MARTIN MARIETTA ENERGY SYSTEMS LIBRARIES

3 4456 0049657 7

DOCUMENT COLLECTION

ORNL-4170
UC-25 – Metals, Ceramics, and Materials

METALS AND CERAMICS DIVISION
ANNUAL PROGRESS REPORT
FOR PERIOD ENDING JUNE 30, 1967

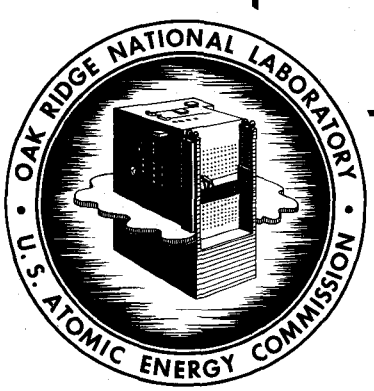

OAK RIDGE NATIONAL LABORATORY
operated by
UNION CARBIDE CORPORATION
for the
U.S. ATOMIC ENERGY COMMISSION

Printed in the United States of America. Available from Clearinghouse for Federal Scientific and Technical Information, National Bureau of Standards, U.S. Department of Commerce, Springfield, Virginia 22151
Price: Printed Copy $3.00; Microfiche $0.65

LEGAL NOTICE

This report was prepared as an account of Government sponsored work. Neither the United States, nor the Commission, nor any person acting on behalf of the Commission:

A. Makes any warranty or representation, expressed or implied, with respect to the accuracy, completeness, or usefulness of the information contained in this report, or that the use of any information, apparatus, method, or process disclosed in this report may not infringe privately owned rights; or

B. Assumes any liabilities with respect to the use of, or for damages resulting from the use of any information, apparatus, method, or process disclosed in this report.

As used in the above, "person acting on behalf of the Commission" includes any employee or contractor of the Commission, or employee of such contractor, to the extent that such employee or contractor of the Commission, or employee of such contractor prepares, disseminates, or provides access to, any information pursuant to his employment or contract with the Commission, or his employment with such contractor.

ORNL-4170

Contract No. W-7405-eng-26

METALS AND CERAMICS DIVISION ANNUAL PROGRESS REPORT

for Period Ending June 30, 1967

J. H. Frye, Jr., Director
J. E. Cunningham, Assistant Director

Section Heads

G. M. Adamson, Jr.
B. S. Borie
W. O. Harms
C. J. McHargue
P. Patriarca

Compiled and Edited by Sigfred Peterson

NOVEMBER 1967

OAK RIDGE NATIONAL LABORATORY
Oak Ridge, Tennessee
operated by
UNION CARBIDE CORPORATION
for the
U. S. ATOMIC ENERGY COMMISSION

MARTIN MARIETTA ENERGY SYSTEMS LIBRARIES

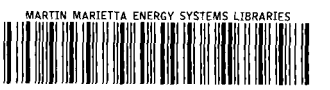

3 4456 0049657 7

Reports previously issued in this series are as follows:

ORNL-28	Period Ending March 1, 1948
ORNL-69	Period Ending May 31, 1948
ORNL-407	Period Ending July 31, 1949
ORNL-511	Period Ending October 31, 1949
ORNL-583	Period Ending January 31, 1950
ORNL-754	Period Ending April 30, 1950
ORNL-827	Period Ending July 31, 1950
ORNL-910	Period Ending October 31, 1950
ORNL-987	Period Ending January 31, 1951
ORNL-1033	Period Ending April 30, 1951
ORNL-1108	Period Ending July 31, 1951
ORNL-1161	Period Ending October 31, 1951
ORNL-1267	Period Ending January 31, 1952
ORNL-1302	Period Ending April 30, 1952
ORNL-1366	Period Ending July 31, 1952
ORNL-1437	Period Ending October 31, 1952
ORNL-1503	Period Ending January 31, 1953
ORNL-1551	Period Ending April 10, 1953
ORNL-1625	Period Ending October 10, 1953
ORNL-1727	Period Ending April 10, 1954
ORNL-1875	Period Ending October 10, 1954
ORNL-1911	Period Ending April 10, 1955
ORNL-1988	Period Ending October 10, 1955
ORNL-2080	Period Ending April 10, 1956
ORNL-2217	Period Ending October 10, 1956
ORNL-2422	Period Ending October 10, 1957
ORNL-2632	Period Ending October 10, 1958
ORNL-2839	Period Ending September 1, 1959
ORNL-2988	Period Ending July 1, 1960
ORNL-3160	Period Ending May 31, 1961
ORNL-3313	Period Ending May 31, 1962
ORNL-3470	Period Ending May 31, 1963
ORNL-3670	Period Ending June 30, 1964
ORNL-3870	Period Ending June 30, 1965
ORNL-3970	Period Ending June 30, 1966

Contents

SUMMARY xiii

PART I. FUNDAMENTAL PROGRAMS

1. CRYSTAL PHYSICS 3
   - Internal Centrifugal Zone Growth of UO_2 Crystals 3
   - The Growth of Rod and Lamellar Eutectic Cermets 4
   - Molten-Salt Growth of Single Crystals 4
     - Paramagnetic Resonance of Gd^{3+} in CeO_2 Single Crystals 5
     - Electron Spin Resonance Spectra of Dy^{3+} in ThO_2 and CeO_2 5
   - Hydrothermal Synthesis 6
     - Lanthanide(III)-Doped YOOH 6
     - Synthesis of Grunerite and Other Phases in the System SiO_2NaOH-Fe-H_2O Near the Critical Temperature of Water 6
     - Further Studies in the System RbOH-SiO_2-Fe_2O_3/Fe-H_2O 6
   - Crystal Growth by the Verneuil Method 6
   - Magnetic Properties 7
2. DEFORMATION AND ANNEALING OF METALS 8
   - Development of Preferred Orientation in Cold-Rolled Niobium 8
   - Recrystallization and the Role of Precipitate Particles in Gold-Doped Zone-Refined Aluminum 11
3. DEFORMATION OF CRYSTALLINE SOLIDS 12
   - Analytical Methods of Representing Texture Data 12
   - Deformation and Fracture of Alloys Strengthened by Spinodal Decomposition 13
   - Rolling and Recrystallization Substructure in Very Thin Foils of Copper and Iron 13
4. DIFFUSION IN SOLIDS 15
   - Self-Diffusion in Body-Centered Cubic Titanium-Vanadium Alloys 15
   - Self-Diffusion in Manganese 15
   - The Near-Surface Effect 15
     - The NSE for Diffusion in Silver 16
     - The Near-Surface Diffusion Anomaly in Gold 17
   - Uranium Diffusion in UN_{1+x} and UO_{2+x} 18

5. ELECTRON MICROSCOPY 19
Morphologies of Bubbles and Voids in Tungsten 19
Nature of Creep Cavities in Tungsten 22
Dynamics of Slip Band Formation 23
A Graphical Method for Determining the Schmid Factor 24
Technique and Equipment Development 24
Transmission Electron Microscopy 24
Extraction Replication 25
Precipitation in Hastelloy N 25
6. ELECTRONIC PROPERTIES OF METALS AND ALLOYS 27
Coulomb-Recoil-Implantation Mössbauer Experiments with ^{73}Ge 27
Low-Temperature Specific Heats of Zr-Ti, Zr-Hf, and Zr-Sc Alloys 28
Low-Temperature Specific Heats of Zirconium with Small Additions (0–5 at. %) of Nb, Mo, Re, and Ru 28
Electrical Resistivities of Zirconium Alloys 29
Galvanomagnetic Properties of Zirconium 29
Zone Purification of Zirconium 30
Effects of Heat Treatment and Impurities on Critical Current Density of Transition-Metal Superconductors 30
7. FUNDAMENTAL CERAMICS RESEARCH 32
Uranium Nitride Intergroup Basic Research Program 32
Thermal Conductivity of UN 33
8. PHYSICAL CERAMICS STUDIES 34
Material Transport in Sintering 34
Progressive Shape Changes of the Void During Sintering 35
Deformation of Single-Crystal Uranium Dioxide 35
Substructure Effect on Diffusion of Thorium in ThO_2 36
Compressive Creep of Sol-Gel ThO_2 36
9. PHYSICAL PROPERTIES 37
Heat Transport in Silicon from 100 to 1300°K 37
Electronic Heat Transport Analysis 37
Ferromagnetic Studies 38
Heat Flow Results 39
Radial Systems, 300 to 1300°K 39
Comparative Longitudinal System 39
Absolute Longitudinal System, 77 to 400°K 40
Equipment Development 41
10. THEORETICAL RESEARCH 42
The Calculation of Constant Energy Surfaces for Copper by the Korringa-Kohn-Rostoker Method 42

Effect of Hydrostatic Pressure on the Fermi Surface of Metallic Copper 42
Theory of the Optical Spectrum of Bi^+ in the Molten $AlBr_3$-NaBr Eutectic 43
Crystal-Field Calculations 43
Mass-Spectrometric and Theoretical Evidence for NH_4 and H_3O 43

11. SPECTROSCOPY OF IONIC MEDIA 45
The Ultraviolet Spectrum of the Bi^+ Ion 46
The Optical Spectrum of Bismuth(I) In the Molten $AlBr_3$-NaBr Eutectic 46
Lower Oxidation States of Bismuth. Bi_8^{2+} Formed in $AlCl_3$-NaCl Melts 46
Electronic Spectra and Coordination of Nickel Centers in Liquid LiCl-KCl Mixtures 46
Electronic Spectra and Coordination Geometry of Nickel Centers in Liquid $MgCl_2$-KCl Mixtures 47
Electronic Spectra and Coordination Geometry of Nickel Centers in Liquid Mixtures of $ZnCl_2$ and CsCl 47
Effect of Melting on the Electronic Spectra of Cs_3NiCl_5 and $CsNiCl_3$ 47
Nickel-Doped Alkali Metal Chloride Crystals 47
The Rate of Oxidation of Nitrite Ions in Dilute Solutions of Sodium Nitrite in Molten Lithium Perchlorate 48
Densities of Molten $AlCl_3$ and NaCl-$AlCl_3$ Mixtures 48

12. SUPERCONDUCTING MATERIALS 49
Equipment Development 49
Magnets 49
Test Assemblies 49
Superconductivity of the Technetium-Vanadium Alloy System 49
Metallography of Lanthanum and Cerium 50
A Metallographic Study of the Allotropic Phase Transformations in Cerium 50

13. SURFACE REACTIONS OF METALS 51
Nickel Oxidation 51
Refractory Metal Oxidation 52
Stress Measurements During Oxidation 52
Protective Properties of Oxide Films 52
Alloy Oxide Films 52
Anodic Oxidation of Tungsten 53

14. X-RAY DIFFRACTION 54
Routine Analyses 54
Crystal Structures of Mixed Oxide Compounds Containing BeO 56
Lanthanum Beryllium Oxide 56
Strontium Beryllium Oxide 56
Sodium Beryllium Oxide 57
Other Systems 57
X-Ray Diffraction from Neutron-Irradiated Ceramic Single Crystals 57
Small-Angle X-Ray Scattering 58
Experiment 58
Theory 58

X-Ray Diffraction Measurements of Film Thickness 59
X-Ray Monochromators 59
The Darwin Dynamical Theory of X-Ray Diffraction 59

PART II. HIGH-TEMPERATURE MATERIALS PROGRAM

15. PHYSICAL AND MECHANICAL METALLURGY OF HIGH-TEMPERATURE MATERIALS 65
Mechanical Properties of Refractory Alloys 65
Effect of Fabrication Variables on Creep-Rupture Properties of Molybdenum Alloys 66
Creep-Rupture Properties of SU 16 67
Creep-Rupture Properties of T-222 67
Time-Temperature Parameters for Creep-Rupture of Refractory Alloys 67
Effect of Irradiation on Creep Properties of Refractory Alloys 68
Fatigue of Refractory Alloys at Elevated Temperatures 68
Physical Metallurgy of Refractory Alloys 69
Aging Characteristics of T-222 and Role of Carbon on Creep Properties of Ta-W-Hf Alloys 69
Diffusion of Nitrogen in Nb–1% Zr 70
Vaporization of Haynes Alloy No. 25 Under Stress 71
Joining of Refractory Materials 71
Welding of Advanced Refractory Alloys 71
Brazing Alloy Development 73
Corrosion Loop Component Welding 74
Fabrication of T-111 Tubing 75
Arc Melting and Casting of Ingots 75
Extrusion and Drawing of Tubing 77
Physical Properties of Refractory Materials 77
Physical Properties of T-111 77
Thermocouple Drift Tests 78
Thermal Radiation Exchange from Graphite 79
Nondestructive Testing of Refractory Alloys 79
16. TUNGSTEN METALLURGY 80
Extrusion and Drawing of Tungsten and Tungsten Alloys 80
Tube-Shell and Duplex Extrusions 80
Hot-Plug Drawing Development 81
Chemical Vapor Deposition 81
Direct Production of Long Thin-Walled Tungsten Tubing by Chemical Vapor Deposition 81
Statistical Parametric Studies 83
Nondestructive Thickness Measurements on CVD Tungsten Tubes 84
Deposition of Tungsten-Rhenium Alloys 84
Physical Metallurgy of CVD Tungsten 85
Formation of Internal Gas Bubbles in CVD Tungsten 85
Growth of Grain-Boundary Gas Bubbles in CVD Tungsten 86
Mechanical Behavior of CVD Tungsten at Elevated Temperatures 86
Effect of Fluorine Impurities on Some Metallurgical Properties of CVD Tungsten 88

Creep-Rupture Properties of W–25% Re 89
Bend Yield Stresses in Tungsten Sheet 90
Tungsten Welding Development 90
Physical Properties of Tungsten and Tungsten Alloys 92

17. ALKALI-METAL CORROSION OF HIGH-TEMPERATURE MATERIALS 93
Compatibility of Boiling Alkali Metals with Refractory Alloys 93
Corrosion of Refractory Alloys by Lithium 94
Effect of Oxygen in the Tantalum-Potassium System 96
Determination of Oxygen in Alkali Metals 96

18. NITRIDE FUELS DEVELOPMENT 97
Powder Synthesis and Pellet Fabrication 97
Synthesis and Fabrication Equipment 97
Microstructural Variations in Sintered UN 97
Preparation of Uranium Carbonitride 98
Sintering Behavior of Uranium Mononitride 98
Distribution of Second-Phase Material in Uranium Nitride 99
Molybdenum in Uranium Nitride 99
Thorium Dioxide in Uranium Nitride 99
Electron Microscopy 100
Thermodynamic and Kinetic Studies 100
Equilibrium Nitrogen Pressures and Thermodynamic Properties of UN 100
The Ideality of the UC-UN Solid Solution 100
Kinetics of the Reaction of UC with Nitrogen 101
Analytical Chemistry of Uranium Nitrides and Carbides 101
Thermodynamic Properties of Uranium Carbides 101
An Explanation of the Anomalous Heat Capacity of Uranium Dicarbide 102
Thermodynamic Functions of Nuclear Materials: UC, UC_2, UO_2, ThO_2, and UN 102

PART III. GENERAL FUELS AND MATERIALS RESEARCH

19. DISPERSION IN SOLIDS 105
Dispersion Hardening of Thorium 105
Dispersion Hardening of Nickel- and Cobalt-Base Superalloys by Internal Oxidation 106

20. FUEL ELEMENT FABRICATION DEVELOPMENT 108
Chemical Vapor Deposition of Uranium Oxide by the Flame Reactor Technique 108
Conversion of Uranium Chlorides to Uranium Dioxide 108
Formation of Uranium Nitrides by Chemical Vapor Deposition 109
Chemical Vapor Deposition of BN 110
Chemical Vapor Deposition of SiC 110
Swelling of UAl_3-Aluminum Compacts 111
Fabrication Development of Instrumented-Plate ATR Fuel Elements 111
Postirradiation Examination of 240-g ORR Fuel Elements 112

21. MECHANICAL PROPERTIES RESEARCH 115
In-Reactor and Postirradiation Creep-Rupture Properties of Type 304 Stainless Steel 115
Development of Alloys with Improved Resistance to Elevated-Temperature Irradiation Embrittlement 115
Effect of Cyclotron-Injected Helium on the Mechanical Properties of Stainless Steel 117
Measurement of the Nuclear Heating Rate in EBR-II 118

22. NONDESTRUCTIVE TEST DEVELOPMENT 119
Electromagnetic Test Methods 119
Ultrasonic Test Methods 121
Penetrating Radiation 122

23. DEVELOPMENT AND TESTING OF SOL-GEL-DERIVED $(U,Pu)O_2$ FUEL 124
Development of Fabrication Processes 124
Extrusion Studies 124
Pelletizing 125
Sphere-Pac Vibratory Compaction 125
Irradiation Testing 125

24. SINTERED ALUMINUM PRODUCTS DEVELOPMENT 128
Powder Preparation 128
Process Selection for Powder Consolidation 128
Thermogravimetric Analysis of Aluminum Flake 130
Fracture Characteristics of SAP 131
Commercial Product Evaluation 133
Properties of SAP Made from Commercial Atomized Powders 133
Mechanical Properties of Extruded Montecatini Sintered Aluminum Products 133
Nondestructive Testing of SAP 135
SAP-UC Compatibility 137

25. WELDABILITY OF HIGH ALLOYS 138
Special Alloy Fabrication 138
VARESTRAINT Testing Performed Under Subcontract at Rensselaer Polytechnic Institute 139
The Effect of Energy Input on the Mechanical Properties of Austenitic Stainless Steel Welds 139

26. ZIRCONIUM METALLURGY 142
Stress Orientation of Hydride in Zircaloy 142
Texture and Anisotropy of Properties in Zircaloy 143
Determination of the Anisotropy of Yielding and Flow in Zircaloy-2 from a Single Test 143
A Yield Stress and Plastic Strain Theory for Anisotropic Materials 144
Purification and Crystal Growth 144
Deformation Studies of Zirconium and Its Alloys 144
Analysis of Textures in Deformed Zirconium Single Crystals 144

Incorporation of Ions in Anodic Oxide Films on Zirconium and Their Effect on Film Behavior 145
Corrosion of High-Purity Zirconium 145
Oxidation Inhibition by Preanodizing 146

PART IV. REACTOR DEVELOPMENT SUPPORT

27. BONUS REACTOR FUEL ELEMENT DEVELOPMENT 151
Technical Assistance to ORGDP 151
Fuel Rod Spacer Brazing 151
Fuel Rod End-Cap Welding 152
Pressure-Shell Assembly Brazing 152
Nondestructive Testing Development 153
Weldability Testing of Superheater Materials 156
General Advisory Assistance 157
28. DESALINATION 158
Bare-Metal Fast Breeder Fuel Refabrication Study 158
Remote Fabrication of Desalination Reactor Fuel Elements 158
29. EVALUATION OF HASTELLOY N FOR SNAP-8 SERVICE 160
30. FUEL ASSISTANCE AND PROCUREMENT 162
31. GAS-COOLED REACTOR PROGRAM 163
Pyrolytic Carbon Coatings Formed at High Deposition Rates at Low Temperatures 163
Deposition of Silicon Carbide Coatings 164
Heat Treatment of Pyrolytic-Carbon-Coated Oxide Particles 166
Influence of Pyrolytic-Carbon Creep on Coated-Particle Fuel Performance 167
Fast-Neutron-Induced Changes in Pyrolytic Carbons 168
Irradiation Testing of Coated-Particle Fuels 169
Mechanisms and Kinetics of the Conversion of UO_2 to UC 171
Concrete for Prestressed Concrete Pressure Vessels 172
32. HIGH FLUX ISOTOPE REACTOR 173
Fuel Element Manufacture 173
Statistical Evaluation of Metals and Controls Quality-Control Data 175
Fuel Compact Thickness 175
Cladding Thickness 175
Total Uranium and Boron Contents 176
Boron Distribution 176
Advanced Fuel-Plate Fabrication 177
Bonding of Type 1100 to Type 6061 Aluminum 179
U_3O_8 Production 181
HFIR Welding Development 181
Fuel-Plate-to-Side-Plate Welding 181
Coolant Channel Spacer Attachment 183

33. HIGH FLUX ISOTOPE REACTOR TARGET DEVELOPMENT 184
Transuranium Target Fabrication Equipment Status and Operation 184
Inspection and Refurbishment of Target Elements Irradiated at SRL 185
Irradiation Testing of Prototypes 186
Examination of Failed Target Elements 187
Examination at TRU 187
Metallographic Examination of a Failed SRL Target Element 189
Effect of Neutron Irradiation on the Mechanical Properties of the X8001 Aluminum Sheath 189
HFIR Target Failure Analysis 191

34. MOLTEN-SALT REACTOR PROGRAM 192
MSRE Support 192
MSRE Materials Surveillance Program 192
Testing of Hastelloy N Surveillance Specimens 195
Consequences of Contaminating the MSRE Radiator Tubing with Aluminum 196
MSBR Development 197
Improving the Resistance of Hastelloy N to Radiation Damage by Composition Modifications 197
Hastelloy N Welding Studies 198
Dynamic Corrosion Studies 200
Procurement and Evaluation of New Grades of Graphite 203
Irradiation Creep of Graphite 203
Brazing of Graphite 205
Compatibility of Graphite-to-Molybdenum Brazed Joints with Molten Fluoride Salts 205

35. REACTOR EVALUATION 206
Computer Program Development 206
HWOCR Fuel Fabrication Cost Estimates 207
AEC Fuel Recycle Task Force 209

36. THORIUM UTILIZATION 211
Thorium-Uranium Recycle Facility 211
Building 211
Fueled-Graphite Line 212
Fueled-Graphite Development 214
Particle Handling 214
Particle Coating 214
Particle Inspection 216
Bonding of Pyrolytic-Carbon-Coated Fuel Particles 217
Fuel Element Inspection 218
Advanced Fuel Cycle Process Development 218
Sol-Gel Extrusion of Thoria-Base Ceramics 219
Pelletizing of Sol-Gel Thoria-Urania Powders 219
Low-Energy Microsphere Packing (Sphere-Pac) 220
Irradiation of Thoria-Base Bulk Oxide Fuels 220
Drying and Sintering of Sol-Gel Urania Microspheres 223
Isothermal Shrinkage of Sol-Gel Urania Microspheres 223

Changes of Crystallite Size, Surface Area, and Bulk Density 223
Differential Thermal Analyses of Sol-Gel Urania 224
Drying and Sintering Schedule for Sol-Gel Urania Microspheres 226

PART V. OTHER PROGRAM ACTIVITIES

37. ISOTOPIC POWER SOURCE DEVELOPMENT 229
Welding of Refractory-Alloy Capsules 229
Welding Development for SNAP-21 230
Nondestructive Testing Support 230
Brayton Cycle Studies 231
38. METALLOGRAPHY 233
Quantitative Television Microscopy 233
Potentiostatic Metallographic Etching Experiments 234
High-Temperature Microscopy 235
Metallographic Preparation of Cerium Carbides 235
39. ROVER ROCKET NOZZLE MATERIALS 238
Thermal Fatigue Testing of Nozzle Tube Configurations 238
Radiation Damage to Brazing Alloys 241
Elevated-Temperature Testing of Tubing Material 242
Effects of Space Environment on NERVA Materials 244
40. THERMONUCLEAR PROJECT 245
Engineering and Design 245
Desorption of Gases from Metallic Surfaces by Electron Bombardment 245

PAPERS AND PUBLICATIONS

PAPERS AND ORAL PRESENTATIONS 251
PUBLICATIONS 258
ORGANIZATION CHART 269

Summary

PART I. FUNDAMENTAL PROGRAMS

1. Crystal Physics

The internal centrifugal zone-growth (ICZG) technique we developed to grow crystals of UO_2 was improved. In the UO_2-tungsten cermet, both rod and lamellar eutectic structures resulted from the unidirectional solidification inherent in ICZG technique. Molten-salt growth of 2-mm ThO_2 single crystals doped with ^{244}Cm was accomplished; electron-spin resonance and optical-spectra studies are in progress. Hydrothermally, YOOH (up to 2 mm) was grown from LiOH solvent and doped with various Ln^{3+} ions. Crystals of iron (^7Li) ferrite and other ferrites up to 1 cm in diameter and 8 cm long were grown. Good-quality oriented crystals resulted – as judged by neutron-rocking curve-line widths of 0.3° and straight sharp neutron Laue diffraction lines. We are able to measure the temperature dependence of the magnetic susceptibility and magnetization of small samples.

2. Deformation and Annealing of Metals

Inhomogeneities in the preferred orientation of polycrystalline niobium were studied with regard to amount of deformation and position in rolled strip. The main components of the texture in the center can be described as spread from $\{111\}\langle 1\bar{2}1\rangle$ to $\{112\}\langle\bar{1}10\rangle$ at low reductions, centered on $\{112\}\langle\bar{1}10\rangle$ at intermediate reductions, and approximately $\{113\}\langle 110\rangle$ at reductions in thickness of 99.5%. At higher amounts of deformation there are further texture changes. A marked surface texture occurs at deformations of 90 to 97%.

The study of effects of gold in solution and in a precipitate on recrystallization and grain-boundary mobility of zone-refined aluminum was concluded.

3. Deformation of Crystalline Solids

Powerful analytical methods were developed for transforming x-ray texture data into axial or biaxial pole figures, which are required for the complete representation of fiber and sheet textures. Least-squares methods are applicable for the axial case, where one either solves for the coefficients of a series or else solves directly for the density function without recourse to a mathematical model. For the biaxial case, the same methods become very difficult, and an iterative method was much more satisfactory. The method was applied to rolling textures for copper, brass, and aluminum.

Work is under way to establish the important parameters that control the strengthening in alloys exhibiting spinodal decomposition. Important parameters are considered to be the wave length, the degree of segregation, and the strains. Since fracture behavior is important in determining the mechanical properties, this is being investigated also.

Very high deformation in copper and iron by rolling changed both the internal structure and the texture relative to more normal strains. Cross rolling altered both the texture and the structure.

4. Diffusion in Solids

Self-diffusion coefficients were determined over wide temperature ranges for the body-centered cubic phase of titanium-vanadium alloys at 10% increments in composition from pure titanium to pure vanadium. Similar experiments were completed for self-diffusion in the body-centered cubic and face-centered cubic phases of manganese. The non-Gaussian penetration behavior at regions near specimen surfaces was examined for ^{58}Co and ^{60}Co in silver and ^{63}Ni and ^{60}Co in gold;

efforts were made to determine the mechanisms for such a near-surface effect. Cation self-diffusion in UN and UO_2 is being studied in experiments in which material stoichiometry is closely regulated.

5. Electron Microscopy

A fractographic technique was used to study gas bubbles and creep cavities in tungsten. Features of the crystallography and surface structures are described. The effects of temperature and stress on the nature of creep cavities and cracks are explained.

A mathematical model was constructed to calculate the dynamic features of the formation of slip bands. Shear strains and shear strain rates were calculated and the stress concentration at the head of the bands was determined for different grain sizes.

A graphical method is described for rapidly determining the Schmid factor or resolved shear stress on any slip plane, in any slip direction, and for any crystal system.

Some modifications to our equipment for preparing transmission electron microscopy specimens are described along with some techniques for the use of an electron microprobe attachment for one of our microscopes. Some results of a study of precipitation in Hastelloy N with these techniques are presented.

6. Electronic Properties of Metals and Alloys

In Mössbauer studies a new method, Coulomb-recoil-implantation, was developed for study of impurities in solids and applied to ^{73}Ge in chromium. In zirconium alloys with the solutes Sc, Ti, Hf, Nb, Mo, Re, Ru, Rh, Ag, Cd, In, Sn, and Sb, measurements of low-temperature specific heat, superconductivity transition temperature, and electrical resistivity indicate a distinct separation in alloying behavior. Transition metal solutes to the right of zirconium in the periodic table appear to have localized electrons near the solutes. Transition metals in the same column with zirconium, elements to the left (Sc), and B-subgroup solutes appear to show alloying effects related to the band structure. Improvements in the zone-refining apparatus for removal of oxygen impurity from zirconium permit up to 65 passes without seizure. Zirconium purity has been increased (resistivity ratio 1200 to 1300), and we find that the high-purity material can be annealed to increase crystalline perfection without sacrifice in electrical properties.

7. Fundamental Ceramics Research

We have initiated an intergroup program of basic research on uranium nitride, which will include single-crystal fabrication, band-theory calculations, physical-property measurements, deformation mechanism studies, solid-state diffusion studies, low-temperature specific heat measurements, helium bubble migration in a thermal gradient, and surface reaction studies. Hopefully, the results of this work will be a better understanding of this important nuclear ceramic, which is one of the "refractory hard metal" class of ceramics, and a better liaison between applied and fundamental groups within the Division.

8. Physical Ceramics Studies

The effect of isostatic pressing on subsequent sintering of partially sintered oxide powder compacts suggests a dislocation contribution to the material transport processes. Topological studies of sintering copper powder compacts indicated that the void space does not undergo spheroidization until approximately 99% of the theoretical density is attained. Deformation mechanics in UO_2 single crystals under compression are being analyzed. Specimens of sintered ThO_2 sol-gel powder underwent extensive grain-boundary sliding in compressive creep.

9. Physical Properties

Our physical property data on silicon agreed with theoretical estimates of the electronic thermal conduction, but theoretical models for lattice thermal conduction do not explain the experimental behavior in detail. Several methods to evaluate the temperature dependence of the Lorenz number revealed high-temperature deviations for platinum, tungsten, and iron. These deviations directly affect thermal conductivity prediction, and we are systematically measuring

properties of other transition metals in several devices to explore the mechanisms for this behavior. The 35% specific heat discontinuity in iron at the Curie temperature was confirmed, and an improved pulse heating calorimeter was constructed to study the iron-nickel alloys that exhibit ordering and ferromagnetism. The thermal conductivity of beds of vibratorily compacted ThO_2 microspheres was shown to be temperature insensitive but quite sensitive to gas and gas pressure. Our comparative longitudinal apparatus was used to provide data on a variety of oxides including MgO, ThO_2, $(Th,U)O_2$, BeO, Tm_2O_3, and UO_2. Our absolute longitudinal apparatus was used to generate data for critical evaluation on Al, Fe, Pt, In, W, and Cu in the little studied region, 77 to 400°K. The applicability of the ultrahigh-vacuum furnace for measuring electrical resistivity and thermoelectric power to 2200°C at 5×10^{-9} torr was demonstrated.

10. Theoretical Research

Our program of band-theory calculations has proved very promising and is being pursued. Crystal-field theory calculations and one-center molecular calculations are continuing.

11. Spectroscopy of Ionic Media

Hydrogen reduction of Bi(III) in molten $AlCl_3$-NaCl permitted measurement of the ultraviolet absorption spectrum of Bi^+ without interference from Bi^{3+}. Visible and near-infrared spectra of Bi^+ in bromide melts differed as expected from those in chloride. The formula of Bi_8^{2+} was confirmed. The spectra of Ni(II) in several media were interpreted in terms of two different coordination geometries in proportions that varied with temperature and medium composition. We also measured rate of oxidation of nitrite in molten $LiClO_4$ and densities of molten $AlCl_3$ and its mixtures with NaCl.

12. Superconducting Materials

Significant progress was made in the metallurgical characterization of several systems of potential interest in research in superconductivity. We determined the equilibrium phase diagram for the binary system technetium-vanadium at temperatures up to 1500°C and are investigating the kinetics of eutectoid decomposition in alloys containing 30 at. % V. The rather complex dependence of the fcc-dhcp transformation in lanthanum and cerium on time, temperature, grain size, cold work, and purity has been surveyed, and more detailed work is in progress. Magnetization data, including both critical-field and critical-temperature data, were obtained for the alloys of the technetium-vanadium system. Techniques have been developed for determination of critical parameters as a function of field strength and temperature in massive superconducting samples throughout the ranges 2 to 20°K, 0 to 75 kilogauss.

13. Surface Reactions of Metals

Research in this area has emphasized newly recognized factors in the oxidation of metals; namely, the importance of short-circuit diffusion paths in the oxide films, oxygen solution effects, and stress generation during oxidation. A study of the oxidation of nickel was undertaken to test the generality of our model for the oxidation of copper, which rationalized oxidation-rate anisotropy in terms of a corresponding anisotropy of the extent of short-circuit diffusion paths through the oxide. Based on the results of x-ray, electron microscope, and optical studies of NiO films, we believe that the oxidation model for copper also applies to nickel. We have also continued our studies of the oxidation of refractory metals. Oxygen was allowed to diffuse into niobium and tantalum at 800°C at several oxygen pressures, and the buildup of a substantial and complicated stress system was observed. The permeation of anodic Ta_2O_5 films by oxygen was studied with particular attention to the inhibiting effects of phosphorus incorporated into the film to produce an oxide alloy. The Ta_2O_5-Nb_2O_5 oxide alloys were prepared by the anodization of tantalum-niobium alloys in anticipation of a study of the phase relationships in the tantalum-niobium-oxygen system. A high-efficiency anodization technique for tungsten was developed and a chemical stripping solution tested preparatory to a study of low-temperature and short-circuit diffusion in that metal.

14. X-Ray Diffraction

We have continued investigations of mixed oxide compounds containing beryllia with a description of the crystal structure of $La_2Be_2O_5$. This equilibrium phase contains only tetrahedrally coordinated beryllium atoms, in contrast to the trigonal coordination found in the nonequilibrium phases $Ca_{12}Be_{17}O_{29}$ and Y_2BeO_4. We have obtained a glass-like material from quenched melts in the sodium oxide–beryllium oxide system.

Powder diffraction data are given for LiN_3. Some structural properties of irradiated spinel crystals are presented. Since the actual chemical composition proved to be $1MgO:3Al_2O_3$ rather than the ideal 1:1 composition, the lattice defects due to nonstoichiometry could trap radiation-produced defects and lead to smaller net lattice expansions than those found in irradiated alumina.

The presence of measurable orientation-dependent small-angle x-ray scattering from neutron-irradiated copper crystals is reported. Mathematical procedures for correcting small-angle x-ray scattering data for the effects of finite slit height and width were developed, and computer programs were written to apply them.

Pyrolytic graphite monochromators continue to show real promise in x-ray diffraction experiments. We also report a new method for experimentally determining thicknesses of thin unattached films with only the linear x-ray absorption coefficient required as a priori knowledge.

A simple alternative to the Ewald–von Laue dynamical theory of x-ray diffraction is described. The method involves the solution of a system of difference equations similar to those first solved by Darwin.

PART II. HIGH-TEMPERATURE MATERIALS PROGRAM

15. Physical and Mechanical Metallurgy of High-Temperature Materials

This program is concerned with materials problems associated with high-temperature high-performance reactors for advanced propulsive and electric power systems, especially for space applications. Particular emphasis is placed on fabrication and complete physical metallurgical evaluation of tantalum-, niobium-, and molybdenum-base alloys.

In creep-rupture investigations the niobium-modified molybdenum alloy TZM, after solution annealing at 1930°C and warm working at 1370°C, was the strongest of all alloys tested in the temperature range 980 to 1315°C. After annealing at 1600°C and aging 3 hr at 1200°C, SU 16 was the strongest niobium-base alloy in this temperature range. The 1000-hr creep-rupture behavior of T-222 was comparable to that of T-111 and Ta–10% W in the temperature range 980 to 1650°C; welded specimens were slightly stronger than base-metal specimens. Larson-Miller parameters were derived for rupture of T-111, FS-85, and TZM, using a cubic polynomial in the logarithm of stress. Creep curves were obtained for molybdenum specimens during irradiation at 705, 760, and 870°C at stress levels of 18,000, 30,000, and 15,000 psi respectively. The resistance of the niobium alloy D-43 to cyclic strain at 1205°C was as good as or better than that around room temperature.

Significant changes in the mechanical properties of tantalum-base alloys like T-111 that occur on cooling from annealing temperatures were attributed to the distribution of carbon. The diffusivity of nitrogen in Nb–1% Zr was described by the equation $D = 1.4 \times 10^{-5} \exp(-42{,}000/RT)$ and is about three orders of magnitude lower than in unalloyed niobium. Studies on the vaporization of Haynes alloy No. 25 in vacuum between 870 and 1150°C have been extended to include the effects of superimposed stresses on the evaporation kinetics and the determination of the creep properties of this alloy during evaporation.

The effects of embrittling aging reactions in gas tungsten-arc welds of the niobium-base alloys Cb-752 and Cb-753 were evaluated in terms of microhardness traverses. Bend transition temperatures for weld specimens of the niobium-base alloy SU 16 were 90°C after electron-beam welding and 230°C after gas-tungsten-arc welding. Brazing alloys were developed for refractory-metal joining, and impressive shear strengths near 20,000 psi were observed to temperatures within 200°C of their melting points. The brazing alloy Ti–21% V–25% Cr proved outstanding in its ability to wet ceramics. Components of the niobium-base alloy D-43 were welded to form a large forced-circulation corrosion loop.

A double arc-melting technique with intermediate extrusion was developed for production of homogeneous billets of the tantalum-base alloy T-111. Six extrusions – including tube shells, round rod, and sheet bar – were made, and the tube shells were subsequently swaged and drawn at room temperature.

The thermal conductivity, electrical resistivity, and thermoelectric power of T-111 were determined for the temperature range 100 to 1000°C; the hemispherical emittance was measured at 500 to 800°C. An analytical expression involving electrical conductivity was developed for extrapolation of the thermal conductivity to 1400°C. Thermal emf changes equivalent to less than 2°C were observed for Chromel-P vs constantan thermocouples after 400-hr exposures at 10^{-7} torr in the temperature range 300 to 800°C. The radiation exchange between graphite and anodized and Aquadag-coated aluminum was determined in connection with an irradiation test in the HFIR, where heat transfer by forced convection was not desirable.

Techniques were developed and applied for nondestructive testing of refractory alloys.

16. Tungsten Metallurgy

In the tungsten and tungsten-alloy tubing fabrication development program, 37 billets were extruded at temperatures ranging from 1650 to 2200°C and extrusion ratios of 3 to 9. Significant process improvement was effected through modifications in the press controls and hydraulic system, the billet heater, and the mandrel design. The duplex extrusion technique was used to produce thin-walled tubing of W–25% Re and to develop a wrought structure in tubes of chemically vapor deposited (CVD) tungsten. Hot-plug drawing equipment and techniques were developed for secondary working of tubes to temperatures as high as 1000°C. An extruded duplex tube shell containing a CVD tungsten sleeve was reduced 85% in five passes at 700°C to 0.710-in.-OD × 0.01-in. wall thickness with no intermediate recrystallization anneals.

Chemical vapor deposition studies included direct production of thin-walled tubing in lengths up to 4 ft, a statistical evaluation of deposition parameters as related to the structural features of the deposit and deposition-rate-controlling mechanisms, and an evaluation of the parameters controlling the uniformity of composition and properties in deposits of tungsten-rhenium alloys.

Physical metallurgy studies on CVD tungsten containing up to 30 ppm F showed that bubbles formed during annealing at 1400°C develop from clusters or fine unresolvable precipitates of unidentified fluorine impurities in the as-deposited material. The morphology and growth characteristics of bubbles and their effect on metallurgical properties were investigated after heat treatments as high as 2500°C. The effect of stress on bubble growth was determined by electron microscopy of specimens creep-rupture tested at 1650 and 2200°C.

The creep-rupture properties of wrought W–25% Re sheet prepared from arc-cast and from powder-metallurgy-derived materials were compared at 1650 and 2200°C. The arc-cast alloy was generally superior to the powder-metallurgy material, particularly with regard to rupture life and rupture ductility. Inflections related to yielding appeared in the load-deflection curves for tungsten annealed at various temperatures and tested in bending at temperatures just above the ductile-to-brittle transition temperature. The effects of annealing temperature and grain size on bend yield stresses were related to changes in substructure, impurity distribution, or perhaps even impurity content during annealing.

Gas tungsten-arc welding formed reproducible, sound, pore-free welds in tungsten and tungsten alloys derived from arc-cast stock, but fusion-line porosity inevitably developed in powder-metallurgy-based alloys. Pore-free welds were also formed in CVD material containing 10 ppm F or less.

The thermal conductivities and electrical resistivities of four tungsten and tungsten-alloy specimens were measured between –196 and 127°C. The results were treated by several methods to obtain the temperature dependence of the Lorenz number for calculating the electronic contributions to the thermal conductivity.

17. Alkali-Metal Corrosion of High-Temperature Materials

Compatibility studies using refluxing capsules, natural-circulation loops, and forced-circulation loops have brought the cumulative operating time for refractory-alloy–boiling-potassium systems to over 90,000 hr. Almost negligible dissolutive

attack has occurred in either the boiler or condenser region at temperatures up to 1300°C and for times as long as 5000 hr. An engineering-scale pumped loop of the niobium alloy D-43 has operated for 2000 hr at a boiler temperature of 1200°C and a condenser temperature of 840°C.

In thermal-convection loop tests of lithium in Nb–1% Zr, mass transfer of zirconium occurred from the hot- to cold-leg regions. Although small, this effect was 10 times greater at a hot-leg temperature of 1300°C than at 1200°C. Welded specimens of T-111 contaminated with 500 ppm O were attacked intergranularly in the base metal unless they had been heat treated at 1300°C after welding.

Basic studies on the role of oxygen on the corrosion of refractory metals by potassium were extended to the Ta-O-K system at 600 to 800°C. Preliminary results indicate that this system behaves similarly to the Nb-O-K system; that is, oxygen is transferred from the metal to the potassium, even though the thermodynamic properties of known oxides suggest that the opposite should occur.

The fast-neutron activation analysis facility for accurate and rapid determination of oxygen in alkali and refractory metals was completed after several operational difficulties were overcome. A series of refractory-metal specimens with carefully documented oxygen levels was assembled to statistically evaluate the accuracy of the system.

18. Nitride Fuels Development

We are developing nitride fuels for space-nuclear and liquid-metal fast-breeder applications. For the latter, properly designed (U,Pu)N fuel pins can operate at significantly higher linear heat ratings and power densities than mixed oxides and may have some advantages over mixed carbides. The development program involves fabrication, product characterization, thermodynamic studies, and compatibility testing. Plans are also under way for irradiation testing of the mixed nitride fuels. We are also incorporating fine dispersions in UN to improve properties.

In fabrication studies we developed a process for producing UN pellets with less than 500 ppm O and 200 ppm C. Low-oxygen-content uranium carbonitrides are also being produced. Abnormal grain growth in UN was found to be caused by traces of liquid uranium. A revised powder synthesis process eliminated this problem.

Our work with dispersed second-phase material in UN showed that the solubility of molybdenum in UN varies such that fine precipitate particles might be formed through careful heat treatment of sintered samples. We also showed that a fine dispersion of a thorium-rich oxide phase can be formed in a (U,Th)N alloy by internal oxidation.

Our thermodynamic studies have extended the range of measured nitrogen pressures over UN down to the practical temperature of 1300°C and have led to a value of -69.6 ± 1.0 kcal/mole for the standard enthalpy of formation of UN at 25°C ($\Delta H^{\circ}_{298,f}$). Studies on UC-UN solid solutions showed that the system is thermodynamically ideal, and the activity of carbon precipitated from UC by reaction with nitrogen below 1700°C is greater than that of graphite. Studies of the kinetics of the reaction of UC with nitrogen showed that the reaction occurs in two stages with a unique composition at a "way station." In related studies, sintered pellets of a desired composition of U(C,N) were prepared by the reaction of graphite with UN in a pressed compact.

PART III. GENERAL FUELS AND MATERIALS RESEARCH

19. Dispersions in Solids

Boronating thorium powders containing 4.65% Zr in solid solution gave a product twice as hard at 800°C as competitive alloys.

Preliminary studies showed that modified Nichrome- and Vitallium-type alloys containing thorium can be internally oxidized to give an ultrafine dispersion of very stable oxide particles. Good dispersion structures and high-temperature strength were achieved.

20. Fuel Element Fabrication Development

We demonstrated the successful operation of a flame reactor technique for the direct conversion of UF_6 to uranium oxide powder. Other investigations in chemical vapor deposition include deposition of UO_2 from uranium chlorides and lithium reduction of UF_6 to produce uranium nitrides or carbides. Non-fuel-bearing compounds such as boron nitride and silicon carbide were also deposited by reactions of gaseous halides. The effects of some deposition parameters have been studied for each system.

We increased our effort in the area of research reactor fuel dispersions, seeking to elucidate the differences in fabrication behavior of uranium-aluminum intermetallics and the oxide fuels. We successfully completed the fabrication of several instrumented fuel element assemblies to be used in the startup of the Advanced Test Reactor. The swelling of UAl_3-aluminum compacts during initial fabrication operations was studied. Irradiation testing of ORR fuel with a 20% increase in fuel loading was completed with satisfactory operational performance.

21. Mechanical Properties Research

The Mechanical Properties Research and Liquid-Metal Fast Breeder Reactor Materials Development programs are closely related and have as their objectives the understanding of radiation damage to the mechanical properties of reactor materials and the development of modified alloys more resistant to radiation damage.

We found that the in-reactor and postirradiation creep properties of type 304 stainless steel are indeed comparable. However, the rupture life and ductility in both cases were significantly less than those of unirradiated material.

The development of titanium-bearing type 304 stainless steel has continued through the investigation of small (100 lb) and medium sized (1500 lb) heats. The results among the various heats are consistent, and the mechanical properties show considerable improvement over conventional type 304 stainless steel after reactor and alpha-particle irradiations.

We are preparing irradiation experiments for insertion into EBR-II. The first experiments to determine the nuclear heating rate in the reactor have been designed and constructed and are at the EBR-II site awaiting installation in the reactor. Subsequent experiments are under construction.

22. Nondestructive Test Development

We continued development of analytical techniques for the calculation of parameters for an induced electromagnetic field and now have two different methods: The computerized relaxation method and a "closed-form" solution. The former is more versatile, but the latter, though more restricted, has the potential of greater accuracy. Additional evaluation of complex integrals is necessary before the closed-form solution can be fully used. A portable phase-sensitive eddy-current instrument was developed with excellent lift-off compensation, sensitivity, and temperature stability. We improved probes for measurement of coolant-channel space for use in hot cells.

We are correlating ultrasonic response for various types of reference discontinuities used for the inspection of sheet and tubing. Improvements were made on techniques for fabricating both longitudinal and transverse notches in tubing. Both schlieren and photoelastic methods were used for viewing ultrasound.

We developed quantitative data for the radiography of graphite and are measuring radiographic sensitivity of metals as various parameters, such as x-ray energy, specimen thickness, and the presence and thickness of lead screens, are varied.

23. Development and Testing of Sol-Gel-Derived $(U, Pu)O_2$ Fuel

We have started to assess the potential of sol-gel-derived PuO_2-UO_2 fuel for fast reactors, particularly the Liquid Metals Fast Breeder Reactor and the Fast Flux Test Facility. The program comprises (1) the development of fabrication processes, (2) out-of-reactor testing, and (3) irradiation to high burnup in thermal reactors.

The initial progress includes the development of a critical path schedule for process development, property determination, irradiation testing, and economic evaluation of the fuels as well as the preparation of suitable plutonium laboratories and equipment to accomplish the work. A non-instrumented capsule for irradiation of the fuels in the Engineering Test Reactor was designed, and irradiation of the first capsules commenced. In addition, work was initiated on the low-energy compaction of sol-gel microspheres, extrusion of sol-gel clays, and the pelletizing of sol-gel powder. No definitive results have yet been obtained from the program.

24. Sintered Aluminum Products Development

Sintered aluminum products (SAP) are powder-metallurgy-produced alloys that consist of aluminum oxide dispersed within an aluminum matrix. These alloys have a high strength-to-weight ratio,

and this beneficial effect is stable up to temperatures approaching the melting point of aluminum.

Although this alloy is attractive for applications in several reactor systems, commercial SAP materials lack the reproducibility of properties needed for many nuclear components. Our program was initiated to investigate the problems and parameters related to primary billet fabrication of SAP for HWOCR pressure tubes and fuel rod cladding. General process steps involve feed-powder characterization, dispersion preparation, and consolidation.

We have evaluated the parameters necessary to ball-mill suitable SAP alloys on a pilot mill scale. These studies indicate that the oxide content is reproducible within the precision of the measurement techniques. Process selection for consolidation of the milled SAP flake was completed. Two alternate methods are available, but one involves careful control of a packaged billet prior to secondary working to prevent rehydration. Rehydration of SAP flake produces an unstable product that swells and blisters because of hydrogen release during elevated-temperature applications.

The fracture characteristics of SAP were studied. The modes of ductile fracture were described and identified by use of a fractography technique. High-temperature fractures are initiated at single oxide particles or groups of particles. Banding and stringering of oxide particles seriously affect the fracture process. Our nondestructive testing studies have been devoted to development of techniques for the measurement of flake thickness and oxide content.

25. Weldability of High Alloys

We are seeking a more thorough understanding of the role of minor elements, individually and combined, upon the cracking behavior and mechanical properties of welds in nickel- and iron-base alloys. A large number of special alloys of the Inconel 600 (Ni–15.5% Cr–8.0% Fe) and Incoloy 800 (Fe–32.5% Ni–21.0% Cr) types were processed for testing both at Rensselaer Polytechnic Institute under subcontract and at ORNL. Excellent control over the melting and fabrication parameters led to a very-high-purity product.

The VARESTRAINT test developed at Rensselaer was used to evaluate the crack susceptibility of welds in three commercial alloys. The total crack length at 2% augmented strain was approximately 500 mils for Inconel 600 and 1100 mils for Incoloy 800 and Hastelloy X. Thus the Inconel 600 appears to resist hot cracking somewhat better than either of the two other materials.

The effect of heat input on the properties of welds in austenitic stainless steel was also studied. The intercellular spacing of the weld metal increased with increasing heat input and the delta ferrite distribution varied markedly. Welds made at 10,000 j/in. had 10,000-psi greater tensile strength at room temperature than those made at 60,000 j/in. The ductility of the weld metal appears to increase with the amount of delta ferrite in the microstructure in the range observed.

26. Zirconium Metallurgy

We described the stress and strain properties of zirconium alloys in terms of crystallographic texture and made continued progress in our study of the effect of fabrication variables on texture in tubing. Single crystal deformation studies added to our knowledge of basic deformation mechanisms and texture development and control. The orientation of the hydride in zirconium alloys has been examined with respect to texture, cooling rate, and stress cycling.

Our corrosion studies provided the first clear picture of the effect of crystallography on the anisotropy of oxidation in zirconium. We also demonstrated the sensitivity of oxidation rate to impurity content. Finally, these studies produced a promising method for significantly improving the corrosion resistance of zirconium.

PART IV. REACTOR DEVELOPMENT SUPPORT

27. BONUS Reactor Fuel Element Development

Support to the improvement of BONUS Fuel Elements is reported. Technical assistance was provided ORGDP with fuel rod spacer brazing, fuel rod end-cap welding, and pressure-shell assembly brazing. An ultrasonic technique was developed for inspecting tube-to-spacer brazed joints. New methods are being used to screen structural alloys for weldability.

28. Desalination

We analyzed the costs of fabricating and using an unclad uranium metal fuel element in a desalination reactor plant. We also worked on the design and construction of a piece of experimental apparatus to test a method of producing this fuel element.

29. Evaluation of Hastelloy N for SNAP-8 Service

The development of improved versions of the SNAP-8 reactor requires a detailed knowledge of the postirradiation mechanical properties of Hastelloy N in the temperature range from 600 to 800°C. Compositional modifications of Hastelloy N for improved resistance to radiation embrittlement will probably be required. The postirradiation properties of Hastelloy N tubing and rod material from similar heats were consistent. The ductility and strength of the heats were reduced to low values at 650 and 760°C, although the strain-rate sensitivity of the effects differed at these temperatures. Aspects of this program involving the development of improved compositions of Hastelloy N are described in Chap. 34.

30. Fuel Assistance and Procurement

A new program aids the AEC in problems related to procurement of fuels for research reactors, such as the ETR, the ATR, the AF-NETR, and various Army reactors.

31. Gas-Cooled Reactor Program

All-ceramic nuclear fuels consisting of pyrolytic-carbon-coated $(Th,U)O_2$ and $(Th,U)C_2$ fuel particles offer considerable advantages as fission-product-retaining fuel for high-temperature gas-cooled reactors. Our support for the Program consisted mainly in advancing the techniques for fluidized-bed coating of particles and the testing of coating materials and coated-particle fuels. We found that the desirable high-density isotropic coatings could be deposited at very high rates at low temperatures using propane or propylene as reactant. Oxide fuel particles having this type of coating survived heat treatment up to 2600°C, but thermal creep from the high internal carbon monoxide pressure caused large dimensional changes and increases in anisotropy. In other coating studies we developed techniques for fluidized-bed deposition of SiC coatings on fuel particles. We also extended our mathematical analysis of stresses in coatings to include creep, which may significantly extend the life of isotropic pyrolytic carbon coatings under high exposures to fast neutrons. Density and dimensional changes in pyrolytic carbon irradiated to a high fast-neutron dose demonstrated the stability of isotropic structures and indicated that densification is a first-order rate process. Irradiation tests on coated-particle fuels demonstrated that the low-temperature isotropic coatings would withstand high fuel burnup and confirmed our previous favorable observations on the irradiation stability of coated sol-gel oxide fuels.

32. High Flux Isotope Reactor

The quality of the HFIR fuel-element development work has been attested by in-reactor performance. Thirteen assemblies have been burned to an average burnup of 2300 Mwd with no obvious problems. Fuel-element production is proceeding smoothly through completion of the first commercial procurement contract and the starting of a second. Fuel-plate recoveries of 92% have been achieved, with blisters and surface defects being the major causes for rejection. Waivers of acceptance standards, however, have been required on most elements; deviations vary in cause from one unit to another. Data obtained from the fuel fabricator were analyzed to demonstrate what effects changes in the specifications would have on rejection rates. Several areas were found in which specifications could be tightened without economic penalty, while relaxation is desirable in others.

Fuel plates of HFIR geometry but with a 25% increase in fuel loading were fabricated with both U_3O_8 and UAl_3 used as the fuel. The amount of densification during hot rolling differed, with the intermetallic being less dense. New cleaning and rolling procedures were developed to eliminate the need for type 1100 bonding layers on the frame. Previously such layers were required to achieve adequate bonding between frame and cover plates. Also, doubly clad frame stock presents a serious production problem.

Pulsed-arc and electron-beam welding are being investigated as alternate techniques for joining fuel plates during final assembly. The former method did not show sufficient advantage to warrant necessary changes in procedure and equipment. The latter method, however, shows promise of simpler and more closely controlled welding practice, if a suitable side plate material with less tendency for weld cracking than type 6061 can be found.

Longitudinal spacers were ultrasonically welded to plates, which were then curved to the required involute. After being assembled in a test rig, such plates successfully resisted abrasion and flow stresses.

33. High Flux Isotope Reactor Target Development

The goal of the Transuranium project is to produce gram quantities of the heavier transuranium elements for research purposes by successive neutron captures in ^{239}Pu. The ^{239}Pu was converted to ^{242}Pu, ^{243}Am, and ^{244}Cm in Savannah River reactors. At ORNL these products were fabricated into target elements that are being irradiated in the High Flux Isotope Reactor at a flux of approximately 3×10^{15} neutrons cm^{-2} sec^{-1}. The target elements are removed periodically from HFIR and reprocessed in the TRU to separate the product actinides and recover the target actinides, which are fabricated into recycle targets and returned to HFIR for further irradiation.

Our tasks have included the design, fabrication, and validation of suitable targets, the development of equipment and techniques for fabricating them, and monitoring their performance in HFIR. Because of the premature failure of target elements exposed in the HFIR, we are also investigating the cause of failure and fabricating modified target elements that may withstand the HFIR service conditions.

We completed an irradiation program in the ETR for confirmation of the HFIR target element design. The necessary ^{242}Pu targets for the HFIR irradiations were fabricated. We have essentially completed the cold testing of the equipment in the TRU, refurbished targets that had been irradiated previously at Savannah River, and commenced an investigation of the mechanism of failure of targets that had been irradiated at Savannah River and in the HFIR to fission of approximately 25% of the plutonium.

One solution to the HFIR target failures is being investigated. Target elements containing lower loadings and greater pellet porosity have been fabricated and are being irradiated in the HFIR.

34. Molten-Salt Reactor Program

We have maintained an extensive surveillance program in the MSRE to determine the effects of the operating environment on the properties of the two primary structural materials – graphite and Hastelloy N. We removed specimens twice, after 7823 and 32,450 Mwhr of operation. Mechanical property tests on the Hastelloy N from the first group indicated that the properties were equivalent to those of material given a similar neutron exposure in the ORR. The surveillance assembly was found to be damaged when it was removed the first time. Some changes were made in the design and the assembly was in good shape when removed the second time.

A cast Al–5% Zn blower failed at the MSRE, throwing pieces of the alloy into the Hastelloy N tubing of the salt-to-air radiator. We removed all of the contaminant possible but felt it necessary to determine the rate of penetration of aluminum into Hastelloy N. Although there was some reaction, the rate of penetration was not rapid. The radiator has since operated satisfactorily for several thousand hours.

Since Hastelloy N suffers reductions in rupture life and ductility when exposed to a neutron flux, we spent considerable effort in developing a modified alloy that has improved properties. Small additions of titanium, zirconium, and hafnium significantly reduced the radiation damage.

To find why Hastelloy N is susceptible to weld cracking, we are looking at the effects of the filler metal composition on the weldability of standard Hastelloy N; the use of an electrode coated with tungsten carbide looks very promising. Hastelloy N modified with additions of titanium and hafnium seems quite weldable, but the alloy modified with zirconium is very susceptible to weld-metal cracking.

Our corrosion program has been concerned with salts and structural materials for the future. The behavior of a new coolant salt, $48NaF–3KF–49BF_3$, in Croloy 9M and Hastelloy N was tested

in thermal-convection loops. A modified fuel salt containing thorium LiF–23 mole % BeF_2–5 mole % ZrF_4–1 mole % UF_4–1 mole % ThF_4 was also being tested in loops of Hastelloy N and type 304 stainless steel.

Advanced reactors will require a graphite with good dimensional stability to very high neutron doses and a very low permeability of ^{135}Xe. We evaluated several new grades of graphite; none satisfies our requirements. However, we have continued our irradiation damage studies and have measured the irradiation-creep behavior of several grades of graphite as a function of temperature up to doses of about 2×10^{20} neutrons/cm^2. The stresses that are developed as a result of nonuniform dimensional changes across a graphite tube wall at this dose level are well below the fracture stress.

An integral part of our proposed molten-salt breeder reactor is a graphite-to-metal joint. Several promising brazing techniques gave sound joints that resisted attack by fluoride salts.

35. Reactor Evaluation

We have continued to assist the AEC in analyzing the potential of various reactor systems for commercial exploitation by evaluating fuel fabrication costs and fuel element performance for potential reactor systems. Our principal development was the expansion of our library of computer programs for estimating fuel fabrication costs to cover fast reactor fuels. These fuels present a unique problem in that the core fuel elements containing recycle plutonium require remote fabrication, while the radial and the axial blanket fuel contains depleted uranium, which can be fabricated in simple ventilated hoods.

We continued the evaluation of the Heavy-Water Organic-Cooled Reactor by assessing four alternative fuel-element designs from the standpoint of the cost of fuel fabrication and predicted performance. Also, as a member of the AEC Fuel Recycle Task Force, we are participating in the updating of the 1962 *Report to the President on the Civilian Nuclear Power Program.* We have the responsibility for developing fuel-fabrication costs for a variety of reactor types under various economic ground rules.

36. Thorium Utilization

To utilize thorium as a source of energy by conversion to fissionable ^{233}U, it is necessary to develop economical fuels, to characterize the physical and chemical natures of such fuels, and to demonstrate the technical and economic feasibility of recycling such fuels. Our responsibilities are the characterization of fuel, the testing of fuel under irradiation, and the development of processes for refabrication of fuel elements that are prototypic of designs useful for power reactors. The principal current objective is to demonstrate the refabrication of high-temperature gas-cooled reactor fuel elements in the Thorium-Uranium Recycle Facility (TURF), an $8 million research and development facility for demonstration of pilot-scale processes. Its construction should be completed in the Fall of 1967. Therefore, we are developing remotely operated processes and equipment to refabricate fueled-graphite elements.

We developed a variety of devices for handling a large number of particles and batches of particles simultaneously. These developments include a pneumatic fuel transfer system, a high-efficiency shape separation process, a classification process to grade uncoated and coated fuel particles within ± 5 μ with a minimum of screen blinding, and suitable valves and feeder mechanisms to serve the various pieces of the particle-handling system.

A reliable engineering-scale particle-coating system was selected, namely, a 5-in. fluidized bed. Over 400 experimental coating runs were made to define the coating parameters for the system. A process was developed to produce low-density buffer coatings from acetylene on bare 230-μ-diam particles with controlled density from 0.4 to 1.4 g/cm^3. A technique was developed for applying high-density (approximately 1.9 g/cm^3) isotropic outer coatings by the pyrolysis of propane and propylene in the temperature range from 1200 to 1500°C at coating rates up to 3 μ/min.

We tried to develop faster and more accurate techniques for obtaining the density, anisotropy, and thickness of pyrolytic carbon coatings, and techniques for determination of the diameter of bare particles. We investigated the blending of two sizes of fuel particles, one for coated fissile and one for fertile fuel particles. These must be

homogeneously blended and bonded in fuel holes to a packing density of 60 to 64 vol % and then filled with a carbonaceous binder. After checking the conventional techniques for blending particles, we designed and experimented with equipment for blending particles by controlling the feed rates of the two different-size particles as they flowed simultaneously from separate feed hoppers into a simulated fuel hole. The maximum deviation from the ideal blend was less than 5%. Various filler materials and resins for obtaining the bond between the coated particles were studied, principally to decrease the period of time required for polymerization of the resin. Also, we started work to nondestructively determine the homogeneity of fabricated fuel sticks, using through-transmission x-ray methods to detect density differences caused by differences in the packing of two sizes of particles.

The results of irradiation tests continue to indicate that the sol-gel-prepared oxide fuels perform equivalently to ceramics processed by other methods. A particle-performance model that is designed to predict the lifetime of fuel particles operating at certain conditions was tested against actual irradiation experience; it has proved most helpful in the design of coated particles.

Sol-gel techniques provide high flexibility in the forming of ceramic bodies. We extruded sol-gel-derived materials to produce bodies without plasticizers and with controlled densities in the range from 75 to 99% of theoretical; in laboratory-scale work we produced solid and cored thoria extrusions in diameters up to $\frac{1}{2}$ in. and lengths to 3 in. We have demonstrated the feasibility of pelletizing sol-gel-derived materials to sintered densities as high as 97% of theoretical at relatively low temperatures (1100°C). Sphere-Pac fabrication (the use of low-energy vibratory compaction and two size fractions of microspheres) was further demonstrated by the fabrication of 33 test rods ranging in diameter from $\frac{1}{4}$ to $\frac{1}{2}$ in. and lengths up to 2 ft. These rods packed to a density of 83.5 ± 0.5%.

The irradiation testing and evaluation of metal-clad thoria-base bulk oxide fuels continued. We initiated the test of cross progeny $(Th,Pu)O_2$ fuels fabricated by the Sphere-Pac technique. Thoria-base fuels have been irradiated to a burnup of 150,000 Mwd/tonne with a linear heat rating of 400 w/cm. Successful tests have been completed with heat ratings of 1000 w/cm. All of the thoria under test continues to exhibit exceptional performance characteristics.

Our basic study of the sintering and grain growth of sol-gel urania microspheres led to a drying and sintering schedule that, on a laboratory scale, yielded microspheres of high density and low residual carbon content.

PART V. OTHER PROGRAM ACTIVITIES

37. Isotopic Power Source Development

The development of procedures for gas tungsten-arc welding of heavy-walled refractory-alloy (TZM) capsules was undertaken in an effort to produce full-penetration welds for containers of alpha-emitting isotopes. The techniques developed were shown to be feasible and acceptable by metallographic examination and helium leak testing of demonstration capsules.

A second developmental welding program was aimed at sealing of the Hastelloy C capsule for SNAP-21. Gas tungsten-arc welding did not consistently produce welds of sufficient penetration and still permit ultrasonic inspection. These difficulties were overcome by the use of electron-beam welding. Equipment suitable for electron-beam welding in hot cells is being assembled in cooperation with Isotopes Division personnel.

Fluorescent penetrant and ultrasonic inspection techniques were evaluated for the inspection of capsule components, raw material, and welds in fueled capsules.

A materials and design study was made in support of a Brayton cycle system with a radioisotope heat source. Recommendations were made for the stress-bearing encapsulating material as well as materials for a diffusion barrier, oxidation protection, and a high emissivity coating.

38. Metallography

The time-consuming task of obtaining quantitative metallography data has been replaced for most analyses by an image-analyzing computer. The data can be obtained directly from the specimen through a microscope, or with an attachment that accommodates all types of prints and negatives. Potentiostatic etching is being investigated

as a procedure for selectively etching and differentiating phases in the microstructure. In the early stages of experimentation, ideal alloys have been selected; however, sufficient work with more complex alloys indicates this procedure may be very helpful in microstructural analysis. By high-temperature microscopy we observed the transformation of UAl_3 to UAl_4 in an aluminum matrix. This observation of the shape change and wedging process of the fuel particles due to the transformation helped to explain the swelling problem. The development of a chemical, and electrolytic, and a protective oil method for specimen preparation extended our capabilities for metallographic examination of reactive CeC_2.

39. Rover Rocket Nozzle Materials

Hastelloy X tube bundles simulating rocket nozzles were cycled between $-200°F$ and elevated temperatures; endurance was related to temperature, hold time, and the presence of dents on the tubes. Shear-stress–strain curves were compared for unirradiated and neutron-irradiated Hastelloy X joints brazed with three different alloys. Tensile properties were measured at elevated temperatures for Hastelloy X and Allvac 625. Participation in a review of the effects of space environment on nuclear rocket materials led to starting an investigation of the effects of gaseous contaminants on adhesion of initially atomically clean surfaces.

40. Thermonuclear Project

Both applied research and engineering assistance were supplied for the Controlled Thermonuclear Program. The decision to use superconducting magnets has made the design of components for use at liquid-helium temperatures necessary. A weldability study of the 5083 aluminum alloy is summarized as a typical example of the engineering assistance provided.

Because of the importance of adsorbed gases in determining the vacuum conditions in many experimental thermonuclear devices, the desorption of gases by electron bombardment is of interest. The desorption of hydrogen, deuterium, and carbon monoxide from tungsten by electron impact is being studied. The yields of hydrogen are of the order of 2×10^{-4} molecules per incident electron (1000-ev electron energy) when the specimen is at room temperature (with molecular hydrogen adsorbed) and about 2×10^{-5} when the specimen is at 1200°K (i.e., only dissociated hydrogen is present on the specimen surface). The yields increase rapidly with voltage above 300 v. The room-temperature yields for deuterium are similar to those for hydrogen, while the yields of carbon monoxide are more than an order of magnitude higher.

Part I.

Fundamental Programs

1. Crystal Physics

G. W. Clark

The growth of single crystals of refractory materials is our central theme. Single crystals are often required to characterize uniquely many physical phenomena. Some technical devices require very specific single crystals for their operations. Since suitable crystals are frequently difficult to obtain, we are conducting a continuing program to provide crystals needed in research, to devise and improve methods of crystal growth, and to develop increased understanding of crystal growth processes and kinetics. Crystals are being grown by several methods: by internal centrifugal zone growth, from molten-salt solvents, from supercritical aqueous systems, and by the general Verneuil method. Some of these crystals have been used by other groups in investigations of use in a neutron-beam chopper, electron-spin resonance, optical properties, deformation, fission-gas release, magnetic properties, and neutron damage by x-ray analysis. Also, we are investigating selected physical properties, both those related to the crystal-growth process and those important for characterizing new compounds.

INTERNAL CENTRIFUGAL ZONE GROWTH OF UO_2 CRYSTALS

D. E. Hendrix A. T. Chapman[1] G. W. Clark

We are continuing the study of the crystal growth of UO_2 by our internal centrifugal zone growth (ICZG) technique.[2] A preheated UO_2 rod moves slowly through a radio-frequency induction coil, causing progressive melting (2800°C) and recrystallization inside a solid UO_2 shell. Thermal gradients favorable to the formation of a single crystal along the rod axis are promoted by rotation of the rod. Crystals approximately 1 cm in diameter and 4 cm long can be grown within 2° of a desired orientation by seeding the melt. The probability of obtaining crack-free laboratory samples from a run was doubled by a recent change to a lower impedance induction coil, which resulted in a lower voltage drop and hence less likelihood of arcing and attendant sudden temperature decreases.

A comparison of the perfection of UO_2 crystals grown by this method, arc-melted specimens, and vapor-grown crystals is under way using etch-pit patterns, dislocation densities revealed by transmission electron microscopy, and x-ray topography. Preliminary results indicate that although substructure is more pronounced in our ICZG UO_2 than in arc-melted UO_2 (from Battelle Northwest), the dislocation densities are comparable (approximately $10^6/cm^2$), and fewer inclusions exist in the ICZG crystals. Good correlation was obtained among the three analysis techniques.

Melts of UO_2-ThO_2 solid solution of up to 60% ThO_2 have been made using the ICZG technique. Single-crystal grains up to 3 mm in diameter and 10 mm long have been grown of UO_2–50% ThO_2.

The analysis of the effect of the interrelated variables (frequency, power level, coil design, electrical and thermal properties of the material to be melted, and the chemical and mechanical controls) on the process is continuing.

We supplied UO_2 single crystals grown by the internal centrifugal zone technique to workers in both this and other laboratories. Studies under way on these crystals include creep properties, dislocation movement, diffusion measurements,

[1] Consultant from Georgia Institute of Technology, Atlanta.

[2] A. T. Chapman and G. W. Clark, *Metals and Ceramics Div. Ann. Progr. Rept. June 30, 1965*, ORNL-3870, pp. 3–4.

infrared spectroscopy, thermal conductivity, crystalline perfection, and fission-gas release.

THE GROWTH OF ROD AND LAMELLAR EUTECTIC CERMETS

D. E. Hendrix A. T. Chapman[1] G. W. Clark

A eutectic structure resulted from ICZG in a pressed bar containing a mixture of UO_2 with 12.5% W. The unidirectional solidification inherent in our process yielded pronounced alignment of rods of the tungsten second phase in the UO_2 matrix. Figure 1.1 shows such a region. A lamellar structure was also observed in the last small regions to solidify (see Fig. 1.2). Runs containing 5, 9, and 12% W indicated a eutectic composition at roughly 10% W and yielded rods from 1 to 2 μ in diameter with a length-to-diameter ratio on the order of 50 and spacing of about 4 to 5 μ. Thermal conductivity was improved about 30% in the direction of the rod axes. Also, with proper manipulation of the available parameters, we believe we can control the bulk orientation or the eutectic structure sufficiently to increase the radial heat transfer significantly in a large-grained UO_2 bar.

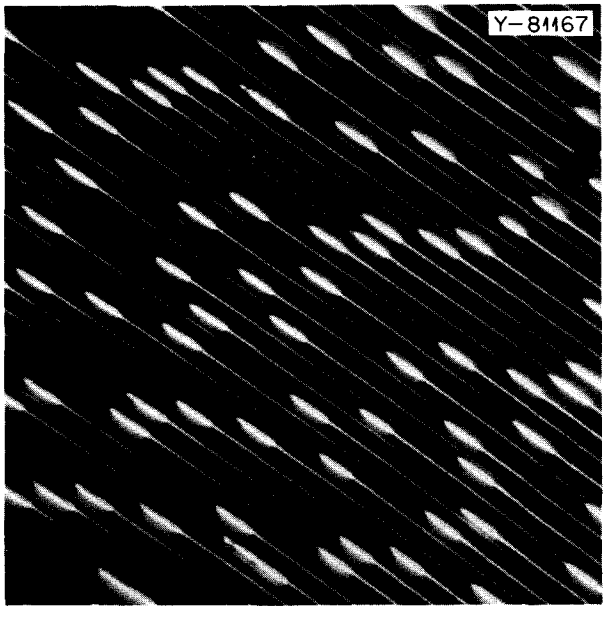

Fig. 1.1. Aligned Tungsten Rods in UO_2. 500×. Dark field.

Fig. 1.2. Tungsten Platelets in UO_2 Matrix. 500×. Dark field.

These early results are most impressive, and the broad implication of controlling rod and lamellar structures in cermets is exciting.

MOLTEN-SALT GROWTH OF SINGLE CRYSTALS

C. B. Finch G. W. Clark

Probably our most significant accomplishment in the area of flux crystal growth was the growth of 2-mm ThO_2 single crystals doped with the radioactive isotope ^{244}Cm (Cm:Th::1:3000). The growth method has been described.[3] Because of the radiation hazard, the crystals were grown in an isolated glove box containing a platinum-wound thermal-gradient furnace and necessary equipment. This was the first experiment performed in the new Transuranium Research Laboratory.

The resulting octahedral Cm^{3+}-doped ThO_2 crystals were initially pink but became nearly colorless after several hours at room temperature. Luminescent and absorption spectra studies are now in progress – data have been obtained at room and liquid-nitrogen temperatures. An electron-spin

[3]C. B. Finch and G. W. Clark, *J. Appl. Phys.* 36(7), 2143–45 (1965).

resonance examination of the crystals at a temperature of 1.5°K revealed the one isotropic peak predicted for trivalent curium, with a measured spectroscopic splitting (Zeeman) factor of $g = 4.488 \pm 0.002$.

Single crystals of the ferrimagnetic spinel $^{7}LiFe_5O_8$ were grown as octahedra up to 1 cm on edge from $Li_2O \cdot 2B_2O_3 \cdot 4PbO$ at 900 to 1150°C. However, these crystals do not scatter neutrons suitably to qualify for the neutron-chopping device for which they were desired. Attempts to improve the neutron-scattering characteristics of flux-grown $LiFe_5O_8$ by adding TiO_2 or Co_2O_3 to the melt led to growth of crystals of size and quality unacceptable for initial testing.

Crystals of a hitherto unreported compound, $LiErMo_2O_8$, of scheelite structure, were grown up to 5 mm in size from $Li_2O \cdot 2MoO_3$ solvent at 1150 to 900°C. The crystals display marked magnetocrystalline anisotropy and will be used for magnetic susceptibility studies.

Described techniques[3,4] were used to grow CeO_2 and ThO_2 single crystals up to 3 mm in size doped with uranium [U:(Ce or Th)::1:200]. These crystals were subjected to electron-spin resonance and optical absorption studies. Crystals of CeO_2 grown from our purest $Li_2O \cdot 2WO_3$ vary from colorless to pale blue. To seek the origin of the blue color, CeO_2 crystals were grown from a $Li_2O \cdot 2WO_3$-CeO_2 solution doped with 10% LiF. The resulting CeO_2 crystals were intensely blue in color. Efforts to characterize the absorption are planned. Crystals of CeO_2 doped with the isotope ^{161}Dy and ThO_2 doped with ^{144}Nd were grown for electron-spin resonance studies.

Paramagnetic Resonance of Gd^{3+} in CeO_2 Single Crystals[5]

M. M. Abraham[6] C. B. Finch
L. A. Boatner[7] E. J. Lee[6]
R. A. Weeks[6]

We incorporated Gd^{3+} into single crystals of CeO_2 (fluorite structure) in cubic sites and observed the ESR spectrum. The temperature dependence of the cubic crystal splitting was measured from room temperature to approximately 2°K and values of g, the fourth order parameter c, and the sixth order parameter d in the spin Hamiltonian treatment for the crystal field potential were obtained with a computer program. The parameters c and d had the same sign, and intensity observations of the temperature dependence of the resonance absorption lines showed that c was negative. The temperature dependence of the total splitting for the magnetic field parallel to [100] was similar to that observed in Gd^{3+}:ThO_2. Forbidden transitions with $|\Delta M_s| > 1$ were observed as well as axial spectra in heavily doped crystals. Lines due to transitions with $\Delta M_s = \pm 4$ were identified in both ThO_2 and CeO_2.

Electron Spin Resonance Spectra of Dy^{3+} in ThO_2 and CeO_2 (ref. 8)

M. M. Abraham[6] L. J. Raubenheimer[9]
C. B. Finch Z. M. El Saffar[10]
R. A. Weeks[6]

Single crystals of ThO_2 and CeO_2 (fluorite structure) doped with 0.5 at. % impurities of isotopically enriched Dy^{3+} (94% even-even isotopes) were grown. Measurements of ESR at $\simeq$ 10 Gc and liquid-helium temperatures revealed spectra with symmetry axes along the 4 crystal [111] axes. For ThO_2 $g_{\parallel} = 1.625 \pm 0.002$, $g_{\perp} = 9.95 \pm 0.05$; and for CeO_2 $g_{\parallel} = 1.632 \pm 0.002$, $g_{\perp} = 9.98 \pm 0.05$.

An additional line is observed and attributed to a $\frac{1}{2} \rightarrow -\frac{1}{2}$ transition between the levels of a ground state Γ_8 quartet in a cubic crystal field. For ThO_2, $g_{[100]} = 4.566$, $g_{[111]} = 4.323$, $g_{[110]} = 4.386$; and for CeO_2, $g_{[100]} = 4.433$, $g_{[111]} = 4.401$, $g_{[110]} = 4.411$ with 0.1% error. These data are sufficient for a calculation of the ratio of the cubic crystal field 4th and 6th order parameters. At

---

[4]C. B. Finch and G. W. Clark, *J. Appl. Phys.* 37(10), 3910 (1966).

[5]Abstracted from *J. Phys. Chem. Solids* 28, 81–92 (1967).

[6]Solid State Division.

[7]Vanderbilt University; part of this work was submitted in partial fulfillment for the requirements of the Ph.D. degree at Vanderbilt University. Current address: Ling-Temco Vought Research Center, Dallas.

[8]Submitted for publication in *The Physical Review;* presented at XIV Colloque Ampere, Sept. 6–11, 1966, Ljubljana, Yugoslavia.

[9]Visitor in Solid State Division from Republic of South Africa.

[10]Visitor in Solid State Division on IAEA Fellowship, Iraq.

20°K no spectra were observed, which made it impossible to detect a low-lying Γ_7 doublet as observed in the case of the isomorphous CaF_2. All line widths were larger than those for other rare-earth ions in these crystals and were 20 to 40 gauss.

HYDROTHERMAL SYNTHESIS

Lanthanide(III)-Doped YOOH

O. C. Kopp[11] G. W. Clark

The growth of single-crystal lanthanide oxyhydroxide (LnOOH) crystals up to 2.5 mm was reported previously.[12] Further studies reveal that analogous crystals of YOOH (up to about 2 mm) can also be grown from LiOH solvent and doped with various Ln^{3+} ions. We conclude from analyzed samples of Gd^{3+}-doped YOOH that the equilibrium distribution coefficient of Gd^{3+} relative to Y^{3+} is close to 1, as was to be expected. Correspondingly a visual change in color intensity was observed for YOOH doped with various amounts of Er_2O_3. We should be able to grow other Ln^{3+}-doped crystals to about 2 mm for electronic-state studies of these ions in a dilute state in this crystal environment.

Synthesis of Grunerite and Other Phases in the System SiO_2-NaOH-Fe-H_2O Near the Critical Temperature of Water[13]

O. C. Kopp[11] L. A. Harris[14]

The amphibole grunerite, $Fe_7(Si_8O_{22})(OH)_2$, was synthesized in the system SiO_2-NaOH-Fe-H_2O under dynamic conditions near the critical temperature of water at a total pressure of about 1.6 kilobars. The grunerite was most abundant near the bases of the vessel (400 to 430°C) but also occurred in the upper part of the vessels (360 to 410°C). It is supplanted by micaceous phases resembling Na-nontronite (or vermiculite) and stilpnomelane and an unusual fibrous "glass" in the upper part of the vessels. The role of sodium ions in the formation of grunerite and the micaceous phases was demonstrated by similar experiments using KOH as a solvent; these produced only the mica ferriannite.

Further Studies in the System RbOH-SiO_2-Fe_2O_3/Fe-H_2O

O. C. Kopp[11] G. W. Clark
L. A. Harris[14]

The presence of a steep boundary curve between rubidium iron mica and rubidium iron zeolite was reported previously.[15] Further study suggests that the temperature of the boundary curve is raised approximately 50°C if Fe_2O_3 is present in the nutrient in addition to the iron available from the liner walls. Additional phases have been noted in the system, including a distinctly greenish mica at temperatures below 350°C and both a feldspar and a possible pyroxene phase at temperatures above 475°C.

CRYSTAL GROWTH BY THE VERNEUIL METHOD

G. W. Clark

An electromagnetic neutron-beam chopper has been proposed by H. A. Mook.[16] The heart of this proposed device is a single crystal of certain magnetic oxide spinels. Historically, Verneuil-grown crystals have not had adequate crystalline perfection to meet the specifications set for this device. When flux-grown crystals failed for other reasons to meet the specifications, we decided to test this method and our skill. Thus, using an

[11]Consultant from the University of Tennessee, Knoxville.

[12]O. C. Kopp and G. W. Clark, *Metals and Ceramics Div. Ann. Progr. Rept. June 30, 1966*, ORNL-3970, p. 4.

[13]Presented at the Southeastern Section of the Geological Society of America, Tallahassee, Florida, March 30–April 1, 1967; summarized from article accepted for publication in *The American Mineralogist*.

[14]X-Ray Diffraction Group.

[15]O. C. Kopp, G. W. Clark, and S. D. Fulkerson, *Metals and Ceramics Div. Ann. Progr. Rept. June 30, 1964*, ORNL-3670, p. 8.

[16]Private communication with H. A. Mook, Solid State Division.

oxyhydrogen Verneuil furnace designed earlier,[17] we embarked on this cooperative program.

For evaluation, we have grown the following ferrites (spinels): nickel-zinc, titanium, iron-lithium, and lithium. In general these crystals have been greater than 8 mm in diameter and 20 mm long. Initial results have been most encouraging. An iron (^{7}Li) ferrite crystal grown on a [331] seed held this orientation and was 1 cm in diameter and 8 cm long. The neutron-rocking curve line width was 0.31° and the neutron Laue diffraction line was sharp and straight. This crystal was judged good enough to be in the first mockup of the electromagnetic neutron-beam chopper. Other crystals will be grown to adjust the composition, perfection, and size to optimize the crystals for this device.

[17]R. A. Lefever and G. W. Clark, *Rev. Sci. Instr.* **33**, 769 (1962).

MAGNETIC PROPERTIES

H. M. Smith G. W. Clark

An electromagnet with shaped 4-in.-diam pole faces and a microbalance were set up and calibrated for measuring the temperature dependence of the magnetic susceptibility and magnetization of small samples. The temperature range possible with this equipment is from 77 to 1000°K. We can measure the saturation magnetization of the ferrites to a precision better than 1%. We are measuring the temperature dependence of this property for our ferrite single crystals as related to composition, growth conditions, and heat treatments in order to optimize their magnetic character for the neutron-beam chopper.

2. Deformation and Annealing of Metals

C. J. McHargue

Our studies are directed toward finding the principles underlying the atom movements that occur during deformation, annealing, and phase transformation in solids. We use these principles to correlate the physical and mechanical properties with the microstructure and to obtain specific properties by suitable thermal and mechanical treatments that modify the microstructure. During this report period we continued to study migration of grain boundaries during annealing and the deformation of body-centered cubic metals.

DEVELOPMENT OF PREFERRED ORIENTATION IN COLD-ROLLED NIOBIUM[1]

J. C. Ogle R. A. Vandermeer

We have continued our investigation of the development of preferred orientation in cold-rolled polycrystalline niobium. In general, the pole figures could be interpreted as ridges of various ideal orientations that spread between two low-index orientations as end points. Each of the orientations along the ridges and between the two ideal end-point orientations shares a common crystallographic direction with all other orientations in the spread and thus is related to the others by a simple rotation about this direction as an axis. Two families of orientation spreads are required to describe the texture of cold-rolled niobium.

Figure 2.1 shows the (110), (200), and (222) x-ray diffraction pole figures of the center material for the most heavily deformed specimen in this study (99.5% reduction in thickness). The two sets of dashed lines follow the ridges that represent the orientation spreads. The stronger of these two spreads is represented by the long dashed lines and is designated as texture A; the weaker one, designated as texture B, is shown as short dashed lines. These two spreads are listed in Table 2.1, which identifies the ideal orientations serving as end points and their common crystallographic rotation axis. The description of the pole figures for this material in terms of orientation spreads alone is not entirely satisfactory, since there are also some discrete intensity peaks in the pole figures. The ideal orientation $(113)[\bar{1}10]$ and $(113)[1\bar{1}0]$ will account for most of these peaks, and the remaining ones result from the superposition of the orientation spreads of texture A and texture B.

An analysis of the development of these center textures for heavily cold-rolled niobium is quite complex; however, some generalizations can be made. After about 60% reduction in thickness the relative strength of texture B is greater than that of texture A, and the ideal orientations $(113)[\bar{1}10]$ and $(113)[1\bar{1}0]$ are not present. Orientations of the type $\{001\}\langle 110\rangle$ appear to be quite strong at

Table 2.1. Description of the Orientation Spreads in the Texture of Heavily Rolled Niobium

Texture	End Point Orientations	Common Crystallographic Directions
A	$(001)[\bar{1}10]$ to $(111)[\bar{1}10]$	$[\bar{1}10]$
	$(001)[1\bar{1}0]$ to $(111)[1\bar{1}0]$	$[1\bar{1}0]$
B	$(111)[\bar{1}2\bar{1}]$ to $(112)[\bar{1}10]$	near $[302]$
	$(111)[\bar{2}11]$ to $(112)[\bar{1}10]$	near $[032]$
	$(111)[1\bar{2}1]$ to $(112)[1\bar{1}0]$	near $[302]$
	$(111)[2\bar{1}\bar{1}]$ to $(112)[1\bar{1}0]$	near $[032]$

[1]Summarized from paper submitted for publication.

ORNL-DWG 67-1851

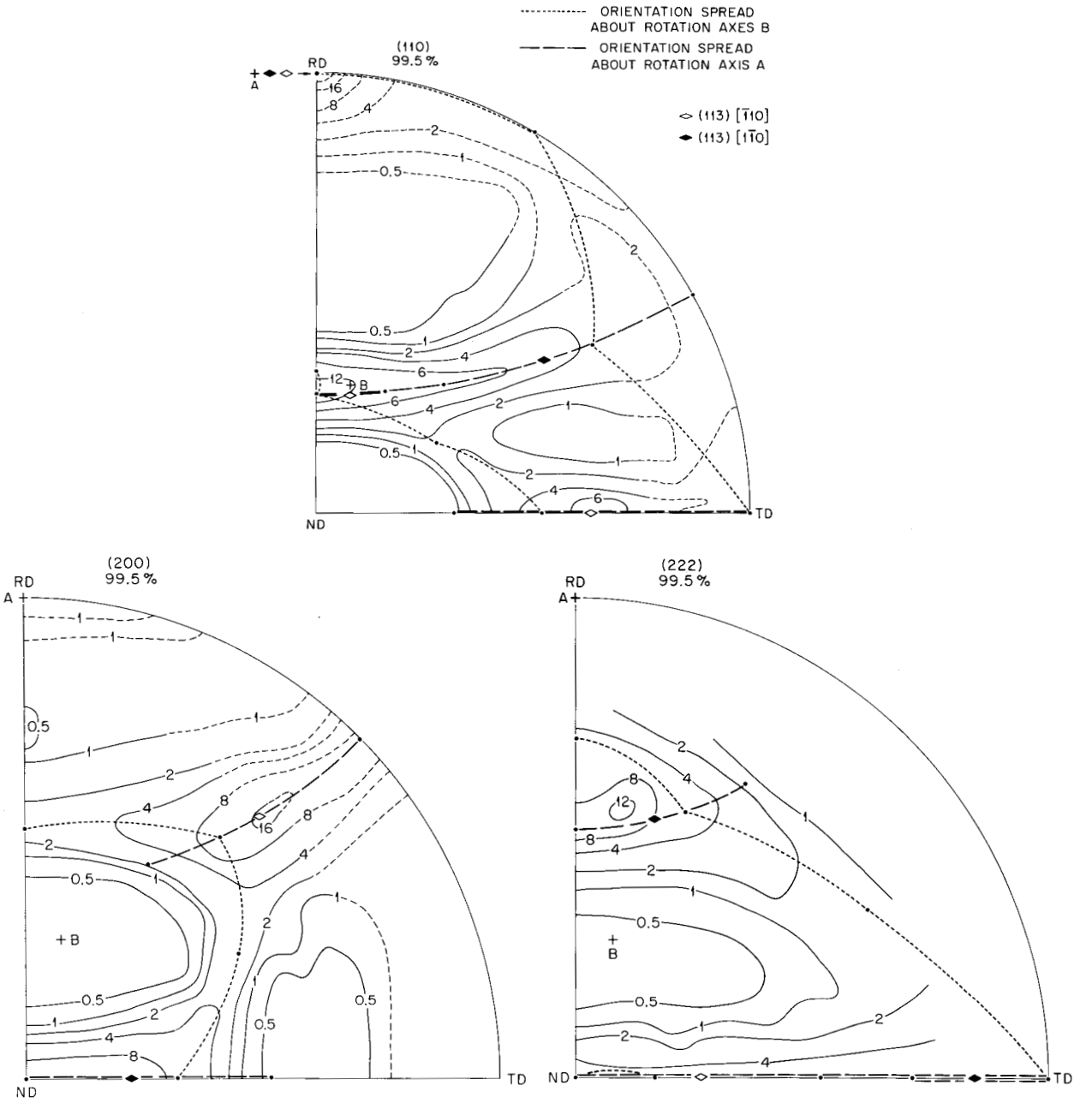

Fig. 2.1. The (110), (200), and (222) Pole Figures of the Center of a Cold-Rolled Niobium Sheet Reduced 99.5% in Thickness.

all reductions between 60 and 99.5%. While many of the grains apparently rotated to these orientations during rolling, these orientations nevertheless tended to be unstable and rotate toward {112}⟨110⟩ orientations. In the intermediate-to-heavy deformation phase of texture development, the {112}⟨110⟩ orientations play a key roll. Generally, material tended to reorient to these orientations.

It should be remembered that the {112}⟨110⟩ orientations, which serve as end points of the spread of texture B, are also members of texture A. However, after very high deformation even these orientations exhibited some degree of instability and the {113}⟨110⟩ orientation emerged as the main texture component.

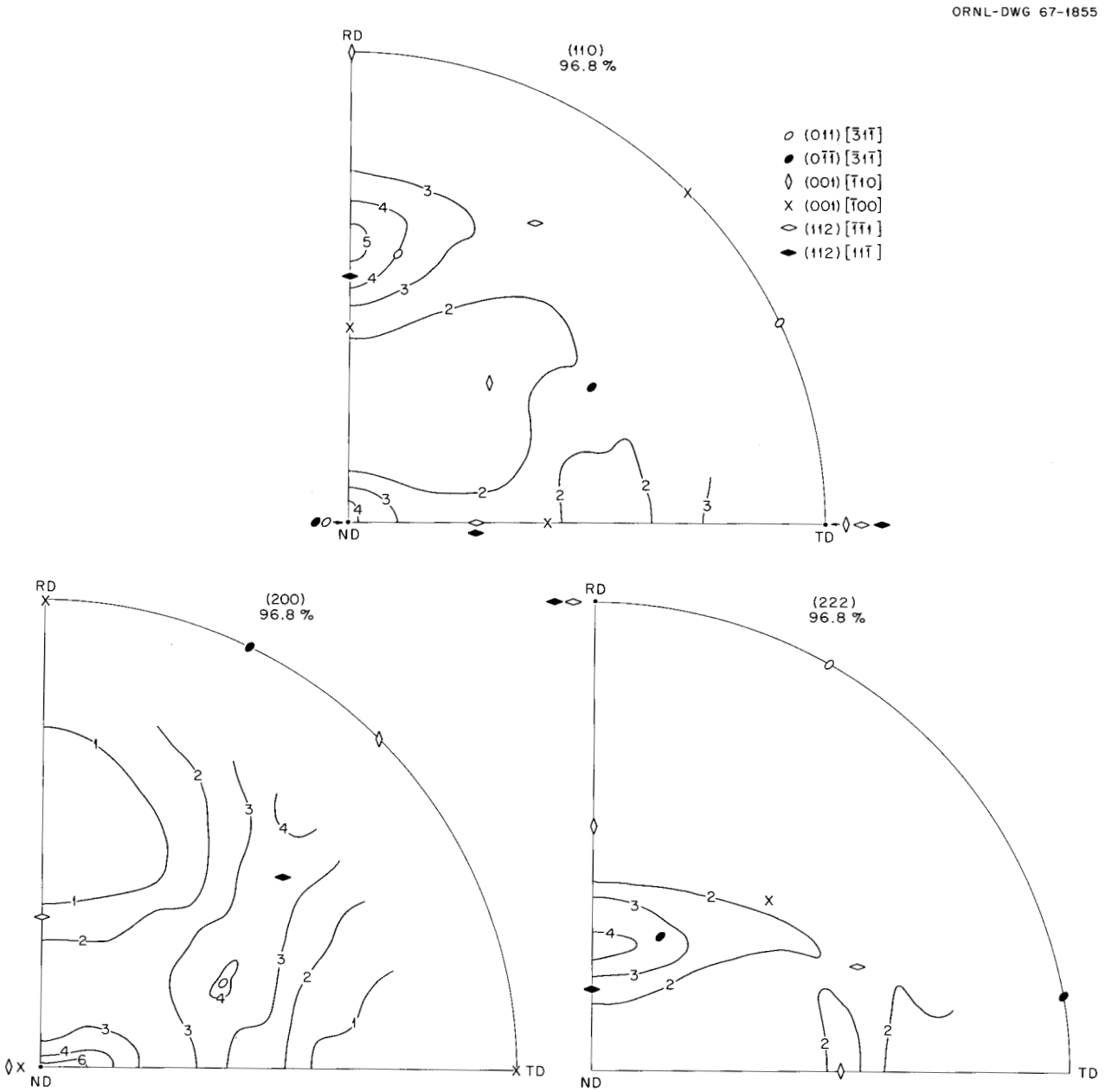

Fig. 2.2. The (110), (200), and (222) Pole Figures of Surface Texture Developed in Cold-Rolled Niobium Sheet at 96.8% Reduction in Thickness.

The textures developed at the surface of cold-rolled niobium are identical to those at the strip center for reductions in thickness up to 87%. At higher reductions a new texture, which is distinctly different from that at the center, appears at the surface. This texture becomes more prominent with increasing deformation up to 96.8% reduction, where it reaches its greatest intensity. Figure 2.2 shows the (110), (200), and (222) pole figures of this new surface texture. Our interpretation of these pole figures indicates that the pair of ideal orientations (011) $[\bar{3}1\bar{1}]$ and $(0\bar{1}\bar{1})$

$[\bar{3}1\bar{1}]$ best describe the strongest components of the surface texture. Other orientations in the pole figure are (001) $[\bar{1}10]$, (001) $[\bar{1}00]$, and the pair (112) $[\bar{1}\bar{1}1]$ + (112) $[\bar{1}1\bar{1}]$, but all of these are considerably weaker than the stronger component.

We are determining how the texture varies from the surface of cold-rolled niobium toward the center of the sheet.

RECRYSTALLIZATION AND THE ROLE OF PRECIPITATE PARTICLES IN GOLD-DOPED ZONE-REFINED ALUMINUM[2]

R. A. Vandermeer

Both the rate of recrystallization and the rate of its component process, grain-boundary migration, were found to depend on thermal history prior to deformation in dilute alloys of gold in zone-refined aluminum. For a given composition, these rates appear to be governed by whether the gold atoms are in solid solution or present in precipitate particles. The rates varied inversely with the degree of supersaturation of the deformed matrix. No change in either the mode of recrystallization or the number of recrystallization nuclei due to the presence of precipitate particles was detected. Specimens containing the most precipitate particles, (i.e., the least supersaturated) showed about the same rates of boundary migration as zone-refined aluminum. This suggests that the precipitate particles themselves have little effect on the boundary-migration rate in this case and act only as disposals for the purification of the solid-solution matrix. The observations agree qualitatively with the impurity-drag theory of grain-boundary migration.

[2]Abstract of paper presented at Annual Meeting, AIME, Los Angeles, February, 1967, and submitted for publication.

3. Deformation of Crystalline Solids

R. O. Williams

We are concerned primarily with the deformation of metals and alloys, especially the effect of structure on mechanical properties. During recent years, considerable effort has been devoted to measuring the change in internal energy during deformation. Work is currently being finished on the nature of the textures formed during rolling, with particular emphasis on developing powerful analytical methods for transforming x-ray data into biaxial pole figures. We presently have considerable interest in the structure of solid solutions and precipitation systems.

ANALYTICAL METHODS OF REPRESENTING TEXTURE DATA[1]

R. O. Williams

Processing of crystalline materials leads to nonrandom orientations of crystals. Knowledge of this nonrandomness, or texture, is of considerable importance in understanding the processing and in the application of materials. Textures are generally studied by x-ray diffraction, but the data do not give directly the identity of the orientations. We have been concerned with methods of converting such data into complete texture information.

The orientation of one axis relative to a single grain is represented by a point in the crystallographic unit triangle for the system. It follows that a large collection of grains exhibiting symmetry around an axis (i.e., a fiber texture) can be represented by a continuous function over this triangle. Such a figure has previously been known as an inverse pole figure, but the term "axial pole figure" is now preferred.

For textures showing lower symmetries, it is necessary to define the orientation of a second axis. This requires that the unit triangle be extended by a new angular variable. The resulting figure is termed a biaxial pole figure.

The experimentally accessible x-ray data correspond to certain kinds of averaging along lines in the axial or biaxial pole figures; hence, the intensity data cannot be directly converted into the desired figure. Rather, one must deduce the optimum distribution that will reproduce the data. Originally this was done by trial-and-error methods for the axial case,[2] but biaxial pole figures are so complex that such methods are very unpromising. The only analytical method that has been used previously employs the Legendre polynomials of spherical harmonics.[3-5] This method has worked more or less satisfactorily for the axial case and has been formally proposed[6,7] for the biaxial case, but no solution has been evaluated.

Our new methods have resulted in marked improvements. In the first place, a general series solution can be used in place of the specialized

[1] Summarized from the papers by R. O. Williams, "Analytical Solutions for Representing Fiber Textures as Axial Pole Figures," to be published in *Journal of Applied Physics*; "Analytical Methods for the Quantitative Representation of Complex Textures by Biaxial Pole Figures," (in preparation); and "The Representation of Rolling Textures of Copper, Brass and Aluminum by Biaxial Pole Figures," submitted to *Transactions of the Metallurgical Society of AIME*.

[2] L. K. Jetter, C. J. McHargue, and R. O. Williams, *J. Appl. Phys.* **27**, 368 (1956).

[3] H. J. Bunge, *Monatsber. Deut. Akad. Wiss. Berlin* **1**, 27, 400 (1959).

[4] R. J. Roe and W. R. Krigbaum, *J. Chem. Phys.* **40**, 2608 (1964).

[5] P. R. Morris, *J. Appl. Phys.* **37**, 358 (1966).

[6] H. J. Bunge, *Monatsber. Deut. Akad. Wiss. Berlin* **3**, 97 (1961).

[7] R. J. Roe, *J. Appl. Phys.* **36**, 2024 (1965).

Legendre solution, and the input data can be weighted so as to obtain a statistically superior answer. Also the solution can be performed for a set of points without recourse to a mathematical model. A more accurate solution by this method has not been proved possible, but this method is easier to set up for computation. The equations for calculating the standard deviation for all three solutions were derived.

Formally, the biaxial case is handled the same as the axial case. There is, however, a significant difference in the degree of complexity. The Legendre method is so complex that no solution has yet been obtained. While the series method is surely applicable, it has not yet been tried. The method in which values are calculated without a mathematical model becomes impractical. We developed an alternate method and find it to be very powerful. In this method, the values of the density at a set of points over the biaxial volume are estimated iteratively from the difference between the experimental and calculated intensity at the points corresponding to the biaxial point. This solution converges to a least-squares solution. One important feature of this solution is that meaningless negative values are prevented. This is not possible by the other methods.

This method was applied to the rolling textures of copper, aluminum, and brass. The results showed that prior texture analyses are only fair. The textures consist of continuous spreads of orientation, which run through or near most of the ideal orientations previously proposed but include other orientations. A cube texture has been identified for the first time in copper and aluminum; its density is slightly less than random.

DEFORMATION AND FRACTURE OF ALLOYS STRENGTHENED BY SPINODAL DECOMPOSITION

R. W. Carpenter

The structural changes associated with spinodal precipitation reactions in metallic alloy systems are of the same type as those required to impede the movement of dislocations during plastic flow. It has been shown experimentally that spinodal decomposition is an effective strengthening mechanism for certain gold-platinum and aluminum-zinc alloys. Yield strengths of about 10^5 psi at room temperature were obtained for an alloy containing 60% Au and 40% Pt in an earlier investigation.[8] The effectiveness of this reaction as a strengthening mechanism in several other alloy systems is the basis of the present investigation. In particular, the strengthening is expected to depend on the wave length and amplitude of the composition fluctuations induced by spinodal decomposition. The alloy systems chosen for the present work permit the variation of these two parameters over an appreciable range and thus permit an evaluation of this strengthening mechanism.

Two different fracture mechanisms have been observed in spinodally strengthened alloys. This first is intergranular shear, and it results in abnormally short elongation to fracture. The second is the usual transgranular shear type, resulting in total strains to failure of 10% or more. Which of these two modes is dominant appears to depend on the amount of incoherent grain-boundary precipitation occurring simultaneously with spinodal decomposition within the grains and on the resistance of the grain-boundary precipitate to plastic flow relative to the surrounding grains. The effect of prior heat treatment upon fracture mode in several alloys of spinodal type is being investigated using drop- and step-quenching techniques.

ROLLING AND RECRYSTALLIZATION SUBSTRUCTURE IN VERY THIN FOILS OF COPPER AND IRON[9]

R. W. Carpenter J. C. Ogle[10]

Annealed polycrystalline sheets of copper and iron were reduced to a thickness of 2 μ by a pack-rolling process. The substructure formed during both straight and cross rolling at reductions of 98.5% was investigated by transmission electron microscopy; deformation and recrystallization textures were determined by an x-ray diffraction method. In the rolled condition neither copper nor

---

[8] R. W. Carpenter, "Deformation and Fracture of Gold-Platinum Polycrystals Strengthened by Spinodal Decomposition," *Acta Met* **15**, 1297–308 (1967).

[9] Abstract of paper to be presented at the 1967 Fall Meeting of the Metallurgical Society, Cleveland, Oct. 16–19, 1967.

[10] Structure of Metals Group.

iron exhibited the dislocation "cell" structure characteristic of these materials in thick deformed specimens. Both showed large areas of high dislocation density with no regular geometric arrangement definable. In addition, copper, and to a lesser extent iron, contained groups of polygonized subgrains with sharp boundaries after rolling at room temperature. Cross rolling favored the appearance of the polygonized subgrains. The copper developed a duplex deformation texture composed of (001) $[\bar{1}00]$ and (001) $[\bar{1}10]$. The (001) $[\bar{1}10]$ component was unstable under cross rolling. The $\{123\}\langle 421\rangle$ type texture usually reported for rolled copper was not observed. Iron developed a (001) $[\bar{1}10]$ texture during rolling. During anneals at relatively low temperatures, both metals recrystallized easily with the subsequent growth of grains considerably larger than the sheet thickness. Recrystallization textures were similar to those reported for bulk materials. The variation of the observed substructures with specimen thickness and deformation temperature are discussed and compared to the behavior of bulk metals.

4. Diffusion in Solids

T. S. Lundy

Past activities have been concerned primarily with self-diffusion in pure substances with emphasis on the refractory body-centered cubic metals and the temperature dependence of their diffusion properties. Other studies have been on cation diffusion in UO_2, on the Ludwig-Soret effect in solids, and on the effects of radiation on diffusion. Herein we report experiments on self-diffusion in the body-centered cubic phase of titanium-vanadium alloys and in the body-centered cubic and face-centered cubic phases of manganese. Characterization of the "near-surface effect" for solute diffusion in silver and in gold is also reported and the possible mechanisms are noted. Experiments were recently started on uranium diffusion in UN and UO_2. Other experiments in preliminary stages include tracer diffusion studies in tungsten (a joint effort with R. E. Pawel of the Reactions at Metal Surfaces Group, Chapter 13) and the effect of hydrostatic pressures on diffusion in body-centered cubic metals and alloys.

SELF-DIFFUSION IN BODY-CENTERED CUBIC TITANIUM-VANADIUM ALLOYS[1]

J. F. Murdock[2] C. J. McHargue

The self-diffusion coefficients for titanium and vanadium diffusing in the body-centered cubic titanium-vanadium alloys at 10% increments over the entire composition range were studied as functions of temperature up to within 50 to 75°C of the solidus. In all instances the data defined a continuously curving line when plotted as ln D versus $1/T$.

The effect of titanium on diffusion in vanadium-rich alloys appears to be primarily a reflection of melting-point effects. In the titanium-rich alloys, however, there are large effects in addition to those associated with melting points. We suggest that strong impurity-vacancy complexes form in the titanium-rich alloys, and the rate-controlling step for both solvent and solute migration is the rate of dissolution of these complexes.

SELF-DIFFUSION IN MANGANESE

J. Askill[3]

Experiments on the diffusion of ^{54}Mn in polycrystalline manganese were completed. Diffusion coefficients varied from 8×10^{-7} cm^2/sec at 1240°C to 1×10^{-7} cm^2/sec at 1170°C for the body-centered cubic delta phase and from 3.5×10^{-7} cm^2/sec at 1150°C to 2×10^{-7} cm^2/sec at 1120°C for the face-centered cubic gamma phase. Of particular interest is the fact that the diffusion coefficients are higher in this system for the more densely packed and lower temperature face-centered cubic phase.

THE NEAR-SURFACE EFFECT

T. S. Lundy

Unidirectional diffusion from a plane source of radioactive tracer into an isotropic homogeneous medium held at a constant temperature T follows

[1]Abstract of paper submitted to the *Transactions of the Metallurgical Society of AIME* for publication.

[2]Present address, USAEC, c/o Puerto Rico Water Resources Authority, Rincon, P.R.

[3]Consultant from Millikin University, Decatur, Illinois.

the Gaussian solution to Fick's second law:

$$c(x,t) = M(\pi Dt)^{-1/2} \exp(-x^2/4Dt) ,$$

where $c(x,t)$ is the concentration of diffusing species at a distance x from the source after a time t at temperature, M is the amount of tracer per unit area at $x = 0$, $t = 0$, and D is the diffusion coefficient. The above expression is valid if D does not depend on concentration changes with position in the specimen. Use of the Gaussian solution for calculation of impurity tracer diffusion coefficients in solids has been justified by the notion that significant concentration variations with position do not occur and by experimental evidence that usually shows a linear dependence of ln $c(x,t)$ on x^2.

In real systems, it is well established that deviations from the Gaussian behavior take place for large penetration distances and that such deviations can be associated with enhanced diffusion along short-circuit paths, such as dislocations or grain boundaries. In recent years, it has also been established that an unusually low rate of migration of tracer atoms may be observed in a region close to the specimen surface. The overall penetration behavior is schematically illustrated in Fig. 4.1, where Region II represents volume diffusion, Region III short circuiting, and Region I the near-surface effect. Various explanations for the near-surface effect (NSE) have been postulated, but no "all-encompassing" answer seems evident.

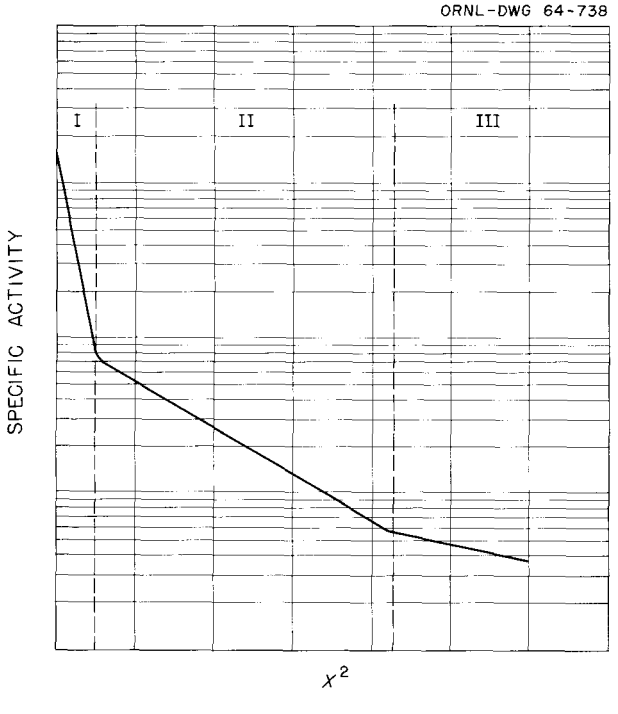

Fig. 4.1. Schematic Penetration Plot for Unidirectional Diffusion from a Plane Source. Region I is due to the near-surface effect (NSE), region II to volume diffusion, and region III to short-circuiting.

In this work, we have attempted to characterize the NSE for diffusion in both silver and gold. Our goal is an understanding of the mechanism or mechanisms for the NSE, so that proper precautions can be taken in treatment of volume diffusion data for solids.

The NSE for Diffusion in Silver

T. S. Lundy R. A. Padgett

Possible explanations for the NSE include (1) a very low concentration of vacancies in the region near the specimen surface, (2) experimental difficulties introducing a large turnup in the data near the surface, (3) presence of an insoluble layer containing the tracer during all or part of the diffusion anneal, (4) existence of an oxide barrier to the diffusion process, (5) a concentration dependence of the diffusion coefficient – even for trace amounts of impurities, and (6) a natural tendency for solute elements to segregate to free surfaces.

To check the possibility of a varying vacancy concentration, we determined penetration profiles for both ^{110}Ag and ^{60}Co in single crystals of silver for various times. As shown in Figs. 4.2 and 4.3, no trace of NSE exists for ^{110}Ag diffusion, while the effect is quite pronounced for ^{60}Co diffusion. Since a shortage of vacancies in the near-surface region would affect diffusion of both tracers, we take these data as proof that no significant vacancy concentration gradients are present. Both sets of experiments were performed by identical techniques (a grinding procedure for the serial sectioning), so we also believe that proper explanation of the NSE in silver is not due to this source.

Next, we varied the concentration of the initially deposited layer of tracer (using ^{60}Co and carrier-free ^{58}Co) from well above the published solubility limit for cobalt in silver of about 4×10^{-6} weight fraction down to about 10^{-6} (for ^{58}Co). The magnitude of the NSE changed drastically

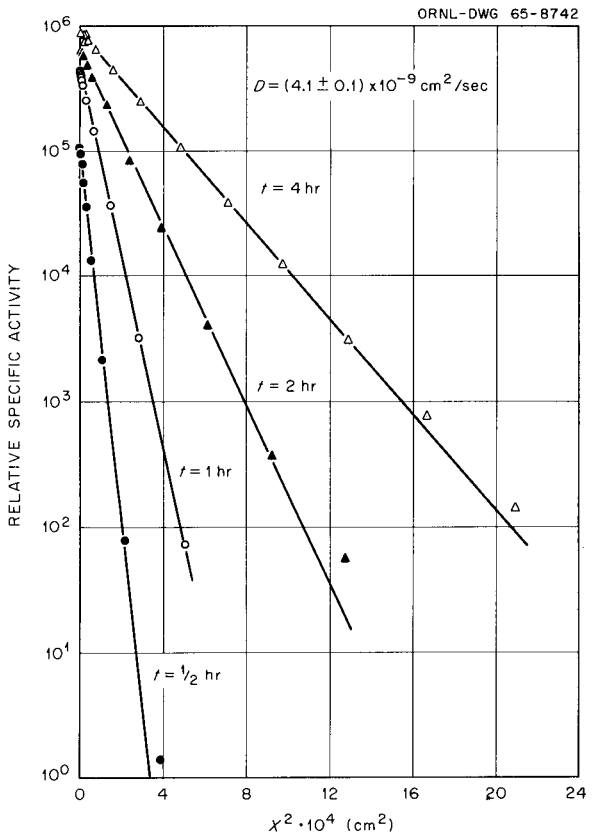

Fig. 4.2. Penetration Plots for ^{110}Ag in Silver at 927°C for Various Times.

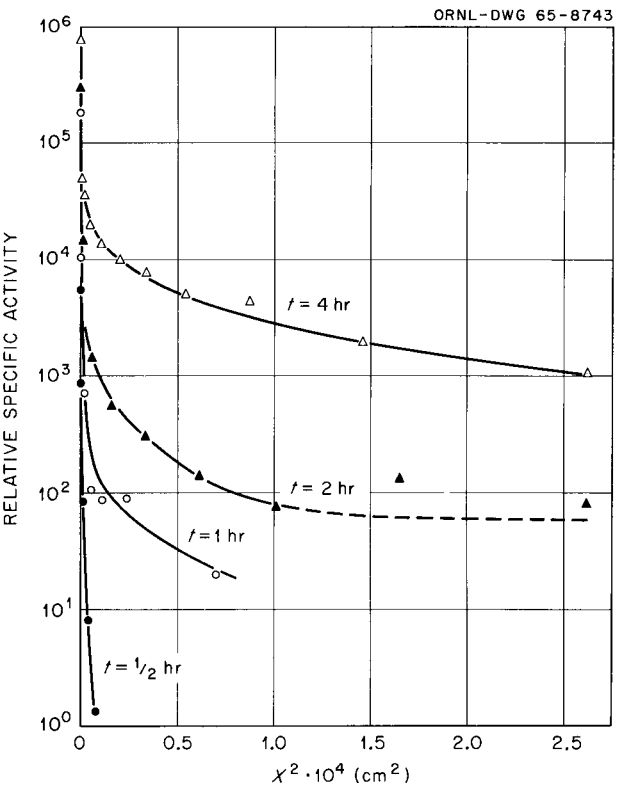

Fig. 4.3. Penetration Plots for ^{60}Co in Silver at 927°C for Various Times.

with these changes in initial concentration but did not vanish. We used three different methods for deposition of the tracer – electroplating, dropwise addition, and vacuum evaporation – without significantly changing the NSE.

The presence of an oxide barrier to diffusion was examined in side-by-side experiments with specimens in two atmospheres, argon and hydrogen. No significant differences in penetration profiles were found between these cases or relative to other experiments in which specimens were diffusion annealed in a vacuum of about 10^{-5} torr.

At the conclusion of these experiments on the NSE in silver we were left with two possible explanations, concentration effects even under conditions well below the solubility limit or a natural tendency for segregation of the cobalt impurity atoms to the silver surface.

The Near-Surface Diffusion Anomaly in Gold[4]

A. J. Mortlock[5]

At several temperatures in the range from approximately 700 to 950°C, ^{60}Co and ^{63}Ni were diffused at tracer concentrations in gold. The diffusion penetration profiles were determined by a serial sectioning technique in which the gold was first anodized and then the anodized layer was dissolved away in acid. In this way layers as small as 250 A could be removed reproducibly.

The region close to the specimen surface was in all cases characterized by irregular behavior in the sense that ln $c(x,t)$ was not linear in x^2. A typical example of this is shown in Fig. 4.4.

Possible reasons for these observations were considered, and we concluded that the present measurements could be explained in part qualitatively by the operation of a short-range attraction or repulsion between the diffusing atoms and the specimen surface. We expect this force to be of thermodynamic origin and associated with the effect of the impurity atoms present on the free energy of the surface.

[4]Summarized from ORNL-4141 (July 1967).

[5]Noncitizen employee from Australia; on leave from Australian National University, Canberra.

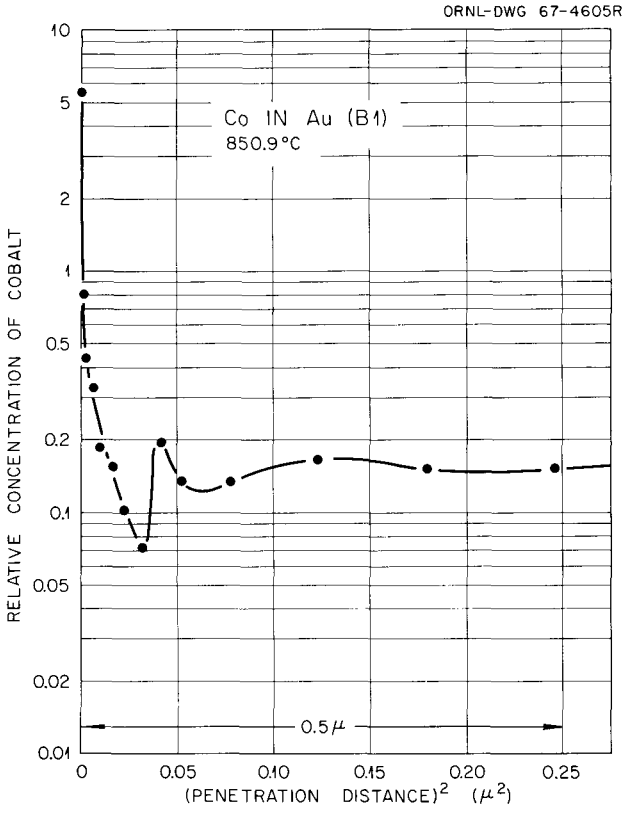

Fig. 4.4. Penetration Plot for ^{60}Co Diffusion in Gold.

URANIUM DIFFUSION IN UN_{1+x} AND UO_{2+x}

D. Reimann[6]

The diffusion of ^{233}U in mono- and polycrystalline UN will be measured for two compositions, one close to the phase boundary between UN and UN + U(*l*) and the other close to the phase boundary between UN and U_2N_3. The desired stoichiometry of the UN_{1+x} will be maintained by an accurately controlled nitrogen pressure in the annealing furnace in the range from about 1 atm to 10^{-10} torr, depending on temperature. The required experimental setup of a tungsten-wire resistance furnace for temperatures up to 2500°C contained within an ultrahigh-vacuum system is being built.

The penetration profile of the tracer after annealing will be determined by alpha spectroscopy with the so-called alpha-energy degradation method, a nondestructive method that makes use of the energy loss of alpha particles by absorption in the matrix material. The diffusion coefficient in one specimen can be measured after each of a series of annealing steps at the same temperature.

Measuring the cation self-diffusion in at least two different compositions of UN_{1+x} will provide a better understanding of the defect structure of the material and probably lead to the determination of the dependence of *x* on nitrogen pressure and temperature and the possible range of *x* in the phase UN_{1+x} without precipitation of a second phase.

Similar experiments will be run on UO_{2+x} single crystals. The required oxygen pressure will be supplied by a CO/CO_2 mixture and measured with an oxygen partial-pressure detector (ZrO_2-CaO solid-electrolyte galvanic cell).

[6]Noncitizen employee from Germany.

5. Electron Microscopy

J. O. Stiegler

The microstructure of a metal or alloy determines its mechanical and physical behavior and its response to its environment. With electron microscopy, we are determining the structures and changes in structure that occur under service conditions in order to understand the corresponding changes in properties. We are using transmission techniques to study dislocation configurations, irradiation-induced defects, and small precipitate particles; replica techniques to examine bubbles, cavities, cracks, and other gross structural features; and extraction techniques to analyze precipitation phenomena by electron diffraction and electron-probe microanalysis. Our etch pitting studies on dislocation motion in body-centered cubic crystals at low temperatures are continuing. We hope to relate these observations to the theoretical analysis of slip bands described in this chapter. The recognition that gas bubbles drastically influence the high-temperature ductility of metals coupled with development of an electron-microscope technique for observing bubbles and cavities under high-resolution conditions has led us to devote a large part of our effort to studies of elevated-temperature fracture. The basic information that we are generating should provide a guide for the development of materials that resist high-temperature radiation embrittlement. We are working closely with the Mechanical Properties Group in this field and with the several groups participating in the Tungsten Metallurgy Program. We report here activities that are primarily microstructural in nature; other work is included in Part II, Chap. 16 of this report.

MORPHOLOGIES OF BUBBLES AND VOIDS IN TUNGSTEN[1]

K. Farrell B. T. M. Loh
J. O. Stiegler

The morphologies of bubbles and voids in tungsten were studied by stereo electron fractography. The tungsten for the examination of gas bubbles was prepared by hydrogen reduction of WF_6 vapor over a heated substrate, the process known as chemical vapor deposition (CVD). When annealed in vacuum at temperatures above 1600°C, CVD tungsten contains many gas bubbles, which grow with increasing annealing time and temperature. The gas involved has not yet been identified, but it probably results from volatile impurities trapped during deposition. The tungsten sheet used for the examination of voids was hot rolled from a sintered powder-metallurgy billet. The voids were creep cavities formed in specimens tested to fracture at a stress of 2000 psi at 2200°C in vacuum. Since both bubbles and voids were formed mainly at the grain boundaries, they could be exposed for examination very conveniently by fracturing the specimens along grain boundaries at room temperature with little distortion from plastic deformation. Direct carbon replicas were made from the newly fractured boundary surfaces and examined by electron microscopy.

Both bubbles and voids appeared to be polyhedral (Fig. 5.1). A stereoscopic technique used to determine the crystallography of the facets on bubbles and voids showed that they are bounded by {100}, {110}, {112}, and {102} faces (Figs. 5.2 and 5.3). In the bubbles the {100} and {112} faces are smooth but terraced, the {102} faces are stepped, and the {110} faces are rough. No terracing, stepping, or roughness is observed on

[1]Summary of a paper to be published in *ASM Transactions Quarterly*.

PHOTO 89113

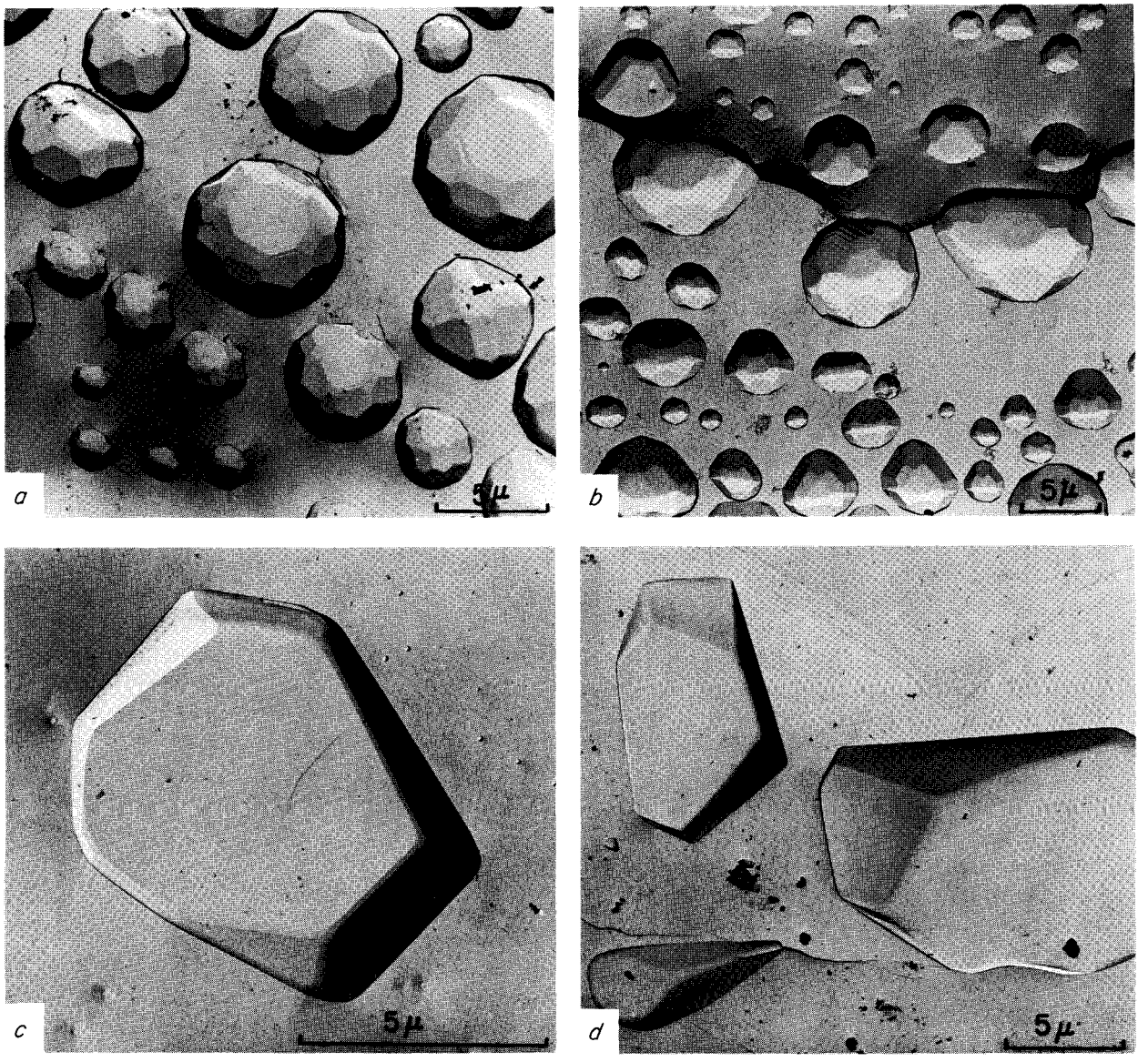

Fig. 5.1. Bubbles and Voids in Tungsten. (*a*) Gas bubbles on grain boundaries of CVD tungsten annealed 5 hr at 2500°C; (*b*) same, including a grain boundary; (*c*) details of a cavity on a grain boundary of powder-metallurgy tungsten after creep at 2200°C under a stress of 2000 psi; (*d*) grouping of such cavities.

PHOTO 89114

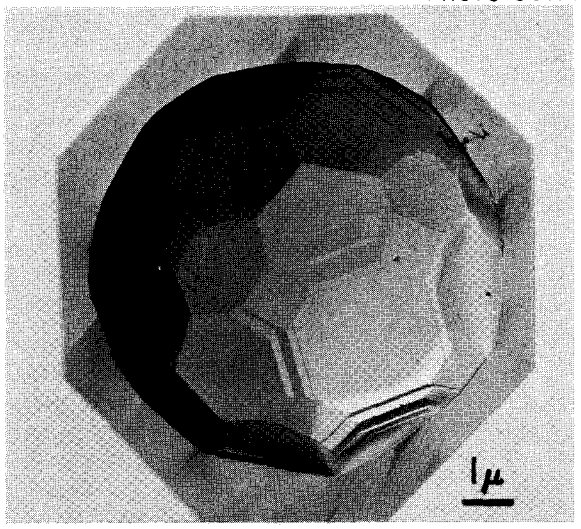

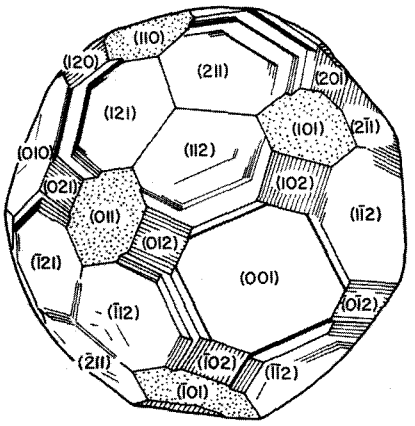

Fig. 5.2. Crystallography of a Bubble.

PHOTO 89115

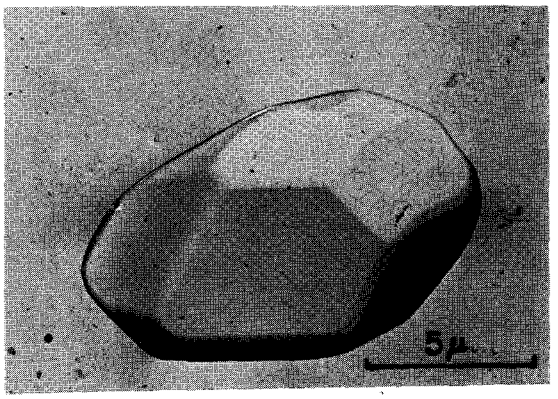

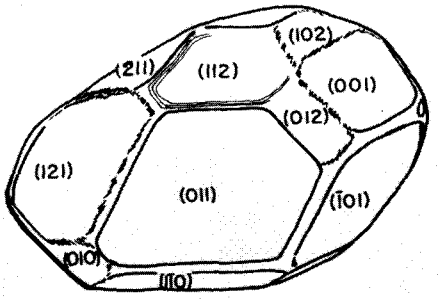

Fig. 5.3. Crystallography of a Creep Cavity.

creep cavities. The {102} faces are thought to be composites of two {112} faces; and, according to theoretical considerations, they should not belong to an equilibrium form. Therefore, the bubbles observed are all in some intermediate nonequilibrium stage (Fig. 5.4). Since small, equiaxed, near-spherical bubbles ought to be closest to the equilibrium shape (bubbles marked A in Fig. 5.4), we have used them to measure relative surface tensions. We find that

$$\gamma\{100\} : \gamma\{112\} : \gamma\{110\} = 1.0 : 1.05 : 1.08 \ .$$

The discrepancies between these values and the predictions of theoretical models may be due to adsorption of the unidentified gas phase from the bubbles.

During the early stages of growth of the bubbles, relative surface areas fall in a different order. We attribute this to kinetic effects involving the rates of growth and dissolution of the different crystallographic faces. We speculate that the rough {110} faces, which dominate in growing bubbles, are not real crystallographic surfaces but rather are composed of four {112} planes forming pointed hills and valleys.

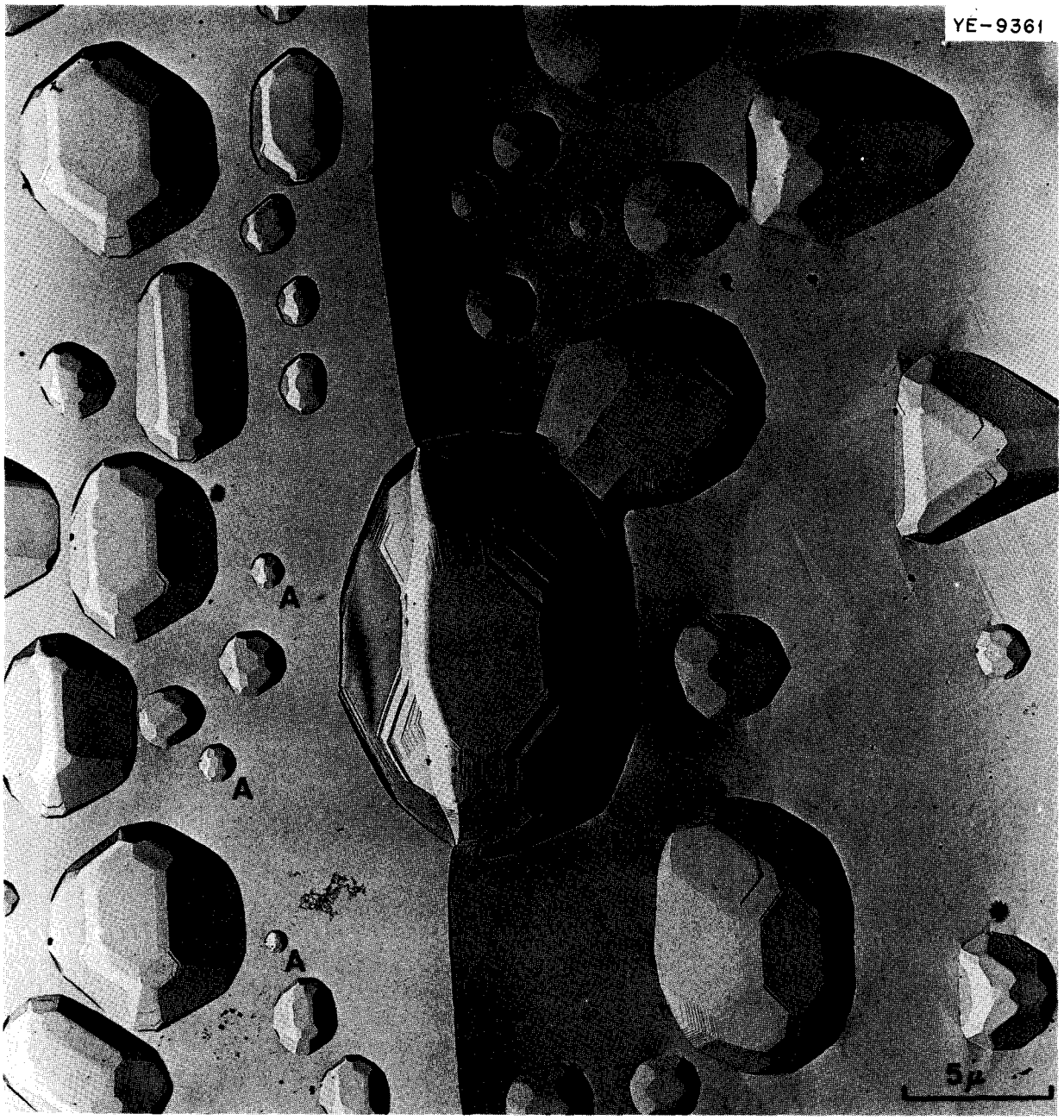

Fig. 5.4. Bubbles at Various Growth Stages. Small bubbles marked A are equiaxed and believed near equilibrium.

NATURE OF CREEP CAVITIES IN TUNGSTEN[1]

J. O. Stiegler
K. Farrell
B. T. M. Loh
H. E. McCoy, Jr.[2]

An electron fractographic technique was used to study grain-boundary cavities formed in tungsten under creep. The appearance of the cavities depends strongly on the conditions of temperature and stress. At lower temperatures and higher stresses, the cavities are shallow and irregularly shaped; they have blunt ends and are best described as being ameoboid (Fig. 5.5). Under lower stresses and higher temperatures, they acquire regular polyhedral shapes (see Fig. 5.3). The different structures are rationalized by consider-

[2]Mechanical Properties Group.

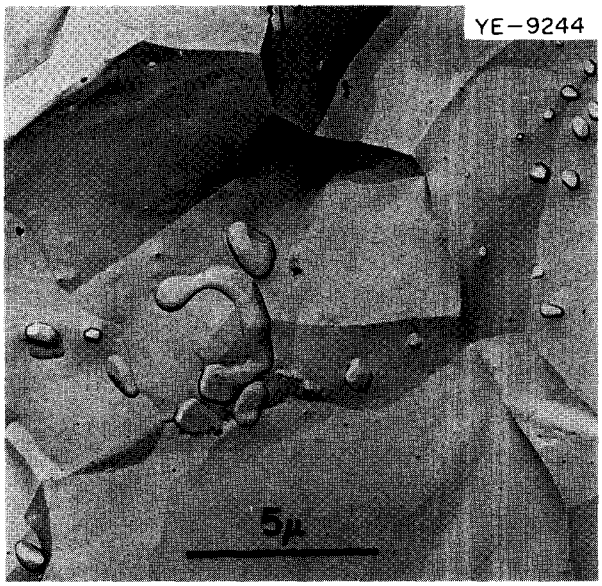

Fig. 5.5. Cavities in Tungsten Produced by Creep at 1650°C at a Stress of 10,000 psi.

ing the competition between growth by plastic deformation or stress-induced vacancy diffusion and internal rearrangement by surface diffusion. In disagreement with observations by optical microscopy, triple grain junctions are not preferred sites of cavity nucleation, although a few occur at them. The most likely mechanism for cavity nucleation involves grain-boundary sliding that is blocked at gross irregularities in the grain-boundary surfaces. Since only large cavities can be detected optically, they have reached a grain-boundary junction, giving the illusion that they are nucleated there. Grain-boundary sliding parallel to triple grain junctions may occasionally open cavities at jogs or irregularities on the junctions or at the points where four grains intersect, but the contribution is minor compared with cavitation at two-grain interfaces.

DYNAMICS OF SLIP BAND FORMATION[3]

B. T. M. Loh

Several investigators have used computer calculations to study the final equilibrium arrangements and the stress fields associated with certain dislocation configurations and the interaction of dislocations with obstacles. In this work, machine computations are employed to study dynamic features of the formation of slip bands originating from a single dislocation source under a variety of stress conditions. Information that can be obtained from such calculations includes not only the dislocation configuration and the stress concentration at the head of the slip band, but also the shear strain and the shear strain rate at any instant during the formation of the band. All are important in considering plastic deformation of crystals. The model used in this calculation is that a dislocation source situated at a boundary of a cubic grain emits a screw dislocation whenever the net stress on the source is larger than the activation stress for generation of a new dislocation. The dislocations move on the primary slip plane toward the opposite grain boundary. The speed of the dislocation is estimated from either Gilman's[4] or Stein and Low's[5] dislocation velocity expressions; however, the stress term in the expressions is replaced by the effective stress exerted on the dislocation. The effective stress is the sum of the applied resolved shear stress and the interaction stresses due to other dislocations on the slip plane. The distance of forward motion of each dislocation between time t and $t + dt$ is the product of the speed and the time interval dt. The time interval dt is regulated so that the displacement of the dislocation with the highest velocity or the highest effective stress in dt is 25 A or approximately 10 Burgers vectors at the beginning of the band formation and is gradually reduced as the dislocations move close to the grain-boundary barrier. Cross slip is allowed in the process only if the effective stress on the cross slip plane is larger than both the effective stress on the primary slip plane and the friction stress on the cross slip plane. Any dislocation reaching the boundary stops there. After every time interval, the effective stresses on all dislocations are recalculated from their relative positions at that instant, and these stresses are then used to compute the new speeds of dislocations and their new positions. The cycle continues until every dislocation reaches its equilibrium position.

[3]Summary of a paper to be presented at the International Conference on the Strength of Metals and Alloys, Tokyo, Japan, Sept. 4–8, 1967.

[4]J. J. Gilman, *J. Appl. Phys.* **36**, 3195 (1965).

[5]D. F. Stein and J. R. Low, *J. Appl. Phys.* **31**, 362 (1960).

A slip band formed without cross slip is actually a single-ended pileup; thus the results of such bands can be compared with the calculation of Eshelby *et al.*[6] The agreement is very good.

By varying the cube edge length, the effect of grain size on the stress concentration, the shear strain, and the shear strain rate can be obtained. The implications of these factors on the lower yield stress are discussed.

Calculations on the formation of a slip band in an infinite crystal are also made to examine the effect of trailing dislocations on the velocity of the leading dislocation. This situation should be considered in those experiments in which dislocation velocity is determined as the ratio of the distance between the leading dislocation and its source to the loading time. Calculated results are compared with the experimental data of Stein and Low. When the applied stress in their expression is replaced by the effective stress, the stress dependence of velocity should be weaker and is time dependent.

A GRAPHICAL METHOD FOR DETERMINING THE SCHMID FACTOR

B. T. M. Loh

In studying dislocation activities and slip behavior of crystals, we often desire to know the shear stresses resolved from the applied load on possible slip planes in the slip direction. The slip plane normal and the slip direction are always perpendicular to each other, and they form a slip system. The resolved shear stress for a given slip system can be calculated from the geometric relation between the crystal orientation and the loading axis and is a product of a geometric factor (usually called the Schmid factor) and the applied stress. When there are many Schmid factors to be calculated, the procedure can be very lengthy; therefore, we developed a quick graphical method that can provide the value of the Schmid factor for *any* slip system in *any* crystal structure. In brief, a double polar net is constructed that consists of two polar nets centered around two reference poles, each pole tilting 45° in opposite directions from the center of the stereographic projection. A Schmid factor map associated with the double polar net is also plotted. This net is used to determine the position of the loading axis on the Schmid factor map for any given slip system that is imagined to coincide with the two reference poles, and the Schmid factor of the slip system can be read immediately from the map. Copies of the double polar net and the Schmid factor map are available on request.

[6] J. D. Eshelby, F. C. Frank, and F. R. M. Nabarro, *Phil. Mag.* **42**, 351–64 (1951).

TECHNIQUE AND EQUIPMENT DEVELOPMENT

Transmission Electron Microscopy

C. K. H. DuBose

Experience during the past year has shown our equipment for preparing foils for transmission electron microscopy to be reliable and applicable to a wide variety of materials. Basically, this equipment consists of a jet polisher for "dimpling" $\frac{1}{8}$-in.-diam specimens and an electropolishing cell with a light detector that is semiautomatic in the final preparation stage. A detailed report describing the equipment and its operation is available.[7] Since publication of the report two notable improvements have been made. In the jet polisher, better control of the "dimple" edges, and thus of the final shape of the dimple, could be obtained by use of capillary tubing for the jet nozzle. The nozzle previously had been hot drawn over a mandrel. A much smoother jet stream is now achieved as well as more accurate control of jet size. A discussion of the effect of current density on dimple shape has been published.[8]

A tenfold increase in sensitivity of the light detector system was achieved by replacing the photo transistor originally used with an improved model (crystalonics FF 600) suggested by T. M. Gayle of the ORNL Instruments and Controls Division. Spectral response is compatible with both infrared and visible light detection. This enables us now to use chromic acid solutions, which are nearly opaque to visible light, for electropolishing.

[7] C. K. H. DuBose and J. O. Stiegler, *Semiautomatic Preparation of Specimens for Transmission Electron Microscopy*, ORNL-4066 (February 1967).

[8] C. K. H. DuBose and J. O. Stiegler, "Controlled Jet Polishing of Specimens for Transmission Electron Microscopy," *Rev. Sci. Instr.* **38**, 694–95 (1967).

Extraction Replication

R. E. Gehlbach

In studying microstructures of complex materials, transmission techniques often prove inadequate. By nature such materials are full of holes and large foreign inclusions and often are chemically inhomogeneous. Because of chemical gradients, dissolution is nonuniform, holes enlarge, and particles fall out. Consequently, it is difficult to obtain large thin areas; and those that occur are suspect, for "better" areas are more likely to thin uniformly, giving rise to sampling bias.

To overcome some of these limitations, we developed techniques for extracting precipitate particles for examination by electron microscopy, electron diffraction, and electron probe microanalysis.[9] We are able to retain the spatial distribution of particles existing in the bulk material, and by eliminating matrix effects we are able to examine the structure and composition of individual particles. The technique is useful both for systems containing extensive but inhomogeneous precipitation and for those in which thin grain-boundary films form that are undetectable by transmission techniques.

By combining the extraction technique with an x-ray microanalyzer attachment for our microscope, we are able to obtain microstructures, diffraction patterns, and chemical analyses of a single area without moving the specimen and without introducing effects from matrix excitation. We are applying these techniques routinely to studies of precipitation in complex nickel-base alloys.

PRECIPITATION IN HASTELLOY N

R. E. Gehlbach H. E. McCoy, Jr.[2]

Hastelloy N, a nickel-base molybdenum-chromium-iron alloy developed at ORNL for its excellent creep strength and resistance to corrosion by molten fluoride salts, exhibits the loss in high-temperature ductility characteristic of nickel-base alloys. It is used as the reactor vessel structural material for the MSRE, and irradiation at the MSRE service temperature has been found to cause further embrittlement, its effect being essentially superimposed on that of the unirradiated material.

Examination of several specimens indicated that extensive grain-boundary precipitation occurred in the temperature range of the ductility decrease. Thus we are investigating the pattern of precipitation in this system – its response to various thermomechanical treatments and its relation to mechanical properties – and identifying those precipitates that may be beneficial as well as those deleterious to maintaining good ductility. We are using several tools, including extraction replication, transmission electron microscopy, bulk microprobe, microprobe attachment for the electron microscope, x-ray and electron diffraction, and autoradiography.

The microstructure is characterized by stringers of massive carbide particles having the composition M_6C. This carbide is high in molybdenum and nickel and is also enriched in silicon (approximately 2.5%) as compared with the matrix (approximately 0.3%). A fine grain-boundary precipitate having the same crystal structure as M_6C forms when the alloy is heated for long periods of time in the temperature range of 600 to 900°C (Fig. 5.6). Several precipitate morphologies can be present in the grain boundaries, depending on the thermal and mechanical history. In air-melted heats, the M_6C does not appear to dissolve appreciably as the temperature is increased. At about 1300°C, the massive M_6C particles begin to transform to an intergranular lamellar product, which is lower in molybdenum and silicon and has a different crystal structure.

Modifications in the composition of Hastelloy N to improve its properties have indicated that decreasing the molybdenum content slightly eliminates nearly all of the M_6C normally present. The addition of a small amount of titanium (<0.5%) results in formation of at least two different phases, one being Ti(C,N). These can assume various morphologies (Fig. 5.7); their effects are being assessed.

[9] R. E. Gehlbach and J. T. Houston, "Application of Electron Metallography to Precipitation Studies of Hastelloy N," to be published with the technical papers of the 21st AEC Metallography Group Meeting held at Brookhaven National Laboratory on May 10–12, 1967.

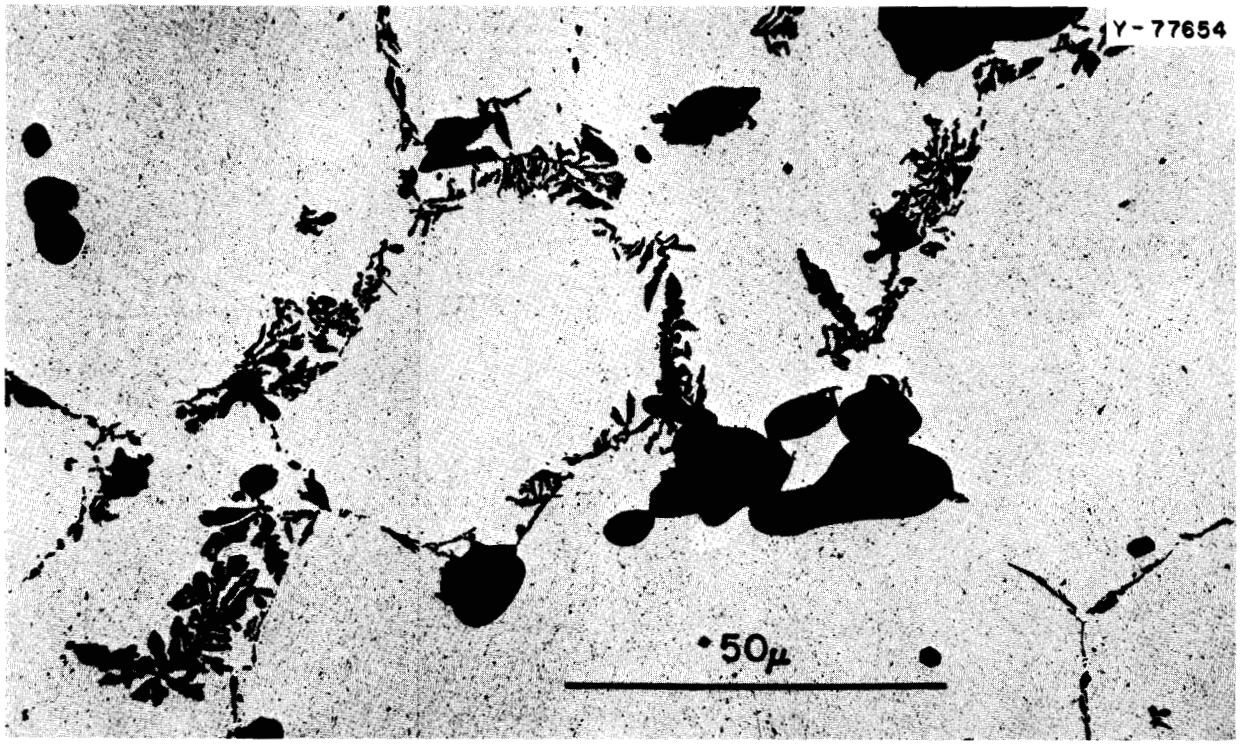

Fig. 5.6. Extraction Replica of Grain Boundary and Blocky M_6C Precipitate in Hastelloy N Aged 4 hr at 870°C.

PHOTO 89116

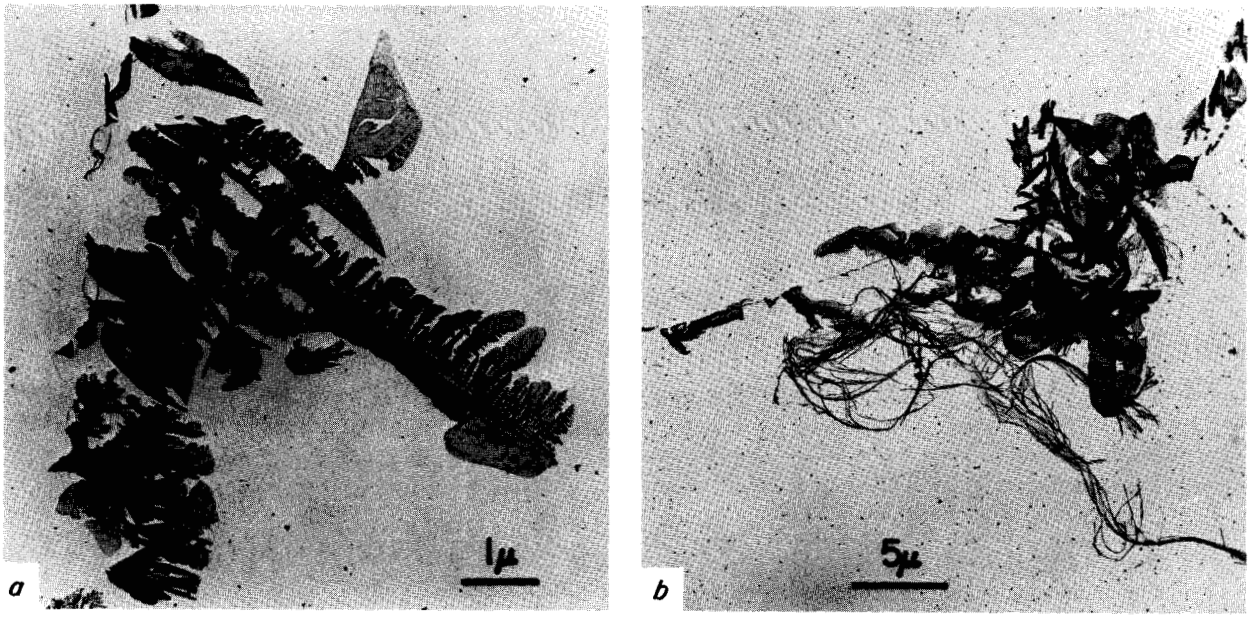

Fig. 5.7. Extraction Replicas Showing Two Forms of Grain-Boundary Precipitate in Titanium-Modified Hastelloy N. (*a*) 0.45% Ti, aged 30 min at 500°C; (*b*) 0.15% Ti, aged 30 min at 650°C.

6. Electronic Properties of Metals and Alloys

J. O. Betterton, Jr.

The object of these studies is basic information on electronic properties of metals and alloys. Experiments consist of (1) Mössbauer spectra for study of electronic states near the nuclei; (2) low-temperature specific heats, superconducting transition temperatures, and electrical resistivities to study transition-metal alloying and superconductivity; and (3) galvanomagnetic experiments on transition-metal crystals to determine connectivity of their Fermi surfaces.

A new Mössbauer technique, Coulomb-recoil-implantation, was developed in collaboration with the Physics Division. This method will be applied to future studies of impurities in solids, with particular emphasis on magnetic properties. We are studying magnetic moments and electronic density at nickel nuclei in nickel alloys with the Mössbauer effect in ^{61}Ni. Initial measurements have begun in the copper-nickel system.

A systematic alloying study has been undertaken of the early transition metal, zirconium. Earlier studies had shown the effects of additions of B-subgroup solutes (i.e., alloys of the type transition metal–simple metal). We completed our study of the effects of transition metals Ti, Hf, and Sc on the low-temperature specific heat of zirconium and nearly completed similar work with Nb, Mo, Re, and Ru. There appears to be a clear separation in alloying behavior between transition-metal solutes to the right of zirconium in the periodic table, which appear to have extra electrons localized near the solutes, and transition metals in the same column with zirconium, elements to the left (Sc), and the B-subgroup solutes, all of which appear to show alloying effects within the framework of the band structure.

The electrical resistivity effects per atomic percent of the transition metals to the right of zirconium were measured and showed widely variable values in a manner very similar to effects of transition-metal impurities on the resistivity of copper and aluminum. Friedel interpreted the latter in terms of virtually bound states near the impurity atoms, and zirconium alloys appear to be another example of the same phenomenon. With further systematic study of zirconium alloys a more detailed separation of various alloying factors, such as those dependent upon electronic density and compositional and structural factors, should be possible.

COULOMB-RECOIL-IMPLANTATION MÖSSBAUER EXPERIMENTS WITH ^{73}Ge (ref. 1)

Gordon Czjzek — John C. Love[2]
J. L. C. Ford, Jr.[3] — Felix E. Obenshain[3]
Horst H. F. Wegener[4]

Nuclear states suitable for Mössbauer studies can be populated by Coulomb excitation.[5–7] We developed a new method, combining the Coulomb-recoil-implantation technique, recently used in conjunction with perturbed angular correlation

---

[1]Abstracted from *Phys. Rev. Letters* **18**, 529 (1967); also in *Phys. Div. Ann. Progr. Rept. Dec. 31, 1966*, ORNL-4082, pp. 82–84.

[2]National Science Foundation Cooperative Fellow from the Ohio State University.

[3]Physics Division.

[4]Temporary employee from the University of Erlangen, Germany.

[5]D. Seyboth, F. E. Obenshain, and G. Czjzek, *Phys. Rev. Letters* **14**, 954 (1965).

[6]Y. K. Lee *et al.*, *Phys. Rev. Letters* **14**, 957 (1965).

[7]G. Czjzek, J. L. C. Ford, Jr., F. E. Obenshain, and D. Seyboth, *Phys. Letters* **19**, 673–75 (1966).

measurements,[8,9] with the Mössbauer effect. This method extends the range of application of Coulomb-excitation Mössbauer experiments, providing a wider selection of host materials for a given target nucleus. In many cases information about solid-state and nuclear properties goes beyond that obtainable by Coulomb-recoil-implantation perturbed angular correlation measurements. In this experiment, we have implanted Coulomb-excited ^{73}Ge into metallic chromium and observed the Mössbauer effect with the 67.0 kev deexcitation radiation.

LOW-TEMPERATURE SPECIFIC HEATS OF Zr-Ti, Zr-Hf, AND Zr-Sc ALLOYS[10]

J. O. Betterton, Jr. J. O. Scarbrough

The specific heats of hexagonal Zr-Ti, Zr-Hf, and Zr-Sc alloys were measured at 1.1 to 4.2°K. Maxima in both the electronic specific heat coefficient γ and in the superconducting transition temperature T_c were observed at 60 at. % Ti in the zirconium-titanium system. No superconductivity was found in the zirconium-scandium system, although γ rose to high values for pure scandium and a minimum in γ occurred near 10 at. % Sc. In the zirconium-hafnium system γ was nearly linear between values for the pure elements. The Debye temperature θ_D, after correction for atomic mass and volume, deviates negatively near 60 at. % Ti in titanium-zirconium, positively near hafnium in zirconium-hafnium, and in an S-type manner in zirconium-scandium. The effects of scandium in depressing γ in the zirconium-rich region are in qualitative agreement with dependence on electron-to-atom ratio indicated by earlier B-subgroup solute effects in zirconium-rich alloys. The γ for zirconium-scandium alloys, after a correction for phonon enhancement and with the assumption of a rigid band in the alloys, correlates fairly well with the electronic density of states for pure zirconium, calculated by Loucks.[11] The rigid band approximation, on the other hand, cannot explain the maxima in γ and T_c in zirconium-titanium alloys, which involve no change of electron-to-atom ratio. Rather, the maximum may arise from differences in the relative energies of the third and fourth bands in titanium and zirconium, with a crossing of these bands in the alloys. The small decrease in γ of zirconium with hafnium additions is also inconsistent with the rigid band model, since no change of electron-to-atom ratio occurs in the zirconium-hafnium system. The γ and T_c are related to both the density of states and the electron-electron interactions, and although clear separation of the two factors is not possible, a reasonable interpretation can be made assuming that the electron-phonon interaction is nearly constant.

LOW-TEMPERATURE SPECIFIC HEATS OF ZIRCONIUM WITH SMALL ADDITIONS (0–5 at. %) OF Nb, Mo, Re, AND Ru

J. O. Scarbrough J. O. Betterton, Jr.

Large increases in the superconducting transition temperature occur in zirconium with additions of Nb, Mo, Re, and Ru. Specific heat studies show that the electronic specific heat coefficient γ, the Debye temperature θ_D, the superconducting transition temperature T_c, and the interaction $(S - J)$ responsible for superconductivity follow with only modest deviations the following linear relations for atomic fraction solute x less than 0.05.

$$\gamma = 2.8 + 44x \quad (\text{mj mole}^{-1}\ ^\circ\text{K}^{-2})$$

$$\theta_D = 291 - 1300x \quad (^\circ\text{K})$$

$$T_c = 0.49 + 73.4x \quad (^\circ\text{K})$$

$$(S - J) = 0.26 - 0.43x \quad (\text{ev atom})$$

The above contrasts sharply with earlier alloying effects of B-subgroup elements Ag, Cd, In, Sn, and Sb on the electronic specific heat of zirconium, $\gamma = 2.8 + 1.6xn$, where n is the solute valency. Further, the former effects do not appear to be modified significantly by change of crystal structure in the Zr-Mo, -Re, and -Ru alloys from hexagonal to cubic (+ small amount of ω) as solute content increases. The indifference to crystal structure and to the number of valency electrons suggests a failure of the rigid band model in these cases of transition-metal solutes to the right of zirconium in the periodic table and the formation of localized states near atoms of these solutes.

---

[8] L. Grodzins, R. Borchers, and G. B. Hagemann, *Phys. Letters* 21, 214 (1966).

[9] F. Boehm, G. B. Hagemann, and A. Winther, *Phys. Letters* 21, 217 (1966).

[10] Abstract of paper submitted for publication in *The Physical Review*.

[11] T. L. Loucks, "Electronic Structure of Zirconium," to be published in *The Physical Review*.

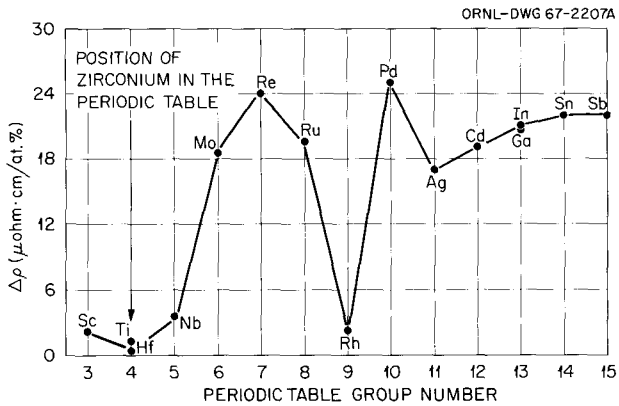

Fig. 6.1. Effects of Solute Elements on the Electrical Resistivity of Dilute Zirconium Alloys at 4.2°K.

ELECTRICAL RESISTIVITIES OF ZIRCONIUM ALLOYS

J. O. Betterton, Jr. D. S. Easton

The change in electrical resistivity with 1 at. % additions of various elements to zirconium varies widely with the group number of the solute in the periodic table. These resistivity coefficients are shown in Fig. 6.1, where the points represent slopes of residual resistivity vs composition curves for a series of alloys with hexagonal structure, except for the solutes molybdenum and ruthenium, which were measured in alloys with cubic structure. The slope of the resistivity curve in the zirconium-rhenium system showed no effect of crystal structure change, hexagonal to cubic, as the rhenium content increased, and the molybdenum and ruthenium points have been plotted on Fig. 6.1 with the assumption that the matrix crystal structure can be neglected.

Variation of the resistivity coefficients of transition metal solutes in copper- and aluminum-base alloys, which was very similar in form to that of Fig. 6.1, was interpreted by Friedel in terms of virtually bound states.[12,13] Such states are formed near solute atoms by resonance of the electrons in the atomic levels of the solute with electrons of the Fermi surface of the matrix metal. Virtual states have also been reported in alloys between transition metals,[14–16] and it is reasonable to interpret the resistivities of zirconium alloys with transition-metal solutes to its right in the periodic table in the same way. This interpretation provides further support for the formation of localized states on the specific heat properties of zirconium.

GALVANOMAGNETIC PROPERTIES OF ZIRCONIUM

J. O. Betterton, Jr. D. S. Easton

A recent calculation of the electronic structure of zirconium by Loucks[11] at Iowa State University is in agreement with the closed and compensated character of galvanomagnetic measurements. One uncertainty in the Loucks theory is whether the third- and fourth-zone holes are continuous along the hexagonal axis in the k-space. Galvanomagnetic properties of crystals whose axes are within 4° of the basal plane indicate that the surface is closed. However, because of the narrowness of the angles over which the open-orbit singularities in magnetoresistance could be present, a crystal oriented closer to the basal plane and having accurate crossing of the magnetic field and the hexagonal axis would be very desirable. We have not made this test, but a goniometer that tilts the crystal rotation axis has been constructed for operation in liquid helium and in the magnetic field for this experiment. Higher purities and higher magnetic fields are needed for investigation of the anomalous transverse voltages in zirconium.[17] Recent increases in the purity of zirconium and the construction of a 76-kilogauss solenoid will increase 30-fold the magnetoresistance and even transverse voltages, which depend upon the square of the effective magnetic field strength.

[12] J. Friedel, *Can. J. Phys.* **34**, 1190 (1956).

[13] E. Daniel and J. Friedel, *Low Temperature Physics LT9, Proceedings of the IXth International Conference on Low Temperature Physics, Columbus, Ohio, August 31—September 4, 1964*, ed. by J. G. Daunt *et al.*, Plenum Press, New York, 1965, pp. 933–54.

[14] Yu. N. Tsiovkin and N. V. Volkenshtein, *Soviet Phys. JETP (English Transl.)* **21**, 527 (1965).

[15] M. P. Sarachik, *J. Appl. Phys.* **35**, 1094 (1964).

[16] P. A. Wolff *et al.*, *J. Appl. Phys. Suppl.* **33**, 1173 (1962).

[17] D. S. Easton and J. O. Betterton, Jr., *Metals and Ceramics Div. Ann. Progr. Rept. June 30, 1966*, ORNL-3970, pp. 29–31.

ZONE PURIFICATION OF ZIRCONIUM

D. S. Easton J. O. Betterton, Jr.

Modifications of an existing electron-beam zone refiner[18] enabled us to make large numbers of zone passes, during which the partial pressures of gases were reduced sufficiently so that contamination did not take place. The increased number of passes allowed zone refining from oxygen; a gradient occurred, with the oxygen concentration diminishing toward the end of the rod as usual for the case of solidus-to-liquidus ratio (K) greater than unity. This gradient can be observed both in the analyzed oxygen content[19] and in the resistivity ratio. The correlation along such a gradient between resistivity at 4°K and oxygen content is shown in Fig. 6.2. The slope of the curve, 7 μohm-cm/at. % O, corresponds well with the average value, 6.8 $\pm$ 1.0 μohm-cm/at. %, given in the literature.[20–22] This shows that the oxygen impurity accounts for most of the change in electrical resistivity along the zoned rod. The intercept of this curve indicates that a significant amount of residual resistivity remains, suggesting possible electron scattering from physical defects and buildup of impurities with $K < 1$, such as carbon, at the end of the zoned length.[23]

Studies of the partial pressures over molten zirconium during zoning showed that most gases were evolved rapidly during the early passes and that hydrogen, methane, ethane, and propane were continuously evolved in all passes. The oxygen partial pressure, 10^{-12} to 10^{-13} torr, is considered to be too low for significant purification or contamination by the transport through the gas phase.

Figure 6.3 illustrates a recent zone-refining experiment. The resistivity ratio attained after 35 passes was 1300, which is the highest yet attained in zirconium. One point illustrated on Fig. 6.3 is that when oxygen and other impurities are low enough so that the resistivity ratio exceeds 800, this ratio is not decreased by annealing. This is important, since it is necessary to anneal the as-zoned rod to produce strain-free crystals.

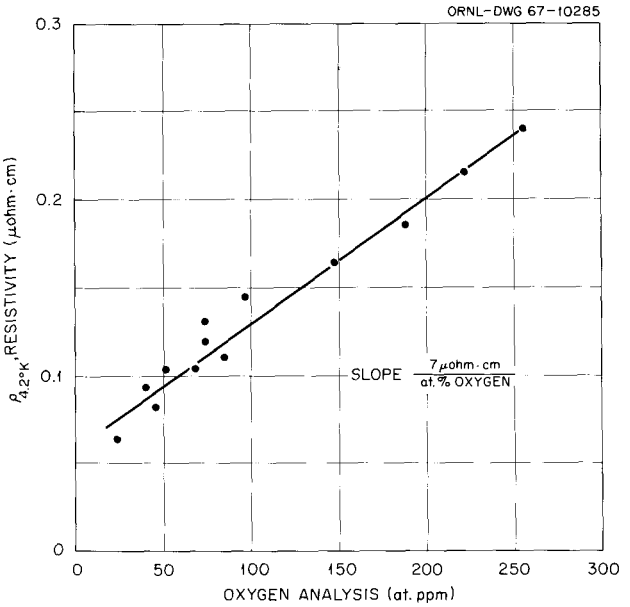

Fig. 6.2. Correlation Between Oxygen Content and Resistivity in Zone-Refined Zirconium. Annealed 48 hr at 800°C.

EFFECTS OF HEAT TREATMENT AND IMPURITIES ON CRITICAL CURRENT DENSITY OF TRANSITION-METAL SUPERCONDUCTORS

J. O. Betterton, Jr. D. S. Easton
J. O. Scarbrough

The program to investigate the role of interstitial impurities in increasing the precipitation enhancement of critical current density[24] was continued by an experiment that showed that Zr–50 at. % Nb alloy after zone purification had very little precipitation enhancement. Another result was that the

[18] D. S. Easton and J. O. Betterton, Jr., *Metals and Ceramics Div. Ann. Progr. Rept. June 30, 1965*, ORNL-3870, pp. 32–33.

[19] Analyses performed under the supervision of W. R. Laing, Analytical Chemistry Division.

[20] R. M. Treco, *Trans. Am. Soc. Metals* **45**, 254 (1953).

[21] D. L. Douglas, *At. Energy Rev.* **1**, 101–4 (1963).

[22] L. Renucci and J. P. Langeron, *Compt. Rend.* **264**, 673 (1967).

[23] Nitrogen impurity less than 3 at. ppm at the low-oxygen end of the bar was too small to be significant for interpretation of the intercept. Nitrogen increased to 12 at. ppm at the high-oxygen end of the rod, and thus nitrogen was zone refined at the same time as oxygen in this experiment.

[24] J. O. Betterton, Jr., G. D. Kneip, Jr., D. S. Easton, and J. O. Scarbrough, U.S. Patent 3275480, Sept. 27, 1966, and U.S. Patent 3215569, Nov. 2, 1965.

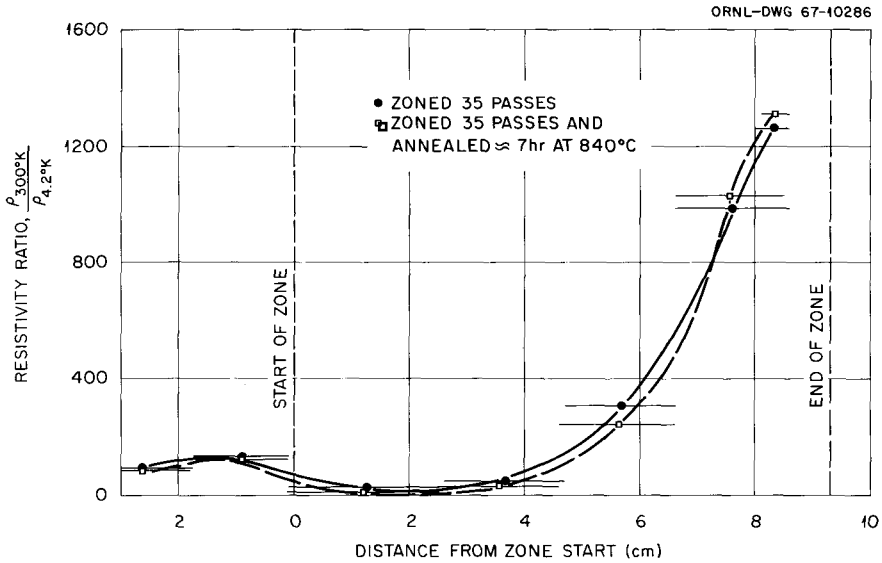

Fig. 6.3. Variation of the Resistivity Ratio Along a Zone-Refined Zirconium Rod.

alloy Ti–30 at. % Ta showed a larger precipitation increase in the oxygen-bearing alloy than in the alloy without oxygen addition. This is in contrast to Ti–60 at. % Ta, where we were unable earlier[25] to show any change in the precipitation enhancement with oxygen additions. Thus, for at least part of the composition range in each of the four alloy systems Zr-Nb, Hf-Nb, Ti-Nb, and Ti-Ta interstitial additives have increased the magnitude of the precipitation enhancement.

[25] J. O. Betterton, Jr., D. S. Easton, and J. O. Scarbrough, *Metals and Ceramics Div. Ann. Progr. Rept. June 30, 1966*, ORNL-3970, pp. 27–29.

7. Fundamental Ceramics Research

W. Fulkerson

The Fundamental Ceramics Research Program has been established to encourage a more coordinated effort of basic ceramics research in the Metals and Ceramics Division by establishing a common program to which several research groups can contribute. We anticipate that a coordinated program will lead to a better understanding of ceramic materials as well as to better exchange of ideas between fundamental and applied groups. As a mechanism for achieving this cohesion, we have decided to focus attention initially on a single material of general interest, uranium mononitride. This compound is a member of an important class of ceramics, the so-called refractory hard metals, and is also an important advanced nuclear fuel candidate.

URANIUM NITRIDE INTERGROUP BASIC RESEARCH PROGRAM

W. Fulkerson

Because of the nuclear fuels research on uranium nitride in the Ceramics Technology Group (see Part II, Chap. 18), good quality pressed-and-sintered specimens are available. Work is now under way in the Crystal Physics Group to grow large single crystals. Thus, research-quality specimens are available, and the prospects for specimens of improved quality are excellent. Furthermore, we will soon know enough about the thermodynamics of the uranium-nitrogen system to enable us to control the stoichiometry of UN during an experiment by regulating the nitrogen overpressure. This background work on UN is incentive for proceeding with more fundamental work on this material, some of which has already been initiated. This will eventually involve the cooperative efforts of 11 groups in the Division.

Uranium nitride is a metallic conducting compound; this explains its relatively high thermal conductivity, one of its important attractions as a reactor fuel. The Physical Properties Group is making careful measurements of thermal conductivity, electrical resistivity, and Seebeck coefficient, as functions of stoichiometry and of alloying with isomorphous actinide compounds. From these measurements, the magnitude and temperature dependence of the lattice and electronic components of the thermal conductivity can be determined. Some preliminary results are presented below.

To have a basis for the theoretical interpretation of transport and other property data for UN, the Theoretical Research Group is modifying its band-theory calculation techniques (see Chap. 10) to handle the UN case of two atoms per primitive cell. Initial calculations have been performed for TiO in order to compare to the augmented plane-wave method results for this material. As a check with experiment, electronic density of states calculated from band theory will be compared to the density of states obtained by the Theory of Alloying Group from low-temperature specific heat measurements.

To understand phenomena dependent on defect structure, such as the diffusion of fission-product impurities and mechanical creep, the self-diffusion coefficients of uranium and nitrogen must be determined. The self-diffusion of nitrogen in UN has been measured,[1] and preparations by the Diffusion in Solids Group are nearly complete to measure

[1] T. J. Sturials and M. A. DeCrescente, *Self-Diffusion of Nitrogen in Uranium Mononitride*, PWAC-482 (October 1965).

the self-diffusion of ^{232}U in UN as a function of stoichiometry for large-grained arc-melted specimens by a nondestructive alpha-spectroscopy method (see Chap. 4).

A number of other studies, including migration of implanted helium bubbles in a thermal gradient, creep, inelastic neutron diffraction, magnetoresistance, and surface reactions are being planned or await the availability of better quality single crystals.

THERMAL CONDUCTIVITY OF UN

J. P. Moore R. K. Williams
D. L. McElroy

Figure 7.1 shows some preliminary thermal conductivity data taken on a pressed-and-sintered UN pellet, 96% of theoretical density, containing about 1000 to 2000 ppm O as second-phase UO_2 (1 to 2 vol %). These data were obtained with the comparative longitudinal heat flow apparatus[2] and were corrected to theoretical density by dividing by the fraction of theoretical density. The oxide second phase was corrected for by assuming that it acts like pores of equal volume. The corrected data lie 12 to 15% lower than results reported by Battelle[3] for arc-melted theoretically dense UN as extrapolated from data above 200°C. An indication that the density correction we used is reasonable is that the electrical resistivity of the ORNL pellet was 156 microhm cm at room temperature, which is about 5% higher than the extrapolated BMI value for arc-melted material. The ORNL thermal conductivity data are near the lower boundary of the range of values reported by Battelle[4] for polycrystalline UN specimens. This range is indicated by the dashed curves on Fig. 7.1 and was obtained by correcting the BMI results to theoretical density and then extrapolating the data to temperatures below 200°C. Also shown on Fig. 7.1 is one point that we[5] obtained several years ago on a 94.5% dense specimen of UN that also had about 2 vol % oxide second phase. This point is about 7% below our present results.

The oxygen concentration in the present specimen will be reduced by heat treatment, and the thermal conductivity and electrical resistivity will be remeasured to demonstrate the effect of this impurity.

---

[2]J. P. Moore, R. S. Graves, T. G. Kollie, and D. L. McElroy, *Thermal Conductivity Measurements on Solids Between 20 and 150°C Using a Comparative-Longitudinal Apparatus: Results on MgO, BeO, ThO_2, $Th_xU_{1-x}O_{2+y}$, and Al-UO_2 Cermets*, ORNL-4121 (June 1967).

[3]R. W. Endebrock, E. L. Foster, Jr., and D. L. Keller, *Preparation and Properties of Cast UN*, BMI-1690 (August 1964).

[4]E. O. Speidel and D. L. Keller, *Fabrication and Properties of Hot-Pressed Uranium Mononitride*, BMI-1633 (May 30, 1963).

[5]T. G. Kollie, D. L. McElroy, R. S. Graves, and W. Fulkerson, "A Thermal Comparator Apparatus for Thermal Conductivity Measurements from 50 to 400°C," pp. 651–76 in *International Symposium on Compounds of Interest in Nuclear Reactor Technology*, ed. by J. T. Waber, P. Chiotti, and W. N. Miner, AIME Metallurgical Society, New York, 1964.

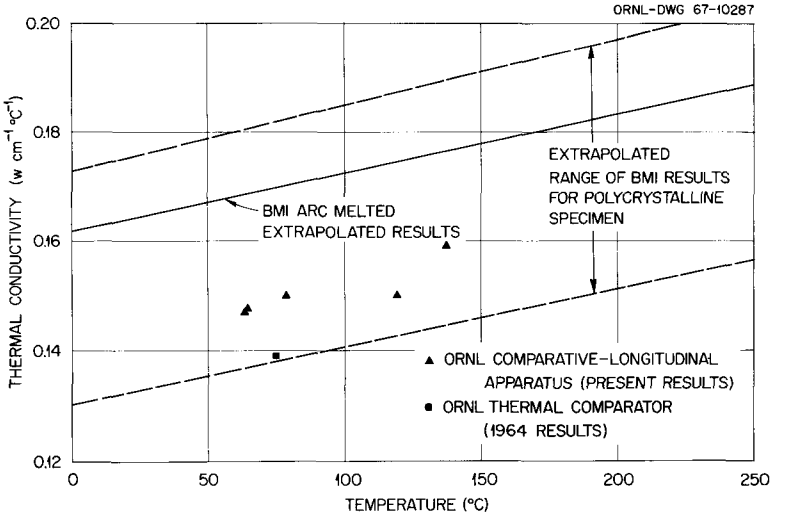

Fig. 7.1. Thermal Conductivity of Uranium Mononitride. Preliminary results for two pressed-and-sintered specimens compared to BMI results on arc-melted material.

8. Physical Ceramics Studies

C. S. Morgan

The increasing application of high-temperature technology has made the understanding of solid-state processes in ceramics more important. Sintering, diffusion, and deformation studies designed to advance our understanding of basic phenomena at high temperature in ceramic materials are being carried out. Densification kinetic studies have demonstrated the significance of plastic flow in sintering. Study of self-diffusion in thoria is intended to correlate the diffusion process with the thoria substructure. Deformation of single-crystal uranium dioxide is being analyzed to determine details of high-temperature dislocation behavior.

MATERIAL TRANSPORT IN SINTERING

C. S. Morgan

Extensive investigation of the initial densification kinetics of highly sinterable oxide powders has suggested that dislocation motion contributes substantially to the material transport.[1,2] Observation of the effect of isostatic pressing on subsequent densification of partially sintered ceramic powder compacts also suggests a dislocation contribution to the material transport. In these experiments powder compacts of thoria were partially sintered, isostatically pressed at 45,000 psi, and resintered. Small amounts of densification occurred, which were attributable to the isostatic pressing.[3] Results are summarized in Table 8.1.

The effect of isostatic pressing is seen more clearly in Fig. 8.1. Here ThO_2 powder compacts were heated to temperature at 3°C/sec without a measurable hold at temperature. The specimens were heated this way four times; they were then isostatically pressed at 45,000 psi and heated again. Additional densification occurred on this last heat treatment. An isostatic pressing effect was not observed on MgO and CaO compacts unless they contained added colloidal particles of ThO_2 or SiO_2.

The results are in agreement with the postulate that dislocations are put into the partially sintered compacts during isostatic pressing. At room temperature the dislocations can not move extensively and tend to pile up at obstacles, but on heat treatment their movement results in densification in addition to what would have occurred without the pressing step.

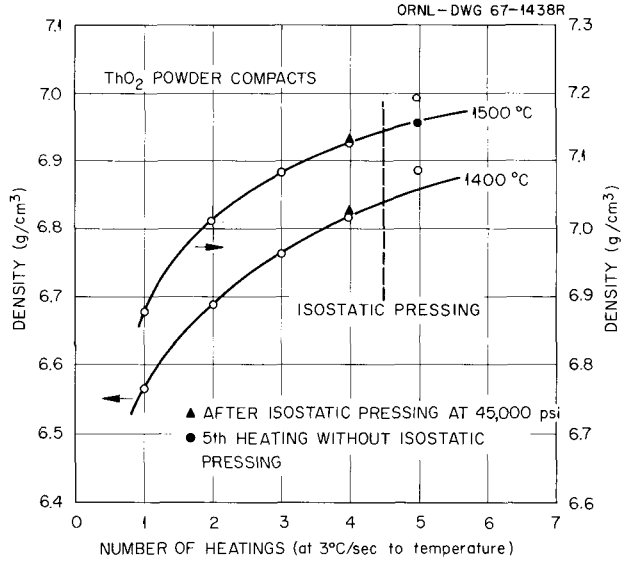

Fig. 8.1. Variation of Density with Number of Firings for ThO_2 Specimens Brought to Temperature Without a Measurable Hold at Temperature. The specimens were isostatically pressed after the fourth heating.

[1] C. S. Morgan and C. S. Yust, *J. Nucl. Mater.* **10**, 182–90 (1963).

[2] C. S. Morgan, C. J. McHargue, and C. S. Yust, *Proc. Brit. Ceram. Soc.* **3**, 177–84 (1965).

[3] C. S. Morgan and L. L. Hall, *J. Am. Ceram. Soc.* **50**, 382–83 (1967).

Table 8.1. Densification Response of Powder Compacts

Initial Firing	Material	Compact Density, g/cm^3			
		After Initial Firing	After Isostatic Pressing at 45,000 psi	After Refiring to 1250°C at 3°C/sec	Increase (from highest previous density)
1 hr at 1250°C	ThO_2	6.31	6.32	6.34	0.02
		6.30	6.30	6.31	0.01
		6.31	6.31	6.33	0.02
To 1450°C at 3°C/sec	ThO_2	8.11	8.10	8.13	0.02
		8.16	8.16	8.19	0.03
To 1450°C at 3°C/sec	ThO_2–1.4% CaO	7.00	7.00	7.06	0.06
		6.91	6.92	6.95	0.03
		6.84	6.84	6.87	0.03

PROGRESSIVE SHAPE CHANGES OF THE VOID DURING SINTERING[4]

Lida K. Barrett[5] C. S. Yust

The geometric changes that occur in the void in a sintering mass of copper particles were examined in detail. The changes in void structure were analyzed by study of two-dimensional cross sections and drawings of three-dimensional void volumes reconstructed from closely spaced serial sections. A phenomenological model of the process of void removal is presented, based on the analysis of the void shape changes. The irregular nature of the stacking of particles and of the particles themselves is accounted for in the model. A mathematical quantity, the proximity number, is defined and used as a tool to facilitate the description of the void removal. The pattern of void removal is largely independent of the original shape of the particle and the green density, although the rate of removal is influenced by these factors. That part of the void having the smallest dimensions and the most complex configuration (i.e., having the lowest proximity number) is removed first, followed by that part of the void having the next lowest proximity number. Isolated porosity occurs first as large definitely nonspherical sections of the void volume. Porosity does not spheroidize until approximately 99% of theoretical density is attained. The void shapes observed in this work are compared with structures observed in other materials. The void removal process described here is contrasted with that described by other sintering models.

[4]Abstracted from *Trans. Met. Soc. AIME* **239**(8), 1172–80 (August 1967).

[5]Consultant from the University of Tennessee.

DEFORMATION OF SINGLE-CRYSTAL URANIUM DIOXIDE

C. S. Yust

Our intent is to achieve an understanding of the deformation of the UO_2 lattice, which, in combination with studies on grain-boundary processes, may lead to useful knowledge concerning deformation of polycrystalline ceramics. Stoichiometric uranium dioxide single crystals for compression testing are prepared in specific orientations in the form of rectangular prisms. The surfaces are chemically polished to remove surface sources of dislocations and to permit the observation of slip traces. Specimens have been deformed at temperatures ranging from 550 to 1400°C. Two different orientations were investigated at 550°C and both of these orientations yielded slip on the anticipated $\{100\}\langle 110\rangle$ slip system. Electron micrographs of the slip plane of deformed uranium dioxide revealed numerous loops, extended in $\langle 110\rangle$ directions (Fig. 8.2). Analysis of the Burgers vector for some of the dislocation loops indicated that the extended sides of the loops are of an edge

Fig. 8.2. Dislocation Loops in Single-Crystal UO_2 Deformed 4.5% in Compression at 1000°C. Loops are extended in a ⟨110⟩ direction. 15,000×.

character. In specimens deformed extensively at a very slow rate at 1400°C, dislocation networks formed as deformation progressed.

SUBSTRUCTURE EFFECT ON DIFFUSION OF THORIUM IN ThO_2

L. E. Poteat[6] C. S. Morgan

The influence of substructure on self-diffusion in ThO_2 is being evaluated by measuring the diffusion coefficient in single crystals, sintered powder compacts, and sol-gel specimens. A wide range of grain sizes is being tested to determine the relative contributions of grain-boundary and volume diffusion. Preliminary results with single crystals indicate that at 1500°C the diffusion coefficient is sharply lower than values obtained on sintered powder specimens, while at 1300°C it is more comparable.

[6]Consultant from Clemson University, Clemson, S.C.

COMPRESSIVE CREEP OF SOL-GEL ThO_2

L. L. Hall C. S. Morgan

Cylindrical specimens of ThO_2 prepared by sintering of pressed sol-gel powder at 1800°C were examined after compressive creep. Extensive grain-boundary sliding and twisting occurred during the creep. This caused the specimen density, which was initially about 91% of theoretical, to rise and then decline as the creep continued. Sol-gel specimens exhibited creep at temperatures as low as 650°C. Deformation of more than 13% was observed at 1450°C. During creep under low constant load at 1500°C, a characteristic three-stage curve was obtained. Strengths approaching 20,000 psi were observed at 1450°C.

9. Physical Properties

D. L. McElroy

We are attempting to understand heat transport phenomena in solids over a broad temperature range from data obtained by use of accurate methods of measuring interrelated physical properties. We are primarily concerned with accurate high-temperature thermal conductivity data, but complementary measurements of other properties such as electrical resistivity, thermoelectric power, specific heat, and thermal radiative properties assist this understanding. Property analysis on certain well-characterized solids permits evaluation of existing theories, and this may lead to reliable property prediction outside the range of available data. This program serves a practical purpose, since needed high-temperature data and the development of measurement capacity are natural by-products.

HEAT TRANSPORT IN SILICON FROM 100 TO 1300°K (ref. 1)

W. Fulkerson, J. P. Moore, D. L. McElroy, R. K. Williams, R. S. Graves

Results are presented of measurements of the thermal conductivity (90 to 1328°K), the electrical resistivity (300 to 1273°K), and the Seebeck coefficient (350 to 1273°K) for single-crystal and large-grained polycrystalline specimens of 99.99+% pure silicon. The thermal conductivity above 387°K was measured by an absolute radial heat flow technique, while below 350°K an absolute longitudinal method was used. Some intermediate thermal conductivity measurements from 300 to 400°K were made on a polycrystalline material with a comparative longitudinal heat flow apparatus. The estimated errors of these three thermal conductivity methods were ±2% ±2°K, ±1.2% ±0.1°K, and ±4.0% ±1°K respectively. The estimated error was ±1.4% ±2°K for the electrical resistivity measurements and ±1.6% ±2°K for the Seebeck measurements. The thermal conductivity values were compared to contradictory data from the literature and corroborate the higher temperature results of Glassbrenner and Slack.[2] We agree with their conclusion that the electronic contribution is reasonably close to theoretical estimates that include a large ambipolar diffusion term. The temperature dependence of the lattice thermal resistance has been compared to various theoretical models, but no approach seems to explain the data in detail. An abrupt slope change in the thermal resistivity at about 670°K is a major cause of the difficulty.

[1] Abstracted from paper to be submitted to *Physical Review* for publication.

ELECTRONIC HEAT TRANSPORT ANALYSIS[3]

W. Fulkerson, J. P. Moore, R. K. Williams, D. L. McElroy

Critical evaluation of the temperature dependence of the Lorenz number is a major part of the analysis of heat transport in metals and alloys. Last year[4] using two approaches we obtained Lorenz numbers for certain metals that deviated from the Sommerfeld limit. Two further more powerful extensions were tested and revealed similar deviations.

[2] C. J. Glassbrenner and G. A. Slack, *Phys. Rev.* 134, A1058–69 (1964).

[3] This section is largely summarized from a paper by W. Fulkerson and R. K. Williams, in preparation.

[4] W. Fulkerson, R. K. Williams, and J. P. Moore, *Metals and Ceramics Div. Ann. Progr. Rept. June 30, 1966*, ORNL-3970, pp. 38–39.

First, the curve plotting approach was extended by use of computer statistical fitting techniques assuming theoretical functional forms for the temperature dependence of the lattice thermal conductivity and the Lorenz number of a pure metal. Two theoretical calculations[5,6] for the temperature dependence of the Lorenz number $L(T)$ were approximated to better than 3% by a simplified equation

$$L(T) = L_\infty[1 - \exp(T/\theta + 0.214)] , \qquad (1)$$

where the exact interpretation of θ is yet to be established. Three lattice thermal conductivity expressions are used: $K_L = 0$; $K_L = A/T$; and $K_L = A/T + B/T^2$. The complexity of the expression chosen is related to the relative magnitude of the ratio of lattice to total thermal conductivity. Data are analyzed, presuming L_∞ and θ are unknowns, to choose θ values corresponding to the minimum standard deviation of the fit to the thermal conductivity and electrical resistivity data input. The θ value at a minimum standard deviation consistent with the data input is used to obtain the lattice thermal conductivity and L_∞, the high-temperature limit of $L(T)$.

A second approach involves analysis of the effect of dilute controlled impurity additions on the lattice and electronic thermal conductivity of a pure element. For certain alloy additions, we assume that the lattice thermal conductivity is unchanged or that the change can be calculated. We further assume that the electronic thermal resistivity can be analyzed in terms of an impurity part and a part characteristic of the pure defect-free element, both parts unrestricted with respect to the temperature dependence of the Lorenz number. Then accurate thermal conductivity and electrical resistivity data at a given temperature on a pure element and a dilute alloy, say tungsten and W–2% Ta, can be treated to yield the Lorenz number of the pure defect-free metal at this temperature. By doing this at several temperatures, the temperature dependence of this Lorenz number can be obtained.[7]

Within experimental uncertainties both methods yield the same results for tungsten. Similar results were obtained for iron. These are the only two elements for which sufficient accurate electrical resistivity and thermal conductivity data exist to permit the comparison. This lack of accurate data is the reason for our increased measurement activity in the 100 to 400°K range. In addition the statistical technique was applied to data available for aluminum, copper, and platinum. The results indicate that the Wiedemann-Franz-Lorenz law is obeyed by aluminum and copper, but for the transition metals high-temperature deviations were noted.

These deviations are of extreme importance in predicting thermal conductivity values outside the range of available data and in understanding heat transport. There are at least three possible causes for high-temperature deviations: (1) ambipolar transport due to band overlap, (2) inelastic electron-electron scattering, and (3) nonnegligible second-order terms in the series solution of the Boltzmann transport equation. We are studying the theories of these mechanisms, and we are attempting to obtain electrical resistivity and thermoelectric power data to high temperatures for interpretation.

FERROMAGNETIC STUDIES

T. G. Kollie D. L. McElroy

The energetics of ferromagnetic materials are being studied by determining specific heat, electrical resistivity, and thermoelectric power of iron, nickel, and iron-nickel alloys.

A pulse calorimeter for measuring the specific heat of electrical conductors from 25 to 900°C was described.[8] The technique employed was unique in that a digital voltmeter, which was capable of recording 400 readings per second to a readability of 0.1% of full scale, was used to measure the transient temperature and power signals. A calculated determinate accuracy of 99% was achieved. Measurements of the specific heat of high-purity iron from 25 to 900°C confirmed this calculated accuracy and were repeatable to within ±0.5%. The calorimeter was capable of measuring the specific heat rapidly at temperature intervals as small as 0.1°C. Modifications are suggested to decrease the measurement errors to 0.5% and to increase the temperature range to from −190 to 1400°C.

[5] A. H. Wilson, *The Theory of Metals*, 2nd ed., The University Press, Cambridge, England, 1958.

[6] J. M. Ziman, *Proc. Roy. Soc. (London) Ser. A* **226**, 436–54 (1954).

[7] W. Fulkerson and R. K. Williams, *Proceedings of the Sixth Conference on Thermal Conductivity, Dayton, Ohio, Oct. 19–21, 1966*, pp. 807–19 (limited distribution).

[8] T. G. Kollie, "Specific Heat Determinations by Pulse Calorimetry Utilizing a Digital Voltmeter for Data Acquisition," accepted for publication in *The Review of Scientific Instruments*.

Using the pulse-heating calorimetric technique described above, we measured the specific heat of a second pure iron from 100 to 850°C. Our previous measurements on a less pure iron were confirmed and the discontinuity in the specific heat of iron was duplicated. The Curie transformation temperature was 7°C lower for the purer iron, probably due to temperature measurement errors. To overcome these and to improve the versatility of the technique, we constructed a second system that incorporates a specimen furnace to allow measurements from −190 to 1400°C.

Our electrical resistivity–thermoelectric power apparatus was modified to provide data continuously on iron to 1450°C. These measurements were completed on triple-zone-refined nickel to 1150°C as a prelude to specific heat measurements.

A study was initiated on iron-nickel alloys of the interaction of two cooperative phenomena – ordering and ferromagnetism. For example, Ni_3Fe has an order-disorder transition temperature of 503°C, a Curie temperature of 600°C in the disordered state, but a Curie temperature of 720°C in the ordered state. The order-disorder transformation is so sluggish that an ordered structure can be maintained above the transition temperature, and in this case the rapid pulse-heating method is ideal for use in property determinations.

HEAT FLOW RESULTS

We obtain accurate thermal conductivity results as a function of temperature for solids by three complementary techniques employing controlled radial or axial heat flow.

Radial Systems, 300 to 1300°K

J. P. Moore R. K. Williams
R. S. Graves D. L. McElroy

The radial system was used to provide data to complete the work quoted above on silicon. The system was also used to determine the thermal conductivity to 1300°K of a 2-in.-tall specimen of T-111 alloy by use of D-43 alloy backup disks to create a 9-in.-tall specimen stack (see Part II, Chap. 15 of this report).

By replacing the specimen stack with an instrumented heavy-wall cylindrical shell and an axial tube core heater, we devised a radial heat flow method for measuring the thermal conductivity of powder specimens contained in the 200-cm^3 annular space. Systematic checks using a MgO-nitrogen powder specimen established this system as capable of obtaining measurements repeatable to ±0.5% and accurate to ±2% between 300 and 1300°K for gas pressures below 2 atm. We measured thermal conductivity between 300 and 1300°K on vibratorily compacted ThO_2 microspheres in helium and argon up to 2 atm. The powder had a density of 84% of theoretical for ThO_2 and was composed of 64% of 400-μ-diam spheres and 20% of 44-μ-diam spheres. According to theory the effective thermal conductivity K_E of a gas-powder system should increase with temperature and K_E(He) should be 4 to 6 times K_E(Ar). However, our results were nearly independent of temperature, and K_E(He) was only twice K_E(Ar) [at 800°K K_E(He) was 0.0120 w cm^{-1}°K^{-1} and K_E(Ar) was 0.0062 w cm^{-1}°K^{-1}]. These results are due to the small size of the voids between particles, which limits the gas mean free path and creates a local high thermal resistance. Since the mean free path is pressure sensitive, one should observe a pressure effect on K_E. Indeed, we noted a 50% increase in K_E(Ar) and a 250% increase in K_E(He) when the pressure was increased from 0.3 to 2.0 atm. At sufficiently high pressures K_E should become pressure invariant. To pursue this, we are developing a dual-purpose radial heat flow system to extend the powder measurements to 10 atm and 1700°K. The same system will allow measurement on 1-in.-diam solid specimens rather than the 3-in. specimens required by the present apparatus.

There has been no significant advance in the development of the high-temperature guarded radial heat flow apparatus for measurements to 1800°K. The major obstacle to overcome is the electrical leakage between the measuring thermocouples and the core heater.

Comparative Longitudinal System[9]

J. P. Moore R. S. Graves
R. K. Williams

We have used a comparative longitudinal apparatus to measure the thermal conductivity between

[9]Many of these results are reported more fully by J. P. Moore, T. G. Kollie, R. S. Graves, and D. L. McElroy, *Thermal Conductivity Measurements on Solids Between 20 and 159°C Using a Comparative-Longitudinal Apparatus: Results of MgO, BeO, ThO_2, $Th_xU_{1-x}O_{2+y}$, and Al-UO_2 Cermets*, ORNL-4121 (June 1967).

300 and 425°K of small uninstrumented specimens sandwiched with indium foils between iron meter bars of known thermal conductivity. An error analysis indicated a measurement uncertainty of from ±2 to ±3%. Indium foils were selected to decrease the interfacial thermal resistance between the specimen and the meter bars. The interfacial resistance with indium foils decreased with increasing pressure in the range from 20 to 5000 psi and was independent of temperature from 300 to 425°K.

Thermal conductivity measurements were made on MgO, sol-gel thoria, and oxalate thoria specimens for a variety of densities, and the results were compared to the equation $K_m/K_{T.D.} = (1 - \rho')/(1 + \beta\rho')$, where K_m is the measured thermal conductivity, $K_{T.D.}$ is the thermal conductivity of theoretically dense material, and ρ' is the pore volume fraction. Experimental values of β obtained for MgO, sol-gel thoria, and oxalate thoria were 1, 6.5, and 1.2 respectively.

Thermal conductivity measurements on $Th_xU_{1-x}O_{2+y}$ with values for $(1 - x)$ of 0.047, 0.061, and 0.063 indicated a thermal conductivity as high as that of pure thoria when the specimens were sintered in hydrogen ($y = 0.0$) but about one-half that of thoria when they were sintered in air ($y = 0.03$).

The effects of neutron irradiation on the thermal conductivity of BeO were measured. Also results on a series of cermets consisting of aluminum and UO_2 were compared to an expression derived by Eucken for the thermal conductivity of two-phase material.

The thermal conductivity of a variety of solids was studied with this apparatus, including the following: (1) 96% theoretically dense UN (see Chap. 7 of this report); (2) silicon as affected by heat treatment and oxygen contamination; (3) Tm_2O_3, a potential radioactive heat source; (4) AlSiMag 222, a machinable refractory; (5) several glassy melts, potentially useful in disposal of radioactive waste materials; (6) spectroscopic carbon rods whose thermal properties govern their performance in analytical use; (7) single crystals of UO_2 grown by the centrifugal floating-zone technique; and (8) Conasauga shale[10] for a hazards evaluation in storage of buried radioactive wastes in the Oak Ridge area.

[10]J. J. Dell'Amico, F. K. Captain, and S. H. Chansky, *Characterization and Thermal Conductivity of Some Samples of Conasauga Shale*, ORNL-MIT-20 (June 1967).

A duplicate of this apparatus for use in the High-Radiation-Level Examination Laboratory was tested with some of the above-mentioned solids and will be installed in 1967. Slight modifications were made to the original device to study the solid-solid interfacial thermal resistance problem common to numerous reactor fuel elements. Data from this study will be used to design a high-temperature thermal conductance simulator.

Absolute Longitudinal System, 77 to 400°K

J. P. Moore R. S. Graves
M. Barisoni[11] N. D. Woodall[12]
D. L. McElroy

We found the range 77 to 400°K to be such a little-studied but rich area for thermal conductivity studies on readily available solids that we duplicated and refined our original absolute longitudinal apparatus.

Accurate measurements[13] of thermal conductivity (±1.8%), electrical resistivity (±0.6%), and Seebeck coefficient (±1.5%) were obtained on 0.3 × 8-in. rod specimens. This apparatus was used for measurements on a variety of solids including platinum, high-purity iron, aluminum, silicon (see above), and thoriated tungsten (see Part II, Chap. 16 of this report).

Our thermal conductivity results on a 99.999% copper specimen from stock previously measured at the National Research Council[14] agree to better than ±½% in the 100°K range of overlap. Our electrical resistivity and thermal conductivity results were compared to existing theoretical equations. Although copper is a simple monovalent metal and an ideal test material, the thermal conductivity results do not agree with available theoretical equations.[15]

[11]Noncitizen employee, on leave from CSM, Rome, Italy.

[12]Co-op student from Auburn University.

[13]J. P. Moore, D. L. McElroy, and M. Barisoni, *Proceedings of the Sixth Conference on Thermal Conductivity, Dayton, Ohio, Oct. 19–21, 1966*, pp. 737–78 (limited distribution).

[14]M. J. Laubitz, National Research Council, Ottawa, private communication (May 1966) of paper prepared for *The Canadian Journal of Physics*.

[15]J. P. Moore, R. S. Graves, and D. L. McElroy, "Thermal Conductivity and Electrical Resistivity of High-Purity Copper from 78 to 400°K," to be submitted for publication in *The Canadian Journal of Physics*.

A systematic study on anisotropic materials was started with measurements on single-crystal and polycrystalline indium rods. These studies will be extended to titanium, zirconium, and hafnium. Thermal conductivity and electrical resistivity results on electron-beam-melted tungsten and a W–2% Ta alloy were used with the two methods described above to separate the lattice and electronic thermal conductivities. Measurements on chromium and molybdenum are in progress.

EQUIPMENT DEVELOPMENT

R. K. Williams D. L. McElroy

As indicated above, we are pursuing several approaches to determine the temperature dependence of the Lorenz number for calculating the electronic thermal conductivity. These results should be correlated with high-temperature electrical resistivity and absolute thermoelectric power data. These data are needed for any meaningful treatment that may produce less restrictive bases for data extrapolation and thermal conductivity estimation. The requisite data will be obtained in our high-temperature ultrahigh-vacuum furnace (5×10^{-9} torr at 2200°C) on ultrahigh-purity metals free of contaminating influences. For instance, this system cleanliness is illustrated by changes in an arc-melted tungsten specimen with a resistivity ratio of 3400, which increased to 4900 on annealing for 5 hr at 2000°C and 6×10^{-9} torr. Similar tests were completed on niobium and tantalum. The components needed to obtain high-temperature property data on a tungsten specimen are currently being assembled in this furnace.

As a result of writing a chapter reviewing the methods based on natural phenomena that are used to measure and control temperature in metals research,[16] we studied the drift of thermal emf of Chromel-P vs constantan thermocouples in vacuum as a function of temperature (see Part II, Chap. 15 of this report).

[16] D. L. McElroy and W. Fulkerson, "Temperature Measurement and Control," in *Techniques in Metals Research*, ed. by R. F. Bunshah, Wiley, New York, in press.

10. Theoretical Research

J. S. Faulkner

We are carrying out theoretical investigations of a number of phenomena in solids and also in atoms and molecules. Much of our effort has gone into band-theory calculations by the Korringa-Kohn-Rostoker method using techniques that we have developed. In addition to the completed work described below, progress has been made on extending these calculations to treat systems with more than one atom per unit cell, to obtain wave functions, and to include relativistic correlations. We have been able to supply theoretical help to other groups and individuals in the Division, particularly in connection with our band-theory and crystal-field-theory calculations.

THE CALCULATION OF CONSTANT ENERGY SURFACES FOR COPPER BY THE KORRINGA-KOHN-ROSTOKER METHOD[1]

J. S. Faulkner Harold L. Davis
H. W. Joy

Constant-energy surfaces are calculated for a number of different energies using three different potential functions for copper. Each surface is specified by values for 26,066 radii in k-space, the radii being calculated with the Korringa-Kohn-Rostoker band-theory method. The Fermi surfaces obtained are used to discuss the available experimental results. Values for the electronic contribution to the low-temperature specific heat that are not clouded by statistical errors or interpolation difficulties are calculated. The density-of-states curve for a range of energies above the *d*-bands is calculated with the Chodorow potential. Questions concerning the convergence of the calculation are treated in detail.

[1] Abstract of a paper accepted for publication in *The Physical Review*.

EFFECT OF HYDROSTATIC PRESSURE ON THE FERMI SURFACE OF METALLIC COPPER

H. L. Davis J. S. Faulkner
H. W. Joy

Calculations were performed relating to the change of the Fermi surface of metallic copper with hydrostatic pressure. We used our constant-energy-search technique, which is based upon the Korringa-Kohn-Rostoker method of band theory. Detailed Fermi surfaces were calculated corresponding to three lattice spacings, a, $0.995a$, and $0.99a$, where a is the normal lattice constant of copper. In obtaining these Fermi surfaces, separate potentials, based on the Mattheiss[2] prescription, were calculated for each lattice spacing using free-atom wave functions. These procedures lead to calculated changes of the Fermi surface with pressures that compare favorably with recent experimental deHaas-van Alphen results of Templeton.[3] Some of our results for the relative pressure change of orbital cross-sectional areas are given in Table 10.1 along with Templeton's experimental results. These results are especially pleasing, since the only previous attempt[4] to calculate any of these quantities predicted a *negative* value for the relative change in area of the neck in the Fermi surface per unit pressure change. We have also calculated other quantities, including the density of states at the Fermi energy, which we predict will decrease upon the application of pressure.

[2] L. F. Mattheiss, *Phys. Rev.* **133**, A1399 (1964).

[3] I. M. Templeton, *Proc. Roy. Soc. (London) Ser. A* **292**, 413 (1966).

[4] D. Caroline and J. E. Schirber, *Phil. Mag.* **8**, 71 (1963).

Table 10.1. Relative Change of Some Orbital Cross-Sectional Areas, per Unit Pressure Change, for the Fermi Surface of Copper

The pressure units are kg/cm^2.

Orbit	Relative Change	
	Calculated	Experimental
Neck	$+1.50 \times 10^{-6}$	$+1.93 \times 10^{-6}$
111	$+4.27 \times 10^{-7}$	$+4.21 \times 10^{-7}$
100	$+4.53 \times 10^{-7}$	Not available
Dog's bone	$+3.96 \times 10^{-7}$	Not available

THEORY OF THE OPTICAL SPECTRUM OF Bi^+ IN THE MOLTEN $AlBr_3$-NaBr EUTECTIC

H. L. Davis

Within the framework of crystal-field theory, a theoretical interpretation was previously given the spectrum of the Bi^+ ion in a molten $AlCl_3$-NaCl eutectic.[5-7] A similar interpretation has now also been given to the spectrum of Bi^+ in the molten $AlBr_3$-NaBr eutectic.[8] This latest work has enhanced the validity of the previous assertion that the Bi^+ spectrum is of a crystal-field nature, since the electron-repulsion parameter is shown to have the expected downward shift over the series: free-ion, ion with chloride ligands, ion with bromide ligands. Experimental aspects of this problem are reported in Chap. 11 of this report.

CRYSTAL-FIELD CALCULATIONS

N. Fogel[9] H. W. Joy

We are using our general-purpose computer program for one-center expansions[10] in a semiempirical manner to interpret ligand-field spectra. We determine an appropriate central charge by fitting the spectrum of the isolated ion, and we obtain the magnitudes and positions of neighboring point charges by fitting the spectrum of the ion in a crystal. For each trial model Hamiltonian we determine the orbitals variationally with the methods built into the program. The approach differs from previous semiempirical methods[11,12] in that it is an attempt to explicitly calculate wave functions for the system, from which various other (some nonspectroscopic) properties may be obtained. Work so far has shown that one can indeed produce the energy levels of crystal-field spectra in this way for those cases in which spin-orbit coupling is unimportant. A more complete treatment requires that the computer program be modified to take account of spin-orbit coupling. These modifications are under way.

MASS-SPECTROMETRIC AND THEORETICAL EVIDENCE FOR NH_4 AND H_3O (Ref. 13)

Charles E. Melton[14] H. W. Joy

The unusual chemical species H_3O and NH_4 have been studied using both experimental and theoretical methods. Experimentally the species were investigated by means of a mass spectrometer equipped with two different reactors designed to produce reactive species. The NH_4 was produced by surface chemistry techniques, whereas H_3O was produced by irradiating water vapor with ionizing electrons. A study of the ionization potential of NH_4 by surface ionization techniques gave a value of 5.9 ev. The ionization potential of H_3O was measured by conventional techniques and a value of 10.9 ev was obtained.

---

[5] N. J. Bjerrum, C. R. Boston, G. P. Smith, and H. L. Davis, *Inorg. Nucl. Chem. Letters* 1, 141–43 (1965).

[6] N. J. Bjerrum, C. R. Boston, and G. P. Smith, *Inorg. Chem.* 6, 1162–72 (1967).

[7] H. L. Davis, N. J. Bjerrum, and G. P. Smith, *Inorg. Chem.* 6, 1172–78 (1967).

[8] N. J. Bjerrum, H. L. Davis, and G. P. Smith, "The Optical Spectrum of Bismuth(I) in the Molten $AlBr_3$-NaBr Eutectic," accepted for publication in *Inorganic Chemistry*.

[9] Research participant from the University of Oklahoma, Norman.

[10] H. W. Joy, *Metals and Ceramics Div. Ann. Progr. Rept. June 30, 1963*, ORNL-3470, p. 11.

[11] G. P. Smith, C. H. Liu, and T. R. Griffiths, *J. Am. Chem. Soc.* 86, 4796–802 (1964).

[12] H. L. Davis, *Metals and Ceramics Div. Ann. Progr. Rept. June 30, 1966*, ORNL-3970, p. 43.

[13] Abstract of a paper accepted for publication in *The Journal of Chemical Physics*.

[14] Chemistry Division.

In the theoretical investigation, the physical parameters of the species were calculated by a one-center expansion method. One- and two-determinant wave functions are given including *s*-, *p*-, and *d*-type orbitals for H_3O and *s*-, *p*-, and *f*-type orbitals for NH_4. The calculations predict a tetrahedral structure with internuclear distances about 1.06 A for NH_4 and a planar H_3O molecule with bond distances about 1.03 A. The ionization potentials of H_3O and NH_4 were estimated to be 3.9 and 3.0 ev.

11. Spectroscopy of Ionic Media

G. P. Smith

Research in this group is concerned primarily with the equilibrium behavior of ionic liquids and solids as revealed by electronic absorption spectroscopy. Topics investigated most extensively have been the coordination geometry and electronic states of impurity ions in crystalline, glassy, and molten salts, oxidation-reduction processes in molten salts, and the effect of melting on coordination geometry in transition-metal compounds.

For a long time bismuth was thought to have only two oxidation states, Bi^{3+} and Bi^{5+}, formed by successively stripping and 6*p* and 6*s* electrons from the bismuth atom. About six years ago we[1] and others obtained preliminary evidence for the formation of Bi^{+} and Bi_4^{4+} when bismuth metal dissolves in its molten trihalide salts. Later, Hershaft and Corbett[2] at Iowa State prepared a crystalline material containing the entity Bi_9^{5+} and showed that it has a very unusual geometry. These results initiated a search for low oxidation states in molten salt systems. Last year we identified Bi^{+} in molten NaCl-$AlCl_3$ and KCl-$ZnCl_2$ and established from its absorption spectrum that it has a partially filled 6*p* electronic shell. Then we proved the existence of Bi_5^{3+} and Bi_8^{2+} and studied some of their chemical reactions. More recently, Corbett[3] prepared crystalline salts containing these polynuclear ions. Similar research on other posttransition elements continues. It has become clear that the posttransition elements in general have a far more intricate chemistry than was previously suspected.

A second productive line of investigation has been concerned with what might loosely be called "complex ions" in molten salts. During the past decade a large number of investigations of the spectra of molten salt systems containing low concentrations of transition-metal ions have had the objective of determining coordination geometry. As the accuracy of the measurements improved it became clear that for a given ion this coordination geometry is an intricate function of temperature and system composition. During the past year we made substantial advances in determining these patterns of behavior for Ni^{2+} ions, and results are reported here for nickel centers in LiCl-KCl, $MgCl_2$-KCl, and $ZnCl_2$-CsCl systems.

During the past year we developed a technique for measuring the absorption spectra of both the crystalline and liquid phases of a compound at the same temperature slightly below the melting point. This technique was applied to Cs_3NiCl_5 and $CsNiCl_3$, which have quite different crystal geometries, to determine any change in the coordination geometry of nickel on melting, and the results are reported here. This study was tightly coupled to the nickel-center studies mentioned above. The information on high-temperature crystal spectra provided data needed in the interpretation of the nickel-center spectra, and the latter provided the basis for interpreting the spectrum of molten $CsNiCl_3$. A related solid-state study deals with the spectra of nickel-doped alkali metal chloride crystals at high temperatures.

Reaction rate studies were conducted on the oxidation of nitrite ions by perchlorate ions in a molten lithium perchlorate solvent.

Liquid densities were determined for pure aluminum chloride and mixtures of aluminum chloride and sodium chloride.

---

[1] C. R. Boston, G. P. Smith, and L. C. Howick, *J. Phys. Chem.* **67**, 1849–52 (1963).

[2] A. Hershaft and J. D. Corbett, *Inorg. Chem.* **2**, 979 (1963).

[3] J. D. Corbett, *Inorg. Nucl. Chem. Letters* **3**, 173–76 (1967).

THE ULTRAVIOLET SPECTRUM OF THE Bi^+ ION[4]

N. J. Bjerrum[5] C. R. Boston
G. P. Smith

Previous work on the lower oxidation states of bismuth gave the visible and near-infrared spectrum of Bi^+ in molten $AlCl_3$-NaCl eutectic. To obtain the ultraviolet spectrum of this ion it was necessary to eliminate Bi^{3+}, which absorbs strongly in this region. Reduction of dilute solutions of $BiCl_3$ in the eutectic solvent with hydrogen instead of bismuth metal was found to produce Bi^+ essentially free of Bi^{3+}. The ultraviolet spectrum of this Bi^+ solution showed very weak bands at about 30,000 and 32,500 cm^{-1} with oscillator strengths of 0.3×10^{-4} and 1.5×10^{-4} respectively. These results confirmed the previous theoretical analysis of the electronic structure of this ion.

THE OPTICAL SPECTRUM OF BISMUTH(I) IN THE MOLTEN $AlBr_3$-NaBr EUTECTIC[6]

N. J. Bjerrum[5] H. L. Davis[7]
G. P. Smith

Previously we showed that the absorption spectrum of Bi^+ coordinated to chloride is rationalized very well in terms of intraconfigurational $6p^2 \rightarrow 6p^2$ transitions split by a ligand field with a symmetry lower than cubic. Because of the important role of the ligands in determining the details of the spectrum, it is interesting to observe the effects of changing from a chloride to a bromide environment. Accordingly, we prepared Bi^+ by reduction of dilute solutions of $BiBr_3$ in the molten eutectic $AlBr_3$–32 mole % NaBr and determined its absorption spectrum in the visible and near-infrared regions. Theoretical analysis of the results shows that the ligand field electron-repulsion parameter decreases in the expected way over the series free ion, chloride ligands, and bromide ligands.

[4]Abstracted from "Lower Oxidation States of Bismuth. Bi^+ and Bi_5^{3+} in Molten Salt Solutions," *Inorg. Chem.* 6(6), 1162–72 (June 1967).

[5]Visitor from Denmark, now at Technical University of Denmark.

[6]Abstracted from "The Optical Spectrum of Bismuth(I) in the Molten $AlBr_3$-NaBr Eutectic," to be published in *Inorganic Chemistry*.

[7]Theoretical Research Group.

LOWER OXIDATION STATES OF BISMUTH. Bi_8^{2+} FORMED IN $AlCl_3$-NaCl MELTS[8]

N. J. Bjerrum[5] G. P. Smith

The entity Bi_8^{2+} was prepared by reaction between excess bismuth metal and dilute solutions of bismuth trichloride in molten mixtures of $AlCl_3$ and NaCl at 130 to 250°C. The reaction equation was

$$22Bi(metal) + 2Bi^{3+}(soln) \rightleftharpoons 3Bi_8^{2+}(soln) .$$

With molten $AlCl_3$–37 mole % NaCl as solvent, spectrophotometric measurements show that this reaction is displaced strongly to the right, so that the oxidation state of the product can be established as $+\frac{1}{4}$ from a measurement of the number of moles of metal that react with a known amount of $BiCl_3$. With molten $NaAlCl_4$ saturated with NaCl as solvent the above reaction leads to an equilibrium with both Bi^{3+} and Bi_8^{2+} present in measurable amounts. Spectrophotometric measurements on such equilibrium mixtures at various Bi^{3+} concentrations permit establishment of the complete reaction stoichiometry and, hence, fix the formula Bi_8^{2+}. These measurements give no information on ligands attached to Bi_8^{2+}.

ELECTRONIC SPECTRA AND COORDINATION OF NICKEL CENTERS IN LIQUID LiCl-KCl MIXTURES[9]

J. Brynestad C. R. Boston
G. P. Smith

The electronic absorption spectra (4000 to 28,000 cm^{-1}) of dilute solutions of $NiCl_2$ in liquid LiCl-KCl mixtures were measured at representative solvent compositions from pure LiCl to pure KCl and temperatures from 363 to 1070°C. Phenomenologically, the spectra respond to changes in temperature at high temperature and changes in solvent composition at low temperatures in ways that are quantitatively very regular. At intermediate temperatures the behavior is more intricate. The data agree well with the following model. Nickel is

[8]Abstracted from paper to be published in *Inorganic Chemistry*.

[9]Abstracted from paper to be published in *The Journal of Chemical Physics*.

partitioned between two types of centers, labeled **T** and **O**, which are in equilibrium. The **T/O** concentration ratio increases with increasing temperature and KCl content in the solvent. At low temperatures the fraction of each kind of center varies linearly with the mole fraction of KCl. The **O**-center concentration falls below the detection limit at 900°C in all solvents and in KCl at all temperatures. The **T** centers have a distribution of coordination geometries about tetrahedral that is narrow and composition invariant at low temperatures but broadens at high temperatures, especially in LiCl-rich melts, and becomes composition dependent. The **O** centers at low temperatures have a relatively broad distribution of geometries that clusters about octahedral and is composition invariant.

ELECTRONIC SPECTRA AND COORDINATION GEOMETRY OF NICKEL CENTERS IN LIQUID $MgCl_2$-KCl MIXTURES[9]

J. Brynestad G. P. Smith

The absorption spectra of nickel centers in $MgCl_2$-KCl mixtures of various compositions were measured from about 5000 to 28,000 cm^{-1} at temperatures up to 1046°C. The observed behavior was qualitatively similar to that previously reported for nickel centers in liquid LiCl-KCl mixtures and, in a general way, fits the same model.

ELECTRONIC SPECTRA AND COORDINATION GEOMETRY OF NICKEL CENTERS IN LIQUID MIXTURES OF $ZnCl_2$ AND CsCl

W. E. Smith[10] G. P. Smith

Research is in progress on nickel centers in the $ZnCl_2$-CsCl system. At low $ZnCl_2$ concentrations the behavior is similar to that in LiCl-KCl and $MgCl_2$-KCl except that certain details show up much more clearly in the $ZnCl_2$-containing system. However, for melts containing high $ZnCl_2$ concentrations a drastically new pattern of behavior is observed, which appears to be associated with the ability of zinc ions to form chloride-bridged networks.

EFFECT OF MELTING ON THE ELECTRONIC SPECTRA OF Cs_3NiCl_5 AND $CsNiCl_3$ (ref. 9)

C. R. Boston J. Brynestad
G. P. Smith

A method is described for measuring the optical absorption spectra of the crystalline and liquid phases of a transition-metal salt close to its melting point. Supercooling the liquid permits measuring both phases at the same temperature. This technique was applied to Cs_3NiCl_5 (m.p. 547°C) and $CsNiCl_3$ (m.p. 758°C). When Cs_3NiCl_5 melted, the approximately tetrahedral arrangement of chlorides about nickel was affected only in minor ways; but when $CsNiCl_3$ melted, the octahedral coordination geometry in the crystal was completely destroyed and replaced by a different distribution of geometries. The spectrum of molten $CsNiCl_3$ and its temperature dependence are closely similar to that of nickel centers in molten $KMgCl_3$ at high temperatures. The latter are known to consist of a single distribution of geometries rather than two distinctly separate distributions. It was previously supposed that there are two different coordination geometries in molten $CsNiCl_3$.

NICKEL-DOPED ALKALI METAL CHLORIDE CRYSTALS

G. E. Shankle[11] G. P. Smith

The spectroscopy of nickel-doped alkali metal chlorides at high temperatures is under investigation. These systems exhibit more or less octahedral coordination about Ni^{2+}, in which deviations from O_h symmetry should be a function of the particular alkali metal ion present. There are also cation vacancies. If these defects lead to a destruction of the center of symmetry, the $g \nleftrightarrow g$ selection rule will be violated with consequent effects on the temperature dependence of the f number.

---

[10] Visitor from Scotland.

[11] Graduate student at the University of Tennessee.

THE RATE OF OXIDATION OF NITRITE IONS IN DILUTE SOLUTIONS OF SODIUM NITRITE IN MOLTEN LITHIUM PERCHLORATE[12]

D. W. James[13]

In dilute solutions of sodium nitrite in molten lithium perchlorate at 245 to 301°C, nitrite ions are oxidized to nitrate ions while perchlorate ions are reduced to chloride ions in a pseudo-first-order homogeneous reaction. The first-order rate constant is 3.51×10^{-4} sec^{-1} at 274°C, and the activation energy is 31.5 kcal/mole. Chlorate ions do not build up during the course of the reaction. The reaction is unaffected by gaseous nitrogen or substantial additions of water, LiOH (5 mole %), or $LiNO_3$ (10 mole %) but is retarded by substantial additions of $NaNO_3$ (10 mole %) and by gaseous oxygen. The evidence suggests the possibility that the rate-determining step involves a direct reaction between a nitrite ion and a perchlorate ion.

DENSITIES OF MOLTEN $AlCl_3$ AND NaCl-$AlCl_3$ MIXTURES[14]

C. R. Boston

The "float" method was used to measure liquid densities of $AlCl_3$ and NaCl-$AlCl_3$ mixtures containing 52.0, 61.8, and 73.0 mole % $AlCl_3$. All melts were studied over a range of temperatures and the data fitted to equations of the form $\rho = \alpha - \beta t$ by a least-squares analysis. Molar volumes showed negative deviations from additivity as large as 22%.

---

[12] Abstract of paper to be submitted for publication.

[13] Visitor from New Zealand, now at University of Queensland, Brisbane, Australia.

[14] Abstract of *J. Chem. Eng. Data* 11, 262–63 (1966).

12. Superconducting Materials

G. R. Love M. L. Picklesimer[1]

We are studying the effects of metallurgical variables on the properties of superconducting materials. Of concern are the effects on current-carrying capacity in a magnetic field of such things as morphology, compositions, and spacings of two-phase structures; mechanical strain; preferred orientation; aging and transformation reactions; and fabrication and heat-treatment procedures. For the studies to be meaningful, we must have a considerable knowledge of the physical metallurgy and phase diagrams of the systems of interest. Few systems have been studied, and they have not been studied in sufficient detail. Consequently, much of the effort is devoted to establishing a background of information on the transformation kinetics and products, morphologies, phase diagrams, precipitation and aging reactions, and rates of formation of intermetallic compounds. The alloy systems of primary interest are those based on niobium and technetium.

EQUIPMENT DEVELOPMENT

G. R. Love C. C. Koch

Magnets

A significant portion of our effort was related to the development of independent capability for testing superconducting properties. The basic components of the testing equipment were the superconducting solenoids purchased from Magnion, Inc. This magnet assembly consists of two nested coils, an outer coil constructed from niobium-zirconium wire capable of a maximum field of about 30 kilogauss, and an inner coil, wound from Nb_3Sn ribbon, with maximum field of about 45 kilogauss. The combined coils produce a maximum field of about 75 kilogauss with ±1% field inhomogeneity over a 1-in.-diam sphere.

Test Assemblies

A test assembly using alternating-current magnetization was constructed and modified. This assembly enables the control and measurement of temperature from about 2 to 77°K, the measurement of applied field to 75 kilogauss, and the measurement of the critical temperature, critical field strength, and critical current density. It appears that the same device, with modifications in the external circuitry, can yield full magnetization curves.

SUPERCONDUCTIVITY OF THE TECHNETIUM-VANADIUM ALLOY SYSTEM[2]

C. C. Koch R. H. Kernohan[3]
S. T. Sekula[3]

The superconducting properties of technetium-vanadium alloys with compositions ranging from 0 to 100 at. % V were investigated in fields up to 15 kilo-oersteds by measurements of the bulk magnetization determined ballistically. A phase diagram of the system was determined by several metallurgical techniques. The sequence of crystal structures at 1500°C with increasing vanadium content is hexagonal close packed → body-centered

[1]Present address: Southern Research Institute, Birmingham, Alabama.

[2]Abstracted from paper submitted to *Journal of Applied Physics*.

[3]Solid State Division.

cubic → CsCl → body-centered cubic. The technetium-rich body-centered cubic phase when quickly cooled to room temperature exhibited superlattice x-ray diffraction lines of the CsCl structure. The superconducting transition temperature of the technetium-rich hexagonal close packed alloys increased with vanadium concentration from 7.73°K to a maximum for the system of 11.3°K at the limit of vanadium solubility (approximately 6.5 at. % V). This transition temperature remained constant for the two-phase alloys. The transition temperature decreased progressively with increasing vanadium content in the CsCl structure, and at compositions in the 50 to 80 at. % V interval no evidence of superconductivity was observed for temperatures as low as 1.4°K. Alloys containing the hexagonal close packed phase showed reversible behavior in the tails of their magnetization curves, while those with the CsCl structure exhibited a high degree of hysteresis in the tails. Estimates of the upper critical field at 0°K using the experimental data and theoretical calculations yielded values of approximately 45 kilo-oersteds for the samples with high transition temperatures. Results of heat treatment at 1100°C on the superconducting parameters of alloys near the 30 at. % V composition are presented.

METALLOGRAPHY OF LANTHANUM AND CERIUM[4]

C. C. Koch M. L. Picklesimer[1]

A technique was developed for the metallographic preparation of lanthanum and cerium. Metallography, the microscopic study of metallic structure, requires polished surfaces for examination. These rare-earth metals are so reactive to the atmosphere that surfaces prepared by conventional techniques are destroyed too soon to permit adequate examination. These metals exist at room and low temperatures in two crystal forms, with hexagonal and cubic symmetries, and this new method permits study of the transformation. This is of special fundamental interest in lanthanum, because both structures exhibit superconductivity. The surface is prepared by chemical polishing with specially developed solutions and then protected by anodizing. Anodizing, not previously applied to rare earths, not only protects the surfaces during examination but also distinguishes the two forms by oxide films of different colors.

[4]Summarized from published paper, *Trans. Met. Soc. AIME* **229**, 759–61 (1967).

A METALLOGRAPHIC STUDY OF THE ALLOTROPIC PHASE TRANSFORMATIONS IN CERIUM[5]

C. C. Koch C. J. McHargue

Some aspects of the phase transformations in cerium were studied by metallography. The temperature dependence of the percentage double hexagonal close packed formed by athermal transformation, as determined by x-ray diffraction, was confirmed by quantitative metallography. The influence of plastic deformation on the transformation was studied by deforming cerium specimens at temperatures above and below M_s. Metallography definitely indicates that deformation promotes the face-centered cubic → double hexagonal close packed reaction. A M_d temperature was determined. A tensile component of deformation appears necessary for the face-centered cubic → double hexagonal close packed transformation. This may explain the conflicting evidence of the effect of deformation on this transformation. The influence of deformation on subsequent athermal transformation and reversion has been studied. The morphology of the transformation was examined and lattice relationships were inferred.

[5]Abstracted from a paper: pp. 416–27 in *Proceedings of the 6th Rare Earth Research Conference, May 3–5, 1967, Gatlinburg, Tennessee*, 1967.

13. Surface Reactions of Metals

J. V. Cathcart

In recent years emphasis in oxidation research has shifted away from the old concept of a uniform oxide film interposing a simple diffusion barrier between a metal and its environment. While such a description may be satisfactory for a few relatively simple reactions, a much deeper insight into the detailed nature of oxidation mechanisms has come with the recognition that factors such as short-circuit diffusion paths in the oxide, oxygen solution effects, and stress generation during oxidation can greatly influence oxidation processes. The research of this group is directed toward the investigation of factors such as these.

We extended our study of structural defects in oxide films to include thin oxide films formed on nickel single crystals. The oxidation-rate anisotropy exhibited by nickel correlated with a corresponding anisotropy of the concentration of structural defects in the oxide. The results are consistent with our previously reported model for the oxidation of copper and copper-nickel alloys.

We also continued our studies of the oxidation of the refractory metals niobium and tantalum. Stress generation by and the distribution of dissolved oxygen in these metals were studied as a function of oxygen pressure. Stresses induced in the oxide films themselves were found to influence the degree of protectiveness of the films. Oxygen transport through the anodic films on niobium and tantalum was studied with special attention being given to the role of phosphorus impurity in increasing the degree of protectiveness of the films. The films from the tantalum-niobium alloys provided an opportunity for the study of an "oxide alloy." We also initiated some anodization work with tungsten as a part of a study of low-temperature and short-circuit diffusion in that metal; this work represents an adaptation of a very sensitive sectioning technique that we previously developed for studying diffusion in tantalum and niobium.

NICKEL OXIDATION[1]

J. V. Cathcart G. F. Petersen

Our previous studies of the oxidation of copper and copper-nickel alloys demonstrated the importance to the overall oxidation process of short-circuit diffusion paths and epitaxial effects in the oxide films. Variations in the concentration of short-circuit diffusion paths were shown to account for an order-of-magnitude difference in the oxidation rate of copper and to provide for the first time a satisfactory explanation of the very pronounced oxidation-rate anisotropy of copper. Our nickel oxidation research is part of an effort to test the generality of these ideas.

The (100), (111), and (110) faces of nickel single crystals were oxidized at temperatures from 400 to 500°C. Under the conditions of our experiments, the relative rates of oxidation of these three crystal planes decreased in the order (110), (100), and (111), the oxidation rates differing by a factor of 2 or 3. The thicknesses of oxide films examined ranged from about 15 to 600 A. The average strain, the mosaic spread, thickness, and epitaxial relationships of the films were studied by an x-ray method developed in our previous work with copper. In addition, both replication and stripped-film techniques were used in an electron-microscopic study of the films. The oxidation rates of the specimens and the optical properties of the films were investigated with an ellipsometer.

[1]This work is being carried out in collaboration with C. J. Sparks of the X-Ray Diffraction Group.

The epitaxial relationships between the NiO films and the substrate were the same as those between Cu_2O and copper. In contrast to the results with copper, however, the average strain in the NiO films, as indicated by average lattice parameter measurements, was virtually zero. The mosaic spread of the (100) and (111) films was half that for films of comparable thickness on copper. These results have interesting implications for the theory of oriented overgrowths but indicate that strain effects probably play only a minor role in the oxidation of nickel.

The oxide on all three of the major planes of nickel consisted of mosaic blocks at most a few hundred angstroms in diameter. Thus in the films a condition existed that assured that a general lack of orientation of the films would result in the development of extensive grain-boundary area within the films. Just such a situation occurred for the oxide on the (110), where the film was initially partially oriented but tended to become polycrystalline as the film thickened. Thus these films were rich in high-angle grain boundaries, which make very effective paths of easy diffusion. The (110) films would, therefore, be expected, as observed, to provide comparatively little protection against continued oxidation.

The oxide on the (111) and (100) was much more precisely oriented but was subject to extensive twinning. Two sets of twins, rotated 90° with respect to each other, formed on the (100), while only one set occurred on the (111). As a consequence, if the distribution of these different orientations are random, the oxide on both these planes contained large numbers of incoherent twin boundaries. These boundaries are almost as efficient as short-circuit diffusion paths as high-angle grain boundaries. The fact that the (100) exhibited a higher rate of oxidation than the (111) can probably be accounted for by the presence of the extra set of twins.

As indicated, the oxidation characteristics of nickel and copper differ significantly, especially with regard to the existence of large strains in the oxide films. However, our results with nickel appear to be completely consistent with the main feature of the oxidation model we proposed for copper, namely, the importance to be attached to the role of short-circuit diffusion paths in determining the overall rate of oxidation.

REFRACTORY METAL OXIDATION

R. E. Pawel J. V. Cathcart

Stress Measurements During Oxidation

We have modified our oxidation apparatus to permit measurements of the flexure of metal specimens during low-pressure oxidation at temperatures up to 900°C. The flexure measurements, converted to appropriate bending stresses, may be interpreted in terms of certain stress distributions in the oxide film and in the metal. Preliminary measurements with niobium specimens oxidized at oxygen pressures of 0.01 to 0.05 torr at 800°C confirmed that oxygen solution effects are important under those conditions.

Protective Properties of Oxide Films[2]

The high-temperature oxidation characteristics of tantalum specimens anodized in phosphoric acid solutions were studied. The anodic oxide films containing phosphorus limited oxygen access to the metal and postponed breakaway oxidation considerably more effectively than phosphorus-free anodic films of the same thickness. Thickness-voltage calibrations for anodization in 0.9 and 14 *M* H_3PO_4 electrolytes allowed quantitative measurements and comparisons of oxidation behavior with that previously found for both plain tantalum and tantalum specimens anodized in dilute aqueous solutions. At temperatures between 500 and 625°C, oxygen permeated films formed in the concentrated acid at approximately one-fifth the rate for the films from dilute acid. The data indicated a 6% increase in the activation energy for oxygen permeation for phosphorus-containing films. Like the plain anodic films, the films containing phosphorus eventually lost their protective properties by local breakdown at flaws in the films followed by lateral growth of the resulting fast-oxidizing regions.

Alloy Oxide Films

Mechanical stripping techniques were used to obtain several alloyed anodic oxide films; these

[2]Summarized from a paper submitted to the *Journal of the Electrochemical Society*.

were subsequently examined with the electron microscope, the electron microprobe, and x-ray diffraction. Tantalum-phosphorus oxides were prepared by the anodization of tantalum in concentrated H_3PO_4; slightly higher temperatures were required to crystallize these films than plain anodic Ta_2O_5. While the electron microscope revealed some differences in morphology of the crystallized regions, neither selected-area electron diffraction nor x-ray diffraction techniques have yet revealed significant structural differences or the presence of secondary phases.

Anodic films were also formed on and stripped from the electropolished surfaces of several tantalum-niobium alloy specimens. These films were amorphous as formed but crystallized upon annealing in the temperature range 500 to 700°C. No significant partitioning occurred during anodization, and such alloy oxide films will be used to study the phase relationships in the Ta_2O_5-Nb_2O_5 system.

Anodic Oxidation of Tungsten

While anodic oxide films form on tungsten in many common electrolytes, many features of anodization important to a microsectioning technique, such as that used in our previous studies of diffusion in tantalum and niobium, are clearly influenced to a large extent by the particular electrolyte and other experimental variables. We examined the anodic oxidation behavior of tungsten in a number of electrolytes and finally established a film thickness–voltage calibration under conditions where the efficiency of film formation was about 99%. A technique for mechanical stripping of the anodic films from the surface of the tungsten specimens has not been found. However, chemical stripping by dissolving the film in a dilute base furnishes an apparently satisfactory method. The dissolution rate of the metal in dilute sodium hydroxide solutions was increased significantly by the presence of oxygen. For solutions made from distilled (but not further deaerated) water, negligible tungsten was dissolved along with the anodic film, and the separations were quantitative. The applicability of these sectioning techniques to the study of tracer diffusion in tungsten is presently being tested in cooperation with the Diffusion in Solids Group.

14. X-Ray Diffraction

H. L. Yakel

Our group functions in a dual role to serve the need for routine x-ray diffraction analyses and to apply diffraction methods to basic scientific problems. In the former area, our work is well within the frontiers of x-ray physics and structural analysis, and its results may have a variable significance in the ultimate solution of the given problem. In the latter area, our work is at these frontiers and its results are pivotal.

We maintain a laboratory adequately equipped to meet the needs of both roles. Determinations of lattice parameters, phase composition, crystal orientation and perfection, phase transition phenomena, and simple crystal structures are rapidly carried out in a routine manner. We also engage in fundamental studies of crystal structures of compounds containing beryllia, and of diffraction effects due to crystalline imperfections caused by solid-solution formation, radiation damage, and precipitation.

ROUTINE ANALYSES

O. B. Cavin R. M. Steele
H. L. Yakel

During the reporting period we completed desired work on over 1300 samples submitted for routine x-ray diffraction analysis by groups within and without the Metals and Ceramics Division. Many results are included in other sections of this report; we present here a few that are of special interest.

Lang x-ray topographic techniques have been applied in reflection geometry to study the perfection of UO_2 crystals. Figure 14.1 is a topograph of a crystal with many small-angle boundaries, grown by the Crystal Physics Group, using the internal centrifugal floating zone method.

We have characterized structures and determined lattice parameters of a series of single-phase solid-solution alloys that have not been described previously. The results appear in Table 14.1. In Table 14.2 we list powder diffraction data for lithium azide, LiN_3, the only alkali-metal azide whose crystal structure is unknown. The material is hygroscopic, crystallizes in an acicular habit, and gives evidence of twinning. A low crystal symmetry, possibly monoclinic or triclinic, is suggested by preliminary single-crystal diffraction data.

We have written and are currently testing computer programs useful in special diffraction problems. One such program UMWEG, predicts multiple scattering effects in single-crystal diffraction experiments. A second, FTRANS and ANTRAN, is a general-purpose Fourier transform calculator and analyzer for diffraction data that are a function of one reciprocal lattice variable. It is

Fig. 14.1. A Reflection Topograph Obtained by Scanning the (200) Reflection from a UO_2 Crystal Grown by the Internal Centrifugal Floating Zone Method. The actual crystal length is 14.5 mm and its height is 8.3 mm. The apparent height on the topograph is foreshortened by setting the film at an oblique angle to the scattered beam direction. The maximum subgrain misorientation in this crystal is 0.6°.

Table 14.1. Crystallographic Data for New Alloys

Composition (at. %)	Crystal System	Lattice Parameter (A)		Remarks
		a_0	c_0	
90 Ho–10 Sc	Hexagonal	3.560 ± 0.001	5.597 ± 0.002	hcp[a]
80 Ho–20 Sc	Hexagonal	3.542 ± 0.001	5.566 ± 0.002	hcp
60 Ho–40 Sc	Hexagonal	3.491 ± 0.001	5.502 ± 0.002	hcp
40 Ho–60 Sc	Hexagonal	3.434 ± 0.001	5.431 ± 0.001	hcp
20 Ho–80 Sc	Hexagonal	3.371 ± 0.001	5.364 ± 0.001	hcp
90 Er–10 Sc	Hexagonal	3.541 ± 0.001	5.578 ± 0.002	hcp
80 Er–20 Sc	Hexagonal	3.523 ± 0.001	5.549 ± 0.002	hcp
60 Er–40 Sc	Hexagonal	3.473 ± 0.001	5.482 ± 0.002	hcp
40 Er–60 Sc	Hexagonal	3.424 ± 0.001	5.415 ± 0.002	hcp
20 Er–80 Sc	Hexagonal	3.366 ± 0.001	5.363 ± 0.002	hcp
95 Er–5 Th	Hexagonal	3.572 ± 0.001	5.597 ± 0.002	hcp
90 Er–10 Th	Hexagonal	3.582 ± 0.002	5.610 ± 0.002	hcp
80 Er–20 Th	Hexagonal	3.581 ± 0.002	5.661 ± 0.002	hcp
90 Ho–10 Th	Hexagonal	3.598 ± 0.002	5.637 ± 0.002	hcp
85 Ho–15 Th	Hexagonal	3.601 ± 0.003	5.655 ± 0.003	hcp
50 Tb–50 Th	Cubic	5.060 ± 0.002		fcc[b]
30 Tb–70 Th	Cubic	5.073 ± 0.002		fcc
20 Tb–80 Th	Cubic	5.079 ± 0.002		fcc
12.5 Fe–12.5 Ni–75 Au	Cubic	3.999 ± 0.001		fcc
20 Fe–20 Ni–60 Au	Cubic	3.923 ± 0.001		fcc
27.5 Fe–27.5 Ni–45 Au	Cubic	3.897 ± 0.001		fcc
35 Fe–35 Ni–30 Au	Cubic	3.798 ± 0.002		fcc
42.5 Fe–42.5 Ni–15 Au	Cubic	3.650 ± 0.002		fcc
$Fe_{2.74}Ti_{0.26}O_4$	Cubic	8.40 ± 0.01		Spinel-type

[a] hcp = hexagonal close-packed.

[b] fcc = face-centered cubic close-packed.

superior to currently available single-variable transform programs for diffraction data in that it (1) can make all necessary corrections (background, Lorentz-polarization, atom form factor, and structure factor) to the data; (2) can use either the Rachinger[1] or Keating[2] method of $K\alpha_1\alpha_2$ doublet separation; (3) computes integrals, with or without the general *n*th-order Lagrangian interpolation of data, by rectangular or parabolic approximation; (4) obtains all characteristics of the intensity distribution (centroid, variance, integral peak breadth, as well as real and imaginary Fourier coefficients referred to the estimated and corrected centroids and to the intensity maximum); (5) can perform Stokes corrections to eliminate instrumental effects; and (6) can use Calcomp plotting routines to plot various intensity and transform coefficient functions.

[1] W. A. Rachinger, *J. Sci. Instr.* **25**, 254 (1948).

[2] D. T. Keating, *Rev. Sci. Instr.* **30**, 725 (1959).

Table 14.2. Powder Diffraction Data for Lithium Azide, LiN_3, Cu Kα Radiation (Ni-Filter); λ Cu Kα = 1.54178 A

Intensity	Spacing[a]	Intensity	Spacing[a]
S–	4.745	M+	1.414
S+	2.826	M	1.356
S	2.714	W	1.307
S+	2.618	M–	1.296
M–	2.368	W	1.232
W–	2.281	W+	1.212
W–	2.196	M–	1.187
M–	2.118	W	1.161
M	2.085	W–	1.146
W–	2.029	W	1.084
M–	1.975	W+	1.071
W+	1.692	W–	1.063
M+	1.658	W–	1.054
S–	1.629	M–	1.051
W+	1.588	W	1.041
W	1.568	W–	1.038
M	1.509	15 more reflections to d = 0.78 A	

[a]Bragg spacings measured with a precision of 0.10% in low-angle region and 0.03% in high-angle region. Qualitative intensity scale: S+ > S > S– > M+ > M > M– > W+ > W > W–.

CRYSTAL STRUCTURES OF MIXED OXIDE COMPOUNDS CONTAINING BeO

L. A. Harris H. L. Yakel

Crystal structures of only a few mixed oxide compounds in systems containing beryllia have been described. Conditions affecting the thermodynamic stability of these phases are not completely understood. In an effort to illuminate this technologically interesting area of structural inorganic chemistry, we have carried out experiments in which known compounds of unknown structure in oxide systems based on BeO have been prepared, crystallized, and analyzed by x-ray diffraction procedures. We have also studied BeO systems in which the existence of stable compounds is uncertain. Some recent results are given below.

Lanthanum Beryllium Oxide[3]

The crystal structure of $La_2Be_2O_5$ has been derived and refined from Mo Kα x-ray diffraction data. The *C*-centered monoclinic cell with a_0 = 7.536 A, b_0 = 7.348 A, c_0 = 7.439 A, and β = 91° 33′ contains four formula weights. The atomic arrangement in this equilibrium phase consists of a three-dimensional framework of corner-sharing beryllium-oxygen tetrahedra with lanthanum atoms irregularly coordinated to ten oxygen atoms. The structure is compared with those of other oxide compounds containing beryllium and, in particular, with the structures of the recently reported non-equilibrium phases $Ca_{12}Be_{17}O_{29}$ (ref. 4) and Y_2BeO_4 (ref. 5), in which trigonal beryllium-oxygen coordinations had been found.

Strontium Beryllium Oxide

Efforts to prepare the reported[6] equilibrium 1:1 and 3:2 phases in the BeO-SrO system resulted in

[3]Abstract of a paper submitted for publication in *Acta Crystallographica*.

[4]L. A. Harris and H. L. Yakel, *Acta Cryst.* **20**, 295 (1966).

[5]L. A. Harris and H. L. Yakel, *Acta Cryst.* **22**, 354 (1967).

[6]E. M. Levin, C. R. Robbins, and H. F. McMurdie, *Phase Diagrams for Ceramists*, The American Ceramic Society, Inc., Columbus, Ohio, 1964.

formation of crystals of the complex disordered phase previously described[7] as 3BeO·2SrO.

We have grown crystals of the 4BeO·SrO equilibrium phase[6] and have observed x-ray diffraction data in good agreement with powder data reported[8] for a phase called $Sr_2Be_9O_{11}$ formed by heating coprecipitated hydroxides. The phase crystallizes in the hexagonal system, Laue group $6/mmm$, with unit cell parameters $a_0 = 4.5961 \pm 0.0000_4$ A, $c_0 = 8.9300 \pm 0.0001$ A. Reflections *hhl* with *l* odd are systematically absent, indicating a c-glide in the *ac* plane. Reflections *hkl* are absent if $h - k = 3n$ and *l* is odd; this is a non-space-group extinction caused by special atom positions in the unit cell. Crystals show a pyroelectric effect normal to the c-axis. The most probable space group is therefore $P\bar{6}2c$. The unit cell parameters are related to those of BeO in that $a_0 \cong \sqrt{3}a_{BeO}$ and $c_0 \cong 2c_{BeO}$. A set of Cu Kα and -β reflection intensity data has been collected and a structure analysis begun.

Sodium Beryllium Oxide

Mixtures of 60 mole % BeO, 40 mole % Na_2O (introduced as Na_2CO_3) were heated on a platinum strip in air to about 1300°C. A molten phase separated from the mixture. On quenching, this liquid solidified to an optically isotropic clear material that produced no sharp crystalline x-ray diffraction pattern. Qualitative electron microprobe and spectrographic analyses of a piece of the glasslike material showed only sodium and beryllium as major metallic constituents. The phase is attacked by atmospheric moisture at room temperature after 24 to 48 hr.

Other Systems

We are attempting to prepare mixed oxide compounds in the systems BeO-BaO, BeO-Nd_2O_3, and BeO-Ho_2O_3. Crystals of additional phases in the BeO-Y_2O_3 and BeO-La_2O_3 systems will also be studied in an effort to determine factors governing the formation of stable and metastable compounds. We have been able to grow small imperfect crystals of the 3BeO·BaO compound reported by Isupova and Keler.[9] Preliminary diffraction results suggest a monoclinic unit cell and are in agreement with the powder data published by the Russian workers.

X-RAY DIFFRACTION FROM NEUTRON-IRRADIATED CERAMIC SINGLE CRYSTALS

H. L. Yakel G. W. Clark[10]

We conducted an irradiation experiment in which a variety of crystals of a ceramic nature were exposed to neutron irradiation in the Engineering Test Reactor.[11] Dose levels of 4×10^{20}, 8×10^{20}, and 10×10^{20} neutrons/cm^2 ($\geq$1 Mev) were achieved, as measured by flux monitors. The irradiation temperature was 140 ± 20°C. Crystals included in this experiment were BeO, Al_2O_3, MgO, "spinel" ($MgAl_2O_4$), SiO_2, Si, Ge, SiC, and beryl ($Be_3Al_2Si_6O_{18}$). Results of x-ray diffraction experiments with the irradiated BeO crystals have been reported.[12]

In the period of this report, we completed preliminary studies of the irradiated "spinel" crystals. Determination of the lattice parameter of an unirradiated control crystal demonstrated that the composition is approximately $MgO \cdot 3Al_2O_3$ rather than the ideal 1:1 spinel composition.[13] There is no evidence of ordering of the lattice defects (probably anion and cation vacancies) that are required by the 1:3 stoichiometry.

The irradiated crystals were only slightly more yellow than the unirradiated controls. Rotation and Weissenberg diffraction patterns obtained from them showed reflections very little broader than those on similar patterns of unirradiated crystals. Fractional lattice parameter variation as a function of neutron dose is shown in Fig.

---

[7] L. A. Harris and H. L. Yakel, *Acta Cryst.* **15**, 615–16 (1962).

[8] R. A. Mercer and R. P. Miller, *J. Inorg. Nucl. Chem.* **28**, 61 (1966).

[9] E. N. Isupova and E. K. Keler, *Zh. Neorgan. Khim.* **9**, 394–402 (1964); *Russ. J. Inorg. Chem. (English Transl.)* **9**, 217–21 (1964).

[10] Crystal Physics Group.

[11] The experiment was possible through the cooperation of G. W. Keilholtz and R. E. Moore of the Reactor Chemistry Division, who permitted us to place crystals in their experiments at the ETR.

[12] H. L. Yakel, *Metals and Ceramics Div. Ann. Progr. Rept. June 30, 1964*, ORNL-3670, pp. 57–60.

[13] F. Rinne, *Neues Jahrb. Mineral. Geol. Palaeontol. A* **58**, 43 (1928).

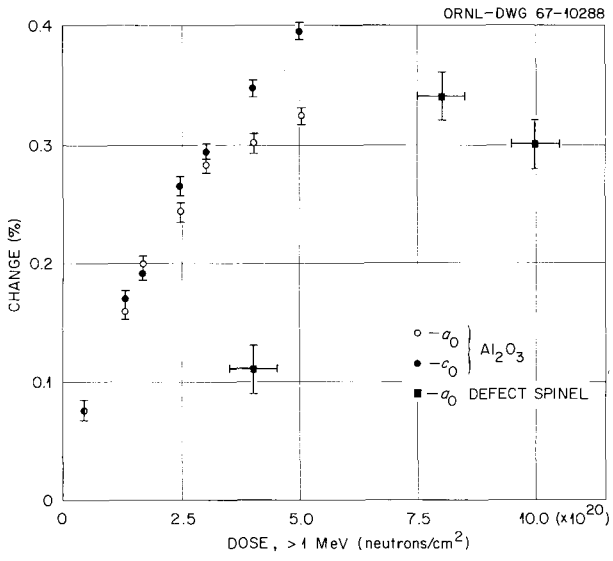

Fig. 14.2. Fractional Variations of Lattice Parameter with Neutron Dose for Al_2O_3 and the Defect Spinel $MgO \cdot 3Al_2O_3$.

14.2. For comparison, the figure also displays the parameter changes reported[14] for Al_2O_3 irradiated at 75 to 100°C. No departures from cubic symmetry, supercell reflections, or appearance of reflections forbidden by the F*d3m* space group were observed in the data from the irradiated defect spinel.

From the results, we conclude that at doses below 1×10^{21} neutrons/cm^2 the fractional lattice expansion of the defect spinel is one-third to one-half those of pure alumina. The reduced expansion should be correlated with the lattice vacancies in the as-grown crystal, which act as traps at which radiation-produced defects may be annihilated.

SMALL-ANGLE X-RAY SCATTERING

R. W. Hendricks

Experiment

Small-angle x-ray scattering measurements were made on irradiated perfect single crystals of copper. Although the intensity detected was very weak, we could observe some dependence of the intensity on sample orientation. We believe that the scattering centers are interstitial disks with diameters in the range of a few hundred angstroms. Research is continuing on thinner samples (to increase the scattered intensity), using absolute intensity techniques in an effort to determine the shape, orientation, and concentration of the scattering centers.

Accurate measurement of the absolute intensity of scattered x-irradiation in the small-angle region has been a difficult problem. We found that, at least for our more intense beams, measurement of the scattering from gaseous octafluorocyclobutane (C_4F_8) provides an excellent measure of the absolute intensity.

Theory

A sequence of computer programs is being written to process automatically collected small-angle scattering data. This sequence consists of PROGRAM EDIT, PROGRAM SAXS, PROGRAM WEIGHT, and PROGRAM COLCOR. PROGRAM EDIT is designed to examine the punched paper tapes generated during data collection for format errors, erroneous data, etc. and provides for manual introduction of corrections and/or deletions to the magnetic tape. PROGRAM SAXS converts the output of a Humphrey Electronics Company model 901-OR stepscanner (number of counts observed in a fixed time at a given angular location) into intensity-angle data. Background scattering is subtracted, and if balanced filters have been used, proper pairwise subtraction of the data from each filter is performed. PROGRAM WEIGHT computes the weighting functions necessary for performing collimation corrections with the geometrical parameters that define the incident x-ray beam. PROGRAM COLCOR will perform the slit-width and slit-length collimation corrections on the raw data.

The calculation of the weighting functions for small-angle scattering data has been extended to include the effects of finite sample thickness and sample misalignment. Preliminary results indicate that slits between the sample and the detector slit introduce angular dependence into the weighting function and the limits of integration in the collimator correction integral equation, thus making the usual methods of performing collimation corrections invalid.

[14] B. S. Hickman and D. G. Walker, *J. Nucl. Mater.* **18**, 197 (1966). Significant reflection broadening for Al_2O_3 is also reported at doses less than 1×10^{21} neutrons/cm^2 by these authors.

X-RAY DIFFRACTION MEASUREMENTS OF FILM THICKNESS

C. J. Sparks

We have developed a new technique for the measurement of thickness of unattached films based on the ratio of the integrated x-ray intensity from the same Bragg peak in reflection to that in transmission. This technique is useful for single-crystal films with the mosaic spread limited to about 10° or for randomly oriented crystallites.

For the geometry shown in Fig. 14.3, the ratio is given by

$$R = \frac{\int^{\text{reflection}} P(\alpha)d\alpha}{\int^{\text{transmission}} P(\alpha)d\alpha}$$

$$= \frac{(2\mu)^{-1}[1 - \exp(-2\mu T/\sin\theta)]}{(T/\cos\theta)\exp(-\mu T/\cos\theta)}$$

$$= \frac{\cos\theta[1 - \exp(-2\mu T/\sin\theta)]}{2\mu T \exp(-\mu T/\cos\theta)}, \qquad (1)$$

where μ is the linear absorption coefficient, θ the Bragg angle, and T the thickness of the film. To determine R for single-crystal films, one need only to rock the film about an axis lying in the surface to gather the total integrated intensity from the reflection, as shown in Fig. 14.3*a*. Then the same measurement is made in transmission with the geometry shown in Fig. 14.3*b*. Having determined μT, one may calculate T using the known absorption coefficient for the particular radiation used.

Since the diffracted intensity is proportional to the volume of film irradiated by the beam, the thickness determined in this way is the same as that for a film of uniform thickness occupying the same volume. One may establish this if the film is of nonuniform thickness by comparing the thickness determined by diffraction to that measured by the attenuation of the incident x-ray beam by absorption.

The accuracy of this method for measuring film thickness depends upon the value of μT. For a value of μT of 0.05 and R measured to a precision of 1%, the thickness is known to a precision of ±10%. For a film of gold using Cu Kα radiation, $\mu T = 0.05$ corresponds to a thickness of about 1200 A. As the thickness increases, the accuracy improves so that an error of about 2% would be expected for a 5000-A gold film.

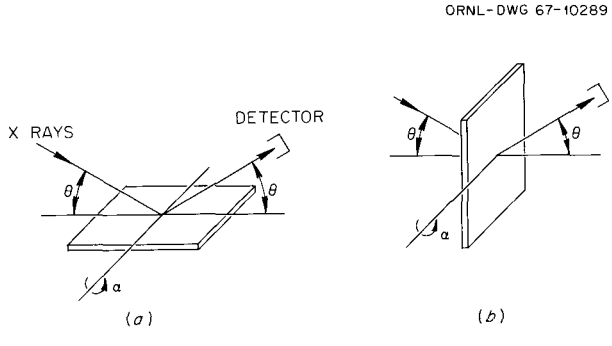

Fig. 14.3. Scattering Geometries for the Estimation of Sample Thickness by X-Ray Diffraction Methods. (*a*) Reflection, (*b*) transmission.

X-RAY MONOCHROMATORS

C. J. Sparks

We previously reported that graphite with highly oriented basal planes is an outstanding diffractor of x rays useful for diffraction experiments.[15] Curved monochromators offer an advantage over flat plates in that the divergent radiation from the source can be focused for more useful intensity. Initial results from singly curved pieces of pyrolytic graphite supplied by the Carbon Products Division of Union Carbide Corporation confirm the optimism of the earlier results. The intensity distribution in the diffracted beam is more uniform than for similar LiF monochromators. Also, the expected fivefold increase in diffracted intensity over LiF is achieved. Further evaluation of graphite for different diffraction geometries will be made.

THE DARWIN DYNAMICAL THEORY OF X-RAY DIFFRACTION

Bernard Borie

The central problem of x-ray crystallography has traditionally been, given a specific array of centers of scattering factor f, to combine the amplitudes and phases of the resultant scattered waves to

[15] C. J. Sparks, *Metals and Ceramics Div. Ann. Progr. Rept. June 30, 1966*, ORNL-3970, pp. 57–58. (A patent application has been filed on this development.)

recover the diffraction pattern associated with the array. Neither quantum mechanics nor electromagnetic theory is normally invoked. The crystallographer simply takes f to be the ratio of the wave scattered by an atom to that scattered by a classical electron and leaves its computation to the theoretical physicist. All of the electromagnetic and quantum theory of the problem is contained in the calculation of f.

The Ewald[16]–von Laue[17] dynamical diffraction theory is a departure from this custom. Here, to obtain the total wave field inside a perfect crystal one solves Maxwell's equations in a medium with a periodic time-dependent complex dielectric constant. The treatment is elegant but rather involved.

We show that that is not necessary, that all of the features of dynamical diffraction including the anomalous aspects of the Borrmann effect are recoverable with the usual tools of x-ray crystallography. No electromagnetic theory is used. The result is achieved by simply solving in Laue geometry the difference equations first solved by Darwin[18] in Bragg geometry.

A preliminary to writing the Darwin difference equations is to calculate the wave scattered by a single plane of scattering material. A family of such planes is then assembled to form a crystal, and the combination of the amplitudes and phases of the scattered waves is expressed by the difference equations.

The result of such a calculation gives

$$ig_0 = \frac{n\lambda}{\cos\theta_1}\frac{e^2 f(0)}{mc^2} \qquad (2)$$

and

$$ig = i\frac{n\lambda\mathcal{K}}{\cos\theta_2}\frac{e^2 f(\theta_1+\theta_2)}{mc^2}\,. \qquad (3)$$

In Eq. (3) $\mathcal{K}$ is a polarization factor, which is unity if the electric vector of the incident wave is parallel to the y-axis or $\cos(\theta_1+\theta_2)$ if the electric vector is in the xz plane. The atomic scattering factor at scattering angle $\theta_1+\theta_2$ is $f(\theta_1+\theta_2)$.

[16]P. P. Ewald, *Ann. Physik* **49**(1), 117 (1916).

[17]M. von Laue, *Ergeb. Exakt. Naturw.* **10**, 133 (1931).

[18]C. G. Darwin, *Phil. Mag.* **27**(315), 675 (1914).

ORNL-DWG 67-10290

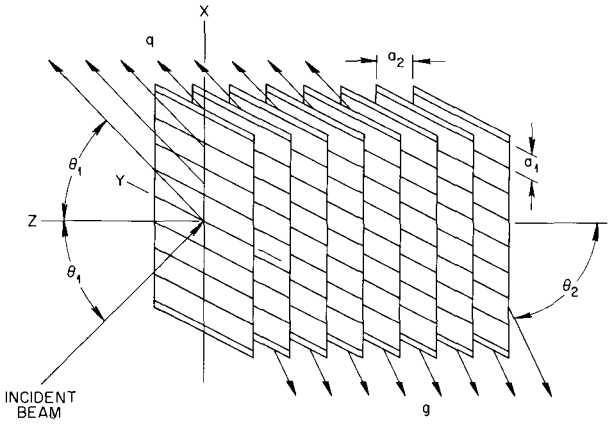

Fig. 14.4. Combination of Fresnel Diffracting Planes to Form a Crystal.

Equation (2) was derived by Darwin by means of a Fresnel zone construction. To obtain Eq. (3), a pseudo-Fresnel zone construction[19] was used. To obtain these equations one assumes a plane wave of x radiation of wavelength λ incident onto a plane containing n atoms per unit area. The direction of incidence makes an angle θ_1 with the normal to the atomic plane. Then ig_0 is the ratio of the complex amplitude of the wave scattered in the direction of incidence just after the plane to that of the incident wave just before the plane. The atomic scattering factor at zero scattering angle is $f(0)$, and e, m, and c are fundamental constants with their usual meanings.

A similar quantity for a wave scattered in a direction defined by θ_2 is ig, as illustrated in Fig. 14.4. Here both the scattered and incident waves are taken to have their directions of propagation in the xz plane. The atoms in each plane must be arranged in rows parallel to the y-axis spaced a_1 apart. Then θ_2 is related to θ_1, a_1, and λ by

$$a_1(\sin\theta_1 + \sin\theta_2) = h\lambda\,, \qquad (4)$$

where h is an integer.

The planes of Fig. 14.4 are numbered 0, 1, 2 ... r, ... and are a_2 apart; T_r is the complex amplitude of the wave in the θ_1 direction just before the rth plane; S_r is that in the θ_2 direction just after the rth plane. Difference equations relating

[19]B. Borie, "The Darwin Dynamical Theory of X-Ray Diffraction," accepted for publication in *Acta Crystallographica*.

these quantities may be written:

$$S_r = igT_r + S_{r-1}(1 + ig_0)e^{-i\phi_2} \tag{5}$$

and

$$T_{r+1} = T_r(1 + ig_0)e^{-i\phi_1} + igS_{r-1}e^{-i(\phi_1+\phi_2)}, \tag{6}$$

where

$$\phi_1 = (2\pi a_2/\lambda)\cos\theta_1$$

and

$$\phi_2 = (2\pi a_2/\lambda)\cos\theta_2 .$$

Equations (5) and (6) may be combined to obtain a single equation in T only. This difference equation may be solved subject to the boundary conditions that $T_0 = 1$ and $S_{-1} = 0$. This solution may be substituted into Eq. (6) to obtain a similar solution for S. The details of the derivation are given in the reference of Borie.[19] The result is

$$T_r = \frac{1}{2}\left\{1 - \frac{(1 + ig_0)\sin\Delta\phi}{[g^2 + (1 + ig_0)^2\sin^2\Delta\phi]^{1/2}}\right\}\beta_1^r + \frac{1}{2}\left\{1 + \frac{(1 + ig_0)\sin\Delta\phi}{[g^2 + (1 + ig_0)^2\sin^2\Delta\phi]^{1/2}}\right\}\beta_2^r \tag{7}$$

and

$$S_{r-1}e^{-i\phi_0} = \frac{1}{2}\left\{\frac{g}{[g^2 + (1 + ig_0)^2\sin^2\Delta\phi]^{1/2}}\right\}\beta_1^r - \frac{1}{2}\left\{\frac{g}{[g^2 + (1 + ig_0)^2\sin^2\Delta\phi]^{1/2}}\right\}\beta_2^r , \tag{8}$$

where $\phi_0 = (\phi_1 + \phi_2)/2$, $\Delta\phi = (\phi_1 - \phi_2)/2$, and

$$\beta = e^{-i\phi_0}\{(1 + ig_0)\cos\Delta\phi \pm i[g^2 + (1 + ig_0)^2\sin^2\Delta\phi]^{1/2}\} . \tag{9}$$

In Eqs. (7) and (8) β_1 corresponds to choice of the positive sign in Eq. (9) and β_2 the negative.

We consider the behavior of Eqs. (7) and (8) in the limit that $\sin^2\Delta\phi \gg g^2$. In that case the coefficients of β_1^r and β_2^r in Eq. (8) are very small, and there is no diffracted beam. The coefficient of β_1^r in Eq. (7) is also negligible, while that of β_2^r is essentially unity. Hence the transmitted beam is given by $T_r = \beta_2^r$. In the limit under discussion, from Eq. (9)

$$\beta_2 = e^{-i\phi_0}(1 + ig_0)e^{-i\Delta\phi} \cong e^{-i\phi_1}e^{ig_0} , \tag{10}$$

since g_0 is very small.

Thus, the phase retardation experienced by T_r as r is advanced to $r + 1$ is not ϕ_1, as we would expect in free space, but $\phi_1 - g_0$. We may think of this as a small advance in phase g_0 of the wave front each time it passes through a plane of scattering material. This causes the effective wave front, and hence the wave propagation vector, to be rotated through a small angle, giving rise to the normal refractive index of the medium.

If g_0 includes a small positive imaginary component, it is clear from Eq. (10) that upon transmission through a plane, the wave experiences not only a phase advance but is slightly attenuated as well. This attenuation is a consequence of the anomalous dispersion correction to f and gives rise to the usual linear absorption coefficient.

Now consider the behavior of Eqs. (7) and (8) when $\Delta\phi = 0$. In that case, they reduce to

$$T_r = \frac{1}{2}\beta_1^r + \frac{1}{2}\beta_2^r \tag{11}$$

and

$$S_{r-1}e^{-i\phi_0} = \frac{1}{2}\beta_1^r - \frac{1}{2}\beta_2^r , \tag{12}$$

where

$$\beta = e^{-\phi_0}\{1 + ig_0 \pm ig\} \cong e^{-i\phi_0}e^{i(g_0 \pm g)} . \tag{13}$$

The condition for diffraction is satisfied, and a wave in the S direction is "turned on." Note from Eqs. (11), (12), and (13) that both the T and S waves are each composed of two components with different refractive indices and absorption coefficients. In fact, if the states of polarization are taken into account, each wave is made up of four components, since Eq. (3) for g includes a polarization factor. Thus, for unpolarized incident radiation, the net wave field inside the crystal is the

sum of eight waves, each characterized by its own propagation direction, state of polarization, absorption coefficient, and refractive index.

If the imaginary part of f is independent of sin θ/λ for that state of polarization for which $\mathcal{K} = 1$, it is clear from Eqs. (2) and (3) that the imaginary parts of g_0 and g are equal. In that case, from Eq. (13), for those waves described by β_2 the linear absorption coefficient vanishes. The result is anomalous transmission, or the Borrmann effect.

A detailed consideration[19] of Eqs. (7) and (8) for $\Delta\phi$ small but not zero yields all of the properties of the wave point and the dispersion surface originally given by the Ewald–von Laue treatment.

Part II.

High-Temperature Materials Program

15. Physical and Mechanical Metallurgy of High-Temperature Materials

W. O. Harms

Research in this program is directed toward the solution of materials problems associated with high-temperature high-performance reactors for advanced propulsive and power applications, especially space devices. Particular emphasis is placed on problems involving tantalum-, niobium-, and molybdenum-base alloys. Tungsten and tungsten-base alloys are investigated in the Tungsten Metallurgy program, which is covered in Chap. 16 of this document. The principal efforts on refractory materials in this activity include fabrication and procurement; development and evaluation of joining procedures; physical metallurgy studies concerning recrystallization, grain growth, interstitial contamination, aging response, and strengthening mechanisms; long-time creep-rupture behavior, including the effects of irradiation; effects of dynamic loading at elevated temperatures; application of advanced nondestructive testing techniques; and measurement of important thermophysical properties.

In the text that follows, frequent reference is made to commercial refractory alloys by their trade designations. The nominal compositions of these alloys are listed in Table 15.1.

Table 15.1. Nominal Compositions of Refractory Alloys

Designation	Base	Alloying Elements (wt %)
B-66	Niobium	5 Mo, 5 V, 1 Zr
C-129 Y	Niobium	10 Hf, 10 W, 0.1 Y
Cb-752	Niobium	10 W, 2.5 Zr
Cb-753	Niobium	5 V, 1.25 Zr
D-43	Niobium	10 W, 1 Zr, 0.1 C
FS-85	Niobium	27 Ta, 10 W, 1 Zr
SU 16	Niobium	11 W, 3 Mo, 2 Hf, 0.08 C
TZM	Molybdenum	0.5 Ti, 0.08 Zr, 0.02 C
Cb-TZM	Molybdenum	0.5 Ti, 0.08 Zr, 0.02 C, 1.5 Nb
TZC	Molybdenum	1.2 Ti, 0.25 Zr, 0.15 C
T-111	Tantalum	8 W, 2 Hf
T-222	Tantalum	9.6 W, 2.4 Hf, 0.01 C

MECHANICAL PROPERTIES OF REFRACTORY ALLOYS

J. R. Weir

In this phase of the program, those properties of greatest importance for long-time service are emphasized, namely, creep, stress to rupture, and fatigue at elevated temperatures. The objectives are (1) to compare the creep and rupture strengths of promising commercial alloys and obtain useful design data extending to at least 1000 hr, (2) to determine the effects of mechanical and thermal treatment and irradiation on the creep-rupture properties of advanced alloys and establish the optimum metallurgical condition on the basis of long-time tests, and (3) to perform those specialized tests, as, for example, under dynamic loading, necessary to qualify a material for a particular engineering application.

Figure 15.1 shows the stress to produce rupture in 1000 hr as a function of temperature for all of the alloys investigated on this program over a

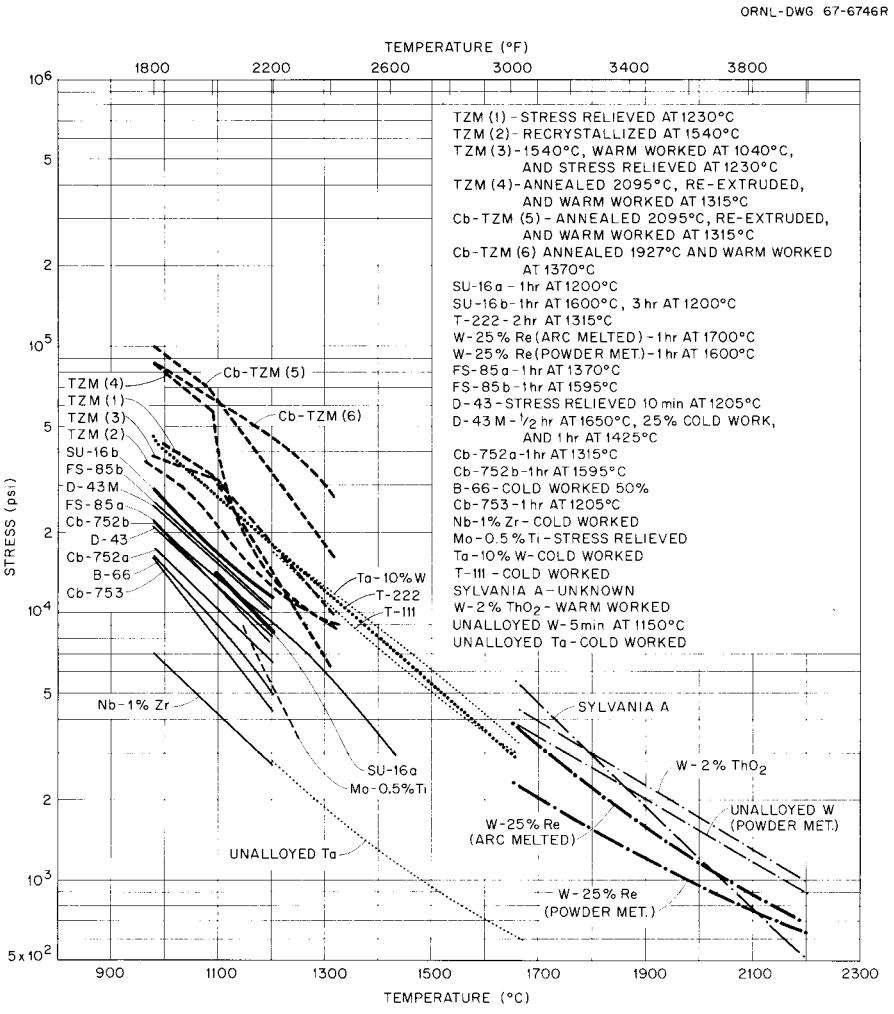

Fig. 15.1. Stress to Produce Rupture in 1000 hr vs Temperature for Selected Refractory Metals and Alloys.

period of several years. Data obtained during the present report period are represented by heavy lines in the figure. Although only single heats are represented, major trends are apparent among the four alloy bases studied – niobium, tantalum, molybdenum, and tungsten.

While the niobium alloys are generally quite fabricable, they are seen to be the weakest of the four sets of alloys investigated. Although the strength of early molybdenum alloys such as Mo–0.5% Ti drops sharply with increasing temperature, more complex alloys such as TZM and Cb-TZM are quite strong at moderate temperatures. The tantalum-base alloys combine good fabricability with useful strength over a broad range of temperatures. Data for tungsten and tungsten alloys are included in this plot for reference purposes and are discussed in more detail in Chap. 16.

It should be noted that the order of merit indicated in Fig. 15.1 might be expected to change due to heat-to-heat variations in composition and microstructure. Also, the order would be different if merit were based on a different design criterion, such as stress to produce 1% creep in 1000 hr or density-compensated rupture or creep strength.

Effect of Fabrication Variables on Creep-Rupture Properties of Molybdenum Alloys

R. L. Stephenson

We are continuing our studies on the effect of fabrication variables on the creep-rupture properties of molybdenum alloys.[1] Alloy TZM was

[1] R. L. Stephenson, *Metals and Ceramics Div. Ann. Progr. Rept. June 30, 1966*, ORNL-3970, pp. 72–75.

studied in four conditions. Stress-relieved TZM and recrystallized TZM, representative of current manufacturing practice, were investigated to provide reference data. Material for a third group of specimens was recrystallized at 1540°C and warm worked at 1040°C, and material for a fourth group of specimens was solution annealed at 2095°C, reextruded, and then warm worked at 1315°C. The stresses to produce rupture in 1000 hr are plotted as a function of temperature for TZM in each of these conditions in Fig. 15.1. It can be seen that the solution-annealed, reextruded, and warm-worked material (condition 4) is the strongest at the lower temperatures, while the recrystallized and warm-worked material (condition 3) is strongest at the higher temperatures.

The 1000-hr rupture stress of niobium-modified TZM (Cb-TZM) in two conditions is also shown in Fig. 15.1. One lot of material, designated Cb-TZM(5), was solution annealed at 2095°C, extruded at 1430°C, and warm worked at 1315°C. Another lot, designated Cb-TZM(6), was solution annealed at 1930°C and warm worked at 1370°C. This latter alloy is the strongest of all the alloys tested in the temperature range 980 to 1315°C. On a density-compensated basis this alloy would compare even more favorably with tantalum- and tungsten-base alloys.

Creep-Rupture Properties of SU 16

R. L. Stephenson

The SU 16 alloy has been investigated in two conditions. One lot of material was annealed 1 hr at 1205°C, and the other was annealed 1 hr at 1600°C, then aged 3 hr at 1200°C. The test results for these materials are compared with other materials in Fig. 15.1. This particular heat of material in the annealed-and-aged condition is the strongest niobium-base alloy we have tested.

Creep-Rupture Properties of T-222

H. E. McCoy

The creep-rupture properties over the temperature range of 980 to 1650°C are presented in Fig. 15.1 for a single heat of T-222. At test temperatures up to 1205°C the fractures were predominantly transgranular. At 1430°C the material recrystallized during testing and failed intergranularly. At 1650°C the specimens were typified by extensive grain growth, intergranular void formation, and intergranular failure. Transverse weld specimens were prepared and tested over the same temperature range as the base metal. The welded specimens were slightly stronger than the base metal, an effect that we attributed to the different orientation of the test specimens. With only one exception, the transverse weld specimens failed in the base metal with only slight deformation of the weld.

Time-Temperature Parameters for Creep-Rupture of Refractory Alloys

R. W. Swindeman

There is a great incentive for developing reliable time-temperature parameters to describe the creep and rupture characteristics of refractory alloys. First, the limitations on equipment make it impractical to extend testing much beyond 1000 hr, whereas some potential applications involve service beyond 10,000 hr; time-temperature parameters are useful in making extrapolations to such times. Second, there are some applications, such as in radioisotope heat sources, where structural materials will experience slowly varying temperature and stress; time-temperature parameters are useful in the design and analysis of such devices.

We have calculated the Larson-Miller parameter for several alloys, using a technique similar to that suggested by Manson and Mendelson.[2] This involves a least-squares fit of the Larson-Miller equation:

$$P = f(\sigma) = T(C + \log t) ,$$

where T is the absolute temperature, t is the time to rupture or to a specific strain, C is a material constant, and P is a function of stress σ and is represented by a cubic polynomial in the logarithm of stress:

$$P = A_0 + A_1 \log \sigma + A_2(\log \sigma)^2 + A_3(\log \sigma)^3 .$$

Typical of the results we have obtained are the three curves shown in Fig. 15.2 for rupture of T-111, FS-85, and TZM. These curves represent a plot of experimental data in which the creep

[2] S. S. Manson and A. Mendelson, *Optimization of Parametric Constants for Creep-Rupture Data by Means of Least Squares*, N-62-70249 (March 1959).

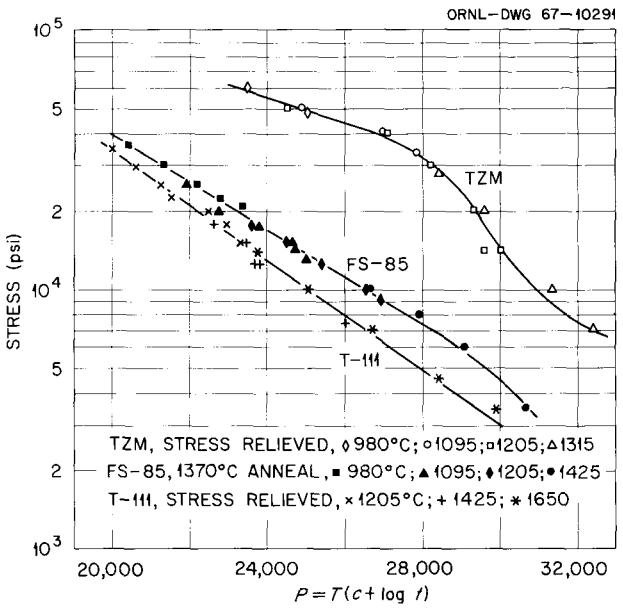

Fig. 15.2. Larson-Miller Parametric Plots for Rupture of Three Refractory Alloys.

stress is the ordinate and the calculated value of the Larson-Miller parameter P is the abscissa.

We intend to expand our studies to include other parametric formulations and to explore the significance of any differences in the reliability of extrapolated data.

Effect of Irradiation on Creep Properties of Refractory Alloys

R. W. Swindeman

We are developing techniques for creep testing of refractory metals under neutron exposure. One experiment containing five molybdenum specimens has been conducted in the poolside facility of the Oak Ridge Research Reactor. The specimens were 0.1-in.-diam rods with a 2-in. gage length and were encapsulated, as illustrated in Fig. 15.3, in an evacuated stainless steel housing. The mechanical loading and extension sensing systems were similar to those employed for Hastelloy N and stainless steel creep experiments, which are described elsewhere.[3]

All five specimens exhibited large thermal gradients along the gage length, but by adjusting heaters outside the capsules we were able to maintain the temperatures at the specimen center and near the reactor within 6°C of one another. The out-of-reactor end measured 30 to 60°C below the other two temperatures. Extension curves for three of the specimens are shown in Fig. 15.4. Interpretation of these data is pending the completion of postirradiation examination of the specimens and the determination of creep curves for the out-of-reactor control specimens. In the meantime, we are redesigning the experiment to include liquid metals as heat-transfer media in an effort to minimize thermal gradients.

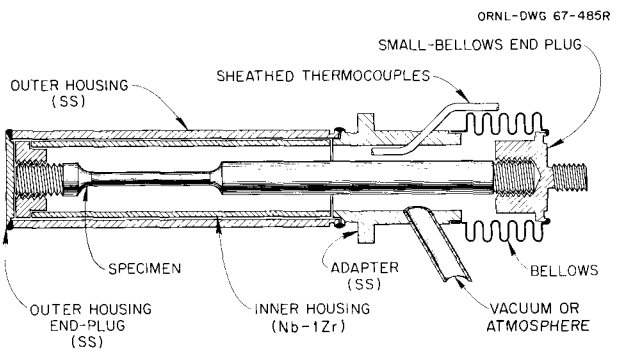

Fig. 15.3. Specimen Assembly for In-Reactor Creep Experiment.

Fatigue of Refractory Alloys at Elevated Temperatures

R. W. Swindeman

We completed a survey of the influence of temperature on the strain-fatigue life of niobium alloy D-43. Tests were conducted in vacuum at a plastic strain range of 1% and a frequency of 1 cps. Test data for the temperature range 20 to 1205°C are shown in Table 15.2. We define the plastic strain range as the width of the stress-strain hysteresis loop at zero stress and the stress range as the total stress change in the loop. The resistance to cyclic strain was as good or better at elevated temperature than around room temperature. As might be expected, the stress corresponding to this level of strain decreases considerably with increasing temperature. Additional testing is in progress at other strain levels to define fatigue curves in the temperature range from 850 to 1200°C.

[3] J. W. Woods, "In-Reactor Mechanical Properties Experiments," *International Symposium on Developments in Irradiation Capsule Technology, Pleasanton, California May 3–5, 1966*, CONF-660511 (March 1967).

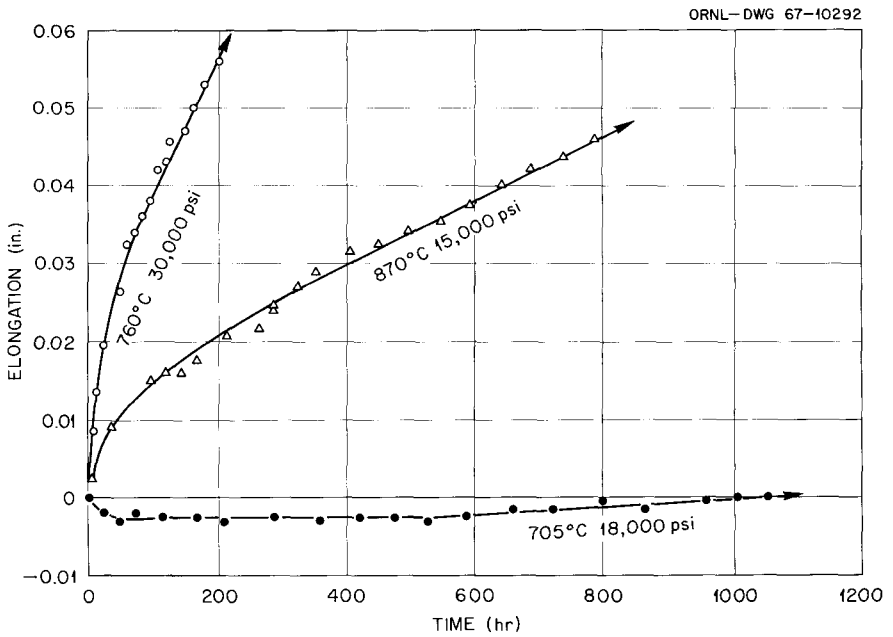

Fig. 15.4. Creep Curves Obtained on Molybdenum Specimens Tested in the Poolside Facility of the ORR.

Table 15.2. Effect of Temperature on the Fatigue Life of D-43 at a 1% Cyclic Plastic Strain Level

Temperature (°C)	Stress Range (psi)	Life (cycles)
20	120,000	2980
300	100,000	6120
540	90,000	6880
760	84,000	7570
870	79,000	3640
980	75,000	8430
1095	69,000	3100
1205	54,000	8920

PHYSICAL METALLURGY OF REFRACTORY ALLOYS

H. Inouye

Aging Characteristics of T-222 and Role of Carbon on Creep Properties of Ta-W-Hf Alloys

D. T. Bourgette

The determination of the aging characteristics of T-222 was a part of a comprehensive program

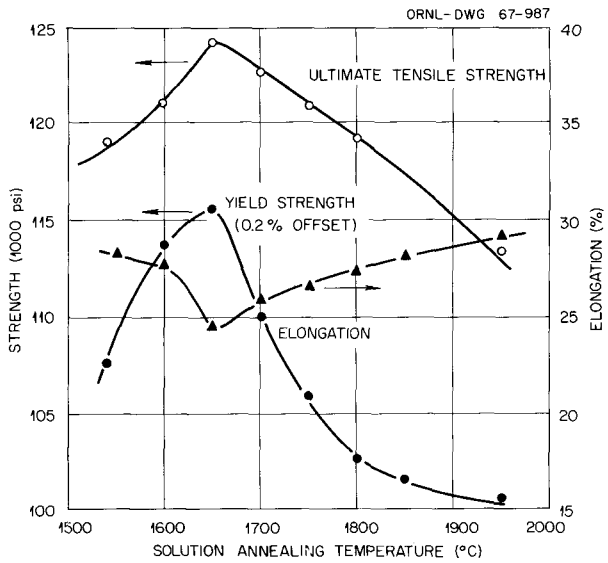

Fig. 15.5. Room-Temperature Tensile Properties of T-222 Solution Annealed for 1 hr at Various Temperatures and 10^{-8} Torr, Then Rapidly Quenched.

that included recovery, recrystallization, grain growth, and aging studies of a family of alloys similar to T-111.

The solutioning behavior of T-222 was very similar to that of T-111. As illustrated in Fig. 15.5, the optimum temperature for maximum tensile strength for a 1-hr anneal was 1650°C when the

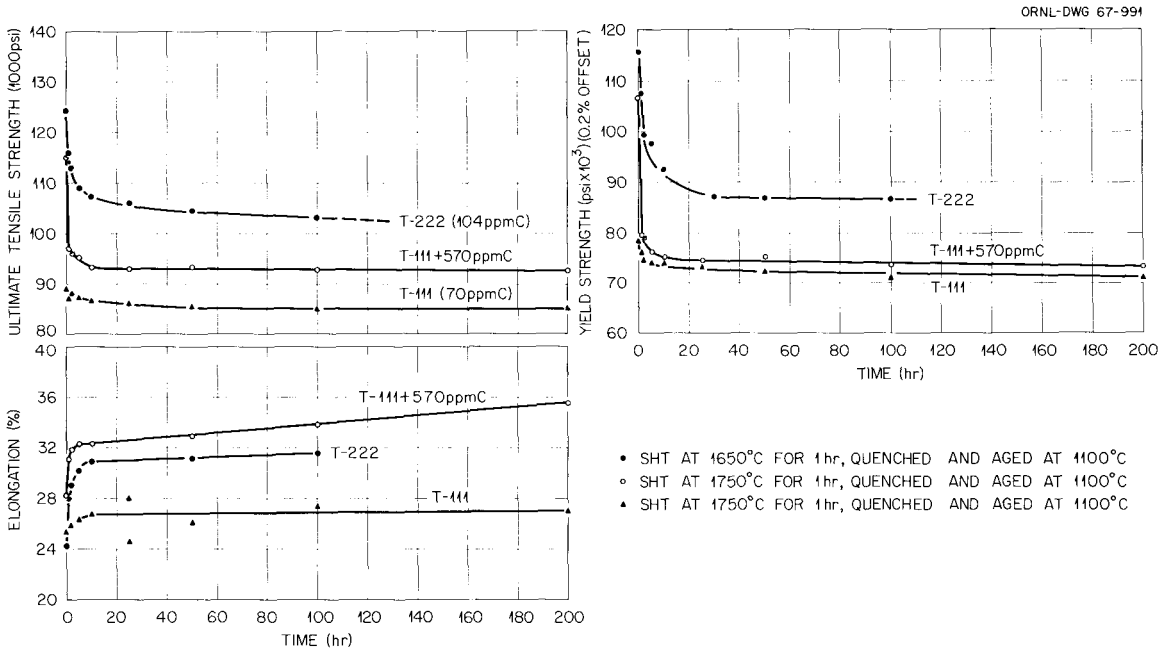

Fig. 15.6. Effect of Duplex Aging Treatments on the Room-Temperature Mechanical Properties of Commercial T-111 and T-222 and T-111 Doped with 570 ppm C.

specimens were quenched. Slow cooling, that is, radiation cooling, the specimens from the annealing temperatures resulted in a reduction of the tensile strength by about 20%. In addition, the slow-cooled alloy did not exhibit minimum or maximum points.

Solution-annealed (1650°C for 1 hr) and then quenched specimens of commercial T-222 were aged for times of 15 min to 100 hr at temperatures of 1100 to 1315°C. As illustrated in Fig. 15.6, a decrease in the room-temperature strength occurred within 10 hr. After this initial decrease, the room-temperature strength remained the same for aging times to 1600 hr (not shown) at 1100°C. The behavior of aged T-222 was very similar to that of commercial T-111 and T-111 doped with 570 ppm C.

The optical microstructure of solution-annealed T-222 and T-111 was single phase when quenched; subsequent aging treatments at 1100 to 1480°C resulted in the precipitation of second phase. This second phase, presumably a carbide, increases in particle size and amount with an increase in aging time. Apparently, T-222, like T-111, is fully aged after the initial solution anneal, and subsequent heat treatments in this temperature range merely result in overaging. The work has been completed, and a final report is being prepared.

Future work will be concerned with the determination of the effects of carbon, oxygen, and changes in the concentrations of tungsten and hafnium on the creep behavior of tantalum-tungsten-hafnium alloys. The strengthening mechanism will be studied by electron transmission microscopy.

Diffusion of Nitrogen in Nb–1% Zr

H. Inouye

The diffusivity of nitrogen in Nb–1% Zr was determined by measuring the sorption rate of nitrogen by the alloy under the conditions listed in Table 15.3. This work is part of a broader program whose aim is to determine the role of interstitials in refractory metals. For these temperatures and pressures the inward flux of nitrogen occurred from a nitride-free surface whose nitrogen concentration C_s was slightly lower than the equilibrium concentration C_e. The diffusivity, which increased with temperature according to the equation $D_N = 1.4 \times 10^{-5} \exp(-42{,}000/RT)$, lowered the nitrogen concentration ratio (denoted as the ratio C_s/C_m in Table 15.3) from about 8 at 1200°C to about 1 at 1450°C.

Table 15.3. Concentration Gradients and Diffusion Coefficients of Nitrogen in Nb–1% Zr

Temperature (°C)	Pressure (torr)	C_e (ppm)	C_s (ppm)	C_s/C_m [a]	D_N (cm^2/sec)
1200	2.5×10^{-7}	1750	1690	7.94	9.2×10^{-12}
1300	4.8×10^{-7}	1140	875	4.37	5.6×10^{-11}
1450	1.8×10^{-7}	255	230	1.15	5.3×10^{-10}

[a]Ratio at C_m = 200 ppm N.

Our results for D_N in Nb–1% Zr are about three orders of magnitude lower than D_N in unalloyed niobium.[4] Internal friction data for Nb–0.8% Zr–nitrogen and niobium-nitrogen alloys[5] show that this amount of zirconium increases the relaxation time by a factor of 700, which is about the ratio found by us for D_N in the Nb–1% Zr alloy and unalloyed niobium.

Vaporization of Haynes Alloy No. 25 Under Stress

D. T. Bourgette

The evaporation kinetics of Haynes alloy No. 25 has been determined for the unstressed condition at temperatures of 870 to 1150°C, and a final report has been issued.[6]

Under certain conditions, stress is known to enhance rate processes such as corrosion and diffusion by vacancy generation and increased dislocation movement. Utilizing this premise and the results of the initial vaporization work, which showed that evaporation of multicomponent alloys was diffusion-rate dependent, a program was initiated to determine the effects of stress on evaporation kinetics and the effects of evaporation on creep behavior. The equipment necessary to conduct adequate experiments in high vacuum has been designed and is currently being fabricated.

[4]W. M. Albrecht and W. D. Goode, Jr., *Reaction of Nitrogen with Niobium*, BMI-1360 (July 1959).

[5]R. W. Powers and M. V. Doyle, "Diffusion of Interstitial Solutes in Group V Transition Metals," *J. Appl. Phys.* 30, 514 (1959).

[6]D. T. Bourgette, *Vaporization Phenomena of Haynes Alloy No. 25 to 1150°C*, ORNL-TM-1786 (May 1967).

[7]R. G. Donnelly, *Metals and Ceramics Div. Ann. Progr. Rept. June 30, 1966*, ORNL-3970, pp. 64–66.

JOINING OF REFRACTORY MATERIALS

G. M. Slaughter

Welding of Advanced Refractory Alloys

R. G. Donnelly

We are continuing to investigate the weldability of advanced refractory alloys and the effects of aging on the properties of welds in these alloys. Investigations on the aging of Cb-752 and Cb-753 have continued and SU 16 was included in our overall weldability evaluation program.

The results of aging gas-tungsten-arc welded sheet specimens of Cb-752 and Cb-753 and subsequently subjecting them to transverse bending at room temperature were reported previously.[7] Hardness traverses of selected weld samples were made and are presented in Fig. 15.7. In each case the hardness of a specimen in the "as welded" condition is presented along with that of a specimen found to be embrittled during aging and subsequent bending (lower temperature heat treatment) as well as one in the overaged condition (higher temperature heat treatment).

From Fig. 15.7*a* it is evident that the Cb-753 alloy did not exhibit any hardness increase in the heat-affected zone or base metal. Indeed, the only hardness increase of any significance on these profiles appears in the weld metal, that is, region C of the specimen aged 200 hr at 760°C. These results correspond to those obtained on bend specimens of Cb-753 containing welds embrittled by this treatment; cracking was always confined to the weld metal.

The hardness profiles of the Cb-752 welds are presented in Fig. 15.7*b*. Note that although zone D is the metallographically detectable heat-affected zone with its attendant recrystallization

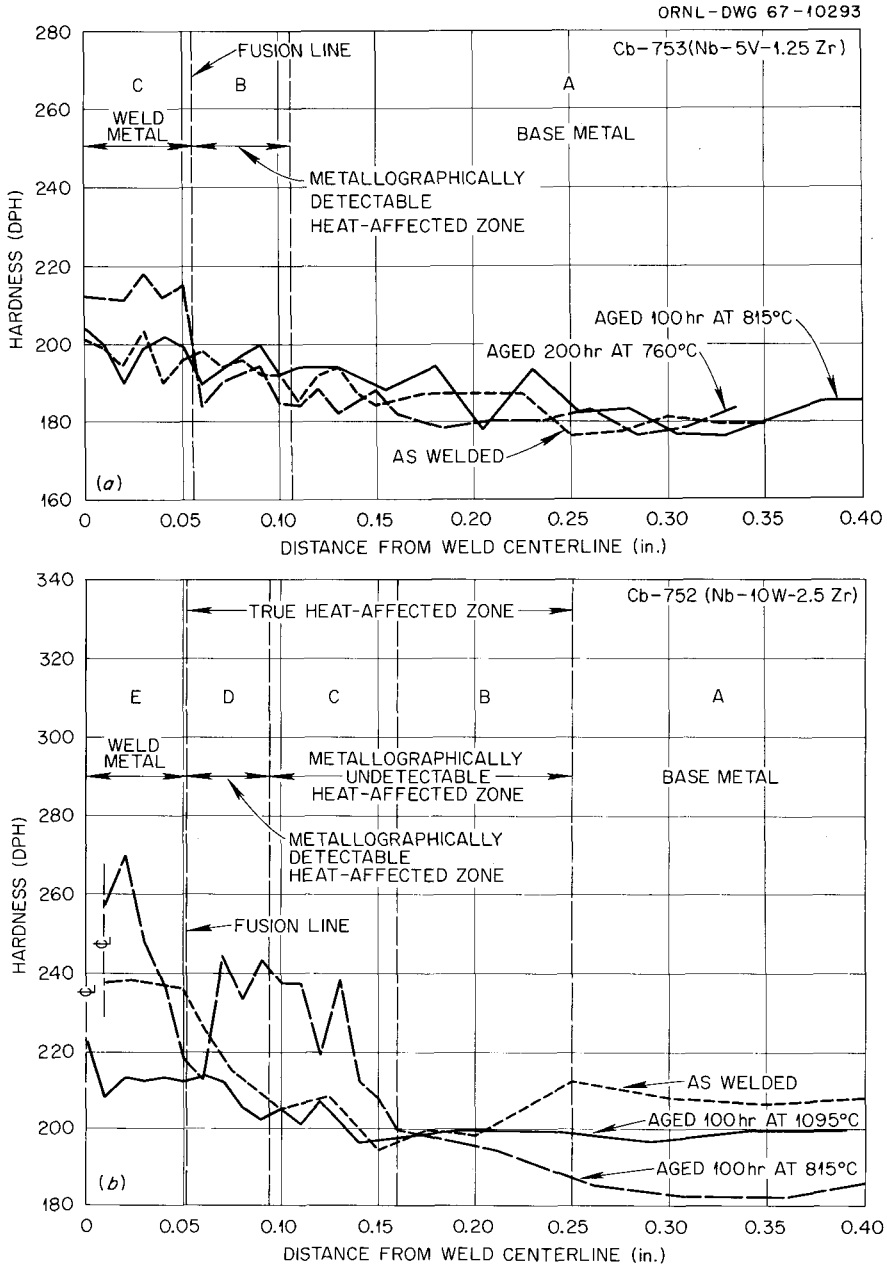

Fig. 15.7. Hardness Profiles of Weldments in (*a*) Cb-753 and (*b*) Cb-752.

and grain growth near the weld fusion line, the hardness traverse shows that the true heat-affected zone encompasses regions B and C as well. Within the weld metal the hardness remained constant, but at a somewhat higher value.

After the as-welded joint was aged for 100 hr at 816°C, the hardness profile was altered considerably. The heat-affected zone had apparently been made sensitive to an aging reaction by the welding operation, and in the weld the hardness values increased toward the weld center line. Metallographic examination of the solidification pattern of the weld metal revealed that the amount of interdendritic material also increased as the weld center line was approached. Thus the interdendritic material is apparently responsible for the hardness increase. Furthermore, examination of joints tested after being exposed to this embrittling treatment showed the cracking to be concentrated in this interdendritic material.

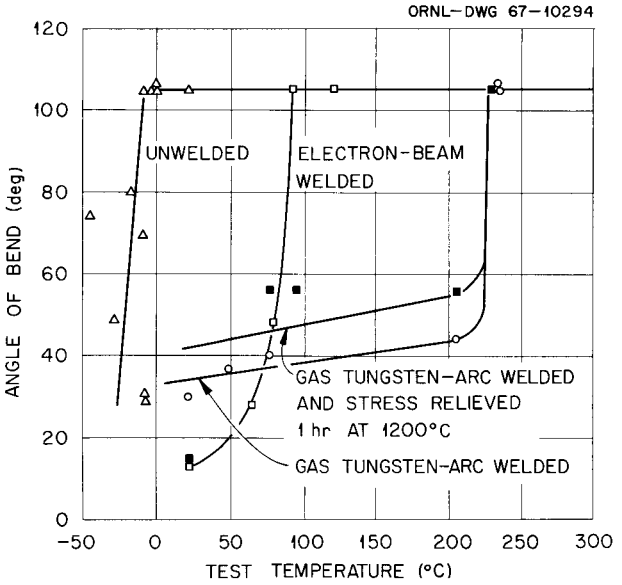

Fig. 15.8. Ductile-to-Brittle Transition Curves for SU 16 Alloy Weld Specimens.

The large hardness increase in the heat-affected zone leads one to expect that cracking might occur during the bending of aged welds. Again, this had been verified metallographically.

The hardness profile of an overaged specimen (100 hr at 1093°C), which was ductile upon bending at room temperature, is also presented in Fig. 15.7*b*. A general moderating of the hardness is evident.

The niobium alloy SU 16, although originally developed for gas-turbine blades,[8] is of potential interest as a structural material for nuclear and space applications. Therefore, we determined the bend ductile-to-brittle transition temperatures for welds in 0.060-in.-thick sheet. The data for 4*T* bend tests on specimens welded by the electron-beam and gas-tungsten-arc processes are shown in Fig. 15.8. Data for unwelded specimens and "stress-relieved" welds are included also.

As expected, the ductile-to-brittle transition occurs at relatively high temperatures. Although the transition temperature of the unwelded sheet is below room temperature, electron-beam welds exhibit a transition of about 90°C and gas-tungsten-arc welds 230°C. The manufacturer's recommended "stress relief" of 1 hr at 1200°C did not lower the undesirably high transition temperature. However, it appears that a slight improvement was obtained in the amount of bending before cracking.

An aging or embrittling reaction also occurred in welds at temperatures in the 800 to 1200°C range. In our tests, the phenomenon was confined to the weld metal and heat-affected zone and was similar to the embrittlement exhibited by all other welded niobium alloys.

Brazing Alloy Development

N. C. Cole D. A. Canonico

Our purpose is to develop brazing alloys for joining refractory metals and ceramics to themselves and to each other. The primary objective concerns alloys for use in the temperature range of 1300 to 1900°C; however, we are not restricted to this range if other alloys are discovered that exhibit unusually attractive features. Studies on the titanium-vanadium-based alloys have been initiated, and work has progressed on other systems discussed previously.[9] Shear strengths were determined on joints brazed with specific compositions that warranted further development. Base metals of TZM and Ta–10% W were selected as being typical of fabricable high-strength materials of interest in brazed systems.

We found that the strength of a brazed joint is dependent upon the base metal. At room temperature the Ta–10% W specimens brazed with the experimental alloys had shear strengths in excess of 40,000 psi; TZM specimens exhibited strengths of greater than 20,000 psi. At elevated temperatures, this advantage of Ta–10% W did not necessarily prevail. However, regardless of the base metal, most of the brazing alloys maintained rather impressive shear strengths (near 20,000 psi) up to temperatures within 200°C of their melting points. Furthermore, the brazing alloy 35% Ti–35% Zr–30% Cr maintained a shear strength of greater than 10,000 psi at a temperature within 25°C of its melting point regardless of the base metal.

One titanium-base brazing alloy containing 21% V and 25% Cr proved outstanding in its ability to wet ceramics. Figure 15.9 shows its excellent wettability and flowability on both Al_2O_3 and tantalum. The penetration of the brazing alloy into the pores of the Al_2O_3 (Fig. 15.10) provides a good mechanical bond in addition to the metallurgical bond. In a qualitative shear test of an Al_2O_3 brazement, failure occurred in the ceramic.

[8] Kawecki Chemical Company, New York, *SU 16 Niobium-Base Alloy*, Bulletin, 1965.

[9] D. A. Canonico, *Metals and Ceramics Div. Ann. Progr. Rept. June 30, 1966*, ORNL-3970, pp. 66–68.

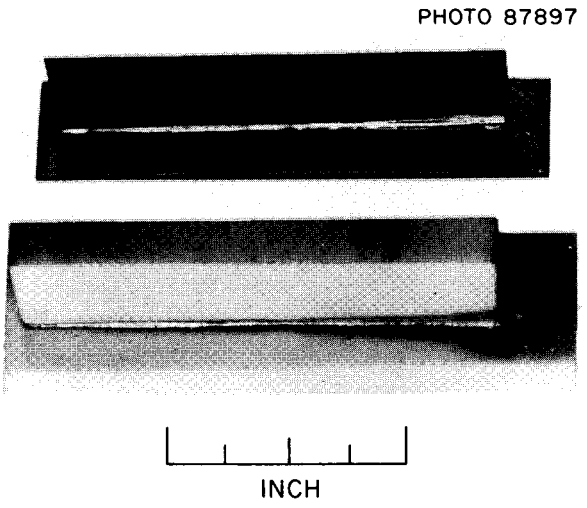

Fig. 15.9. Tantalum (Top) and Aluminum Oxide (Bottom) T-Joints Brazed with Experimental Alloy 13E (Ti–21% V–25% Cr). Excellent flow is evident.

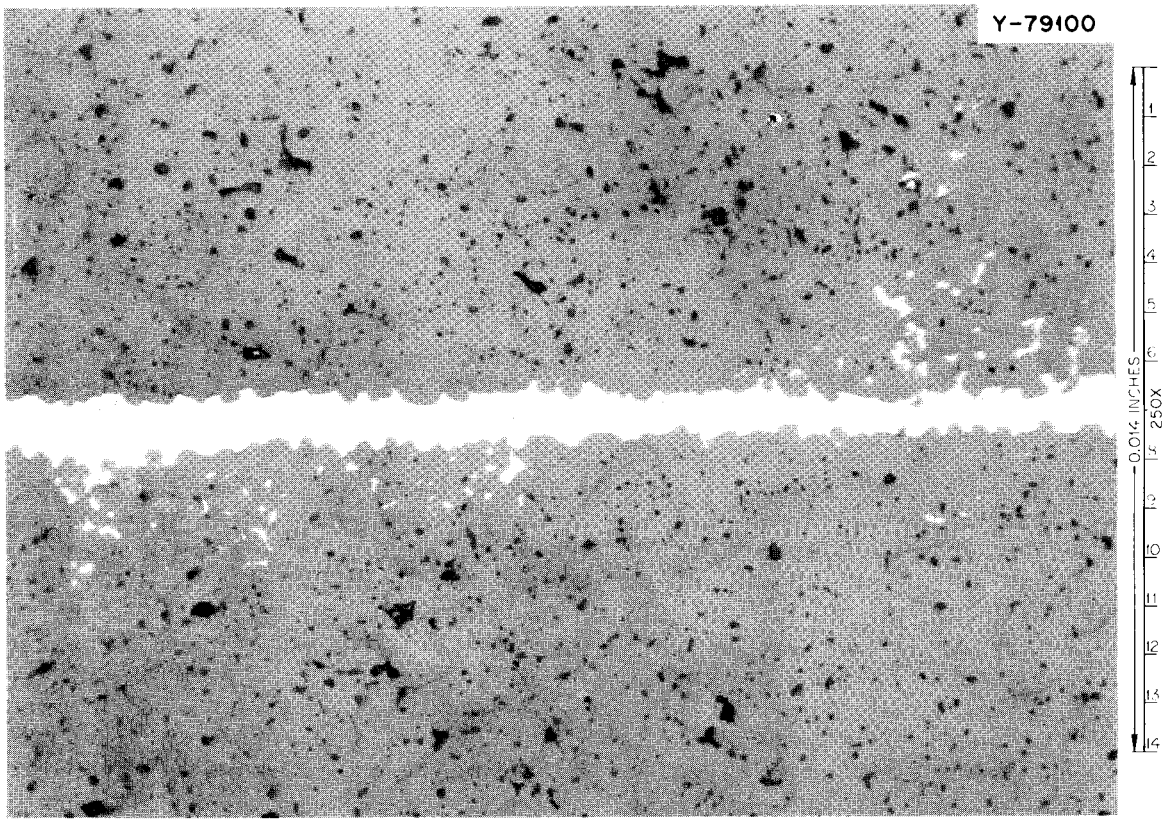

Fig. 15.10. Microsection of Brazed Joint Between Two Pieces of Aluminum Oxide, Showing Good Flow and Penetration.

Corrosion Loop Component Welding

E. A. Franco-Ferreira

A large D-43 forced-circulation potassium corrosion loop (FCL-8) was fabricated. The operation and other aspects of this loop are discussed in Chap. 17. The final qualification of the weldability of the loop material was made when the first weld was deposited. The sequence was arranged such that this weld was the heaviest section weld in the system; it was a mitre-joint in two pieces of heavy-wall pipe. After welding, the joint was

PHOTO 85360

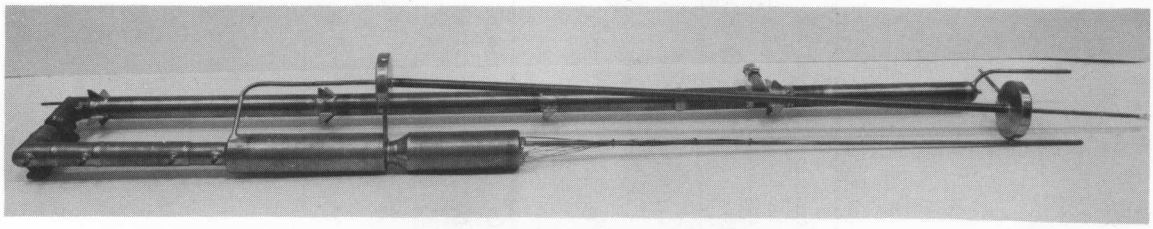

Fig. 15.11. Boiler and Condenser Legs of D-43 Loop FCL-8 Before Completion of Final Butt Weld.

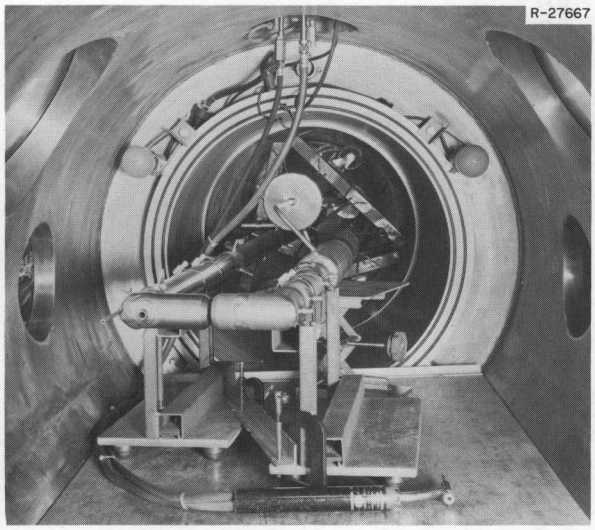

Fig. 15.12. View of D-43 Loop FCL-8 in Welding Chamber in Position for Final Butt Weld.

carefully inspected for defects before any additional loop construction was undertaken. In general, the welding proceeded routinely; however, a few minor cracking problems were encountered. In one case, a small crack was noted in the base metal in the bevel area of the weld after the root pass had been deposited in one of the condenser section welds. This defect was machined out until all dye-penetrant indications were removed. Subsequent rewelding resulted in a sound weld. The other cracking problem was encountered when some heater support lugs were welded to the boiler section over existing welds. Cracks, which probably resulted from stresses set up when the support lugs were welded on, were noted in the surfaces of the original welds. The defects were removed by grinding until all dye-penetrant indications were removed. After subsequent repair welding of the grinding depressions no defects were indicated.

A view of the completed boiler and condenser legs of the loop before completion of the final butt weld is shown in Fig. 15.11. Figure 15.12 is a view of the welding chamber with the loop in position for the final butt-welding operation.

FABRICATION OF T-111 TUBING

W. R. Martin

Arc Melting and Casting of Ingots

R. E. McDonald C. W. Dean
J. M. Jones

The melting parameters for the T-111 alloy development program have been established. Four electrodes prepared by "sandwiching" tantalum strip, tungsten foil and wire, and hafnium rods were consumably arc melted into 4-in.-diam by approximately 7-in.-long ingots. Due to composition inhomogeneities, particularly tungsten segregation, these ingots were given a second vacuum arc melt with an intermediate extrusion step. This double-melt, intermediate-extrusion process assures a homogeneous product.

The melting of this alloy requires approximately 6200 amp of current at 30 v. To begin melting, the strike is made at 5000 amp and almost immediately an additional rectifier is brought in at 1200 amp. This sequence is necessary to prevent the electrode from sticking to the bottom of the mold and to initiate melting. If the current is held at a lower level, a low-voltage plasma forms and concentrates on the mold wall, resulting in a burn-through. The electrode cross-sectional area must not exceed one-fourth that of the mold. Vacuum is maintained at 5×10^{-5} torr during melting to remove volatile impurities.

Table 15.4. Summary of Extrusion Data for T-111

Extrusion	Billet Dimensions (in.)			Weight (lb)	Temperature (°C)	Extrusion Ratio	Force (tons)		Speed (in./sec)	Extrusion Constant	Extrusion Dimensions (in.)		
	OD	Length	ID				Maximum	Minimum			OD	ID	Length
Round Rods													
0356[a]	3.950	6.00		39.2	1650	8.8							
0380	3.930	6.875		46.2	1850	4.1	980	900	14.9	106,100	1.999		27.6
Tube Shells													
0365	3.985	7.60	1.125	56.0	1750	4.1	1040	950	16.5	113,200	2.001	1.064	30.8
0417	3.915	5.75	1.125	33.0	2000	4.7	1180	860	1.4	117,200	2.010	1.009	21.51
0418	3.915	5.25	1.125	30.1	2000	4.1	900	740	10.2	78,100	2.125	1.050	18.0
Sheet Bar													
0357	3.860	6.75	1.125	41.1	1750	7.1	1100	1060	13.7	86,400	1.506 × 3.064[b]		16.0

[a]Extrusion failed.

[b]Thickness and width, respectively, for sheet bar.

One of the problems encountered early in this alloy development program was the loss of hafnium during vacuum arc melting. To stay within the 1.8 to 2.2% specification range, we determined that 3.0% Hf must be charged. At that time no indication was given that tungsten was lost during melting. However, chemical analysis now shows that the hafnium loss is not as great as originally reported and some tungsten is also lost. Each heat of the alloy that has been melted has a total interstitial impurity content (C + O + H + N) of less than 100 ppm, with the carbon levels averaging 25 ppm.

Since T-111 is still in the developmental stages, we are also making the alloy electrodes by an alternate method, powder metallurgy. Electrodes have been formed by blending powders of tantalum, tungsten, and hafnium hydride, isostatically pressing at 30,000 psi, and sintering to enhance the integrity of the electrodes and to remove as much of the volatile impurities as possible. These electrodes have been arc melted once in vacuum and are to be extruded as tube shells and processed into tubing.

Extrusion and Drawing of Tubing

R. E. McDonald C. W. Dean G. A. Reimann

Six T-111 extrusions have been made. The extrusion parameters are given in detail in Table 15.4. One primary extrusion (No. 0356) broke apart because of excessive tungsten segregation. A sheet bar (No. 0357) was extruded and a portion of it is being used to study subsequent fabrication parameters. Three tube shells have been extruded as Nos. 0365, 0417, and 0418 and are being machined for subsequent fabrication into tubing.

The drawing procedures necessary for the production of T-111 tubing for corrosion loop FCLLL-1 (see Chap. 17) have been tentatively developed. All of this work is conducted at room temperature with the chain-driven drawbench, using hardened steel mandrels.

One T-111 as-extruded tube shell was machined to remove surface defects and ensure bore concentricity. It was then reduced by mandrel-swaging to a diameter small enough (less than 1.5 in.) to be accommodated by the drawbench. While the wall was quite heavy, drawbench capacity limited the reduction in area per pass; however, 25% reduction per pass was possible after several passes had thinned the wall. A fluorocarbon lubricant worked very well and provided sufficient film strength for reductions over 25%. Particular attention must be paid to drawing dies so that they are smooth and scrupulously clean, because scratches and adhering metal nullify the effectiveness of the lubricant.

Because good-quality mandrel rods could not be obtained in a reasonable time, hardened drill rod was used for mandrels in the T-111 drawing development effort. This caused some difficulties because lengths were limited to 3 ft, and the rods warped on heat treatment. The warpage made it necessary to expand the tubes considerably to remove the mandrels, and some scoring of the inside surface resulted when the mandrels were withdrawn. The excessive amount of cold reduction to compensate for the expansion to remove the warped mandrels limited the amount of wall reduction obtainable by drawing; the tubes cracked during mandrel removal. This required more frequent annealing. When the desired mandrels arrive, the established tube reduction schedule will be made more efficient.

PHYSICAL PROPERTIES OF REFRACTORY MATERIALS

D. L. McElroy

We are concerned with measuring, correlating, and understanding the high-temperature thermophysical properties of refractory materials. Their characteristics are sought by accurate measurements of thermal conductivity λ, electrical resistivity ρ, thermoelectric power S, specific heat C_p, and total hemispherical emittance E_t.

Physical Properties of T-111

J. P. Moore R. S. Graves T. G. Kollie

A special assembly of the radial heat flow apparatus was used to measure λ between 50 and 1000°C for a limited supply of T-111. A 9-in.-tall × 3-in.-diam disk stack was used and consisted of 7 in. of D-43 backup disks and 2 in. of T-111 disks located in the central portion. Table 15.5 lists smoothed values of λ, corrected for core heater expansion, that are accurate to ±1.5%. We see that λ increases with temperature to 1000°C, a

Table 15.5. Physical Properties of T-111

Temperature (°C)	Thermal Conductivity, λ (w cm^{-1} $°C^{-1}$)	Electrical Resistivity, ρ (μohm-cm)	Thermoelectric Power,[a] S ($\mu v/°C$)	Total Hemispherical Emittance	
				Thermal Polish	11-μin. Finish
100	0.418	22.40	5.90		
200	0.447	26.56	7.90		
300	0.466	30.62	9.89		
400	0.483	34.48	11.92		
500	0.498	38.34	14.05	0.086	0.259
600	0.511	42.05	16.22	0.096	0.287
700	0.524	45.66	18.42	0.111	0.315
800	0.537	49.12	21.61	0.126	0.343
900	0.545	52.71	22.83		
1000	0.549	56.21	25.04		
1100	0.559[b]	59.68	27.35		
1200	0.567[b]	63.14	29.75		
1300	0.574[b]	66.52	32.24		
1400	0.580[b]	69.91	34.85		

[a]With respect to platinum.

[b]Calculated from $\lambda = 2.404 \times 10^{-8}\ T/\rho + 9/T$.

behavior similar to that of pure tantalum. These values are 3 to 17% below literature[10] values for T-111. Table 15.5 includes smoothed values of ρ and S of T-111 obtained to 1400°C on a rod specimen. The ρ values for T-111 are nominally 5 μohm-cm above literature[11] values for tantalum.

These data may be related to ±0.6% by

$$\lambda = 2.404 \times 10^{-8}\ T/\rho + 9/T\ ,$$

where T is the absolute temperature in °K. The coefficient 2.404×10^{-8} is the Lorenz number and is slightly less than the Sommerfeld limit of 2.443×10^{-8} $(v/°K)^2$. The $9/T$ term represents the lattice contribution, which is generally small in niobium- and tantalum-base alloys. This equation was used to obtain the λ values above 1000°C from the ρ measurements.

Total hemispherical emittance values for two surface conditions of T-111 are also given in Table 15.5. The pulse-heating calorimeter described in Part I, Chap. 9 of this report was used for these measurements. The thermally polished specimen had been repeatedly heated to 1500°C and yielded low E_t values. The specimen with 11-μin. surface finish was cold swaged and lapped to produce a finish similar to that of ground glass. The 300% difference represented by these results illustrates the importance of surface finish on E_t and the need for studies to allow proper surface characterization for prediction of E_t for real surfaces.

[10]J. C. Hedge, C. Kostenko, and J. I. Lang, *Thermal Properties of Refractory Alloys*, ASD-TDR-63-597 (June 1963).

[11]R. P. Tye, pp. 168–74 in *Niobium, Tantalum, Molybdenum, and Tungsten*, ed. by A. G. Quarrell, Elsevier Publishing Company, New York, 1961.

Thermocouple Drift Tests

D. L. McElroy

The large thermoelectric power of the Chromel-P vs constantan thermocouple makes it attractive for use from −195 to 800°C; however, evaporation from small wires in vacuum makes it suspect. Consequently, thermal emf drift tests were conducted for 400 hr at 10^{-7} torr between 300 and 800°C on bare thermoelements with four different diameters – 0.005, 0.010, 0.020, and 0.032 in. Thermal emf changes equivalent to less than 2°C

were noted for these test conditions. Initial drifts due to cold working and annealing effects were followed by small constant drifts due to evaporation.[12]

Thermal Radiation Exchange from Graphite

T. G. Kollie

Temperature control of certain irradiation tests at high temperatures can be simplified if radiant heat exchange can be used rather than forced convection to remove gamma and neutron heating. In a planned irradiation test in HFIR of graphite generating 37 w/cm and held in an anodized aluminum closed container, passive means (gaseous conduction and convection and thermal radiation, but no forced convection) were to be used to maintain the graphite at 700°C, if a thermal radiation exchange of 12 w/cm could be achieved. Unfortunately, mockup tests of this configuration indicated a radiant exchange for graphite at 700°C of 7.6 w/cm for an anodized aluminum receiver and 9.2 w/cm for an Aquadag-coated aluminum receiver. These tests indicated an E_t value for graphite at 700°C of 0.796 and at 20°C of 0.504 for anodized aluminum and 0.679 for Aquadag-coated aluminum. All of these values are lower than normally assumed for these materials.

[12]D. L. McElroy, *Proceedings of Fifth Temperature Measurements Society Conference and Exhibit, Hawthorne, California, March 14–15, 1967* (in press).

NONDESTRUCTIVE TESTING OF REFRACTORY ALLOYS

R. W. McClung K. V. Cook

We have continued our nondestructive evaluation of refractory alloys. The specific techniques employed were selected according to the materials and their configurations. Fluorescent penetrants were used to evaluate the outer surfaces of the alloys, and very few significant discontinuities were detected by this procedure. Penetrant examination of tantalum alloys proved satisfactory only after the surface had been etched. At least one ultrasonic technique was used for the detection of internal flaws, and in some instances radiography and eddy currents were also applied.

A large portion of our work was devoted to the preparation of appropriate reference standards and subsequent evaluation of materials under study. For the ultrasonic evaluation of sheet, bar, plate, and tubing, we found that electric discharge machining yields the most accurate and reproducible reference notches. Additional work of this type is discussed under Nondestructive Test Development in Part III, Chap. 22 of this report.

16. Tungsten Metallurgy

W. O. Harms

Tungsten is attractive for advanced high-temperature reactor systems because of its high melting point, excellent high-temperature strength, high thermal and electrical conductivities, and good compatibility with many fuel materials and coolants. However, it suffers from a lack of ductility at low temperatures, which hampers both fabrication and application. The present program encompasses two areas of tubing fabrication and a complete physical-metallurgical evaluation of products of both. One fabrication method is direct chemical vapor deposition (CVD) for heavy-metal halides, and the other is modification of more conventional techniques based on extrusion and warm drawing. The program also includes more basic studies designed to elucidate the mechanisms involved in the low-temperature mechanical behavior of tungsten and the role of selected alloying elements.

EXTRUSION AND DRAWING OF TUNGSTEN AND TUNGSTEN ALLOYS

W. R. Martin

The objective of our metalworking program in this activity is to devise new or improved techniques for the production of tungsten tubing that offer better quality products and lower costs. Our fabrication development involves the extrusion and drawing of tungsten and tungsten alloys using improved tooling and techniques with conventional metalworking equipment.

Tube-Shell and Duplex Extrusions

R. E. McDonald G. A. Reimann
C. W. Dean

The investigation of tungsten and tungsten-alloy tubing extrusion has continued, and 37 billets were extruded in the past year. Extrusion temperatures ranged between 1650 and 2200°C and extrusion ratios varied between 3 and 9. The extrusion press controls and hydraulic system were modified to greatly increase press response as well as ram speed during extrusion, thereby minimizing billet heat losses to the tooling. The billet heater was modified to facilitate maintenance and repair and to eliminate sticking of the hot billet to the pedestal block. The mandrel design was altered to reduce billet transfer time and to ensure ejection of extrusions from the tooling.

Additional effort with W–25% Re duplex billets[1] demonstrated their suitability for reextrusion into thin-walled tubing. Also, the duplex billet design was employed successfully to obtain a wrought structure in tubular CVD tungsten.

Improved extrusion surfaces resulted from employing billet temperatures in the vicinity of 1850°C and inserting 0.005-in. molybdenum foil into the press container prior to loading the billet. Since lower billet temperatures restrict the extrusion ratio somewhat, heavy-walled tube shells are produced. Higher temperatures (to 2200°C) to permit extrusion of thinner-walled tubing result in accelerated tooling attrition and promote surface defects in the extrusion related to interactions with molten iron from the container sleeve.[2] These problems appear to negate the advantages gained from higher extrusion ratios obtained as a result of employing higher temperatures. Considerable

[1] R. E. McDonald and G. A. Reimann, *Metals and Ceramics Div. Ann. Progr. Rept. June 30, 1966*, ORNL-3970, pp. 61–64.

[2] G. A. Reimann and R. E. McDonald, *The Extrusion of Tungsten and Tungsten-Alloy Tubing* (in preparation).

development appears necessary to obtain suitable tooling designs, materials, and techniques before routine extrusion at temperatures above 2000°C becomes practical and economical.

Heavy-walled tube shells are satisfactory when reextrusion as a duplex billet is intended. However, if tube shells are to be reduced on the drawbench, the longer, thinner-walled configuration is desired. Using optimized extrusion parameters, we feel that the maximum reduction ratio obtainable on W–25% Re at 1850°C is about 6.5, which produces a 1.5-in.-OD × 1.0-in.-ID tube shell.

Hot-Plug Drawing Development

G. A. Reimann

A state-of-the-art investigation disclosed that no successful method has been devised for direct hot-plug drawing (above 700°C) of as-extruded tungsten-alloy tube shells. Prior investigations have been hampered by insufficient drawbench capacity, lack of necessary auxiliary equipment, inability to achieve desired drawing temperature, lack of suitable lubricants, and the inability of conventional tooling materials to survive the rigors of drawing tungsten alloys at elevated temperatures. Thus, we embarked on a program to develop a relatively economical process that would enable direct conversion of as-extruded tube shells into semi-finished tubing by plug drawing.

Vitrified zirconia was selected for dies and drawing plugs to withstand the 1000°C deemed necessary for the initial tube-shell reductions. A heated die head maintains the dies at 450°C, and drawbench modifications are in progress to provide improved tube-shell heating capability, a means of rapid mandrel advance and retraction, equipment for ensuring drawing speed control, and instrumentation to monitor processing variables.

To establish the feasibility of our approach to hot-plug drawing, several as-extruded molybdenum-alloy tube shells were selected, because molybdenum at somewhat lower temperatures behaves similarly to tungsten. A 45% area reduction could be obtained in a single pass when TZM was heated to 700°C. Seven passes at 700°C reduced as-extruded $1\frac{1}{4}$-in. OD × $\frac{1}{4}$-in. wall to 0.725-in. OD × 0.027-in. wall, a total area reduction of 92%. A duplex extrusion with a CVD sleeve was reduced 85% in five passes, and dissolution of the molybdenum covering yielded a wrought CVD tube, 0.710-in. OD × 0.010-in. wall. No intermediate recrystallization anneal was necessary in either of the above trials.

While our hot drawing facility is incomplete, our preliminary efforts for the hot-plug drawing of refractory alloys are quite encouraging. Should we achieve target tube sizes in tungsten alloys using this technique, we will have made a significant advance in developing a commercially adaptable process that may improve the properties of the finished tubing and reduce processing costs.

CHEMICAL VAPOR DEPOSITION

W. R. Martin

The chemical vapor deposition technique is being developed to produce high-purity tungsten and tungsten alloys in a wide range of forms as shown in Fig. 16.1. Our primary effort is threefold: (1) the direct production of thin-wall tubing in lengths up to 4 ft, (2) an empirical and statistical investigation of deposition parameters as related to the structural features of the deposit and the mechanism that is rate-controlling during deposition, and (3) an evaluation of the parameters controlling the uniformity of composition and properties in deposits of tungsten-rhenium alloys.

Direct Production of Long Thin-Walled Tungsten Tubing by Chemical Vapor Deposition

R. L. Heestand[3] W. R. Martin

The general process for depositing relatively short lengths of tubing by reduction of WF_6 with hydrogen has been described previously.[4] Recently, we developed an improved technique, using a resistance-heated mandrel for deposition of tubing having uniform wall thickness to 3- to 4-ft lengths. The deposition is carried out in a water-cooled chamber fitted with insulated electrodes at each end. The apparatus is operated in the vertical position, and straightness of the resistance element is maintained by applying a weight to the

[3]Present address, Battelle Memorial Institute, Columbus, Ohio.

[4]R. L. Heestand, J. I. Federer, and C. F. Leitten, Jr., *Preparation and Evaluation of Vapor-Deposited Tungsten*, ORNL-3662 (August 1964).

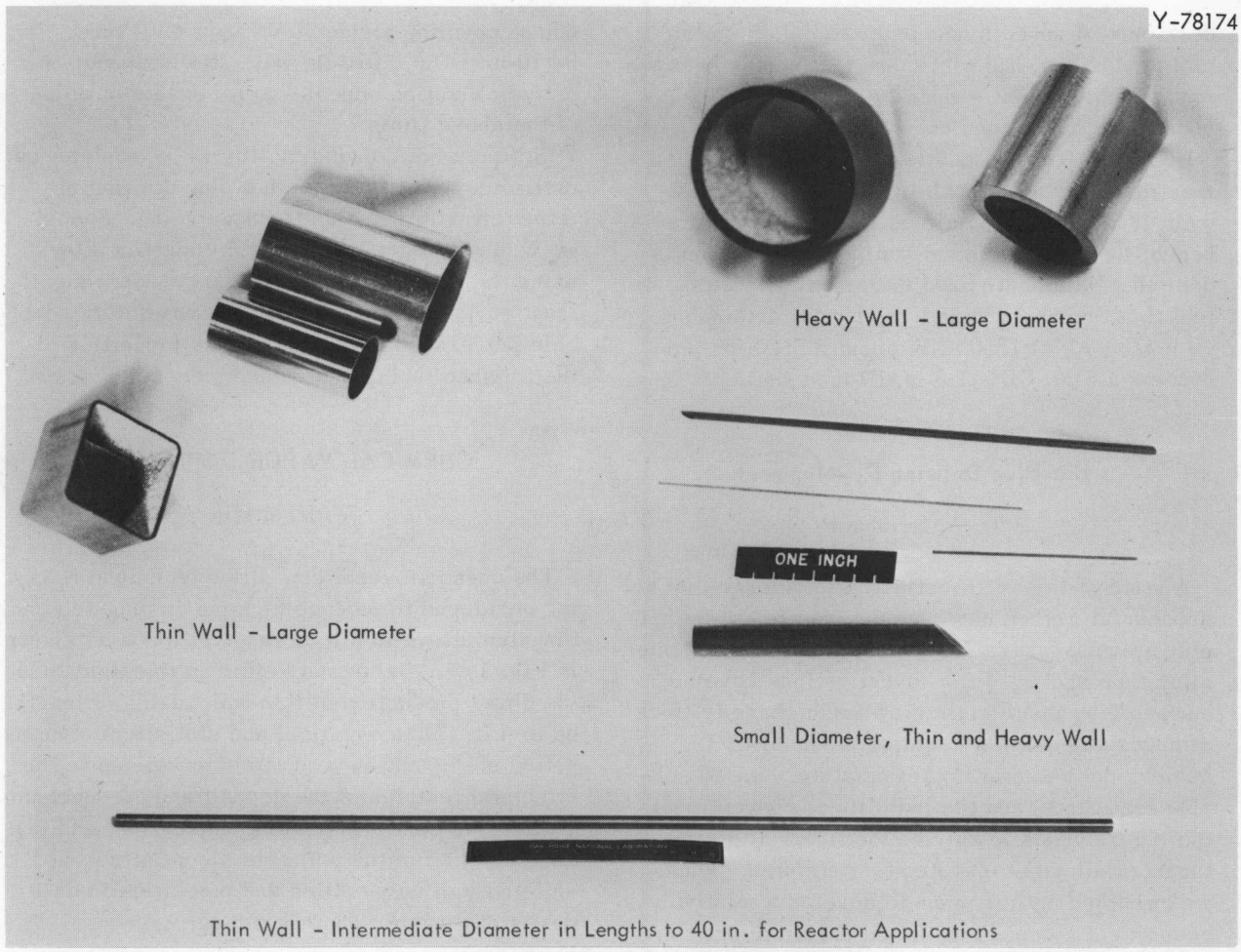

Fig. 16.1. Tungsten and Tungsten-Alloy Products Formed by Chemical Vapor Deposition. In this composite, the 1-ft scale was photographed with the long tube at the bottom and the 1-in. scale with the other pieces.

retractable bottom electrode. Thin-wall stainless steel tubing is drawn to an outside diameter equal to the inside diameter of the tungsten tube required. This tubular mandrel, in addition to giving suitable resistance for heating, allows installation of an internal thermocouple to monitor the deposition temperature. The power supply for the resistance heating is a 300-amp welding machine in which the power output can be continuously adjusted to maintain the desired deposition temperature.

Thickness uniformity is enhanced in this scheme by the resistance behavior of the deposit. Relatively thin regions have a higher current density, which raises the temperature locally, thus increasing the deposition rate and thickness. This method, of course, requires that sufficient amounts of reactants be present to ensure a uniform tube wall. For a 0.200-in.-ID tube deposited at 650°C, 100 cm^3/min WF_6, 2100 cm^3/min H_2, and a pressure of 10 torrs, the deposition rate was 0.0055 in./hr and the efficiency was greater than 90%. At this deposition rate, a 40-in. tube with a wall thickness up to 0.030 in. can be produced in one day.

Because of the difference in the thermal coefficient of expansion between the stainless steel mandrel and the tungsten deposit, the tungsten tube can be readily removed from the mandrel after cooling. No parting agent is necessary, because the tungsten does not bond to the thin oxide film that forms on the stainless steel mandrel.

Tubing of the type under consideration is suitable for use in the as-deposited condition but may be ground to enhance the outer finish. It may also be drawn, as described in the previous section. The smoothness of the inner surface depends upon the surface condition of the mandrel used during deposition.

Statistical Parametric Studies

W. C. Robinson, Jr.

Factors affecting the chemical vapor deposition of tungsten are being evaluated in a statistically designed parametric study. We required 81 experiments in the WF_6-H_2 deposition system to provide a third-order polynomial correlation between the response parameters and the independent system parameters over the experimental range of 450 to 820°C, 9 to 20 torrs, 60 to 370 cm^3/min WF_6, and 752 to 5240 cm^3/min H_2. The system parameters were H_2/WF_6 ratio, total flow rate, temperature, and pressure. The initial response parameters of total deposition, deposition efficiency, and thickness uniformity were determined for an internal deposit in a 15-in. length of an 0.807-in.-ID copper mandrel. The deposition rate of tungsten at HF mole fractions of 0.02, 0.05, 0.10, and 0.20 was also determined for each experiment and correlated with the system parameters.

Examples of the curves resulting from these correlations are shown in Figs. 16.2 and 16.3. Figure 16.2 shows the thickness of tungsten deposited in 5 hr at the point on the mandrel at which the gas stream contained 5 mole % HF. The thickness, which is readily converted to deposition rate for these constant-time runs, is plotted as profiles against temperature and pressure at a constant value of total gas flow and H_2/WF_6 ratio in the gas stream. Figure 16.3 depicts the total mass of tungsten deposited in 5 hr in a 15-in. length as a function of temperature and pressure at constant values of inlet total gas flow and H_2/WF_6 ratio. These curves are drawn by fitting the experimental data with an empirical equation involving 35 constants. The forms of the equations relating the response parameters of total deposition and deposition efficiency have been developed

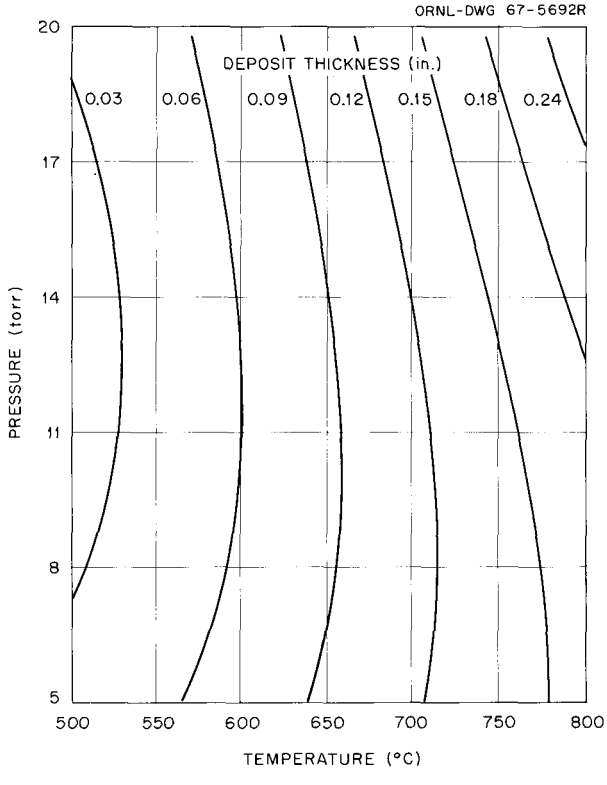

Fig. 16.2. Thickness of Tungsten Deposited in 5 hr as a Function of Temperature and Pressure for Conditions of 4000 cm^3/min Total Gas Flow Rate, HF Mole Fraction of 0.05, and 5.0% WF_6 in Feed Gas.

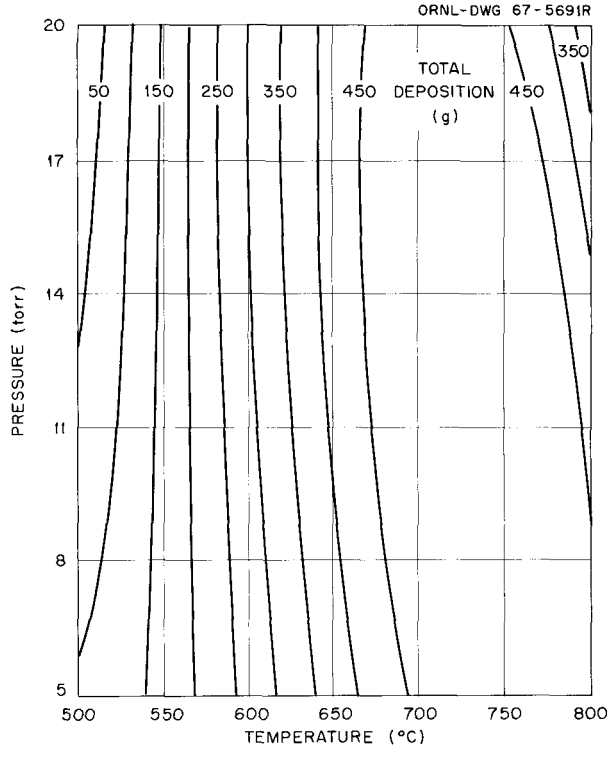

Fig. 16.3. Total Tungsten Deposition in 5 hr as a Function of Pressure and Temperature for Total Flow Rate of 4000 cm^3/min and 5.5% WF_6 in Feed Gas.

from diffusion, fluid-flow, and reaction theory. This theoretically derived equation contains only three constants and fits the data as well as the empirical equation. Refinement of this theoretical equation should indicate the particular rate-controlling processes in each experimental area.

Nondestructive Thickness Measurements On CVD Tungsten Tubes[5]

B. E. Foster S. D. Snyder

A through-transmission x-ray attenuation technique[6] was developed and used to measure the thickness of CVD tungsten deposited on the inner surface of copper tubes. We tested 86 tubes in connection with the statistical parametric studies described above.

Deposition of Tungsten-Rhenium Alloys

J. I. Federer W. R. Martin

Development of a CVD process for preparing tungsten-rhenium alloys in tubular and sheet form has continued.[7] The process uses the hydrogen reduction of WF_6 and ReF_6. Tubular deposits having compositional uniformity in both the axial and radial directions were prepared by use of an injector to deliver the WF_6-ReF_6 mixture directly into the uniformly heated portion of $\frac{5}{8}$-in.-ID mandrels. Deposition conditions were $H_2/(WF_6 + ReF_6)$ ratio of 15, 5-torr system pressure, and temperatures of 800 to 900°C for alloys containing nominally 5 and 25% Re, respectively. The deposition temperatures were based upon thermodynamic calculations for the codeposition process. Typical axial variations in rhenium content were ±0.5 and ±1% Re in arbitrary lengths of deposits containing 7 and 22% Re respectively. The electron microprobe traces for a W–22% Re alloy in Fig. 16.4 show that the composition was substantially uniform through the thickness of a typical tubular deposit. Deposition rates of about 12 mils/hr were obtained. The grain structure was columnar and the surface texture was similar to that of unalloyed tungsten deposits. Almost 100% of the metal content of the metered fluorides were recovered in the deposits.

We next tried to scale up the process to prepare sheet material for measurement of mechanical properties. Tubular mandrels of square, pentagonal, and octagonal cross sections were used so that the flat sections could be separated into $\frac{3}{4}$-in.-wide strips after deposition. However, deposits prepared under conditions suitable for $\frac{5}{8}$-in.-ID mandrels always had a nodular grain structure with associated porosity and rough surface textures. In addition, alloys prepared in the largest mandrel (2-in. OD, octagonal cross section) always contained substantially less than the intended 5 or 25% Re content. Thus, deposition conditions could not be translated to the three different mandrel geometries and had to be redetermined.

Deposition temperatures were decreased while we maintained the $H_2/(WF_6 + ReF_6)$ ratio of 15 and pressure of 5 torrs in tubular mandrels having approximately the same surface areas as octagonal mandrels to be used for sheet material. Nodular deposits were still obtained at 750°C, but alloys deposited at 650°C had a smooth surface texture, a dense columnar grain structure, and uniform composition. These results indicate that conditions that produce uniform composition in alloy deposits are sensitive to mandrel geometry and, until the codeposition process is better understood, must be determined for each case. Sheet material is presently being deposited under the optimum conditions determined in this study.

A study of the A15-type structure occurring in CVD tungsten-rhenium alloys was completed, and the results have been reported.[8] An A15-type phase in CVD tungsten-rhenium alloys was identified by x-ray diffraction, metallography, and hardness measurements. The composition range of this A15-type phase varied with temperature but was near W_3Re.

In the temperature range investigated, 1000 to 1500°C, the phase occurred alone or coexisted

---

[5] A paper summarizing this work was presented at the convention of the Society for Nondestructive Testing, Chicago, Nov. 2, 1966.

[6] B. E. Foster and S. D. Snyder, *Metals and Ceramics Div. Ann. Progr. Rept. June 30, 1966*, ORNL-3970, pp. 123–24.

[7] J. I. Federer and C. F. Leitten, Jr., *Metals and Ceramics Div. Ann. Progr. Rept. June 30, 1966*, ORNL-3970, pp. 105–7.

[8] J. I. Federer and J. E. Spruiell, "Formation and Characterization of an A15-Type Structure in Chemical Vapor Deposited Tungsten-Rhenium Alloys," pp. 443–58 in *Proceedings of the Conference on Chemical Vapor Deposition of Refractory Metals, Alloys, and Compounds*, ed. by A. C. Schaffhauser, American Nuclear Society, Hinsdale, Ill., 1967.

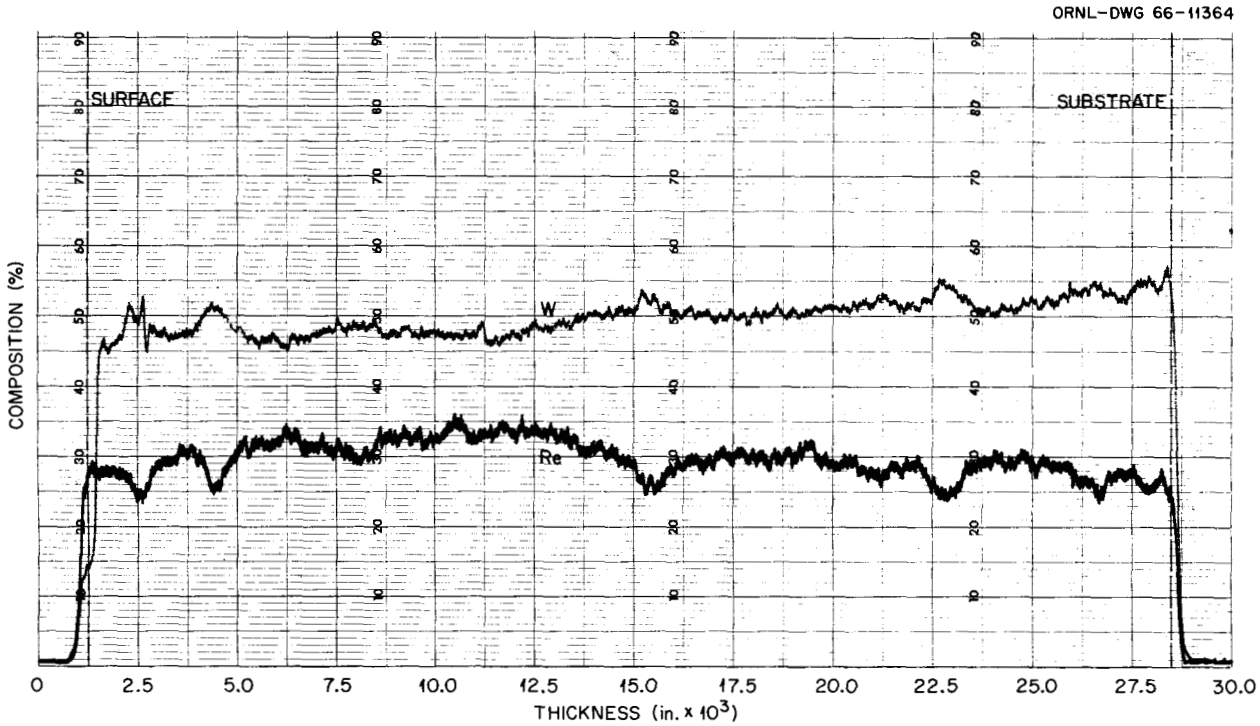

Fig. 16.4. Electron-Probe Microanalyzer Traces for a Tungsten-Rhenium Alloy Deposited in a Moving Mandrel at 900°C with a WF_6-ReF_6 Injector. Average composition 22% Re. The instrument calibration was not adjusted to true percentage composition.

with the tungsten-rich terminal solid solution (β) or with sigma phase (σ). Because the phase was about four times as hard as the β phase, alloys containing the phase as a major constituent would have limited usefulness. Transformation to β or $\beta + \sigma$ during long-time anneals at deposition temperatures showed that the phase was metastable. Thus, the A15-type phase would not be expected to form in β or $\beta + \sigma$ alloys subjected to service at elevated temperatures.

PHYSICAL METALLURGY OF CVD TUNGSTEN

The production of tungsten by hydrogen reduction of WF_6 has many advantages, and the material has properties which in many cases are superior to those of unworked or recrystallized tungsten produced by other methods. However, CVD tungsten containing relatively high levels of fluorine impurities swells on annealing at high temperatures due to internal gas bubble formation and growth. Extensive void growth leading to premature fracture is encountered when this material is tested under stress at high temperatures.

This phase of the program has included studies of the formation and growth of gas bubbles by electron microscopy and other techniques in an effort to provide a better understanding of the behavior and effect of bubbles on the properties of CVD tungsten. The work has involved studies of many other metallurgical properties, such as the as-deposited grain structure, hardness, deformation behavior, ductility, and the grain stability at high temperatures, which also are related to fluorine impurities.

Formation of Internal Gas Bubbles in CVD Tungsten

A. C. Schaffhauser

The formation of gas bubbles on annealing CVD tungsten is being studied as a function of fluorine content and annealing treatment. As-deposited material containing < 1 to 30 ppm F is fully dense, and no bubbles or precipitates can be detected by electron microscopy. The hardness increases linearly with fluorine concentration in this range.

However, at the higher fluorine concentrations the hardness drops significantly on annealing at 1400°C. The drop coincides with the first observation of grain-boundary bubbles by electron microscopy. The annealing behavior indicates that the fluorine impurities precipitate as gas bubbles.

Electrical resistivity and x-ray diffraction line broadening are being measured to determine the nature and state of the fluorine impurities. The resistivity ratio is 127 for as-deposited samples containing 30 ppm F and 542 for samples containing 6 ppm F. The x-ray diffraction line width, which is a measure of the inhomogeneous microstrain in the material, was halved when samples containing 20 ppm F were annealed at 1400°C. These results show that the fluorine impurities are either clustered in solution or exist as extremely fine gaseous or solid precipitates in the as-deposited material.

Growth of Grain-Boundary Gas Bubbles in CVD Tungsten[9]

K. Farrell J. T. Houston
A. C. Schaffhauser

The growth of grain-boundary gas bubbles developed on heating tungsten deposited from WF_6 was studied as a function of annealing time and temperature and fluorine content. Measurements of the size and number of bubbles were obtained by quantitative electron fractography. In material containing 25 ppm F, bubbles were found on the boundaries for annealing temperatures as low as 1450°C, but at these temperatures the distribution of the bubbles was highly heterogeneous. Size-frequency histograms were plotted for bubbles in specimens annealed at temperatures between 1600 and 2500°C. Bubble growth was continuous with time at temperatures below 2200°C and was accelerated at higher temperatures. Some examples of grain boundary bubbles are shown in Fig. 16.5.

Bubble growth was consistent with a coarsening process causing swelling. At temperatures of 2000°C and below, the grain-boundary bubbles coarsened solely at the expense of other grain-boundary bubbles. When the temperature was raised to 2200°C, more gas was attracted to the grain boundaries from within the grains. This phenomenon occurred early in the annealing treatment, but with increasing time further coarsening took place by rearrangement of the gas already in the boundaries. At 2500°C bubble growth was rapid and was assisted by an influx of gas from within the grains and by bubbles merging with each other when they touched.

Although the gaseous species in the bubbles was not identified, the incidence of bubbles on the boundaries correlated well with fluorine content and was sensitive to the area of grain boundaries in the specimens. The total volume of bubbles was shown by density measurements to vary directly with fluorine content.

Mechanical Behavior of CVD Tungsten at Elevated Temperatures[10]

H. E. McCoy J. O. Steigler

Many applications of CVD tungsten require that the material be stressed at elevated temperatures. We have run creep-rupture tests at 1650 and 2200°C on this material and compared its properties with those of a typical heat of wrought powder-metallurgy-derived (PM) tungsten.[11] At 1650°C, the CVD product exhibited lower fracture strains and a lower minimum creep rate. At high stresses the rupture life was shorter than that of the PM material, but at low stresses the rupture lives were about equivalent. At 2200°C the minimum creep rate was higher and the rupture life lower for the CVD product.

We carried out extensive microstructural observations to explain this behavior. The bubbles observed at grain boundaries on annealing the CVD product grew dramatically on stressing at elevated temperatures, probably by stress-induced diffusion of vacancies. Failure occurred when they linked up to form cracks. At low stresses the bubbles expanded into stable voids (Fig. 16.6), but above some critical stress they grew indefinitely (Fig. 16.7) and linked up (Fig. 16.8), causing premature

[9] Abstracted from pp. 363–90 in *Proceedings of the Conference on Chemical Vapor Deposition of Refractory Metals, Alloys, and Compounds*, ed. by A. C. Shaffhauser, American Nuclear Society, Hinsdale, Ill., 1967.

[10] Abstract from pp. 391–425 in *Proceedings of the Conference on Chemical Vapor Deposition of Refractory Metals, Alloys, and Compounds*, ed. by A. C. Shaffhauser, American Nuclear Society, Hinsdale, Ill., 1967.

[11] H. E. McCoy, *Creep-Rupture Properties of Tungsten and Tungsten Alloys*, ORNL-3992 (August 1966).

PHOTO 89118

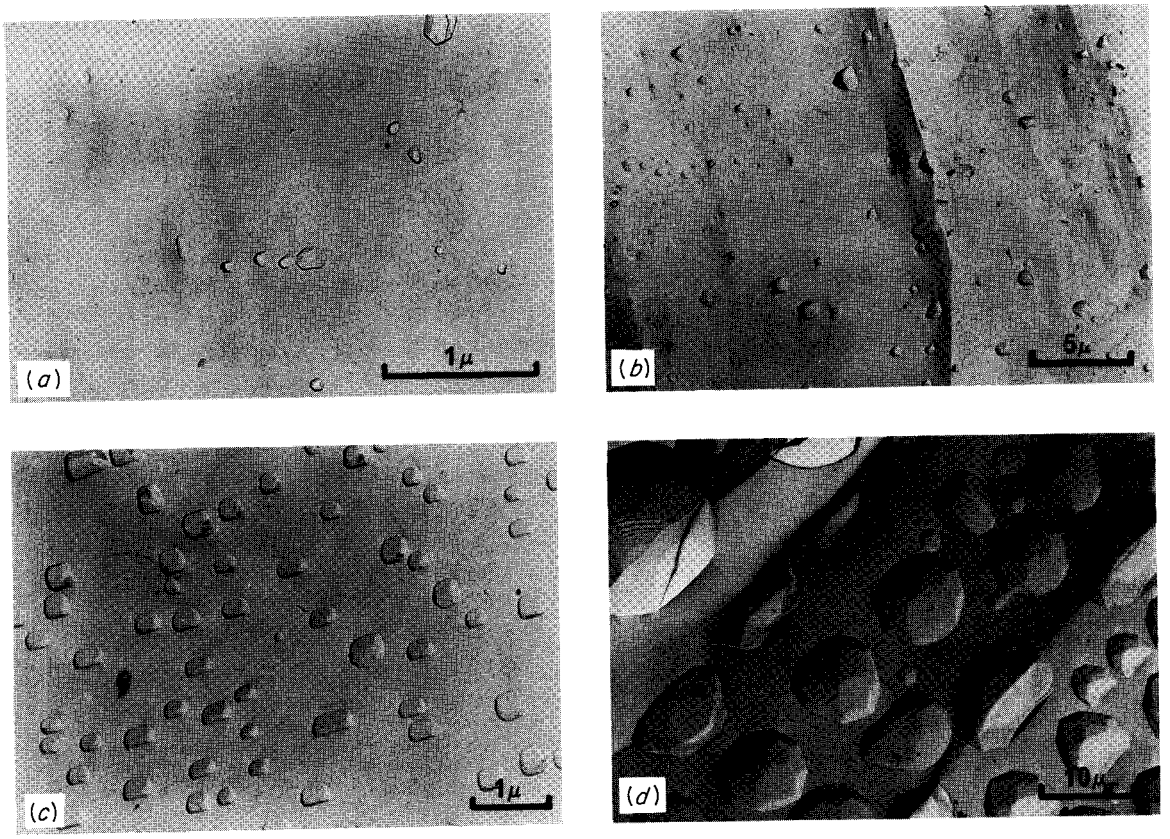

Fig. 16.5. Electron Fractographs Showing the Effect of Heat Treatment on Grain-Boundary Bubbles in CVD Tungsten Containing 25 ppm F. (*a*) 100 hr, 1600°C; (*b*) 10 hr, 2000°C; (*c*) 2 hr, 2200°C; (*d*) 10 hr, 2500°C.

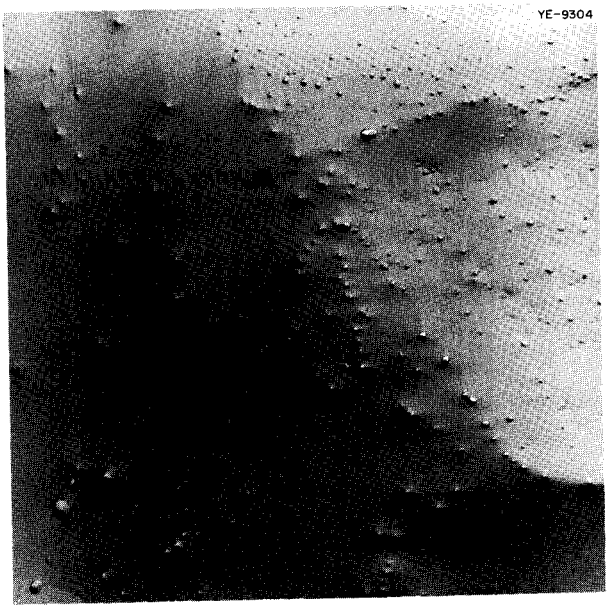

Fig. 16.6. Gas Bubbles Expanded into Stable Voids in CVD Tungsten Tested at 1650°C and 4000 psi for 413 hr.

Fig. 16.7. Unstable Voids in CVD Tungsten Formed from Gas Bubbles by Testing at 1650°C and 6000 psi for 12.8 hr.

rupture. The columnar grain structure prevented extensive grain-boundary sliding, so much of the elongation observed arose from formation of the voids. At 2200°C the rate of void formation was high enough to give the CVD product the higher minimum creep rate.

Fig. 16.8. Voids Linking Up to Form Cracks in CVD Tungsten Tested at 1650°C and 6000 psi.

Effect of Fluorine Impurities on Some Metallurgical Properties of CVD Tungsten

A. C. Schaffhauser R. L. Heestand[12]

Many of the metallurgical properties of CVD tungsten are related to the fluorine impurities.[13,14] To systematically study these relationships, we produced a series of deposits having fluorine contents in the range of < 1 to 30 ppm without significantly changing the concentration of other impurities by careful control of deposition parameters. The very-low-fluorine samples were deposited on the external surface of a mandrel at 600°C in a water-cooled chamber at a system pressure of 10 torrs.

The grains in the low-fluorine specimens were slightly less columnar than in the higher fluorine

[12]Present address, Battelle Memorial Institute, Columbus, Ohio.

[13]A. C. Schaffhauser and R. L. Heestand, "Effect of Fluorine Impurities on the Grain Stability of Thermochemically Deposited Tungsten," pp. 222–27 in *1966 IEEE Conference Record of the Thermionic Conversion Specialist Conference Nov. 3 and 4, 1966, Houston, Texas*, Institute of Electrical and Electronic Engineers, New York, 1966.

[14]J. V. Festa and J. C. Danko, "Some Effects of Fluorine Content on the Properties of CVD Tungsten," pp. 349–61 in *Proceedings of the Conference on Chemical Vapor Deposition of Refractory Metals, Alloys, and Compounds*, ed. by A. C. Schaffhauser, American Nuclear Society, Hinsdale, Ill., 1967.

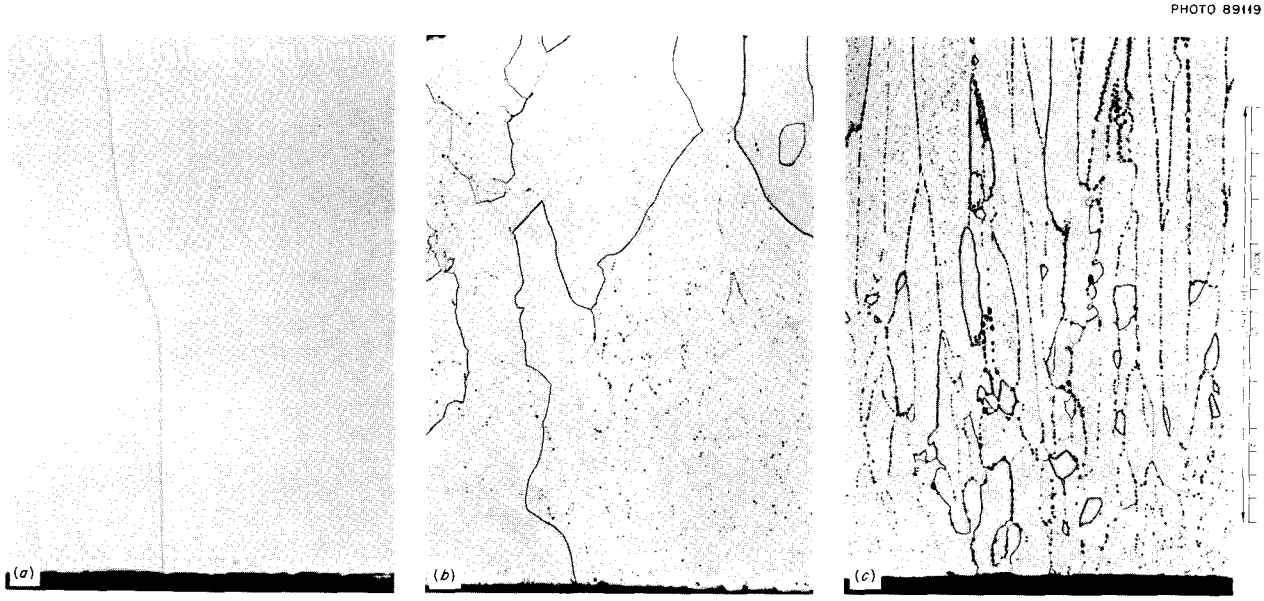

Fig. 16.9. Effect of Fluorine Content on Microstructures of CVD Tungsten After Annealing 1 hr at 2500°C. Etchant: $NH_4OH + H_2O_2$. 200×. (*a*) < 1 ppm F; (*b*) 6 to 7 ppm F; (c) 30 to 31 ppm F.

deposits. The amount of preferred [100] orientation decreased from about 80 times that corresponding to a random distribution for the samples containing 20 to 30 ppm F to 6 times random for the sample with less than 1 ppm F. The hardness of the as-deposited samples increased linearly from 380 to 470 DPH with increasing fluorine content. A large decrease in hardness of the higher fluorine samples was observed on annealing at 1400°C, and after annealing at 2500°C all material had a hardness of 350 to 360 DPH, independent of fluorine content. No consistent change in fluorine content on annealing was observed.

The ductile-to-brittle transition temperature (DBTT) (90° bend for $4T$ punch radius at 0.1-in./min deflection rate) of as-deposited specimens containing 5 and 25 ppm F was 250 and 400°C respectively. Heat treatment between 1000 and 2000°C lowered the DBTT to 185 to 225°C. Higher annealing temperatures for the high-fluorine samples produced large gas bubbles, which covered a large fraction of the grain-boundary area and thus reduced the fracture area and raised the DBTT.

The relationship between fluorine content, gas bubble density, and high-temperature grain stability for samples annealed 1 hr at 2500°C is clearly shown in Fig. 16.9. Grain-boundary gas bubbles are obviously effective in stabilizing the columnar grain structure of deposits containing approximately 20 ppm F or greater to temperatures as high as 2500°C. Small grain-boundary bubbles formed at 1800°C, which can be observed only by electron microscopy, also stabilize the grain structure, as is desirable for some applications.

CREEP-RUPTURE PROPERTIES OF W–25% Re

R. L. Stephenson

We are studying the creep-rupture properties of W–25% Re to provide a comparison between arc-melting and powder-metallurgy processing. We made comparison tests on one lot of each of these materials, which had been similarly processed at the Albany Metallurgy Research Center, Bureau of Mines. The stress to produce rupture in 1000 hr for both materials is compared with that of tungsten alloys previously reported in Fig. 15.1. In most cases, both are weaker than the other tungsten alloys previously studied.

The contrast between the arc-melted and the powder-metallurgy W–25% Re is more apparent when the creep curves are compared on a linear time scale. Figure 16.10 shows creep curves for a short-time and a long-time creep test at 1650°C for each material. The inferior ductility and rupture life of the powder-metallurgy material are apparent. Similar curves are compared for the 2200°C test temperature in Fig. 16.11. Although the disparity in rupture life is not as great, the rupture ductility of the powder-derived material at long times is spectacularly low.

The secondary creep rates are plotted as a function of stress for both materials in Fig. 16.12. The results for the powder material indicate that over the range of stress studied the 1650°C curve has a steeper slope than the 2200°C curve. However, the creep rate at 1650°C can be reduced by

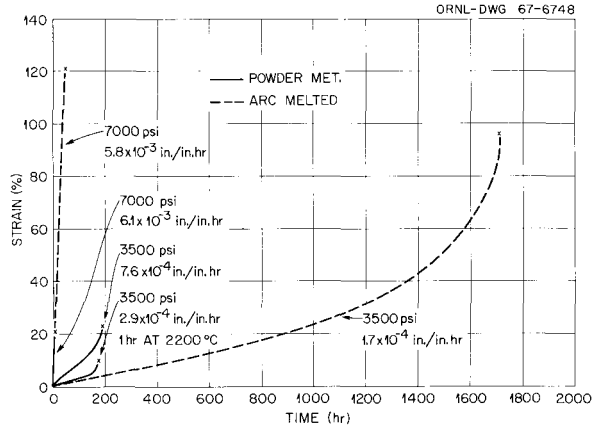

Fig. 16.10. Creep Properties of W–25% Re at 1650°C.

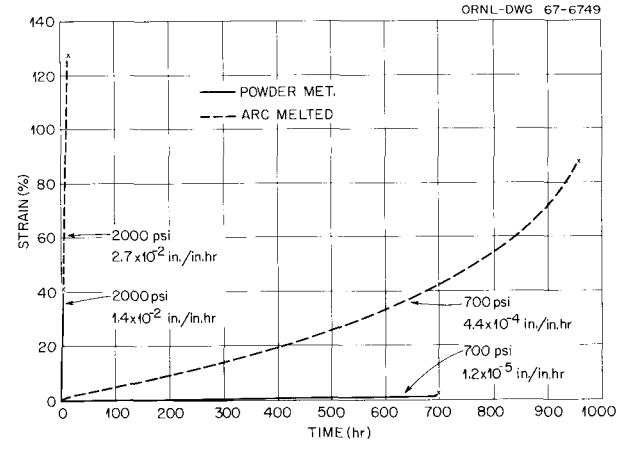

Fig. 16.11. Creep Properties of W–25% Re at 2200°C.

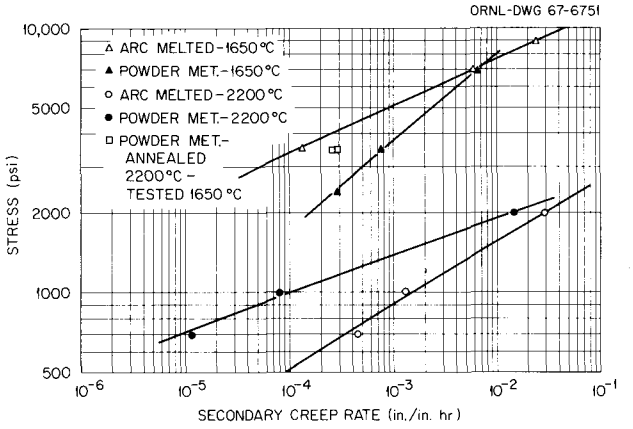

Fig. 16.12. Secondary Creep Rate vs Stress for W–25% Re.

annealing 1 hr at 2200°C prior to testing. Optical and electron microscopy will be used in seeking explanations for these observations.

BEND YIELD STRESSES IN TUNGSTEN SHEET[15]

K. Farrell A. C. Schaffhauser
J. O. Steigler

Recrystallized tungsten sheet tested in bending at temperatures just above the ductile-to-brittle transition temperature displays marked discontinuities on the load-deflection curve, which bear a striking resemblance to yield-point inflections. Their temperature dependences are the same as those reported for tensile yield stresses in tungsten. They also show a strong dependence on grain size on a Hall-Petch type plot. However, better relationships are obtained by using an exponent other than $-\frac{1}{2}$ or by breaking the $d^{-1/2}$ curve into segments corresponding to different parts of the grain-size–annealing-temperature curve. This suggests that the variation of yield stress with grain size in the tungsten sheet depends to some extent on the annealing treatments used to produce the grain sizes. The yield-stress–annealing-temperature relationship probably reflects changes in substructure, impurity distribution, or perhaps even impurity content. Thus, the marked changes in yield stress at the lower annealing temperatures are connected with the substructural changes involved in recrystallization. At intermediate annealing temperature the yield stress is relatively insensitive to temperature and may be related to minor changes in structure and impurity distributions. The effect of the higher annealing temperatures is to cause major rearrangement and perhaps losses of impurities, both of which promote substantial grain growth. The matter of how much of the decrease in yield stress during these stages is caused by grain growth per se and how much is caused by other internal changes is as yet unresolved.

[15] Summary of *J. Less-Common Metals* 13(5), 548–58 (1967).

TUNGSTEN WELDING DEVELOPMENT

N. C. Cole G. M. Slaughter

The use of tungsten and its alloys for very-high-temperature applications demands that adequate joining techniques be developed. Since a basic understanding of the welding metallurgy of tungsten is obviously necessary, we are expanding the joining investigations initiated previously.[16] The scope of our program includes the welding of powder-metallurgy, arc-cast, and CVD material as unalloyed tungsten, W–5 at. % Re, W–26 at. % Re, and W–25 at. % Re–30 at. % Mo in forms of sheet, plate, and tubing.

Bead-on-plate studies showed that the as-welded hardness of weld metal deposited with W–26% Re filler wire is significantly greater than that deposited with unalloyed tungsten (425 vs 350 DPH). In general, less porosity occurs in the welds made with W–26% Re filler metal than in those made with unalloyed tungsten. We assumed that this difference in porosity relates in part to differences in purity of the two commercial filler wires. Porosity tends to be especially prevalent along the fusion line of the welds in unalloyed tungsten base metal, as shown in Fig. 16.13.

Less grain growth occurred in the weld heat-affected zone when tungsten-rhenium filler metal was used than when unalloyed tungsten was used. This is probably because of the lower temperature required for welding.

To determine the effect of preheat on the welding parameters and metallurgical properties of the welded material, we built an apparatus incorporating cartridge heaters in a copper chill block. We ascertained that a preheat of 540°C will prevent

[16] R. G. Gilliland, *Joining of Tungsten*, ORNL-TM-1606 (October 1966).

Fig. 16.13. Unalloyed Tungsten Welded with Unalloyed Tungsten Filler Metal. 75×. Etchant: NH_4OH and H_2O_2. Reduced 32%.

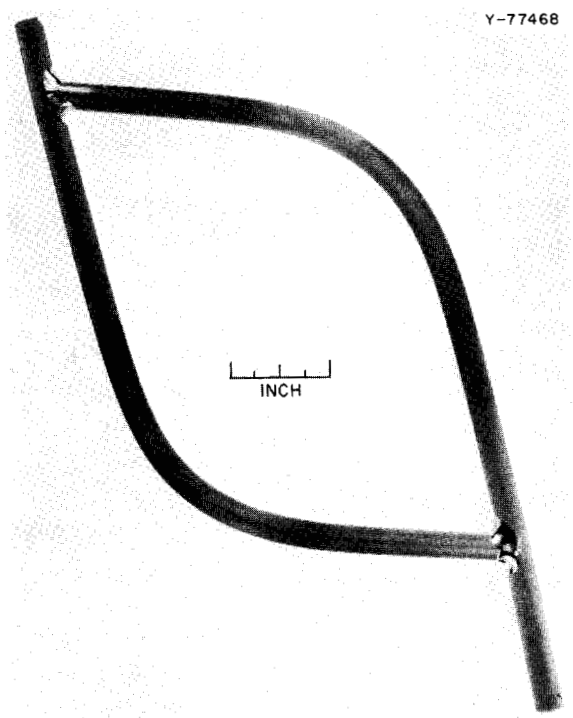

Fig. 16.14. Demonstration Loop Fabricated by Bending and Welding CVD Tungsten Tubing.

cracking during the butt welding of $\frac{1}{16}$-in.-thick unalloyed tungsten sheet, and we are now determining if a lower temperature will be sufficient.

We are also determining the feasibility of fabricating test components from tungsten and tungsten alloys. A demonstration assembly simulating a corrosion loop was successfully welded and is shown in Fig. 16.14. It was constructed from small-diameter thin-walled (0.275-in.-OD × 0.035-in.-wall) chemically vapor deposited (CVD) tungsten tubing. It was welded manually in a chamber under a high-purity inert-gas atmosphere with W–25 at. % Re filler metal. Nondestructive inspection revealed the welds to be helium leak-tight and crack-free.

Metallographic examination of these prototype welds revealed that they had complete penetration, no cracks, and only a small amount of fine porosity. Figure 16.15 shows the difference in grain growth exhibited by the two tungsten tubes.

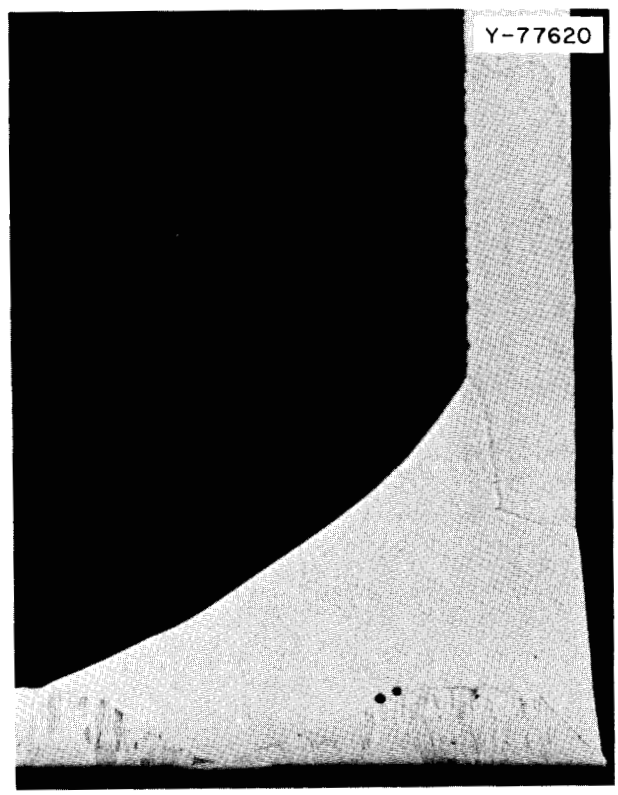

Fig. 16.15. Prototype Weld Between CVD Tungsten Tubes. No cracks and only very fine porosity can be seen. The difference in grain growth exhibited by the two different tubes is evident. 20×. Etchant: NH_4OH and H_2O_2.

In the bottom tube, the grains grew very little as compared to the one large grain of the vertical tube. Others[13] have found that the amount of grain growth depends upon the amount of impurities (primarily fluorine) present in the tungsten. Since the porosity shown is along the fusion interface of the fine-grained tungsten tube, this observation has been attributed to differences in fluorine content of the two sections of tubing.

PHYSICAL PROPERTIES OF TUNGSTEN AND TUNGSTEN ALLOYS

N. D. Woodall[17] J. P. Moore
D. L. McElroy

With the absolute longitudinal heat flow apparatus we measured accurately the thermal conductivity (±2%) and electrical resistivity (±0.5%) of four tungsten and tungsten alloy specimens in the range 77 to 400°K (−196 to 127°C), and smoothed values are given in Table 16.1. These results were treated by several methods to obtain the temperature dependence of the Lorenz number, needed for calculating the electronic thermal conductivity of tungsten. The calculated Lorenz values were less than the Sommerfeld limit at very low temperatures but greater above about 200°K. The temperature dependence of the electrical resistivity of the thoriated tungsten is steeper than that of electron-beam-melted tungsten, which is similar to the behavior observed in sintered aluminum products containing dispersed oxide phases. The electrical resistivity of thoriated tungsten at a given temperature can be described by $1.044(\rho_{EBM} + 0.094)$, where ρ_{EBM} is the electrical resistivity of electron-beam-melted tungsten.

[17] Coop student from Auburn University.

Table 16.1. Thermal Conductivity and Electrical Resistivity of Tungsten and Tungsten Alloys

Temperature		Thermal Conductivity (w cm^{-1} $°C^{-1}$)				Electrical Resistivity (μohm-cm)			
(°K)	(°C)	Electron Beam Melted Tungsten[a]	99.98% Pure Tungsten[b]	W–2% ThO_2	W–2% Ta	Electron Beam Melted Tungsten[a]	99.98% Pure Tungsten[b]	W–2% ThO_2	W–2% Ta
100	−173	2.140	1.998	1.968	1.234	1.04	1.20	1.16	2.52
150	−123	1.963	1.878	1.857	1.297	2.14	2.30	2.29	3.64
200	−73	1.893	1.816	1.780	1.328	3.24	3.40	3.44	4.75
250	−23	1.859	1.768	1.712	1.345	4.34	4.49	4.59	5.87
300	27	1.784	1.709	1.648	1.350	5.44	5.60	5.75	6.98
350	77	1.672	1.634	1.587	1.348	6.54	6.70	6.91	8.10

[a] Very high purity indicated by an electrical resistivity ratio of 4900.

[b] Hot extruded from powder-metallurgy tungsten.

17. Alkali-Metal Corrosion of High-Temperature Materials

J. H. DeVan A. P. Litman
W. O. Harms

Auxiliary electrical or ion-propulsion requirements for space vehicles necessitate power plants of high efficiency that will operate at high temperatures. Nuclear power systems have been proposed for these applications in which alkali metals transfer heat from the reactor, power a turbogenerator, and lubricate rotating components.[1] Accordingly, we are studying the corrosion properties of candidate alkali metals, specifically lithium and potassium, under conditions of interest for space applications. Because of the relatively high temperatures (>1000°C), the studies are largely concerned with refractory-metal container materials.

COMPATIBILITY OF BOILING ALKALI METALS WITH REFRACTORY ALLOYS

J. R. DiStefano D. H. Jansen
B. Fleischer

A program to investigate the compatibility of refractory metals with boiling alkali metals has been in progress using refluxing capsules, natural-circulation loops, and forced-circulation loops.[2] Tests are being conducted at 1100 to 1400°C with durations ranging from 100 to 5000 hr. Materials under investigation include alloys based on niobium, tantalum, molybdenum, and tungsten.

The major part of our investigation of boiling and condensing conditions has involved refluxing capsules and natural-circulation loops. Both types of tests incorporate insert specimens in the condenser section to provide quantitative data on the rate of dissolutive attack. To obtain a better simulation of boiling circuitry we are also operating engineering-scale pumped loops that provide data on the corrosion-erosion resistance of potential nozzle and turbine blade materials.

Table 17.1 summarizes the conditions and results of tests conducted during the past year. These tests have effectively completed our study of developmental niobium- and tantalum-base alloys in potassium and have brought the cumulative operating time for refractory-metal–boiling-potassium systems to over 90,000 hr. Examinations of these systems showed almost negligible dissolutive attack in either the boiler or condenser regions at temperatures up to 1300°C and for times as long as 5000 hr.

Included in our experimental program this year was a 3000-hr pumped loop (FCL-6) fabricated of Nb–1% Zr. The loop contained a TZM nozzle-blade test section, which operated at an 1100°C vapor inlet temperature. Metallurgical examination is still in progress, but we have found that each of three blade specimens showed a slight weight gain and a thin deposit. Slight erosion damage was noted on the blade impingement area adjacent to the low-quality (82%) high-velocity (3000 ft/sec) nozzle. The other two blade specimens, which were subjected to much higher quality vapor, showed no evidence of attack or erosion. Another pumped loop (FCL-8) of a similar design is presently operating. This loop, fabricated of D-43 and containing D-43 nozzle-blade specimens, has completed 2000 hr at 1200°C test-section inlet temperature.

Future study of refractory metals in potassium will be directed toward tungsten-base alloys and toward the role played by oxygen in the corrosion of niobium and tantalum.

[1] A. P. Fraas, *Nucleonics* **22**(1), 72 (1964).

[2] J. H. DeVan, J. R. DiStefano, and D. H. Jansen, *Metals and Ceramics Div. Ann. Progr. Rept. June 30, 1966*, ORNL-3970, pp. 176–77.

Table 17.1. Summary of Boiling-Potassium–Refractory-Alloy Compatibility Tests

Material[a]		Temperature (°C)		Test Duration	Condensing Rate	Weight Change	Results
Insert	Container	Boiler	Condenser	(hr)	(g min^{-1} cm^{-2})	(mg/cm^2)	
Refluxing Capsules							
T-111	T-111	1200	1180	5000	0.32	−0.1 to −1.7	No evidence of attack
TZM	TZM	1300	1250	5000	0.32	−0.3 to −1.6	No evidence of attack
Nb–1% Zr	Nb–1% Zr	1190	1170	5000	0.35	−0.3 to +1.5	No evidence of attack
C-129Y	C-129Y	1325	1250	5000	0.36	+0.6 to +1.1	~1 mil attack on end of one insert
W	W	1315	1240	5000	0.33		Examination in progress
Nb	Nb		1200	1500	0.31		Test in progress
Nb–1% Zr	Nb–1% Zr	1240	1210	1100	0.30		Test in progress
Natural-Circulation Loops							
T-111	T-111	1250	1040	3000	0.47	−0.4 to +2.5	No attack. C and O pickup by loop material
TZM	D-43	1250	1040	3000	0.35	+0.3	No attack. O pickup in loop material in areas of decarburization
FS-85	FS-85	1250	750	1200	0.26	+2.5 to −23	Loop being repaired
TZM	TZM	1240	1160	200	0.29		Test in progress
Forced-Circulation Loops							
TZM	Nb–1% Zr	1200	450	3000	165 g/min		Examination in progress
D-43	D-43	1300	840	*b*	280 g/min		Test in progress

[a]Compositions of alloys identified here and in the text of this chapter by commercial names are listed in Table 15.1.

[b]Loop has completed 2000 hr of a scheduled 3000-hr test.

CORROSION OF REFRACTORY ALLOYS BY LITHIUM

C. E. Sessions J. H. DeVan
B. Fleischer

Interest in lithium stems from the attractive properties of this metal as a heat-transfer fluid in high-performance nuclear reactor systems. Refractory alloys based on niobium, tantalum, tungsten, or molybdenum have demonstrated low solubilities in lithium, and, by virtue of their superior high-temperature strength, appear ideally suited for containing lithium. Accordingly, we are investigating the detailed corrosion behavior of refractory metals in lithium from the standpoint of mass transfer resistance and the effects of oxygen on grain-boundary penetration.

We are investigating mass transfer in thermal-convection loops, which circulate lithium for 3000 hr at maximum temperatures in the range 1200 to 1300°C. Weight changes of insert specimens placed end-to-end around the loop are recorded for all loop positions after the test. Operating conditions of tests completed or in progress during this past year are shown in Table 17.2. We are correlating the results of a Nb–1% Zr loop (TCL-5R), which operated at 1300°C, with results of earlier 1200°C loops[3] to evaluate the effects of hot-leg temperature on mass transfer rates. Figure 17.1 compares the weight change profiles obtained for the Nb–1% Zr alloy at the two test temperatures. The total amount of material lost (0.4 g) in

[3]J. H. DeVan and C. E. Sessions, "Mass Transfer of Niobium-Base Alloys in Flowing Nonisothermal Lithium," *Nucl. Appl.* **3**, 102–9 (February 1967).

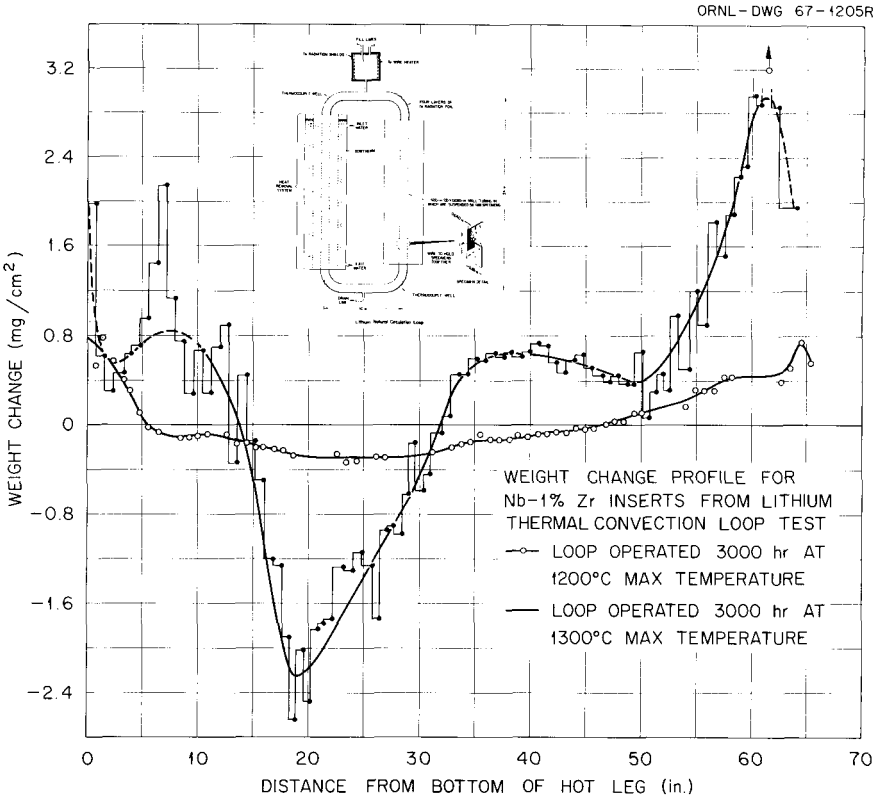

Fig. 17.1. Comparison of Nb–1% Zr Weight Change Profiles for 1200 and 1300°C Lithium Thermal Convection Loop Tests.

Table 17.2. Operating Conditions for 3000-hr Thermal-Convection Loops Used to Test Refractory Metals in Lithium

Loop	Alloy	Temperature (°C)		Lithium Flow Rate (fpm)
		Maximum Hot Leg	Minimum Cold Leg	
TCL-5R	Nb–1% Zr	1315	1115	4.8
TCL-6R[a]	T-222	1350	1150	5.0

[a]Loop currently operating.

the 1300°C test was twice that lost at 1200°C; however, the maximum weight loss at 1300°C was ten times that in the 1200°C test. Both loops showed a depletion of zirconium from hot-leg surfaces and an enrichment of zirconium, primarily as ZrN, along cold-leg surfaces. For the maximum weight loss area, electron microprobe analyses revealed depths of zirconium depletion 0.002 and 0.007 in. in the 1200 and 1300°C loops, respectively. Zirconium diffusion rates at these two temperatures, based on the assumption of a constant surface concentration, were calculated to be 3.5×10^{-13} and 6×10^{-12} cm^2/sec respectively. The values of diffusivity at these temperatures agree with published data in which short-circuiting along grain boundaries accounts for the bulk of the material transport.

These thermal-convection loop results will be supplemented by mass-transfer studies under forced flow. We have undertaken the design, pump development, and construction of a T-111 alloy loop to operate at temperatures in the range 1370 to 1650°C. The loop is being designed as a test-bed system to accommodate removable insert specimens and will operate with a maximum fluid velocity of 20 ft/sec at a flow rate of 6 gpm. Following each test series, the heater and economizer sections along with insert specimens will be replaced with various tantalum- and tungsten-base alloys. Preliminary to this pumped loop experiment, we conducted a series of static capsule

tests to evaluate the effect of oxygen contamination in T-111 and T-222 welds during exposure to lithium. Coupons of each alloy were doped with oxygen to approximately 500 ppm, welded in argon, and tested in lithium at 750 and 1200°C for 100 hr. No corrosion was found within the weld bead of either alloy at the 500 ppm O level; however, intergranular corrosion was observed for both alloys in the base metal away from the heat-affected zone. Heat treatment at 1300°C, which precipitates oxygen as HfO_2, effectively eliminated the base-metal attack.

EFFECT OF OXYGEN IN THE TANTALUM-POTASSIUM SYSTEM

R. L. Klueh

Our studies of the role played by oxygen in the corrosion of refractory metals by potassium have shifted from the niobium-potassium system to the tantalum-potassium system. A series of static capsule tests at 600, 800, and 1000°C has been programmed to investigate (1) the partitioning of oxygen between tantalum and potassium, (2) the dissolution of the tantalum in potassium, (3) the formation of corrosion products, and (4) the kinetics of these processes. Oxygen effects are being investigated from the standpoint of the concentration of oxygen in the tantalum as well as in the potassium.

Preliminary results for the Ta-O-K system at 600 and 800°C have followed closely the patterns observed for the Nb-O-K system. That is, although the thermodynamic properties of the known oxides of potassium and tantalum predict that oxygen should be gettered from potassium by tantalum, the opposite is observed. In capsule tests at 600°C, tantalum specimens with 50 ppm O exposed to potassium containing 100 to 3300 ppm O lost weight in proportion to the oxygen content of the potassium. After 500 hr, all of the tantalum specimens had lost oxygen, irrespective of the oxygen level of the potassium. Studies are now in progress to define the chemical reactions by which both the oxygen and tantalum enter potassium.

DETERMINATION OF OXYGEN IN ALKALI METALS

J. E. Strain[4] J. H. DeVan

A fast-neutron activation analysis facility was completed during the past year to expedite the analysis of oxygen in alkali and refractory metals. However, operation of the system has been hampered by debugging problems encountered first with the counting equipment, subsequently with the sample vacuum system, and currently with the palladium leak valve within the neutron generator. The latter problem is associated with the leakage of Freon from the insulated accelerator dome into the valve. The cause of the leakage was located, and the manufacturer of the accelerator is sending a replacement valve and feed system to eliminate the problem. The sample stopping and unloading device was also redesigned to reduce the travel time of the sample from irradiation to counting position. A series of refractory-metal specimens with carefully documented oxygen levels was assembled to statistically evaluate the accuracy of the present system.

[4]Analytical Chemistry Division.

18. Nitride Fuels Development

J. L. Scott W. O. Harms

Uranium mononitride continues to show promise as a nuclear fuel for space and fast breeder reactors because of its excellent high-temperature stability, high density, and high thermal conductivity. These features permit its operation in metal-clad elements at heat ratings surpassing those attainable with the more standard UO_2. Unlike uranium monocarbide, its chief competitor in these high-power applications, uranium nitride is easily made stoichiometric, thus lessening fuel-cladding interactions. Also, since UN has a higher melting point (2850°C at 2.5 atm N_2) than UC (2450°C), nitride fuels hold promise of exhibiting better irradiation performance than the carbides.

A portion of our work is directed toward development of the carbonitride concept. A carbonitride fuel might offer significant advantages over either pure carbide or nitride fuels because (1) the activities of the nitrogen and carbon could be adjusted to minimize fuel-cladding reactions, (2) the stoichiometry, with respect to either free carbon or free uranium, could be readily controlled, and (3) the vapor pressure of nitrogen over such a solution would be lower than over the pure nitride. This solid-solution material should also be more economical to prepare than either pure carbide or nitride.

Mixed uranium-plutonium nitrides or carbonitrides appear to be particularly attractive as fuel for liquid-metal-cooled fast breeder reactors. Our studies indicate that, for sodium- or helium-bonded stainless steel fuel rods, mixed nitride fuel offers a linear heat rating at least twice that of a mixed oxide fuel. We are developing a facility for preparing and studying these mixed uranium-plutonium nitrides and carbides.

Uranium nitride is an interesting material from a fundamental viewpoint and is being investigated under the Fundamental Ceramics Research Program described in Part I, Chap. 7. In addition, a program is under way to study the motion of injected helium gas bubbles in UN.

POWDER SYNTHESIS AND PELLET FABRICATION

R. A. Potter

Synthesis and Fabrication Equipment

We placed in operation a new synthesis rig and associated glove box system that has greatly increased our production capability for high-quality UN and its alloys. The powder synthesis equipment, shown in Fig. 18.1, consists of an Inconel retort heated by a resistance furnace that is mounted on horizontal tracks.

The retort is loaded with clean uranium metal within an argon-filled glove box, valved off, removed from the box, and connected to the vacuum-gas header at the synthesis station. The furnace is then moved into position, the synthesis is made, and the retort is returned to the glove box for unloading. The glove box system contains all equipment necessary for pellet fabrication through the cold pressing steps; the UN powder is always exposed to a purified argon atmosphere. Results indicate that with this new setup we can routinely produce a sinterable powder that contains less than 400 ppm O.

Microstructural Variations in Sintered UN

We have often seen regions of cannibalistic grain growth in our sintered specimens made from both commercial and our own powders. We believe that

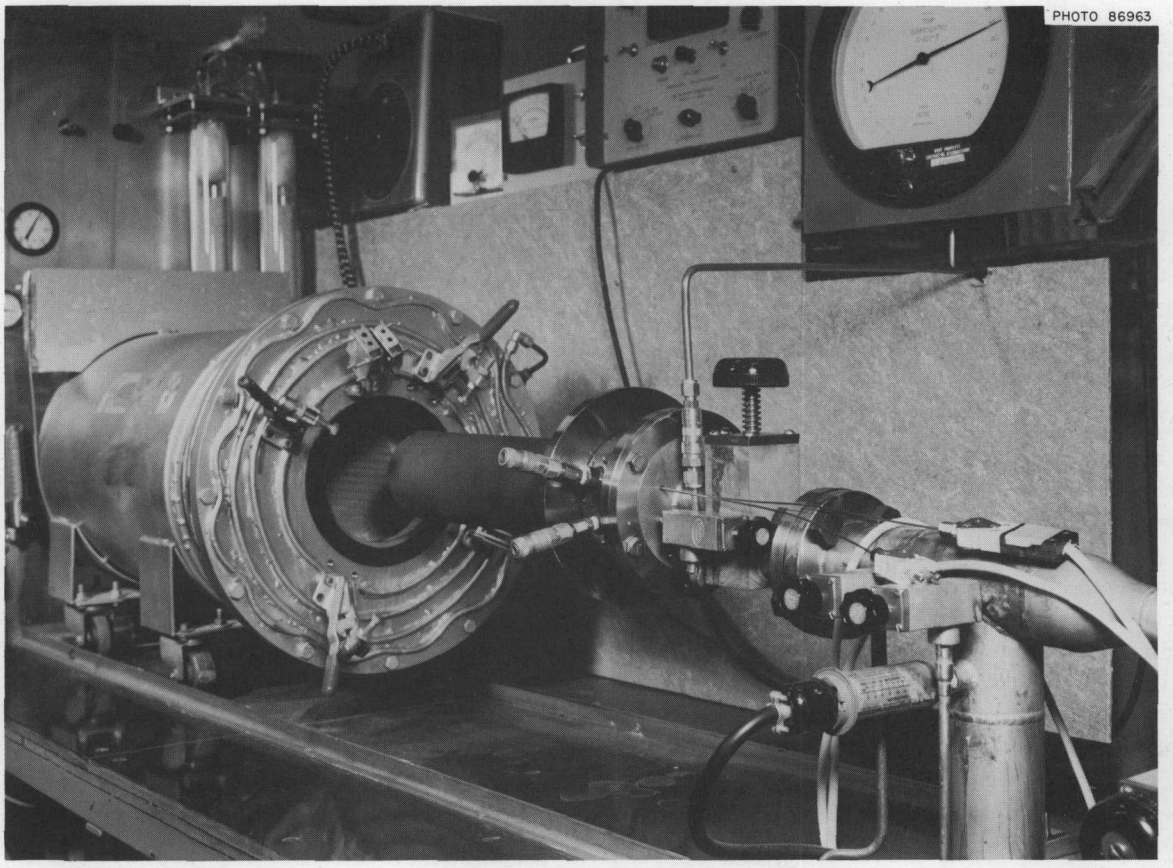

Fig. 18.1. Uranium Nitride Synthesis Apparatus. The furnace is retracted to show the Inconel retort.

these regions result from traces of uranium metal in the UN powder. During the nitriding step of the synthesis, the strongly exothermic reaction produces enough heat to fuse the very fine uranium powder in some areas. This fused metal then resists further nitridation. If we give the nitrided material an additional hydriding-dehydriding treatment, the free uranium is reactivated and is nitrided in the subsequent step. No evidence of gross microstructural variations has been observed on any materials prepared by this new procedure.

Preparation of Uranium Carbonitride

We have begun to examine ways of preparing uranium carbonitride and have selected the reaction of graphite with UN for the initial work. We intimately mixed graphite flour and UN powder in the proportion necessary to form $U(C_{0.25}N_{0.75})$. Pressed pellets of the mixture were heat treated to 2100°C under nitrogen pressures calculated to yield the desired composition as derived from the thermodynamic studies reported later in this chapter. X-ray diffraction analysis indicated that a homogeneous solution with the composition $U(C_{0.27}N_{0.73})$ was obtained. Thus, it appears that U(C,N) of a desired composition can be obtained readily by this procedure.

Sintering Behavior of Uranium Mononitride[1]

R. A. Potter V. D. Fréchette[2]

The effects of time and temperature on the final stages of densification and grain growth of compacted UN powders were investigated. Densification rates were obtained over the temperature range 1600 to 2230°C.

---

[1]Abstract of paper presented at the meeting of the American Ceramic Society, New York, May, 1966, and submitted for publication to the Bulletin of the American Ceramic Society.

[2]Consultant from State University of New York College of Ceramics at Alfred University, Alfred.

Specimens of a typical commercial-grade powder – cold-pressed to 58% density, heated in vacuum to 1500°C in 2 hr, and then heated to 1900°C in 1 atm N_2 in 5 min – reached 90% density and a grain size of 7 μ in 1 hr. Specimens heated in the same manner to 2230°C and held for 1 hr reached 95% density with a grain size of 16 μ. Metallography showed only UN with minor amounts of UO_2. Extended heat treatment at 2230°C was attended by weight loss (30 mg/cm^2 in 8 hr) and disappearance of UO_2 from the surface zone. Analysis of the data suggests that oxygen is lost by a diffusion-controlled process.

DISTRIBUTION OF SECOND-PHASE MATERIAL IN URANIUM NITRIDE

T. G. Godfrey J. M. Leitnaker
R. A. Potter

A thermally stable dispersion of very small second-phase particles might greatly enhance the irradiation performance of fuels through provision of nucleation and pinning sites for fission gases. We are continuing our efforts to provide such a dispersion in UN through incorporation of either molybdenum or thorium dioxide. We are also developing procedures for electron microscopy of UN, the primary method for studying the morphology and distributions of the dispersions.

Molybdenum in Uranium Nitride

We have previously discussed results obtained on heat-treated mixtures of molybdenum and UN, which suggested that this system might lead to a fine precipitate dispersion.[3] Experiments on more homogeneous material prepared by nitriding arc-melted uranium-molybdenum alloys established the solubility relationship depicted in Fig. 18.2. Room-temperature lattice parameters of the nitride-molybdenum samples after the various heat treatments indicate that the solubility of molybdenum reached a maximum value at about 2350°C. Metallography revealed second-phase molybdenum in all specimens sintered and annealed below 2350°C,

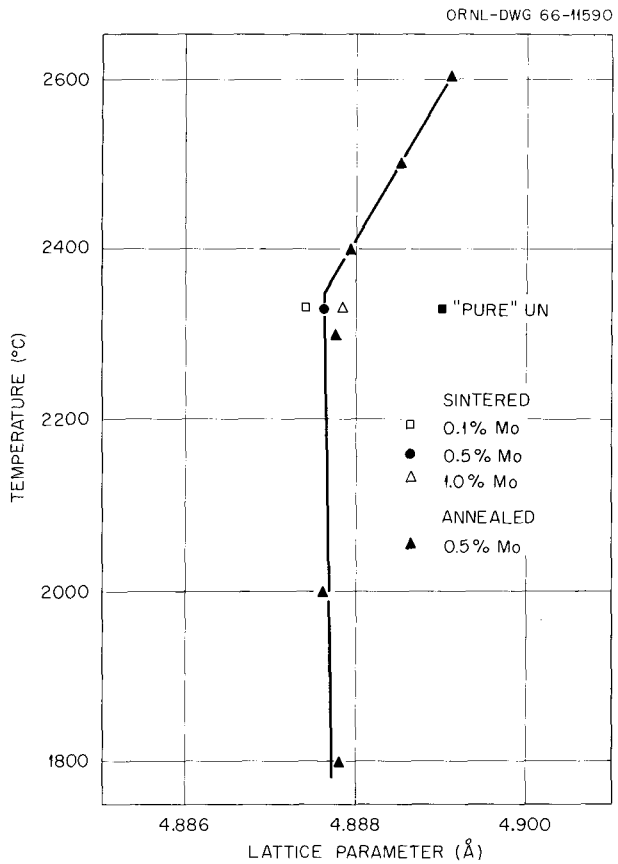

Fig. 18.2. Room-Temperature Lattice Parameters of UN-Molybdenum Specimens and a Pure UN Sample as a Function of Heat Treatment.

although the amount was very small in the 0.1% Mo sample. This indicates that the solubility is somewhat less than 0.1% at 2350°C. In samples heat treated above 2350°C, the molybdenum apparently reacted with UN to form a uranium-molybdenum liquid phase, which removed molybdenum from solution. Thus, we feel that sintering at about 2300°C followed by an annealing at a lower temperature shows considerable promise of leading to the desired fine dispersion of molybdenum precipitate particles in UN.

Thorium Dioxide in Uranium Nitride

We believe, for reasons stated previously,[3] that a suitable dispersion of fine precipitate particles of ThO_2 in UN is feasible. We have now shown that a thorium-rich oxide phase is indeed formed in situ by internal oxidation of solid solutions of (U, Th)N synthesized from arc-melted alloys. The

[3]T. G. Godfrey, J. M. Leitnaker, and R. A. Potter, *Metals and Ceramics Div. Ann. Progr. Rept. June 30, 1966*, ORNL-3970, pp. 92–93.

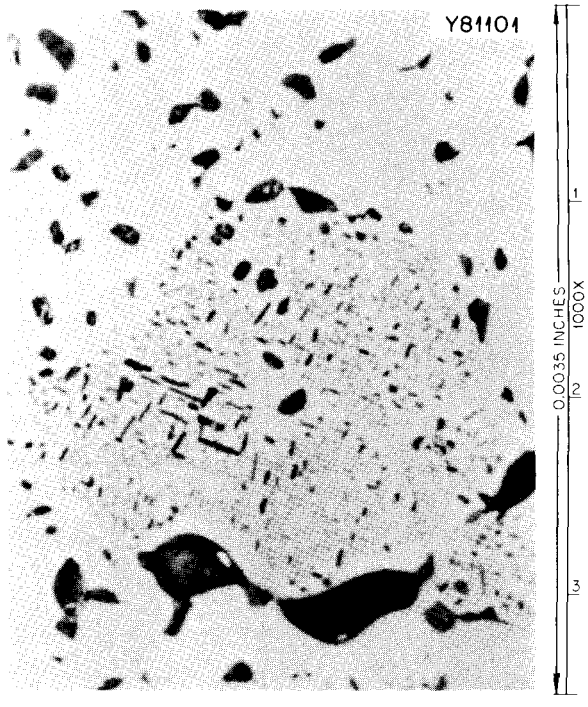

Fig. 18.3. Microstructure of (U–2% Th)N–5% UO_2 Sample Sintered at 2300°C, Showing Distribution of Gray Oxide Phase. As polished.

UN-ThN system obeyed Vegard's law at least up to 5% ThN. Oxygen is supplied by UO_2 intimately mixed with the nitride powder. During the sintering process, oxygen diffuses into the nitride phase and preferentially reacts with thorium to form an oxide within the nitride matrix. Figure 18.3 illustrates the type of very fine oxide particles that we have observed in several specimens. The small platelets and particles of oxide seem to be crystallographically oriented with respect to the nitride subgrains, suggesting a degree of coherency between the two phases. We are now investigating ways of producing this dispersed oxide phase on a uniformly fine scale.

Electron Microscopy

We chose to prepare our electron microscopy specimens by fracturing the sample, shadowing the fresh surface with platinum, and replicating with evaporated carbon. We feel that this method is more likely to reveal the true nature of the sample than the alternate technique of replicating a selectively etched sample prepared metallographically.

To avoid possible oxidation artifacts on the fresh fracture surface of this pyrophoric material, we fracture the specimen while it is immersed in a volatile organic liquid, transfer it – still covered with liquid – to the vacuum shadowing unit, remove the liquid under vacuum, and immediately shadow the specimen.

The very fragile and lacy replica could be freed from the specimen by repeatedly dipping the specimen into hot 40% HNO_3. This procedure eliminates the formation of large gas bubbles, which tend to fragment the replica.

THERMODYNAMIC AND KINETIC STUDIES

J. M. Leitnaker

Among the parameters necessary for the design of reactor fuel systems are the thermodynamic properties of the individual constituents. We are determining these thermodynamic properties of UN by several different techniques and are also investigating solid solutions of UC and UN. Ultimately, this work will lead to studies on mixed uranium-plutonium nitrides and carbonitrides for advanced breeder reactor concepts.

Equilibrium Nitrogen Pressures and Thermodynamic Properties of UN (ref. 4)

H. Inouye J. M. Leitnaker

Pressures of nitrogen over UN(*s*) + U(*l*) were measured between 1300 and 1500°C by an equilibration technique. Such measurements have now been made over a pressure range of nearly 11 orders of magnitude and a temperature range of 1550°C. These data, coupled with literature data, indicate that the heat of formation of UN, $\Delta H^\circ_{298,f}$, is –69.6 ± 1.0 kcal/mole. The second and third law calculations agree satisfactorily.

The Ideality of the UC-UN Solid Solution[5]

J. M. Leitnaker

We studied the equilibrium of the reaction of UC with nitrogen at temperatures from 1500 to 1900°C

[4]Abstract of paper submitted for publication to the *Journal of the American Ceramic Society*.

[5]Abstract of paper to be presented at the IAEA Symposium on Thermodynamics of Nuclear Materials with Emphasis on Solution Systems, Vienna, Austria, Sept. 4–8, 1967.

to determine the thermodynamic properties of the UC-UN solid solution and, using the known properties of UC, to obtain $\Delta H^{\circ}_{298,f}$ of UN. By assuming Vegard's law, we found $\Delta H^{\circ}_{298,f}$ of UN to be -70.4 ± 0.9 kcal/mole over a wide nitrogen pressure range corresponding to 0.3 to 0.9 mole fraction UN. This value compares well with the -69.6 ± 1.0 kcal/mole obtained from examination of all vapor pressure measurements on UN. We reason that an observed trend with temperature in ΔH°_{298} for the reaction

$$UC(s) + \frac{1}{2}N_2(g) \rightleftharpoons UN(s) + C(graphite)$$

is caused by precipitation of carbon in a more active state (by approximately 0.6 kcal/mole at 1500°C) than graphite below 1700°C. This is substantiated by experiments in which UN was reacted with graphite.

Kinetics of the Reaction of UC with Nitrogen

J. M. Leitnaker T. G. Godfrey
C. M. Fitzpatrick

A study of the kinetics of the reaction of UC with nitrogen was a necessary part of the equilibrium UC-UN studies described above and was of interest in its own right in view of the possible importance of uranium carbonitrides and the ways of producing them.

We found the reaction to be a two-stage process. In the first stage, regardless of the starting conditions, a singular carbon-rich U(C,N) composition was reached very quickly. If we accept ideal behavior of the UC-UN solid solution and assume that the singular composition of U(C,N) corresponds to the one in equilibrium with graphite and UC_2, we calculate for the reaction

$$UC(s) + 0.91C(graphite) \rightleftharpoons UC_{1.91}(s)$$

a ΔH°_{298} of 2.85 kcal/mole, which agrees well with previous results of the thermodynamic analysis of the uranium-carbon system.[6] This supports the assumption of ideality in the UC-UN system and indicates that the singular point [which is one apex of the UC_2-U(C,N)-graphite composition triangle] is a "way station" in the overall reaction. The second stage of the reaction leads ultimately to the equilibrium composition for that temperature and pressure and is relatively slow.

The speed of the two-stage reaction is dictated by the nature of the starting materials, as shown by Hanson;[7] "aged" samples react significantly faster than do "fresh" samples. We showed that this aging effect can be reversed: if a sample is heated in vacuum for a few minutes before nitrogen is admitted, the rate of reaction is remarkably slower.

Analytical Chemistry of Uranium Nitrides and Carbides

J. M. Leitnaker K. E. Spear
W. R. Laing[8]

Much of the work discussed in this chapter demands accurate and precise chemical analysis. It is generally recognized that analyses on uranium nitrides and carbides are difficult and often fraught with subtle complications. We found that some of the supposed problems arise simply from sample handling and preparation steps. However, a basic problem may exist in the analysis of free and combined carbon. We feel that this may be related to the fact that carbon, as stated in the UC-UN discussion above, may be precipitated on a submicroscopic scale in a form that is activated with respect to graphite. This supposition has profound implications with regard to much of the information in the literature concerning carbides in general.

Thermodynamic Properties of Uranium Carbides[9]

J. M. Leitnaker T. G. Godfrey

Thermodynamic and phase information relative to the uranium-carbon system was analyzed and shown to be consistent. The anomalously high heat capacity of UC_2 is justified in the analysis. Thermal functions are calculated for UC and UC_2, using a value of 0.6 cal $mole^{-1}$ $°K^{-1}$ for S°_0 of the dicarbide. For uranium, $\Delta H^{\circ}_{298,vap}$ is calculated to be 123.7 ± 1.3 kcal/mole.

---

[6] J. M. Leitnaker and T. G. Godfrey, *J. Nucl. Mater.* 21, 175–89 (1967).

[7] L. A. Hanson, *J. Nucl. Mater.* 19, 15 (1966).

[8] Analytical Chemistry Division.

[9] Abstracted from *J. Nucl. Mater.* 21, 175–89 (1967).

An Explanation of the Anomalous Heat Capacity of Uranium Dicarbide[10]

T. G. Godfrey J. M. Leitnaker

Published enthalpy data on uranium dicarbide indicate a heat capacity of 32 cal $mole^{-1}$ $°K^{-1}$ at 2000°K. Since this value is considerably higher than one would expect for a triatomic solid, it has been viewed with some suspicion. However, three lines of evidence indicate that the measurements are of acceptable accuracy. First, metallographic evidence indicates that a phase change takes place over a range of temperature below approximately 2000°K. Second, high-temperature x-ray diffraction data indicate an unusual behavior in the lattice parameters of the dicarbide below 2000°K. Third, use of the enthalpy measurements with other published information completes a thermodynamic cycle in the uranium-carbide-oxygen system. A nonzero $S^{\circ}_{0^{\circ}K}$ is a reasonable assumption.

Thermodynamic Functions of Nuclear Materials: UC, UC_2, UO_2, ThO_2, and UN (ref. 11)

T. G. Godfrey J. A. Woolley[12]

J. M. Leitnaker

The thermodynamic functions, $H^{\circ}_T - H^{\circ}_{298}$, C°_p, S°_T, and $(F^{\circ}_T - H^{\circ}_{298})/T$, of five compounds of nuclear interest (UC, UC_2, UO_2, ThO_2, and UN) were calculated from literature data and tabulated at increments of 100°C. Estimates of accuracy were included, and the fit of the original enthalpy data to the calculated curve was shown graphically in each case.

---

[10]Abstracted from ORNL-TM-1595 (October 1966).

[11]Abstracted from ORNL-TM-1596 Revised (December 1966).

[12]Summer employee, 1965.

Part III.

General Fuels and Materials Research

19. Dispersion in Solids

J. P. Hammond

The purpose of this program is to apply the principles of fine-particle dispersion hardening and whisker reinforcement to the advancement of nuclear fuel, cladding, and structural materials. Hard stable particles are used for obstructing dislocation flow[1] in structural materials and anchoring precipitated fission gases[2] in nuclear fuels. For optimum performance, particles should be around 0.03 μ in size and spaced 0.1 to 0.3 μ apart.

During the past year, studies were continued on dispersion hardening of thorium, and new efforts were begun on aluminum-base alloys and nickel- and cobalt-base superalloys. Studies of controlled precipitation in uranium nitride are described in Part II, Chap. 18 of this report.

DISPERSION HARDENING OF THORIUM

J. P. Hammond

The permissible operating temperature and burnup potential of thorium matrix fuels could be improved by dispersion hardening. We examined a number of methods for introducing stable fine dispersions in thorium; representative hot-hardness results are given in Table 19.1. Excellent dispersion structures were achieved in thorium derived from the fragile hydride ball-milled with ultrafine ThO_2. Extruded rods of this material displayed[3] good hardness and strength at 800°C. However, restricting carbon pickup and controlling the final oxide content proved difficult. That carbon has a deleterious effect on hardness at 800°C is seen by comparing specimens 5 and 3 of Table 19.1 (and by inference 4 and 2).

A fine dispersion of intermetallic UBe_{13} in thorium prepared by the SLIS technique[4] also gave moderately good hardness at 800°C (specimen 6). However, by far the best hardness results were obtained by a new internal-boronation process devised to form a stable zirconium boride dispersion in thorium (specimens 7 and 8).

In the boronation process, a small amount of separated ^{11}B isotope in the form of 200-A soot is blended into an ultrafine powder of thorium containing 4.65% (10 at. %) Zr in solid solution. As in the case of the ThO_2-hardened material, the thorium is rendered fine by ball-milling it as hydride. Boron is then introduced and the mixture consolidated and hot extruded in the form of a rod. It will be noted that the boronated alloys picked up substantial carbon ($\frac{3}{4}$ to 1%), as did two of the ThO_2-hardened specimens (Nos. 4 and 5), from the hydrocarbon grinding liquid used in milling. However, the boronated alloys showed twice the hardnesses at 800°C of competitive alloys despite carbon contamination. That not carbon, but boron in conjunction with zirconium accounts for the high hot hardness was proven by a supplemental experiment in which carbon was introduced while boron was excluded from the thorium-zirconium alloy (specimen 9). Without boron, these alloys exhibited very low hot hardness.

---

[1] A. Kelly and R. B. Nicholson, "Precipitation Hardening," p. 324 in *Progress in Materials Science*, Vol. 10, The MacMillan Company, New York, 1963.

[2] R. S. Barnes, *A Theory of Swelling and Gas Release for Reactor Materials*, AERE-R-4429 (October 1963).

[3] J. P. Hammond, *Metals and Ceramics Div. Ann. Progr. Rept. June 30, 1966*, ORNL-3970, pp. 101–2.

[4] Consists of quenching molten particles of an alloy having a solute that is *soluble* in the *liquid* state but *insoluble* in the *solid* state. Nuclear Metals, Inc. prepared Th–1.3% Be alloy powder for us by this method.

Table 19.1. Hot Hardness of Dispersion Hardened Thorium Alloys

Specimen	Method of Hardening[a]	Additives (wt %)	Chemical Analysis (wt %)			Hardness[b] (DPH) at				
			B	C	O	25°C	500°C	600°C	700°C	800°C
1	None	None				85	30	22	15	
2[c]	ThO_2 embedment	5 ThO_2				123	53	41	29	21
3[c]	ThO_2 embedment	10 ThO_2		0.14		220	91	63	43	31
4[d]	ThO_2 embedment	5 ThO_2				326	126.5	68.5	23	7
5[d]	ThO_2 embedment	10 ThO_2		1.05		296	91.5	60.5	21.5	5.5
6[e]	SLIS	1.3 Be				139	86	71	45	28
7[f]	Boronation	4.65 Zr–0.54 B	0.43			427	129.5	92	70.5	74.5
8[f]	Boronation	4.65 Zr–0.14 B	0.15	0.91	0.53	403	152	94	62	53
9[g]	Carburization	4.65 Zr		0.77		280	88	33	16	10

[a]Thorium used to prepare each alloy was from a calcium-reduced grade analyzing 99.8% Th, 340 ppm C, 2000 ppm O, and 180 ppm N.

[b]Each value is an average of two measurements.

[c]Fine dispersion was prepared by dry ball-milling 0.03-μ ThO_2 with hydrided thorium in ordinary mill, followed by vacuum hot pressing in graphite at 1000°C and extruding at 900°C.

[d]Fine dispersion was prepared by ball-milling 0.03-μ ThO_2 with hydrided thorium in a high-energy mill, followed by dehydriding, cold pressing, vacuum sintering at 800°C, and extruding at 750°C. The high carbon content was attributed to carbon picked up from a hydrocarbon grinding liquid used in ball-milling.

[e]Fine dispersion is based on the $ThBe_{13}$ intermetallic and was prepared from powder made by the SLIS technique. Powders were consolidated by hot-upset-extrusion at 600°C.

[f]Fine dispersion was prepared by boronating a finely ground thorium alloy powder containing 4.65% Zr in solid solution. The alloy was hydrided, ball-milled in a high-energy mill, and then dehydrided, and a 200-A boron soot was introduced by dry blending. Consolidation was by vacuum sintering at 800°C and extruding at 750°C. The high carbon content was attributed to carbon gained from a hydrocarbon grinding liquid used in ball-milling.

[g]Processed the same as specimens 7 and 8 except that no boron was added.

DISPERSION HARDENING OF NICKEL- AND COBALT-BASE SUPERALLOYS BY INTERNAL OXIDATION

J. P. Hammond J. Y. Chang[5]

Preliminary studies were undertaken to dispersion harden heat-resisting alloys by internal oxidation. Although previously only the less corrosion-resistant alloys (i.e., those lean in additives conferring scaling resistance) were hardenable by internal oxidation, now this mechanism may be exploited to boost the high-temperature load-carrying capabilities of nickel- and cobalt-base superalloys.

Alloys patterned after Nichrome and Vitallium but containing approximately 7 at. % Th as an oxidizable additive were prepared as powders and successfully internally oxidized. The powders were cold pressed and sintered as $1\frac{1}{4}$-in.-diam pellets and then worked by hot extrusion and swaging.

A replica electron micrograph of the internally oxidized Nichrome alloy is shown in Fig. 19.1 and illustrates the fineness and uniformity of dispersion obtainable at this stage of development. Tensile tests conducted at 1095°C on the internally oxidized Nichrome gave an ultimate tensile strength of 11,000 psi, which compares favorably with T.D. nickel. The oxidation resistances of internally oxidized Nichrome and Vitallium at 1095°C are compared in Table 19.2 with results for unmodified Nichrome and Vitallium. The alloys not only gained substantially less weight than their commercial counterparts, but, equally important, the thin protective surface films formed were very tenacious and resistant to thermal cycling.

[5]Noncitizen employee from Korea.

Fig. 19.1. Replica Electron Micrograph of Extruded Rod of Internally Oxidized Modified Nichrome Alloy (Transverse Section).

Table 19.2. Oxidation Resistance of Extruded Internally Oxidized Superalloys[a]

Alloy	Composition (wt %)	Weight Gain[b] (mg/cm^2)
Internally oxidized		
Nichrome-thorium (V59)	63.7 Ni–15.33 Cr–20.2 Th	0.0601
Nichrome-thorium (V47)	63.7 Ni–15.33 Cr–20.2 Th	0.0747
Vitallium-thorium (Co-5-1)	53.3 Co–17.64 Cr–3.15 Ni–4.28 Mo–21.2 Th	0.1402
Standards		
Nichrome	80 Ni–20 Cr[c]	0.2379
Vitallium	64.5 Co–27.5 Cr–2.5 Ni–5.5 Mo[c]	0.7911

[a]Tested for 100 hr at 1095°C in static air.

[b]Average of two determinations.

[c]Nominal.

20. Fuel Element Fabrication Development

G. M. Adamson, Jr.

Our program is to devise new fabrication techniques for fuel, cladding, and structural materials and to improve the performance of these materials. Chemical vapor deposition of uranium dioxide, uranium nitride, and plutonium oxide have been investigated using several processes. This new approach appears adaptable to fuel recycle as well as to preparation of initial fuel charges. The chemical vapor deposition of tungsten-rhenium alloys is reported in Part II, Chap. 16 of this report.

We are seeking new knowledge on aluminum-base fuel elements to increase fuel loading, utilize less expensive fuels, and gain a better assurance that the practice of commercial fabricators will produce satisfactory fuel elements. Investigations of the fuels for application to the High Flux Isotope Reactor are reported in Part IV, Chap. 32 of this report.

CHEMICAL VAPOR DEPOSITION OF URANIUM OXIDE BY THE FLAME REACTOR TECHNIQUE

W. C. Robinson, Jr. F. H. Patterson[1]
W. R. Martin

An apparatus for the direct conversion of UF_6 to uranium oxide powder was constructed and is being operated. The reaction of hydrogen and fluorine heats the gases so the oxide products precipitate as powder from the gas phase rather than form a massive deposit on a surface. This "flame reactor" concept is used at ORGDP for the conversion of UF_6 to UF_4 and for production of refractory-metal powder. However, the apparatus at ORGDP operates at pressures of 0.5 atm and above, which are too high to allow complete conversion of UF_6 to a UO_2 product, since condensable intermediates such as UO_2F_2 and UF_4 can form. Previous work at ORNL had demonstrated that UF_6 could be converted to UO_2 in a one-step high-temperature low-pressure hydrogen reduction. Furthermore, at sufficiently high temperatures the reaction would occur away from the deposition mandrel to form a fine powder product. Finally, a self-starting hydrogen-fluorine flame was stabilized at very low pressures. The combination of these ideas led to the present apparatus (see Fig. 20.1), which is constructed to simultaneously introduce H_2, F_2, O_2, and UF_6 gases into a reaction chamber and to catch the uranium oxide product of the resulting reaction. This may be a high-rate economical route for reprocessing uranium fuels to fine uranium oxide powder.

The preliminary experience with the process is most encouraging. The apparatus is very easy to operate. Moreover, nearly 100% of the UF_6 was directly converted to a U_3O_8 and UO_2 combination powder product in the initial three runs. Optimization of experimental variables is under way.

CONVERSION OF URANIUM CHLORIDES TO URANIUM DIOXIDE

W. C. Robinson, Jr. F. H. Patterson[1]
W. R. Martin

Uranium chlorides are obtained from the chlorine volatilization process considered for recovery of Zircaloy-clad fuels. We investigated[2] the feasibility of converting these gaseous chlorides to

[1] Present Address, Battelle Memorial Institute, Columbus, Ohio.

[2] F. H. Patterson, W. C. Robinson, Jr., and C. F. Leitten, Jr., *Conversion of Uranium Chlorides to Urania by Gas-Phase Reduction Hydrolysis*, ORNL-TM-1701 (April 1967).

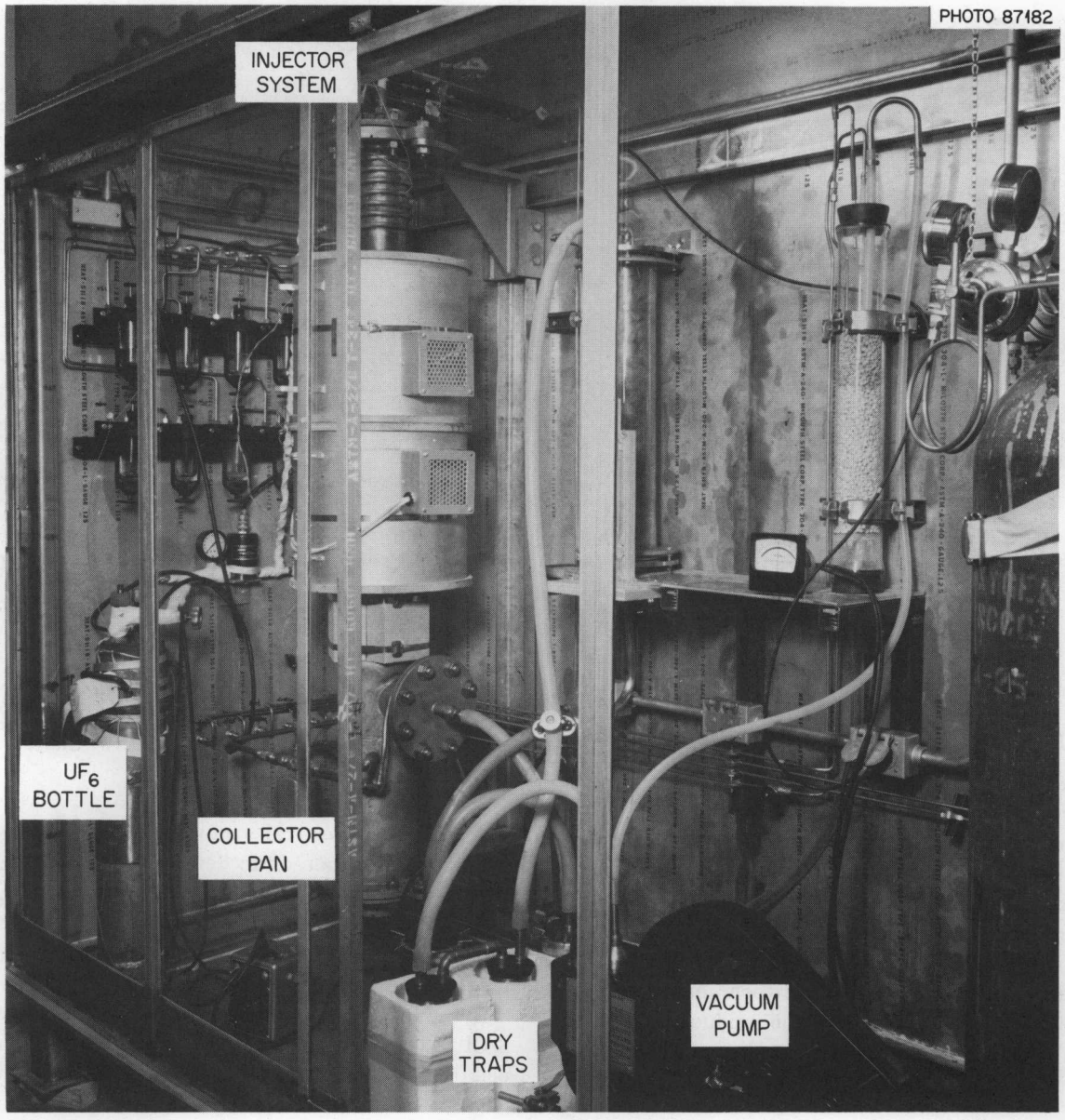

Fig. 20.1. Flame Reactor for Conversion of UF_6 to Urania.

uranium oxide powder by reaction with hydrogen and water vapor.

The parameters investigated in these feasibility studies included a temperature range of 660 to 960°C and pressures of 1 to 6 torrs. The uranium chloride was successfully converted to microfine urania powder. This established the feasibility of a simple conversion of the product of the chloride volatilization process back to usable fuel material.

FORMATION OF URANIUM NITRIDES BY CHEMICAL VAPOR DEPOSITION[3]

W. C. Robinson, Jr. W. R. Martin

We investigated[3] the feasibility of using an alkali-metal reductant to achieve products impossible to obtain with hydrogen. The direct gas-phase reduction of UF_6 to uranium metal according

[3]Summarized from *A Feasibility Study – Formation of Uranium Nitride Compounds Using Chemical Vapor Deposition Techniques*, ORNL-TM-1812 (May 1967).

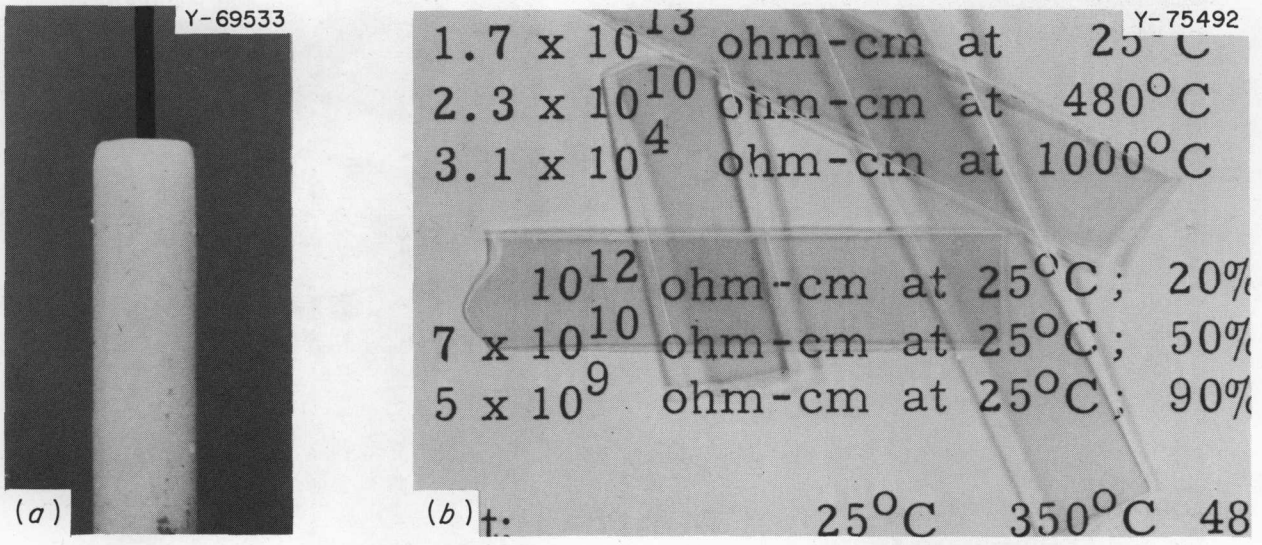

Fig. 20.2. Vapor-Deposited Boron Nitride. (*a*) Milky white deposit similar to commercially deposited material. 4×. (*b*) Newly discovered transparent boron nitride, usable to 3000°C in inert environments. 2.5×.

to the reaction

$$UF_6(g) + 6Li(g) \longrightarrow U(s) + 6LiF(g)$$

was demonstrated. Nitrogen was then introduced into the chamber simultaneously with UF_6 and lithium vapor to form a uranium-nitrogen compound. At temperatures and pressures selected, thermodynamic data indicate uranium nitride to be stable. The reaction produced UN, UN_2, U, LiF, and complex (U, Li, F) compounds. We proved that uranium nitride could be formed by this technique; however, clean separation of the reaction products was not feasible in our apparatus.

CHEMICAL VAPOR DEPOSITION OF BN

W. C. Robinson, Jr. W. R. Martin
R. L. Heestand[1]

The feasibility of depositing BN from the reaction of BCl_3 and NH_3 was investigated. Variation of the deposition parameters led to three different types of BN product: milky white, chocolate brown, and transparent. Examples of the milky-white and transparent materials are shown in Fig. 20.2. Further development of the transparent material is awaiting a specific application. The milky-white material is already being used as part of a tungsten-BN-tungsten coaxial temperature probe.[4]

CHEMICAL VAPOR DEPOSITION OF SiC

W. C. Robinson, Jr. D. W. Short[5]
R. L. Heestand[1]

A series of chemical vapor deposition experiments was conducted[6] to determine the feasibility of controlling the stoichiometry and surface structure of silicon carbide deposits. The silicon carbide was deposited by the reduction of $SiCl_4$ in the presence of hydrogen and CH_4.

By adjusting the temperature and proportions of $SiCl_4$, CH_4, and H_2, the morphology and stoichiometry can be controlled. Pressure affected the deposition rate and surface roughness but had little effect upon composition. Smooth coatings were obtained when the deposit was rich in silicon. These experiments indicate the modifications required to obtain particular compositions. The resulting deposits of this investigation are being characterized more thoroughly. If justified, a parametric study will seek conditions for producing product with optimum characteristics.

---

[4]R. L. Heestand and W. J. Leonard, *Metals and Ceramics Div. Ann. Progr. Rept. June 30, 1966*, ORNL-3970, p. 247.

[5]Summer employee.

[6]D. W. Short and R. L. Heestand, *Chemical Vapor Deposition of Silicon Carbide* (in preparation).

SWELLING OF UAl_3-ALUMINUM COMPACTS[7]

J. L. Gregg[8] R. S. Crouse
W. J. Werner

Satisfactory ATR-type fuel elements have been fabricated with UAl_3 fuel. However, during fabrication of these elements, swelling of the cold-pressed fuel compacts was observed after degassing at 590°C.

Examination by low-magnification microscope, room-temperature and heating-stage metallography, and x-ray diffraction confirmed the transformation of UAl_3 to UAl_4. Very little volume change occurs when UAl_3 converts to UAl_4 in an aluminum matrix, so the swelling was thought to take place due to fuel particles changing shape and forcing the poorly bonded aluminum grains apart. This shape change and wedging process was actually observed as it happened in a heating-stage metallograph.

FABRICATION DEVELOPMENT OF INSTRUMENTED-PLATE ATR FUEL ELEMENTS[9]

J. H. Erwin W. J. Werner
M. M. Martin

A procedure was developed for fabricating special plates to be used to determine the effects of fuel channel blockage during start-up of the ATR (Advanced Test Reactor). These full-size assemblies are unique in that two plates and the accompanying water channel are combined into a single plate for two positions in an element. This plate contains two normal-size cores separated by a thick aluminum center section into which holes are drilled for thermocouples to be inserted. Such plates were prepared with both U_3O_8 and UAl_3 as the dispersion fuel. The fabrication and assembly of instrumented fuel elements have been completed, and these finished fuel elements have been transferred to Idaho Nuclear Corp.

Deviations from normal ATR fuel element processing comprise a solid-state powder reaction to prepare stoichiometric UAl_3, roll bonding of split-cored plates, and maintaining the plate in compression during marforming. During fabrication development, we observed noteworthy differences in the fabricability of U_3O_8- and UAl_3-bearing plates of equivalent uranium loading and geometry. When compared to U_3O_8, the UAl_3-aluminum dispersion showed excessive growth in vacuum anneals, severe thickening or "dog-boning" near the core ends, and separation of tandem cores during rolling. Typical measurements of both types of plates are given in Table 20.1.

Table 20.1. Cross-Sectional Measurements of ATR Duplex Fuel Plates

Location of Measurement	Dimensions (in.)	
	UAl_3	U_3O_8
Intended dimensions		
Cladding	0.015	0.015
Core	0.020	0.020
Core separation	0.108	0.108
Average plate dimensions excluding core and compact ends		
Top cladding	0.0145	0.0152
Top core	0.0213	0.0209
Core separation	0.1061	0.1052
Bottom core	0.0213	0.0212
Bottom cladding	0.0148	0.0155
Average plate dimensions at core ends		
Top cladding	0.0085	0.0155
Top core	0.0320[a]	0.0232
Core separation (extrapolation)	0.0910	0.1025
Bottom core	0.0365[a]	0.0216
Bottom cladding	0.0100	0.0152
Average plate dimensions at compact ends[b]		
Top cladding	0.0121	0.0155
Top core	0.0245	0.0210
Core separation (extrapolated)	0.1029	0.1045
Bottom core	0.0252	0.0220
Bottom cladding	0.0133	0.0150

[a]Note the increased core thickness at the core ends.

[b]The fuel cores were made from more than one compact; these locations are between the separate compacts.

[7]Abstracted from ORNL-4056 (January 1967).

[8]Consultant from Cornell University.

[9]Summarized from report in preparation.

POSTIRRADIATION EXAMINATION OF 240-g ORR FUEL ELEMENTS

A. E. Richt

Potential savings in fuel costs provide considerable incentive to increase the fuel loading of the ORR fuel elements from 200 to 240 g of ^{235}U. To ascertain whether the more heavily loaded elements would perform satisfactorily in service, we fabricated three 240-g fuel elements specifically for irradiation tests in the ORR. These elements, details of which are shown in Table 20.2, were irradiated at a process water temperature of 52°C to an average burnup of 60% depletion of ^{235}U (8.3×10^{21} fissions/cm^3) with no indications of failure. Two of the elements, NL-24 and NL-30S (Al–30% UAl_3 dispersion), are being examined in the hot cells. Examination of the third element (NL-26) awaits further decay.

Table 20.2. Details of ORR 240-g Irradiation Test Fuel Elements

Element	Fuel	Aluminum Cladding Alloy	Element Condition
NL-24	Al–22% U alloy	1100	20% cold worked
NL-26	Al–22% U alloy	6061	Fully annealed
NL-30S	Al–30% UAl_3 dispersion	6061	Fully annealed

Although we have not completed the examination of these elements, preliminary results indicate that both the alloy and dispersion fuel elements performed quite satisfactorily in the ORR even with the increased loadings. Dimensional measurements showed that the elements had not bowed, warped, or twisted. No evidence of significant changes in the width, height, or coolant channel spacings of the elements was found. The fuel plates of both elements had increased slightly in thickness. The increase appeared to be directly proportional to burnup; however, at comparable burnup levels, plates fueled with the Al–22% U alloy consistently showed slightly greater thickness increases than the plates fueled with the Al–30% UAl_3 dispersion. At peak burnup areas (74% depletion of ^{235}U or 10.2×10^{20} fissions/cm^3), the alloy-fueled plates had increased approximately 0.0025 in. in thickness, compared to 0.0015 in. in the dispersion-fueled plates.

Metallographic examination of sections from the irradiated elements indicated that changes in fuel-plate thickness were a result of the combined effects of fuel swelling and the buildup of a corrosion-product film on the fuel-plate surfaces. The greater thickness increase in the alloy-fueled plates can be attributed partially to a thicker oxide film on the surfaces of these fuel plates. However, our results also indicate that the alloy fuel swelled slightly more than the dispersion fuel at comparable burnup levels. The lower swelling of the dispersion fuel appears to be related to the porosity present in the UAl_3 particles of the as-fabricated fuel plate. During irradiation, swelling of the fuel particles is at least partially accommodated by consumption of this porosity. This effect is clearly shown in Fig. 20.3, where the voids in the UAl_3 particles of the as-fabricated fuel plate have completely disappeared after irradiation to a high burnup level. The alloy fuel, however, has essentially no pores in the as-fabricated condition and thus swelled at the normal rate during irradiation.

Specimens cut from the minimum and maximum burnup regions of the fuel plates were heat-treated to determine if the breakaway swelling temperature of the two types of fuel differed significantly. As shown in Fig. 20.4, the blistering temperature of the UAl_3 dispersion fuel was slightly higher than that of the alloy.

Although results of this examination program indicate that the UAl_3 dispersion is slightly more stable than the alloy, both types of fuel appear to be quite satisfactory for the 240-g ORR elements. Consequently selection of the fuel material for additional 240-g elements should probably be based upon economic considerations.

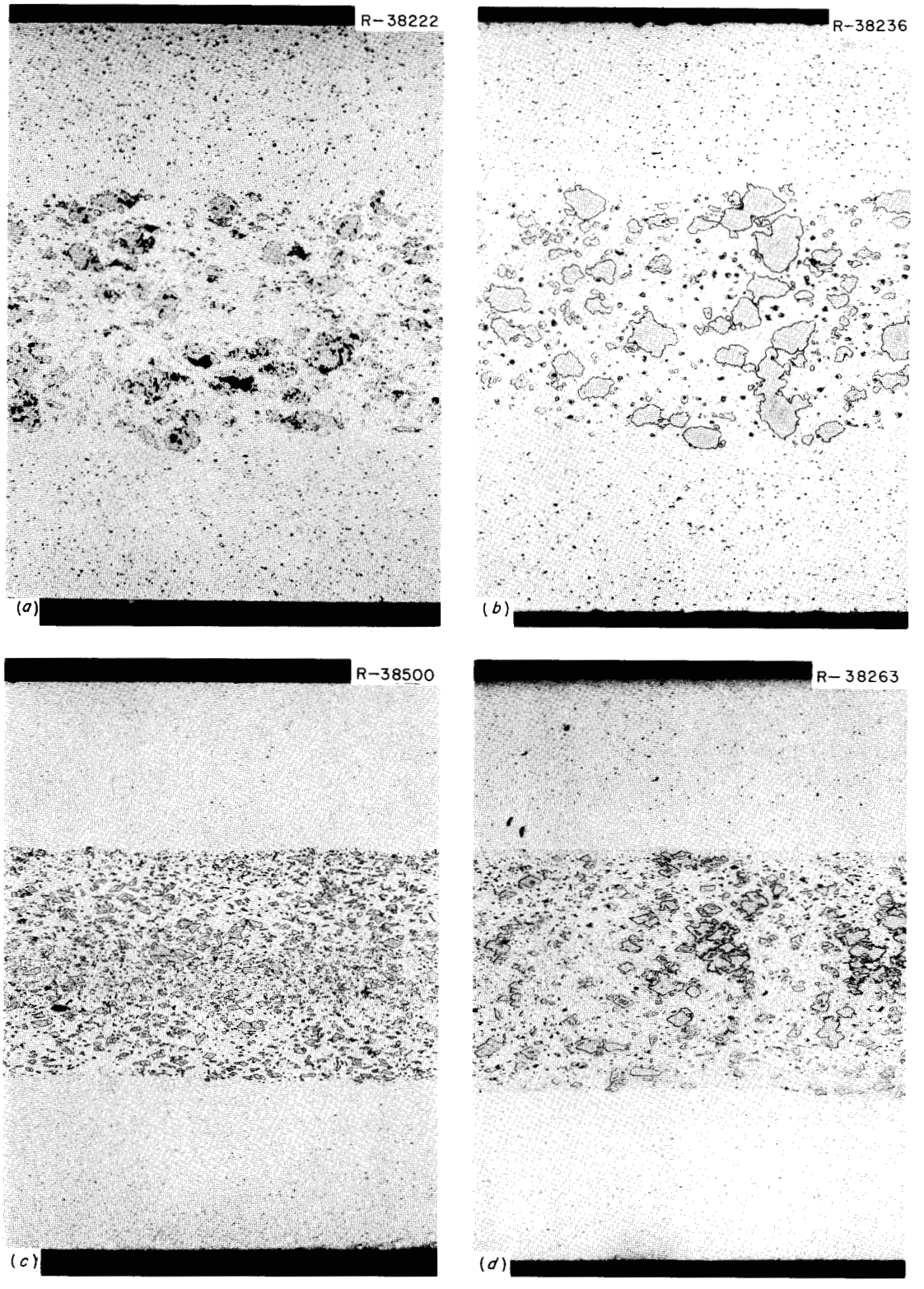

Fig. 20.3. Typical Microstructure of Fuel Plates from the 240-g ORR Fuel Elements. (*a*) Unirradiated Al–30% UAl_3 dispersion; (*b*) Al–30% UAl_3 dispersion after 10.2×10^{20} fissions/cm^3; (c) unirradiated Al–22% U alloy; (*d*) Al–22% U alloy after 10.2×10^{20} fissions/cm^3. As polished. 100×.

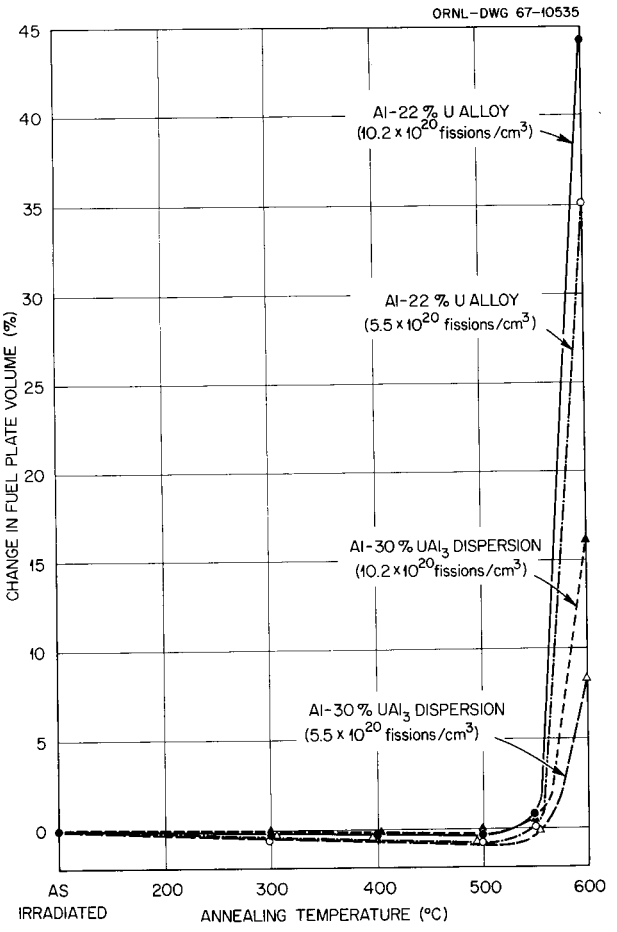

Fig. 20.4. Results of Postirradiation Heat Treatment on Dimensional Stability of ORR-Type Fuel Plates.

21. Mechanical Properties Research

J. R. Weir, Jr.

The Mechanical Properties Research and Liquid Metals Fast Breeder Reactor Materials Development programs are very closely related, and although the support for the programs is from different AEC sources, both are reported here. The objectives of the programs are (1) to understand the radiation damage to the mechanical properties of cladding and structural materials and (2) to develop modified alloys having improved resistance to the effects of reactor irradiation. The programs involve the use of the Oak Ridge Research Reactor, Cyclotrons at ORNL and ANL, the Experimental Breeder Reactor II, and potentially the High Flux Isotope Reactor for irradiation testing.

The emphasis of the program has been the investigation of the high-temperature radiation damage to austenitic alloys. We recognize that at high neutron flux in fast reactors, displacement damage effects may persist to higher temperatures than observed in thermal test reactors having lower neutron flux.

Similar work on nickel-base alloys is reported in Part IV, Chaps. 29 and 34, of this report.

IN-REACTOR AND POSTIRRADIATION CREEP-RUPTURE PROPERTIES OF TYPE 304 STAINLESS STEEL[1]

E. E. Bloom J. R. Weir, Jr.

The creep-rupture properties of a commercial heat of type 304 stainless steel were determined in the unirradiated condition and for irradiated specimens tested both during and after irradiation. The final anneal prior to testing was 1 hr at 1038°C and developed a grain size of ASTM 6 (average grain diameter of 45 μ). Tests were performed at 650°C and at stresses ranging between 15,000 and 35,000 psi. In-reactor tests were conducted at a poolside position of the Oak Ridge Research Reactor. The thermal flux was 6×10^{13} neutrons cm^{-2} sec^{-1}, and the fast flux (>2.9 Mev) was 5×10^{12} neutrons cm^{-2} sec^{-1}. Postirradiation tests were performed on specimens irradiated at 650°C to a dose of 2×10^{20} neutrons/cm^2 (thermal) and 2×10^{19} neutrons/cm^2 (>2.9 Mev).

No significant differences were observed between results of tests performed during or after irradiation. Ductility, as measured by either elongation or reduction in cross-sectional area, was reduced to very low values by the irradiation. For the stresses used in this investigation the loss of ductility became more severe as the strain rate (or stress) was reduced. As a consequence of the lower ductility, the rupture life of the irradiated alloy was reduced by a factor of 3 to 5. Creep rates for both in-reactor and postirradiation tests were a factor of 2 to 5 higher than those of the unirradiated alloy. However, the irradiated specimens failed in times approximately equal to the time required for the establishment of secondary creep in the unirradiated alloy. Hence, we feel that the apparently higher creep rates associated with the irradiated specimens were due to their failure while still in the primary stage of creep.

[1]Summary of paper presented at the American Nuclear Society, San Diego, Calif., June 11–15, 1967.

DEVELOPMENT OF ALLOYS WITH IMPROVED RESISTANCE TO ELEVATED-TEMPERATURE IRRADIATION EMBRITTLEMENT

E. E. Bloom J. R. Weir, Jr.

The effects of neutron irradiation upon the mechanical properties of the austenitic stainless

steels have been extensively reported. At test temperatures above approximately 600°C, irradiation affects the ability of the alloy to resist intergranular fracture, and as a result the ductility as measured in a tensile test and the ductility and rupture life as measured in a uniaxial creep-rupture test are severely reduced. These effects are a result of helium produced by (n,α) reactions during irradiation. Martin and Weir[2] discussed several possible solutions to this problem; among these was the addition of amall amounts of titanium to an alloy having the nominal composition of type 304 or type 304L stainless steel. The addition of approximately 0.2% Ti to small laboratory heats gave significant increases in ductility for both the unirradiated and irradiated alloy.

We have now obtained several small (50 to 100 lb) and one moderately large (1500 lb) commercial heats of the titanium-modified alloy to substantiate the beneficial effect of titanium and optimize the properties with regard to fabrication variables and preirradiation microstructures.

In some cases the alloy as received from the vendor contained a second phase, which has been identified as ferrite and which results from nonequilibrium freezing of the ingot. In all instances, however, this second phase could be dissolved by a high-temperature (1200°C) anneal to produce a fully austenitic structure. No other problems have been encountered in fabrication of the titanium-modified alloy.

In the unirradiated condition the elevated-temperature tensile ductilities of the modified alloy were significantly higher than those exhibited by a standard type 304 stainless steel having equivalent carbon content and grain size. Yield and ultimate tensile strengths were approximately the same. Creep strength of the modified alloy at 740°C, in terms of both rupture life and minimum creep rate, was as much as 5 to 10 times higher than those of standard type 304 having equivalent pretest heat treatment. Creep-rupture fractures of the modified alloy were a mixture of transgranular and intergranular, compared to the completely intergranular fracture that occurs in the unmodified alloy.

The Oak Ridge Research Reactor was used to determine the effects of neutron irradiation upon the properties of the modified alloy. Tensile ductility was reduced by irradiation; however, in all cases studied it was still much improved when compared to standard type 304 or 304L stainless steel irradiated under similar conditions. Optimum postirradiation ductility in both tensile and creep-rupture tests was achieved when a preirradiation anneal of 1 hr at 900 to 925°C was used. Figure 21.1 shows the postirradiation creep-rupture ductility of both the standard and modified alloys as a function of calculated helium concentration. Differences in ductility cannot be attributed to grain size alone, since the ductility of the standard alloy having a comparable grain size falls far short of that exhibited by the modified alloy.

Results of an investigation to determine the effects of preirradiation annealing temperature upon the modified alloys are summarized in Table 21.1.

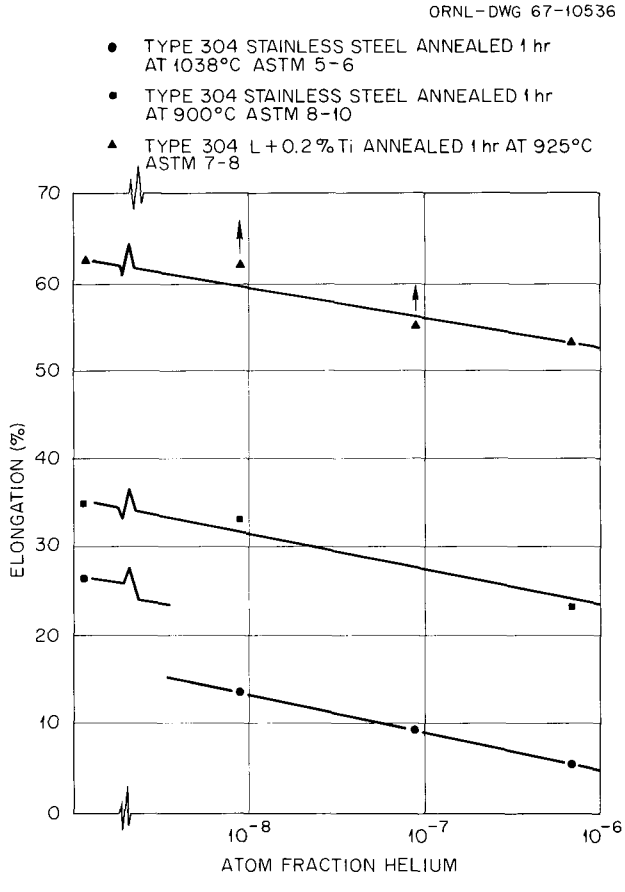

Fig. 21.1. Effect of Helium on the Stress-Rupture Ductility of Type 304 and Modified 304L Stainless Steel Irradiated at 50°C, Tested at 704°C and 15,000 psi. Arrows on points indicate that the ductility plotted was reached without failure of the specimen.

[2]W. R. Martin and J. R. Weir, "Solutions to the Problems of High-Temperature Irradiation Embrittlement." Paper presented at the Sixty-Ninth Annual Meeting ASTM, Atlantic City, N.J., June 27, 1966, to be published in the proceedings.

Table 21.1. Effect of Preirradiation Annealing Temperature, as Reflected by the Grain Size, on Postirradiation Creep of Type 304 and Modified Stainless Steels

Material[a]	ASTM Grain Size No.	Temperature (°C)		Stress (psi)	Creep Rate (%/hr)	Rupture Life (hr)	Elongation (%)	Reduction in Area (%)	Atom Fraction He (calculated)
		Irradiation	Test						
304 SS	5–6	650	650	30,000	0.50	12.0	8.4	9.1	1×10^{-6}
				25,000	0.139	24.4	4.9	4.2	
				20,750	0.014	123.4	2.9	4.0	
				17,000	0.006	314.4	3.7	0.4	
				15,000	0.0018	956.9	2.8	0.2	
304 SS	5–6	650	704	20,000	0.85	7	8.5	1.8	2×10^{-6}
				15,000	0.098	67	8.5	0.7	
M304 SS	5–6	650	704	15,000	0.12	138.1	26.6	21.1	10×10^{-6}
M304L SS	4–5	650	704	20,000	2.3	10.3	29.5	28.5	10×10^{-6}
M304L SS	6	650	704	15,000	0.26	77.2	25.8	21.5	2×10^{-6}
				10,000	0.00066	>1260	>12	>13	
M304L SS	7–8	650	704	15,000	0.68	31.2	27.5	26.9	10×10^{-6}
				10,000	0.097	249.8	40.0	15.1	
M304L SS	7–8	800	704	15,000	0.61	37.0	38.1	30.4	10×10^{-6}
				10,000	0.066	350.7	46.7	30.0	
M304L SS	8	650	704	15,000	0.63	42.5	38.7	41.2	2×10^{-6}
				10,000	0.083	327.7	45.4	14.0	
M304L SS	9	650	704	15,000	0.38	58.3	30.1	25.5	2×10^{-6}
				12,500	0.17	144.8	32.5	23.3	
				10,000	0.0036	636.4	31.6	31.2	

[a]M denotes modified alloy.

The ductility of irradiated type 304 stainless steel decreases to very low values when the rupture life is extended beyond 100 hr. In comparison, the ductility of the modified alloy remains at a relatively high level for rupture lives up to 1000 hr. In addition these data suggest that for those reactor applications in which the somewhat lower creep strength of the fine-grain material cannot be tolerated, the use of a coarse grain size will give improved strength while maintaining adequate ductility.

EFFECT OF CYCLOTRON-INJECTED HELIUM ON THE MECHANICAL PROPERTIES OF STAINLESS STEEL[3]

R. T. King J. R. Weir, Jr.

Direct experimental evidence was obtained to support the hypothesis that trace amounts of helium cause a severe nonrecoverable decrease in the high-temperature ductility of type 304 stainless steel. Previously published indirect evidence indicated that helium produced by (n,α) transmutations in neutron-irradiated stainless steel was responsible for observed ductility losses in tension and creep tests.

Helium was injected into flat tensile samples by scanning the samples through a beam of cyclotron-accelerated α-particles whose energy was periodically degraded to produce a uniform deposit of helium throughout the samples. Samples of type 304 stainless steel containing 10^{-7} and 10^{-6} atom fraction of cyclotron-injected helium suffered losses of tensile ductility from 700 to 900°C, accompanied by intergranular fracture. Samples ir-

[3]Abstracted from paper to be presented at the AIME Meeting, October 1967, Cleveland.

radiated in neutron fluxes to produce the same helium content by transmutations behaved similarly. The other tensile properties of this material remained substantially unchanged regardless of the source of the helium. Bombardment of samples with alpha particles having sufficient energy to pass completely through the samples did not cause the drastic ductility loss, demonstrating that it is associated with the presence of helium.

In contrast, a type 304L stainless steel containing a 0.2% Ti addition was not affected as severely as the type 304 stainless steel by cyclotron-injected helium nor by transmutation-produced helium. The beneficial effect of titanium may be related to its role in reducing the tendency of stainless steel to fracture intergranularly. An alternate explanation is based on the observation that titanium alters the precipitate structure of stainless steel. The precipitate may trap helium and prevent the accumulation of large concentrations of helium at grain boundaries, where gas bubbles have been observed to form.

MEASUREMENT OF THE NUCLEAR HEATING RATE IN EBR-II

E. E. Bloom A. F. Zulliger[4]
J. R. Weir, Jr.

An experiment has been designed and constructed to measure the axial distribution of nuclear heating in nonfissionable materials in Row 2 and Row 7 positions of the EBR-II. These positions are representative of those to be used in ORNL materials irradiations. Nuclear heat susceptors will be placed in the central pin of Mark B-7 subassemblies. The gas composition, gap size, and susceptor material were selected on the basis of heat transfer calculations performed on an IBM system 360 computer. The code for determining susceptor temperature includes radial heat transfer from the susceptor by conduction and radiation and accounts for axial conduction losses through the specimen and support pins. Thermal conductivity, susceptor dimensions, and emissivity values as a function of temperature are incorporated into the program. Susceptors were designed on the basis of published heat rates to produce susceptor center-line temperatures between 500 and 800°C. Melt wires having melting points over a range extending both above and below the design temperature to cover the range of ±50% of the published heating rate were placed in each susceptor. The experiment will consist in bringing the reactor to the desired power level and irradiating for approximately 24 hr. Post-irradiation examination will place the actual operating temperature between a lower and an upper value (determined by which melt wires have melted). Then calculations based on temperature and susceptor dimensions will give the nuclear heating rate to ±10%. The results of this experiment will allow mechanical properties test specimens to be irradiated within ±25°C of the desired temperature when a susceptor of similar design is used.

[4]General Engineering and Construction Division.

22. Nondestructive Test Development

R. W. McClung

This program is designed to develop new and improved methods of examining reactor materials and components. To achieve this we study the pertinent physical phenomena, develop instrumentation and other equipment, devise application techniques, and design and fabricate reference standards. Among the subjects being actively pursued are electromagnetics (with major emphasis on eddy currents), ultrasonics, and penetrating radiation.

ELECTROMAGNETIC TEST METHODS

C. V. Dodd W. E. Deeds[1]

We have continued both analytical and empirical research concerning electromagnetic phenomena. As a part of the program, we are studying the mathematical determination of the vector potential of a coil as a function of coil dimensions, frequency, specimen electrical conductivity, and coil-to-specimen spacing (lift-off). We now have two different techniques to calculate the vector potential: (1) the relaxation technique, which is very versatile and can be applied to almost any problem; and (2) a closed-form solution, which has the potential of being very accurate. The closed-form solution has been derived for only two general cases: (1) the case of a coil above one metal clad on another, and (2) the case of a coil encircling a rod with one metal clad on another. Once the vector potential has been determined, any physically observable electromagnetic induction phenomenon can be calculated from it. We calculated the vector potential of a coil above a conducting plane for two conditions (with and without a ferrite cup surrounding the coil) to study the effect of ferrite toward shaping the electromagnetic field or vector potential. Since the eddy-current density is proportional to the vector potential in a conductor, the contours in Fig. 22.1 represent contours of constant eddy-current flow in the conductor with and without the use of the ferrite cup. The response to actual defects can be related to the current intensity.

Many induction problems other than eddy-current testing can be calculated from the vector potential solutions. For example, electromagnetic forces may be calculated, as described in one of our recent reports,[2] an abstract for which appears below.

Relaxation averaging formulae are derived for magnetic induction problems involving axially symmetric fields with sinusoidal or pulsed time dependence in media that may be linear or nonlinear, homogeneous or inhomogeneous. Solutions have been obtained from a high-speed digital computer for time-harmonic fields in linear inhomogeneous media. From these solutions, the electromagnetic forces are calculated and compared with experimental measurements. The computed and measured values agreed quite well, and most of the discrepancy can be explained by the fact that the permeability of the ferrite used in the measurements was different from that assumed in the calculations.

A paper was prepared and presented describing the application of the analytical solution to the design of eddy-current tests.[3] The abstract is presented below:

An analytical solution of eddy-current coil problems was sought in order to improve eddy-current tests. A

[1]Consultant from the University of Tennessee.

[2]C. V. Dodd and W. E. Deeds, *Electromagnetic Forces in Conductors*, ORNL-TM-1835 (May 1967).

[3]C. V. Dodd and W. E. Deeds, "Computer Design of Eddy-Current Tests," to be published in the proceedings of the Fifth International Conference on Nondestructive Testing, Montreal, Canada, May 21–26, 1967.

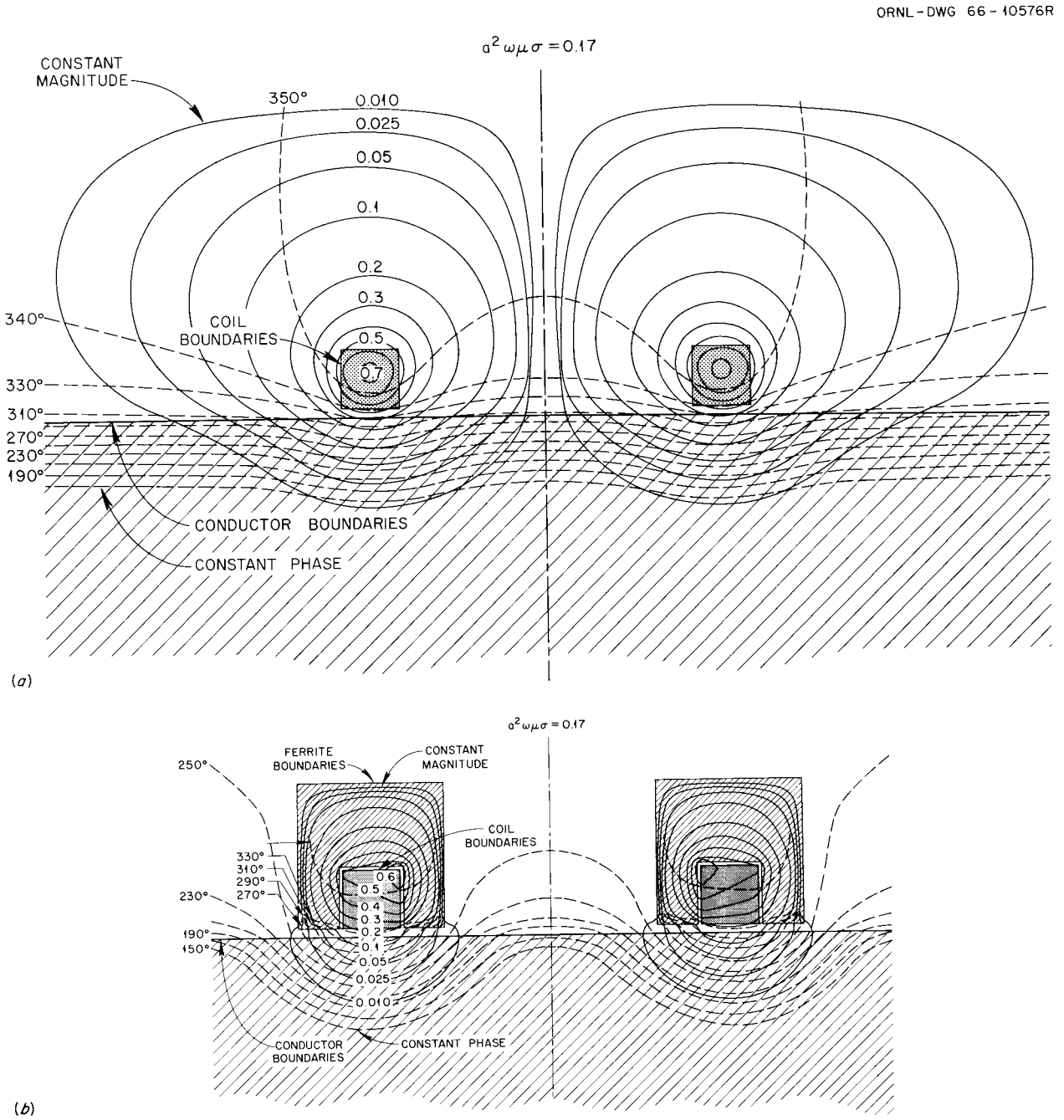

Fig. 22.1. Vector Potential Contours of a Coil Above the Plane Surface of a Conductor. (*a*) Without and (*b*) with a ferrite cup over the coil.

method was developed for analyzing the physical properties of an eddy-current coil with the help of a large digital computer. These physical properties include eddy-current coil impedance, actual eddy-current distribution in the sample (and hence the sensitivity to small defects), and the induced voltages in various pickup coils. The technique has been applied to several specific cases including a coil with and without a ferrite cup above a conducting plane and a coil encircling a rod. This technique gives both further physical insight into and actual numerical results of eddy-current tests.

We continued development of a portable phase-sensitive eddy-current instrument and improved the temperature stability of the portable instrument and coils independently over a temperature range from −17 to +55°C. At 50 kc the temperature drift corresponds to a conductivity change of 0.3%/°C. The lift-off compensation circuits in the instrument were also improved. At 500 kc the apparent conductivity change due to a variation in lift-off of 0 to 0.010 in. of a 0.200-in.-diam coil is ±0.5%.

With the excellent lift-off compensation we have been able to use smaller coils and have constructed coils as small as 0.040 in. in diameter. These coils have a greater sensitivity to small defects and allow us to inspect small parts with less effect of curvature and proximity of the specimen edge.

We designed a series of new coolant-channel spacing probes for use in hot cells. Sturdier probes were needed to allow mechanical handling, and the longer lengths of cable required some electronic circuit modifications. We built a mold and cast the probes of both fiber glass and a flexible epoxy covered with Teflon tape. The epoxy probes are more flexible than fiber glass, but the Teflon tears on a sharp object. The fiber glass probe, being more rigid than the epoxy probe, has a much harder finish that can be scratched but will not tear.

We modified the bridge circuit of the Dermitron so that one side of the coil is at ground and then used a single shielded cable to drive the coil. This feature reduced the capacitance between the "hot" lead and ground and also reduced the error due to capacitance change as the probe was inserted into the coolant channel.

ULTRASONIC TEST METHODS

K. V. Cook
H. L. Whaley
L. S. Snyders[4]
R. W. McClung

We have continued our studies on the behavior of ultrasound in thin sections; the principal effort was an attempt to correlate ultrasonic response from electric-discharge-machined (EDM) notches, drilled holes, and flat-bottomed holes of various sizes. We have been working with two sheet materials, 1100 aluminum and type 304 stainless steel, for the initial studies. However, we intend to also correlate the ultrasonic response for similar discontinuities in small-diameter tubing. Figure 22.2 shows typical data and is a collection of curves relating the incident angle to the number of decibels insertion required to achieve constant amplitude for a 0.080-in.-thick sheet of aluminum. These curves were generated by use of a 5-Mc lithium sulfate transducer and a $\frac{1}{4}$-in. cone collimator.

We are continuing to work on the problems encountered in tubing inspection. A major problem is the establishment of realistic ultrasonic notch standards for calibration. Since EDM appears to be a reliable method for making both inner- and outer-surface notches, we are continuing our fabrication studies.[5] A paper on this subject has been published.[6] An abstract is given below.

Electro-discharge machining was investigated for the preparation of artificial defects in reference materials of plate, sheet, bar, and tubing configurations. Difficulties were overcome in machining these reference discontinuities by developing reproducible methods of establishing a start-of-cut position and by preshaping the cutting tool. Techniques were also developed for measuring depths of notches, using replication methods and/or subsequent differential focusing techniques with a microscope. Longitudinal notches were machined within ±0.0001 in. of nominal depths and have been placed in tubing with an inner diameter as small as 0.065 in. Circumferential notches were machined within ±10% of nominal depths and have been placed in tubing with an inner diameter of 0.380 in.

Since this paper was written, we have increased our capabilities for machining both longitudinal and transverse notches in small-diameter tubing. Longitudinal notches can now be placed inside tubing with inner diameters as small as 0.050 in. (depending on the required notch depth). However, our precision and reproducibility for these smallest notches are slightly decreased. Transverse notches can now be machined inside 0.210-in.-ID tubing, and we feel that the limit will be approximately 0.180 in.

We prepared a paper[7] summarizing our work with the optical system described previously.[5] The abstract is presented below.

[4]Visitor from South Africa.

[5]K. V. Cook, *Metals and Ceramics Div. Ann. Progr. Rept. June 30, 1966*, ORNL-3970, pp. 120–22.

[6]K. V. Cook and R. W. McClung, "Electro-Discharge Machined Reference Discontinuities," *Mater. Eval.* 25(2), 36–40 (February 1967).

[7]H. L. Whaley, K. V. Cook, R. W. McClung, and L. S. Snyders, "Optical Methods for Studying Ultrasonic Propagation in Transparent Media," to be published in the proceedings of the Fifth International Conference on Nondestructive Testing, Montreal, Canada, May 21–26, 1967.

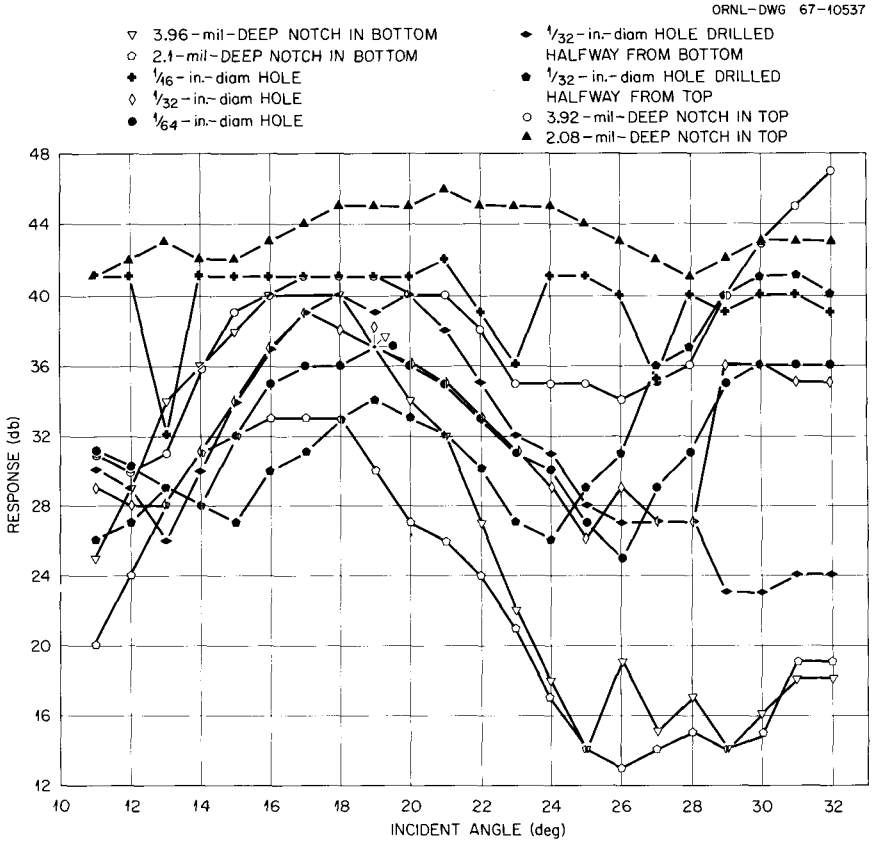

Fig. 22.2. Response from Various Reference Discontinuities in 0.080-in.-Thick Aluminum Sheet as a Function of Incident Angle of Ultrasound.

The schlieren and photoelastic methods for viewing continuous and pulsed ultrasonic waves propagating in transparent media were investigated. Limitations, possible applications, and results of the investigation of each system are discussed. Emphasis is placed on equipment improvements for the development of optimum systems for nondestructive testing applications.

A more detailed report was prepared on experimental work using photoelastic phenomena for observing pulses of ultrasound in transparent solids.[8] Quantitative measurements of attenuation were made using a unique specimen containing static bending stresses. Optical superimposition of the stresses due to the ultrasound introduced a change in the photoelastic image, which was photographed and measured with a microdensitometer. Good experimental comparison was found with miniature strain gages.

[8]L. S. Snyders, *The Photoelastic Observation of Ultrasonic Waves in a Transparent Plate*, ORNL-TM-1671 (January 1967).

Extensive technical editing was provided for the translation of a lengthy German dissertation,[9] which discussed the ultrasonic detection and significance of flaws in such steel components as turbine rotors, small forgings, tubes, and bonded joints. The translation was performed at the request of the Fuels and Materials Development Branch, Division of Reactor Development and Technology, AEC.

PENETRATING RADIATION

R. W. McClung R. R. Wamorkar[10]

In a continuation of development of low-voltage radiographic techniques, we made quantitative

[9]H. Krautwedel, S. Peterson, and R. W. McClung, translators and editors, *The Results of Ultrasonic Testing in the Practice of Machine and Boiler Construction Concerning the Material and Strength Properties of Components*, by Hans-Juergen Meyer, ORNL-tr-1369 (May 1967).

[10]Visitors from the Atomic Energy Establishment, Trombay, Bombay, India.

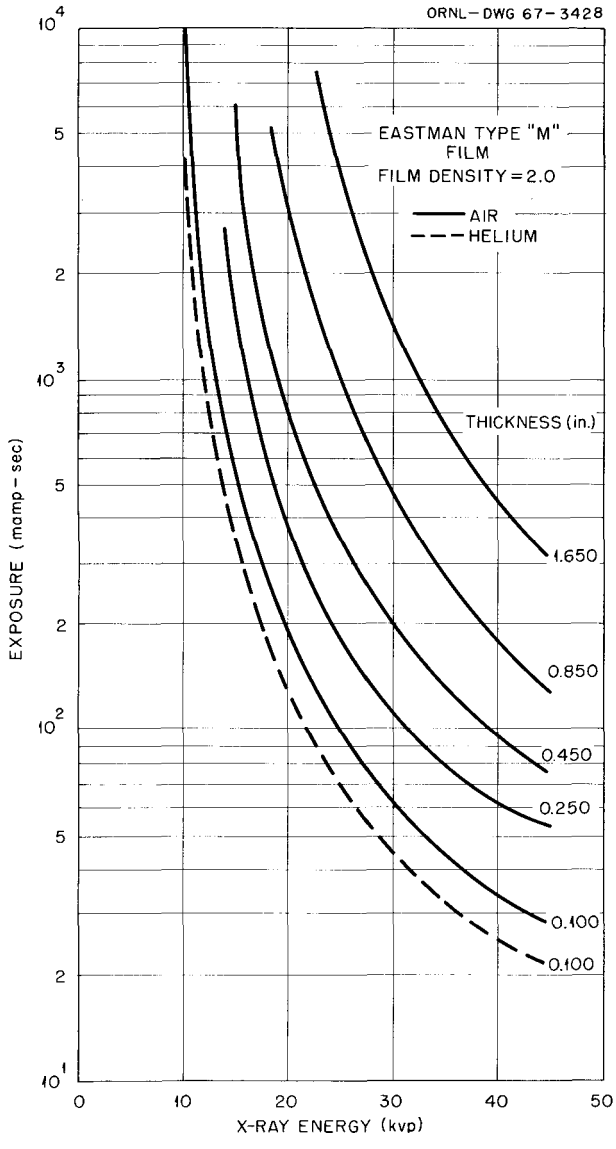

Fig. 22.3. Exposure Chart for Radiography of Various Thicknesses of Graphite with Air and Helium.

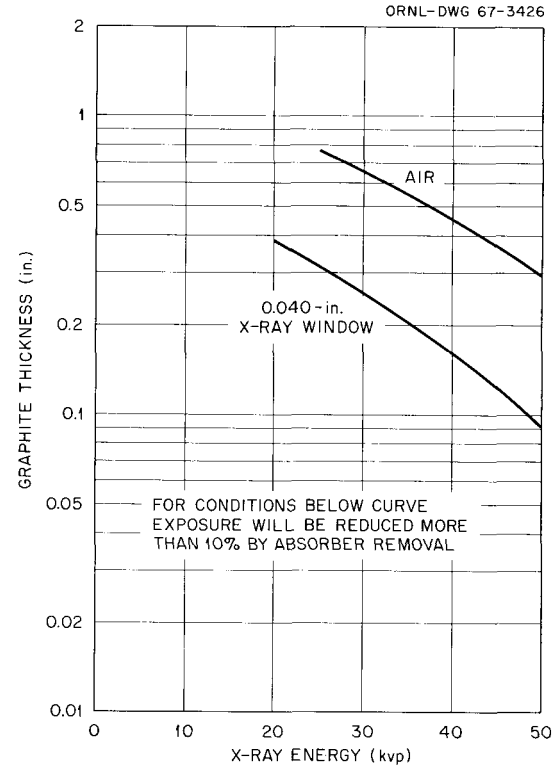

Fig. 22.4. Conditions Under Which Absorber Removal Will Effect 10% Change in Exposure Requirements for Radiography of Graphite.

studies for the radiography of thin sections of graphite. A step wedge with thicknesses from 0.100 to 1.650 in. was radiographed with energies from 10 to 45 kv peak at exposures to achieve a wide range of film densities for each step thickness. The exposures were made with intervening atmospheres of both helium and air. The data allowed plotting of comprehensive exposure charts and calculation of optimum operating conditions. Figure 22.3 relates x-ray energy (kv peak) to exposure factor (ma-sec) for various thicknesses of graphite and both helium and air atmospheres. Figure 22.4 displays the conditions under which a 10% change in exposure requirement will be achieved by removal of the specified absorber. A paper[11] describing the studies and applications has been prepared.

We are quantitatively studying radiographic sensitivity as various parameters, such as x-ray energy, specimen thickness, and thickness of lead intensifying screens, are varied. The materials being examined are stainless steel, aluminum, and copper. Special penetrameters for the steel and aluminum were prepared to allow evaluation of small changes in sensitivity. The penetrameters are thin sheets containing many small drilled holes whose diameter and depth vary in small increments with position in an ordered array. For copper we are using small-diameter wire to indicate image quality. Preliminary results indicate that thin lead screens are beneficial at energies as low as 70 kv peak. This contrasts with previously accepted values of approximately 120 kv peak.

[11] R. W. McClung, "Low Voltage Radiography and Microradiography of Graphite," presented at Symposium on Nondestructive Testing of Graphite, ASTM Annual Meeting, Boston, Mass., June 27, 1967.

23. Development and Testing of Sol-Gel-Derived $(U,Pu)O_2$ Fuel

A. L. Lotts

The sol-gel process is a versatile process, the end product of which can be obtained in a variety of forms suitable for fabrication into fuel rods by alternate techniques. In the previous work with thoria-base fuels, we emphasized the vibratory compaction of dense angular particles from tray drying and calcining. The sol-gel process will also produce dense microspheres suitable for vibratory compaction, a concentrated sol suitable for extrusion, or a powder for standard pellet production. A development program to investigate the economic and performance potential of each of these methods of fabrication for $(U,Pu)O_2$ fuels for fast breeder reactor applications was started late in the year.

We established a critical path schedule for the program, which includes process development, property determinations, irradiation testing, and economic evaluation. Much of our initial effort has been to complement our existing plutonium equipment with additional equipment to accomplish the work. Fabrication and irradiation of the first capsules commenced.

DEVELOPMENT OF FABRICATION PROCESSES

A. R. Olsen

Our development program on the fabrication of sol-gel derived $(U,Pu)O_2$ fuels is based on our extensive experience with sol-gel thoria-base fuels reported previously[1-3] and in Chap. 36 of this report.

[1] A. L. Lotts, R. B. Fitts, J. D. Sease, and A. R. Olsen, *Metals and Ceramics Div. Ann. Progr. Rept. June 30, 1966*, ORNL-3970, pp. 218–20.

[2] M. J. Bannister, H. Beutler, and J. W. Prados, *Metals and Ceramics Div. Ann. Progr. Rept. June 30, 1966*, ORNL-3970, pp. 220–22.

[3] R. G. Wymer and A. L. Lotts (compilers), *Status and Progress Report for Thorium Fuel Cycle Development Dec. 31, 1966* (in preparation).

Extrusion Studies

J. G. Stradley R. L. Hamner
J. M. Robbins

Fitts and Sease[1] have shown that thoria shapes can be extruded from sol-derived pastes called "clays," which are normally prepared by concentrating thoria sols to about 12 *M* and adding fractions of partially calcined and fully calcined sol-gel powders to control shrinkage, minimize cracking, and control final density. We have extended this work, using the same techniques, to a study of the feasibility of extruding sol-derived urania. We hope to apply the technology developed in these studies to the extrusion of UO_2-PuO_2 sol-derived materials.

Unlike nitrate-prepared thoria sols, nitrate-prepared urania sols of low molarity (0.7 *M*) could not be concentrated by evaporation of liquid to the required 12 *M* without gelling. However, they were concentrated satisfactorily by freezing with liquid nitrogen and evaporating the moisture from the solid state. The fine sol-gel powders (−325 mesh) that we add to the clays to adjust properties were prepared without grinding by completely freeze drying the sols.

We had very little difficulty preparing clays from chloride-prepared sols, which do not gel during concentration as readily as nitrate-prepared sols. However, extrusions made with this material retained 130 ppm Cl after our usual sintering treatment, heating in hydrogen for 1 hr at 1600°C. Presintering these extrusions in steam–argon–4% hydrogen at 1000°C for 1 hr reduced the chlorine content to less than 1 ppm.

Using a 30 wt % powder addition, we obtained bulk densities of 68 and 72% of theoretical on ex-

trusions from the nitrate- and chloride-prepared clays, respectively.

Pelletizing

J. G. Stradley J. M. Robbins
R. L. Hamner

We started developing a process for pelletizing sol-gel-derived UO_2 powders. The powders were obtained from both nitrate and chloride sols by vacuum drying and grinding and from nitrate sols by freeze drying. Precalcined (400°C) and uncalcined powders were cold pressed and sintered under a variety of conditions. Although this development is in the early stages, we have derived the following tentative conclusions: (1) powders from more highly concentrated sols (9.75 *M*) yield pellets of higher green densities; (2) steam added to an Ar–4% H_2 atmosphere during heating to 1000°C appears to increase the final density of the sol-gel urania pellets; and (3) presintering in the steam–Ar–4% H_2 atmosphere followed by final sintering at 1600°C in hydrogen produces sol-gel urania pellets of the same density regardless of the prior fabrication history.

Sphere-Pac Vibratory Compaction

A. R. Olsen R. B. Fitts

Development of a process to produce high-density $(U,Pu)O_2$ microspheres from the sol-gel process is the responsibility of the Chemical Technology Division. This development has been reported[3] and has reached the stage where experimental quantities are available for product characterization and irradiation testing. Details of the development of the low-energy vibratory compaction (Sphere-Pac) fabrication technique for fabricating fuel rods from these microspheres is reported in Chap. 36 of this report.

IRRADIATION TESTING

A. R. Olsen R. B. Fitts

The in-reactor performance of a nuclear fuel is strongly influenced by its properties as established by the fuel preparation and fabrication technique. We have initiated a program to determine the irradiation performance of the sol-gel-derived $(U,Pu)O_2$ fuels as a function of sol-gel process variables and fabrication techniques. Initial screening tests are being conducted in the Engineering Test Reactor using the capsule shown in Fig. 23.1. This capsule permits the testing of four $\frac{1}{4}$-in.-OD fuel elements at high cladding-surface temperature with minimum restraint on the cladding. The four elements operate with a variety of heat generation rates because of the flux gradient in the reactor. The bottom element operates at an average power approximately half that in the center elements. The test elements are held together by spacers, which also center them in the $\frac{1}{2}$-in.-OD capsule. The fuel cladding is $\frac{1}{4}$-in.-OD × 0.010-in.-wall type 304 stainless steel.

Sol-gel microsphere fuel fabricated by the Sphere-Pac technique is presently being irradiation tested. Other sol-gel-derived fuel forms will be tested as they reach an appropriate stage of development. We have fabricated and are testing fuel elements containing microspheres of $(^{235}U_{0.8}Pu_{0.2})O_2$, and $(^{238}U_{0.85}Pu_{0.15})O_2$. Twenty rods were loaded for these tests by the Sphere-Pac technique to 84 ± 0.5% of theoretical; the variation arises from variation in the density of the microspheres. Details of the fuel preparation and rod fabrication are reported elsewhere.[4] The first five capsules in this irradiation test series have been fabricated, and two have been irradiated.

The first two capsules irradiated, ORNL 43-99 and ORNL 43-100, contained two elements each of $(^{235}U_{0.8}Pu_{0.2})O_2$ fuel at 76% smear density (weight of fuel divided by volume as determined from the inside diameter of the tube) and two of $(Th_{0.95}Pu_{0.05})O_2$ fuel (also Sphere-Pac) at 84% smear density. These tests were intended to operate at a calculated maximum cladding surface temperature of 475°C and linear heat rating of 650 w/cm. These tests were to be compared with the results of fast reactor irradiations of the same $(U,Pu)O_2$ fuels to be conducted by Argonne National Laboratory. Both capsules attained an estimated burnup of approximately 10,000 Mwd/tonne of uranium and plutonium (1% fissions per initial metal atom) during a continuous 16-day reactor full-power operating period before a failure in capsule 43-99 necessitated their

[4] F. G. Kitts, R. B. Fitts, and A. R. Olsen, "Sol-Gel Urania-Plutonia Microsphere Preparation and Fabrication Into Fuel Rods," to be presented at AIME 1967 Nuclear Metallurgy Symposium on Plutonium Fuels Technology and published in a volume of the *Nuclear Metallurgy Series*.

removal. The failure occurred about 1.5 hr after a return to full power operation following a short reactor shutdown. The capsule failure was detected when a hole in the outer Zircaloy-2 capsule released part of the NaK heat transfer medium. A 3-in. length of cladding melted on the highest rated $(U,Pu)O_2$ fueled rod in the region of the capsule failure. The other three fuel rods in the capsule were intact.

Capsule 43-100 did not evidence any failure in-reactor. The predisassembly gamma scan of this capsule during postirradiation examination showed no change in the fuel locations or lengths for any of the fuel rods but did show an anomalous activity peak approximately 0.5 in. long in the region of the bottom fuel rod end plug. After removal of the NaK and disassembly of this capsule, failures in both the $(U,Pu)O_2$ fuel rods were evident. A hole in the cladding, approximately $\frac{1}{2}$ in. above the top of the original fuel column, was found in the rod with the highest heat rating, and the bottom end of the bottom rod was melted off. Preliminary metallographic examinations of the $(U,Pu)O_2$ fuel from both the intact rod and the remaining portion of the hottest rod from ORNL 43-99 show microstructures consistent with operation with central fuel melting.

The cause of these failures is not yet known. The most likely causes are overpowering (i.e., operation at much higher heat ratings than intended), the development of localized bubbles in the NaK after the short reactor shutdown, or a combination of both conditions. The results of the burnup analysis, not yet available, will establish the actual operational heat ratings and thus permit a better evaluation.

The operating conditions for these tests were calculated by various techniques, which yield widely varying results. This is due principally to the high absorption cross section of these fuels relative to standard low-enrichment UO_2 fuels and the resonance absorption cross sections for plutonium isotopes for neutron energies slightly above thermal. These two factors render most of the standard calculational techniques quite inaccurate when applied to plutonium-bearing fuels. We have employed a manual numerical integration of the fission rate as a function of neutron energy with reasonable results for these fuels. This technique, however, is subject to several poor assumptions. We are now exploring the use of computer codes based on transport theory to calculate the fission rate as a function of fuel radius for a multigroup neutron-energy spec-

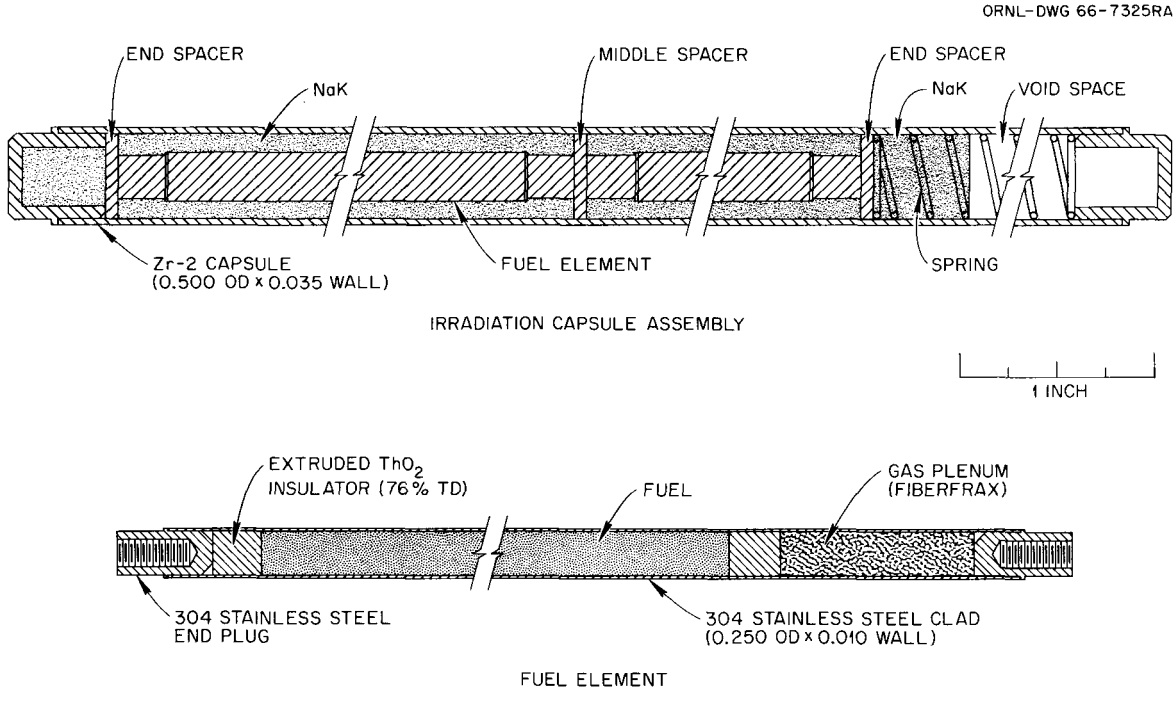

Fig. 23.1. Capsule for Irradiation Tests.

trum. The results of these calculations will be compared with experimental results to verify the reliability of this approach.

The remaining three capsules fabricated this year are scheduled for insertion in the ETR in July. Capsule ORNL 43-103 contains three test elements of low-density (87.7%) UO_2 microspheres at 73.5% smear density and a UO_2 pellet element for an internal standard. It will be operated at 500 w/cm calculated maximum linear heat rating with a cladding-surface temperature of 400°C to a 2% fissions per initial metal atom burnup. This test will compare the performance of low-density microspheres with standard UO_2 pellets and, in conjunction with later tests, determine the effect of microsphere density on the performance of Sphere-Pac beds.

The other two capsules, ORNL 43-112 and ORNL 43-113, each contain three test elements of (^{238}U–15% Pu)O_2 at 80.5% smear density and one of the low-density UO_2 microsphere rods described above. These tests will also operate at 500 w/cm and 400°C surface temperature. They are scheduled to attain burnups of 2 and 10% fissions per initial metal atom respectively. These tests will yield information on the effect of plutonium concentration, extended burnup, and various heat ratings on the performance of these fuels.

24. Sintered Aluminum Products Development

W. R. Martin

Sintered aluminum products (SAP) are powder-metallurgy-produced alloys that consist of aluminum oxide dispersed within an aluminum matrix. These alloys have a high strength-to-weight ratio, and this beneficial effect is stable up to temperatures approaching the melting point of aluminum.

Although this alloy is attractive for applications in several reactor systems, commercial SAP materials lack the reproducibility of properties needed for many nuclear components. Our program was initiated to investigate the problems and parameters related to primary billet fabrication of SAP for HWOCR pressure tubes and sheaths for fuel rods. General process steps involve feed-powder characterization, dispersion preparation, and consolidation. We are attempting to optimize the conditions of each operation to arrive at a more reliable and consistent product, using the typical metallurgical tools for evaluation. Concurrent with the development of a suitable billet fabrication process, we have endeavored to develop suitable nondestructive techniques to aid in process evaluation.

POWDER PREPARATION

G. L. Copeland

Ball-milling was selected for dispersing the desired amount of oxide in the aluminum. The process was scaled up to the pilot plant stage, and parameters were determined for producing nominal 9% oxide flake.

The pilot plant mill is 16 in. long × 36 in. in diameter. We believe it to be representative of the longer mills used commercially for producing aluminum flake, since the critical dimension for milling action is the diameter. A linear increase in oxide content is observed as the mill diameter increases from 10 to 48 in. with constant milling conditions and times. The mill is ribbed and is filled to 33% of its volume with $\frac{1}{2}$-in.-diam hardened steel balls. Atomized aluminum powder charged into the mill amounts to 4% of the weight of the balls. For our pilot plant mill, we use 27 lb of −100 mesh aluminum. Mineral spirits equal to twice the weight of the aluminum powder is used as the milling vehicle. Stearic acid amounting to 3% of the weight of the aluminum powder is used as the lubricant. The mill rotates at the critical speed of 44 rpm and is water cooled to maintain a temperature of no greater than 40°C. Air is circulated through the mill to assure a normal air atmosphere during milling.

The oxide content is a linear function of milling time, at least up to 12% oxide. A series of ten batches run under essentially identical conditions for milling times of 20 hr indicated that the oxide content is reproducible within the precision of the measurement techniques. The mean and expected deviation for a 20-hr milling time are 8.70 ± 2.80% oxide by fast-neutron activation analysis and 8.22 ± 1.54% oxide by the gaseous HCl dissolution technique. The indicated deviation is based on 95% confidence that 95% of a normal distribution will be within this range.

The use of the steel mill and balls results in the inclusion of approximately 0.5% tramp iron in the flake product. Magnetic separation can remove it.

PROCESS SELECTION FOR POWDER CONSOLIDATION

M. M. Martin

The primary purpose of consolidation is to compact the SAP powder into a suitable billet for extrusion to a semifinished product with the aluminum oxide in a stable form of predictable morphology. The direct extrusion of powder is not practical,

since the bulk density is about 10% that of the extruded rod. We investigated several combinations of cold pressing, vacuum annealing, vacuum hot pressing, and vacuum fusion. On the basis of superior mechanical properties with minimum variability, we selected vacuum hot pressing for more detailed evaluation and scaleup for pilot production of nominal 9%–Al_2O_3 SAP billets. Our aim is to achieve a product that is equivalent to commercially available SAP-895, which contains approximately 10% oxide. Conditions that were or are currently being investigated are the temperature for vacuum annealing the powder, the density of the consolidated billets, permissible levels of iron, carbon, and hydrogen impurities, and the necessity of vacuum annealing the billets after consolidation.

Our work encompassed a series of 2-in.-diam SAP billets that were produced by six different processes (listed in Table 24.1) from commercially supplied Al–6 wt % Al_2O_3 flake powder. Vacuum hot pressing was done in graphite dies at a maximum pressure of 0.8 tsi. The procedure included holding the powder at 600°C for 2 hr and then pressing for 0.5 hr, all under vacuum. In vacuum fusion, cold pressed compacts were heated at 700°C for 15 min or 1 hr. The density of all billets immediately before extrusion was 70 to 80% of theoretical.

The billets were extruded at a reduction ratio of 30 through a shear die at 435°C to $\frac{3}{8}$-in.-diam × 40-in.-long rods and subsequently straightened by swaging at 450°C with a reduction ratio of 1.02. Data from tensile tests performed at 450°C and a low strain rate of 0.0002 min^{-1} are shown in Table 24.2.

Processes B and C produced material whose tensile strength depended significantly on specimen position. Oxide content and texture differences failed to account for the consistent decrease in strength along the rods. Although data were limited, material from processes E-2 and F-2 exhibited high oxide contents near the nose of the extrusions, and their strength variations behaved similarly to those from processes B and C. Elimination of the high-oxide areas from the evaluation yielded the tensile values presented in Table 24.2. In all processes, the uniform elongation was less than 2% at 450°C and the low strain rate. Process D appears to be the most attractive in the magnitude and uniformity of strength of its product; the product closely approximates the properties of SAP-895 at significantly lower oxide content.

The effects of secondary extrusion and initial billet density were examined in a series of 4-in.-diam compacts consolidated according to processes B and D. Process D billets, which were prepared from a new batch of commercial flake containing 5% Al_2O_3, extruded without difficulty through a shear die with a reduction ratio of 5.4, a billet temperature of 500°C, and a tooling temperature of 200°C. Process B billets were consolidated from material with 6% Al_2O_3 by vacuum annealing 17.5 hr at 600°C and then immediately transferring without cooling to the extrusion press preheat furnace. The billets were extruded similarly to those from

Table 24.1. Billet Consolidation Processes

Process	Powder Treatments			Billet Treatments	
	Vacuum Anneal[a]	Cold Pressing	Vacuum Hot Pressing[a]	Vacuum Anneal[a]	Vacuum Fusion[b]
A		used		$<10^{-2}$	
B			$<10^{-2}$	$<10^{-2}$	
C-1	$<10^{-4}$	used			
C-2	$<10^{-2}$	used			
D	$<10^{-4}$		$<10^{-2}$		
E-1		used			15 min
E-2		used			1 hr
F-2	$<10^{-2}$	used			1 hr

[a]At 600°C. If used, pressure is given in torrs.

[b]700°C for time indicated.

Table 24.2. Effect of Billet Consolidation Process on Oxide Content and Tensile Strength of Extruded Rod

Consolidation Process	Oxide Content[a] (wt %)	Ultimate Tensile Strength[b] (psi)	Expected Deviation[c] of Ultimate Tensile Strength	
			(psi)	(%)
		$\times 10^3$	$\times 10^3$	
A	7.7–9.6	9.4	±0.65	6.9
B	6.6	12.2 − 0.055*L*	±0.96	8.6
C-1	8.2–9.4	13.7 − 0.039*L*	±1.34	10.4
C-2	8.2–9.4	15.5 − 0.086*L*	±0.75	5.4
D	8.2	11.9	±0.82	6.9
E-1	8.5–11.5	11.9	*d*	*d*
E-2	8.5–11.5	11.5	*d*	*d*
F-2	10.1–14.3	10.9	*d*	*d*
SAP 895[e]	11.5	12.1	±0.77	6.4

[a]The range of values represents the maximum and minimum of at least four determinations along the rod length.

[b]If the strength varied significantly along the rod, it is given as a function of the distance *L* in inches from the nose of the extruded rod.

[c]Statistical tolerance limits.

[d]Insufficient tests to derive meaningful value.

[e]Values for commercial material.

Process D, except at a billet temperature of 600°C. These 1.75-in.-diam primary rounds were further processed the same as the 2-in.-diam rounds described above, except that swaging was not needed, and conical dies were used to simulate fabrication of tubing.

In tests performed at 450°C and 0.002-min^{-1} strain rate, ultimate tensile strength depended slightly on density but not on sample location along the length of the extrusions for both B and D processes. Billets of 80 and 98% of theoretical density extruded to rods with average ultimate strengths of 10,300 and 9830 psi respectively. The uniformity of strength within a particular extruded rod was excellent; variations were less than 5% of the average value. At this time, the available data are insufficient to evaluate variability among extrusions.

Primary extrusions of 4-in.-diam billets that had been consolidated according to process B procedures contained less than 5 ppm H and are equivalent to SAP-895. To achieve less than 10 ppm H with process D, the vacuum annealed flake and vacuum hot pressed billets must not be allowed to rehydrate during delays in processing. Storage in sealed plastic bags with desiccant accomplishes this end.

It is apparent that process B or D can be used to consolidate SAP powder flake into billets that yield tensile properties that vary less than 5% and are equal in magnitude to those of a commercial SAP alloy that contains significantly more oxide.

THERMOGRAVIMETRIC ANALYSIS OF ALUMINUM FLAKE

M. M. Martin

The primary purpose of vacuum annealing SAP flake is to convert the aluminum oxide hydrate to a stable form of Al_2O_3 and to remove volatile contaminants. To select optimum heat-treatment time and temperature, commercial Al–6% Al_2O_3 and our ball-milled powder containing 10% Al_2O_3 were subjected to vacuum thermogravimetric analysis. The study included exposure of degassed materials to moist air at 1 atm. Figure 24.1 depicts the differential weight loss curve that was determined for our 10% Al_2O_3 product upon heating to 600°C at a rate of 100°C/hr; the commercial flake behaved similarly.

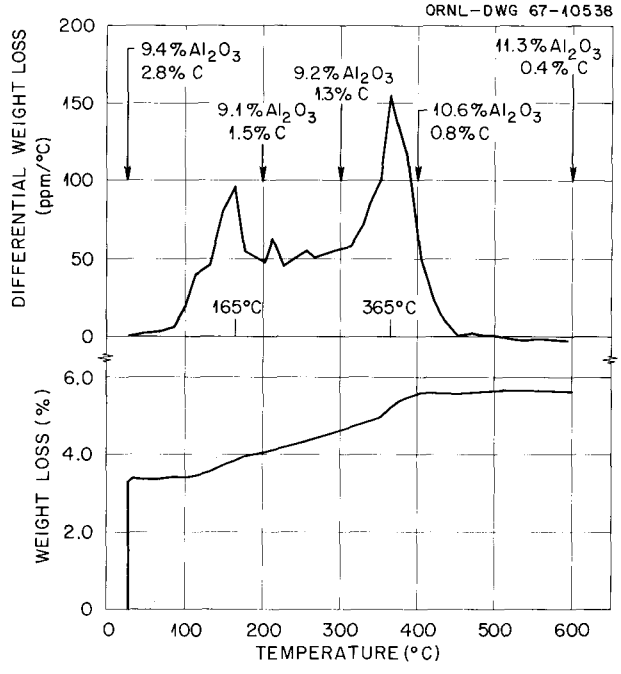

Fig. 24.1. Effect of Temperature on Degassing Experimental SAP Flake at Approximately 5×10^{-4} torr. The oxide and carbon contents were determined at the stages indicated.

Prior to heating, the analytical system was evacuated to slightly less than 10^{-3} torr. The reduced pressure permitted approximately 60% of the total weight loss of 5.6% to occur during the pumpdown at room temperature.

In Fig. 24.1 the peak shown at about 165°C results primarily from the release of loosely attached water and carbonaceous materials. Approximately 50% of the carbon is released at this temperature. The aluminum hydrate decomposes around 365°C, although some volatile hydrocarbons are still being released during this period of rising temperature. The temperature must be raised to 600°C to reduce the carbon level to less than 0.5%. The stable forms of aluminum oxide on powder heated to 600°C were identified as χ-Al_2O_3 and η-Al_2O_3.

When exposed to 11°F-dewpoint air, the degassed material gains weight at the rate of 18 ppm/min. With further exposure, the rate of water adsorption decreases exponentially to about 0.5 ppm/min at the end of 120 hr. The material loses approximately half of this weight gain upon reheating to 600°C. Heating to above the melting point did not produce an additional weight change.

Therefore, we expect that heat treatment of powder at 600°C is required to remove volatile hydrocarbons to levels less than 0.5% C and that rehydration of SAP flake produces a more stable hydrate and must be avoided if alloys are to be made with low hydrogen contents.

FRACTURE CHARACTERISTICS OF SAP

D. G. Harman T. A. Nolan[1]

A unique fractographic analysis technique was developed to study the initiation and propagation of the high-temperature fracture of SAP-type alloys. The formation of voids at the Al_2O_3 sites early in the high-temperature tensile test was verified, and their growth throughout the fracture process was studied.

The study involves the fractographic analysis of low-temperature fractures of SAP specimens that had been prestrained various amounts at elevated temperature. This technique is feasible because of the significant difference in appearance of surfaces formed at the two temperatures.

Figure 24.2 shows a fractograph of a specimen that was tested and fractured at 450°C as well as of specimens prestrained 0.2, 1.0, and 1.6% at 450°C and then pulled to fracture at −200°C. These electron micrographs show fracture cavities ranging from 2 to 5 μ in diameter, with their size increasing with increasing strain at 450°C. The larger features are the areas that had separated at the higher temperature, and they are surrounded by the fine-scale −200°C fracture features.

We also reported[2] the results from the examination of fracture surfaces of XAP-001 dispersion-hardened aluminum in the electron microscope using two-stage replication. The fracture surfaces were obtained from rod tensile specimens tested from −200 to 450°C or creep tested at 450°C. Three modes of ductile fracture are described and identified by fractography. High-temperature fractures were initiated at single oxide particles or groups of particles. Banding and stringering of oxide particles seriously affected the fracture process.

---

[1] Physics Department, Technical Division, ORGDP.

[2] D. G. Harman, *Mechanical Properties of Al-Al_2O_3 Alloys: Testing Procedures and Evaluation of Data*, ORNL-TM-1802 (May 1967).

PHOTO 89199

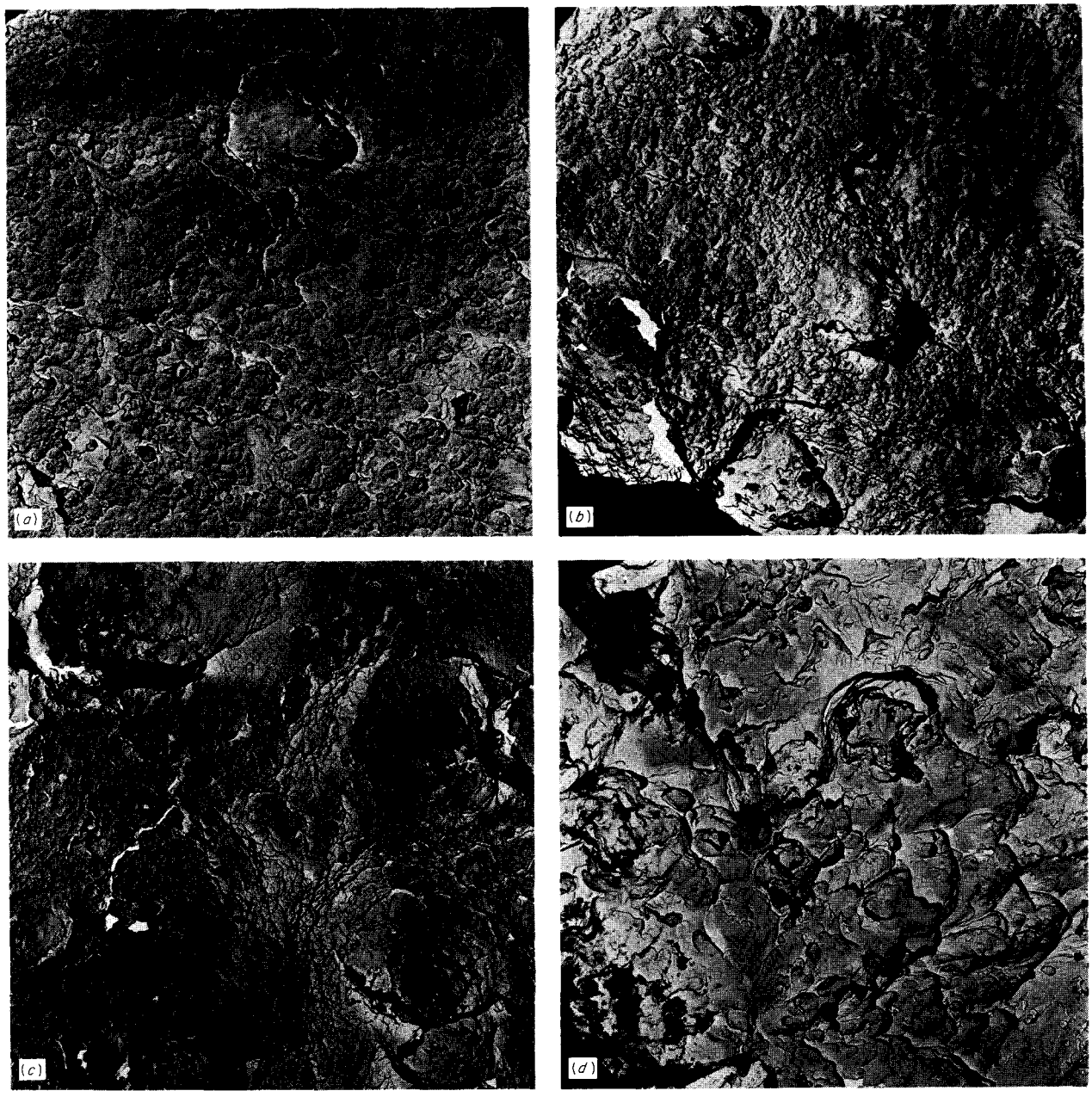

Fig. 24.2. Electron Fractographs Showing Fracture Initiation and Propagation in SAP Material at 450°C. 6500×. (*a*) Specimen prestrained 0.2% at 450°C, then fractured at −200°C. A single high-temperature fracture void is shown surrounded by the fine scale −200°C fracture features. (*b*) 1.0% prestrain. High-temperature fracture voids have increased in both size and density. (c) 1.6% prestrain. Voids have grown to about 5 μ in diameter. (*d*) 450°C fracture. Reduced 47%.

COMMERCIAL PRODUCT EVALUATION

D. G. Harman D. H. Turner[3]

Properties of SAP Made from Commercial Atomized Powders

Short-time tensile properties of rod extruded from the five grades of atomized powder listed in Table 24.3 were measured at room temperature and elevated temperature. Some swaged rod was also tested. The oxide contents of the extruded rods varied from 1 to 15%. Milling lubricants, extrusion ratios, and billet preheat temperatures were studied.

It was apparent that the several variables involved were not adequately treated for any firm conclusions; however, certain trends among the five powders were used for some cursory comparisons. The high-temperature strength of SAP from Alcoa's Albron 101 powder was consistently low (for a given oxide content), while Valley Metallurgical's H-3, H-5, and H-10 were all at an approximately identical higher strength level. Alcan Metal's MD X-65 had the highest strength, which was probably due in part to the lubricant used. At oxide levels of less than 4%, SAP from 101 grade powder showed the highest ductility (total elongation). There was appreciable scatter in the ductility data, and no other trends were evident with respect to powder grade.

[3]On loan from Atomics International.

The effects of milling conditions and lubricants were appraised by considering the data on the VMP H-5 powder. There was no strength difference between materials milled with stearic acid and with silicone as lubricants; however, the material milled with oleic acid showed 30% higher strengths at the same oxide level. The incorporation of lifter bars in the ball mill increased the high-temperature strength of VMP H-5 SAP by about 30%, whether aluminum or stainless steel balls were used. Those VMP H-5 powders milled with stearic acid showed the highest ductility, while those milled with silicone showed the lowest.

In addition to these milling studies, the effects of hot swaging after extrusion were studied for four grades of powder. The high-temperature strength and ductility were improved for three of the four grades.

Mechanical Properties of Extruded Montecatini Sintered Aluminum Products

To provide base-line data for ORNL SAP, current commercial material is being evaluated. A 2-in.-diam SAP 895 billet produced by Montecatini and obtained from Atomics International was tested at ORNL in the as-received condition and after hot extrusion to $\frac{3}{8}$-in.-diam rod.

The effect of strain rate on the elevated-temperature mechanical properties is shown graphically in Figs. 24.3 and 24.4 and compared with our data from a similarly tested XAP-001 extrusion. Figure 24.3

Table 24.3. Characteristics of Spherical Aluminum Powders Used as Starting Material

Powder	Manufacturer	Average Size (μ)	Surface Area (m^2/g)	Oxide Content (%)	Crystallite Size (A)	Atomizing Medium
Albron 101 (−325 mesh fraction)	Alcoa	12				Air
MD X-65	Alcan Metal Products	6.5	0.754	0.3	790	Air
VMP H-3	Valley Metallurgical Processing Corporation	3.5	0.996	0.4	1050	Helium
VMP H-5	Valley Metallurgical Processing Corporation	6	0.803	0.7	910	Helium
VMP H-10	Valley Metallurgical Processing Corporation	10	0.594	0.2	910	Helium

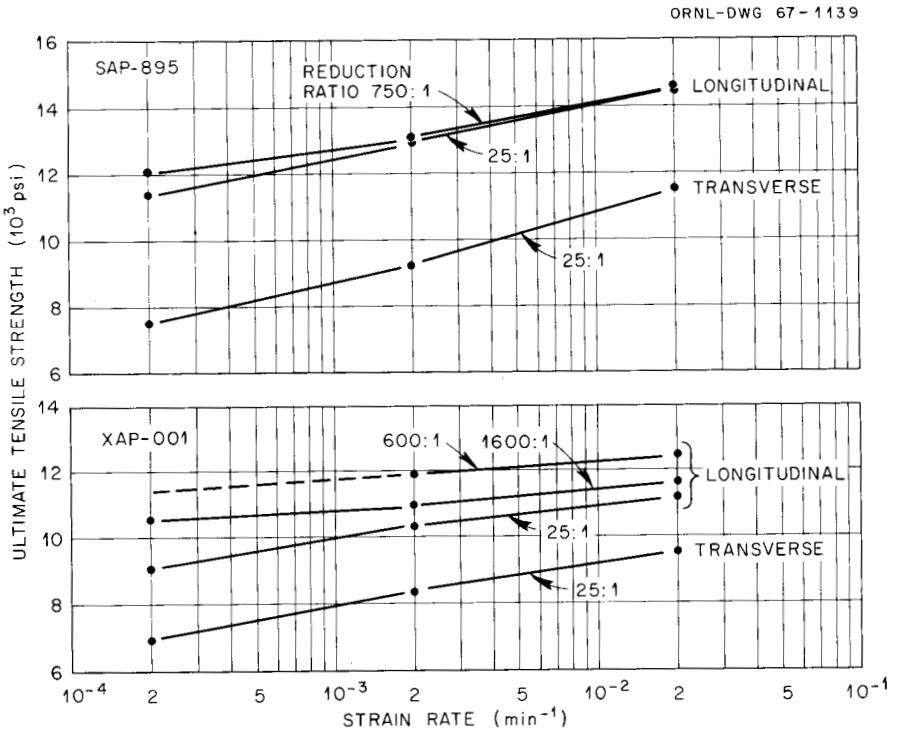

Fig. 24.3. Tensile Strength of Commercial SAP Alloys of Various Reduction Ratios at 450°C.

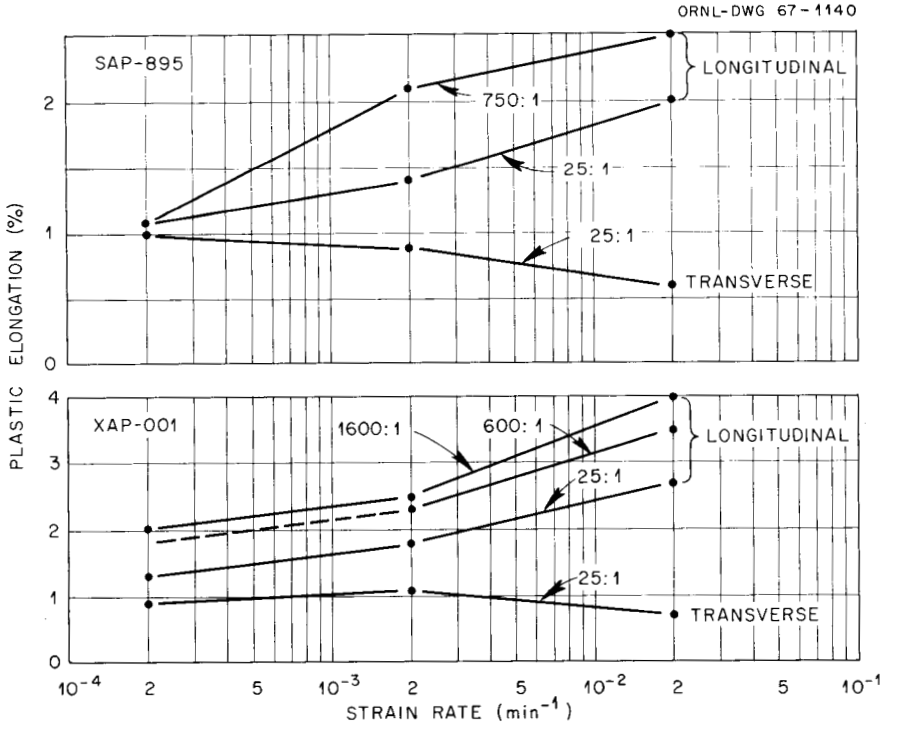

Fig. 24.4. Ductility of Commercial SAP Alloys of Various Reduction Ratios at 450°C.

shows that as the strain rate is decreased, the difference in strength between longitudinal and transverse directions remains essentially constant for as-received billets (reduction ratio 25) of each alloy. This difference was about 3500 psi for the SAP 895 and about 2000 psi for the XAP-001. Notice that the SAP 895 (approximately 11% Al_2O_3) is only 440 psi stronger in the transverse direction than is the XAP-001 (approximately 6% Al_2O_3). Figure 24.4 shows that changing the strain rate by two orders of magnitude had very little effect on the ductility for either alloy measured in the transverse direction. The material showed transverse elongations of 1% or less at all strain rates. On the other hand, the longitudinal ductility essentially doubled with the 100-fold increase in strain rate.

NONDESTRUCTIVE TESTING OF SAP

H. L. Whaley

We have been working primarily on two problems associated with the SAP material development program this year: measurement of flake thickness and oxide content of SAP powders.

For the first problem, our survey of existing particle classifying instruments found none applicable. A technique of dispersing the flakes in air in a vertical column, injecting them into a horizontal laminar stream of air, and collecting them as they settle out of the air stream under the influence of gravity was developed. Calculations show that the distance traveled in the laminar stream before settling is inversely proportional to the thickness of a given flake. An apparatus for accomplishing this thickness-dependent settling was designed and built (Fig. 24.5), and early work demonstrated that such separation appeared to occur when the process was conducted at atmospheric pressure. However, due to the very slow vertical component of the terminal velocities of the thinner flakes, they were passing completely through the horizontal settling chamber. Two approaches to facilitate quicker settling were considered; use of a gas other than air and use of reduced air pressure. Calculations showed that the latter was more practical.

A large, reinforced Plexiglas box was built to contain the settling apparatus at the desired reduced pressure. Significant problems were overcome in getting the electrical systems to perform appropriately at reduced pressure (0.02 to 0.5 atm). Since the powder is dispersed by blowing air upon it, significant modifications were necessary to allow dispersion at reduced pressure.

Samples of as-received MD-3100 powder were successfully dispersed and collected at 0.30, 0.167, 0.120, and 0.067 atm. These were sent to Metallography where they were put in a form allowing measurement of the flake thickness. When straight lines were drawn through plots of flake thickness vs set-

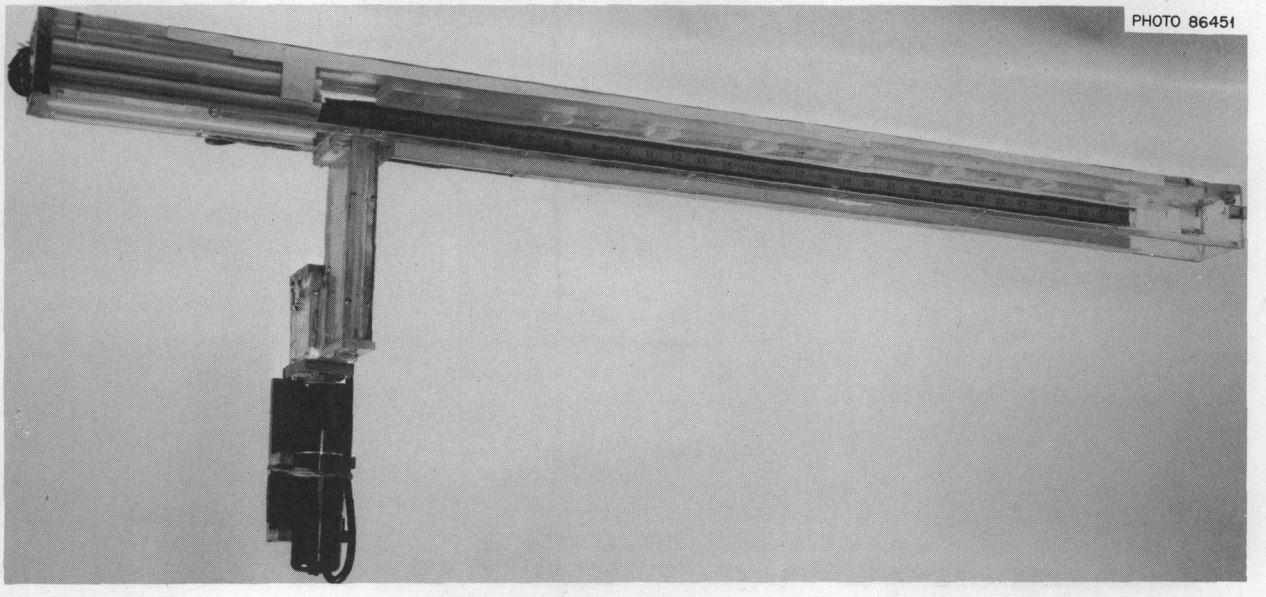

Fig. 24.5. Flake Thickness Separating Apparatus.

tling distance for these samples, the slopes diminished as pressure increased. The thickness range collected at a given pressure covered only about 0.5 μ and was centered near 1.0 μ. More samples of MD-3100 for test and calibration are now being collected and processed. Plans have been made to analyze powder from an experimental ball mill designed and fabricated at ORNL.

On the oxide content problem, the feasibility of using eddy-current techniques to measure conductivity differences in SAP due to different oxide contents was demonstrated with extruded SAP billets. However, our goal was a quick determination of oxide content from powder direct from a ball mill; therefore, extruded SAP could not be used.

Wafers 1 in. in diameter and about 0.100 in. thick were required for the eddy-current tests. Neither cold compacting to 50 tsi nor vacuum hot pressing to high pressure yielded a wafer with sufficiently high conductivity. Vacuum fusing followed by cold pressing produced a compact with conductivity between those of 1100 and 2024 aluminum. We are trying to obtain less variation in conductivity as measured at various points on the face of a sample and less variation between wafers processed the same way from the same starting powder. The present variation in conductivity over the face of a wafer is equivalent to about a 1% oxide variation. The present goal is to obtain sufficient reproducibility and homogeneity for the fusing process and then calibrate over the oxide range of interest. Photographs of the interior of the fused wafers (Fig. 24.6) showed very bad cracking parallel to the faces, which contributes to the conductivity variation. Gamma attenuation has also been investigated as a backup technique on the oxide content problem.

Some work has also begun to determine the homogeneity of preextrusion compacted billets by gamma scanning to see if this correlates with postextrusion billet integrity.

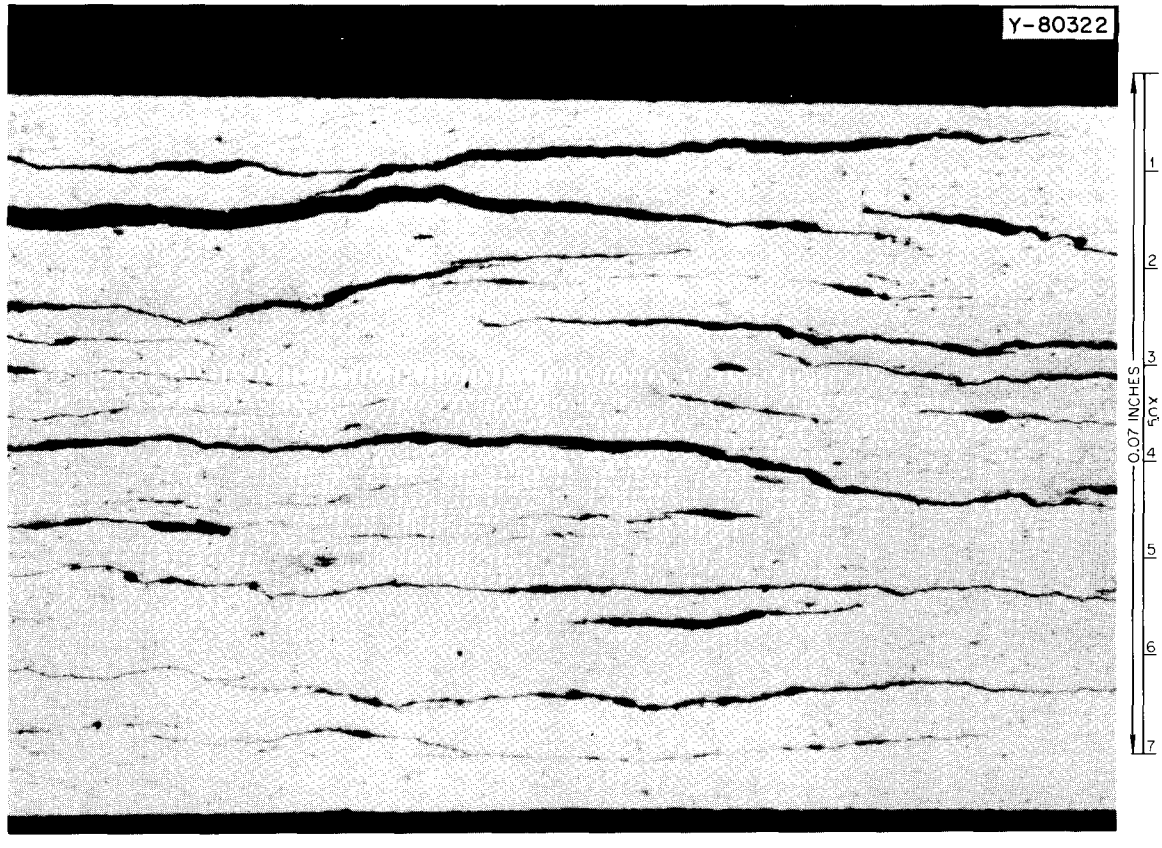

Fig. 24.6. Cracking in Fused SAP Wafer. 50×.

SAP-UC COMPATIBILITY

J. T. Venard

A series of experiments to investigate the compatibility between SAP and UC was performed. We tested SAP containing 10 wt % oxide against hypostoichiometric, stoichiometric, and hyperstoichiometric uranium monocarbide over the temperature range 450 to 625°C.

The spring-loaded compatibility capsules used in these experiments did not produce as much reaction product as had been observed by other experimenters. The amount of reaction product observed and the capsule loading conditions are, however, probably representative of a fuel rod in an unpressurized reactor. X-ray analysis of extracted reaction product has not yet identified the material.

The activation energy for the growth of the reaction product in UC containing 4.8% C was 83.6 kcal/mole. The corresponding value for 5.1% C samples was 92.4 kcal/mole. Results for 4.6% C samples were very erratic, presumably because of the presence of free uranium, and have not given any useful information.

A report covering the details of these experiments and their analysis has been drafted.

25. Weldability of High Alloys

G. M. Slaughter

This program has a twofold objective. The first is to obtain a more thorough understanding of the role of minor elements, individually and combined, upon the cracking behavior and mechanical properties of welds in high alloys. These minor elements can be either those specifically added or those present as unwanted residuals. Much effort was expended in procuring high-purity raw materials and processing them into special alloys for testing weldability both at Rensselaer Polytechnic Institute under subcontract and at ORNL.

The second objective of the program is concerned with a more thorough understanding of the influence of welding parameters on the weldability of conventional alloys. Weld energy input is a basic variable in welding, and its effect on the properties of stainless steel welds has been studied.

SPECIAL ALLOY FABRICATION

W. J. Werner R. E. McDonald
D. A. Canonico

Raw materials were purchased on the basis of purity, cost, and delivery data. Table 25.1 shows typical chemical analyses of the melting stock. Melting and fabrication were essentially completed on two groups of alloys: one a nickel-base alloy (Inconel 600, Ni–15.5% Cr–8.0% Fe) and the other an iron-rich alloy (Incoloy 800, Fe–32.5% Ni–21.0% Cr).

The elemental components of the special alloys were consolidated by inert-atmosphere arc melting. The resultant 12-in.-long half-rounds were welded into cylindrical 2-in.-diam electrodes and then melted into 4-in.-diam ingots. These were extruded and hot swaged or hot rolled to the final desired rod or plate configurations.

The Incoloy-800 composition was chosen in view of its current importance for a variety of fuel element and nuclear steam generator applications. Variations in aluminum and titanium content within the fairly wide range permitted by ASTM were incorporated. These two minor element additions were selected for study because of their probable (but undetermined) major influence on weldability. Additional alloys were prepared that contained nominal amounts of aluminum and titanium together with controlled additions of sulfur and/or phosphorus. A pure ternary alloy was included for comparison.

The study of the Inconel 600 alloy consists of two portions, VARESTRAINT testing and hot-ductility testing. In the first case, controlled sulfur and phosphorus additions were made to a nominal alloy containing 0.03% C, 0.04% Cu, 0.20% Mn, and 0.20% Si. Pure ternary and pure nominal alloys were included for comparison.

Table 25.1. Chemical Analyses of Melting Stock

Impurity Element	Impurity Content of Melting Stock (wt %)		
	Fe	Cr	Ni
C	0.005	0.002	0.007
Si	0.0002	0.0002	0.005
P	0.002	0.004	0.0005
S	0.004	<0.002	<0.002
Fe		0.11	0.001
Cu	0.05	0.0005	0.00002
Pb		0.0013	0.00001
Al	<0.02	0.004	0.00001
N		0.014	
O	0.012	0.033	
H	0.0009	0.0003	

Six 125-lb heats of the pure Inconel 600 ternary were melted for the VARESTRAINT studies at RPI. We produced 6-in.-diam extrusion ingots by air-induction melting of the elemental components into 4-in.-diam electrodes and vacuum-consumable melting these. A commercial fabricator extruded them into sheet bar (1 × 4 in. cross section).

Excellent quality, reproducibility, and fabricability were obtained for the more than 50 heats of special alloys manufactured in-house. Close control over all melting and fabrication parameters was maintained at all times, and the contamination during melting and fabrication was minimal.

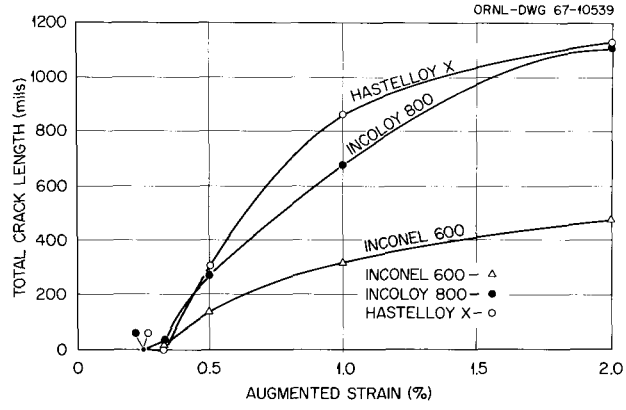

Fig. 25.1. Effect of Augmented Strain on Total Crack Length in VARESTRAINT Test. Data recorded from as-welded surface at 60× magnification. Data points represent the average of the data from two heats of each material with two replications at each augmented-strain per heat.

VARESTRAINT TESTING PERFORMED UNDER SUBCONTRACT AT RENSSELAER POLYTECHNIC INSTITUTE[1]

D. A. Canonico W. J. Werner

The weldability of nickel-bearing alloys is being investigated by use of the VARESTRAINT test developed at Rensselaer Polytechnic Institute.[2] This VAriable RESTRAINT test, which is new and relatively inexpensive, permits the evaluation of base-metal weldability as well as the determination of the effect of a particular welding process and associated welding variables on hot cracking. Standard ½- × 2- × 12-in. test specimens of commercial heats of Inconel 600, Incoloy 800, and Hastelloy X were tested as one part of the program.

Figure 25.1 compares the generalized sensitivity to hot cracking for the three types of material studied. The data points were obtained by averaging the results (at equivalent augmented strain) of the tests on two heats of the same material. Note that the cracking threshold (minimum augmented strain to cause cracking) is 0.33% for Hastelloy X and 0.25% for both Inconel 600 and Incoloy 800, indicating a superior hot-cracking resistance for the Hastelloy X material at low strain levels. However, this superiority is lost at all higher levels of augmented strain, and Inconel 600 exhibits a pronounced superiority over both Hastelloy X and Incoloy 800 at augmented-strain levels of 0.5, 1, and 2%. Thus the commercial Inconel 600 apparently exhibits the greatest overall hot-cracking resistance of the three materials studied, and commercial Hastelloy X and Incoloy 800 are roughly equivalent.

The total crack length at 2% augmented strain is approximately 500 mils for the Inconel 600 and 1100 mils for the Incoloy 800 and Hastelloy X. In general, the crack length at 2% strain has been found to be directly proportional to the range of temperature in which the material is sensitive to hot cracking. Thus the Inconel 600 material exhibits a smaller hot-cracking temperature range than either the Incoloy 800 or Hastelloy X material.

Similar experiments are being run on several heats of the special alloys to determine threshold compositions for cracking. Hot-cracking mechanisms are being studied through the use of electron microscopy and microprobe analysis of fracture surfaces.

THE EFFECT OF ENERGY INPUT ON THE MECHANICAL PROPERTIES OF AUSTENITIC STAINLESS STEEL WELDS

D. A. Canonico W. R. Martin

The mechanical properties of carbon- and low-alloy steel welds are significantly affected by variations in welding parameters. These changes in mechanical properties are largely related to refinement or coarsening of the ferritic microstructure during cycling

[1]Work performed under direction of W. F. Savage and C. D. Lundin, Department of Materials Engineering, Rensselaer Polytechnic Institute, Troy, N. Y. Subcontract is funded jointly with BONUS Core II Superheater Research and Development (Part IV, Chap. 27, of this report).

[2]W. F. Savage and C. D. Lundin, "The Varestraint Test," *Welding J. (N.Y.)* 44(10), 433-s–442-s (1965).

through the allotropic transformation from face-centered cubic to body-centered cubic. Unlike welds in ferritic steels, austenitic stainless steel welds do not undergo allotropic transformations and, therefore, cannot be affected in this way.

However, one possible way of controlling the mechanical properties of weld metal in such an alloy is to change the mode of solidification. To evaluate the influence of weld energy input on the solidification mode in tungsten-arc welds, a cursory bead-on-plate study was undertaken, using welding conditions producing 10,000, 20,000, and 40,000 j/in. Type 308 stainless steel filler metal was deposited on type 304 stainless steel base metal by use of a cold-wire feed mechanism. Obvious microstructural differences (i.e., dendrite spacing, delta ferrite distribution, etc.) did indeed prevail; furthermore, microhardness studies indicated that strength differences should exist between welds made with the three energy inputs.

The program was then extended to actual butt welds on highly restrained plates. The joint designs were selected to provide both all-weld-metal and transverse (base metal, heat-affected zone, and weld metal) specimens. The transverse specimens and one set of all-weld-metal specimens were made with one heat of filler metal (W-1). A second set of all-weld-metal specimens was made with a different heat of filler metal (W-2). The energy-input level 60,000 j/in. was also included. The two filler metals had essentially identical delta ferrite quantities (approximately 8%), as determined from the Schaeffler diagram.[3]

The effect of heat input on the W-2 weld-metal microstructure is shown in Fig. 25.2. The white phase seen in these photomicrographs is austenite, while the darker and more defined phase is delta ferrite. The approximate intercellular distances for the microstructures are 7, 12, 16, and 20 μ, respectively, for the 10,000, 20,000, 40,000, and 60,000 j/in. welds.

In metallographic samples of these welds, relative amounts of each phase were directly measured with the quantitative television microscope (QTM). The results indicated that the ferrite level for a given heat input ranged from approximate 4 to 9% (the predicted value from the chemical composition of the filler wire was 8%).

The effect of heat input on the ultimate tensile strength of both heats of weld metal is shown in Fig. 25.3. The welds made at 10,000 j/in. are approximately 10,000 psi stronger at room temperature than those made at 60,000 j/in. This advantage decreased as the testing temperature increased.

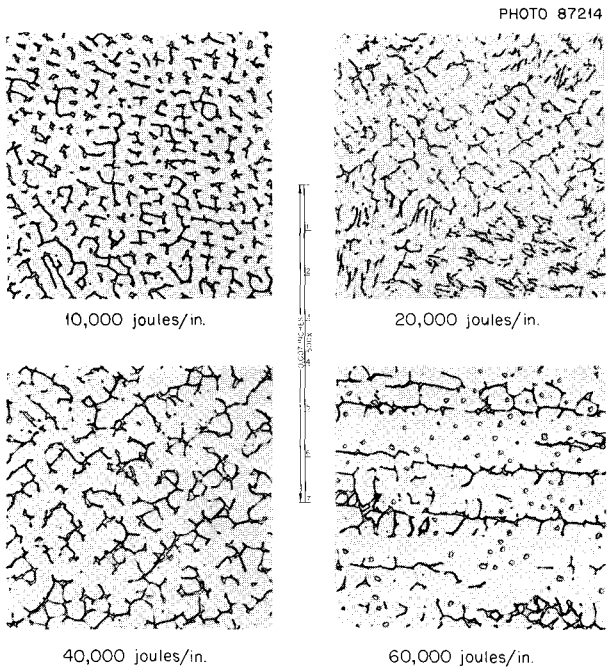

Fig. 25.2. Effect of Heat Input on the Microstructure of Type 308 Stainless Steel Weld Metal. Electrical parameters: 220 amp, 12 v.

The ductility measurements for welds made with the two heats of filler metal were quite similar at both the 10,000 and 20,000 j/in. energy inputs. However, they were conspicuously different for the higher levels of heat input. At the 40,000 value, the W-1 welds had ductilities (as measured by elongation) from 20 to 50% of that obtained for W-2. A metallographic investigation showed that the W-1 weld deposited at 40,000 j/in. contained no ferrite.

Weld metal deposited in the 40,000 j/in. W-1 weld showed a distinct loss of chromium. This lower chromium equivalent results in a decrease in the amount of delta ferrite in the weld metal; in confirmation, the Schaeffler diagram indicated a nominal delta ferrite level of 3.5% in the weld metal. (It should be pointed out that the Schaeffler diagram is empirical and can be used only as a guide; it does not provide absolute values.)

Our results indicate that heat input significantly affects the mechanical properties of stainless steel weld metal. This effect is probably related to such factors as intercellular distance and actual delta ferrite content.

[3] A. L. Schaeffler, "Selection of Austenitic Electrodes for Welding Dissimilar Metals," *Welding J. (N.Y)* 26, *601-s–620-s (November 1947).*

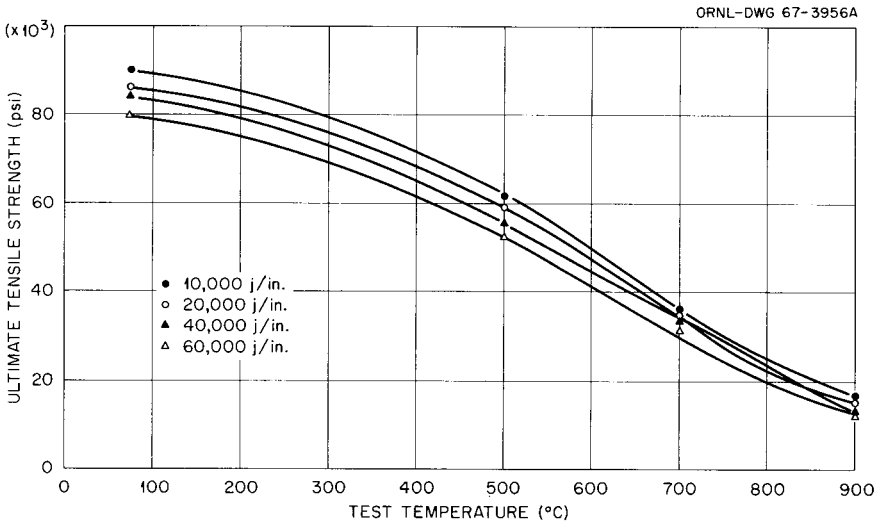

Fig. 25.3. Tensile Strength of Weld Metal Deposited at Different Levels of Energy Input. A 10,000-psi difference is noted at room temperature.

26. Zirconium Metallurgy

P. L. Rittenhouse M. L. Picklesimer[1]

Several α-zirconium alloys are either in use or exhibit good potential for use as fuel cladding, pressure tubing, and structural material in water-cooled or -moderated nuclear reactors. To achieve the objectives of advanced reactor designs, the strength of zirconium alloys must be increased at no cost of neutron economy and their corrosion properties and resistance to hydrogen embrittlement must be improved. Our studies of the development and control of texture and the effect of texture on anisotropy of plastic properties should permit us to obtain the necessary increase in design strength. We are attempting to reduce corrosion rates by anodic treatments. The studies of texture and corrosion are also appropriate to the solution of the hydrogen problem.

STRESS ORIENTATION OF HYDRIDE IN ZIRCALOY

P. L. Rittenhouse

We precipitated hydride in Zircaloy-2 and -4 stressed to 20,000 psi (elastic) at cooling rates of from 4 to 170°C/min. The rate has no measurable effect on the orientation of the hydride platelets but causes major differences in morphology. At 4°C/min, large intergranular platelets are formed. The platelets precipitated at 170°C/min are much smaller and many are intragranular.

Other specimens were temperature cycled (100 → 400 → 100°C) under stress (15,000 psi) to alternately dissolve and precipitate hydride. We saw no change in the orientation of the hydride platelets in specimens cycled 1, 5, and 10 times, but duplicate 20-cycle tests resulted in a significant increase in the number of platelets oriented

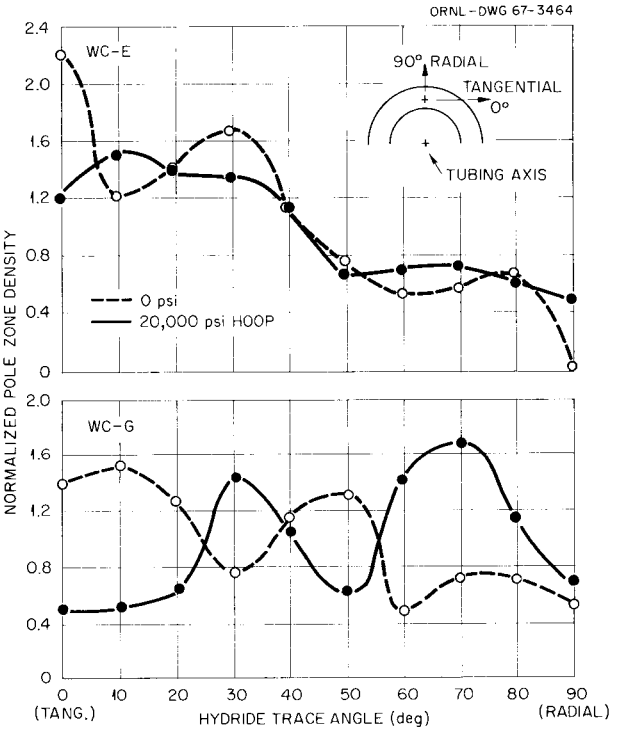

Fig. 26.1. Hydride Platelet Distribution in Zircaloy Tubing. The concentration of basal poles parallel to the tangential direction θ in material WC-E is only half as great as that in a "random" material. There is relatively little difference in hydride orientation with and without stress. In WC-G the basal poles are twice "random" parallel to θ, and there is a large difference in the orientation precipitated under stress. A random distribution of hydride corresponds to a uniform normalized pole density of 1.0.

[1]Present address: Southern Research Institute, Birmingham, Ala.

perpendicular to the stress direction. Additional cycling, up to 88 cycles, did not increase the percentage of platelets perpendicular to the stress.

We also examined the distribution of hydride in 15 lots of annealed Zircaloy tubing. The hydride was allowed to precipitate either with or without an applied elastic hoop stress of 20,000 psi. In the unstressed tubing, the fraction of hydride platelets at any given orientation was proportional to the concentration of basal planes parallel to that orientation. The orientation of the hydride precipitated under stress was unchanged relative to that in unstressed specimens except when there was an appreciably greater than random concentration of basal poles parallel to the tangential direction (see Fig. 26.1).

TEXTURE AND ANISOTROPY OF PROPERTIES IN ZIRCALOY

P. L. Rittenhouse

We have examined the textures developed in Zircaloy tubing fabricated by a variety of techniques. In tube-reduced material the texture obtained is influenced dramatically by whether the final reduction is accomplished by "ironing" or "sinking." Heavy wall reduction with little diameter reduction (ironing) promotes a texture with basal poles parallel to the tubing radius. If, however, the diameter is reduced more than the wall during the final pass (sinking), the basal poles are tangent to the tube wall.

We demonstrated the effect of texture on plastic strain anisotropy of Zircaloy. When tubing is stressed uniaxially, the natural strains that occur by diameter reduction ($\bar{\epsilon}_\theta$) and wall reduction ($\bar{\epsilon}_R$) are inversely proportional to texture coefficients in those directions. (The texture coefficient, $TC_{(0001)}$, is the concentration of basal poles parallel to a direction expressed as a multiple of that in a "random" sample.) This is demonstrated in Table 26.1 for five lots of tubing.

The strength of Zircaloy can also be related directly to texture. We show this in Fig. 26.2. Both the tension and compression yield strengths are linear functions of $TC_{(0001)}$ parallel to the test direction.

Biaxial yield loci have been generated for materials of various textures. We have done this by several methods including Knopp microhardness anisotropy, uniaxial yield strength and strain anisotropy, and biaxial testing.

Table 26.1. Relationship Between Texture Coefficients and Strains in Zircaloy Tubing

Material Code	$TC_{(0001)_R} / TC_{(0001)_\theta}$	$\bar{\epsilon}_\theta / \bar{\epsilon}_R$
Y-2	1.6	1.4
E-1	0.30	0.22
E-2	3.2	2.7
R-2	1.8	1.6
S-1	1.0	1.0

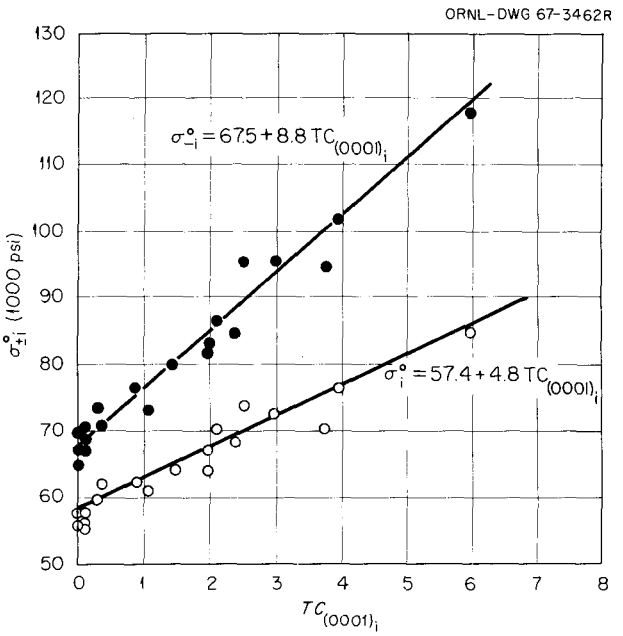

Fig. 26.2. Correlation Between Yield Strength and Texture for Zircaloy. σ°_{+i} and σ°_{-i} are the uniaxial tension and compression yield strengths respectively. The least-squares equation for each set of data is shown.

DETERMINATION OF THE ANISOTROPY OF YIELDING AND FLOW IN ZIRCALOY-2 FROM A SINGLE TEST[2]

P. L. Rittenhouse

The anisotropy of plastic properties of Zircaloy-2 is an important consideration in its use. A rapid

[2]Abstract of paper accepted for publication in *Journal of Nuclear Materials*.

and simple method of evaluating and characterizing these properties would be a valuable aid to the designer. Experimental yield and strain data on lots of Zircaloy-2 with varied crystallographic texture were used to develop empirical correlations that relate yield strength and strain behavior parameters. These correlations allow the calculation of tension and compression yield strengths and strain anisotropy constants for the principal fabrication directions from the data obtained in a single test. The correlations are also valuable for material specification, quality control, and internal consistency checks on experimental data.

A YIELD STRESS AND PLASTIC STRAIN THEORY FOR ANISOTROPIC MATERIALS[3]

D. C. Bogue[4]

A yield stress and plastic strain theory is developed for anisotropic materials showing the Bauschinger effect. The theory is a generalization of Hill's anisotropic theory. The quadratic (Hill) terms are common to and predominate in both the yield stress criterion and the plastic strain equations; there are additional constants in both cases, which are not interrelated. The formulation is motivated by the behavior of Zircaloy-2 and is tested with data from highly textured material.

PURIFICATION AND CRYSTAL GROWTH

J. C. Wilson

We have performed routine zone-refining and crystal-growth operations on zirconium, hafnium, and at least 15 other metals and alloys. Large single crystals, up to $\frac{1}{2}$ in. wide × 8 in. long, were grown in Zircaloy-2 and -4 by solid state (β phase) zoning after quenching. We have built a new zone refiner and a solid-state electrolysis apparatus and are constructing an ultrahigh-vacuum annealing and quenching furnace.

[3]Abstracted from ORNL-TM-1869 (July 1967).

[4]Consultant from the University of Tennessee.

DEFORMATION STUDIES OF ZIRCONIUM AND ITS ALLOYS

D. O. Hobson

We have deformed zirconium and zirconium alloy single crystals in shear to force flow in specific crystallographic planes and directions. Specimens oriented for $\{10\bar{1}0\}\langle 11\bar{2}0\rangle$ slip yielded at a very low stress. Twinning was not observed. Crystals aligned for $\{10\bar{1}1\}\langle 11\bar{2}3\rangle$ flow twinned profusely and did not yield until the stress was 10 times that for shear in the $\{10\bar{1}0\}\langle 11\bar{2}0\rangle$ specimen. We now believe that $\langle 11\bar{2}3\rangle$ slip, if it exists, occurs only at high temperatures where deformation by twinning ceases.

Several single crystals of Zircaloy-2 and -4 were loaded to fracture in uniaxial tension. The ultimate tensile strength for specimens oriented almost ideally for $\{10\bar{1}0\}\langle 11\bar{2}0\rangle$ slip was about 40,000 psi. Accurate modulus and yield strength values are being determined. Zircaloy-2 specimens failed or fractured along a single slip plane, but other slip traces were seen. Zircaloy-4 specimens showed every indication of duplex slip and necked to a knife-edge before failing.

ANALYSIS OF TEXTURES IN DEFORMED ZIRCONIUM SINGLE CRYSTALS

D. O. Hobson

To control texture in fabricated zirconium alloy products, it is necessary to know the effect of various fabrication procedures in developing the final texture. We are using x-ray and polarized light methods to follow the texture changes that occur when specifically oriented "perfect" textures (single crystals) are fabricated by rolling and drawing. In all instances, we have been able to identify the operative deformation systems and to correlate the resulting textures with the initial orientations of the crystals. By assuming that twinning is responsible for texture change and that the majority of the macroscopic strain occurs by slip, we can show why a texture tends to perfect at high fabrication reductions. Early in the fabrication, the appropriate twinning systems will move the average specimen orientation to a position or positions where the slip systems are subjected to the maximum resolved shear stress. This texture will remain stable to additional deformation by the same fabrication technique.

INCORPORATION OF IONS IN ANODIC OXIDE FILMS ON ZIRCONIUM AND THEIR EFFECT ON FILM BEHAVIOR[5]

J. C. Banter[6]

Transmission spectra of anodically formed ZrO_2 films show that certain anions – such as phosphate, sulfate, and several carboxylates – are incorporated in these films when they are formed from solutions containing these ions. Furthermore, hydrous ZrO_2 films result from anodizing in strongly oxidizing electrolytes. Films formed in many other solutions contain no incorporated ions. Film conductivity and thickness measurements indicate that incorporated ions increase the electrical resistance of the films and also limit their growth. We suggest that these effects arise from lowered rates of diffusion of electrons and oxygen atoms through the films and that the lowered diffusion rates result from the space charge created by the incorporated ions.

CORROSION OF HIGH-PURITY ZIRCONIUM

J. C. Wilson

We determined the effect of crystallographic orientation on oxidation of zone-refined zirconium by observing the interference colors developed on single crystal spheres. Figure 26.3 shows earlier work[7–9] on crystal bar zirconium and a summary of our data for approximately the same conditions.

Spherical single crystals oxidized for several hours in steam at 500°C show the features described by Wanklyn[10]: (1) regions of initially rapid oxide growth, (2) interference color regions (slowly growing oxide), and (3) micron-sized mounds of oxide (pustules) on the interference color region. The rapidly growing oxide corresponds to the dark areas in Fig. 26.3*d*. We found that the pustule density, distribution, and morphology are related to the orientation of the underlying metal. After a relatively short time most of the weight gain occurs by nonuniform oxide (pustule) growth.

Thermal oxidation produced at least a fourfold variation in thickness with orientation, but films produced by anodic oxidation varied only 25%. For anodized films less than 1500 A thick the film variation pattern is similar to Fig. 26.3*d*, but at greater thicknesses some differences occur.

---

[5]Abstracted from *J. Electrochem. Soc.* **114**(5), 508–11 (1967).

[6]Consultant from Florida Atlantic University, Boca Raton.

[7]J. P. Pemsler, *J. Electrochem. Soc.* **105**, 315 (1958).

[8]A. E. Bibb and J. R. Fascia, *Trans. Met. Soc. AIME* **230**, 415 (1964).

[9]J. N. Wanklyn, *Am. Soc. Testing Mater. Spec. Tech. Publ.* **358**, 58 (1964).

[10]J. N. Wanklyn *et al.*, *J. Electrochem. Soc.* **110**, 856 (1963).

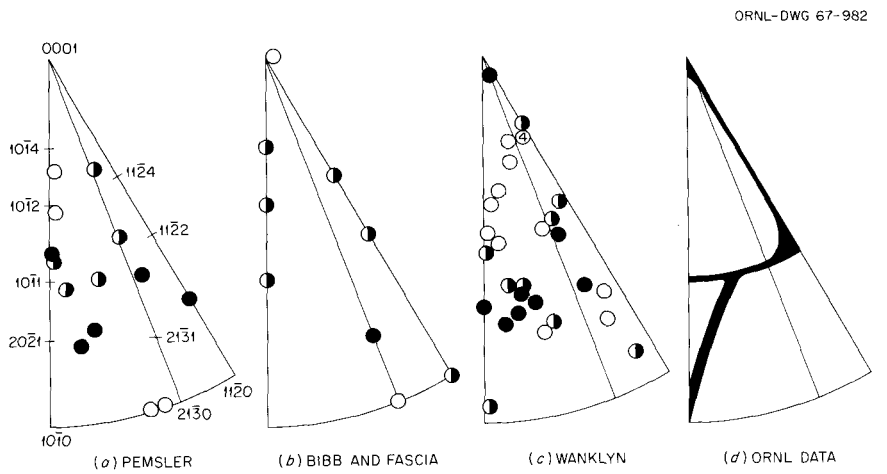

Fig. 26.3. *Qualitative Comparison of* Oxide Thickness as a Function of Crystallographic Orientation. Zirconium oxidized (*a*) in air at 400°C by Pemsler, (*b*) in water at 360°C by Bibb and Fascia, (c) in steam at 500°C and 15 psia by Wanklyn, and (*d*) summary of our data for all these conditions. Darker areas or points indicate thicker oxide. Ratio of thickest to thinnest oxide is about 4 in our work.

We also determined the anisotropy of oxidation of zone-refined hafnium in air at 400°C and steam at 500°C. Figure 26.4 shows that, except for the areas noted in the caption, hafnium film thickness-orientation behavior is similar to that of zirconium.

We corroded specimens from four regions of a zone-refined rod and from the crystal bar zirconium stock used for refining to study the effect of purity on oxidation. The crystal bar stock oxidized heavily (100 mg/dm^2) during three days in water at 360°C, but all of the zone-refined specimens were still covered with a dark, protective oxide film. We could see under a microscope that there were differences in oxide morphology on specimens from different positions along the refined bar. In similar tests in steam at 500°C, we observed weight gains differing threefold along the refined bar. As the difference in total impurity content from end to end in the refined bar is less than 50 ppm, these tests show how extremely sensitive oxidation is to impurity content.

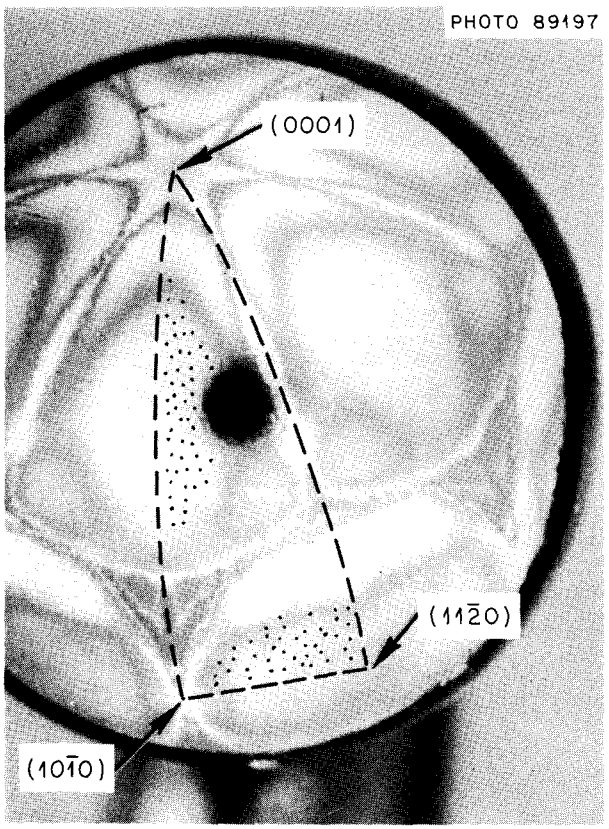

Fig. 26.4. Oxidized Hafnium Single-Crystal Sphere. This 1-cm-diam sphere was oxidized for 24 hr in steam at 500°C and 15 psia. The stereographic triangle of Fig. 26.3 is outlined by dashed lines. The stippled areas indicate orientations where hafnium forms a thick oxide but zirconium does not. Except in these areas, the anisotropy of oxidation is similar in hafnium and zirconium.

OXIDATION INHIBITION BY PREANODIZING

J. C. Wilson

The weight gain of arc-melted crystal-bar zirconium exposed for 500 hr in steam at 500°C and 15 psia can be reduced by two-thirds by preanodizing in phosphoric acid. These experiments were suggested by Banter's observation [11] that films formed in phosphate-containing solutions were dissolved more slowly into the metal than films produced in other solutions. Banter later found that phosphorus was incorporated into the anodic film and suggested that the lowered dissolution rate might improve oxidation resistance at higher temperatures. [12]

The data in Fig. 26.5 show that a 120-v film (3000 A thick) formed in 85% H_3PO_4 significantly reduces both the oxidation rate and weight gain. Even a 30-v film (800 A) gives improved resistance. We took two of the five unanodized control specimens exposed for 268 hr and anodized them at 150 v in 85% H_3PO_4. Although only a negligible amount of oxide could have formed, it provided sufficient protection to temporarily reduce the oxidation rate.

Preanodizing in 1% aqueous KOH also gave measurable protection, but we suspect that transfer of phosphorus in the corrosion apparatus may have affected these results. This is the first reported instance of an anodic film protecting zirconium from oxidation in the thick-film region. Other workers have reported that anodic films have no effect [13] or decrease the oxidation resistance of zirconium. [14]

The appearance of the oxide on preanodized specimens indicates that the anodic film is effective in reducing localized oxide growth at pustules, on grain boundaries, and at hydride. Preanodizing also seems to reduce the growth rate or retard the breakdown of the uniform oxide film into pustules.

---

[11] J. C. Banter, *Electrochem. Technol.* 4, 237 (1966).

[12] J. C. Banter, *J. Electrochem. Soc.* 114, 508–11 (1967).

[13] J. J. Polling and A. Charlesby, *The Inhibition of Gas Phase Reactions of Zirconium by Anodic Oxide Films. Part I,* AERE-M/R-1040 (1952), and *The Inhibition of Gas Phase Reactions of Zirconium by Anodic Oxide Films. Part II,* AERE-M/R-1040A (1953).

[14] C. F. Britton, J. F. Authurs, and J. N. Wanklyn, *J. Nucl. Mater.* 15, 263 (1965).

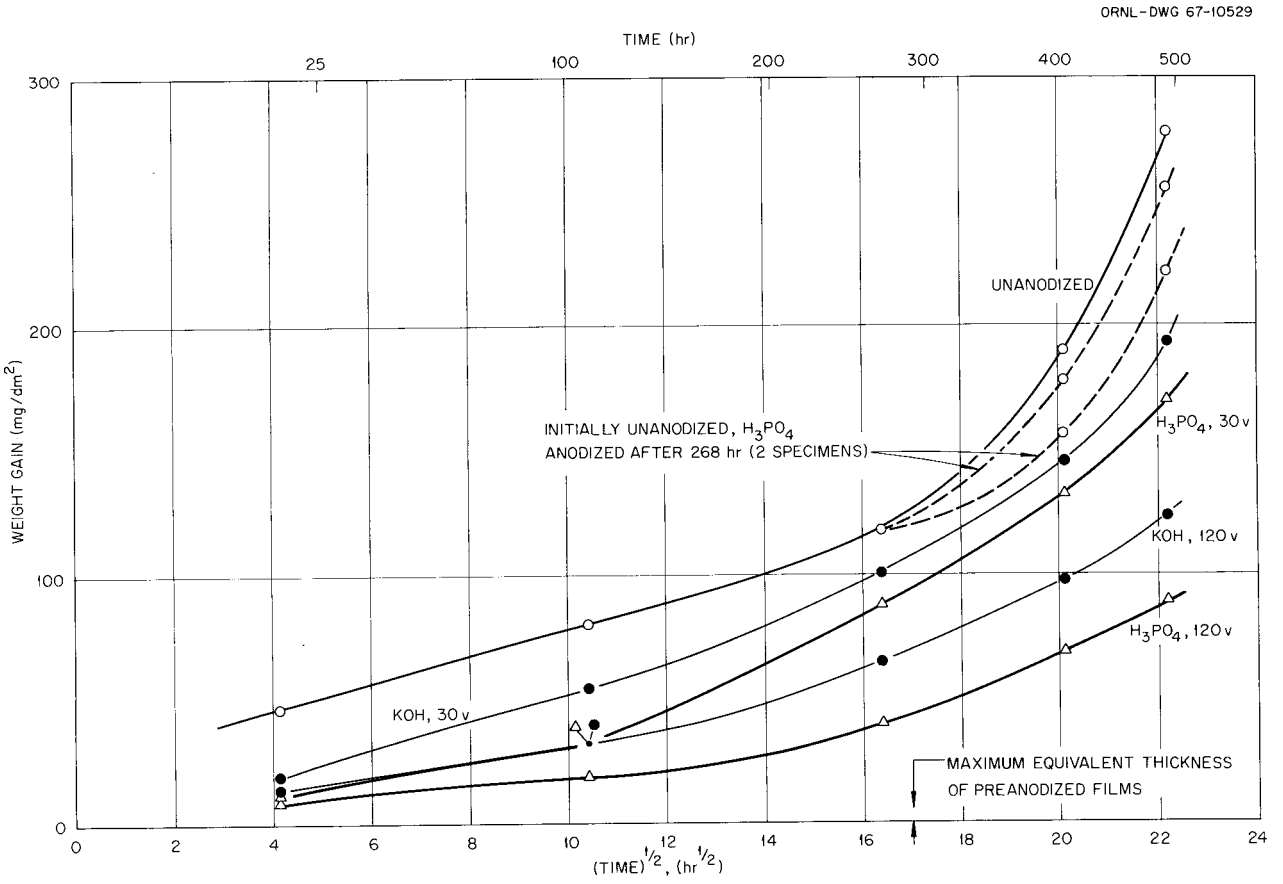

Fig. 26.5. Weight Gain for Oxidized Crystal Bar Zirconium. These curves show weight gain as a function of time for arc-melted crystal bar zirconium (vacuum annealed 4 hr at 800°C) strip oxidized in steam at 500°C and 15 psia. All specimens were electropolished in 2% $HClO_4$ in methanol at −70°C. The weight gain of unanodized specimens at 500 hr is three times that of metal anodized in H_3PO_4. Anodizing solutions were concentrated (85%) H_3PO_4 and 1% aqueous KOH.

Part IV.

Reactor Development Support

Note: The program LMFBR Cladding and Structural Materials Development is combined with the closely related Mechanical Properties Research in Part III, Chap. 21.

27. BONUS Reactor Fuel Element Development

E. A. Franco-Ferreira

At the request of the USAEC, a modest effort has been under way for the past 2.5 years in support of the Boiling Nuclear Superheat (BONUS) Reactor.[1,2] The main objectives have been: (1) to find the source of fission-product leakage as well as to establish the nature and extent of damage to Inconel-clad UO_2 fuel components that failed in service; (2) to devise design and manufacture modifications to prevent recurrence of failure and to demonstrate the feasibility of these changes by rebuilding a failed unit for testing in the reactor core;[3,4] (3) to assist in specification revision and to provide needed materials research, development, and trouble shooting for Oak Ridge Gaseous Diffusion Plant (ORGDP) in the task of fabricating a number of advanced superheater assemblies for reactor service; (4) to consult and advise on technical problems associated with the malfunction of other reactor components, such as control rods and the preheater-drier piping system; and (5) to evaluate and select new engineering materials for construction of superheater fuel assemblies. All major support activities are expected to be completed by November 1, 1967.

[1] J. E. Cunningham, *Metals and Ceramics Div. Ann. Progr. Rept. June 30, 1965*, ORNL-3870, pp. 293–99.

[2] G. M. Slaughter and G. M. Adamson, Jr., *Metals and Ceramics Div. Ann. Progr. Rept. June 30, 1966*, ORNL-3970, pp. 141–45.

[3] J. E. Cunningham, E. L. Long, E. A. Franco-Ferreira, and D. G. Harman, *BONUS Reactor Superheater Fuel Assemblies – An Investigation of Failure and Method of Correction*, ORNL-3910 (December 1965).

[4] G. M. Slaughter, E. A. Franco-Ferreira, E. C. Kirstowsky, K. K. Klindt, E. L. Long, Jr., and G. M. Tolson, *Fabrication of Rebuilt BONUS Reactor Superheater Fuel Assembly*, ORNL-4072 (June 1967).

TECHNICAL ASSISTANCE TO ORGDP

E. A. Franco-Ferreira G. M. Slaughter
L. C. Williams

Technical assistance is being given to ORGDP in revising specifications, procuring material, and developing fabrication and inspection procedures for eight advanced superheater fuel assemblies. Much of the specification and procurement work was accomplished during FY 1966 and has been previously reported.[2] More recent work has been in the area of direct assistance on the actual fabrication operations for the eight fuel assemblies. Most of the innovations being used on these assemblies evolved during the rebuilding[4] of BONUS Superheater Fuel Assembly No. 29. A few of the activities associated with this support program will be outlined below.

Fuel Rod Spacer Brazing

Studies were conducted to optimize procedures for the brazing of five triangular sheet-metal spacers on each of the 32 fuel cladding tubes required in the assembly. Both the tubes and spacers were made of Incoloy 800, a high-nickel austenitic alloy (nominally containing 21% Cr, 34% Ni, and balance Fe). This work included the specification of a suitable time-temperature cycle for brazing, the optimum method of brazing alloy preplacement, and the selection of an outside vendor capable of performing the job satisfactorily.

Since the Incoloy 800 material also contains approximately 0.5% total aluminum plus titanium, an extremely dry hydrogen atmosphere is needed to achieve adequate wetting and flow of the Ni-Cr-P

brazing alloy. The search to find a qualified vendor involved testing job samples from five different plants before a vendor was found who could provide an atmosphere of sufficiently high quality. Once a suitable vendor was found, the brazing operation was carried out satisfactorily with a very high yield rate. A cross-sectional view of a typical tube-to-spacer braze is shown in Fig. 27.1.

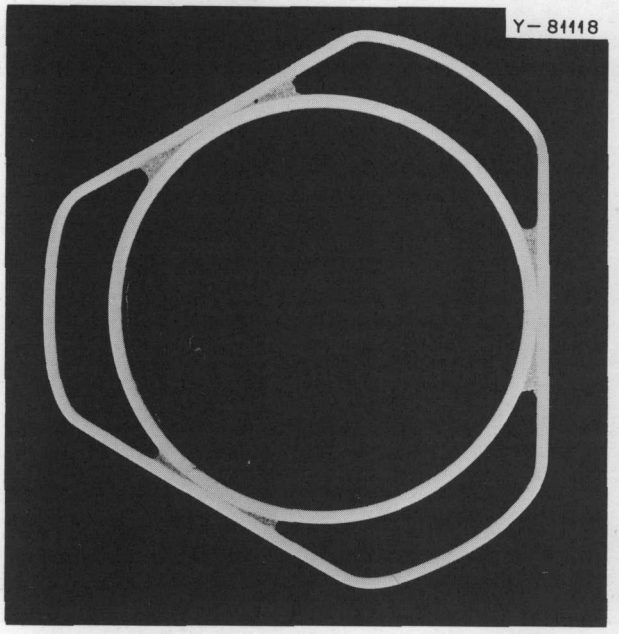

Fig. 27.1. Cross Section of a Typical BONUS Spacer-to-Tube Brazed Joint. 5×. As polished. Reduced 17%.

Fuel Rod End-Cap Welding

The joint designs and welding procedures for welding the upper and lower Incoloy 800 end caps into the fuel cladding tubes were based on developments during the rebuilding[4] of Assembly No. 29. Only slight changes in welding parameters were necessary to adapt the original procedures, developed for Inconel 600, to the Incoloy 800 joints.

Pressure-Shell Assembly Brazing

In the rebuilding of Assembly No. 29, the original pressure shell built by Combustion Engineering was reused. This brazed unit, however, had some weak points that could profitably be eliminated in new construction to gain additional life. One such weakness was the excessive runoff of brazing alloy shown in Fig. 27.2. This particular view shows the underside of the lower tube sheet and details of the pressure-tube-to-tube-sheet joints.

Some basic improvements were made in the original design, but before adoption their worth was demonstrated on a job sample. The first of these changes was welding the pressure tubes to the bottom side of the lower tube sheet, thus anchoring them in place and preventing any run-through of brazing alloy. Small stainless steel rings were placed around each tube on the bottom

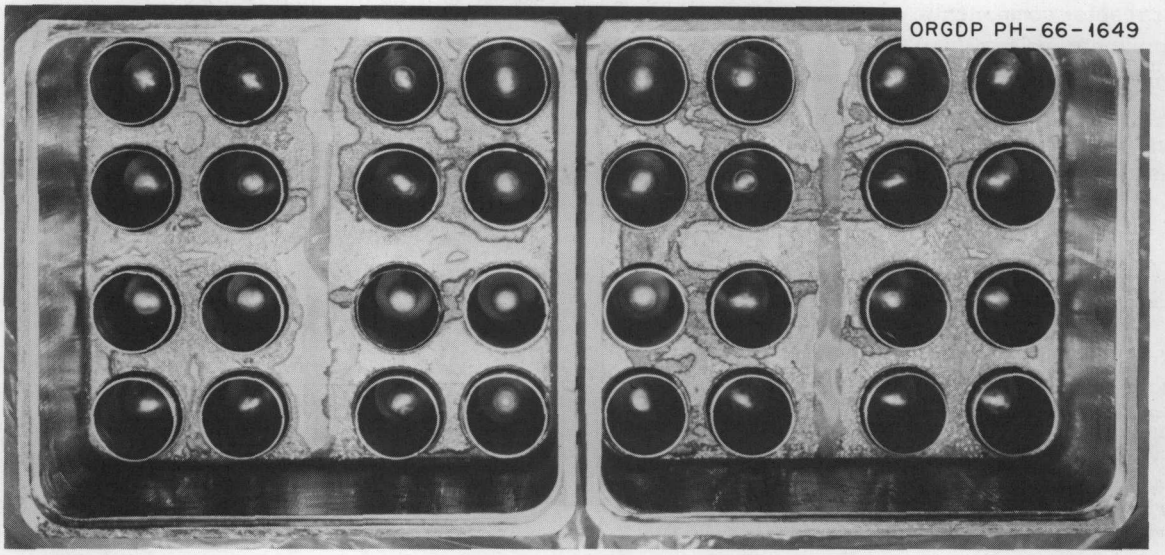

Fig. 27.2. Bottom View of Lower Tube Sheet from Assembly No. 29 Pressure Shell. Note excessive brazing alloy run-through.

sides of the joints between the tubes and the cooling pan and upper tube sheet. The purpose of these rings was to provide enough extra capillarity to control run-through on the upper joints, which could not be welded on one side. A view of these rings on the job sample prior to brazing is shown in Fig. 27.3. An additional control exercised over the quality of the brazing job was to specify close tolerances on joint fitup, amount of brazing alloy preplaced on each joint, and the duration and temperature of the brazing cycle.

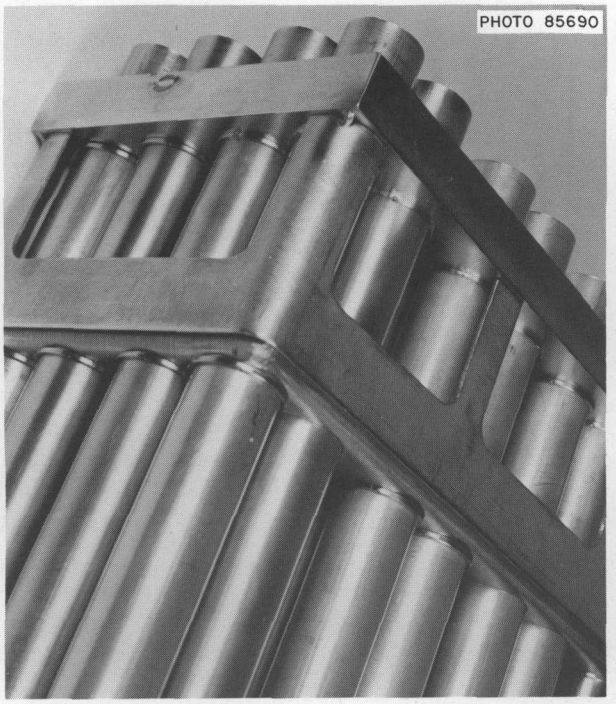

Fig. 27.3. Underside of Upper Tube Sheet and Cooling Pan from Improved Pressure Shell Job Sample. Note stainless steel rings around tubes to control brazing alloy run-through.

A prototype pressure-shell assembly incorporating these improvements was successfully brazed at the plant of an outside vendor. Figure 27.4 shows the tube-to-tube-sheet welds on the lower side of the bottom tube sheet on this prototype, while Fig. 27.5 is an overall view of the prototype in the assembly jig with all but the last 8 of its 32 tubes installed.

NONDESTRUCTIVE TESTING DEVELOPMENT

K. V. Cook

Nondestructive testing studies are being conducted to develop improved techniques for inspecting the BONUS fuel elements. The problem areas include examination of spacer-to-tube brazed joints, fuel cladding, and the several welds in the fuel, coolant, and pressure tubes. Our technique for inspecting the brazed joints is reported here.

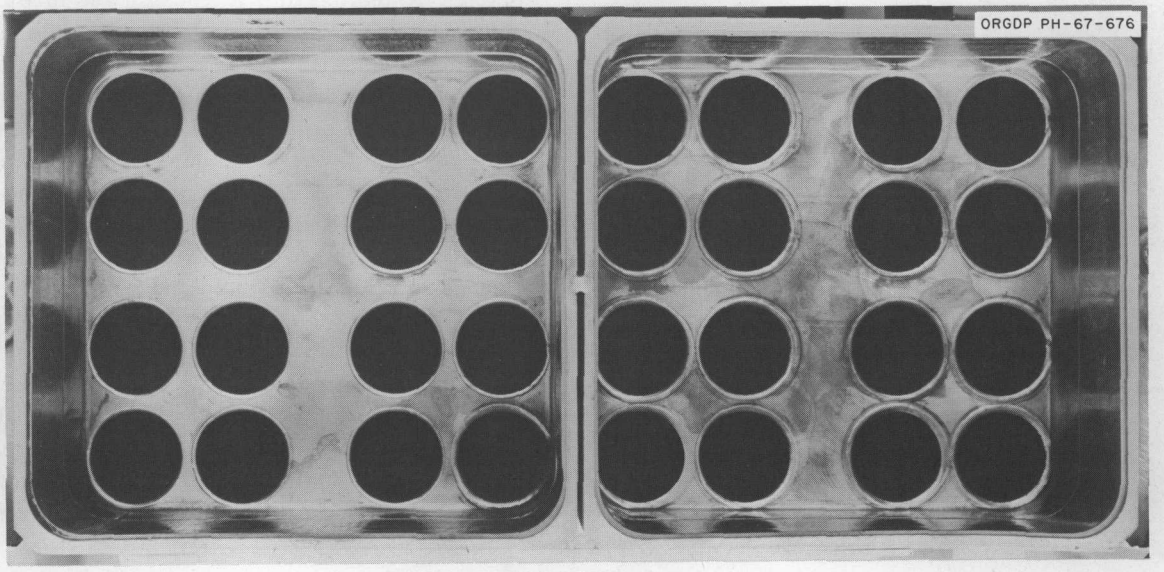

Fig. 27.4. Underside of Lower Tube Sheet from Improved Pressure Shell Prototype, Showing Tube-to-Tube-Sheet Fusion Welds.

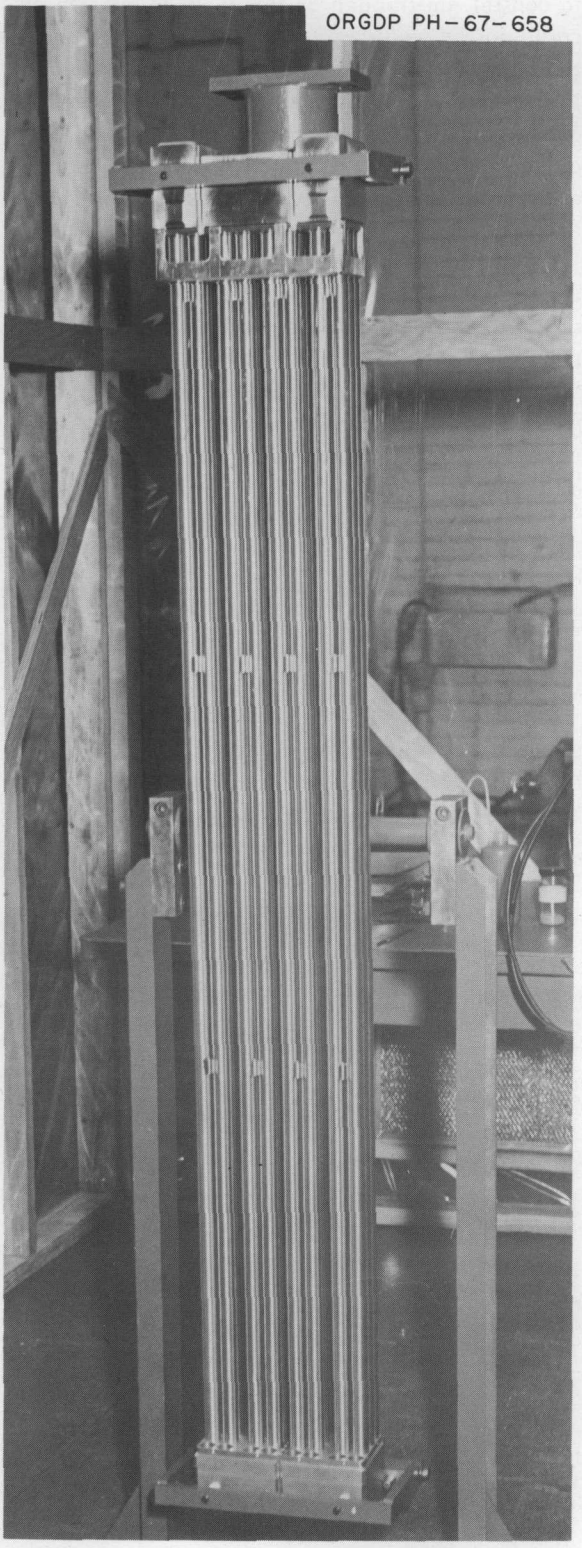

Fig. 27.5. Overall View of Prototype Pressure Shell in Assembly Jig.

We have developed and successfully applied an ultrasonic through-transmission method to evaluate the fuel-tube-to-spacer joints for nonbonding. This technique uses a scanning procedure with a very narrow rectangular beam of ultrasound to inspect the entire bond width in incremental steps along its length.[5]

Preliminary scans were run on a number of joints to select a reference braze joint of sound quality. Strip-chart records from all other inspected joints were arbitrarily compared to this joint. Figure 27.6 compares typical recordings obtained for a relatively good joint and a rejectable joint as well as the "peeled" joints after spacer removal. The nonbond signal appears as an upward deflection of the recorder pen, and its amplitude and trace length are related to the amount of nonbonding. Ultrasonic diffraction by the edges of the spacer also appears as upward deflection signals. Data for joints containing bonds ranging from 25 to 95% correlated well with destructive "peel" tests.

After demonstrating feasibility, we inspected approximately 350 production fuel tubes containing 15 joints per tube. Each transverse section through the tube and attached spacer should intersect at least 0.040 in. of bond at each of the three joints. Since our beam was approximately $\frac{1}{8}$ by $\frac{1}{16}$ in., any bonding within it that would allow identical ultrasound transmission as that for a 0.040-in. transverse strip by $\frac{1}{16}$-in.-width bond was acceptable. A decibel (db) attenuator was incorporated to insert known attenuation values to simulate various braze conditions. In addition, a joint containing a small nonbond was also used to establish sensitivity levels prior to the actual inspection.

After developing the technique and calibration procedures, we modified our chain-drive tubing-inspection tank[6] to allow a relatively fast inspection of the tube-to-spacer joints. We removed the chuck rotation drive chain and replaced the tubing guides with a Teflon "V" groove slide. Figure 27.7 shows the dolly assembly with a BONUS fuel tube in place. The spacers fit the groove in the Teflon guide and automatically align themselves as they slide into it. This alignment is assured by the spring-loaded wheel shown on the left of the search-tube-and-transducer assembly

[5]K. V. Cook, *Metals and Ceramics Div. Ann. Progr. Rept. June 30, 1966*, ORNL-3970, p. 144.

[6]R. B. Oliver, R. W. McClung, and J. K. White, *Nondestructive Testing* **15**, 140–44 (1957).

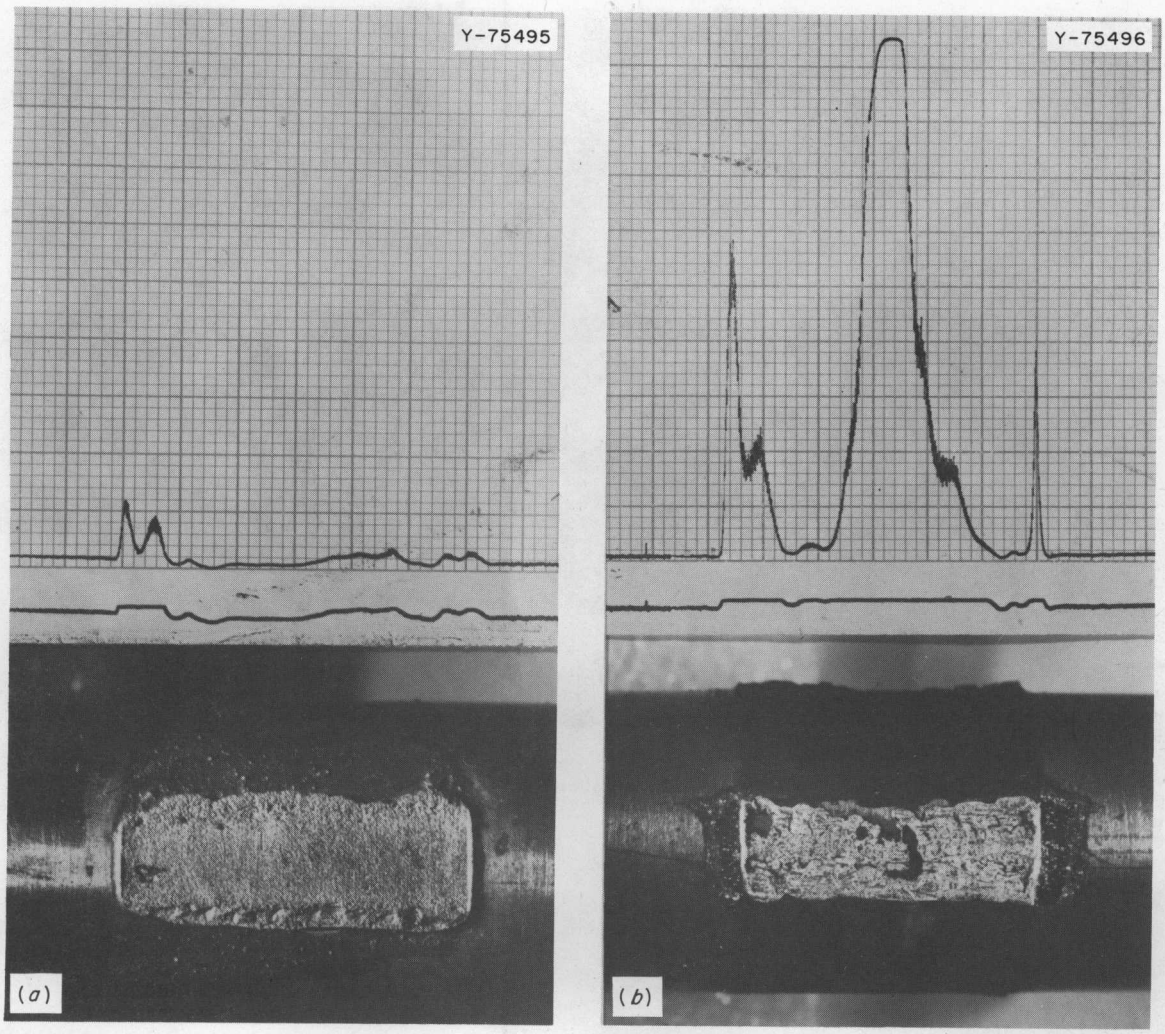

Fig. 27.6. Correlation of Ultrasonic Trace with "Peel" Tests for Fuel-Tube-to-Spacer Brazed Joints. (*a*) Sound joint. (*b*) Unsound joint.

(Fig. 27.7). Directly under the wheel is a partial spacer attached to a short fixed tube to serve as a tail stock. The opposite end is similar except the tube is held by the chuck normally used for tubing inspection. Since the drive chain to the chuck has been removed, this end is free to rotate slightly, allowing automatic alignment of the spacers in the Teflon guide. The partial spacer arrangements allow rapid loading and unloading of the tubes.

The dolly passes along the fuel tube length three times, inspecting one joint on each of the five spacers on each pass. Figure 27.8 shows the external transducer and the inner probe as the latter enters a tube-to-spacer mockup assembly. This mechanical system was used for our initial studies; however, the same transducer arrangement is required in the tubing-tank facility. Of course, the internal probe must be mechanically coupled to the same drive chains that translate the dolly to assure simultaneous probe and external transducer (or dolly) movement.

We have inspected approximately 400 tubes (over 6000 joints) and detected various braze conditions. The scanning speed was about 60 in./min; each tube requires approximately 15 min. About half of the time consumed is necessary for plug gaging, handling, and generating permanent strip-chart recordings. At least one joint was rejected per tube on the first joints; however, after the ultrasonic test was used to select the vendor, the quality improved greatly so very few tube rejections were necessary.

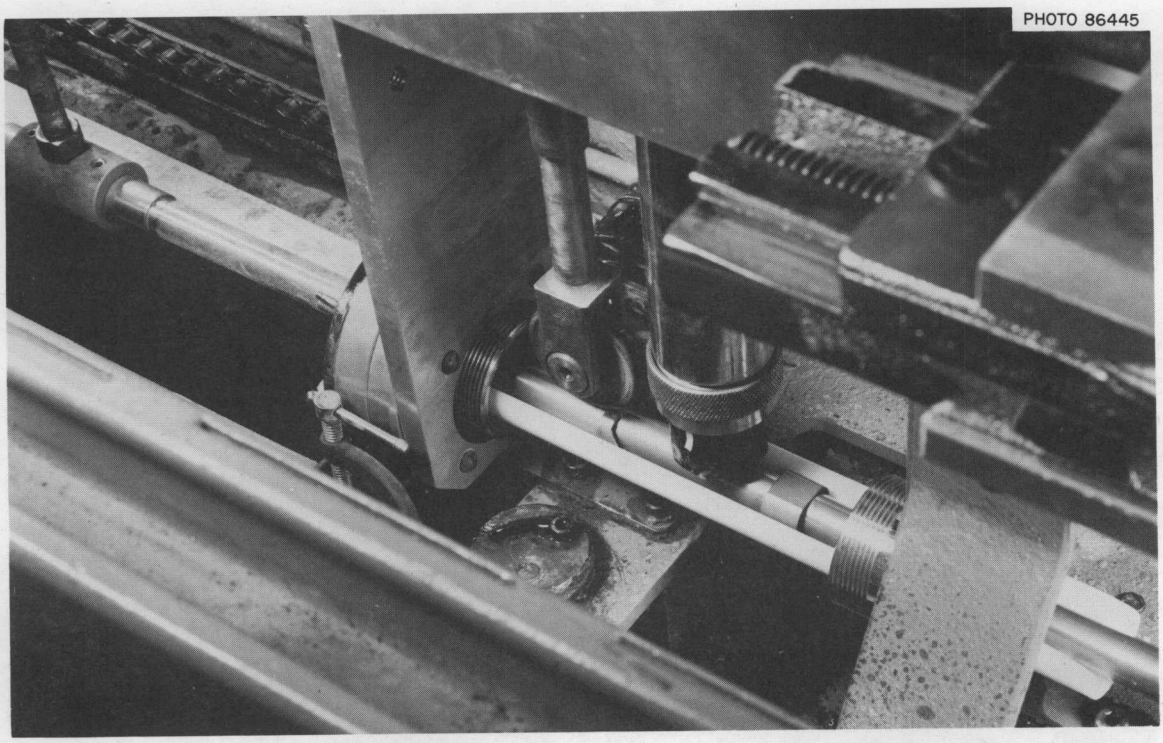

Fig. 27.7. Tubing Tank Dolly Modified for Nonbond Inspection of Tube-to-Spacer Brazed Joints.

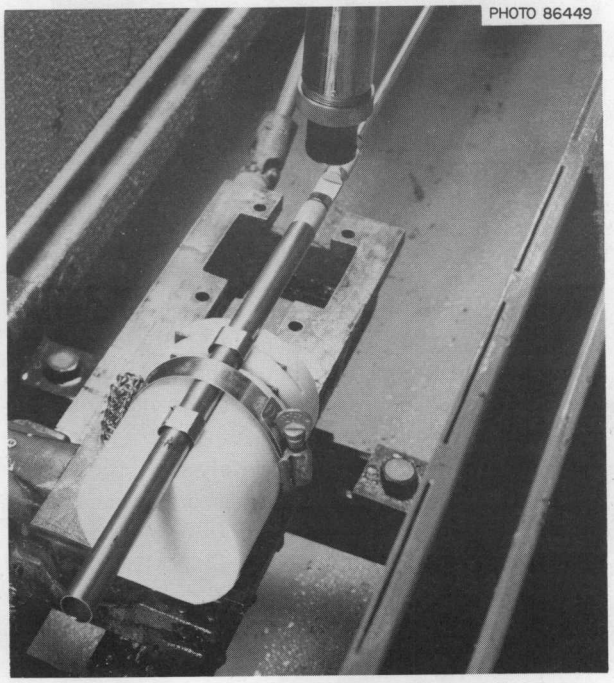

Fig. 27.8. Preliminary Scanner System Showing the Ultrasonic Probe Transducer Entering the Bore of a Tube-to-Spacer Mockup Assembly.

WELDABILITY TESTING OF SUPERHEATER MATERIALS[7]

G. M. Slaughter

Rensselaer Polytechnic Institute is testing weldability on three materials of interest for a variety of superheat applications, Inconel 600, Incoloy 800, and Hastelloy X. A large portion of this work concerns the testing of both commercial and specially processed heats. A description of progress in this phase of the program is presented in Part III, Chap. 25 of this report.

Another phase of the work concerns the evaluation of newly devised tests for weldability. The VARESTRAINT test used for the program mentioned above has been shown to be very useful in determining relative weldability and hot-cracking susceptibility of a wide range of materials.[8] The

[7]Performed under subcontract at Rensselaer Polytechnic Institute under supervision of W. F. Savage and C. D. Lundin, Department of Materials Engineering. Subcontract is funded jointly with Fuels and Materials Branch of DRDT, AEC, Washington.

[8]W. F. Savage and C. D. Lundin, "The Varestraint Test," *Welding J. (N. Y.)* 44 (10), 433-s–442-s (1965).

ORNL-DWG 67-645A

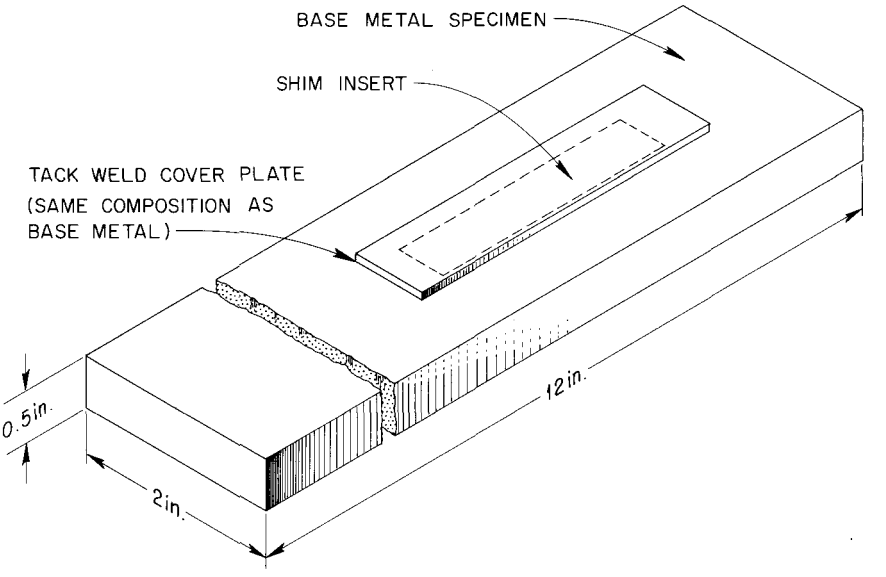

Fig. 27.9. Modified VARESTRAINT Test Specimen with "Shim" Insert.

$\frac{1}{2} \times 2 \times 12$ in. specimens required for the test, however, are quite large, considering the expense of the specially formulated and processed heats required by the ORNL-funded program.

As one means of minimizing the cost and time delays in preparing relatively large amounts of the special alloys, Rensselaer has developed the modified VARESTRAINT test specimen shown in Fig. 27.9. The body of the specimen is composed of a commercial heat of material, while the "shim insert" is composed of the base composition and varying amounts of minor elements. As the welding arc passes over the insert, it is melted and fused into the body of the specimen. Thus, by a factorial experiment, the individual and combined effects of several elements at various levels of contamination can be determined.

A second-generation VARESTRAINT-type device, nicknamed the TIG-A-MA-JIG, has also been designed to utilize the good points of its predecessor and to add several refinements. The basic principles of operation are similar to the VARESTRAINT test; however, the specimen is considerably smaller and the weld is of the stationary gas tungsten-arc type. We hope that this test will facilitate the evaluation of minor compositional effects, and, in addition, simulate the conditions of multipass welding.

GENERAL ADVISORY ASSISTANCE

G. M. Slaughter

Continuing advisory assistance is being provided to the BONUS Project in such fields as materials selection and steam corrosion. Inconel 600 was recommended as the material to be used in the replacement BONUS Reactor preheater-dryer piping installation. This recommendation was based on service conditions, recent steam-corrosion research, general availability, and overall fabricability.

Review of reports concerning superheated steam-corrosion data throughout the world is continuing. In this way, the experiences of others with a wide variety of advanced superheat materials can be used to advantage.

28. Desalination

E. A. Franco-Ferreira

The desalination program at ORNL consists of two main areas of interest. One concerns the reactor and the other the distillation plant. The problems relating to the heat source are under the cognizance of the AEC, while the evaporator-condenser is under the direction of the Office of Saline Water in the Department of the Interior.

We analyzed the costs of fabricating and using an unclad uranium metal fuel element in a desalination reactor plant. We also worked on the design and construction of a piece of experimental apparatus to test a method of producing this fuel element.

BARE-METAL FAST BREEDER FUEL REFABRICATION STUDY

A. E. Goldman T. N. Washburn

We studied the economics of refabricating a bare-metal fuel element for a low-temperature fast breeder reactor for desalting. The hexagonal fuel slug proposed for this reactor concept is shown in Fig. 28.1. Primary effort was expended on economic evaluation of potential fuel refabrication methods, because the anticipated short exposure (8000 Mwd/tonne max) of unclad uranium-plutonium-fission-product alloy suggests that the cost of refabrication would be a significant portion of the total fuel cycle cost.

A refabrication rate of 1230 kg per calendar day would be required for a 10,500 Mw(thermal) reactor complex. Detailed studies were made of processes involving melting in a graphite crucible under a halide slag and either (1) casting into a permanent molybdenum alloy mold or an expendable graphite mold or (2) casting as a solid ingot and subsequently machining finished fuel slugs from the ingot. Several other processes were reviewed in a more cursory fashion. Cost estimates for the processes ranged from $11.50/kg for the shaped mold methods to $21.50/kg for the casting and machining process. The evaluations involved estimates of manpower, capital equipment, flowsheets, consumable materials, and operating costs.

REMOTE FABRICATION OF DESALINATION REACTOR FUEL ELEMENTS

C. W. Dean R. E. McDonald
F. H. Patterson[1] E. A. Franco-Ferreira

The complex uranium alloy body shown in Fig. 28.1 has been chosen as a suitable configuration for a desalination reactor fuel. We are attempting to develop a fabrication process that would produce these bodies economically using remote facilities. Consideration of space requirements, overall costs, and reproducible quality of the end product led us to the choice of an elevated-temperature die casting technique for the production of this fuel body.

We designed the die casting machine to operate remotely at a maximum die temperature within the range 800 to 900°C in an inert or vacuum environment. The casting machine components are machined from the molybdenum alloy TZM and are internally cooled by liquid metal. Reactor Division personnel have designed and fabricated the liquid-metal cooling system to be used in conjunction with the casting machine. To date, all components have been machined and assembly is in progress. A view of the partially completed core-finger base with its

[1]Present address, Battelle Memorial Institute, Columbus, Ohio.

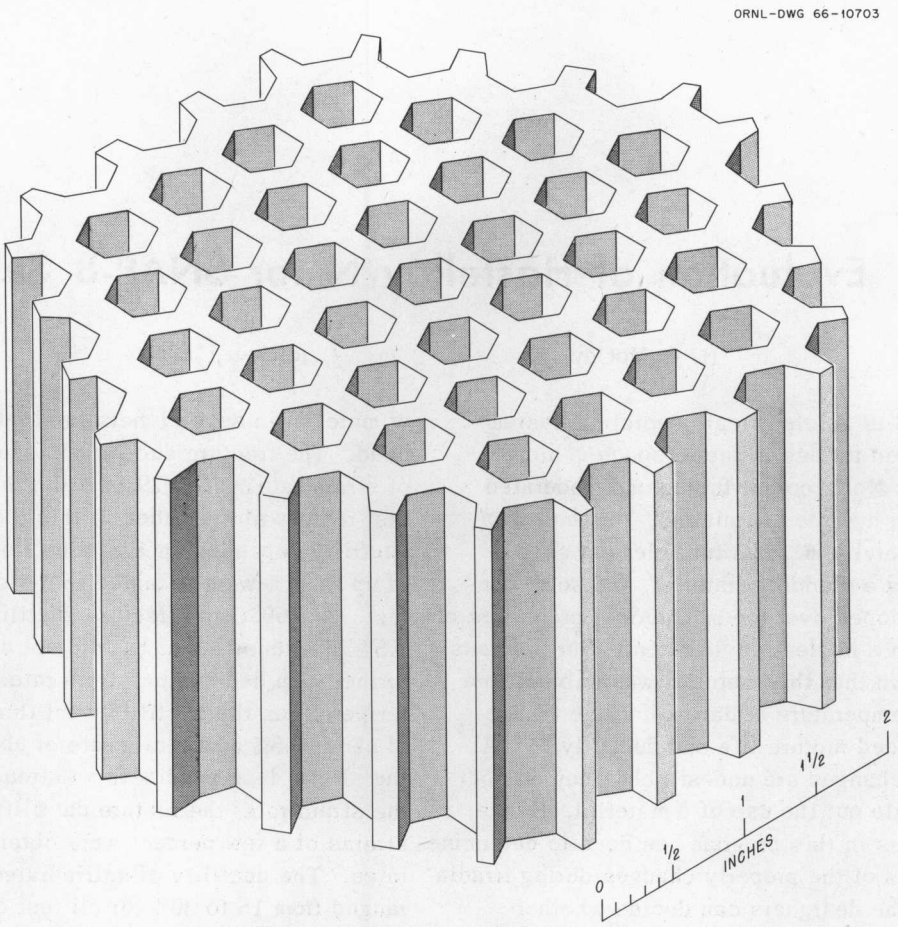

Fig. 28.1. Bare-Metal Fuel Element for Fast Breeder–Desalination Reactor.

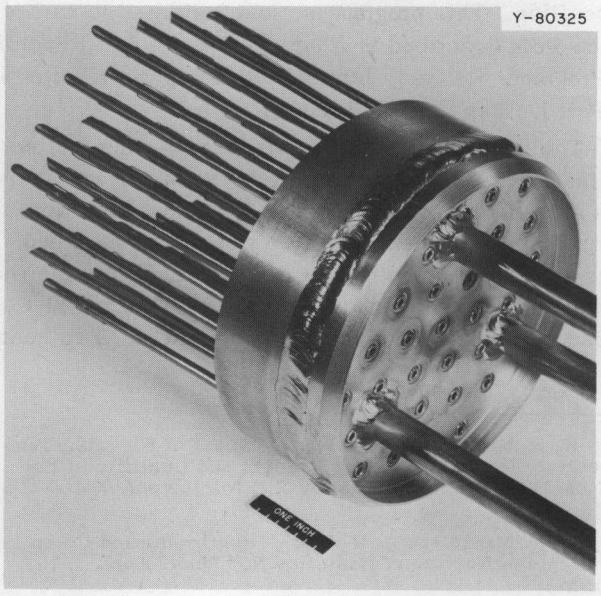

Fig. 28.2. Partially Completed Core-Finger Base Showing the Internal Cooling Tubes for Each Hexagonal Core-Finger.

coolant tubes is shown in Fig. 28.2. Some unexpected difficulty has been experienced in joining of the TZM parts. Radial and circumferential cracking was encountered in welding some of the thick walls to thin walls. We have taken remedial action and anticipate that the machine will be completed and used to evaluate the die casting technique as a plausible means of fabricating this complex shape of uranium-bearing material.

29. Evaluation of Hastelloy N for SNAP-8 Service

H. E. McCoy, Jr. J. R. Weir, Jr.

The SNAP-8 is an electrical-generating system being developed for use in future space vehicles. The reactor is NaK cooled, fueled and moderated with zirconium hydride containing ^{235}U, and reflected with beryllium. The fuel element uses Hastelloy N as a cladding material, and some concern has developed over the mechanical properties of Hastelloy N in a nuclear environment. Our previous work has shown that this material was subject to a type of high-temperature radiation damage that resulted in reduced rupture life and ductility.[1,2] Although these changes are undesirable, they do not necessarily rule out the use of a material. Hence, one of our roles in this program has been to determine the magnitudes of the property changes during irradiation, so that the designers can decide whether Hastelloy N can be utilized in a nuclear system of the proposed type. A second objective was to seek ways of improving the properties by thermal-mechanical treatments or by changes in alloy composition. This program is closely related to part of the work described in Chap. 34, Molten-Salt Reactor Program. Related electron microscopy is reported in Part I, Chap. 5 of this report.

The first experiments on standard vacuum-melted Hastelloy N involved small tensile specimens with a gage section $\frac{1}{8}$ in. diam $\times$ $1\frac{1}{8}$ in. long that were irradiated and then subjected to tensile and creep tests. These specimens were irradiated to a thermal dose of 2.3×10^{20} neutrons/cm^2 at 650 and 760°C and tested at the irradiation temperature. Two heats of material in several metallurgical conditions were used. The fracture ductility is shown as a function of strain rate in Fig. 29.1; both creep and tensile test results are included in this plot.[3] At 650°C the ductility depended upon strain rate; fracture strains of up to 11% were obtained in a slow-strain tensile test. At 760°C the fracture ductility was only 1.0 to 1.5% in a tensile test but did not decrease much further with decreasing strain rate. For both test temperatures the ductility went through a minimum of about 0.5% at a strain rate of about 0.5%/hr. As the stress decreased with an attendant decrease in the strain rate, the rupture ductility increased so strains of a few percent were obtained at low strain rates. The ductility of unirradiated specimens ranged from 15 to 30% for all test conditions investigated. Other significant conclusions from these experiments are:

1. At 760°C the rupture life was decreased by irradiation about two orders of magnitude at high stresses. The stress-rupture curves for irradiated and unirradiated specimens converged slightly with decreasing stress.
2. At 760°C, the minimum creep rate at high stresses was reduced by irradiation but was the same for irradiated and unirradiated specimens at stresses below about 10,000 psi.
3. At 650°C, the rupture life was decreased by irradiation only about one order of magnitude, and sufficient data were not available to make a conclusion about convergence at low stresses.
4. At 650°C, the minimum creep rate was unaffected by irradiation.

[1] W. R. Martin and J. R. Weir, "Effect of Elevated Temperature Irradiation on the Strength and Ductility of the Nickel-Base Alloy, Hastelloy N," *Nucl. Appl.* 1, 160 (1965).

[2] W. R. Martin and J. R. Weir, "Postirradiation Creep and Stress Rupture of Hastelloy N," *Nucl. Appl.* 3, 167 (1967).

[3] The metallurgical conditions identified symbolically on the graph will be explained by H. E. McCoy, Jr., *Effects of Irradiation on the Mechanical Properties of Two Vacuum-Melted Heats of Hastelloy N*, report in preparation.

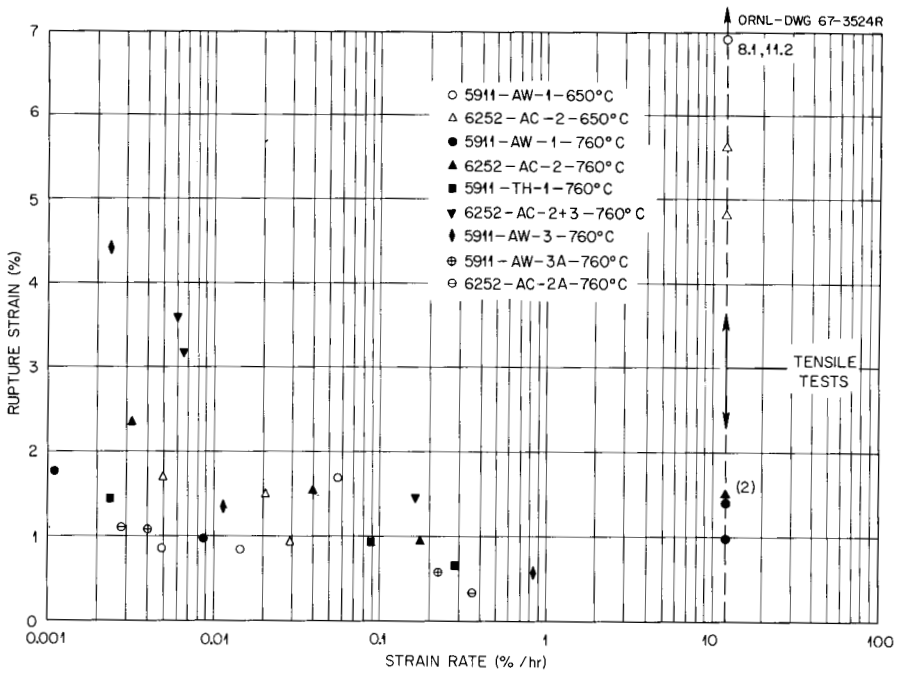

Fig. 29.1. Fracture Ductilities for Hastelloy N Under Several Test Conditions.

5. None of the metallurgical variables studied (two heats and various metallurgical states) appeared to significantly affect the postirradiation properties.

Since the service application involves tubes about $\frac{1}{2}$ in. in diameter, we ran several experiments where tubes were pressurized in the reactor.[4] The failure time and the strain at fracture were obtained by this technique. The thermal flux was 4×10^{13} neutrons cm^{-2} sec^{-1}, and the temperature was 760°C. Several significant observations were made in this study.

1. The rupture life was reduced by about an order of magnitude when the thermal-neutron dose was only of the order of 10^{18} neutrons/cm^2. The stress-rupture curves of the irradiated and unirradiated materials remained parallel.
2. The tangential rupture strains decreased from values of 7 to 10% for the unirradiated tubes to 0.1 to 2% for the irradiated tubes.
3. The creep rates were estimated and appeared to be unaffected by irradiation.

The results of the tests on rods and tubes were compared. The differences in properties could be accounted for on the basis of differences in stress state and dose at the time of failure.

The properties of Hastelloy N were improved significantly by slight changes in chemical composition. Additions of about 0.5% Ti, Zr, and Hf were studied individually, and each produced improved properties under SNAP-8 operating conditions. The details of this work are discussed in Chap. 34.

[4]H. E. McCoy, Jr., and J. R. Weir, Jr., *In- and Ex-Reactor Stress-Rupture Properties of Hastelloy N Tubing*, ORNL-TM-1906 (to be published).

30. Fuel Assistance and Procurement

R. J. Beaver

This program was initiated in the latter part of this fiscal year with the objective of assisting the Division of Reactor Development, Washington, D.C., in their engineering management of test and research reactor fuel fabrication. This assistance includes efforts to standardize specifications, review technical requirements of procurement packages, and participate in fuel procurement as well as quality control audits of fuel fabricators.

During the current fiscal year, specifications for the Engineering Test Reactor and the Advanced Test Reactor fuel elements were reviewed, specific aspects of PM type 4 core procurement were evaluated, and technical liaison and inspection were conducted in the procurement of fuel elements for the Air Force Nuclear Engineering Test Reactor.

31. Gas-Cooled Reactor Program

J. H. Coobs

Our materials effort in support of the Gas-Cooled Reactor Program is directed primarily toward development of unclad ceramic fuel elements for high-temperature gas-cooled converter reactors (HTGR's), such as the Fort St. Vrain Reactor being designed by General Atomic for Public Services Corporation of Colorado. Such elements fueled with $(Th,U)O_2$ or $(Th,U)C_2$ offer distinct advantages for high-temperature operation and neutron economy. Proposed prototype elements consist of prismatic graphite blocks containing coated-particle fuels and are designed to retain much of the fission-product activity within the fuel element to simplify maintenance.

Our program consists principally in refining the technology for depositing pyrolytic carbon coatings and preparing and testing pyrolytic-carbon-coated oxide and carbide fuel particles and coating materials. A substantial part of this effort has involved preparing and characterizing coated fuel particles for numerous irradiation tests. Results from three such experiments are included. The testing of coating materials and coated particles by heat treatment has continued, and results from fast-neutron irradiation experiments on pyrolytic carbons has assisted in understanding the behavior of coated-particle fuels and perfecting the mathematical model[1] for predicting their performance.

A small supporting effort included development of techniques for depositing silicon carbide coatings in a fluidized bed. Other supporting research consisted of a thermodynamic study of the mechanisms for conversion of oxide particles to carbides and an investigation of the materials and properties of concrete for use in prestressed concrete vessels for large power reactors.

[1]J. W. Prados and J. L. Scott, "Mathematical Model for Predicting Coated-Particle Behavior," *Nucl. Appl.* 2(5), 402–14 (October 1966).

PYROLYTIC CARBON COATINGS FORMED AT HIGH DEPOSITION RATES AT LOW TEMPERATURES

R. L. Beatty D. M. Hewette, II
J. L. Scott

Pyrolytic-carbon-coated microspheres of uranium-thorium oxide or carbide are attractive for use in fuel elements for advanced gas-cooled reactors such as the Fort St. Vrain Reactor being developed by General Atomic for the Public Service Corporation of Colorado. Normally the pyrolytic carbon coating is a composite structure having a low-density inner layer, to provide void volume to accommodate fuel swelling and fission-gas release, and a high-density outer layer, which acts as a pressure vessel. The inner layer is usually deposited from acetylene[2] and has a density in the range 0.6 to 1.1 g/cm^3. The outer layer should be isotropic and have a density greater than 2.0 g/cm^3 for adequate resistance to fast-neutron-induced distortion.[3]

One problem in coated-particle manufacture has been the difficulty of obtaining high-density isotropic coatings. Methane is commonly used as a source of carbon, but temperatures above 2000°C are required to produce isotropic structures that have densities greater than 2.0 g/cm^3. The low deposition rates (35 to 60 μ/hr) and high temperatures contribute to high fabrication costs. We found that much higher deposition rates are possible when either propane or propylene is used as the source of carbon. In

[2]H. Beutler, R. L. Beatty, and J. H. Coobs, "Low-Density Pyrolytic-Carbon Coatings for Nuclear Fuel Particles," *Electrochem. Technol.* 5(5–6), 189–94 (May, June, 1967).

[3]R. J. Price and J. C. Bokros, "Mechanical Properties of Neutron-Irradiated Pyrolytic Carbons," *J. Nucl. Mater.* 21(2), 158–74 (February 1967).

studies of structures produced at various temperatures and at several supply rates of these reactants, we could produce isotropic coatings with densities above 2.0 g/cm^3 at rates as high as 600 μ/hr at 1250°C. High-density coatings can also be obtained from methane at 1250°C, but these deposits are not isotropic. Like methane,[4] propane will produce a variety of structures if one varies the reactant supply rate and deposition temperature.[5] The anisotropy and density of deposits derived from propane are shown as contour maps in Fig. 31.1. The large region in which all deposits are isotropic and the maximum density at the lowest temperature are worthy of note in this system. Similar coatings may be produced from propylene, and the lower heat of decomposition of propylene makes it the preferred reactant in many cases. A distinct advantage of these coatings is the low level of surface contamination associated with deposits formed at low temperatures and high rates.

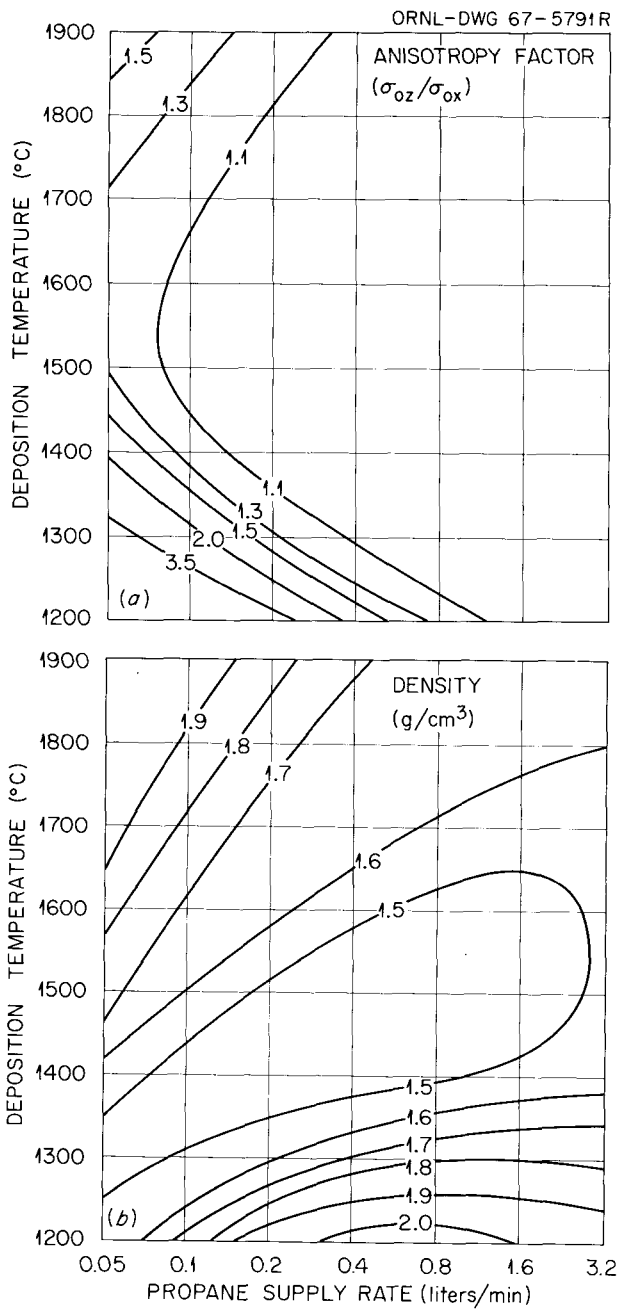

Fig. 31.1. (*a*) Anisotropy Factors and (*b*) Densities of Coatings Applied to 50 g of 450-μ-diam ThO_2 Particles in a 1-in.-diam Coater with a Total Flow Rate of 6 liters/min.

Two batches of pyrolytic-carbon-coated sol-gel UO_2 microspheres having dense outer coatings deposited from propylene were tested under irradiation at 1400°C in a sweep-capsule experiment. After 16.3 at. % heavy-metal burnup, the release-to-birth rate ratio of noble-gas fission products was about 10^{-7}. This result is equivalent to the best previously obtained with coatings derived from methane.

DEPOSITION OF SILICON CARBIDE COATINGS

H. Beutler[6]

Silicon carbide coatings designed as barriers between pyrolytic carbon coatings or as a substitute for pyrolytic carbon coatings are of potential interest for high-temperature gas-cooled reactors. The effectiveness of SiC coating for retaining some of the solid fission products (barium and strontium) has been demonstrated by the Dragon Project[7] and Battelle.[8] In addition, the physical and mechanical

---

[4] R. L. Beatty, F. L. Carlsen, and J. L. Cook, "Pyrolytic-Carbon Coatings on Ceramic Fuel Particles," *Nucl. Appl.* 1(6), 560–66 (December 1965).

[5] R. L. Beatty, *Pyrolytic Carbon Deposited from Propane in a Fluidized Bed*, ORNL-TM-1649 (December 1966), M. S. Thesis, the University of Tennessee.

[6] Noncitizen employee from Switzerland.

[7] H. J. de Nordwall and J. B. Sayers, "The Value of a Silicon Carbide Barrier in H. T. R. Fuels," paper presented at AIME Nuclear Metallurgy Symposium, Delavan, Wis. Oct. 3–5, 1966.

[8] H. S. Rosenburg *et al.*, *Postirradiation Fission-Product Release from Coated Fuel Particles*, BMI-1734 (July 1965).

properties of pyrolytically deposited silicon carbide as well as the excellent stability of SiC under fast-neutron irradiation make this material particularly attractive for coated particles. The eventual incorporation of SiC coatings in coated-particle fuel for future HTGR's will, however, depend on factors like fabrication and processing costs as well as on neutron economy. To furnish more data for such evaluations and to determine the performance of SiC coatings in comparison and in conjunction with our pyrolytic carbon coatings, we are investigating the application of SiC coatings. Silicon carbide can be derived by thermal decomposition of methyltrichlorosilane (a compound that contains silicon and carbon in the required atomic proportions) according to the following equation:

$$CH_3SiCl_3(l) \xrightarrow[H_2]{\text{heat}} SiC(s) + 3HCl(g) .$$

Since the deposition of SiC coatings from methyltrichlorosilane in a fluidized bed has been studied elsewhere,[9] we have limited our work to establishing suitable deposition conditions and studying their effect on the product properties in the range of interest for possible production applications. We investigated the effect of deposition temperatures in the range of 1200 to 1800°C using an initial charge of 35 g ThO_2 sol-gel microspheres (460-μ nominal diameter particles precoated with 45 μ of pyrolytic carbon). We ran some additional experiments at a deposition temperature of 1600°C with a 70-g charge of the same material and charges of smaller particles (225-μ-diam particles precoated with 27 μ of pyrolytic carbon) having equivalent surface areas.

The density of the silicon carbide coatings as determined by density gradient column on deposits removed from graphite disks was unaffected by deposition temperature between 1400 and 1800°C. The densities obtained varied between 98.4 and 99.7% of the theoretical density of β-silicon carbide (3.21 g/cm^3). Neither bright-field nor polarized-light metallographic examination revealed structural differences between any of these deposits. The as-polished material, shown in Fig. 31.2, appeared to be single phase and featureless. However, the deposit obtained at 1300°C was slightly less dense, and its microstructure indicated the presence of a finely dispersed unidentified second phase. X-ray diffraction showed all the deposits to be β-silicon carbide. The crystallite size varied between 250 and 460 A. We have not yet been able to correlate the variations in crystallite size with any of the controlled coating parameters (e.g., temperature, charge surface area, or contact time).

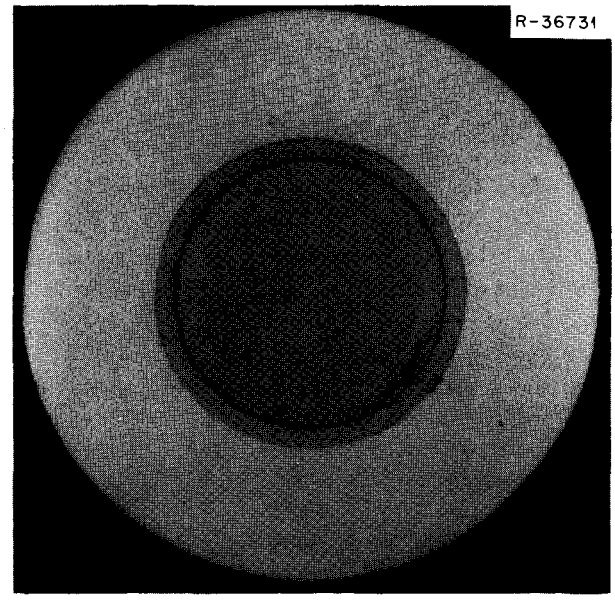

Fig. 31.2. Microstructure of SiC Coating Deposited from Methyltrichlorosilane at 1600°C on ThO_2 Microspheres Precoated with Pyrolytic Carbon. As polished. 200×. Reduced 21%.

The deposition efficiency, as calculated from the weight increase in the charge and the volume of methyltrichlorosilane consumed, increased with temperature from 18.8% at 1300°C to 74.4% at 1700°C. Increasing the charge surface area from 596 to 1186 cm^2 did not affect the density of the deposit, but the deposition efficiency changed from 72 to 80% for large particles and from 69 to 73% for small particles. All the deposits obtained were very uniform in thickness. We confirmed that SiC can be applied with no apparent difficulties by the pyrolysis of methyltrichlorosilane vapors at convenient deposition rates (1.4 to 3.9 μ/min). All the deposits obtained were high in density and appeared to be insensitive to a wide range of coating conditions; thus the process is attractive for large-scale production.

[9] R. A. U. Huddle, J. R. C. Gough, and H. Beutler, "Coated Particle Fuel for the Dragon Reactor Experiment," pp. 344–74 in *Ceramic-Matrix Fuels Containing Coated Particles*, TID-7654 (November 1962).

HEAT TREATMENT OF PYROLYTIC-CARBON-COATED OXIDE PARTICLES

H. Beutler[6] R. L. Hamner

We heat treated pyrolytic-carbon-coated oxide fuel particles at high temperatures (1) to identify high-temperature failure mechanisms that might be significant in reactor hazards evaluations, (2) to determine whether residual carbon contained in the oxide kernel has a significant effect on the thermal stability of coated particles, (3) to investigate the feasibility of graphitizing a carbon-matrix fuel element containing coated particles, and (4) to obtain estimates of the mechanical properties (particularly high-temperature rupture strength and creep behavior) of pyrolytic-carbon-coating materials.[10]

We heat treated multiple lots of coated UO_2, ThO_2, and $(Th,U)O_2$ particles in the temperature range between 2000 and 2600°C for 2-min intervals. We limited our study to coating structures and designs that, according to model predictions,[1] should survive moderate to high burnup.

All the particles tested survived heat treatments up to 2400°C without apparent failure. The only coated particles that survived the 2600°C heat treatment were those with kernels of ThO_2 and $(Th,U)O_2$ and one batch of coated UO_2 that had a high ratio of coating thickness to kernel diameter (0.87). After heat treatments at 2300°C and above, all particles showed migration of fuel into the porous coating and formation of a gap between particle and outer coatings. We attribute this gap to thermal creep induced by the internal carbon monoxide pressure.

We investigated the thermal creep behavior of outer coatings on individual particles under carefully controlled conditions. We observed large expansions (up to 42%) of the total particle diameter and concurrent thinning of the coating on UO_2 particles after heat treatments for 10 min at 2500°C. In separate experiments we investigated the effect of heat-treatment time on the dimensional changes of two outer carbon coatings that had similar properties but different conditions of deposition. Both coatings had high density, isotropic structures, and identical dimensions; they were deposited over a porous inner layer on UO_2 particles that had been obtained from the same batch. The outer coating in the first experiment was deposited from methane at 2000°C, whereas that in the second was deposited from propylene at 1250°C.

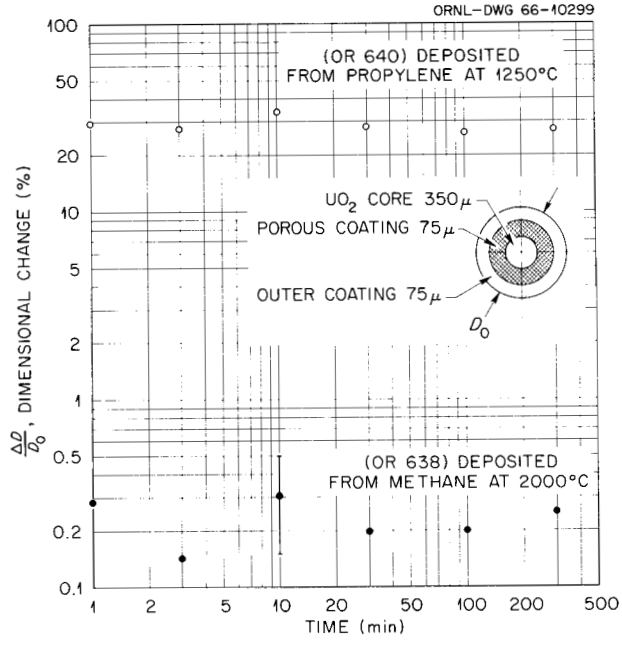

Fig. 31.3. Effect of Heat-Treatment Time on Dimensional Changes of Coated Particles at 2300°C.

As shown in Fig. 31.3, the most significant change in each coating had already occurred within 1 min, and no additional expansion could be measured after exposures up to 300 min. This behavior is somewhat surprising, since the large expansion and concurrent thinning of the outer coating observed in some coatings results in a drastic increase in stress level (up to 90%); yet, after the initial plastic deformation the coating became resistant to creep, suggesting a considerable increase in coating strength.

The initial expansion measured on coatings deposited from propylene at 1250°C was approximately 100 times that of coatings deposited from methane at 2000°C. The high-temperature coating could also be deformed to the same degree; however, approximately 10 times higher stress levels were required to produce the same effect.

We investigated structural changes of heat-treated particles by metallography. Polarized-light examination revealed an increase in preferred orientation in the pyrolytic carbon coating as a result of heat treatments. This effect was observed in initially isotropic coatings derived from methane, propane, and propylene. For ThO_2 particles with identical coatings, no effect

[10] H. Beutler, R. L. Hamner, and J. W. Prados, "Heat Treatment of Pyrolytic-Carbon-Coated Oxide Particles," *GCR Program Semiann. Progr. Rept. Sept. 30, 1966*, ORNL-4036, pp. 10–22.

of heat treatment on preferred orientation and dimensional changes was observed. Therefore, reordering of crystallites must be associated with a strain effect rather than with temperature or heat-treatment time. This is consistent with previous heat treatment results[11] on unstrained isotropic pyrolytic carbon disks, which did not reveal any changes in preferred orientation.

INFLUENCE OF PYROLYTIC-CARBON CREEP ON COATED-PARTICLE FUEL PERFORMANCE

J. W. Prados[12] J. L. Scott

We previously described a mathematical model for predicting coated-particle behavior;[1,13] it aids in identifying significant features that control coated-particle performance and assists in the planning of irradiation tests and interpreting the data. Agreement between the model's predictions and results from a high-burnup irradiation test at low fast-neutron exposure have been encouraging.[14] However, our model neglected the effect of creep, which may be significantly enhanced by fast-neutron irradiation at normal fuel temperatures.[3] Such creep could relieve coating stresses resulting from fast-neutron damage, and, thus, an elastic model's predictions of failure under high fast-neutron exposure to low burnup may be overconservative. Hence, we extended our analysis of stress and strain in spherical pyrolytic carbon coatings to include creep and performed calculations to demonstrate its influence on mathematical-model predictions of coated-particle failure.

The analysis of stress and creep in a spherical pyrolytic carbon shell subjected to internal pressure and possible anisotropic dimensional changes poses formidable mathematical difficulties due to the nonlinearity of the governing equations. However, an iterative numerical technique for creep analysis, proposed by Mendelson and his coworkers,[15] provides a means of obtaining solutions well within the accuracy of existing data by a method of successive elastic approximations. The working equations, which are presented elsewhere,[16] must be solved by trial and error for each time increment. In addition, a second trial-and-error solution is required to determine the fission-gas pressure within the particle coating as a function of fuel-kernel properties, burnup, and inner-coating free volume.[1,13]

These calculations were programmed for the CDC-1604A computer at ORNL, and results were obtained for some typical coated-particle dimensions, properties, and operating conditions. At present, the functional dependence of coating creep on temperature, stress, and fast-neutron flux and exposure are poorly defined, as are the appropriate criteria for coating failure (i.e., limiting stresses and/or strains). We have performed calculations with the radiation-creep relation suggested by Price and Bokros[3] – steady creep rate of approximately 1×10^{-27} [psi (neutrons/cm^2)]$^{-1}$ in a fast-neutron flux (>0.18 Mev) – to predict fast-neutron dose and burnup at failure for a typical two-layer-coated particle under the assumption that failure will occur when the tangential tensile stress in the outer coating exceeds 30,000 psi. Similar calculations were performed for the same particle based on a 20% higher creep rate, a 100% higher creep rate, and zero creep. The curves relating fast-neutron dose and burnup at failure for each creep assumption are known as failure loci[1,13] and are shown in Fig. 31.4 for each creep relation assumed. (These are the curves that converge on the abscissa near 20% burnup.) The relation between fast-neutron dose and burnup for several types of fuel kernels in different flux spectra are shown in the same figure; the intersection of one of these latter curves with a given failure locus represents the predicted burnup and fast-neutron dose at failure for the given fuel kernel and the coating represented by the failure locus. The significance of these relations is discussed more fully elsewhere.[1,13]

In the present case, it is interesting to note that radiation creep exerts little influence on predicted coated-particle performance for fuel kernels with

---

[11] F. L. Carlsen, Jr., "Effects of Heat Treatments on Pyrolytic Carbon," *GCR Program Semiann. Progr. Rept. Sept. 30, 1965*, ORNL-3885, pp. 28–33.

[12] Consultant from the University of Tennessee.

[13] J. W. Prados and J. L. Scott, "Mathematical Simulation of Coated-Particle Behavior," *GCR Program Semiann. Progr. Rept. Sept. 30, 1965*, ORNL-3885, pp. 53–59.

[14] J. H. Coobs, R. L. Beatty, A. R. Olsen, H. L. Krautwedel, J. W. Prados, and J. L. Scott, "Testing of a Design Analysis for Coated-Particle Fuels," *Trans. Am. Nucl. Soc.* 9(2), 421–22 (October–November 1966).

[15] A. Mendelson *et al.*, "A General Approach to the Solution of Practical Creep Problems," *J. Basic Eng.* 89, 585–98 (1959).

[16] J. W. Prodos, "Calculation of Creep in Spherical Pyrolytic-Carbon Shells Under Combined Radiation Damage and Internal Pressure," *Trans. Am. Nucl. Soc.* 9(2), 382–83 (1966).

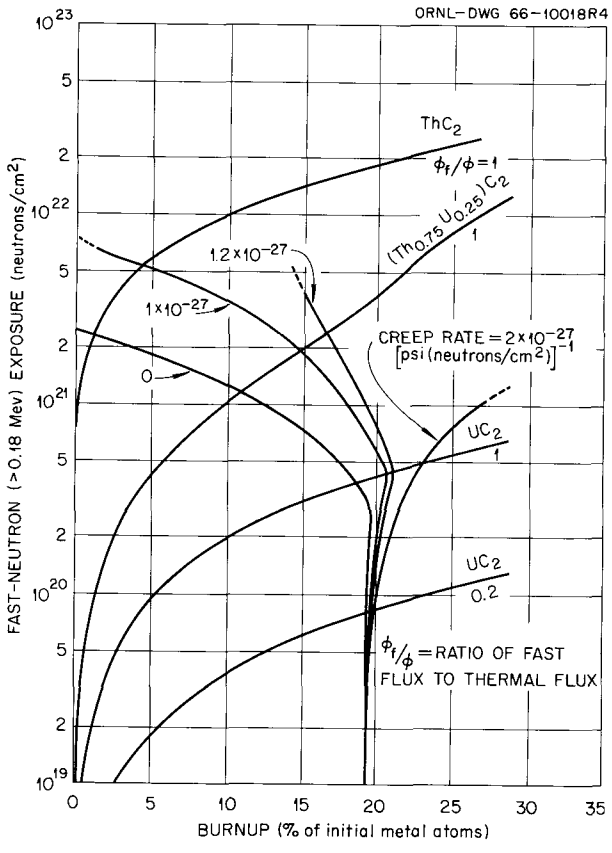

Fig. 31.4. Influence of Irradiation Creep on Predicted Failure Conditions for a Typical Coated Particle. 240-μ-diam, fully-dense $(Th,U)C_2$ kernel; 40-μ inner pyrolytic carbon layer, 37% available volume; 40-μ high-density outer pyrolytic carbon layer, anisotropy factor = 1.4.

high ^{235}U content at low fast-neutron flux. However, for kernels with high thorium content, where appreciable fast-neutron doses may be absorbed before significant fuel burnup can occur, radiation creep may serve to extend life significantly beyond that predicted by an elastic model. In fact, with sufficiently high creep rates fast-neutron-induced failure would not be predicted at all, as indicated by termination of the failure loci for the higher creep rates assumed in the present case.

We need far more precise knowledge than is presently available regarding pyrolytic carbon creep rates and failure conditions as functions of irradiation environment to assess the quantitative significance of these results. Fast-neutron irradiations of pyrolytic-carbon-coating materials are currently being planned at ORNL to aid in providing this information.

FAST-NEUTRON-INDUCED CHANGES IN PYROLYTIC CARBONS

D. M. Hewette, II

We prepared two series of samples of pyrolytic carbon disk specimens and coated particles to study their stability under fast-neutron irradiation. One series consists of specimens having high density, low anisotropy, and varying crystallite size, and the second set has high density and large crystallites with increasing anisotropy. Some specimens are in test in the Dounreay Fast Reactor, and a second experiment is being assembled.

We previously irradiated a series of coated disk specimens that had anisotropy factors ranging from 1.0 to 3.0, a wide range of densities (1.29 to 2.05 g/cm^3), and c-direction crystallite sizes L_c = 30 to 130 A. These specimens were coated along with particles for several irradiation experiments. The samples were irradiated at 950°C to a fast-neutron (>0.18 Mev) exposure of about 1.9×10^{21} neutrons/cm^2 in the B8 position of the ORR. The shrinkage parallel to the deposition plane varied from 2.3 to 11.7%, and densification of the coatings ranged from 4 to 36%. These changes were greatest in a low-density anisotropic specimen and smallest in a high-density isotropic coating, as expected.

Based on the analysis of density changes proposed by Bokros and Schwartz,[17] we plotted the changes in density with respect to the initial density defect (theoretical density minus actual) of the as-deposited material. Using the slope of a straight line fitted to these data, as shown in Fig. 31.5, a densification constant K_d of 3.33×10^{-22} (neutrons/cm^2)$^{-1}$ was calculated according to the following expression:

$$\frac{\Delta_\rho}{\rho_{theo} - \rho_0} = 1 - e^{-K_d \gamma} ,$$

where γ is the fast-neutron dose, ρ_{theo} is the theoretical density, ρ_0 is the initial density, and Δ_ρ is the density increase. This constant agrees favorably with the value of 2.8×10^{-22} (neutrons/cm^2)$^{-1}$ determined by Bokros and Schwartz[17] for pyrolytic carbons irradiated at about 1000°C to fast-neutron doses of 2.2 to 2.4×10^{21} neutrons/cm^2. For comparison, their data are also shown in Fig. 31.5.

[17] J. C. Bokros and A. S. Schwartz, "Irradiation-Induced Densification of Pyrolytic Carbons," *Trans. AIME* 239(1), 7–13 (1967).

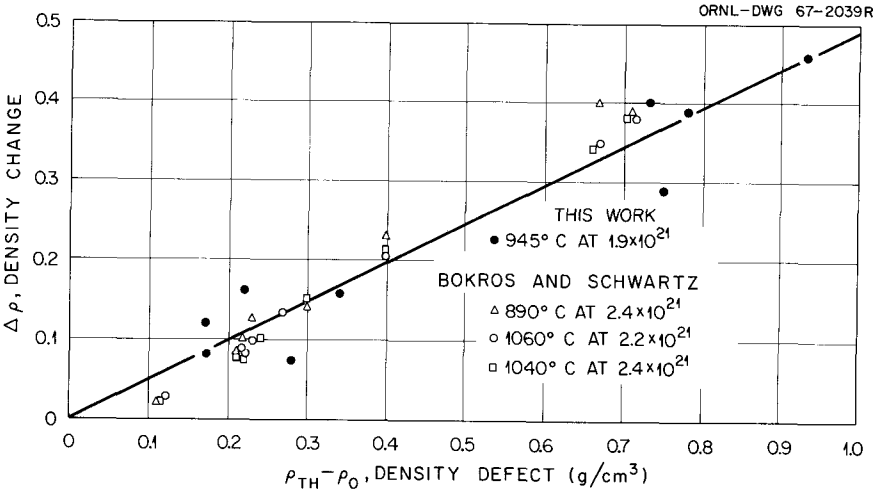

Fig. 31.5. Relationship Between Density Defect and Density Changes for Pyrolytic Carbon Irradiated at 945°C to a Fast-Neutron (> 0.18 Mev) Dose of 1.9×10^{21} neutrons/cm^2.

IRRADIATION TESTING OF COATED-PARTICLE FUELS

A. R. Olsen J. W. Prados[12]
J. H. Coobs E. L. Long, Jr.
H. L. Krautwedel[18]

Irradiation testing of sol-gel-derived UO_2 and $(Th,U)O_2$ microspheres as coated-particle fuels for use in High-Temperature Gas-Cooled Reactors is a cooperative effort of the Thorium Utilization (Chap. 36) and Advanced Gas-Cooled Reactor Programs. The irradiation tests completed have established the satisfactory performance of sol-gel-derived coated-particle fuels.[19,20] In addition, the usefulness of the Prados-Scott mathematical model[21] for predicting coated-particle performance has been established.[14]

The purpose of this program is to establish reliable performance predictions that can be combined with the process development results to establish optimum economic specifications for coated-particle fuels for a variety of specific reactor requirements. In an operating high-temperature gas-cooled reactor, both the fuel composition and the irradiation conditions will vary, and optimum coated-particle parameters must be adjusted accordingly. We have analyzed the various parameters included in the mathematical model and developed a critical path schedule for irradiation tests required to establish quantitative values for these parameters. The experiments in this program include both instrumented and noninstrumented tests of coated-particle fuels and pyrolytic carbon deposits. We use the mathematical model to design the experiments, and irradiation test results in turn provide data that are used to refine the parameters used in the model.

We completed examination of the second capsule in a series of irradiation experiments (designated as the X-basket series), which used a static noninstrumented capsule designed for simultaneous high- and low-temperature testing of annular arrays of loose coated particles in individual containers. The design of the capsule and the results of the first experiment were reported previously.[22,23] The

[18] On assignment from Kernforschungszentrum (Nuclear Research Center), Karlsruhe, West Germany.

[19] A. R. Olsen, J. H. Coobs, and J. W. Ullmann, "Current Status of Irradiation Testing of Thorium Fuels at Oak Ridge National Laboratory," paper presented at the Second International Thorium Fuel Cycle Symposium, Gatlinburg, Tenn., May 3–6, 1966; ORNL-TM-1631 (September 1966).

[20] R. G. Wymer and J. H. Coobs, "Preparation, Coating, Evaluation and Irradiation Testing of Sol-Gel Oxide Microspheres," *Proc. Brit. Ceram. Soc.* 7, 61–79 (February 1967).

[21] J. W. Prados and J. L. Scott, "Mathematical Model for Predicting Coated-Particle Behavior," *Nucl. Appl.* 2(5), 402–14 (October 1966).

[22] J. H. Coobs, A. R. Olsen, H. L. Krautwedel, J. W. Prados, and J. L. Scott, *Metals and Ceramics Div. Ann. Progr. Rept. June 30, 1966*, ORNL-3970, pp. 154–57.

[23] J. H. Coobs, H. L. Krautwedel, J. W. Prados, D. M. Hewette, R. L. Beatty, A. R. Olsen, J. L. Scott, and E. L. Long, Jr., "Analysis of Results from ETR X-Basket Experiment ORNL 43-89," *GCR Program Semiann. Progr. Rept. Sept. 30, 1966*, ORNL-4036, pp. 31–45.

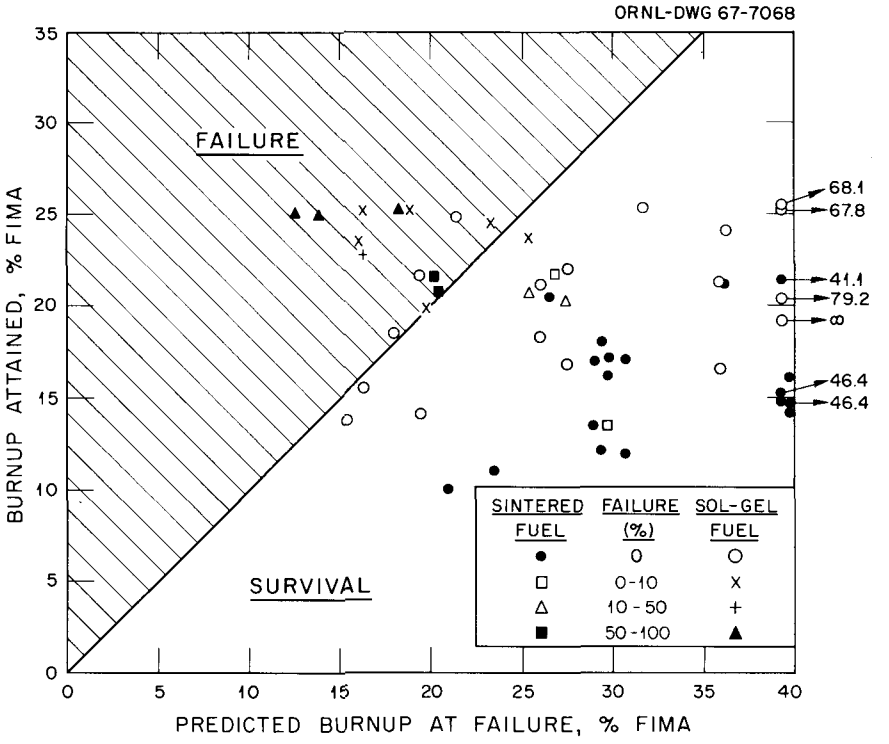

Fig. 31.6. Predicted Burnup (Fissions per Initial Metal Atom) Based on 30,000 psi Rupture Stress, 100% Release of Fission Gas from Kernels, 25% of Total Inner Coating Porosity Available as Free Volume (Except 50% for Porous Inner Coatings), and Irradiation Creep Rate of 1.5×10^{-27} [psi (neutrons/cm^2)]$^{-1}$. The particles were irradiated at temperatures in the range 350 to 1400°C, with large numbers at 400, 1000, and 1400°C.

second experiment was designed to compare the performance of coated sol-gel UO_2 microspheres with the sintered UO_2 coated particles tested in X Basket 1. The coating parameters were essentially duplicates of the first set. Inner coatings nominally 50 μ thick consisted of low-density isotropic, porous, low- or high-density laminar deposits. High-density granular or high-density isotropic deposits about 70 μ thick were used as outer coatings. Ten coating combinations on 220-μ-diam UO_2 microspheres were tested.

Figure 31.6 compares the actual fuel burnup attained by each lot of experimental particles at both high and low temperature with the burnup at failure predicted by our revised model, which includes the effects of irradiation-induced creep in the pyrolytic carbon deposits. Results are shown from both X Baskets 1 and 2. As reported recently,[24] we concluded from the evaluation of these tests that: (1) coated particles fabricated from sol-gel UO_2 microspheres perform as well as similar coated particles of sintered UO_2 or UC_2 and (2) the mathematical model does indeed predict the performance of coated-particle fuels, although the precision of these predictions is restricted by the lack of mechanical and physical property data for various pyrolytic carbon deposits. In particular the effects of temperature and irradiation on changes in these properties are not well defined. This is borne out by the different performances of identical coated particles exposed in the two experiments. The same batch performed better in X Basket 2 at a calculated irradiation temperature of 1400°C than in X Basket 1 at a calculated irradiation temperature of 1000°C.

Currently three additional X-basket capsules are being irradiated in the ETR. The conditions and objectives of all experiments in the X-basket series are listed in Table 31.1.

[24] A. R. Olsen, J. H. Coobs, D. M. Hewette, II, H. L. Krautwedel, A. W. Longest, E. L. Long, Jr., J. W. Prados, and J. L. Scott, "Performance of Pyrolytic-Carbon-Coated Sol-Gel UO_2 Microspheres in High-Burnup Irradiation Tests," *Trans. Am. Nucl. Soc.* 10(1), 96–97 (June 1967).

Table 31.1. Summary of the X-Basket Series of Irradiations of Coated Particles

X Basket	Fuel Varieties	Particle Size (μ)	Number of Coated Particle Variations[a]	Peak Burnup (% FIMA)[b]	Status	Objective[c]
1	Sintered UO_2 and UC_2	220	12	~25	Examined	Compare coated particle model performance characteristics with fuel performance
2	Sol-gel and sintered UO_2	210	13	~25	Being examined	Compare sol-gel microsphere performance with sintered spheroids
3	Sol-gel $(U,Th)O_2$	230	10	~25	In-reactor	Determine the effects of the thorium-to-uranium ratio on fuels with the same fissile content
4	Sol-gel $(U,Th)O_2$	280	15	~20	In-reactor	Test fuel particles prepared for irradiation in Dragon; investigate coating optimization and fast flux effects on particle performance
5	Sol-gel $(Th,U)O_2$ and $(Th,U)C_2$	450	10	~12	In-reactor	Evaluate the performance of fertile fuels and fast flux effects including radiation creep on coated-particle behavior

[a]Coated-particle variations include both coating parameter and fuel composition variables to make up the different batches of coated particles that are normally loaded into separate graphite containers for each batch during irradiation. Each capsule contains 28 to 30 such containers.

[b]Fissions per initial metal atom.

[c]All tests are planned on the basis of the Prados-Scott coated-particle performance model, which is constantly being revised as the results of these and other tests become available. Fuel in the individual containers is irradiated at either 400 or 1400°C.

MECHANISMS AND KINETICS OF THE CONVERSION OF UO_2 TO UC

Terrence B. Lindemer

The conversion of microspheres of UO_2 to UC_2 via solid-state reaction with carbon or carbon-bearing material may be the most economical process for producing UC_2 microspheres. Since UC is an intermediate phase in the reaction, a study of the kinetics and mechanisms for the conversion of UO_2 to UC was deemed important for a complete understanding of the overall conversion process.

Several conclusions could be drawn from the initial experiments performed to establish the experimental conditions necessary for the conversion process.[25] First, a uniform reaction was not obtained when the carbon source was a porous pyrolytic carbon coating on the UO_2 microspheres; it was necessary to react the UO_2 in a dynamic bed of powdered graphite to get a uniform reaction. Second, the main transport mechanism for carbon appeared to be volume diffusion; this requires intimate contact of the carbon with the microsphere during the conversion process. Third, the "UC" product phase produced under the present experimental conditions was shown by x-ray techniques to be nonstoichiometric.

[25]T. B. Lindemer and J. M. Leitnaker, "Mechanisms and Kinetics of the Conversion of UO_2 to UC," *GCR Program Semiann. Progr. Rept. Mar. 31, 1967*, ORNL-4133, pp. 3–10.

A kinetic model that exists in the literature[26] is apparently applicable by a standardized procedure to the experimental data now being produced. This model permits the evaluation of the reaction rate constant k by two independent methods. Preliminary data at 1612°C indicate that the values of k determined by the two methods agree within 10% or less; we consider this agreement to be very good.

CONCRETE FOR PRESTRESSED CONCRETE PRESSURE VESSELS

J. G. Stradley

Prestressed concrete pressure vessels are expected to be used for many future reactors. It is generally believed that prestressed concrete offers a cost and safety advantage over steel, and, more importantly, it allows larger vessels to be field erected than would be possible with steel.

During the past year, we reviewed the literature on the concrete materials used for prestressed concrete pressure vessels. We concluded that construction of such vessels from the current designs would not require any major technological breakthrough in concrete materials. However, basic information on the materials is needed to assure the capability and endurance of these vessels for nuclear service. We recently started to seek information about concrete in four general areas: (1) characterization of the concrete being used in the ORNL creep studies,[27] (2) mechanisms for the rheology or workability of concrete, (3) mechanisms of moisture movement in concrete under stress and temperature gradients, and (4) effects of irradiation on concrete.

[26] R. E. Carter, *J. Chem. Phys.* 34(9), 2010–15 (1961).

[27] J. M. Corum, "Basic Program for Investigating the Time-Dependent Deformation of Concrete Under Multiaxial Stress Conditions in Prestressed Reactor Vessels," *GCR Program Semiann. Progr. Rept. Sept. 30, 1966*, ORNL-4036, pp. 256–62.

32. High Flux Isotope Reactor

G. M. Adamson, Jr.

The High Flux Isotope Reactor (HFIR) is a beryllium-reflected, light-water-cooled and -moderated unit with a thermal power output of 100 Mw. It was designed by ORNL with special core features to operate at an average power density of 2000 w/liter and to attain an unperturbed flux of 5×10^{15} neutrons cm^{-2} sec^{-1} in the central trap region for production of research quantities of the transplutonium elements. The reactor core consists of two concentric arrays of involute-contour fuel plates containing highly enriched ^{235}U in the form of an aluminum-clad dispersion of U_3O_8 in aluminum.

During the first year of full-power operation, 13 of these high-power fuel assemblies operated for an average core lifetime of 2300 Mwd and presented no operating difficulties. While performance to date has been outstanding, there is considerable operational and economic incentive to reduce cost and upgrade performance. Consequently the present materials effort is being directed toward cost reduction of the presently designed components and exploring reliable means for achieving higher fuel loading to extend lifetime and increase the temperature capability.

FUEL ELEMENT MANUFACTURE

R. W. Knight

We are assisting Metals and Controls, Inc.,[1] the production contractor for the HFIR fuel elements, in refining their manufacturing processes to reduce cost, to make the operation more foolproof, and to improve the quality of the finished fuel element. After a review of new bid proposals, another contract was let with Metals and Controls for an additional three years supply of HFIR fuel assemblies; hence, the rate of production has been increased from two to three per month. The manufacturing process used for HFIR fuel elements has been described.[2,3]

In May of 1967, the final fuel element of the first contract was completed and shipped to ORNL. None of the 33 fuel assemblies has met all of the specifications; however, after careful review by ORNL, all elements have been accepted for use at design power. The deviations from the specification are random, and there is no indication that relaxing the specifications in any specific area would greatly benefit the fuel element production. Figure 32.1 shows the frequency of typical infractions. It should be noted that more than one infraction of a given category may occur in the same fuel element. The largest number of deviations from the specifications are dimensional and are associated with the side plate final machining. These side plates after machining are so thin that just laying the individual fuel elements on their sides in cradles will cause them to go out of round.

Fuel homogeneity is a problem area, not because of a large number of rejections, but because rejections that do occur and all questionable areas must be evaluated by ORNL reactor engineers to determine the suitability of the rejected fuel plate.

[1] Division of Texas Instruments, Inc., Attleboro, Mass.

[2] J. Binns, G. M. Adamson, Jr., and R. W. Knight, *Fabrication Procedures for Manufacturing High Flux Isotope Reactor Fuel Elements*, ORNL-TM-1628 (November 1966).

[3] R. W. Knight, J. Binns, and G. M. Adamson, Jr., *Fabrication Procedures for Manufacturing High Flux Isotope Reactor Fuel Elements*, ORNL report in preparation.

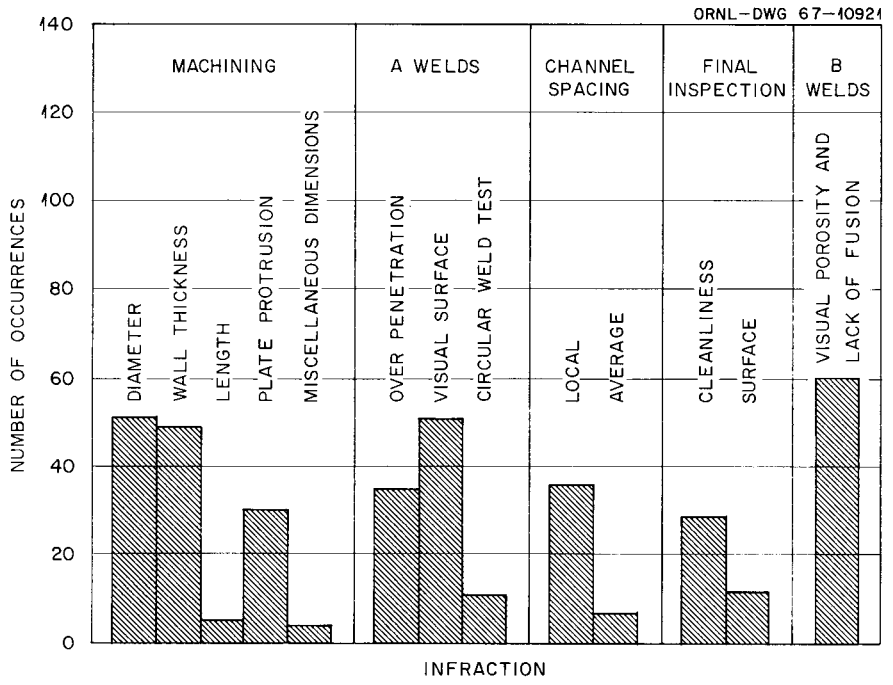

Fig. 32.1. Out-of-Specification Items on 30 Outer and 30 Inner Fuel Elements.

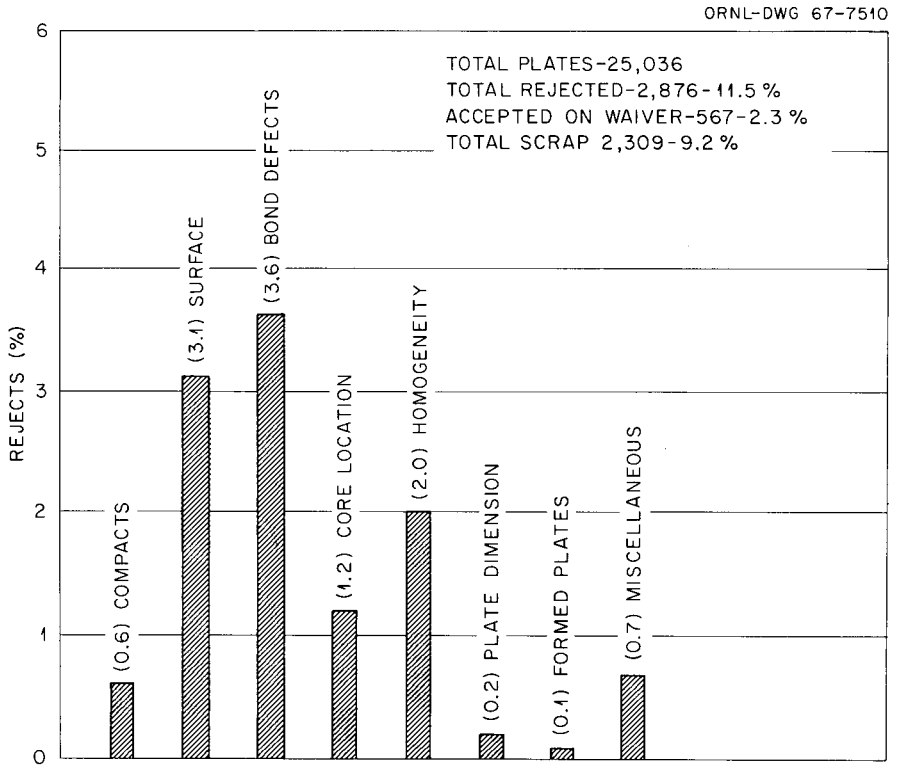

Fig. 32.2. HFIR Fuel Plate Recovery Data.

This problem stems from the fact that the specifications cover only the worst operating conditions and, in addition, the homogeneity scanners evaluate different lots of fuel differently. Uranium oxide with a high surface area will show an apparent high fuel loading on the scanner, thus causing increased rejections.

The welding of the fuel elements continues to be another problem area. Porosity standards for the type B (side-plate-to-end-fitting) welds have been modified to permit more porosity, thereby reducing the rejection rate. The type B weld parameters being used at this time appear to be the best compromise between porosity and lack of fusion that can be achieved with the equipment being used. Occasional overpenetration for short lengths is a continuing problem with the type A (fuel-plate attachment) welds. Although in most instances the amount is within that permitted by the specifications, it is sufficient to indicate a lack of adequate control.

Fuel-plate spacing has been good; however, some problems have been encountered at the bottom end of the outer annulus. The pressure on the fuel plates of the welding trunion rings resulting from side-plate shrinkage occasionally will cause them to deform. New trunion rings have been designed, and a repair procedure has been approved. We expect that this problem will be short lived. Within the bodies of the fuel elements, the fuel-plate spacings have been consistently good.

Fuel-plate production has been running smoothly. In continuing production of 25,036 fuel plates, an excellent overall rejection rate of only 9.2% was encountered (Fig. 32.2). The major causes of rejections were bond defects (blisters) and surface damage. Reasons for these rejections are continually being investigated, and short-term gains are achieved periodically.

Starting material for second-round production has been ordered. The new aluminum powder and B_4C that have been received are sufficiently different from the original material to require a demonstration as to their suitability for HFIR use. The aluminum powder contained more –325 mesh material. The B_4C differed in chemical content of boron and foreign materials. Investigation of the aluminum powder is complete, and the new material is acceptable and will be used in production shortly. The B_4C is still being investigated.

STATISTICAL EVALUATION OF METALS AND CONTROLS QUALITY-CONTROL DATA

M. M. Martin

The quality control data from representative lots of HFIR production fuel plates at Metals and Controls were examined statistically to better evaluate the current product specification and/or fabrication process. The requirements[4] subjected to analysis were (1) thickness variability of degassed fuel compacts (±0.003 in.), (2) cladding thickness (average greater than 0.010 in., minimum greater than 0.008 in.), (3) variability of total uranium (±1%) and boron (±10%), and (4) variability of boron within the inner-annulus plates (±35% in 0.20-in.^{2}-area samples).

Fuel Compact Thickness

The permissible deviation of the individual thickness measurements made on each core is ±0.003 in. Such a value results in an acceptance rate of 99.0%. Rates of 93 and 99.9% would be predicted if values of ±0.002 and ±0.004, respectively, were used. Even at the ±0.004 value, which has been accepted on waiver, no deleterious effects – such as blistering, cladding thinning, and severe edge bowing or end feathering of the core in the rolled fuel plate – were encountered.

For each compact, a mean thickness is determined from five measurements, and these means are averaged for each lot of 24 compacts. The mean values for 99% of the compacts differed less than ±0.002 in. from the average values for their lots. The average lot thicknesses depend on the pressing pressure, which varies from batch to batch of material. Of the 57 lots in the analysis, the total range of lot averages was only ±0.001 in.

Cladding Thickness

The specification requires that all fuel plates shall have an average cladding thickness on each surface greater than 0.010 in. and a minimum of 0.008 in. Conformity to these requirements for each annulus of the fuel assembly is established

[4]G. M. Adamson, Jr., and J. R. McWherter, *Specifications for High Flux Isotope Reactor Fuel Elements*, ORNL-TM-902 (August 1964).

through destructive testing of at least one fuel plate that is representative of that element. A total of 68 observations from three complete cross sections (ten measurements per section per side) and the core ends (two measurements per end per side) represents the data for average cladding thickness. The minimum cladding thickness from each of the five metallographic samples is also determined over 100% of the exposed cladding surface.

Our analysis encompassed 18 inner and 29 outer plates from 44 lots. In general, the results on average cladding thickness indicate no significant difference between (1) inner and outer plates, (2) fuel and filler side cladding, and (3) the three complete cross sections as well as the ten measurement locations per section per side. The complete absence of dogboning in the HFIR fuel gradient core is confirmed, since the cladding over the core ends is approximately 0.2 mils thicker than at the three center sections. The plates within either the inner- or outer-annulus group are considered, however, to be different statistically, although the total range for average plate cladding is only from 10.8 to 11.6 mils. For the fixed measurement locations, the maximum point variation that is expected around the particular plate average is ±1.6 mils at the 99.9% confidence level.

While the major concern with cladding is with the minimum thickness, techniques are not available for determining such a value. Therefore, the specification was separated into two independent parts; a maximum depth of scratches and surface defects (0.002 in.) and the minimum wall thickness measured metallographically in the samples discussed above (0.008 in.). The latter measurement in mainly an indication of the penetration of the individual hard U_3O_8 particles into the cladding.

Figure 32.3 shows how fuel-plate recovery would be affected by specifying various minimum cladding values. These data were determined from the 47 examined plates. The significant separation of the two curves results from the U_3O_8 particles at the top surface protruding into the filler section and not into the cladding as at the bottom. The location of the minimum thickness is independent of both the five sampling sections and the position within the sections. Obviously, for the bottom cladding the minimum thickness is a stringent requirement, and high rejections would result from any additional tightening. However, a more detailed examination of the data reveals that not many cladding areas approach the minimum, and few deep scratches or surface defects are found on any one plate. Since the chance of the two occurring at the same spot in coincidence with an area of maximum temperature or corrosion is quite remote, some relaxation may be possible.

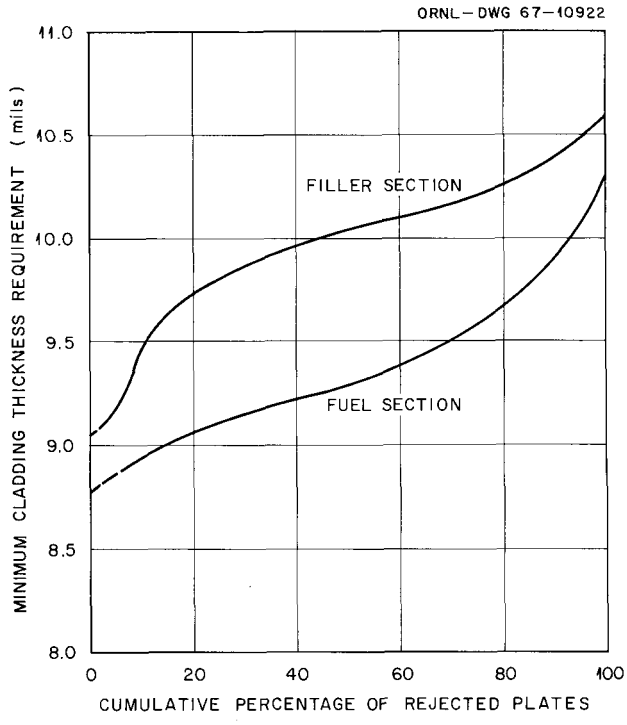

Fig. 32.3. Effect of Minimum Cladding Thickness Requirements on Rejection Rate of HFIR Fuel Plates.

Total Uranium and Boron Contents

We examined the fuel (U_3O_8) and poison (B_4C) loadings that were assigned to 1107 outer and 513 inner fuel plates. Only the inner plates contain boron. The maximum actual deviations of uranium from that specified were, respectively, 15.18 g ^{235}U ± 0.6% and 18.44 g ^{235}U ± 0.2% for inner and outer plates. The total range for boron around the specified mean of 0.0164 g was only ±2%. The permissible variations of ±1% for uranium and ±10% for boron are definitely loose requirements and can be tightened, if the need exists, without a significant increase in rejection rate.

Boron Distribution

To minimize the radial peak-to-average power-density ratio in the HFIR, the poison surface densities of the inner-annulus plates vary nonlinearly

Table 32.1. Statistical Analysis of Boron Distribution in 13 Inner-Annulus Fuel Plates

Row	Coordinates of Punchings (in.)		Number of Replicate Punchings	Boron Content (μg)					Tolerance Limits[a] (%)
				Specified		Found			
	Distance from Reference Edge of Plate	Distance from Center of Plate		Minimum	Maximum	Minimum	Maximum	Average	
1	0.545	0, ±4	39	316	656	384	469	437	±14
		±8	26	316	656	414	536	465	±14
2	1.935	0, ±4	39	102	212	131	178	155	±26
		±8	26	102	212	134	179	160	±26
3	2.955	0, ±4	39	185	383	218	292	270	±16
		±8	26	185	383	262	310	284	±16

[a]Tolerance limits calculated at the 95% confidence level to include at least 99% of the distribution for a sample size of 61.

across the width but are constant along the length. The specification requires that the amount of boron in 15 fixed regions of 0.20-in.^{2} area must be distributed to within ±35% of the nominal loading. The data from 13 plates that were randomly selected from 85 lots are statistically evaluated in Table 32.1. Row 2 is located on the longitudinal traverse of minimum boron content and rows 1 and 3 are near the edges of the fuel core. As indicated in the table, the average boron content is significantly larger near the core ends than near the middle. Plates fabricated at ORNL have exhibited this identical effect, in that increasing distance from the center gave higher boron contents.[5] The predicted tolerance limits and maximum and minimum observation, however, are well within the permissible variation. A more stringent requirement of ±30% from nominal should not result in an increased rejection rate.

ADVANCED FUEL-PLATE FABRICATION

M. M. Martin

We are investigating the fabricability of HFIR fuel plates containing a 25% increase in uranium loading. The investigation includes use of "dead burned" U_3O_8, which is equivalent to that now being used for HFIR fuel elements, and UAl_3-type intermetallics. In general, the study comprises (1) the characterization of the uranium-bearing compounds and aluminum-matrix powder; (2) compressibility of the duplex fuel compacts; (3) evaluation of possible fabrication difficulties, such as uranium segregation, thinning of the cladding near the core ends, and excessive fuel particle degradation during rolling; and (4) calibration of our continuous x-ray attenuation homogeneity scanner for the various fuel materials.

Our study is incomplete to date; yet, from present results, no deleterious effects in fabrication are expected from the increase in loading for the U_3O_8 fuel. Based on previous U_3O_8 calibration work, two inner-annulus plates that contain fuel sections of Al–31.2% U_3O_8 and Al–37.1% U_3O_8 exhibited fuel distribution that met the HFIR specifications on homogeneity.

The outer plate containing the higher loading of 49.8% U_3O_8, however, attenuated the x-ray beam to levels beyond our calibration. New correlations for attenuation vs uranium content are required for all of the UAl_3-bearing plates, and the work is now in progress.

The in-reactor performance of aluminum-base dispersion-type fuel plates is believed to depend

[5]M. M. Martin and C. F. Leitten, Jr., *Metals and Ceramics Div. Ann. Progr. Rept. June 30, 1965*, ORNL-3870, p. 218.

Table 32.2. Densification of Experimental Fuel Dispersions

Type of Fuel	Dispersoid Concentration (wt %)	Dispersoid Concentration (vol %)	Pressed[a] Density of Compacts (% of Theoretical)	Increase in Density by Rolling: Actual Increase[b] (%)	Increase in Density by Rolling: Relative to Maximum (% of Maximum Theoretical[c])
U_3O_8-Al	31.2	12.2	94.4	3.0	52.7
	37.1	15.4	94.3	2.7	44.4
	42.5	18.2	93.8	2.4	36.5
	49.8	22.8	92.6	2.9	35.5
UAl_3-Al	36.1	17.0	92.8	4.9	63.8
	43.3	21.3	91.9	4.9	56.4
	49.9	25.7	90.8	5.1	51.9
	58.9	32.2	88.9	4.7	38.6
$UAl_3Si_{0.4}$-Al	36.8	17.5	92.5	4.9	65.2
	44.2	21.9	91.3	5.8	64.5
	50.8	26.2	89.8	5.9	56.9
	59.9	32.9	88.0	5.7	42.2

[a]Compacts cold pressed at 22.5 tsi.

[b]Increase in density, $D = 1 - \rho_{pressed}/\rho_{rolled}$.

[c]Maximum theoretical increase, $D_{th} = 1 - \rho_{pressed}/\rho_{theoretical}$.

somewhat upon the amount of void volume initially present in the clad core. The unoccupied regions, if in the near vicinity of the fuel particle, should provide a place to accommodate particle swelling and fission gases. Control of the proper quantity of voids and their location will then extend the maximal operating temperature and burnup conditions.

Some densification of the HFIR fuel compacts occurs in rolling of the plates. As shown in Table 32.2, the fuel section densifies independently of uranium concentration and initial density, but the UAl_3 and U_3O_8 behave differently. The difference between dispersions of stoichiometric UAl_3 and thermally stabilized $UAl_3Si_{0.4}$ in aluminum do not appear to be significant.

Figure 32.4 shows the total amount of unoccupied space that remains in the various roll-clad dispersions after fabrication. The volume percent of voids does not differ greatly for the present inner and outer plates and the inner plates that contain

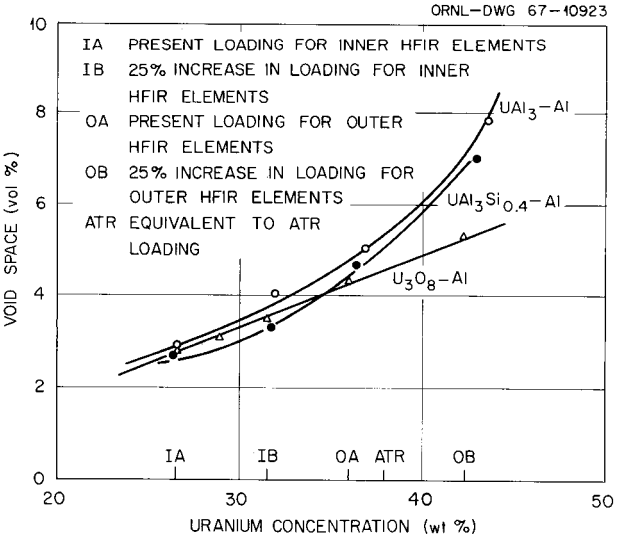

Fig. 32.4. Effect of Type and Concentration of Fuel Compounds on Volume of Voids That Remain in Roll-Clad Aluminum Fuel Dispersions.

a 25% increase in fuel. The outer-annulus dispersion of highest loading exhibited significantly more voids, which can conceivably accommodate increased quantities of fission gases without deleterious swelling. We plan to test this hypothesis in miniature irradiation sample plates.

BONDING OF TYPE 1100 TO TYPE 6061 ALUMINUM

J. H. Erwin

Procurement of blister-free type-1100-alclad 6061 aluminum for HFIR has become increasingly more difficult, particularly in plate at least as thick as the 0.350 in. required for frame materials. Type 1100 aluminum cladding promotes bonding in both the fuel and control plates during hot rolling. The plates must be blister free, and all internal mating must exhibit grain growth across more than 50% of the bond line length.

To circumvent the need for the type 1100 aluminum cladding on the frame material, we investigated the quality of bond produced between bare type 6061 frames and the type 1100 aluminum clad on cover plates as a function of (1) rolling temperature, (2) total billet reduction at a constant rate of reduction per mill pass, and (3) surface preparation of billet parts. Our evaluation of bonding is made primarily from the interruption of interfacial grain growth observed in a minimum of two 1-in.-long metallographic samples representing a group of identical plates.

We found no effect, as shown in Table 32.3, in the bond between scratch-brushed type 1100 and type 6061 aluminum that was accountable to rolling temperature in the range 475 to 550°C with reductions of about 24% per mill pass. However, the interfacial grain growth increased parabolically as the total billet reduction ratio increased in the range 6.1 to 27.1.

The attractiveness of chemical etchants as a replacement for surface preparation by scratch brushing the billet parts is shown by the data presented in Table 32.4. Chemical etchants, including both acid and caustic, without and in combination with scratch brushing, were used to treat the surfaces of the type 1100 cladding on the cover plate and the bare type 6061 frame prior to assembly of the standard production-size billet. The reduction schedule followed production practice: two passes at 15%, then six at 24%, and finally two at 15%. The bond at the interfaces in the plates rolled from acid-cleaned parts, when assembled directly after cleaning, showed considerable improvement over the scratch-brushed parts (interfacial grain growth of roughly 75 and 40% respectively). The "Mil Etch"-cleaned plates exhibited 85 and 86% interfacial grain growth and the "Oakite 160" plates exhibited 89% interfacial grain growth. In addition, these plates

Table 32.3. Interfacial Grain Growth in Roll Bonded Type 6061 Aluminum to Alclad Cover Plate for Various Reductions and Rolling Temperatures[a]

Rolling Temperature (°C)	Grain Growth for Various Reduction Ratios[b] (%)									
	6.1		9.6		12.6		15.6		27.1	
475	29	34	39	51	54	55	62	70	76	79
475[c]	19	35	31	53	46	46	48	61	74	75
500	35	38	44	42	53	55	64	49	73	64
525	24	25	40	50	55	52	54	68	73	63
550	23	28	41	55	42	48	66	54	38	45

[a] All surfaces were scratch brushed.

[b] For each reduction ratio, the first percentage is for a transverse section and the second for a longitudinal section.

[c] These values were remeasured after the specimens had been reground and repolished.

Table 32.4. Evaluation of Surface Preparations for Roll Bonding 6061 Aluminum to 1100-Alclad 6061 Aluminum at 500°C and a Total Reduction Ratio of 9.6 (7.6 Hot)

Surface Preparation	Number of Plates Fabricated	Number Rejected		Interfacial Grain Growth[a] (%)	Bond Rating[b]			
		Blisters	Nonbond		A	B	C	D
Scratch brush only	20	0	0	39	13.1	1.3	165	67
				37	20.5	0	108	67
Caustic etchant followed by acid pickle								
Mil Etch[c]	20	0	2	86	0	23.7	37	154
				85	0	39.0	38	272
No. 1268 etchant[c]	14	0	1	74	0	29.2	71	300
				71	0	27.6	64	346
Acidic etchant only								
Chromate cleaner[d]	20	1	1	85	0	22.2	49	222
				72	0	19.0	48	137
$H_3PO_4 + HNO_3$ mixture	20	0	1	77	0	20.0	68	145
				76	0	16.7	59	177
Etchant followed by scratch brush								
NaOH	20	0	0	51	1.3	4.0	95	90
				54	0	4.9	71	107
$H_3PO_4 + HNO_3$ mixture	20	0	0	71	0	11.8	58	135
				68	0	10.3	59	131
Surface treatment followed by 35 min, 500°C preheat of frame								
Scratch brush	10	0	0	39	9.9	1.2	117	92
				42	14.3	1.8	110	71
Oakite 160[e]	20	0	1	89	0	28.6	29	168
				89	0	39.0	31	234
$H_3PO_4 + HNO_3$ followed by scratch brush	20	0	0	44	3.9	0	118	68
				43	16.1	0	138	68

[a]The first line for each surface treatment is for a transverse specimen, the second longitudinal.

[b]Bond rating from metallographic samples:

A = number of measuring increments showing no interfacial grain growth per 100 increments (40 mils)

B = number of measuring increments showing full interfacial grain growth per 100 increments (40 mils)

C = maximum length (mils) of no interfacial grain growth shown by sample

D = maximum length (mils) of full interfacial grain growth shown by sample.

[c]Wyandotte Chemicals, Wyandotte, Mich.

[d]Industrial Colloids and Chemicals Inc., Knoxville, Tenn.

[e]Oakite Products, New York, N. Y.

exhibited only short lengths (about 30 mils) without metallurgical bond and relatively long lengths of continuous bond.

After the previously described work, we roll-bonded four unfueled standard size HFIR fuel plates and one unfueled standard size control plate in which the interface was type 6061 to type 6061 aluminum. The parts were cleaned with "Oakite 160" just previous to billet assembly. The fuel-plate billet was reduced to 0.0625 in. thickness in 30% reduction increments at 500°C; the control plate billet was rolled according to standard practice – about 13.5% reduction increments at 500°C with the billet evacuated. The metallurgical bond in these plates appeared to be equal to that obtained with the present practice using the alclad materials. No blisters were observed, the cladding could not be stripped from the core, and samples of the fuel plate examined by metallography indicated interfacial grain growth equal to 90% of bond line length with maximum lengths of 26 mils showing no grain growth interruption.

U_3O_8 PRODUCTION

R. W. Knight

Production of U_3O_8 at the Y-12 Plant is continuing. An additional order for 1500 kg was placed as fuel for 108 fuel assemblies. Quality of the U_3O_8 has been good and has easily met specifications except for surface area, which has fluctuated between 0.045 and 0.068 m^2/g. This range of surface area does not affect fuel plate manufacture but is troublesome during homogeneity inspection. The x-ray scanner cannot differentiate between surface area changes and fuel loading changes. An increased surface area in a fuel plate will appear as an increased fuel loading.

The Y-12 plant has sought experimentally and found means to control surface area to 0.05 ± 0.005 m^2/g. Fuel plates are being fabricated from fuel with several known surface areas. These plates will be scanned with the x-ray scanner and the apparent fuel loading will be calculated. These data will be plotted against surface area in an attempt to find a more desirable range of surface areas.

If a more desirable range of surface area becomes apparent, new standards for the x-ray scanner will be made and the new range of surface areas will be specified.

A report[6] has been issued discussing the method used to produce the U_3O_8 and comparing the properties of several types of U_3O_8.

HFIR WELDING DEVELOPMENT

Fuel-Plate-to-Side-Plate Welding

R. G. Donnelly

Several alternative methods have been investigated to improve the controllability and quality of the joints between fuel plates and side plates of the HFIR fuel elements. These methods have included pulsed-arc welding, electron-beam welding, and fluxless brazing.

As reported previously,[7] pulsed-arc welding seemed to have several potential advantages. These included (1) lower total heat input, which would tend to minimize shrinkage and distortion; (2) better arc controllability; and (3) the ability to use larger diameter wires, which, in turn, would simplify wire feeding. However, we found that, while satisfactory welds could be made, none of these advantages were of sufficient significance to justify replacing the existing low-energy gas metal-arc welding process.

Electron-beam welding, however, did seem to exhibit several distinct advantages over the present arc-welding techniques. These include (1) no filler-metal addition required, (2) no weld grooves required, (3) excellent control of weld penetration, (4) much less distortion, and (5) much less cleanup machining required. To demonstrate the feasibility of this process, a flat test section was assembled and electron-beam welded at the Y-12 Plant. Since the very heavy wall of the standard side plate was not required, $\frac{1}{4}$-in.-thick side plates were used and were slotted on one side only for the fuel plates. Welding conditions were developed on single $\frac{1}{4}$-in.-thick plates, and the optimum conditions were then used to weld the test assembly.

---

[6] W. J. Werner and J. R. Barkman, *Characterization and Production of U_3O_8 for the High Flux Isotope Reactor*, ORNL-4052 (April 1967).

[7] R. G. Donnelly, *Metals and Ceramics Div. Ann. Progr. Rept. June 30, 1966*, ORNL-3970, pp. 169–70.

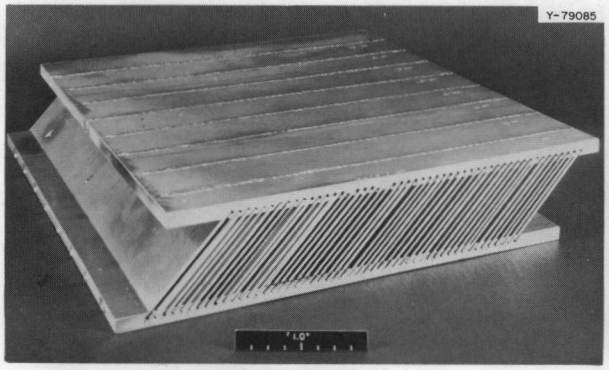

Fig. 32.5. Flat-Plate Test Sample Dummy Fuel Plates Electron-Beam Welded to Type 6061 Aluminum. Note poor fit-up.

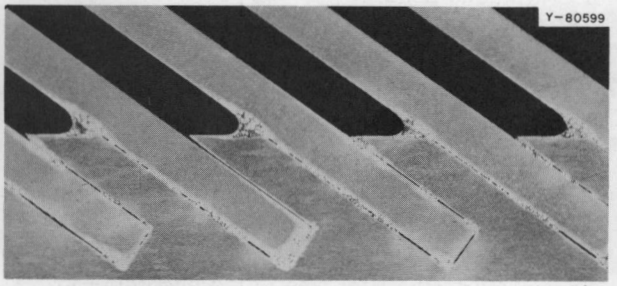

Fig. 32.7. Fluxless-Brazed Fuel-Plate-to-Side-Plate Joints. Although the process appears highly promising, methods of obtaining improved flow are necessary. 10×. Etch: H_2O, HF, HCl, HNO_2. Reduced 49%.

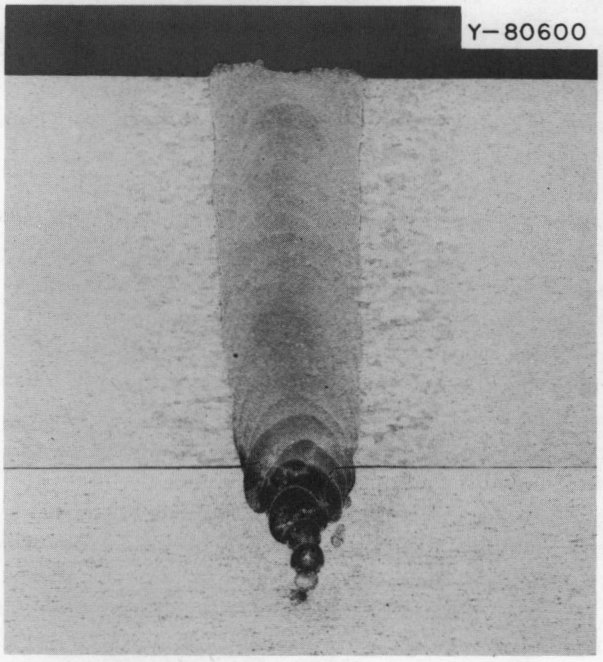

Fig. 32.6. Fuel-Plate-to-Side-Plate Electron-Beam Weld. (No filler-metal addition). 10×. Etch: H_2O, HF, HCl, HNO_2.

As can be seen from Fig. 32.5, very little cleanup machining would be required. A cross section of one on the welds is shown in Fig. 32.6. Penetration was consistent and did not seem sensitive to fuel-plate fit-up. One difficulty with this technique is that, since type 6061 aluminum was the material joined, cracking was found in every joint; a more weldable alloy will be required for the side plates. The weld-metal cracking problem is overcome in the present arc-welding procedure by using type 4043 aluminum alloy filler metal.

Brazing of aluminum fuel elements offers the potential advantages of lower cost, high fuel-plate-to-side-plate bond strengths, reduced and more uniform distortion, and more rigidity. However, conventional aluminum brazing techniques are not acceptable because they require highly corrosive halide-containing fluxes, which are extremely difficult, if not impossible, to remove completely. In addition, the conventional aluminum-base brazing alloys flow at temperatures somewhat above the blister-annealing temperature used for the fuel plates. A fluxless method of brazing aluminum has been developed in the aerospace industry; it uses Al–10% Si or Al–12% Si alloys (brazing temperature 570 to 580°C) as filler metals. The parts are brazed in highly purified argon at reduced pressure. For evaluation, we prepared a flat sample assembly and sent it to Avco Corporation for fluxless brazing. A photomicrograph of a section from this assembly is presented in Fig. 32.7. The results of this first test are promising; however, only partial bonding was obtained, and additional studies to optimize joint clearance and alloy preplacement procedures are obviously indicated.

If further experiments indicate that the process can be applied advantageously to the HFIR fuel-element fabrication problem, a modest effort to develop improved alloys with somewhat lower flow temperatures appears to be in order.

Coolant Channel Spacer Attachment

C. H. Wodtke

Previously, we reported[8] development work and production of the first flow-test element having wire ribs ultrasonically joined to simulated fuel plates. An additional similar test element with flat plates was produced in cooperation with the Plant and Equipment Division Fabrication Department. Here, ribs were machined to provide 0.002 in. nominal clearance between rib and adjacent plate. (In the first element, clearance was 0.004 in. nominal.)

In the latest flow-test element, shown in Fig. 32.8, simulated fuel plates have the involute contour of HFIR fuel plates. In this case, the clearance between the rib and the adjacent plate was intended to be in the range 0.002 to 0.004 in. The group of plates was given backup support by filling the extraneous space with epoxy.

The previously developed ultrasonic joining procedure was applied to attach the wire ribs to flat plates (before forming). Slight dimensional changes in plate width and rib location necessitated minor modifications to the fixture. Plates were subsequently press-formed to the required contour after the ribs had been machined to proper height. Bonds between rib and plate appeared sound under visual examination, even though the ribs were on the convex side during forming. The assembly adequately withstood the flow test, and fretting-type corrosion did not seem to be a problem.

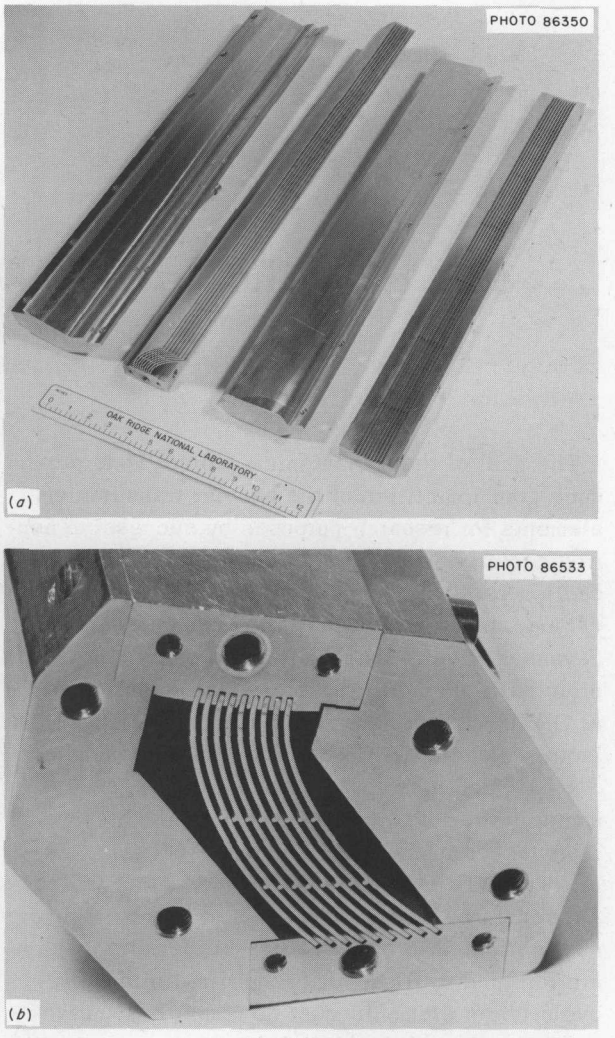

Fig. 32.8. Flow-Test Element with Ultrasonically Welded Spacer Ribs. (*a*) Partially assembled. (*b*) Completed assembly.

[8]C. H. Wodtke and J. W. Tackett, *Metals and Ceramics Div. Ann. Progr. Rept. June 30, 1966*, ORNL-3970, pp. 171–72.

33. High Flux Isotope Reactor Target Development

A. L. Lotts

The goal of the transuranium project is to produce gram quantities of the heavier transuranium elements for research purposes by successive neutron captures in ^{239}Pu. The first part of the production path, the conversion of ^{239}Pu to ^{242}Pu, ^{243}Am, and ^{244}Cm, was carried out in reactors at Savannah River. Target elements containing principally these three isotopes were fabricated at ORNL and are being irradiated in the High Flux Isotope Reactor (HFIR) at a flux of approximately 3×10^{15} neutrons cm^{-2} sec^{-1}. The target elements are removed periodically from the HFIR and reprocessed in the Transuranium Processing Facility (TRU). At the TRU, the product actinides are separated and the target actinides are recovered and fabricated into recycle target elements, which are returned to HFIR for further irradiation. Recycle target elements must be remotely manufactured because of the high gamma and neutron radiation associated with the contained isotopes.

Our tasks have included the design and validation of the original targets, the development of equipment and techniques for fabricating these elements both in a glove box and remotely, the monitoring of the performance of the target elements in HFIR, and the design and fabrication of modified targets that may withstand the HFIR service conditions.

At this point we have completed the irradiation program for confirmation of the HFIR target element design; we have fabricated the necessary ^{242}Pu targets; we have essentially completed the cold testing of the equipment in the transuranium facility; we have refurbished targets that were irradiated at the Savannah River Laboratory; and we have commenced an investigation of the mechanism of failure of targets that had been irradiated at Savannah River and in the HFIR to fission of approximately 25% of the plutonium. In addition, a program for short-range and long-term solution of the limited burnup problem of the targets was initiated.

TRANSURANIUM TARGET FABRICATION EQUIPMENT STATUS AND OPERATION

J. E. Van Cleve E. J. Manthos
M. K. Preston, Jr.[1]

During irradiation in the HFIR, the target actinide oxides are encased in an assembly consisting of 31 individual elements. Each target element[2] consists of 35 individually jacketed pressed pellets, each composed of a mixture of 12 vol % actinide oxides dispersed in aluminum. The pellets are contained in a type X8001 aluminum tube with discontinuous fins. These fins are subsequently attached to the target rod sheath, which positions the element in the target array and through which cooling water flows during reactor operation. Manufacture of the targets consists of three parts, (1) pellet fabrication, (2) assembly and welding of the target element, and (3) inspection of the finished element.

The development of the equipment to remotely fabricate these targets in the TRU has been essentially completed, the equipment has been installed, and part of it has been used for the inspection and refurbishment of irradiated target elements. During remote checkout of the target fabrication process some of the components were modified to improve their reliability.

---

[1]General Engineering and Construction Division.

[2]M. K. Preston, Jr., J. E. Van Cleve, J. D. Sease, and A. L. Lotts, *Metals and Ceramics Div. Ann. Progr. Rept. June 30, 1966*, ORNL-3970, pp. 179–81.

After equipment installation was completed at the TRU, a detailed set of operation and maintenance procedures was completed. These procedures had been under development for some time but could not be completed until the equipment had been installed and operated in the TRU.

During the past year, 18 ^{242}Pu rods, fabricated at ORNL and irradiated in a Savannah River reactor for approximately one year, were inspected and refurbished before they were irradiated in the HFIR. Details of this work are covered below.

Cell 3 in the TRU contains the equipment necessary to fabricate and inspect pellets. The inability to maintain accurate calibration of the various weighing systems resulted in poor reliability of this equipment. A systematic examination of this problem is presently under way. Short periods of operation have allowed the examination of the remaining equipment, and it has operated satisfactorily.

Cell 2 contains the equipment required to load a target rod with inspected pellets, weld the top end plug, and helium leak test the welded target rod. Difficulties with the pellet inspection and loading equipment were traced to fasteners having been loosened by the vibratory action of the pellet feeders. Each of these pieces has been secured with a locking compound. The remaining auxiliary equipment appears to be satisfactory.

The assembly machine is being used out of the cell until a spare unit is fabricated. Several alignments and relocations of components have been performed to make remote maintenance easier. The construction of a spare unit is approximately 70% complete.

Final assembly, inspection, and cleaning of the target element are performed in cubicle 1. Most of the equipment in this cell was extensively used during inspection of the SRL target elements. Minor adjustments and modifications were made on some of the equipment. This confirmed the procedures envisioned for removal and maintenance of equipment components. All three of the inspection systems were used, and the dimensional inspection apparatus was removed for calibration and is the only piece of equipment not yet operational in cell 1. Final checkout of the device is awaiting the fabrication of redesigned components. The helium leak test station and the radiography station operated satisfactorily.

To eliminate the fretting discussed in the next section from future fabricated target elements, the hex-can staking fixture has been redesigned to include one additional staking assembly for staking the three additional sets of fins. This subassembly has been fabricated and is being adjusted and checked out before being installed remotely on the in-cell unit.

The operation of the remainder of the equipment has in general been excellent, with very few malfunctions of equipment or operator errors. The procedures for this cubicle are in excellent condition, since this particular cell has been in use for an extended period of time, primarily in refurbishing SRL target elements.

A final report covering the engineering and developmental testing of the equipment is being prepared.

INSPECTION AND REFURBISHMENT OF TARGET ELEMENTS IRRADIATED AT SRL

E. J. Manthos M. K. Preston, Jr.[1]

Eighteen HFIR target elements that had been irradiated at Savannah River for approximately one year were inspected and refurbished at the TRU Facility during the period June 1 to September 1, 1966, before they were inserted in the HFIR for further irradiation.

Each SRL target element originally contained 10 g of ^{242}Pu, dispersed in 35 aluminum pellets. These rods were identical in design, except for ^{242}Pu loading, to the targets that were to be irradiated in HFIR only.[3] Each target was centered in an outer hex-can sheath by four sets of target rod positioning fins. The upper three sets of fins each contained three fins spaced 120° apart, and the lowest set of fins contained six fins positioned 60° apart. The outer sheath was mechanically attached or staked to the target rod at the bottom six positioning fins only.

Each of the 18 SRL rods was transferred to TRU and examined visually with a telescope, dimensionally inspected, helium leak tested, and refurbished before it was further irradiated in HFIR.

Suspicions that the unattached fins had been damaged by fretting during reactor operations at Savannah River were confirmed. We observed fin

[3] J. D. Sease, *The Fabrication of Target Elements for the High Flux Isotope Reactor*, ORNL-TM-1712 (March 1967).

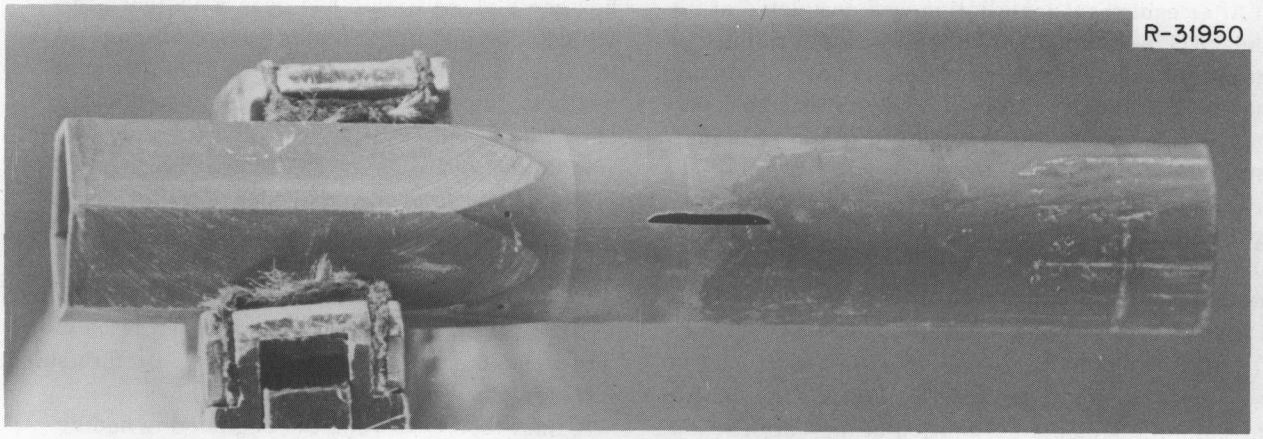

Fig. 33.1. Top of Hex-Can Sheath from HFIR Target Rod, Showing Hole Worn in Sheath by Positioning Fin. 1.4×.

wear on all of the unattached target rod fins. Half of the target elements examined also had a hole in the top of the hex-can sheath where a fin had worn through just below the hex portion of the sheath, as shown in Fig. 33.1. All of the damaged sheaths were removed, and new sheaths were installed and staked to the lower six positioning fins.

A spider-type spacer, a $\frac{3}{8}$-in.-long split ring with either three or six legs to fit the inside of the hexagonal area, was placed in the hexagonal area of the refurbished rods to center the target in the sheath. Three-legged spiders were installed on the first two refurbished rods and six-legged spiders were installed on the remainder.

Expect for the fin damage, the integrity of the elements was good. We saw no evidence of localized swelling, the appearance of the welds and cladding was normal, and none of the elements showed a leak during helium leak testing. On those rods where the hex-can sheath was removed, the positions of the pellets were visible because of differences in oxide coloring on the rod. We transferred 17 of the 18 target rods to the HFIR for further irradiation. One of the rods was retained at TRU for dissolution and chemical analysis.

The design of future target rods has been modified to reduce the possibility of fretting. All fin positions will contain six equally spaced fins, and the sheath will be staked at each fin location. We removed 29 previously manufactured unirradiated ^{242}Pu target rods of the three-fin design from the HFIR storage vault and staked them at each fin location.

IRRADIATION TESTING OF PROTOTYPES

A. R. Olsen J. D. Sease
A. E. Richt J. P. Moore

The postirradiation examination of the four prototype target elements in the ETR to validate the target element design was reported previously.[4,5] The four rods, which had been loaded with ^{239}Pu, performed satisfactorily to burnup levels of 2.4×10^{21} fissions/cm^3. However, the extent of reaction between the dispersed PuO_2 and the aluminum matrix was found to be strongly temperature dependent. In addition, preliminary work on the fabrication of the dispersion had indicated a strong influence of oxide particle size on the thermal conductivity of the dispersion. Consequently, a detailed investigation of the effects of actinide oxide particle-size distribution and volume percent loading on the thermal conductivity of the cermet was initiated.

This investigation is not completed, but some preliminary conclusions can be derived from the available data. Surprisingly, the thermal conductivity is essentially constant up to 120°C, the upper temperature limit of our comparative thermal conductivity apparatus. This behavior for those

[4]A. R. Olsen, J. D. Sease, A. E. Richt, J. W. Ullmann, and S. D. Clinton, *Trans. Am. Nucl. Soc.* 9(1), 66 (1966).

[5]A. R. Olsen, J. D. Sease, A. E. Richt, and J. W. Ullmann, *Metals and Ceramics Div. Ann. Progr. Rept. June 30, 1966*, ORNL-3970, pp. 182–84.

specimens where the oxide is the continuous phase requires further investigation. The volume percentage of the oxide has a significant effect but is secondary to the oxide size-distribution effect on the thermal conductivity. The addition of particle sizes less than 325 mesh (44 μ) greatly reduces the thermal conductivity. The use of ceramic grade powders, that is, particle sizes less than the 5 μ typical of powders precipitated from solutions, must be avoided, since they reduce the thermal conductivity to approximately 5% of that of a comparable volume loading of larger size oxide. With usable-size particles of oxide, the sintering associated with the thermal degreasing of the pressed cermet pellets (3 hr at 550°C) increases the cermet density 3% and approximately doubles its thermal conductivity. We have substituted UO_2 for the higher actinides to obtain a thermally induced reaction between the aluminum and the oxide. The effect of this reaction on the thermal conductivity has not yet been determined.

EXAMINATION OF FAILED TARGET ELEMENTS

A. L. Lotts E. J. Manthos
J. E. Van Cleve

Irradiation of 17 HFIR target rods that had been exposed in the Savannah River Reactors (SRL) for approximately 12 months and in the HFIR for approximately 5 months was terminated when curium activity was discovered in the HFIR primary water coolant system. Suspect target rods were isolated in HFIR, and inspection of these rods revealed that 5 of 17 SRL rods had failed.

Actually, two groups of target rods were being irradiated in the HFIR at the time of failures. In addition to the group of target rods irradiated in the SRL reactors for approximately 12 months and subsequently stored in water for 8 months, a second group of targets (14) had been irradiated only in HFIR. Before irradiation in HFIR, the SRL targets were inspected in the TRU Facility, and new outer sheaths were installed on 9 of the 17 rods, as described above.

Both groups of targets were of similar design, except that the SRL targets contained 10 g of ^{242}Pu each while the virgin targets contained 8 g. Each target contained 35 individually jacketed aluminum-matrix pellets, in which the ^{242}Pu was dispersed as PuO_2. The target rod cladding and outer hex-can sheath were fabricated from X8001 aluminum. Both the SRL and virgin targets were irradiated for approximately the same length of time in HFIR; however, the SRL targets were distributed in the outer circumference of the target array and consequently received a greater fast-neutron dose. We are presently investigating the mechanism of failure of these elements, and the results of our preliminary work are reported below.

Examination at TRU

E. J. Manthos J. E. Van Cleve

Nine suspect SRL target elements were inspected at TRU. We determined that five of these rods (56A, 34A, 6A, 10A, and 35A) had failed; we definitely saw cracks on the cladding of four of the rods. Element 56A was selected for detailed examination. We inspected it visually, obtained diameter measurements, and x-rayed, leak-tested, and pressure-tested the end plug welds at the TRU.

The end plugs, including the welds, were removed and tested to ascertain that the failure was not caused by a defective weld that had allowed water to enter the rod. Radiographs of both welds showed that they were normal. The welds were leak checked with 80-psi air while the end plugs were submerged under water, and we saw no evidence of a leak. They were also hydraulically tested with water at pressures exceeding 7000 psi; we saw no leakage of water through the welds. Since none of the above tests indicated that the welds were defective, subsequent rods were inspected only visually, dimensionally, and for fission gas activity buildup on a charcoal trap in a nitrogen sweep test. Heat generated by the targets prevented vacuum leak testing for helium.

Rod 56A contained the target tubing crack as shown in Fig. 33.2. Oriented 90° from the crack and slightly below it was a mechanically damaged region (a chatter mark), Fig. 33.3, which was covered with oxide similar in appearance to the oxide on the remainder of the rod. Two of the other rods each contained two cracks in the same line; one of these failures is shown in Fig. 33.4. A fourth visibly failed rod contained three cracks; two were in line and the third was 120° away.

All of the cracks occurred in the same general region, at the midpoint of the pellet column, which also coincided with the maximum neutron flux in the rod. The as-received target-rod tubing con-

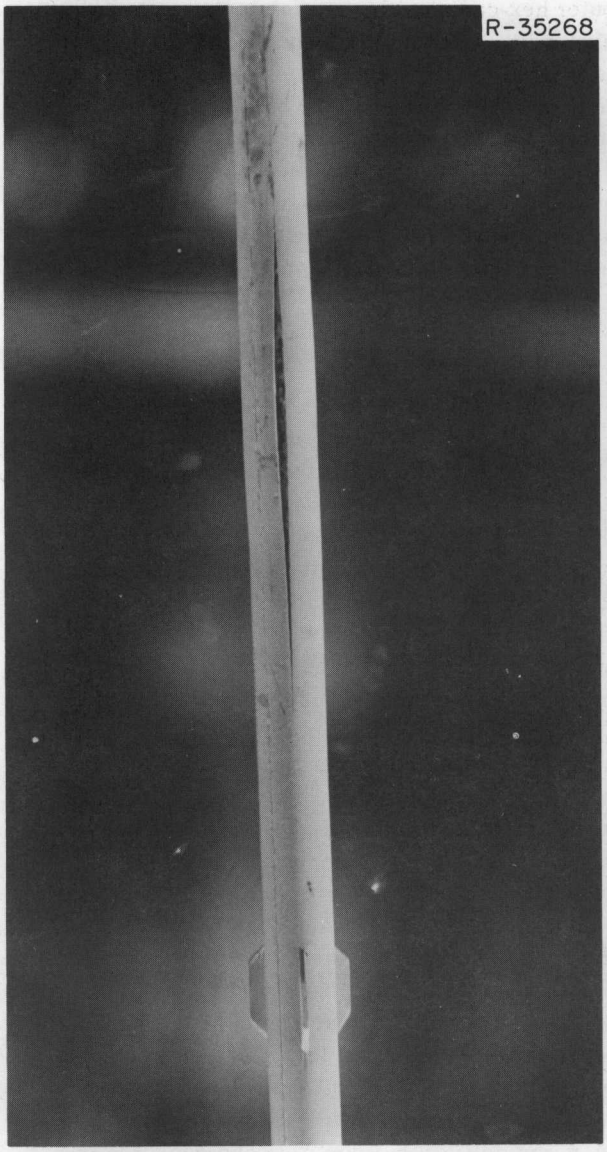

Fig. 33.2. Appearance of Failure on SRL-HFIR Target Rod. 1×.

tained six full-length extruded fins, 60° apart; they were partially machined off to provide discontinuous fins, which supported the outer sheath. Some of these fins are visible in Figs. 33.2 and 33.4. Every crack occurred on one of the original fin lines. In rupture tests of unirradiated machined target-rod tubing, it ruptured along the original fin lines at pressures ranging from 4000 to 4700 psi. Full-length-finned tubing ruptured at pressures ranging from 5100 to 5400 psi, and it appears that the presence of full-length fins probably would not have prevented the failures but perhaps delayed them.

We attempted to remotely measure the outside diameter of all nine target rods with hand micrometers at points along the target rod corresponding to preirradiation measurements. However, we were not able to obtain accurate and reproducible measurements.

Several types of specimens were obtained from the failed rods and their sheaths and submitted for metallography and mechanical properties testing. Metallographic samples, including both the pellet and cladding, were sectioned from rods 56A and 34A. Sections of the sheath from the maximum flux region of three targets that had been exposed in both SRL and HFIR were obtained. A section from the maximum flux region of a sheath that had been exposed in HFIR only was also obtained.

The remaining sections of the failed rods are now being chemically processed. Before they were dissolved, all of the positioning fins were removed from the rods in the event that any further examinations are required. The hex-can sheaths from all nine of the rods that were inspected are also available for further examination if necessary.

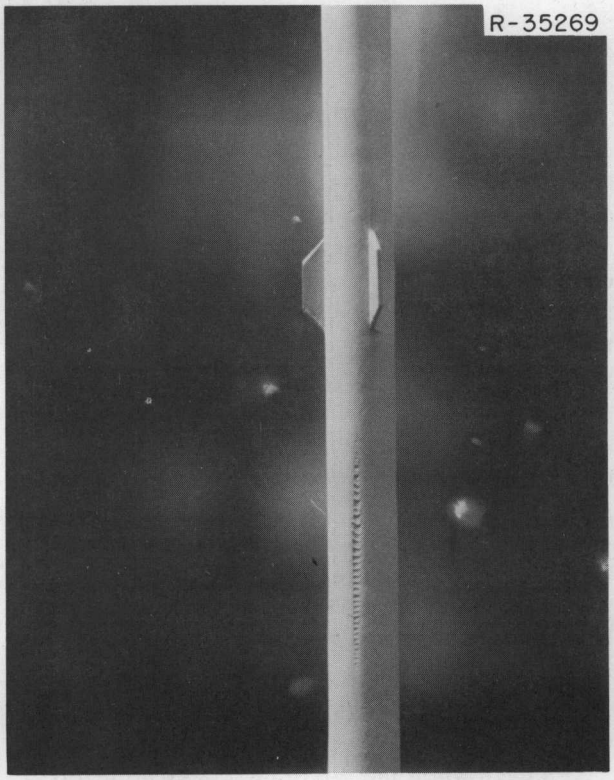

Fig. 33.3. Appearance of Abraded Region on SRL-HFIR Target Rod 56A. 1×.

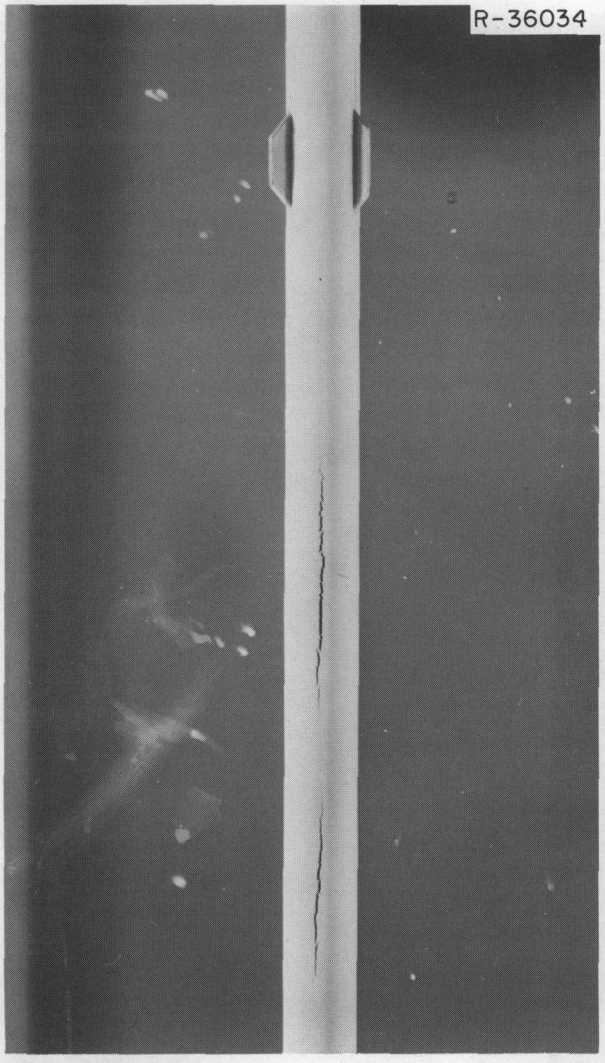

Fig. 33.4. Appearance of Failure on SRL-HFIR Target Rod 6A. 1×.

Metallographic Examination of a Failed SRL Target Element

E. L. Long, Jr.

Two specimens were sectioned from the failed region of HFIR target rod 56A at the TRU Facility and transferred to the HRLEL for metallographic examination. The specimens were transverse sections taken at the end and about midlength of the fracture in the cladding. The specimens included both cladding and target pellet; the specimen taken near the end of the fracture included a "chatter" mark that apparently had occurred prior to reactor service.

Figure 33.5 shows the specimen taken from near midlength of the cladding failure. The fracture was intergranular and extended through the cladding and pellet liner and well into the target dispersion. In the cladding we saw numerous microcracks that originated at the inner surface, and several extended over halfway through the wall thickness. The fracture in the cladding was of a brittle nature; there was no measureable reduction in wall thickness. Although the target material showed evidence of plastic flow and swelling in the fracture region, there was no evidence of melting or gross reaction between the target pellet material and the aluminum matrix. Numerous fission-gas bubbles were present in the target particles.

Examination of the section taken near the end of the cladding fracture showed that this crack was intergranular and extended only through the cladding; the pellet remained intact. However, the pellet diameter had increased by about 5 mils (approximately 2%) over the as-fabricated diameter. In contrast to the specimen described earlier, no other fractures or microcracks were noted that originated at the inner surface of the cladding. One microcrack that did not completely penetrate the cladding was noted; it occurred in the region of mechanical damage (described at the beginning of this section). No gross reaction had occurred between the fuel and the aluminum matrix. Numerous fission-gas bubbles were present in the fuel particles.

The cladding specimens examined were coated with about 2 mils of a dense tightly adherent aluminum oxide, and there was no evidence of localized corrosion or pitting. Microhardness measurements of the cladding showed over a 2.5-fold increase as a result of irradiation.

Effect of Neutron Irradiation on the Mechanical Properties of the X8001 Aluminum Sheath

R. T. King J. R. Weir

The mechanical properties of the irradiated X8001 aluminum sheath material were investigated to gain understanding of the failure of the HFIR target cladding. Since suitable tensile samples could not be prepared from the cladding, ring tensile samples were cut from the hex-can sheath. The sheath and cladding material neutron doses were 6.38×10^{22} neutrons/cm^2 thermal and 1.07×10^{22} neutrons/cm^2 fast (>0.82 Mev). However, the hex can had been

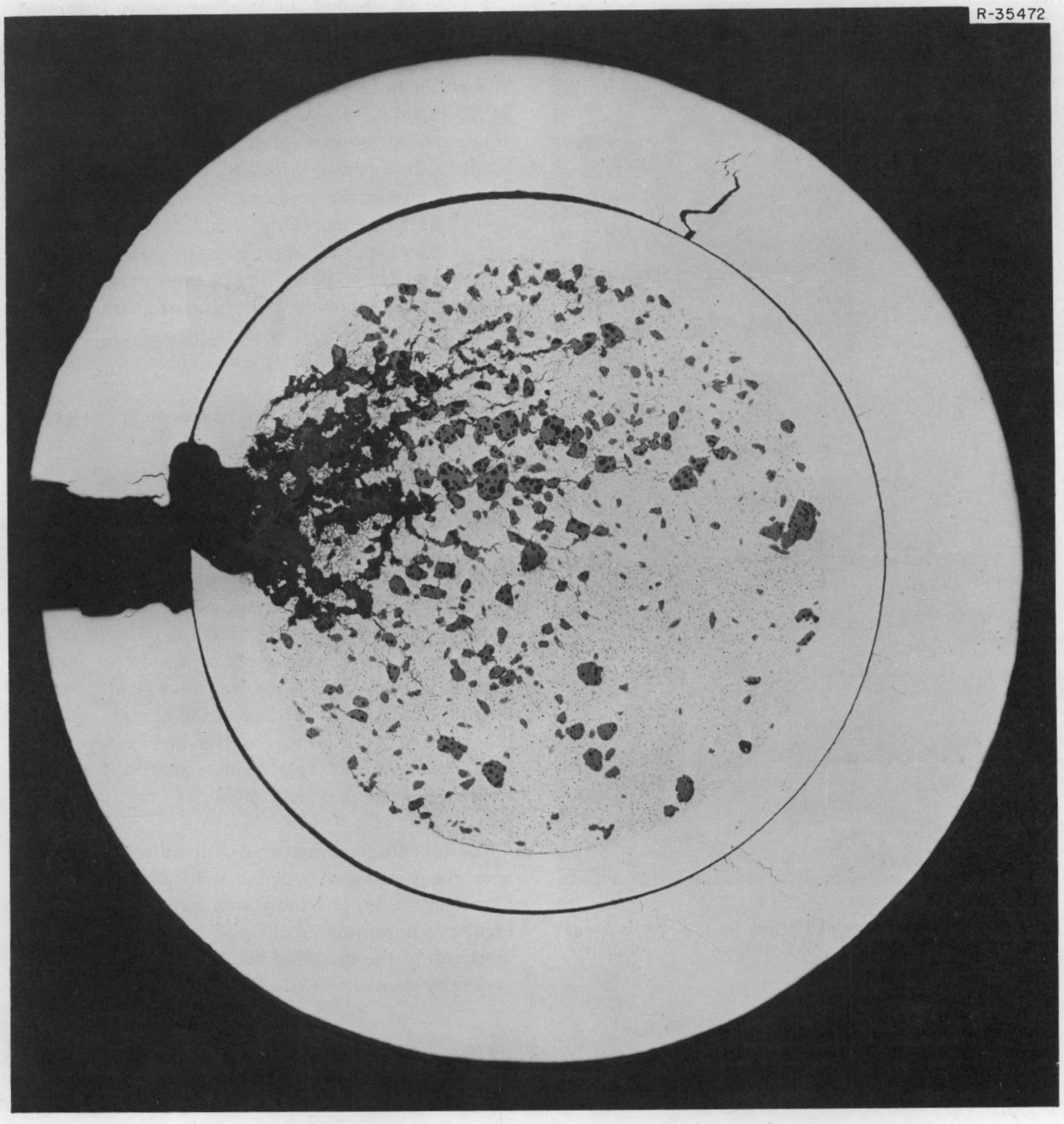

Fig. 33.5. Appearance of the Transverse Section Taken Through the Failed Region of Target Rod 56A. As polished. 20×. Reduced 20%.

irradiated at approximately 130°F, while the cladding operated at approximately 275°F.

Samples from an unirradiated sheath and from the sheath exposed both in SRL and HFIR were tested in air at temperatures ranging from room temperature to 650°F. In testing ring samples, the ultimate stress and crosshead travel to fracture are readily determined quantities measuring strength and ductility respectively.

An irradiation-induced increase in the ultimate strength existed at testing temperatures as high as 500°F. The ratio of ultimate strengths of irradiated material to unirradiated material ranged from 1.65 at room temperature to 2.3 at 500°F. The

ductility of the unirradiated sheath increased with increasing testing temperature. The ductilities of the irradiated and unirradiated hex cans were the same at room temperature, but the ductility of the irradiated hex can decreased to a minimum near 250 or 300°F. It is significant that the ductility minimum in the hex can occurred near the operating temperature of the cladding.

Because of differences in the metallurgical history and irradiation temperatures of the cladding and hex-can material, the in-reactor failure mode of the cladding may not have been duplicated in these tests. A program for a more detailed investigation of the effects of irradiation on aluminum alloys is being outlined.

HFIR Target Failure Analysis

R. E. Adams

Cladding failures have occurred in several HFIR target rods at maximum burnup equivalent to fission of about 25% of the plutonium. All of the failures were longitudinal cracks in the cladding at regions of highest burnup. The failures are typical of those expected from excessive internal fission gas pressures. However, similar prototype rods irradiated in the ETR did not fail at fission of 69% of the plutonium.

Data from both types of rods were analyzed. The ETR rods contained ^{239}Pu to permit high fission burnup in the test program. HFIR rods were loaded with ^{242}Pu. Exposure in HFIR resulted in a much higher fast neutron exposure for the HFIR target rods. Thus HFIR target cladding accrued a fast neutron dose (>0.82 Mev) of about 1×10^{22} neutrons/cm^2 while 25% of the plutonium fissioned, but the fast exposure of the ETR rods was 1/15 as much (0.7×10^{21} neutrons/cm^2) during fission of 69% of the plutonium.

Pellets for each type of rod contained 10% porosity to accommodate fuel swelling and to facilitate release of fission gases to end plenums. In the ETR test, less than 5% of the fission gas was found in the end plenums,[4] and the HFIR failures did not release significant amounts of fission gases to the reactor system.

An analysis of the ETR rod indicates that at fission of 69% of the plutonium, cladding stresses caused by fuel swelling and retained fission gases would remain below the failure stress only if the cladding yielded to allow the diameter to increase about 9 mils. Measured expansion ranged between about 5 and 13 mils.

We postulate that the HFIR rods failed at lower burnup because the high fast flux reduced the ductility of the cladding so that it could not yield to relieve fission-gas pressures. If no cladding expansion occurs, calculations suggest that excessive cladding stresses would develop in a standard pellet when about 35% of the plutonium has fissioned. Such calculated internal pressures are quite sensitive to initial void volume in the fuel pellet. Variations between individual pellets (within the fabrication tolerances used at the time the pellets were made) could result in 30% variation in initial void volume. Calculations based on the smaller void volumes indicate excessive internal pressures could occur at 25% fission.

We designed and fabricated HFIR target rods that contain 20 and 25% porosity in the pellets and 8 and 6 g of plutonium per rod (in contrast to the previous rods, which contained 10% porosity and 10 g of plutonium per rod). Calculations indicate that such rods would be expected to achieve 50 to 75% fission before excessive internal pressures develop. Six such experimental rods are now being irradiated in HFIR.

34. Molten-Salt Reactor Program

H. E. McCoy, Jr. G. M. Adamson, Jr.

The Molten-Salt Reactor Program is an ORNL program for thermal breeder development. The main effort to date has been the construction and operation of the Molten-Salt Reactor Experiment (MSRE). This reactor used a liquid fuel salt containing LiF–29.1 mole % BeF_2–5 mole % ZrF_4–0.9 mole % UF_4, a graphite moderator, and Hastelloy N as the metallic structural material; it operates at 650°C.

The MSRE went critical on June 1, 1965, and had operated 32,450 Mwhr as of May 9, 1967. (Normal power level is about 7.5 Mw.) The main purpose of this reactor is to demonstrate the feasibility of the molten-salt concept and to gain experience with operating this type of system. We have followed the property changes in the graphite and the Hastelloy N by a detailed surveillance program. We have also been involved in a consulting capacity to ensure that the structural materials have satisfactory thermal, mechanical, and chemical conditions for operation.

The successful operation of the MSRE has stimulated work toward the development of suitable materials for a Molten-Salt Breeder Reactor (MSBR). The breeder is complicated by the fact that graphite is a primary structural material. The present concept uses concentric tubes of high-density low-permeability graphite for the fuel channels. A thorium-bearing blanket salt will be circulated around the fuel tubes, and modified Hastelloy N will be used for the pressure vessel. Our work has been concerned primarily with the two principal structural materials – graphite and modified Hastelloy N.

MSRE SUPPORT

MSRE Materials Surveillance Program

W. H. Cook

The effects of the MSRE environment on its moderator (grade CGB graphite) and its primary structural alloy (Hastelloy N) are being monitored periodically by a surveillance program. The details of the surveillance fixture and specimens have been presented previously.[1] A cross section of the surveillance assembly is shown in Fig. 34.1. Each stringer consists of a graphite section and two Hastelloy N rods. The graphite section comprises various types of specimens and the Hastelloy N rod has reduced sections so that tensile specimens can be cut directly from the rod. The assembly is designed so that individual stringers can be removed and replaced by new ones (Fig. 34.1*b* and c). These specimens are mounted axially approximately 3 in. away from the center line of the reactor core and are referred to as core specimens. A second set of Hastelloy N specimens is mounted approximately 4.5 in. outside the reactor vessel, where the specimens are exposed to the N_2–approximately 2% O_2 atmosphere of the reactor cell. The thermal neutron dose on the core specimens is about 20 times that on the pressure vessel.

The reactor core specimens were sampled on July 28, 1966, after 7823 Mwhr and again on May 15, 1967, after 32,450 Mwhr of reactor operation. The second sampling corresponded to a dose of 1×10^{21} neutrons cm^{-2} sec^{-1} fast and 4×10^{20} thermal. The reactor vessel specimens were sampled only after 32,450 Mwhr of operation.

In the first sampling both the Hastelloy N and graphite were mechanically damaged independently of the nuclear conditions. The damage was most severe just above the midpoint of the stringer for approximately 9 in. of its overall length of 62 in., as shown in Fig. 34.2. We concluded that the relatively high thermal expansion of the tensile specimen rods of Hastelloy N allowed the seven metal-banded tongue-and-groove joints of the graphite in

[1] W. H. Cook and A. Taboada, *Metals and Ceramics Div. Ann. Progr. Rept. June 30, 1966*, ORNL-3970, pp. 193–95.

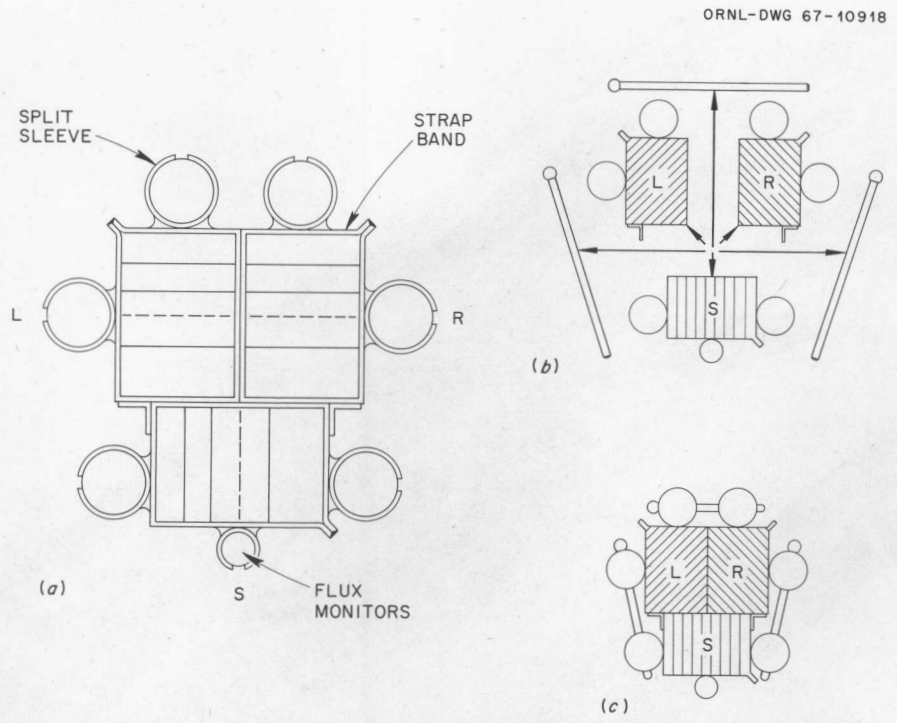

Fig. 34.1. MSRE Surveillance Specimens. (*a*) Detailed plan view. Sketches showing fixture (*b*) unassembled and (*c*) assembled.

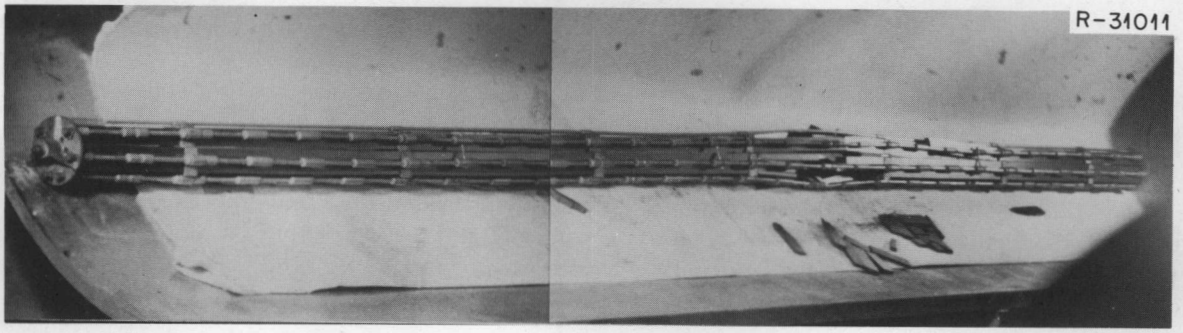

Fig. 34.2. Surveillance Specimens of Grade CGB Graphite and Hastelloy N Removed from the MSRE after 7823 Mwhr.

each stringer to separate and to be penetrated by molten salt. Upon reactor shutdown and subsequent cooldown, salt trapped in the joints froze and made the graphite stringers longer than their original 62 in. The tensile specimen rods of Hastelloy N thermally contracted to their original 62-in. lengths and loaded the graphite specimens, causing some of them to buckle and break. The gage sections of the Hastelloy N specimens were bent in the zones where this happened. Sufficient undamaged specimens were available for the data sought. The fission-product data were obtained by the Reactor Chemistry Division,[2] and corrosion, carburization, and mechanical data on the Hastelloy N were obtained by the Metals and Ceramics Division.

To alleviate the mechanical damage with this assembly, we prepared a new one in which the following changes were made:

[2]S. S. Kirslis, *MSR Program Semiann. Progr. Rept. Aug. 31, 1966*, ORNL-4037, pp. 165–89.

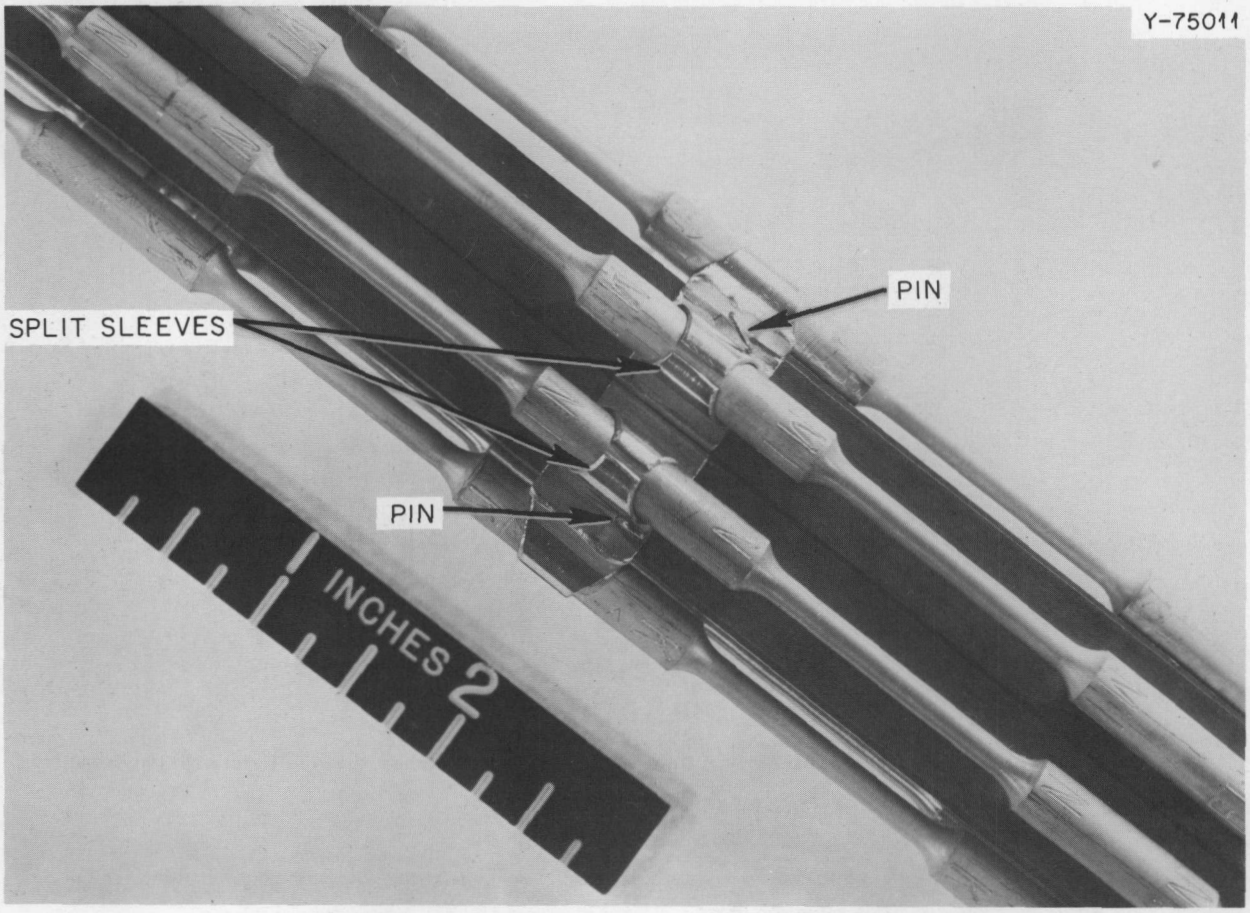

Fig. 34.3. Design Modifications of Surveillance Specimens. Graphite joints pinned, graphite column shortened, sleeves slit to provide better salt drainage and alleviate binding.

1. We pinned the tongue-and-groove graphite joints with 30-mil-diam pins within their metal bands to prevent their separation and subsequent salt entrapment (Fig. 34.3).
2. The slip-type sleeves that hold the tensile specimen rods at the bands were shortened and split (Fig. 34.3).
3. The graphite sets were pinned to the Hastelloy N rods near their midpoints; this in effect halved the travel that the thermal expansion would cause.
4. The graphite sets were shortened so that they could not be end loaded by the upper and lower metal plates of the assembly in case salt froze in the graphite joints.

A new set of specimens in an assembly with these modifications was placed in the core of the MSRE. After 32,450 Mwhr the surveillance assembly was removed and found to be in excellent mechanical condition. One of the stringers was removed and replaced, and the assembly is back in the reactor core.

The typical appearance of the materials in the stringer removed after 32,450 Mwhr is shown in Fig. 34.4. Note that the Hastelloy N tensile specimens are reflected in the bright surface of the graphite, showing that the graphite surface was unchanged by exposure with the exception of a few adhering salt droplets. The Hastelloy N surface was dulled. The reactor vessel specimens were, of course, darkened by their exposure to the nitrogen-oxygen atmosphere at elevated temperatures.

We have broadened our testing program to include materials for future use as well as MSRE materials. In the specimens just removed, some tensile specimen rods were made of Hastelloy N modified to increase its radiation damage resistance. One of the rods had an addition of 0.52% Ti and the other 0.43%

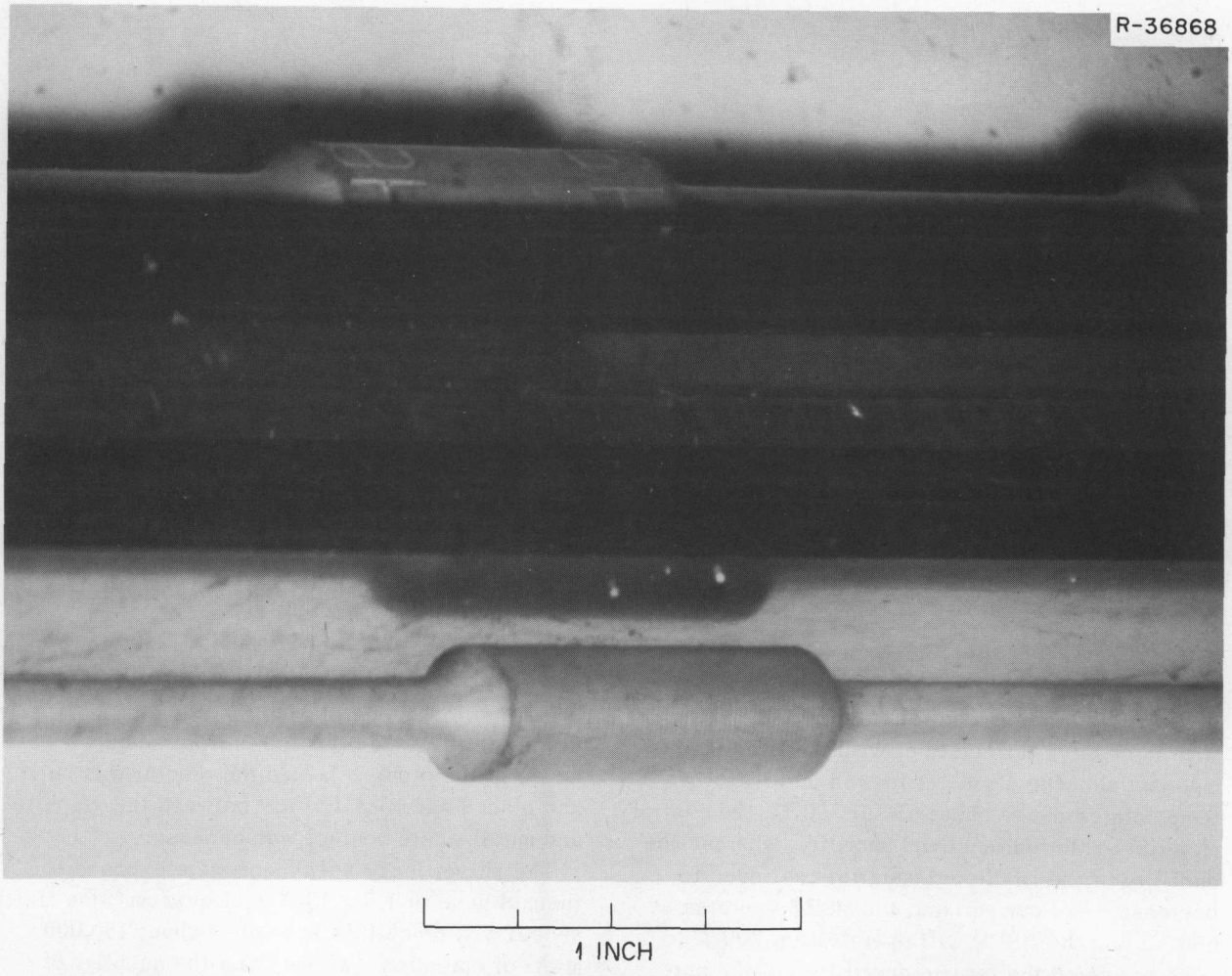

Fig. 34.4. A portion of the Graphite and Hastelloy N Surveillance Specimens After Their Removal from the MSRE After 32,450 Mwhr.

Zr. In addition to radiation effects on these modified alloys, their corrosion resistance in the MSRE environment can be studied. In the new set of specimens recently charged into the MSRE, the testing of alloy modifications is being continued with one rod containing 0.5% Ti + 2% W and one with 0.5% Hf. These rods will be removed later and examined with respect to mechanical properties and corrosion. The new graphite samples included the anisotropic MSRE graphite, isotropic graphite, pyrolytic graphite, and a graphite-metal brazed joint. Our primary purpose in this program is to ensure the safe operation of the MSRE, so we are continuing to retain at least 65% of the assembly for the MSRE grades of Hastelloy N and graphite.

Testing of Hastelloy N Surveillance Specimens

H. E. McCoy, Jr.

The core specimens pulled after 7823 Mwhr of operation have been tested. The details of this study have been reported.[3]

Several of the surveillance and control specimens were tensile tested. The total elongation at fracture for specimens deformed at a strain rate of 0.05 min^{-1} is shown as a function of temperature in Fig. 34.5. Both heats show some exposure-induced reduction in ductility at low temperatures,

[3]W. H. Cook and H. E. McCoy, *MSR Program Semiann. Progr. Rept. Feb. 28, 1967*, ORNL-4119, pp. 95–103.

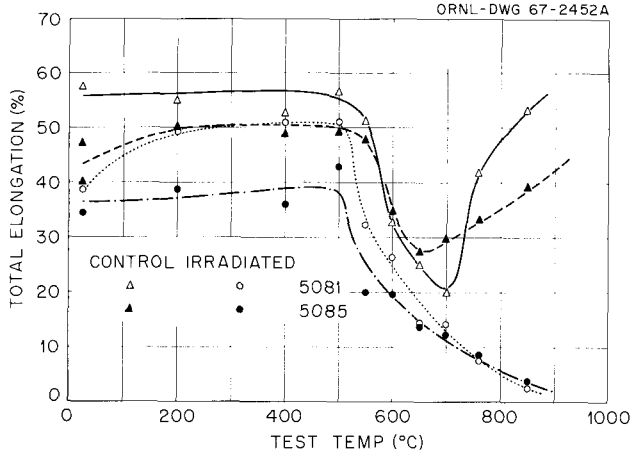

Fig. 34.5. Tensile Ductilities of MSRE Hastelloy N Surveillance Specimens and Their Controls at a Strain Rate of 0.05 min^{-1}. Separate curves are given for the two heats tested.

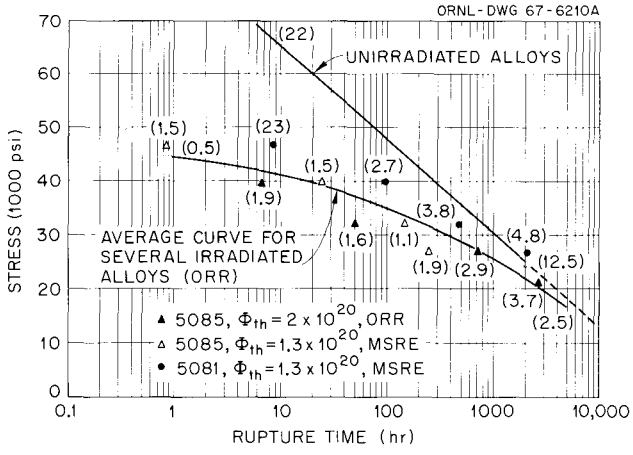

Fig. 34.6. Comparison of MSRE Hastelloy N Surveillance Specimens with Specimens Irradiated in the ORR. Numbers in parentheses indicate ductilities.

with a greater reduction being observed for heat 5085. At temperatures above 500°C the ductility of the irradiated and control materials decreased with increasing temperature, with the irradiated material showing a greater loss in ductility. At temperatures above about 650 or 700°C, the control material exhibited improved ductility, whereas the ductility of the irradiated material continued to decrease. For comparison, the MSRE operates at 650°C, and the MSBR will operate near 700°C.

We compared the tensile ductilities of the surveillance specimens with those for specimens irradiated in other experiments[4] without salt present. The results agreed very well, indicating no significant added effect of the salt environment.

Creep-rupture tests were also run. The results were in excellent agreement with those obtained previously on specimens irradiated without salt present. The results in Fig. 34.6 show a decrease in rupture life and ductility.

Metallographic examination of the Hastelloy N showed the presence of a surface film at points where the graphite and Hastelloy N had been in intimate contact. This product was present at such points on both the surveillance and the control specimens. Electron microprobe examination showed that the carbon content of the edge of the specimen ranged from 0.3 to 1.2%, compared with 0.05% for the interior of the sample. No evidence of attack or carburization was found on metal surfaces that were separated from the graphite $\frac{1}{16}$ in. This carburization is not a concern for the MSRE, since we were aware of the problem before the reactor was built and placed sacrificial shims between the graphite and metal where contact was necessary.

The surveillance specimens were exposed to a thermal dose of 1.3×10^{20} neutrons/cm^2; the MSRE vessel will reach this dose after about 150,000 Mwhr of operation. We feel that the quantity of helium produced in the material at this dose due to the $^{10}B(n,\alpha)$ transmutation is sufficient to cause a saturation of the level of damage. Hence, the properties of the Hastelloy N probably will not deteriorate further. The present ductility and strength levels appear to be adequate for the successful completion of the Molten-Salt Reactor Experiment.

[4]W. R. Martin and J. R. Weir, "Effect of Elevated-Temperature Irradiation on Hastelloy N," *Nucl. Appl.* 1, 160–67 (1965).

Consequences of Contaminating the MSRE Radiator Tubing with Aluminum

D. A. Canonico

On July 17, 1966, a cast Al–5% Zn alloy blower failed at the MSRE site, throwing small shrapnel across the Hastelloy N tubing of the salt-to-air radiator. As a result of the failure the radiator temperature rose from 575°C to about 650°C for 5 hr. Hence, we investigated the effect of the molten aluminum-zinc alloy on the radiator tubing. Since

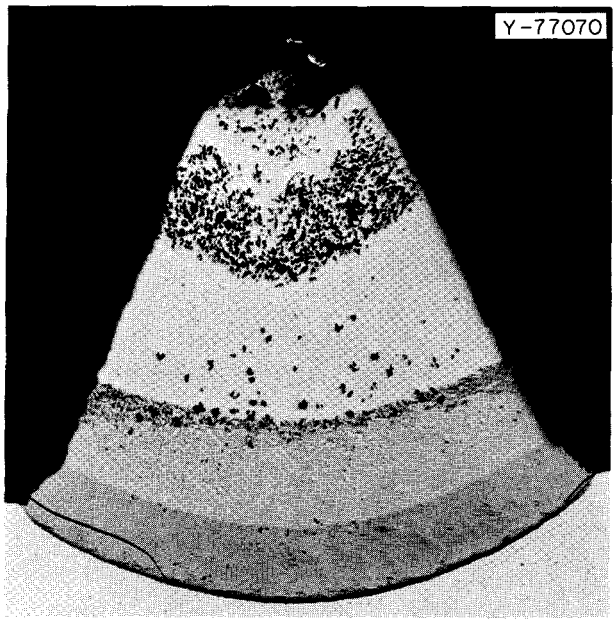

Fig. 34.7. Metallographic Section Through Aluminum Cone and Hastelloy N Tube. Sample was held at 650°C for 1000 hr. 50×. As polished. Reduced 9%.

the actual tubing could not be removed and sectioned metallographically, only specimens simulating the exposure could be prepared and examined. Small segments of the failed blower were tested in contact with representative samples of the tubing over the temperature range 620 to 675°C.

Laboratory experiments[5,6] showed that it was extremely difficult to wet the Hastelloy N tubing with aluminum in an environment characteristic of that at the time of the failure. An oxide film formed on the aluminum, and even at a temperature of 675°C (which exceeds the actual radiator tubing temperature), the molten aluminum was contained within the scale.

When the oxide skin was broken (by mechanical abrasion, shock, etc.), wetting did occur. Figure 34.7 is a photomicrograph of an aluminum–Hastelloy N couple after 1000 hr at 650°C. The appearance of this specimen is essentially identical (except for the microstructure of the aluminum) to one that was held at 650°C for 5 hr. The penetration into the Hastelloy N was approximately 10 mils (16% of the tube-wall thickness) for both the 5- and 1000-hr exposures. This study indicated that if any undetected aluminum was present on the tubes, the danger of its penetration was minimal.

Prior to startup of the reactor, the tubes were thoroughly inspected, and the few areas that showed indications of aluminum contamination were carefully cleaned.

In May 1967, the MSRE was shut down after successfully completing several thousand hours of operation since the blower failure. The tubes were reinspected, and there were no indications of any damage due to the blower-fan failure.

MSBR DEVELOPMENT

Improving the Resistance of Hastelloy N to Radiation Damage by Composition Modifications

H. E. McCoy, Jr. J. R. Weir, Jr.

Although Hastelloy N has suitable properties for long-term use at elevated temperatures, we have found that the ductility and strength deteriorate when it is exposed to neutron irradiation. This type of radiation damage manifests itself through a reduction in the creep-rupture life and the rupture ductility. This damage is a function of the thermal neutron dose and is thought to be associated with the helium that is produced by the $^{10}B(n,\alpha)$ transmutation. However, the threshold helium content required for damage is so low that the property deterioration cannot be prevented by reducing the ^{10}B level in the alloy. We have found that slight modifications to the composition offer considerable improvement.

Our studies have shown that the normal massive precipitate, identified[7] as M_6C, can be eliminated by reducing the molybdenum level to the 12 to 13% range.[8] The strength is not reduced significantly and the grain size is more uniform and more easily controlled. The addition of small amounts of titanium, zirconium, or hafnium reduces the irradiation damage problem significantly. Figure 34.8 illustrates the fact that several alloys have been developed with postirradiation properties that are

[5] D. A. Canonico and D. M. Haseltine, *MSR Program Semiann. Progr. Rept. Aug. 31, 1966*, ORNL-4037, pp. 103–7.

[6] D. A. Canonico and D. M. Haseltine, *MSR Program Semiann. Progr. Rept. Feb. 28, 1967*, ORNL-4119, pp. 116–17.

[7] R. E. Gehlbach and H. E. McCoy, Jr., Part I, Chap. 5 of this report.

[8] H. E. McCoy, Jr., and J. R. Weir, Jr., *Materials Development for Molten-Salt Breeder Reactors*, ORNL-TM-1854 (June 1967).

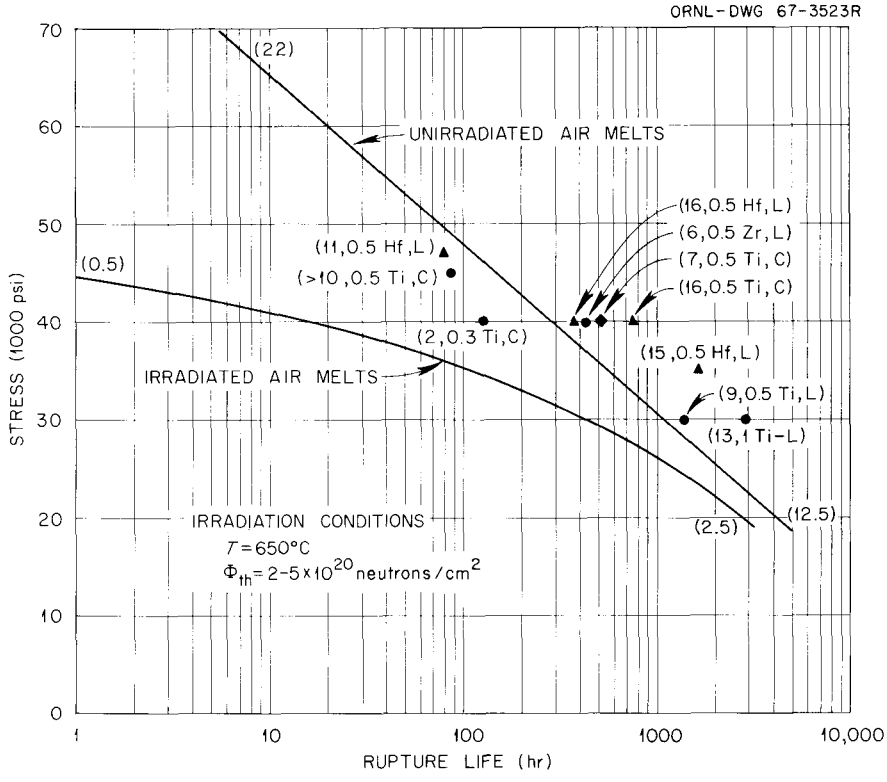

Fig. 34.8. Comparison of the Postirradiation Creep of Several Variations of Hastelloy N at 650°C. Solid curves represent values for the unmodified alloy. Individual points give values for irradiated modified alloys. The percentage fracture strains are given in parentheses, followed by the alloy addition and whether the source is this laboratory (L) or commercial (C).

superior to those of unirradiated standard Hastelloy N. We are beginning work to optimize the compositions and heat treatments of these alloys. We are also initiating the procurement of 1500-lb commercial melts of some of the more attractive alloys.

The properties of the modified Hastelloy N in the unirradiated condition seem very attractive. Strengths are slightly better than standard Hastelloy N and fracture ductilities are about double.

Hastelloy N Welding Studies

D. A. Canonico H. E. McCoy, Jr.

Our research effort on the weldability of Hastelloy N during the past year can be divided into two areas: the continuation of the study of conventional Hastelloy N (Ni–16% Mo–7% Cr–4% Fe) and the initiation of studies on modified Hastelloy N (Ni–12% Mo–7% Cr) with additions of titanium, zirconium, and hafnium to improve its resistance to irradiation damage.

The studies on conventional Hastelloy N covered the effect of base-metal melting practice (air melting vs vacuum melting) and modifications of the welding filler metal. The objectives were to determine and, if possible, to improve the mechanical properties of gas tungsten-arc welds. Particular emphasis was placed on their stress-rupture properties. Two heats of air-melted and one of vacuum-melted base metal were studied. The two air-melted base metals were joined with air-melted filler metal from two heats and with vacuum-melted filler metal. The vacuum-melted heat was joined with filler metal prepared from the same heat. In addition, air-melted plates were joined with filler metal that had been prepared by spray coating $\frac{1}{8}$-in.-diam air-melted rods with Al_2O_3 and WC.

The elongations at room temperature and at 650°C for these welds and the respective base metals are given in Table 34.1. The weldment strengths are all within 10% of each other, regardless of the base metal and filler metal. The elongation values at 650°C are similar for all of the weldments except

Table 34.1. Fracture Elongations of Hastelloy N Welds

Weld	Heats Used		Melting Method		Fracture Elongation[a] (%)	
	Base	Filler	Base	Filler	Room Temperature	650°C
b	5065, 5067		air		56	33
1	5065, 5067	5101	air	air	28	12.5
4	5065, 5067	5101	air	air	26	15
5	5065, 5067	5055	air	air	34	16
6	5065, 5067	65–552	air	vacuum	41	19
7	5065	5090[c]	air	air	34	14
8	5065	5090[d]	air	air	39	25
b	2477		vacuum		55	42
3	2477	2477	vacuum	vacuum	37	14.5

[a]Strain rate, 0.05 min^{-1}.

[b]Values for unwelded base metal.

[c]$\frac{1}{8}$-in.-diam rod spray coated with Al_2O_3.

[d]$\frac{1}{8}$-in.-diam rod spray coated with WC.

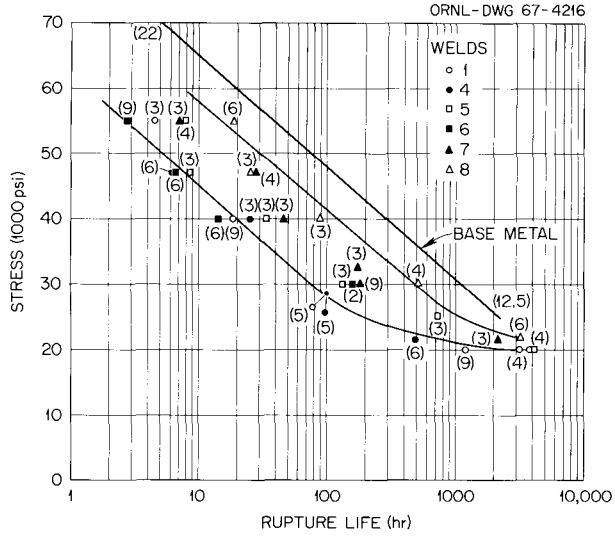

Fig. 34.9. Comparative Stress-Rupture Properties of Several Hastelloy N Welds at 650°C. The numbers in parentheses indicate the strain at fracture.

weld 8, which was made with the tungsten-carbide-coated filler metal. At room temperature weld 8 again demonstrated good ductility. Welds 6 (air-melted base metal, vacuum-melted filler metal) and 3 (vacuum-melted base and filler metal) also showed good ductility at room temperature.

The results of the stress-rupture studies at 650°C are given in Fig. 34.9 Welding air-melted material reduced the rupture life for a given stress level by a factor greater than 10. The lower line is a best fit for welds 1, 4, and 5. These all contain air-melted base metals welded with air-melted filler metal. Spray coating the filler metal with tungsten carbide (weld 8) increased the life of the joint approximately eightfold. Weld 3 (vacuum-melted base and filler metals) had excellent creep-rupture properties in the as-welded condition. However, the data for weld 6 indicate that the properties are quite poor if only the filler metal is vacuum melted.

It is evident from these studies that air-melted base metal that has been joined with air-melted filler metal possesses mechanical properties considerably poorer than those of the base metal. Coating the filler metal with tungsten carbide improved the weldment properties in all respects. Vacuum-melted materials exhibited as-welded properties that are superior to those of air-melted alloys, although combinations of the two types of material offer little improvement.

The advantages of the modified Hastelloy N base metal have been discussed previously. Since the elements that are being added to improve its irradiation damage resistance may degrade its weldability, we started to study the weldability of this modified alloy. Sound welds were made in $\frac{1}{2}$-in.-thick plates of experimental alloys containing titanium and hafnium. However, the alloys containing zirconium exhibited extensive cracking.

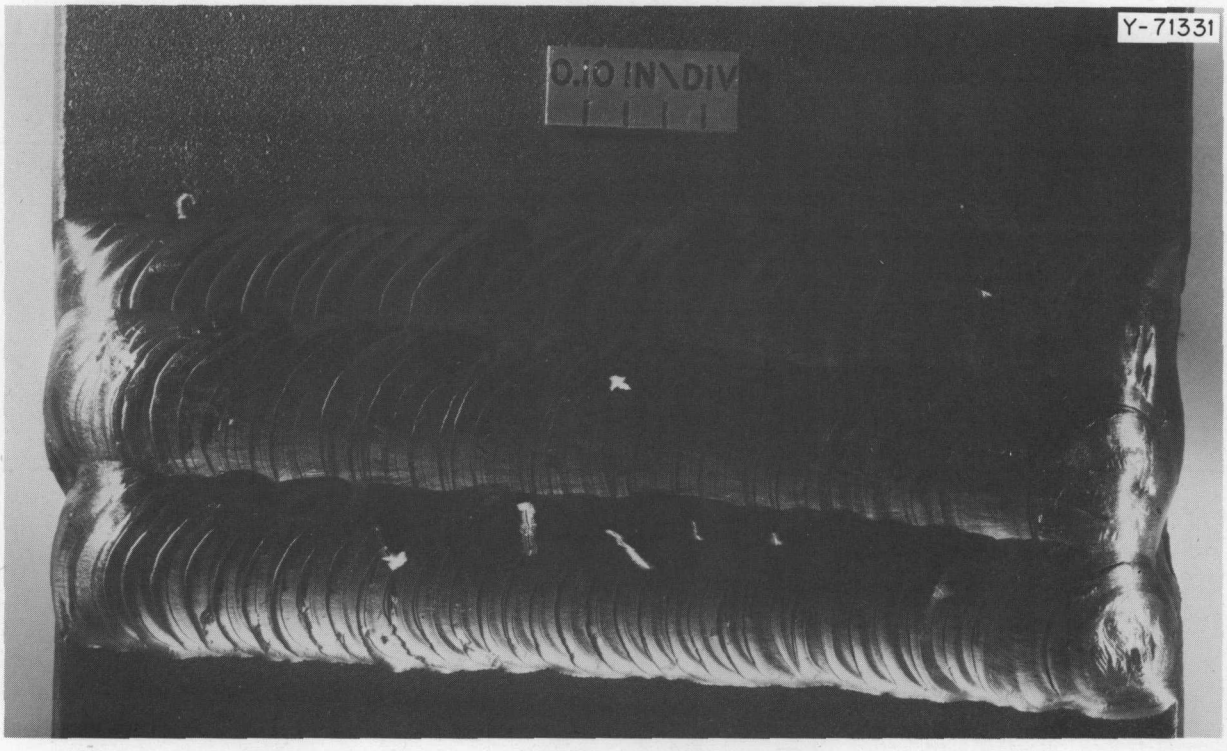

Fig. 34.10. Welds in Hastelloy N Containing 0.05% Zr. Slight cracking in the weld metal is revealed by fluorescent penetrant.

Cursory studies were made on the weldability of experimental heats of the Ni–12% Mo–7% Cr alloy with 0.05 and 0.5% Zr. These heats were rolled to ½-in.-thick plate and welded with filler metal of the same composition. The gas tungsten-arc welds that were made in the 0.5%-Zr material contained innumerable hot cracks in the weld metal; decreasing the zirconium level to 0.05% considerably reduced the susceptibility to cracking. Figure 34.10 is a photograph of the top surface of the 0.05% Zr welds, in which fluorescent penetrant was used to expose the hot cracks. Clearly, the behavior of the weld metal of both alloys is unsatisfactory.

Such hot cracking may also be a problem in the heat-affected zone. To study its behavior in these zirconium-bearing alloys, a hot-ductility test (using the Duffer's Gleeble[9]) was conducted on experimental alloys containing 0, 0.1, 0.3, 0.5, 0.7, and 1% Zr. The Gleeble test uses ductility (measured by reduction in area) as the criterion for determining the heat-affected zone behavior. The difference between the temperature at which the ductility reaches zero during exposure to a simulated weld thermal cycle and the melting temperature of the bulk alloy is an indication of the weldability of the base metal. Furthermore, the ability to recover ductility after an exposure to the zero-ductility temperature (ZDT) is an even better measure. Typical results of this study were that the addition of 0.3% Zr to the Ni–12% Mo–7% Cr decreased the ZDT from 1290 to 1160°C, a rather precipitous drop. However, the recovery of ductility was quite good, indicating moderate resistance of the heat-affected zone to hot cracking.

[9]E. F. Nippes *et al.*, "An Investigation of the Hot-Ductility of High-Temperature Alloys," *Welding J. (N.Y.)* 34, 183-s–196-s (1955).

Dynamic Corrosion Studies

A. P. Litman

The Reactor Materials Engineering Group is continuing to study the compatibility of fluoride salts with structural materials of interest for molten-salt reactors in natural circulation loops. Although we presently plan to use Hastelloy N as the metallic structural material in the MSBR, cooler parts of the

Table 34.2. Thermal Convection Loop Operation Through June 30, 1967

Loop	Loop Material	Hot-Leg Specimens	Heat Transfer Medium	Maximum Temperature (°C)	Temperature Drop (°C)	Time Operated (hr)
1255	Hastelloy N	Hastelloy N + 2% Nb[a]	$LiF-BeF_2-ZrF_4-UF_4-ThF_4$ (70-23-5-1-1 mole %)	705	89	49,950
1258	Type 304L stainless steel	Type 304L stainless steel[b]	$LiF-BeF_2-ZrF_4-UF_4-ThF_4$ (70-23-5-1-1 mole %)	675	100	34,675
10	Hastelloy N	None	$NaK-KF-BF_3$ (48-3-49 mole %)	610	147	8,765[c]
12	Croloy 9M	Croloy 9M[a]	$NaF-KF-BF_3$ (48-3-49 mole %)	610	145	1,440[d]

[a]Permanent specimens.
[b]Removable specimens.
[c]Scheduled loop shutdown May 23, 1967.
[d]Loop plugged on September 26, 1966.

system could be constructed of a cheaper iron-base alloy. Thus, our program has been diversified to include Croloy 9M and type 304 stainless steel. Current loop operation is summarized in Table 34.2.

Loop 1255, constructed of Hastelloy N and containing a simulated MSRE fuel salt plus 1 mole % ThF_4, has operated for five years without difficulty.

Loop 1258, constructed of type 304L stainless steel, has now logged four years of circulation with only minor changes in flow characteristics. To examine the corrosive behavior of the relatively old simulated fuel salt, ten fresh specimens were placed in the hot leg of loop 1258 this past January. Rapid attack occurred in the first 50 hr of exposure, but the rate of weight loss declined with time. While several perturbations in the rates occurred at longer times, the rate loss has generally remained constant between 1 and 2 mils/yr equivalent uniform attack. This is, of course, many times the corrosion rate observed for Hastelloy N under similar conditions.

Loops 10 and 12, both of which have ceased operation, contained a developmental fluoroborate coolant salt. Loop 12, constructed of Croloy 9M, plugged after 1440 hr of circulation due to growth of essentially pure iron crystals. The plug was located in approximately the coldest portion of the loop. Similar crystals were found adhering to specimens in the hot leg. A green deposit with a composition that varies in the range Fe, 15 to 17%; Cr, 11 to 14%; B, 2 to 4%; Mn, 1.5%; Na, 10 to 15%; F, 46%

PHOTO 74314A

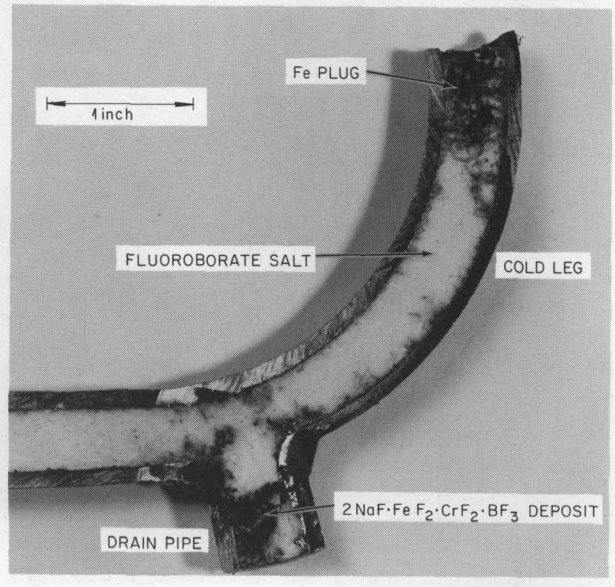

Fig. 34.11. Plugging in Croloy 9M Loop 12 Containing $NaF-KF-BF_3$ (48-3-49 mole %) After 1440 hr at 610°C. Temperature drop, 145°C. 1.6×.

was found in the drain line attached to the cold horizontal leg of the loop, as shown in Fig. 34.11. The composition of the deposit approximates $2NaF \cdot FeF_2 \cdot CrF_2 \cdot BF_3$. Metallographic examination of the hot-leg specimens disclosed only moderate surface roughening.

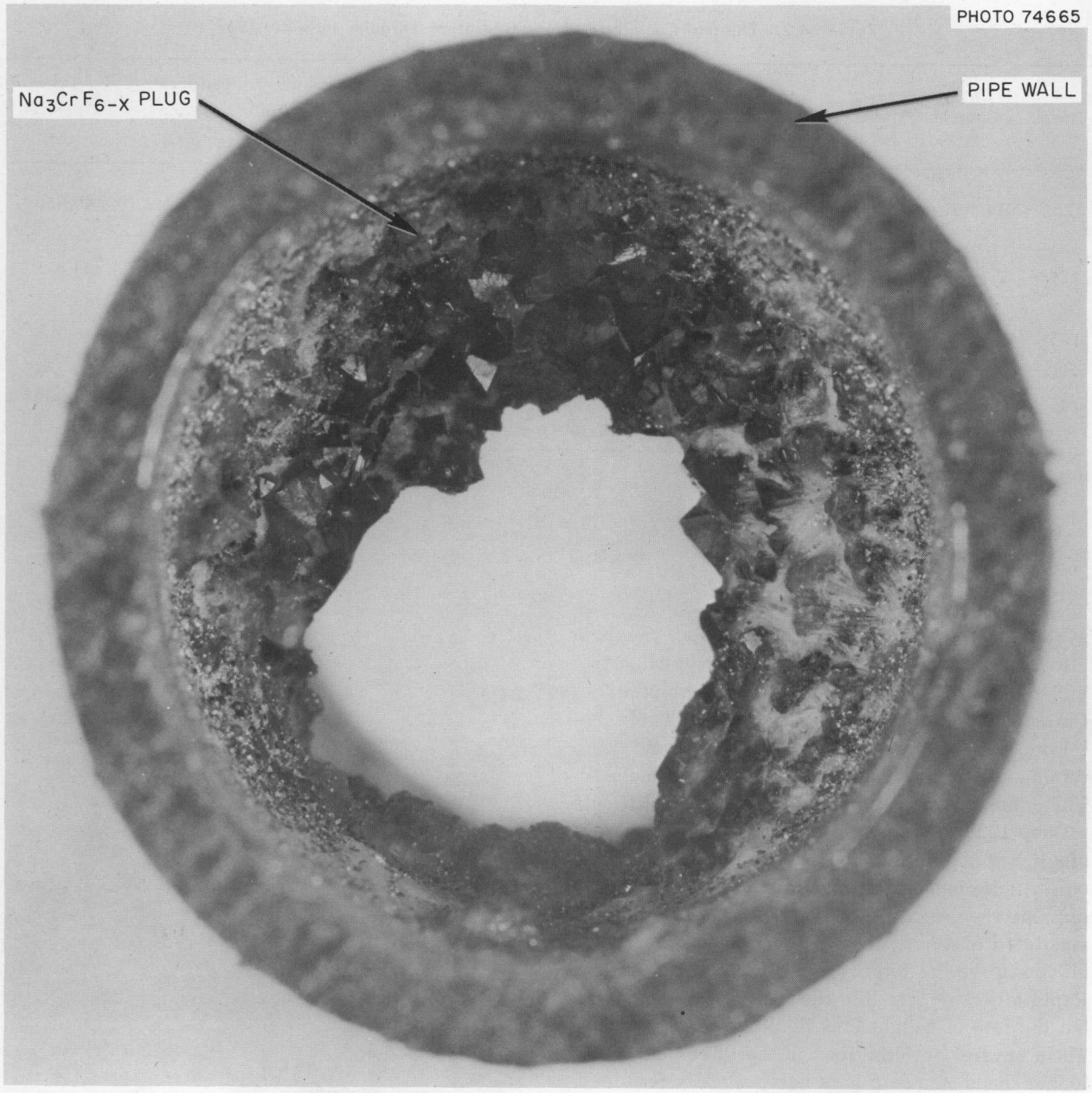

Fig. 34.12. Plug Formed in Hastelloy N Loop 10 Containing NaF-KF-BF_3 (48-3-49 mole %) After 8765 hr at 610°C. Temperature drop, 147°C. 8×. Reduced 13%.

Loop 10 fabricated from Hastelloy N operated without incident for 8335 hr; then the hot-leg temperature increased about 30°C and the cold-leg temperature decreased the same amount. A perturbation of this type usually indicates plugging; however, the temperature fluctuations ceased after 1 hr, and operation was continued. The loop was shut down after its scheduled one year of operation. Examination of the loop piping disclosed a partial plug in the lower portion of the cold leg, shown in Fig. 34.12. The plug, which closed approximately 75% of the cross-sectional area of the pipe, was emerald green and composed[10] of essentially single crystals of Na_3CrF_{6-x}. The uncertainty in the composition is due to a lack of a comparative

[10]Private communication from R. E. Thoma, Reactor Chemistry Division, June 14, 1967.

standard for this compound. Examination of this loop is proceeding.

Extensive efforts were made to remodel the thermal-convection loop area for advanced studies on the compatibility of MSBR salts with Hastelloy N and modified Hastelloy N (0.5% Ti). All instrumentation has been or is being upgraded, outmoded furnaces are being replaced, and special facilities are being installed to handle toxic BF_3 gas. Our plans include natural-circulation and possible forced-circulation loop studies with the prime candidate fuel, blanket, and coolant salts[11] for the MSBR; a study of the compatibility of brazed joints between graphite and Hastelloy N with fuel salt; and capsule tests to determine the effect of BF_3 pressure on compatibility of the coolant fluoroborate salt.

Procurement and Evaluation of New Grades of Graphite

W. H. Cook

Work has continued on the evaluation of anisotropic and isotropic grades of graphite as potential materials for the molten-salt breeder reactors.[12,13] The properties of MSRE graphite, Grade CGB, are being used as a basis for comparison. Grade CGB is a needle-coke, anisotropic graphite that has been fabricated to have low permeability to molten salts and gases but is not stable under irradiation. The isotropic grades of graphite are more stable under irradiation, but they are new. Past development has not been directed toward the production of material having the low gas permeability and small pore entrance diameter required of graphite for molten-salt breeder reactors.

The emphasis is on the well-graphitized (with a high degree of crystal perfection) isotropic graphite because of its relative radiation stability. The main characteristics of primary importance are that (1) the pore entrance diameters be less than 1 μ (to keep the molten salt out of the graphite) and (2) the permeability to helium be between 10^{-7} to 10^{-5} cm^2/sec (to keep the ^{135}Xe from entering the graphite). The plot of typical pore entrance diameters for various grades of anisotropic and isotropic graphite in Fig. 34.13 shows that none of the types of graphite evaluated to date meets the pore spectrum requirement. Neither have any of the graphites exhibited the desired low permeability. Another factor is that many of the isotropic grades are poorly graphitized and thus would not have the desired degree of dimensional stability under irradiation.

We have not obtained a grade of graphite that meets all of the molten-salt breeder requirements, but some materials examined appear to have potential. Several vendors have initiated development programs that should lead to a more suitable grade of graphite for use in the MSBR. We are also investigating the use of coatings (molybdenum, niobium, nickel, and pyrolytic carbon) as a means of reducing the permeability.

Irradiation Creep of Graphite

C. R. Kennedy

The primary purpose of our experiments has been to determine the creep behavior of graphite under irradiation in order to resolve the stress generation problem caused by differential growth. The creep coefficients determined for graphite at 700 and 1000°C and reported previously[14] were found to be in error. After-test measurements of the specimen indicated a rather large discrepancy between the displacement readings indicated by the in-reactor transducer output and the post-test specimen measurements. We found that the transducers were overheated in the higher temperature creep experiments; severe resistance changes occurred and resulted in large apparent displacement readings. Although the after-test measurements yielded values for the creep coefficients, these values include uncertainties as to the extent of primary creep and differential growth strains. Therefore, a new experiment with shielded transducers has been initiated to creep-test graphite grades AGOT and CGB at 800 and 1000°C.

The preliminary results of this experiment after 2×10^{20} neutrons/cm^2 are compared in Fig. 34.14 with those reported previously[14] and with those calculated from post-test measurements. The calculated values at 1000°C are low compared with

[11] Fuel salt, LiF–34 mole % BeF_2–0.5 mole % UF_4; blanket salt, LiF–29 mole % ThF_4; coolant salt, $NaBF_4$.

[12] R. B. Briggs *et al.*, *MSR Program Semiann. Progr. Rept. Feb. 28, 1966*, ORNL-3936, pp. 107–8.

[13] W. H. Cook, *MSR Program Semiann. Progr. Rept. Aug. 31, 1966*, ORNL-4037, pp. 108–10.

[14] C. R. Kennedy, *Metals and Ceramics Div. Ann. Progr. Rept. June 30, 1966*, ORNL-3970, pp. 161–62.

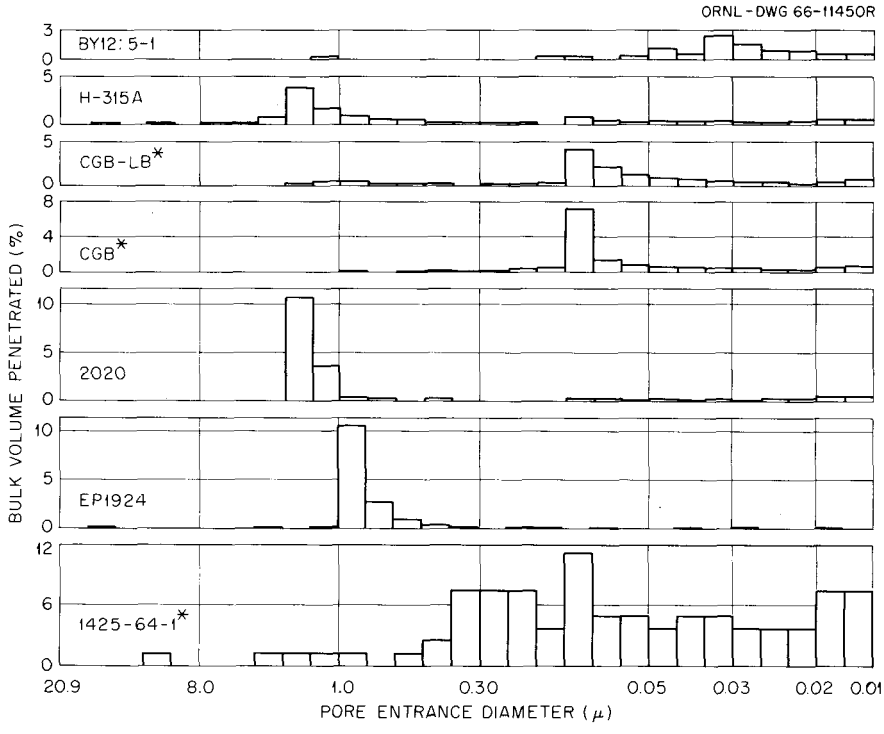

Fig. 34.13. A Comparison of the Distributions of the Pore Entrance Diameters for Various Grades of Anisotropic (Marked with an Asterisk) and Isotropic Graphite.

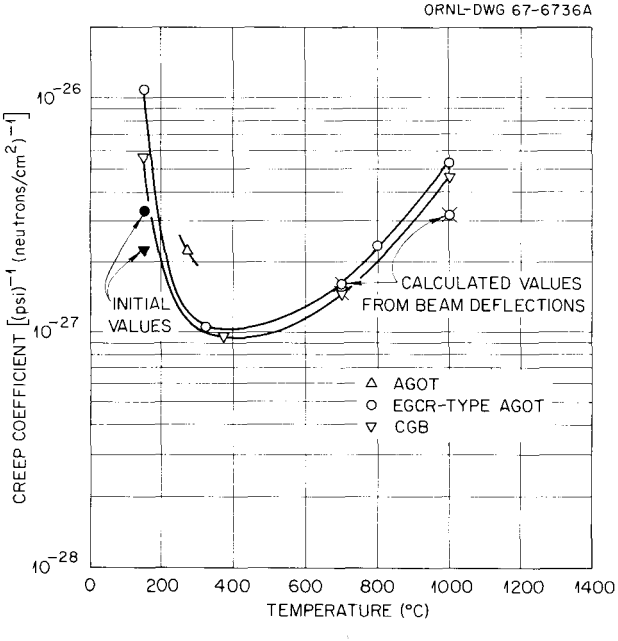

Fig. 34.14. The Effect of Temperature on the Creep Coefficient of Graphite Under Irradiation.

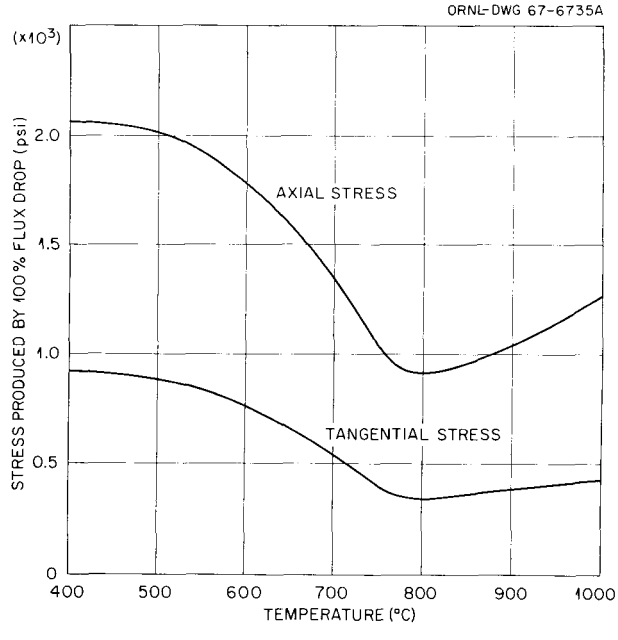

Fig. 34.15. Maximum Stresses Generated in an AGOT Graphite Tube.

the new values; however, the 700°C calculations appear to be in excellent agreement. These experimental results should be considered tentative until they can be confirmed by after-test measurements.

These results offer a reasonable concept of the creep behavior of graphite, from which the differential growth stresses can be calculated. A generalized solution to the problem utilizing existing elastic solutions expanded to consider the anisotropic behavior of graphite growth and creep has been developed. The results of a tubular analysis, which can usually approximate most structures, is shown in Fig. 34.15. The solution is independent of the tubular dimensions with the exception that the flux drop will increase with increasing wall thickness. Most reactor concepts do not have flux gradients greater than 20% in the graphite, and from Fig. 34.15 the maximum stress generated would be 410 psi at 400°C and 180 psi at 800°C. These stress levels are certainly within the strength range of most graphites.

Brazing of Graphite

W. J. Werner

Advanced molten-salt reactor concepts require the joining of graphite fuel tubes to the structural material Hastelloy N. In particular, a high-quality leak-tight braze is needed to join the tubes to a Hastelloy N header and thereby isolate the fuel salt from the blanket salt. The major difficulties encountered are associated with the poor wettability of graphite and the large difference in thermal expansion between graphite and Hastelloy N.

The differential thermal expansion problem is further complicated by the fact that, at the neutron dose rates expected, the graphite may contract considerably during reactor operation. Therefore, if the joint design circumvents the thermal expansion problem through the use of low-expansion materials (such as molybdenum or tungsten) between the Hastelloy N and graphite,[15,16] the braze joint stresses may shift from compressive to tensile during irradiation. This situation is undesirable for a material such as graphite with low tensile strength and ductility. Development work has been focused on (1) a direct joint of Hastelloy N to graphite by a method that leaves the graphite in compression, and (2) the transition joint involving the same low-expansion intermediate materials.

Further study of the Pd–35% Ni–5% Cr alloy discussed previously[16] demonstrated that this alloy has considerable attractiveness for joining graphite to molybdenum or Hastelloy N. Unfortunately, the alloy exhibits poor flowability on high-density graphite; however, its marginal flow is enhanced by preplacing it as foil in the joint.

We are continuing to develop brazing alloys with better wettability and flowability for joining graphite to Hastelloy N. Several new alloys based on the molten-salt-corrosion-resistant Ni-Pd, Cu-Pd, Ni-Cu, and Ni-Nb systems have been prepared for testing.

Compatibility of Graphite-to-Molybdenum Brazed Joints with Molten Fluoride Salts

W. H. Cook

In addition to proper joint design and metal selection, the braze must be compatible with the molten fluoride salts. Specimens of graphite brazed to molybdenum with Pd–35% Ni–5% Cr were exposed for 100, 1000, 5000, and 10,000 hr to molten fluoride salt at 700°C. Some of the results from this series have been reported previously.[17–19] A 20,000-hr test is still in progress. Although no attack is apparent on the braze, some palladium has diffused from the matrix to the surface of the brazed joints. Chemical analyses of the salt used in the tests through the 5000-hr exposure do not show any corrosion products. Examination of the Hastelloy N capsules used in the 5000-hr salt test did not show any transfer of palladium to the capsule surfaces.

These observations show that the brazing alloy does "sweat" palladium to its surface but is not attacked by salt in 10,000 hr under the conditions described above. Additional salt corrosion data on this alloy will be obtained. A joint made with this alloy was included in the surveillance fixture in the MSRE core. Any changes in the braze metal composition will be investigated by suitable corrosion tests.

---

[15] R. G. Donnelly and G. M. Slaughter, "The Brazing of Graphite," *Welding J. (N.Y.)* 41(5), 461–69 (May 1962).

[16] J. M. Jones and R. G. Donnelly, *Metals and Ceramics Div. Ann. Progr. Rept. June 30, 1966*, ORNL-3970, pp. 198–200.

[17] W. H. Cook, *Metals and Ceramics Div. Ann. Progr. Rept. June 30, 1966*, ORNL-3970, pp. 200–2.

[18] W. H. Cook, *MSR Program Semiann. Progr. Rept. Aug. 31, 1966*, ORNL-4037 pp. 115–17.

[19] W. H. Cook, *MSR Program Semiann. Progr. Rept. Feb. 28, 1967*, ORNL-4119, pp. 111–15.

35. Reactor Evaluation

A. L. Lotts

The total cost of producing heat or power by nuclear energy is composed of a multitude of interacting relationships. Capital costs, operating costs, and fuel-cycle costs are some of the general terms used to collectively identify categories. To achieve a meaningful reduction in cost, one must consider the problem in its entirety and recognize the effect that changes made in one area may have on others. The Laboratory is engaged in studying this general problem, and our role is to examine fabrication costs and fuel-element performance as they relate to the fuel cycle and other cost areas. Accordingly, we work in conjunction with chemical processing personnel in the Chemical Technology Division and the physicists and design engineers in the Reactor Division. Thus, we report here only fragments of much broader studies.

COMPUTER PROGRAM DEVELOPMENT

T. N. Washburn F. R. Winslow

An indispensable factor in the evaluation and comparison of various proposed reactor systems is the cost of fuel-element fabrication. Accordingly, we have assisted the evaluation of reactor concepts by providing extensive studies of this cost.

The prediction of fabrication costs involves the selection of fabrication procedures and flowsheets and the calculation of operating costs, capital costs, and the costs of materials used in the processes. Also, one must apply certain factors such as the fabrication environment, the prospects of success for the process, and the method of financing. Because a large number of variables are involved in calculating fabrication costs, we previously[1] developed three computer programs to perform the calculations on a limited number of fuel-element types.

The programs work in the following way. All the information concerning the process and the costs involved in the process are stored in the computer program. When the fuel element, the plant in which it is to be fabricated, and the manner in which the plant is to be operated and financed are described, fuel fabrication costs can be calculated for a number of production rates.

Our efforts for this year in computer code development for calculating fuel fabrication costs consist primarily of extension of the codes to include fast-reactor fuels. These fuels present a unique problem in that the core fuel elements containing recycle plutonium require remote fabrication, while the radial and axial blanket fuel contains depleted uranium and can be fabricated in simple ventilated hoods. Two characteristics of fast-breeder-reactor fuel elements are small fuel diameter (less than 0.350 in.) and short lengths (about 30 in.). Since both of these dimensions restrict the quantity of fuel per fuel rod, they produce an increase in fuel fabrication costs relative to current light-water reactor designs. Thus, for fast-breeder-reactor fuels, fabrication costs assume an even more significant role in determining fuel cycle costs.

A typical simplified fabrication flowsheet for breeder reactor fuel is shown in Fig. 35.1. A single fabrication plant produces both radial blanket and core fuel elements for a given reactor type. The plant is physically divided into two areas; one is suitable for remote fabrication of equilibrium-cycle mixed oxide (UO_2-PuO_2), while

[1] A. L. Lotts, *Metals and Ceramics Div. Ann. Progr. Rept. June 30, 1964*, ORNL-3670, pp. 254–55.

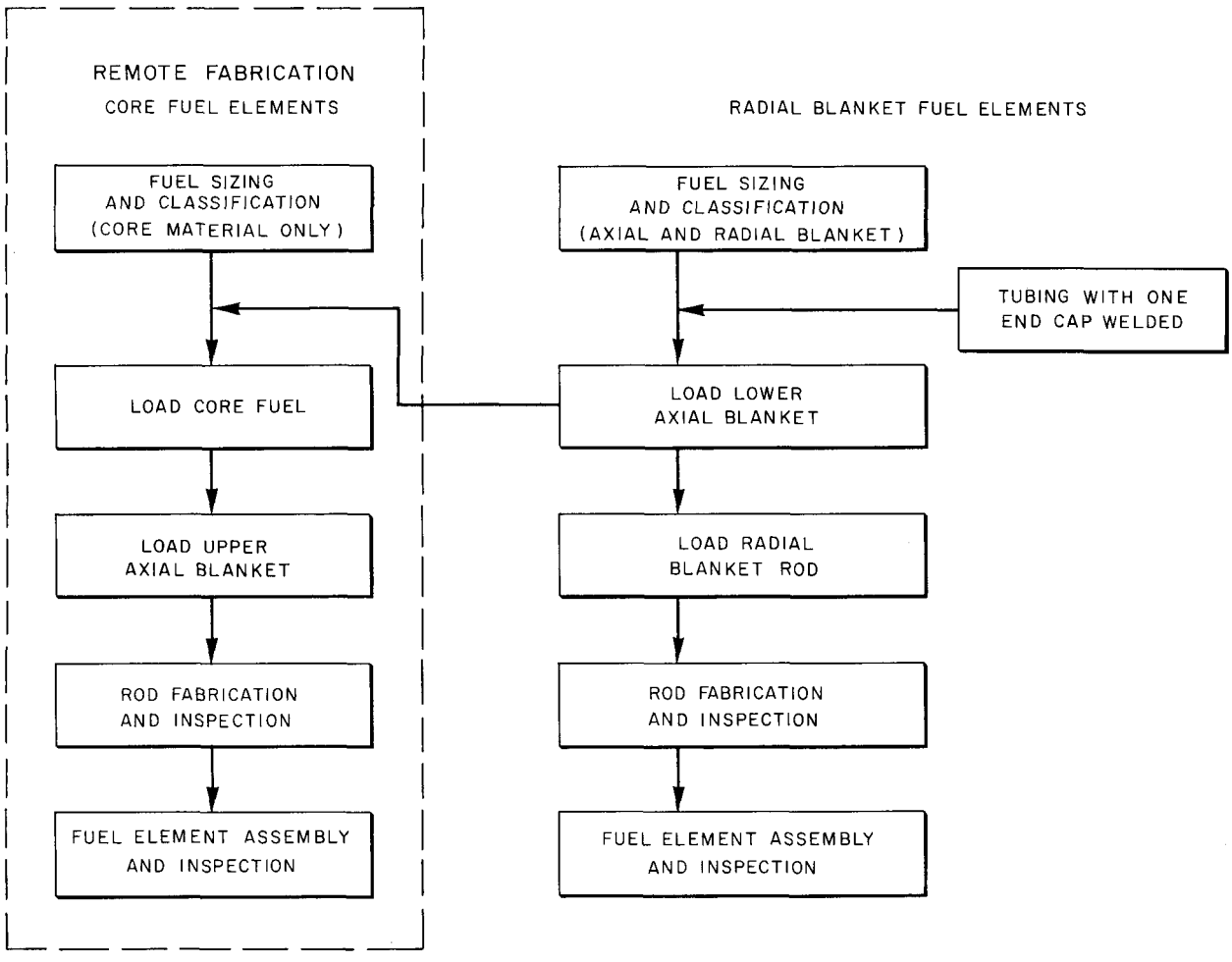

Fig. 35.1. Simplified Flowsheet for Fabrication of Breeder Reactor Fuel by Vibratory Compaction.

the adjacent area for fabricating radial blanket fuel is comparable to existing plants producing light-water-reactor fuel. Axial blanket fuel is sized and classified along with the radial blanket material (both are depleted UO_2). Fuel for the lower region is loaded into the cladding tubing and transferred to the remotely operated section of the plant for loading of core fuel and the upper axial blanket.

HWOCR FUEL FABRICATION COST ESTIMATES

T. N. Washburn

One of the principal tasks undertaken during the year was the continuation of the Heavy-Water Organic-Cooled Reactor (HWOCR) evaluation to assess alternative fuel element designs. Our evaluation of the initial fuel element designs was previously reported.[2,3] Four additional fuel element designs were evaluated. Two, proposed by Atomics International–Combustion Engineering (AI–CE), were natural-enrichment uranium monocarbide with SAP cladding and natural uranium metal coextruded with Zircaloy cladding as annular

[2]T. N. Washburn and A. L. Lotts, *Metals and Ceramics Div. Ann. Progr. Rept. June 30, 1966*, ORNL-3970, pp. 205–08.

[3]P. R. Kasten, R. E. Adams, R. S. Carlsmith, R. H. Chapman, E. P. Epler, E. H. Gift, F. E. Harrington, M. L. Myers, R. C. Olson, J. T. Roberts, R. Salmon, J. P. Sanders, R. S. Stone, D. R. Vondy, C. S. Walker, T. N. Washburn, L. B. Yeatts, and F. C. Zapp, *An Evaluation of Heavy-Water-Moderated Organic-Cooled Reactors*, ORNL-3921 (January 1967).

rings. The other two designs were submitted by the Babcock and Wilcox Company (B & W). One of these consisted of thorium-uranium oxide vibratorily compacted in SAP cladding; the other consisted of thorium-uranium alloy coextruded with Zircaloy cladding as annular rings. The details of each design have been described.[4,5]

The method of estimating fuel fabrication costs was consistent with and similar to that used in the advanced converter evaluation.[6] Both operating and capital costs were stored in the computer program for performing each step of the fabrication process over a wide range of production rates. Costs of tubing, end caps, and other items of fuel-element hardware were specified, with values covering the ranges of physical dimensions, quality level, and procurement rates required for different evaluations. Input data for each particular case included a specification of the fuel element parameters, the fabrication process selected, annual capital charge rate, an estimated reject rate, plant utilization factor, and the production rates of interest. The computer program then selected the appropriate cost for each step of the process and accumulated and manipulated these costs for each specified set of conditions to calculate the fuel fabrication cost in dollars per kilogram of heavy metal.

Input material to the fabrication plant is ceramic-grade UO_2 for the uranium monocarbide design, metal billets for the natural uranium metallic fuel design, sol-gel-produced high-density thoria-urania fragments for the oxide case, and thorium powder briquettes with fully enriched uranium metal for the metallic fuel case. For each of these fuels, output of the fabrication plant consists of fuel assemblies packaged for shipment and suitable for loading into the reactor.

Table 35.1 compares the fuel-element design parameters and fabrication costs of these four alternate HWOCR design concepts. The natural-fueled designs have low fuel fabrication costs per unit weight for three basic reasons: (1) large fuel loadings per piece fabricated, (2) absence of criticality problems, and (3) minimum health hazards to fabrication personnel. The thorium-fueled concepts are designed to operate at higher specific powers and thus require thinner fuel sections; they contain fully enriched uranium, which involves stringent criticality-control procedures; and the health hazards associated with recycle thorium dictate the need for remote fabrication facilities.

The scale of production to supply fuel for a 15,000-Mw(electrical) industry is a large extrapolation of existing technology and experience for each of the fuel types. Thus the cost estimates obtained are based primarily on engineering estimates and judgments. A significant amount of pilot-plant fabrication of uranium monocarbide has been reported.[7] Uranium has been coextruded with Zircaloy cladding successfully on a production basis for a number of years. Also, thorium-uranium alloys have been coextruded with Zircaloy cladding at Hanford,[8] Savannah River,[9] and Nuclear Metals, Inc. There is no experience, however, relative to remote fabrication by this process. Therefore, the accuracy of the cost estimate for the metallic thorium-uranium fuel assembly is probably less than that for the uranium assembly.

The major area of extrapolation for fabrication of the thorium cores is the large-scale application of remote operations required for recycle fuel. While sol-gel thoria-urania fuel has been vibratorily compacted at the ORNL Kilorod Facility,[10-12] and B & W has evaluated the process on a pilot-plant

---

[4] P. R. Kasten, *An Evaluation of Heavy-Water-Moderated Organic-Cooled Reactors*, ORNL-3921, suppl. A (to be published).

[5] P. R. Kasten, *An Evaluation of Heavy-Water-Moderated Organic-Cooled Reactors*, ORNL-3921, suppl. B (to be published).

[6] M. W. Rosenthal *et al.*, *A Comparative Evaluation of Advanced Converters*, ORNL-3686 (January 1965).

[7] D. K. Magnus, *ESADA Fuel Fabrication Development Program Terminal Report*, AI-8700, Vols. I–IV (December 1963).

[8] R. S. Kemper *et al.*, *Fabrication of Zircaloy-2 Clad Thorium-Uranium Alloy Fuel Elements*, HW-79843 (March 1964).

[9] S. R. Nemeth, ed., *Thorium–1.4 wt % ^{235}Uranium Metal Fuel Tubes – Fabrication and Irradiation in HWCTR*, DP-943 suppl. (April 1965).

[10] J. D. Sease, F. C. Davis, and A. L. Lotts, *Thorium–Uranium-233 Oxide (Kilorod) Facility – Rod Fabrication Process and Equipment*, ORNL-3539 (April 1964).

[11] C. C. Haws, J. L. Matherne, F. W. Miles, and J. E. VanCleve, Jr., *Summary of the Kilorod Project – A Semiremote 10-kg/day Demonstration of $^{233}UO_2$-ThO_2 Fuel-Element Fabrication by the ORNL Sol-Gel Vibratory-Compaction Method*, ORNL-3681 (August 1965).

[12] J. E. VanCleve, Jr., J. J. Varagona, and A. L. Lotts, *Time Study of Fuel Rod Fabrication in the Kilorod Facility*, ORNL-3740 (October 1965).

Table 35.1. Comparison of Fuel Element Design Parameters and Fabrication Costs[a] – HWOCR

	AI–CE		B & W	
Fuel composition	UC	U	$(Th,U)O_2$	Th,U
Fabrication cost				
$/kg	19.26	8.90	40.89	27.96
mills/kwhr (electrical)	0.30	0.16	0.22	0.18
Fuel diameter, in.	0.629			
Ring 1, OD		3.168		4.730
Ring 1, ID		2.642		4.530
Ring 2, OD		2.477		4.130
Ring 2, ID		1.891		3.830
Ring 3, OD		1.754		3.430
Ring 3, ID		0.928		3.020
Ring 4, OD				2.620
Ring 4, ID				2.136
Large rods (31)			0.471	
Small rods (6)			0.298	
Fuel length, in.	41.5	43.0	42.7	45.0
Fuel per rod, kg heavy metal	2.73		0.85	
Ring 1		9.0		12.4
Ring 2		7.5		16.2
Ring 3		6.5		17.9
Ring 4				15.6
Rods per assembly	19	3	37	4
Fabrication rates				
kg U/day	6722	7859	2385	2740
rods (rings)/day	2460	216	2805	175
assemblies/day	130	72	76	44
Burnup, Mwd/MT	8000	6700	21,900	19,600

[a]Based upon 15,000 Mw(electrical) industry, 260 operating days/year for fabrication plant, 22% annual capital charge rate.

scale in a hooded facility,[13] there is no experience to date on operation of a remotely operated fabrication plant as envisioned. However, a detailed engineering design of both facilities and equipment for remote fabrication has been accomplished[14] for the Thorium-Uranium Recycle Facility (TURF) at ORNL. In addition, design studies and evaluation of factors involved in plant extrapolations have been done extensively in other work at ORNL.

AEC FUEL RECYCLE TASK FORCE

T. N. Washburn

We are participating in the activities of the AEC Fuel Recycle Task Force in their contribution to updating the 1962 *Report to the President on the Civilian Nuclear Power Program.* We have the responsibility for developing fuel fabrication costs

[13]G. Schileo and L. R. Weissert, "A Pilot Plant for the Production of Th-U^{233} Recycle Fuels," paper presented at the VIII Congresso Nucleare of the Comitato Nazionale per L'Energia Nucleare, Rome, Italy, June 17–23, 1963.

[14]A. R. Irvine, A. L. Lotts, and A. R. Olsen, "The Thorium-Uranium Recycle Facility," *Proceedings of the 13th Conference on Remote Systems Technology, 1965,* Am. Nucl. Soc., Hinsdale, Ill., 1966.

for a variety of reactor types. These include pressurized-water and boiling-water reactors (including plutonium recycle for each); Heavy-Water-Moderated Organic-Cooled Reactors with alternate fuels of low-enriched uranium monocarbide, natural uranium monocarbide, natural uranium metallic fuel, thorium-uranium oxide, and thorium-uranium alloy; Heavy-Water-Moderated Boiling-Light-Water Reactors with natural UO_2 fuel; High-Temperature Gas-Cooled Reactor; Steam-Cooled Breeder Reactor; Gas-Cooled Fast Reactor; and Liquid-Metal-Cooled Fast Breeder Reactors. In addition to estimating these fuel fabrication costs with computer codes developed at ORNL, we are conducting studies into two closely associated areas:

1. Development of a model for determining the economic optimum quantity of fuel material backlogged at the fabrication plant as working inventory. This quantity is influenced by the value of the material, the inventory charge rate, the scale of production, and the penalties suffered by downtime because of an inadequate supply of material to process.

2. Evaluation of an economically optimum schedule for the addition of fuel fabrication capacity as a function of projected growth rate of installed nuclear electric generating plants. The alternatives of building fabrication capacity on an "as-needed" basis, expansion of existing plants, and overbuilding capacity based upon future projected needs are being investigated.

All of this work is currently being conducted, and the results are not yet available for publication.

36. Thorium Utilization

A. L. Lotts

The simplification and cost reduction of the thorium fuel cycle as it pertains to the processing of bred fuels has been the aim of a joint effort of the Chemical Technology and Metals and Ceramics Divisions for several years. Since the recent evaluations of reactors that would use the Th-^{233}U fuel cycle have shown that the high-temperature gas-cooled reactor has the greatest potential for utilization of this cycle, the direction of our program has changed to place more emphasis on the fueled-graphite elements required for such reactors. The development is aimed specifically at the advanced reactor fuel element designs by General Atomics Division of General Dynamics Corporation, as exemplified by the fuel element for the Fort St. Vrain Reactor of the Public Service of Colorado. The project is to culminate in a demonstration of the refabrication of fuels of the type that would be used in that reactor and larger power reactors using similar fuel. Also included in the program is a demonstration of recycling fuel to the Peach Bottom reactor of the Philadelphia Electric Corporation. Fuel elements for Peach Bottom would be of the same type, but much smaller.

We are comprehensively developing pilot-scale processes and equipment for recycle of advanced HTGR fuels. The work includes process development, engineering development, equipment design, pilot-scale demonstration of processing, product evaluation, and irradiation testing. The program is tied quite closely to the Gas-Cooled Reactor Project, particularly that aspect of the program dealing with the testing of coated-particle fuels, which is reported in Chap. 31 of this report.

THORIUM-URANIUM RECYCLE FACILITY

A. L. Lotts

The final objective of the thorium-utilization program is to furnish data and information on reprocessing and refabrication required for various fuel elements of the thorium fuel cycle. The assessment of such recycling technology and economics requires the development of data at pilot-scale production level for the recycle processes. There may be economic advantages in recycling fuel through low-decontamination processes and then remotely refabricating fuel elements. Also, the ^{232}U decay in the recycle fuel produces increasing radioactivity and necessitates biological protection. Consequently, we are now completing the construction of the Thorium-Uranium Recycle Facility, which will permit the development and evaluation of a variety of integrated fuel processing and refabrication schemes at the necessary pilot-scale levels.

Concurrently with the construction of the facility, research and development are proceeding on the first fabrication line to be installed in TURF, and the design of the line has been initiated. It will prepare sol-gel microspheres and refabricate prototype HTGR elements.

Detailed information on this program may be obtained from another report.[1]

Building

J. M. Chandler[2] J. W. Anderson[3]

The Thorium-Uranium Recycle Facility (TURF), a heavily shielded radiochemical treatment–fuel

[1] R. G. Wymer and A. L. Lotts (compilers), *Status and Progress Report for Thorium Fuel Cycle Development Dec. 31, 1966* (in preparation).

[2] Chemical Technology Division.

[3] General Engineering and Construction Division.

element fabrication plant,[4] is being constructed; shakedown operations of the facility will be completed by January 1968. The construction contract for this $7,250,000 facility was awarded May 6, 1965, to the Blount Brothers Construction Company of Montgomery, Alabama. It now appears that the fixed-price construction by Blount Brothers Construction Company will be completed in the Fall of 1967. At the completion of the fixed-price contract, a cost-plus-fixed-fee contractor will begin the final phase of the TURF construction project, which includes the installation of the manipulator and crane systems, waste sampling equipment, viewing windows, cell penetration closures, and equipment mounting fixtures. This contractor will also rework some construction items remaining from the Blount contract. Giffels and Rossetti, Inc., Detroit, Michigan, is the architect-engineer for the TURF design and the fixed-price construction phase of the contract.

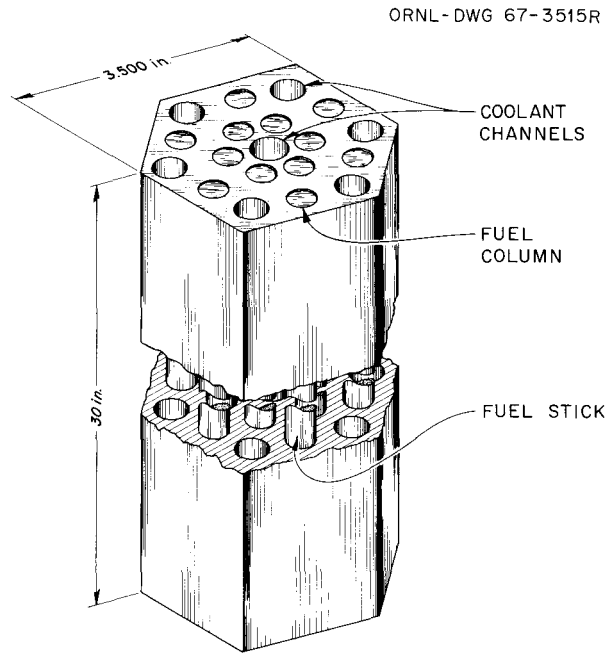

Fig. 36.1. Modified PSC Element for the Peach Bottom Reactor.

Fueled-Graphite Line

J. D. Sease S. E. Bolt[5]
F. C. Davis[3]

We continued the development and design of a remote fabrication line that will be installed in TURF to demonstrate the refabrication technology of High-Temperature Gas-Cooled Reactor (HTGR) fuel elements. Advanced HTGR fuel elements consist of graphite blocks with holes for fuel and for the passage of the coolant gas. The fuel holes are filled with pyrolytic-carbon-coated microspheres of thoria and urania in a carbonaceous matrix. For the design of the fabrication line, the reference fuel element is based on the design of the Public Service of Colorado Fort St. Vrain Reactor (PSC) fuel element and consists of a 3.5-in.-diam hexagonal block modified to fit the existing Peach Bottom core. In Fig. 36.1, a segment of the reference fuel element shows the pertinent design features. Even though the modified Peach Bottom element will be the design reference, only a minimum amount of retooling will be required to make the larger elements for PSC (14.5-in.-diam hexagonal block containing 216 fuel holes). The design production rate for the fabrication line has been established at 10 kg/day of fissile material and 10 kg/day of fertile material. The flexibility of the design will permit us to handle and fabricate any combination of $^{235}UO_2$, $^{233}UO_2$, and ThO_2 that may be selected for the optimum fuel cycle. The production capacity of the present design in a 24-hr day, with a 70% plant factor, is approximately 30 Peach Bottom segments 30 in. long or 2 PSC elements 30 in. long.

The process flow diagram for the TURF fueled-graphite refabrication line is shown in Fig. 36.2. A general division of this process line in the TURF hot cells based on contamination levels is represented by the shading around segments of the flowsheet. The operations that involve potential contamination or direct contact with fuel particles will be carried on in cell D; the relatively clean operations of element assembly and inspection will be carried on in cell E. In the particle-coating operations, particles will be transferred by a pneumatic system.

Scaled-down production-type equipment will be used for the fueled graphite line to provide technical and economic information applicable to a production facility. The equipment for cell D,

[4]A. R. Irvine, A. L. Lotts, and A. R. Olsen, "The Thorium-Uranium Recycle Facility," pp. 19–24 in *Proceedings of the 13th Conference on Remote Systems Technology, 1965*, American Nuclear Society, Hinsdale, Ill., 1966.

[5]On loan from Reactor Division.

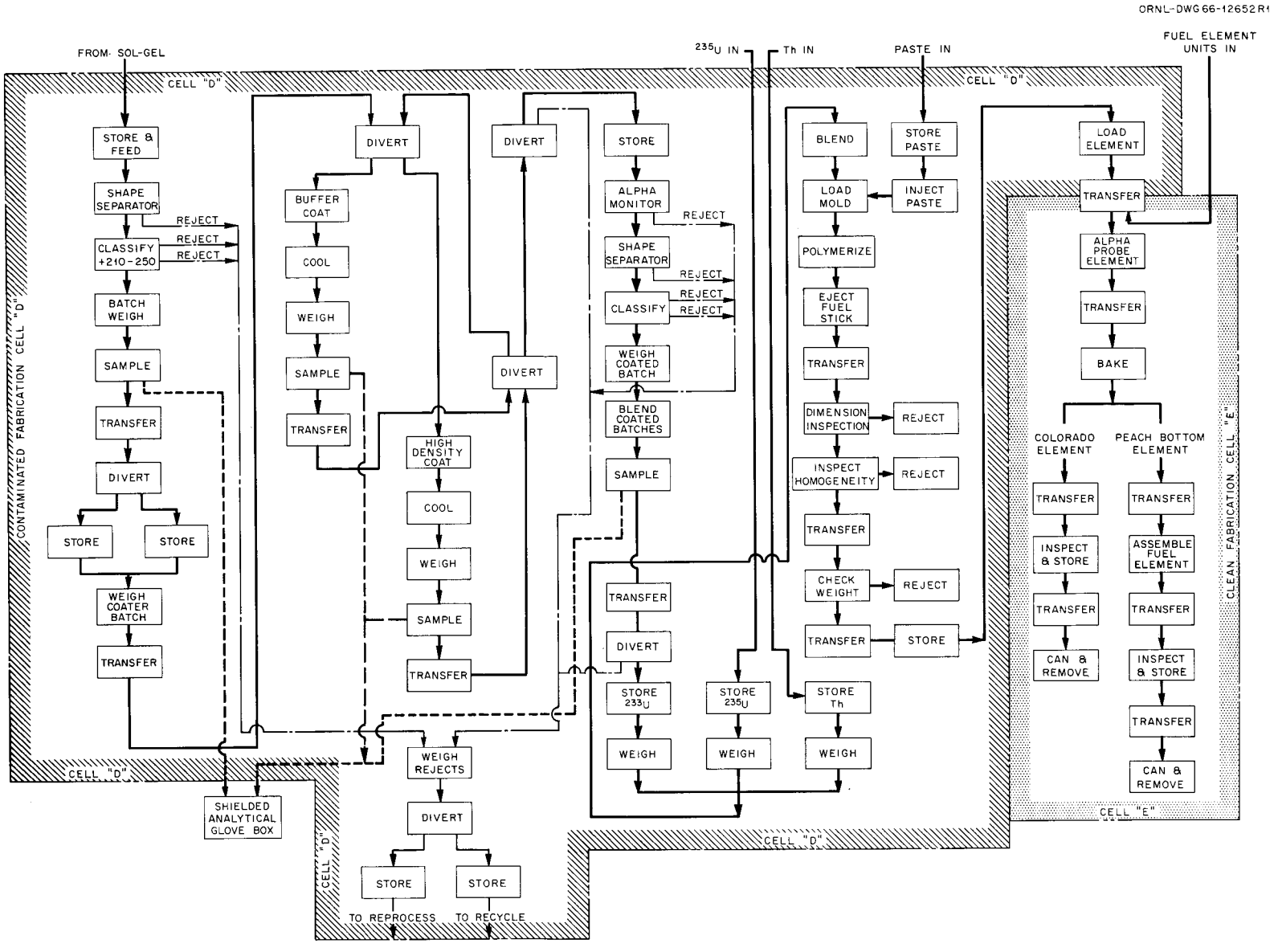

Fig. 36.2. Process Flow Diagram for Recycle HTGR Fuel in TURF.

because of the high probability of contamination, will be capable of installation, maintenance, and removal by the cell remote-handling equipment. In cell E, where little contamination is expected, provisions for maintenance by manipulators will not be extensive.

We have completed the conceptual design of 90% of the process equipment in cell D and 10% of the equipment in cell E. We completed a detailed study of the process control and data handling requirements, which represents approximately 75% of the conceptual design of this phase of our engineering effort. Our detailed design effort was concentrated on the prototype remote coating and effluent handling system. This design, representing 5% of the cell D detailed design requirement, was completed, and the equipment is being fabricated.

A critical-path schedule was developed and is being used in the execution of the project. The scheduled date for completion of fabrication and installation of the process in the TURF and the initiation of cold processing runs is late 1969.

FUELED-GRAPHITE DEVELOPMENT

J. D. Sease

Our development of fueled-graphite processes is directed towards fulfilling the requirements of the design of the TURF fueled-graphite line. Our main concern is to develop simplified processes that will result in the lowest fuel-cycle costs. In some cases we must develop special processes to meet the requirements of the TURF remote environment. The work is in five parts: particle handling, particle coating, particle inspection, particle blending and bonding, and fuel element inspection.

Particle Handling

J. T. Meador[5]

In passage through the fabrication line, 10 kg or 10^8 particles per day of fissile materials must be stored, weighed, transferred, coated, classified, shape-separated, inspected, blended, and dispensed. Another 10 kg of fertile material is added at the blending and dispensing step. We have developed a variety of devices to satisfy these requirements. A pneumatic fuel-transfer system was developed, which can transfer coated particles without damage through at least 50 ft of $\frac{1}{4}$-in.-OD tubing with verticle lift of 16 ft at rates near 500 g/min. A new high-efficiency shape-separation process was developed, which minimizes particle interference during separation and allows gradation of the particles by shape. The classification process to grade uncoated and coated fuel particles within $\pm 5\ \mu$ and with a minimum of screen blinding was developed; it uses precision etched screens and a natural-frequency vibratory feeder unit.

Particle Coating

R. B. Pratt S. E. Bolt[5]

The coating of nuclear fuel particles with pyrolytic carbon probably represents the most expensive step in fabricating HTGR fuel elements. The principal requirement is that the particles should have duplex pyrolytic carbon coatings, the interior layer having a low density of less than 1.2 g/cm^3. We are seeking the best combinations of processing parameters, gases, and equipment to meet these specifications on an engineering scale.

After investigation of a number of coating systems,[6,7] the fluidized-bed coater appears to be the best for remote operation; therefore, essentially all of our efforts have been concentrated on the development of fluidized-bed coating and the design of a prototype remote fluidized-bed coating system.

A 5-in.-diam coating chamber with a single-inlet nozzle was used in most of our experiments. Over 400 experimental coating runs were made in defining the coating conditions of this system. First, a process was developed to produce buffer coatings with controlled density from 0.4 to 1.4 g/cm^3 on bare 230-μ-diam particles in batches up to 1500 g of $(Th,U)O_2$ particles. The coating is deposited at approximately 1200°C with acetylene as the carbon supply. The variation in densities was obtained primarily by controlling the total gas flow and the partial pressure of acetylene in a dilution gas such as helium. Temperature variation of the

[6]H. J. Flamm, *An Entrained-Fluidized-Bed System for Pyrolytic Carbon Coating of Microspheres*, ORNL report in preparation.

[7]A. L. Lotts and R. L. Pilloton, "Fueled-Graphite Development," *Status and Progress Report for Thorium Fuel Cycle Development for Period Ending Dec. 31, 1965*, ORNL-4001, pp. 69–92.

ORNL-DWG 67-2691R

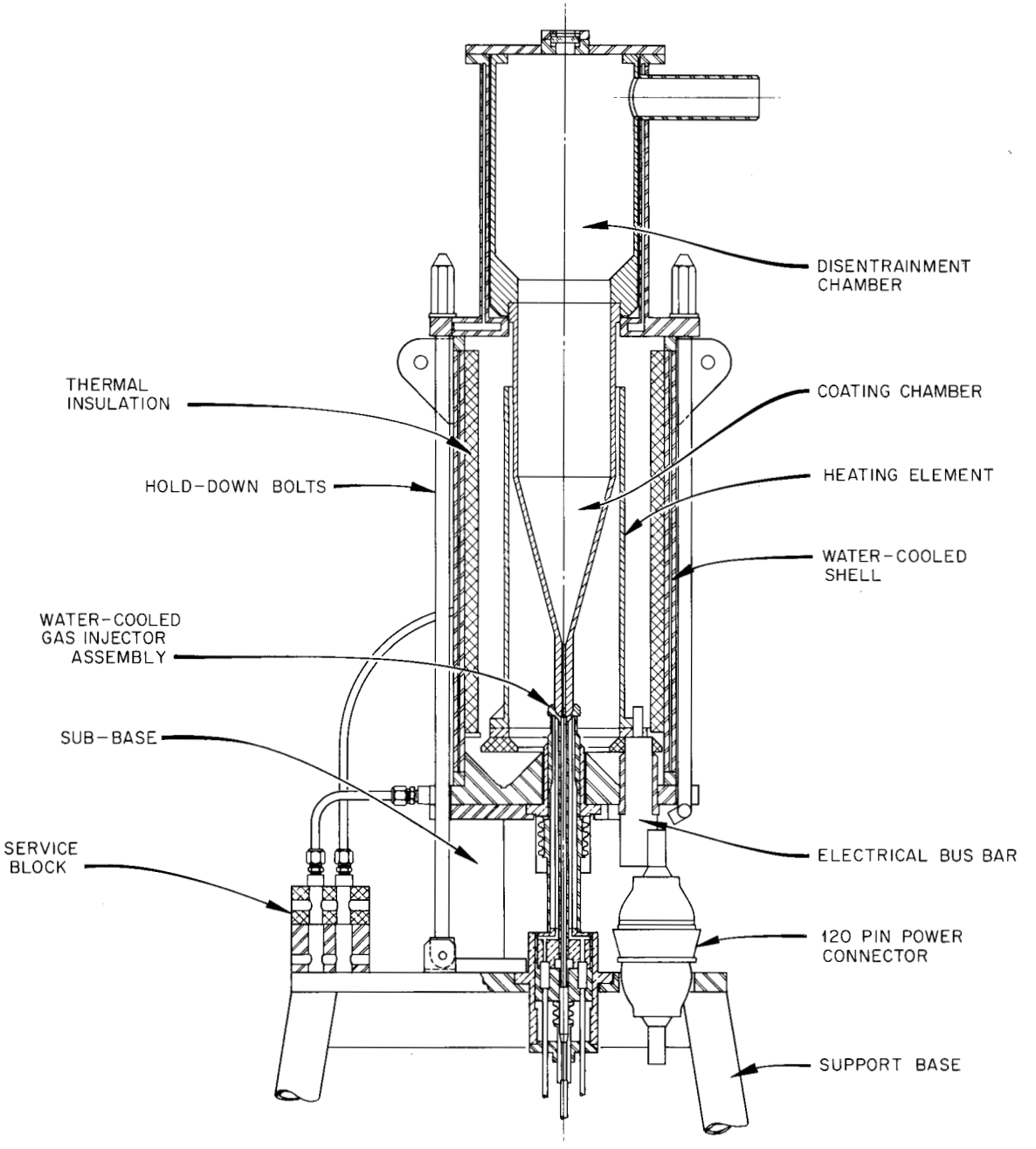

Fig. 36.3. Prototype Remote Fluidized-Bed Coater.

coating chamber between 1000 and 1300°C had minimal effects on the coating properties.

In developing the high-density isotropic outer coating, we have concentrated our efforts on a low-temperature coating process (1200 to 1500°C) using propane and propylene as the carbon-supply gases. These gases have several advantages over methane, the gas most generally used in the coating of nuclear fuel particles. In comparison with methane, propane and propylene can produce an isotropic high-density coating at a deposition temperature of 500 to 600°C lower and with a deposition rate of 4 to 5 times greater. We have defined the temperatures and gas flow conditions to produce isotropic (Bacon anisotropic factor <1.1) coatings with densities of about 1.9 g/cm^3

at coating rates up to 3 μ/min. These coatings are deposited on buffer-coated particles from both propane and propylene.

Based on our experience with the 5-in. coating system, a prototype remote fluidized-bed coating system was designed and is now being fabricated. It consists of a 5-in.-diam fluidized-bed coater, services, loading and unloading system, and instrumentation to monitor and control the process. The coating furnace portion of this system is shown in Fig. 36.3.

Particle Inspection

W. H. Pechin B. E. Foster
S. D. Snyder

In the present concept of the fueled-graphite line, particle inspection will be performed in a shielded analytical glove box on a small representative sample of each lot of particles. Properties to be determined will include density of the buffer coating and the outer coating, mean values and standard deviations for the kernel diameter and the thickness of the buffer coating and outer coating, shape of the final product, sealing efficiency of the coating, and strength of the coating.

The main effort so far has been on coating thickness and density. In support of the coating development work, the coating density has been calculated from the density of the whole particle as determined with a mercury porosimeter and the coating weight determined by burning the carbon off the ThO_2 kernels.

The effects of the experimental errors in weight and mercury porosimeter determinations were investigated and found to result in a standard error of ± 0.026 g/cm^3 for the low-density coating and ± 0.011 g/cm^3 for the high-density coating. Other methods were compared with the mercury porosimeter, including helium pycnometer, sink-float test of a disk stripped from a carbon substrate coated along with the particles in the fluidized bed, and gradient density determinations on both the disk and coated particles. The sink-float and gradient density determinations were found to be from 0.03 to 0.12 g/cm^3 higher than the mercury porosimeter results. The gradient density determinations on whole particles agreed on the average with the mercury porosimeter, but since the gradient density method requires the use of saturated solutions that must be kept at constant temperature above room temperature, they require considerably greater effort and care. The difference between gradient density results on the disks and on the whole particles was attributed to the fact that organic solutions that were used for the former wet the carbon more readily and caused greater infiltration of open porosity.

The variation in coating thickness is determined by measurement from a microradiograph. The shape factor presently being used is the ratio of the minimum to the maximum diameter on a microradiograph of the coated particle. No work has yet been done on coating strength or sealing efficiency.

The mercury porosimeter and burn-off methods apply to particles with a single coating; however, when the high-density coat is applied over a low-density coat there is an infiltration of the low-density coating increasing its density. This effect was investigated by including undersized bare particles with each batch of buffered material charged to the furnace for overcoating. After the run, the undersized material was sifted out of the charge and analyzed to determine the density of the overcoat. With a known overcoat density, the increase in density of the buffer coat could be determined. The density increase was found to be a function of starting density, gas flux, temperature, and hydrocarbon gas. The effect has been evaluated on the basis of the fraction of the open pore volume of the buffer coat that was filled with carbon during the overcoating process. This fraction varied from 20 to 70% and was a maximum in the 1200 to 1300°C temperature range for propane and propylene. The effect was less pronounced with propylene, for which the maximum for a gas flux of 2.0 cm^3/sec per square centimeter of particle surface was 55% at 1280°C, compared to a maximum of 70% at 1250°C for propane.

Metallography has been used to estimate the anisotropy factor of the coatings, based on the intensity of the cross formation observed under plane-polarized light. The quantitative determination of anisotropy is based on an x-ray diffraction analysis, which measures the ratio of the intensities of the 0.02 diffraction peaks from basal planes parallel and perpendicular to the deposition plane.

In addition to the more conventional analytical techniques, we are investigating a number of systems for coating analysis that will be more amenable to requirements of the TURF operation.

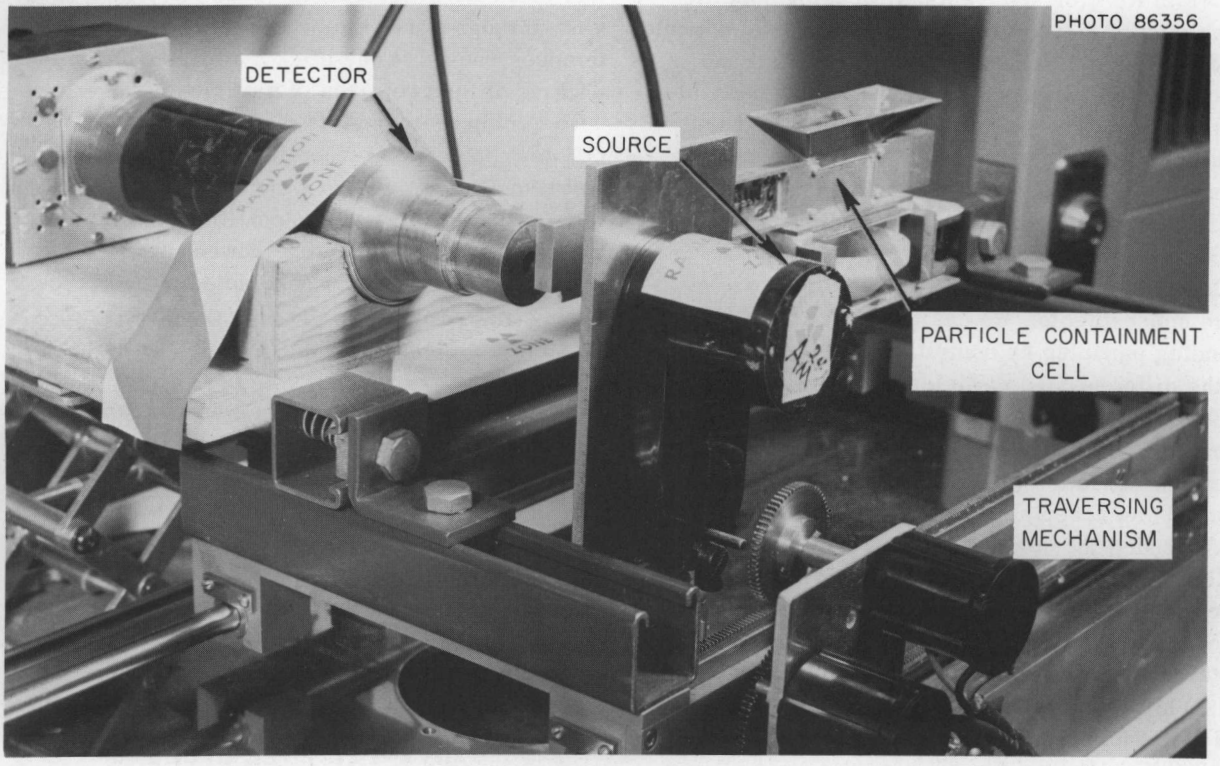

Fig. 36.4. Particle Coating Thickness Scanner.

An automatic particle counter and size analyzer has been procured and is being investigated as a means to provide the coating thickness and density data in less time and for a larger sample.

An in-line process monitor for measuring the average thickness of pyrolytic carbon on ThO_2 microspheres is being developed. For this system, we have chosen an x-ray attenuation technique using ^{241}Am as the radiation source and a NaI(Tl) crystal optically coupled to a photomultiplier tube as the detector.

Figure 36.4 shows the scanner mechanism, detector, and electronic instrumentation. The containment cell for the microspheres is made of 0.020-in.-thick beryllium. The inside cell dimensions are $\frac{1}{16}$ in. wide × 2 in. long × 1 in. high. The cell is filled with the coated microspheres and moved into the radiation beam for measurement. The scintillation detector monitors the transmitted radiation intensity. Through proper calibration, the transmitted intensity can be related to the coating thickness on a specific kernel diameter. The output current is read directly in coating thickness units (μ).

The system has been used quite successfully on specific kernel diameters within the range of 230 to 380 μ with carbon coating thicknesses of 10 to 170 μ. The equipment must be recalibrated for different kernel diameters. This is accomplished by use of accurately sized kernels with known uniform coating thicknesses. The coating thickness for initial calibration is achieved by measuring the thickness with low-voltage microradiographs of single-layer microspheres.

A similar technique using lower x-ray energies is being developed to measure the coating densities.

Bonding of Pyrolytic-Carbon-Coated Fuel Particles

J. M. Robbins R. L. Hamner

We studied methods for loading coated fuel particles into the fuel holes of graphite fuel elements similar to the design proposed for the Fort

St. Vrain Reactor.[8,9] Tentative loading specifications require that the fissile and fertile fuel particles be of two sizes, be homogeneously blended and loaded into the fuel holes to a packing density of 60 to 64 vol %, be bonded together so that they would not spill freely into the reactor if a fuel element were broken, and be provided with as much carbon as possible in the bonding material for cesium absorption.

Conventional techniques for blending particles were unacceptable. We designed equipment for blending particles by controlling the feed rates of the different-size particles as they flowed simultaneously from separate feed hoppers into a simulated fuel hole. By this technique, the maximum deviation from the ideal blend was less than 5%, an acceptable value.

We bonded the coated fuel particles into solid cylindrical rods (which we call fuel sticks) by injecting phenolic resin and powdered charcoal into the interstices of particles contained in metal molds and heating the assembly at 80°C for 40 hr to polymerize the resin. After removing the fuel sticks from the molds, we heated them at 1000°C in helium to carbonize the resin.

We made fuel sticks 0.5 in. in diameter and 12 to 30 in. long with fuel loadings of 60 to 64 vol % and bonding matrix carbon concentrations of 0.7 to 0.8 g/cm^3. We found that (1) shrinkage of the bonding matrix during carbonization did not affect the dimensions of the fuel stick; (2) particles having methane-deposited coatings were satisfactorily bonded; (3) particles having porous propylene-deposited coatings were so strongly bonded to the matrix that the coatings cracked during shrinkage of the matrix and also upon fracture of the fuel sticks; and (4) particles having smooth, nonporous coatings of silicon carbide or of pyrolytic carbon deposited from propylene were not bonded at all.

We propose ultimately to insert the fuel sticks into the fuel holes and to carbonize them in the fuel block.

Fuel Element Inspection

B. E. Foster S. D. Snyder

In fuel element inspection our work has been mainly confined to testing the homogenity of the fuel stick prepared with particles of two different sizes to simulate the fissile and fertile fuel in the fuel element. Our technique uses the principle of x-ray through transmission to detect density differences caused in the stick by differences in the packing of the two sizes of particles.

The equipment consists of a Norelco 50-150 kv constant potential commercial x-ray unit, a beryllium-window 150-kv constant potential x-ray tube, a NaI(Tl) crystal-photomultiplier combination detector, a high-voltage power supply, a strip-chart recorder, and associated signal processing instrumentation. The x-ray beam is collimated to a diameter of 0.078 in. at the surface of the specimen.

Approximate preliminary calibration of the system was obtained through the use of aluminum thicknesses equivalent in x-ray attenuation to that of the fuel sticks with an x-ray energy and intensity of 120 kv constant potential and 0.25 ma, respectively. To establish more confidence in the technique and its calibration, additional fuel sticks differing in average fuel loading will be evaluated with the system.

ADVANCED FUEL CYCLE PROCESS DEVELOPMENT

A. R. Olsen

A preliminary economic analysis has been made for four alternate fuel-rod fabrication techniques based on the unique properties of various sol-gel process products. The fuel-rod fabrication costs, independent of the sol-gel process costs, show the Sphere-Pac process to be least expensive, followed by extrusion, vibratory compaction, and pellet pressing in that order. Since these economic analyses are based on the current state of development, which is limited in some cases, we are continuing the development of all the alternate fabrication techniques at least until the economic studies indicate which development should be discontinued. The fabrication development is closely coordinated with concurrent sol-gel process developments. In addition, the techniques developed for one fuel type are used to guide the development for other fuel types.

---

[8] R. L. Patterson and R. F. Walther, *Trans. Am. Nucl. Soc.* 9(1), 313 (June 1966).

[9] J. M. Robbins and R. L. Hamner, *GCR Program Semiann. Progr. Rept. Mar. 31, 1967*, ORNL-4133, pp. 16–24.

Sol-Gel Extrusion of Thoria-Base Ceramics

R. B. Fitts J. D. Sease

Sol-gel extrusion is the combination of extrusion, which is a high-production-rate fabrication technique, and the sol-gel process. The sol-gel process yields a homogeneous clay-like material that will sinter at low temperature (1150°C for ThO_2) and is suitable for extrusion.[10–12] The sol-gel clay is formed by precipitation from a sol of the desired oxide material. This sol-gel clay at 10 to 12 *M* may be extruded with standard ceramic extrusion equipment to form high-density bodies (about 99% of theoretical density). The sol-gel clay may also be mixed before extrusion with sol-gel-derived powders to produce bodies with controlled densities in the range from 75 to 98% of theoretical, as shown in Fig. 36.5. We demonstrated this process in laboratory-scale work, producing solid and cored thoria extrusions in diameters up to 0.5 in. and lengths to 3 in. The general effects on extrusion density, microstructure, and dimensional tolerances of preaddition heat treatment of the sol-gel powders and of various drying techniques were defined in this work. This process, proven in the thoria system, may enable improvement and economy in the fabrication technology for ceramic shapes of materials such as urania, plutonia, zirconia, alumina, and other ceramics that can be made by the sol-gel process.

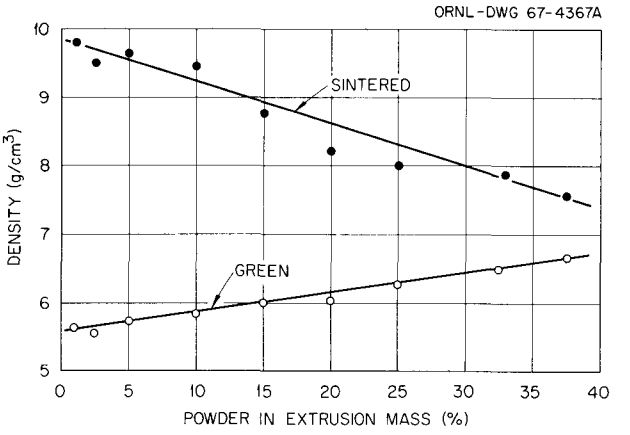

Fig. 36.5. Effect of Powder Additions to Sol-Gel Clay on Green and Sintered Densities of Extruded ThO_2.

Pelletizing of Sol-Gel Thoria-Urania Powders

J. G. Stradley J. M. Robbins

The interest in sol-gel fuel materials for nuclear applications stems from the amenability of the sol-gel process to the recycle of fuels and to its ability to produce homogeneous mixtures of fissile and fertile materials that can be sintered to high densities (>97% of theoretical) at low temperatures (approximately 1150°C). In the past, these materials have been prepared in two forms: fragments, for use in metal-clad fuel elements, and microspheres, which could be either coated with pyrolytic carbon for use in graphite-matrix fuel elements or used bare in metal-clad elements. We extended the technology of fabricating sol-gel materials to the preparation of pellets by cold pressing and sintering.[13]

The material used in our studies was a −200 mesh powder derived from a thoria-urania sol-gel containing 6.5% U. In these studies we considered the following fabrication variables:

Powder calcination temperature: Uncalcined, 200, 400, and 750°C

Powder moisture content: 1 and 5%

Forming pressures: Uniaxial forming at 2000, 3500, and 6500 psi followed by a second forming stage of isostatic pressing at 20,000, 40,000, and 60,000 psi for each uniaxial pressure level

Sintering atmosphere: Air, helium, and hydrogen

[10] R. B. Fitts and J. D. Sease, *Metals and Ceramics Div. Ann. Progr. Rept. June 30, 1966*, ORNL-3970, pp. 219–20.

[11] R. B. Fitts, A. B. Meservey, J. D. Sease, and A. L. Lotts, "Extrusion of Thoria Bodies from Sol-Gel Clay," presented at the American Ceramic Society Annual Meeting in New York, May 1967.

[12] R. B. Fitts, J. D. Sease, and A. L. Lotts, "Preparation of Ceramic Nuclear Fuels by Sol-Gel Extrusion," presented at the AIChE Symposium on Preparation of Nuclear Fuel Materials, Salt Lake City, Utah, May 1967; to be published in a *Chemical Engineering Progress Symposium Series* volume on Nuclear Engineering.

[13] J. M. Robbins and J. G. Stradley, "Fabrication of Sol-Gel Derived Thoria-Urania by Cold Pressing and Sintering," paper presented at the American Ceramic Society Meeting, New York, May 2, 1967; to be published.

In preliminary experiments, we sintered sol-gel pellets at temperatures ranging from 1200 to 1650°C to establish an optimum sintering temperature for our studies. The densities increased about 3% from 1200 to 1425°C, and no further densification occurred between 1425 and 1650°C. We therefore sintered all pellets prepared for these studies at 1425°C for 1.25 hr.

The green strength, green density, and sintered density of the pellets decreased as the powder calcination temperature was increased. However, the effect of calcination temperature on the sintered density was much less for pellets formed at very high pressures (60,000 psi). The effect of the uniaxial forming pressure on the sintered density was not significant. The sintered densities of pellets were increased by increasing the isostatic pressure in the second stage of forming. Also, the structure of the sintered pellets appeared to be more strongly influenced by the isostatic forming pressure than by the other variables studied.

An increase in the moisture content of powders calcined under the same conditions caused an increase in the sintered density and tended to equalize the effect of forming pressure. The pellets were densest when sintered in air, slightly less dense when sintered in helium, and appreciably less dense when sintered in hydrogen. It was necessary, however, to treat the air-sintered pellets with hydrogen to reduce the oxygen-to-uranium ratio from 2.67 to 2.00, but this did not appreciably affect the sintered density.

Under the most favorable conditions of powder calcination temperature, powder moisture content, forming pressures, and sintering atmosphere, we produced 0.5-in. right cylindrical pellets with densities as high as 95% of theoretical. However, we produced pellets having a wide range of densities (down to 78% of theoretical) by selectively adjusting the fabrication variables.

For thermal conductivity measurements, we prepared $(Th,U)O_2$ specimens 2 in. in diameter and 0.5 in. thick ranging from 85 to 93% of theoretical density. However, attempts to achieve very high densities ($\geq$95% of theoretical) in such large pellets resulted in cracking during sintering.

Low-Energy Microsphere Packing (Sphere-Pac)

A. R. Olsen R. B. Fitts

The sol-gel microsphere forming process yields a dense spherical particle that is ideally suited for fabrication of oxide nuclear fuel rods by low-energy vibratory compaction. The initial work on this technique[14] demonstrated that we could produce oxide fuel rods with density 83.5% of theoretical by volume packing of microspheres, utilizing readily available ThO_2 sol-gel spheres. This was accomplished by Sphere-Pac, the sequential loading of coarse and fine microspheres with low-energy vibration to facilitate the infiltration of the fine spheres into the coarse bed.

We have since extended the application of Sphere-Pac fabrication to produce fuel elements for irradiation testing of UO_2, $(U,Pu)O_2$, and $(Th,Pu)O_2$ sol-gel microsphere fuels.[15] We produced 33 test rods in diameters from $\frac{1}{4}$ to $\frac{1}{2}$ in. and lengths up to 2 ft. All of these rods packed to a sphere packing density of 83.5 ± 0.5%.

The principal unknown property that will influence the use of this fabrication technique for reactor fuels is the thermal conductivity. Initial studies on this property are described in Part I, Chap. 9 of this report and in more detail elsewhere.[16]

IRRADIATION OF THORIA-BASE BULK OXIDE FUELS

A. R. Olsen

The irradiation testing and evaluation of metal-clad thoria-base bulk oxide fuels is continuing.

---

[14] A. R. Olsen and J. D. Sease, *Metals and Ceramics Div. Ann. Progr. Rept. June 30, 1966*, ORNL-3970, p. 220.

[15] F. G. Kitts, R. B. Fitts, and A. R. Olsen, "Sol-Gel Urania Plutonia Microsphere Preparation and Fabrication Into Fuel Rods," to be presented at the AIME Nuclear Metallurgy Symposium, "Plutonium Fuels Technology," October 1967 and published in a volume of *Nuclear Metallurgy*.

[16] J. P. Moore, T. G. Kollie, R. S. Graves, and D. L. McElroy, *Thermal Conductivity Measurements on Solids Between 20 and 150°C Using a Comparative-Longitudinal Apparatus: Results on MgO, BeO, ThO_2, $Th_xU_{1-x}O_{2+y}$ and Al-UO_2 Cermets*, ORNL-4121 (June 1967).

Previously reported results[17–23] have shown that sol-gel-derived thoria-base fuels fabricated by high-energy vibratory compaction perform as well as pelletized thoria fuels and that all thoria-base fuels are superior to urania-base fuels in irradiation performance characteristics. We are continuing to investigate the effects of extended burnup, higher heat ratings, and sol-gel processing on the performance of these fuels. We initiated tests on crossed progeny fuels, (Th–5% Pu)O_2 microspheres, fabricated into fuel rods by the Sphere-Pac technique. The current irradiation test program is outlined in Table 36.1.

Currently we have nine fuel rods under postirradiation examination. Three of these rods contained pellets of (Th–4.5% U)O_2 and have been irradiated to a burnup level of approximately 150,000 Mwd per tonne of Th + U (15% FIMA, fissions per initial metal atom). To date only cladding diameter measurements are available, and these indicate a plastic strain of less than 1%, which supports the previous conclusion[21] that the fission-product-induced swelling is in part accommodated by volume changes resulting from the transformation of thorium to uranium and protactinium.

We also started the examination of the two rods in the MTR II group that have been exposed to a burnup of approximately 100,000 Mwd per tonne of Th + U (10% FIMA), at a peak linear heat rating of approximately 600 w/cm. These rods contained vibratorily compacted sol-gel (Th–5% U)O_2 powder. Each of these 56-cm-long rods has a 5-cm-long bulge in the cladding near the end that was down during irradiation. One rod was operated with the fuel bed in contact with the lower end plug. The maximum diameter change at the bulge on this rod was 0.12 cm, representing a plastic strain in the cladding of 15%. The fuel bed in the other rod was separated from the lower end plug by a 1-cm-long gas plenum containing Fibrafax. The maximum change in diameter for this rod was only 0.07 cm or 9% plastic cladding strain. The postirradiation gamma scans showed no significant change in fuel-column height for either rod or penetration of fuel into the Fibrafax. The maximum strain occurred approximately 0.6 cm from the end of the fuel column. We have no logical explanation for this apparently anomalous swelling.

The remaining four rods currently being examined are listed in Table 36.1 as the Sphere-Pac group. These rods were irradiated in the ETR in two capsules of the design described in Part III, Chap. 23 of this report. The fuel was sol-gel-derived (Th–5% Pu)O_2 microspheres packed to a smear density (weight of fuel divided by volume determined from the inside diameter of the tube) of 84% of theoretical. The linear heat ratings were 570 and 440 w/cm and the cladding temperature was approximately 400°C. Although the examination is incomplete, metallographic examination of the fuel beds indicates only incipient sintering of these microspheres in the center of the highest rated rods. These tests were terminated prematurely at a burnup of approximately 7000 Mwd per tonne of Th + Pu because of the failure of the outer secondary cladding on one of the capsules.

Six new irradiation test rods were inserted in the ETR during the past year. These are Sphere-Pac-fabricated rods of mixed progeny fuels identified as the ETR-IV group. The use of plutonium from current power reactors as the fissile enrichment in thorium-base fuels may offer both economical and technological advantages. Pending the development of fast breeder reactors, plutonium may be more economical than highly enriched ^{235}U as a fissile additive to ThO_2 fuels. Also, bred ^{233}U can be separated from the plutonium

---

[17] R. G. Wymer and A. L. Lotts (compilers), *Status and Progress Report for Thorium Fuel Cycle Development Dec. 31, 1966* (in preparation).

[18] A. R. Olsen, J. W. Ullmann, and E. J. Manthos, *Status and Progress Report for Thorium Fuel Cycle Development Dec. 31, 1965*, ORNL-4001, pp. 102–12.

[19] S. A. Rabin, J. W. Ullmann, E. L. Long, Jr., M. F. Osborne, and A. E. Goldman, *Irradiation Behavior of High-Burnup ThO_2–4.45% UO_2 Fuel Rods*, ORNL-3837 (October 1965).

[20] A. R. Olsen, D. B. Trauger, W. O. Harms, R. E. Adams, and D. A. Douglas, "Irradiation Behavior of Thorium-Uranium Alloys and Compounds," pp. 246–91 in *Utilization of Thorium in Power Reactors, Report of a Panel Held in Vienna 14–18 June 1965*, International Atomic Energy Agency, Vienna, 1966; ORNL-TM-1142 (June 1965).

[21] A. R. Olsen, D. A. Douglas, Y. Hirose, J. L. Scott, and J. W. Ullmann, *Proc. Brit. Ceram. Soc.* 7, 289–310 (1967); ORNL-TM-1297 (November 1965).

[22] A. R. Olsen, J. H. Coobs, and J. W. Ullmann, "Current Status of Irradiation Testing of Thorium Fuels at Oak Ridge National Laboratory," paper presented at the Second International Thorium Fuel Cycle Symposium, Gatlinburg, Tennessee, May 3–6, 1966; ORNL-TM-1631 (September 1966).

[23] A. R. Olsen, J. W. Ullmann, Y. Hirose, and E. J. Manthos, *Metals and Ceramics Div. Ann. Progr. Rept. June 30, 1966*, ORNL-3970, pp. 215–18.

Table 36.1. Thoria-Base Fuel Rods Currently Being Irradiated or Examined[a]

Designation	Number of Rods	Type of Oxide	Density (% of Theoretical)	Fuel Rod Dimensions (cm)			Linear Heat Rating (w/cm)	Peak Burnup (Mwd per tonne of metal)	Objective	Status
				Length	OD	Wall				
MTR-II	2	Sol-Gel S ThO_2–4.5% UO_2 Vi-Pac	88 to 89	57	0.8	0.06	600	100,000	Obtain higher heat rating by increasing enrichment	Being examined
MTR-III	6	Sol-Gel 35 ThO_2–4.5% UO_2 Vi-Pac	86 to 89	30	1.1	0.06	820	100,000	Compare oxide calcining atmospheres and higher heat ratings obtained by increasing diameter	In reactor
ETR-II	6	BNL Sol-Gel ThO_2–4% $^{233}UO_2$ Vi-Pac	90	48	1.3	0.09	630	30,000 to 100,000	Study effects of remote fabrication and oxide recalcining	1 Being examined 5 In reactor
ETR-III	7	Sol-Gel ThO_2	88	48	1.3	0.09	770	10,000 to 70,000	Study ThO_2 blanket material with gradually increasing heat rating and provide high-protactinium low-fission-product material for chemical processing	3 Rods in process 4 Rods in reactor
ETR-IV	6	Sol Gel	84	24	1.3	0.09	650 to 7000	20,000 to 100,000	Study sol-gel ThO_2-PuO_2 microsphere performance as vibratorily compacted beds at various heat ratings and burnup levels	In reactor
Sphere-Pac	4	Sol-Gel ThO_2–5% PuO_2 Sphere-Pac	84	19	0.64	0.025	650 to 1000	10,000	Test sol-gel ThO_2-PuO_2 microspheres with high cladding temperatures	Being examined
Pellet Rods	3	ThO_2–4.5% UO_2	91	11.4	0.79	0.06	400	150,000	Investigate swelling and gas release of ThO_2-base fuels at very high burnup	Being examined

[a]ETR-II, ETR-III, and ETR-IV rods are clad with Zircaloy-2; all other fuel rods are clad with type 304 stainless steel.

during reprocessing; thus the ^{236}U contamination associated with ^{235}U enrichment is avoided. This group of tests at three linear heat ratings, 650, 850, and 1000 w/cm, with peak burnup levels from 2 to 10% FIMA, is designed to evaluate the irradiation characteristics of sol-gel-derived $(Th,Pu)O_2$ fuels fabricated by the newly developed Sphere-Pac technique.

No additional irradiation tests on metal-clad thoria-base bulk oxide fuels are planned unless a power reactor concept designed to utilize the exceptional performance characteristics of these fuels is developed.

DRYING AND SINTERING OF SOL-GEL URANIA MICROSPHERES

H. Beutler[24] R. L. Hamner

We are studying the drying and sintering behavior of sol-gel urania microspheres to determine conditions suitable for production as well as to establish the operative mechanisms.[17,25] For vibratorily compacted fuel rods containing sol-gel microspheres as the fuel, the densities of the particles must be high ($\geq$95% of theoretical) to meet fuel loading requirements.

During the past year, we emphasized the study of the drying and sintering behavior of sol-gel urania microspheres. We determined the isothermal shrinkage kinetics of sol-gel UO_2 microspheres by hot-stage microscopy and measured changes in x-ray crystallite size and BET surface area during sintering. In addition, we studied the drying and sintering behavior of sol-gel urania by differential thermal analyses. Based on our characterization study, we specified a drying and sintering schedule, which on a laboratory scale yielded microspheres of high density and of low residual carbon content.

Isothermal Shrinkage of Sol-Gel Urania Microspheres

Individual urania gel microspheres were held at carefully controlled temperatures in a hot-stage microscope, and the process of shrinkage was followed by sequence photography. We carried out isothermal shrinkage determinations in dry hydrogen in the temperature range 680 to 1000°C. To differentiate between dimensional changes due to drying and sintering, we employed a soaking treatment for 12 hr at 400°C prior to each determination. During this soaking treatment, which removed the volatiles, we observed consistently a linear shrinkage of 8 to 10%. As in the case of thoria particles, the shrinkage followed a law of the form $\Delta L/L_0 \propto t^n$ at constant temperature. The isotherms differ, however, from those expected from simple sintering theory in that log-log plots of the fractional shrinkage vs time are not linear but decrease in slope with increasing shrinkage. The slope of the shrinkage isotherms decreases from 0.20 to 0.1 as $\Delta L/L_0$ values increase from 0.04 to around 0.1. The maximum linear shrinkage that we observed was 24% after 1 hr at 990°C, compared to the 26% predicted for theoretical density.

Changes of Crystallite Size, Surface Area, and Bulk Density

We carried out two series of isothermal heat treatments on sol-gel UO_2 microspheres to investigate the effects of time and temperature on crystallite size, BET surface area, and bulk density. We selected temperatures of 300, 500, 700, and 900°C and heat treatment times of 1 to 24 hr. In the first series of experiments, we used a sintering atmosphere of dry Ar–4% H_2; in the second series, we saturated the argon-hydrogen mixture with water at room temperature. For each heat-treated sample, we determined the x-ray crystallite size (from the broadening of 111, 220, and 311 reflections), the BET surface area, and the bulk density by mercury porosimetry. In a dry Ar–4% H_2 atmosphere, we did not observe crystallite growth or change in surface area at heat treatments for 24 hr at 500°C and below. The crystallite size increased above 500°C, and the BET surface area decreased with both time and temperature.

When the specimens were heated for 24 hr at 900°C, the average crystallite increased in size from 69 A (crystallite size of original gel) to 247 A, and the surface area decreased from 69.7 m^2/g (BET surface area of original gel) to 1.03 m^2/g,

[24] Noncitizen employee from Switzerland.

[25] P. A. Haas, F. G. Kitts, and H. Beutler, "Preparation of Reactor Fuels by Sol-Gel Processes," presented at the AIChE meeting at Salt Lake City, Utah, May 1967; to be published in a *Chemical Engineering Progress Symposium Series* volume on Nuclear Engineering.

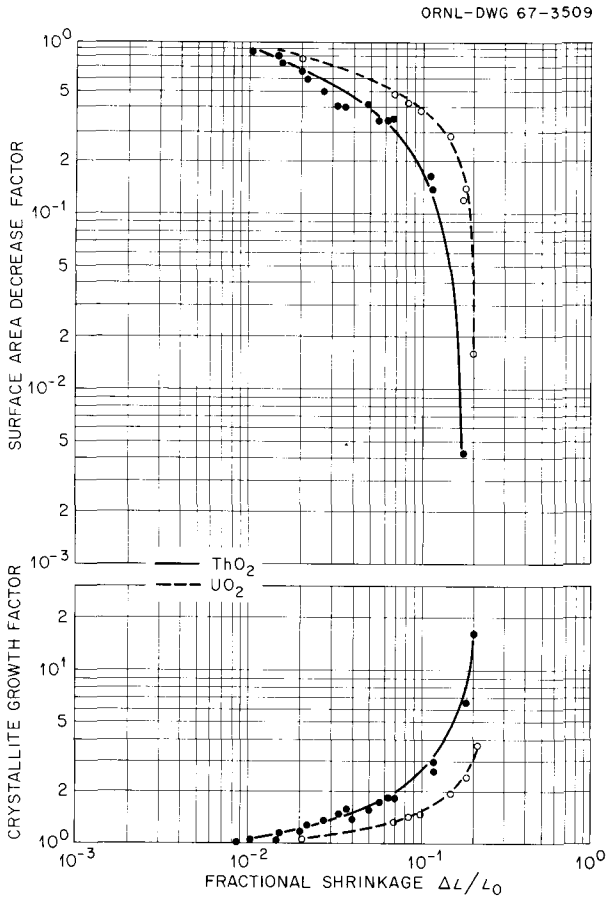

Fig. 36.6. Relationship Between Changes in BET Surface Area, Crystallite Size, and Fractional Linear Shrinkage of Sol-Gel UO_2 and ThO_2.

which is approximately 500 times larger than the geometrical surface area of the microspheres used. The bulk density increased even after heat treatments at 300°C, although no changes in crystallite size and BET surface area occurred. As previously discussed, the density increase at low temperature is associated with the removal of volatiles and subsequent reordering of crystallites to a closer packing. The change in bulk density with both time and temperature agrees well with our previously discussed shrinkage data obtained by hot stage microscopy on single microspheres.

The relationship between fractional shrinkage, crystallite growth, and surface area decrease is shown in Fig. 36.6. Data previously[26,27] obtained for the densification of thoria are shown for comparison. The relationships between shrinkage, crystallite growth, and surface area decrease for thoria and urania are remarkably similar and appear independent of temperature.

The presence of water vapor lowered the temperature at which crystallite growth and surface area reduction started and enhanced the process of densification over the whole range of conditions that we investigated. After heating the samples for 24 hr at 900°C in wet Ar–4% H_2, we found that the density increased to 10.14 g/cm^3, the crystallite size increased to 620 A, and the surface area decreased to 0.008 m^2/g, a value only four times higher than the geometrical surface area of the spheres used.

The increase in densification rate because of the addition of water vapor (which we observed either directly in changes of bulk density or indirectly in changes of crystallite growth and surface area reduction with time) corresponds to a temperature increase of 100 to 150°C in treatments in a dry atmosphere.

Differential Thermal Analyses of Sol-Gel Urania

We employ differential thermal analyses (DTA) as an additional means of investigating the drying and sintering behavior of sol-gel urania. A typical DTA pattern, which we obtained during the heating of crushed UO_2 microspheres in Ar–4% H_2 at a uniform rate of 10°C/min is shown in Fig. 36.7; in this pattern, two pronounced energy-absorption peaks at 170 and 470°C are interrupted by a strong energy-release peak at 220°C; a release of surface energy, detected at 730°C, peaks at 870°C. We attribute the endothermic peaks to the vaporization of residual volatiles. The sharp exotherm starting at 220°C is typical of both thoria and urania microspheres. Since this exotherm is observed only in case of gels that contain residual organic solvents and surfactants, we attribute this energy release to the oxidation of organic compounds by nitrate. This reaction has caused severe cracking of microspheres heat treated in bulk charges. We have demonstrated by DTA that the organic-nitrate reaction can be

[26] M. J. Bannister, *Status and Progress Report for Thorium Fuel Cycle Development Dec. 31, 1965*, ORNL-4001, pp. 113–16.

[27] M. J. Bannister, H. Beutler, and J. W. Prados, "Sintering and Grain Growth of Sol-Gel Thoria and Urania," *Metals and Ceramics Div. Ann. Progr. Rept. June 30, 1966*, ORNL-3970, pp. 220–22.

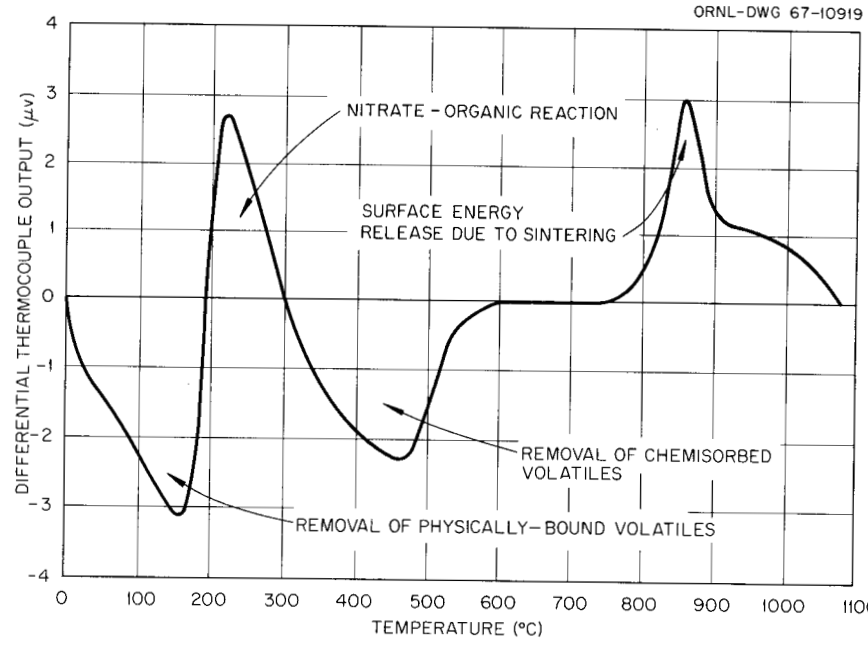

Fig. 36.7. Differential Thermal Analysis (DTA) Pattern of Sol-Gel UO_2 Microspheres.

successfully suppressed by exposing the microspheres to superheated steam at 150°C for 8 hr prior to passing the critical temperature region (200 to 250°C).

We investigated the effects of steam-Ar–4% H_2 and carbon dioxide atmospheres on the surface energy release pattern. The addition of water vapor shifted the surface energy release peak approximately 100°C downward in temperature, but the intensity and general pattern of the peak remained remarkably similar to the one obtained in dry Ar–4% H_2. The carbon dioxide atmosphere caused a drastic lowering of the temperature at which surface energy release started (see Fig. 36.8). The release occurred within a very narrow temperature range and was completed at 650°C.

We confirmed that CO_2 greatly enhances sintering and crystallite growth by isothermally heat treating microspheres at 600°C for 24 hr. As measured by both mercury porosimetry and helium pycnometry, the bulk density of the microspheres after this treatment was 10 g/cm^3, indicating complete closure of surface pores. X-ray diffraction revealed preferential crystallite alignment in the [220] direction. We have not been able to determine whether these effects are associated with oxidation of urania during sintering in CO_2.

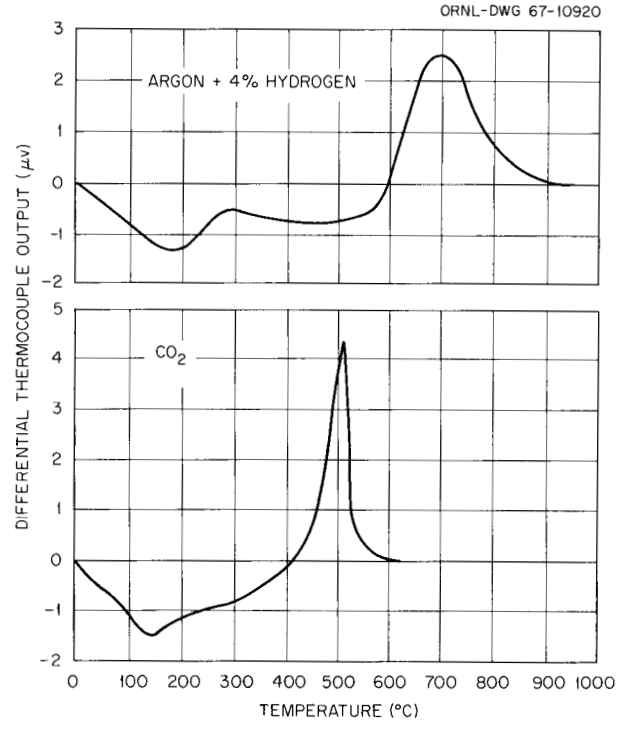

Fig. 36.8. Comparison of Differential Thermal Analysis (DTA) Patterns of Sol-Gel UO_2 Fragments Heated at 10°C/min in Two Atmospheres. Samples had been precalcined 4 hr at 400°C in Ar-4% H_2.

We conclude that the study of the surface energy release by DTA is a convenient means to characterize the sinterability of sol-gel materials.

Drying and Sintering Schedule for Sol-Gel Urania Microspheres

Based on our preliminary characterization of sol-gel urania microspheres by differential thermal analyses, hot stage microscopy, crystallite size determinations, and BET surface area measurements, we sought to establish a drying and sintering schedule to obtain high-density low-carbon-content urania microspheres. Our approach was to remove as large a quantity of residuals (nitrate, organics, carbon) as possible prior to the beginning of sintering. The atmosphere and heating schedule to 1000°C were the major variables considered.

In the past, CO_2 has been used extensively as the atmosphere for sintering urania microspheres, mainly because it is effective in removing carbon. Microspheres sintered in a CO_2 atmosphere, however, often have low densities (<95% of theoretical). Our hypothesis regarding these low densities is that the residuals in urania microspheres are not removed to an appreciable degree in a CO_2 atmosphere before the beginning of sintering at a temperature just above 400° C; consequently, they become trapped during the early stages of sintering and cause low densities.

In our experiments with a steam-Ar–4% H_2 atmosphere, we found that (1) the urania microspheres would start to sinter just above 450°C, (2) the nitrate and carbon contents could be reduced to low levels (40 to 400 ppm respectively) by soaking at 450°C, and (3) the organic-nitrate reaction occurring at about 220°C could be suppressed by soaking at 150°C. Therefore, we based our sintering schedule on a steam-Ar–4% H_2 atmosphere with soak periods at 150 and 450°C.

By using soak periods of 2 hr at 150°C and 16 hr at 450°C, we produced urania microspheres in 5 to 10-g batches with bulk densities of 97 to 99% of theoretical, carbon contents of 30 to 40 ppm, and oxygen-to-uranium ratios of less than 2.001 to 2.003 after sintering for 1 hr at 1000°C. Our heating rate after the soak periods was 300°C/hr.

To optimize the schedule, we determined the carbon level in the microspheres after soak periods ranging from 2 to 24 hr at 150 and 450°C. We found that carbon removal was much more temperature dependent than time dependent, that 400 ppm C remained in the microspheres that had a bulk density of 98% of theoretical, and that a carbon content of 40 ppm could be produced without a soak period at 450°C provided a soak period of 2 hr at 150°C was included in the sintering schedule. Within the limits of our investigation, we consider this to be the optimum schedule for sintering small batches of urania microspheres to specifications.

We are now determining what adjustments must be made in our sintering schedule to achieve the same results in sintering large batches of microspheres.

Part V.

Other Program Activities

37. Isotopic Power Source Development

R. J. Beaver R. G. Donnelly

The materials program in support of isotopic power source development programs was continued. The stringent engineering and safety requirements involved demand very-high-quality materials for containing the isotopic fuels and procedures for sealing these containers. The materials of interest for these applications are the superalloys and refractory-metal alloys.

Our efforts were centered mainly on welding development, nondestructive testing, and a design study on a Brayton cycle power system. Welding development was conducted on refractory-metal capsules of the molybdenum alloy TZM as well as on Hastelloy C capsules for SNAP-21. The nondestructive testing effort was devoted to the evaluation of capsule components and more recently to the inspection of welded fuel-containing capsules for the SNAP-21 program.

In addition, a paper was presented describing work on the compatibility of curium fuels with candidate container materials.[1]

WELDING OF REFRACTORY-ALLOY CAPSULES

R. G. Donnelly

The sealing of containers for alpha-emitting isotopic heat sources requires that sound welds having full penetration be made in heavy-walled refractory-metal capsules. This requirement stems from the fact that the helium generated by the decay of the isotope is of sufficient magnitude that these capsules must serve as pressure vessels.

Previously,[2] we described equipment used for making joints of this type by electron-beam welding. However, under certain conditions it may not be desirable or feasible to use the electron-beam welding process. Therefore, we evaluated the conventional gas tungsten-arc welding process as a method for making joints of this type.

With the electron-beam method, adequate atmosphere purity during the welding operation is assured by the high vacuum (approximately 5×10^{-5} torr) inherent with the process. However, to prevent contamination of refractory metals by interstitial elements such as C, O, H, and N during arc welding, the operations must be carried out in a chamber purged of air and containing only high-purity argon or helium. Using a specially designed and constructed chamber, the welding of end caps to molybdenum alloy TZM containers with a 0.150-in.-thick wall was investigated. The heat buildup inside the capsule while making full-penetration welds of this type was so intense that a vent was needed for the expanding gas. After the primary weld had been made, the small-diameter vent could be welded shut with much less total energy input.

Techniques using this procedure were developed to make full-penetration primary welds successfully and repeatedly. A typical weld of this type is shown in Fig. 37.1. As can be seen from the figure, the weld is sound and has a penetration of at least the wall thickness of the capsule. This particular joint design employed a recess in the cap in the area of the weld to assist in assuring full penetration. The conditions used in making this weld were: welding current, 360 amp; travel speed, 10 in./min; revolutions, 1. The vent hole

[1] J. R. DiStefano and W. D. Box, "Compatibility Studies for High-Temperature Radioisotopic Power Source Applications," paper presented at the 1966 IEEE Thermionic Conversion Specialist Conference, Nov. 3 and 4, 1966, Houston (classified).

[2] R. G. Donnelly, *Metals and Ceramics Div. Ann. Progr. Rept. June 30, 1966*, ORNL-3970, pp. 225–27.

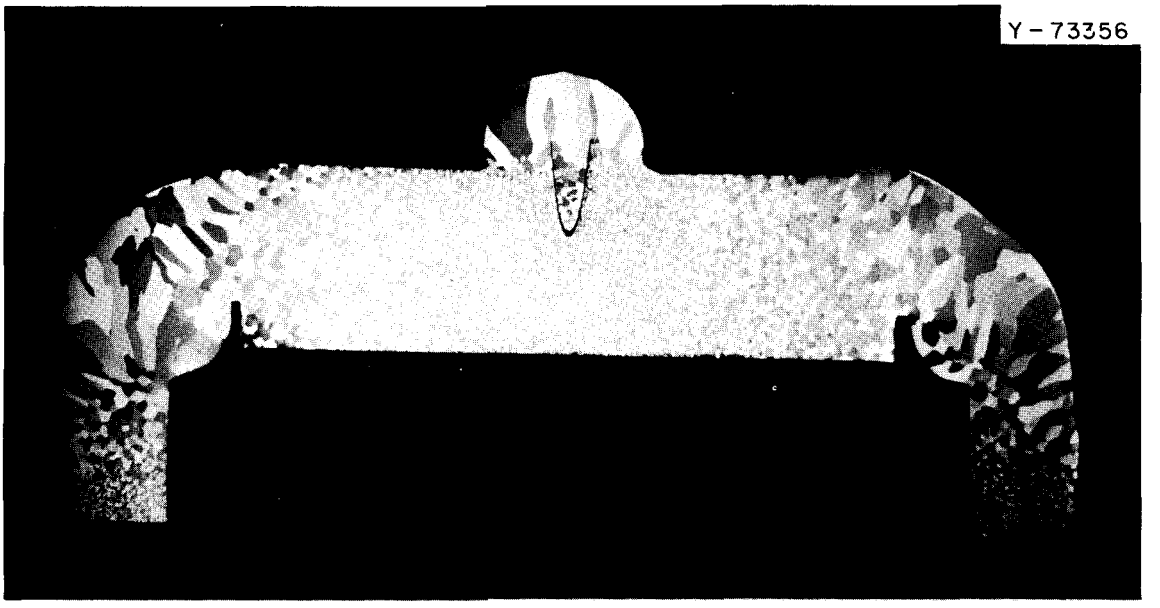

Fig. 37.1. Typical Primary Closure Weld of a TZM Container. 3.5×. Note that the weld is sound and that full penetration was achieved.

was subsequently sealed by inserting a tapered pin to help fill the hole and then welding for 7 sec at 230 amp, using the same equipment that was used for the primary weld.

WELDING DEVELOPMENT FOR SNAP-21

R. G. Donnelly

The SNAP-21 heat source is being developed by ORNL in cooperation with the 3M Company. This $^{90}SrTiO_3$ source will generate 200 w (thermal) and is intended for use under the sea. The capsule is $\frac{1}{4}$-in.-thick Hastelloy C and must be sealed by welding to ensure mechanical strength and leak-tightness. A requirement of the joint design is that the weld be inspectable by ultrasonic techniques. Ideally, this means that the top outside edge of the capsule should remain undisturbed by welding; at least, the weld penetration must be greater than the depth of edge melting. If these conditions are not met, the joint to be inspected is masked by the surface of the weld.

Figure 37.2 compares joints made by three techniques. Initial gas tungsten-arc welding experiments failed to attain the required 0.100 in. of defect-free weld-metal penetration without edge melting (Fig. 37.2*a*). This weld was obtained with the end cap beveled at a 30° angle for 0.100 in. Adequate weld penetration was obtained by melting over the edge of the capsule as shown in Fig. 37.2*b*, but this violated the requirement for ultrasonic weld inspection.

The desired combination of weld penetration and inspectability was ultimately provided by electron-beam welding. Figure 37.2*c* shows an electron-beam weld made at 30 kv with 130 ma of beam current and a travel speed of 35 in./min. Equipment capable of making welds of this type is presently being assembled in cooperation with Isotopes Division personnel for installation in the hot cells.

NONDESTRUCTIVE TESTING SUPPORT

K. V. Cook

Because of the toxic and radioactive nature of the core materials contained in isotopic heat sources, the integrity of the container must be assured through a reliable nondestructive testing program. Most of the isotope-enclosure materials are refractory alloys or superalloys, and there is very little nondestructive testing experience with these materials. Our purpose is to satisfy two basic requirements: (1) to assure the material integrity and (2) to build a background of familiarity with the testing characteristics of these materials.

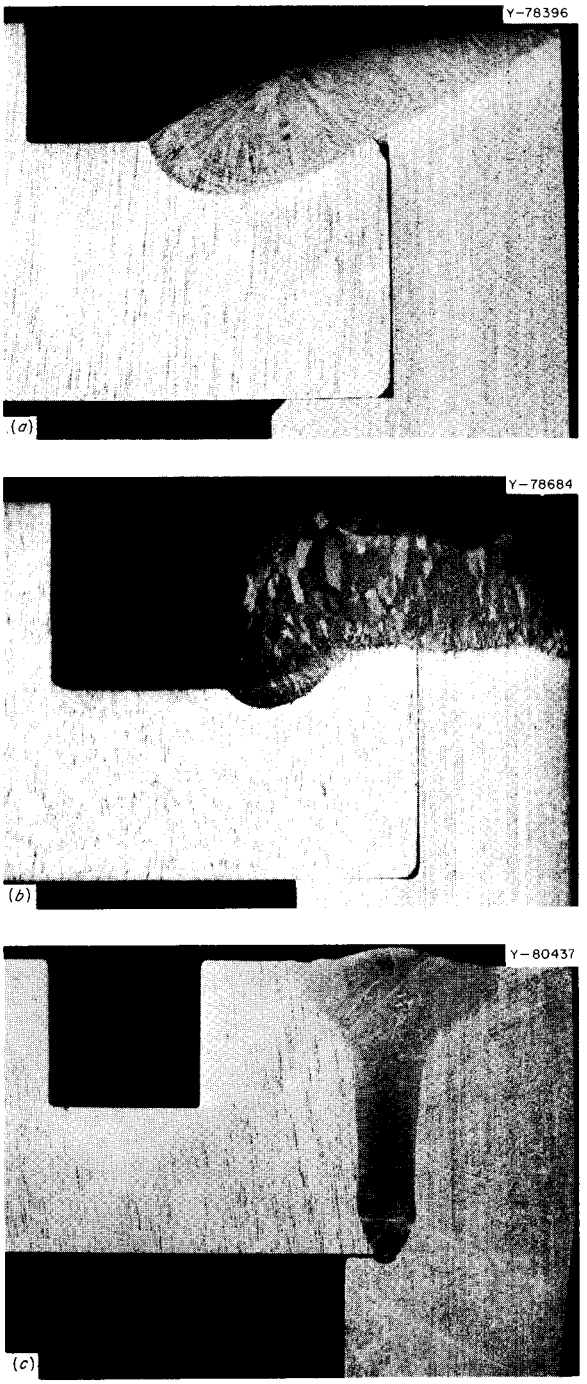

Fig. 37.2 Experimental Hastelloy C Welds for SNAP-21 Heat Source Program. 10×. (*a*) Tungsten-arc weld made with beveled joint. Insufficient weld penetration was obtained. (*b*) Tungsten-arc weld with adequate penetration but unacceptable because the capsule edge contour prevents weld inspection. (*c*) Electron-beam weld having both adequate penetration and acceptable edge contour. Reduced 42%.

Basically, we are adapting or developing nondestructive testing techniques for two separate tasks. The first is testing the capsule material before loading. The second is remote inspection of the closure weld following the capsule loading.

For the raw material evaluations, we have generally used fluorescent penetrant and ultrasonic inspection methods, although at times other techniques have been required. While the penetrant test is relatively easy to adapt to the isotope program, one must be careful because meaningless results are possible. For instance, with tantalum-base alloys, we found that smearing of the surface during capsule machining could close cracks or discontinuities normally open to the surface and thus render them undetectable by the penetrant examination. A very light etch removes this smearing and allows a meaningful test to be performed.

The ultrasonic pulse-echo technique normally used for plate, sheet, bar, and tubing inspections is presently being applied to the inspection of capsule materials. Our major problems in applying the ultrasonic technique have involved the fixtures necessary for adequate mechanical scanning of the various capsule configurations and the establishment of reliable and reproducible reference discontinuities.

Our work involving the second-stage evaluation has dealt entirely with the SNAP-21 Program. The Pacific Northwest Laboratory was assigned the responsibility by the 3M Company for developing an inspection technique and remote inspection equipment to evaluate the closure weld on the SNAP-21 capsule. Our responsibility is to follow this development to assure a smooth transfer of technology, to ensure a well-designed remote inspection facility by supplying necessary design criteria, and, following the delivery and installation of the system at ORNL, to operate the remote system for hot-cell testing of both fueled and unfueled capsule weldments.

BRAYTON CYCLE STUDIES

R. J. Beaver

As part of an integrated effort at ORNL, we reviewed materials that appeared attractive as encapsulating materials for isotopic heat sources with energy potential for powering a 25-kw Brayton

engine for space application.[3,4] The results of these studies indicated that either of the tantalum-base alloys T-111 or T-222 was acceptable for the stress-bearing encapsulating member. However, because of their poor oxidation resistance at elevated temperatures, these alloys would have to be protected with a thin cladding of platinum. Thoria was suggested as a barrier to prevent diffusion between the tantalum and the platinum, and iron titanate was recommended as a coating for the platinum to achieve an acceptable value of emissivity.

---

[3]R. A. Robinson, R. J. Beaver, D. W. Burton, T. C. Chapman, C. W. Craven, Jr., S. T. Ewing, A. J. Miller, J. P. Nichols, and R. L. Stephenson, *Brayton-Cycle Radioisotope Heat Source Design Study Phase I (Conceptual Design) Report*, ORNL-TM-1691 Del. (NASA CR-72090) (August 1967).

[4]R. A. Robinson *et al.*, *Brayton-Cycle Radioisotope Heat Source Design Study Phase II (Preliminary Design) Report*, ORNL-TM-1829 (NASA CR-72151) (August 1967).

38. Metallography

R. J. Gray

Our major responsibility is to provide metallographic service assistance to the Metals and Ceramics Division and other divisions at this Laboratory. This assistance is in the form of specimen preparation, examination, interpretation, and recording and transmitting of data. We are also responsible for special services such as microprobe analyses, high-temperature microscopy, high-temperature hardness testing, metallography in color, and postirradiation metallographic examinations. Our efforts are denoted throughout this report and in most of the reports originating in the Metals and Ceramics Division as well as other divisions requiring microstructural studies of metals and ceramics. In providing this service, we try to improve our techniques and our skills in this field and keep abreast of new aids through newly developed equipment, as reported below.

QUANTITATIVE TELEVISION MICROSCOPY

T. M. Kegley, Jr.

The metallography laboratory now has a newly developed instrument, the quantitative television microscope (QTM),[1-5] which greatly extends the application of quantitative metallographic techniques to metallurgical investigations. Usual quantitative metallographic procedures such as point counting, linear analysis, and particle sizing are time consuming, quite tedious, and fatiguing to the eye. The QTM overcomes the tedium associated with these procedures.

The QTM can be operated with either a microscope or an epidiascope. With the microscope attached to the QTM, the microstructure of metallographic specimens can be analyzed, and with the epidiascope attachment larger items, such as photographic prints and negatives, electron micrographs, transparencies, and microradiographs, can be analyzed. The image obtained with either the microscope or the epidiascope is projected onto the television camera tube located in the QTM control unit. By electronically analyzing the output from the television camera, the QTM quickly yields the following data: (1) the area fraction of constituents, (2) the number of intercepts of the television line scan with feature boundaries, (3) the number of features in the field, and (4) the size distributions. The measurement of the number of intercepts of the television line scan with the feature boundaries, which is in effect a projection measurement, can be related directly to the average linear intercept distance or the grain size.

We plan to evaluate the performance of the QTM by analyzing with the aid of the epidiascope attachment known standards such as area fraction and grain size charts. An indication of its performance is seen in a QTM area fraction measurement (0.327), which was well within 1% of the area fraction (0.325) of the prepared standard. In the series of QTM grain-size measurements presented in Table 38.1, the greatest deviation from the nominal grain size was 0.28, while the average deviation from the nominal was ±0.13.

[1] Quantimet Image Analyzing Computer, manufactured by Metals Research, Ltd., Cambridge, England.

[2] M. Cole, *The Microscope and Crystal Front* **15**(4), 148–60 (1966).

[3] C. Fisher, "The Metals Research Image Analysing Computer," paper presented at Particle Size Analysis Conference, Loughborough, England, Sept. 14–16, 1966, to be published by Society for Analytical Chemistry, London, pp. 77–94.

[4] D. Radtke and D. Schreiber, *Steel Times*, pp. 246–59 (Aug. 19, 1966).

[5] John Schuck, *Research/Development* **17**(4), 28–36 (April 1966).

Table 38.1. Grain Size of ASTM Grain Size Charts[a] as Determined by QTM

Nominal ASTM Grain Size	Number of Intercepts per Unit Length, N_L[b] (cm^{-1})	Calculated Grain Size,[c] G
8	493.1[d]	7.88
7	346.9[d]	6.87
6	250.0[d]	5.92
5	183.1[d]	5.02
4	136.9[d]	4.19
3	84.7[e]	2.80
2	61.0[e]	1.85
1	50.0[e]	1.28
0	32.4[e]	0.03

[a]ASTM E 112, Plate I.

[b]N_L calculated from $N_L = P/L$ where P is the average QTM projection reading and L is the length of the QTM blank frame.

[c]Calculated from Hilliard's formula, $G = -10.00 + 6.64 \log N_L$, *Metal Progr.* **85**(5), 99 (1964).

[d]2.5-in. focal length objective employed.

[e]1-in. focal length objective employed.

POTENTIOSTATIC METALLOGRAPHIC ETCHING EXPERIMENTS[6]

J. B. Buhr[7] T. M. Kegley, Jr.
R. J. Gray

The potentiostat, which is an instrument for maintaining any desired electrical potential relative to a standard electrode, provides a means for maintaining a particular optimum potential at which a specific phase in the microstructure can be selectively etched electrolytically and differentiated from the remaining phases. The particular potential for optimum selectivity must be found experimentally, and the potentiostat aids in this by allowing the potential to be varied as desired. By means of the potentiostatic etching apparatus, shown schematically in Fig. 38.1, anodic polarization curves were determined. Current maxima exhibited by these curves were then associated with the preferential etching of a particular phase, as in the example shown in Fig. 38.2. Our purpose was to obtain experience in the application of a potentiostat to the etching of metallographic specimens and to acquaint ourselves with the possible use of potentiostatic etching for phase identification.

The experiments performed concerned (1) the etching of two-phase alloys of tin and zinc in which little or no solid solubility is exhibited, (2) the etching of austenitic stainless steels con-

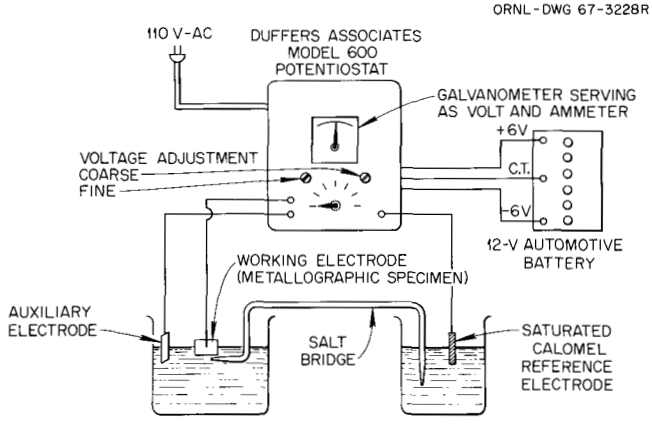

Fig. 38.1. Potentiostatic Etching Apparatus.

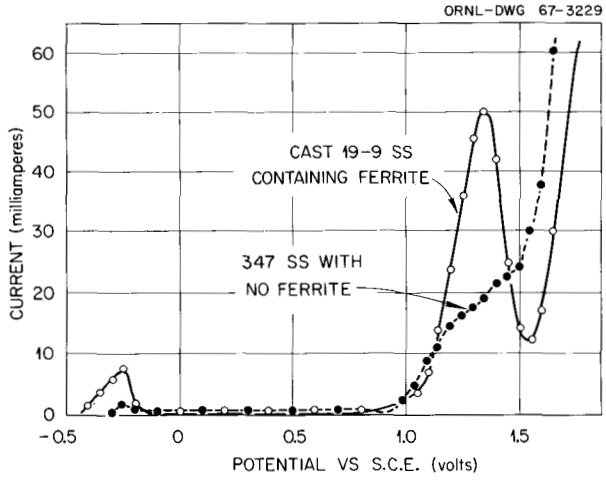

Fig. 38.2. Anodic Polarization Curves for Cast 19-9 and Type 347 Stainless Steels. 1 N H_2SO_4 electrolyte.

[6]Abstract of paper to be published in the technical papers of the Twenty-First AEC Metallography Group Meeting, held May 10–12, 1967 at Brookhaven National Laboratory, Upton, N.Y.

[7]The experiments were performed by James B. Buhr during the summer of 1966 in a summer trainee program conducted at ORNL by the Oak Ridge Associated Universities.

taining ferrite and free of ferrite, and (3) the etching of heat-treated type 310 stainless steel containing sigma phase. In the tin-zinc alloys the zinc phase was selectively etched in 1 *N* NaOH at −1.2 v (vs S.C.E.) and the tin phase was selectively etched at −0.9 v (vs S.C.E.). The ferrite phase of cast 19-9 stainless steel etched preferentially in 1 *N* H_2SO_4 at 1.35 v (vs S.C.E.) (Fig. 38.3). After the cast 19-9 specimen was etched in 1 *N* HCl, the ferrite etched preferentially at −0.42 v (vs S.C.E.) and the austenite etched preferentially at −0.16 v (vs S.C.E.). We were unable to preferentially etch the sigma phase of the type 310 stainless steel in either 1 *N* HNO_3 or 1 *N* HCl at any potential. We did observe that recrystallized austenite (formed in 25% cold worked type 310 stainless steel at 650°C) surrounding the sigma-phase particles could be preferentially etched at 0.00 v (vs S.C.E.) in 1 *N* HCl electrolyte that had been in use and contained dissolved metallic ions.

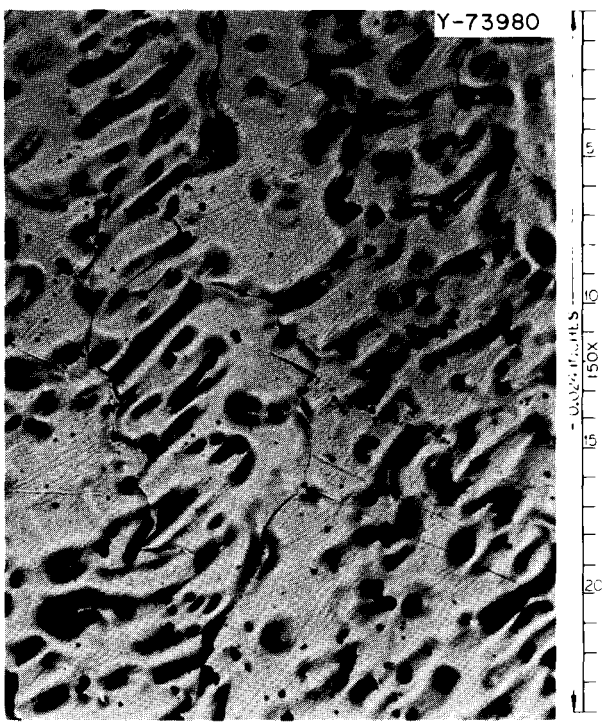

Fig. 38.3. Cast 19-9 Stainless Steel Etched Potentiostatically for 2 min at 1.35 v (vs. S.C.E.) in 1 *N* H_2SO_4. The ferrite phase was attacked preferentially.

HIGH-TEMPERATURE MICROSCOPY

R. S. Crouse

Direct observation of microstructural changes related to temperature variations is invaluable. Examination of such phenomena as thermal etching, grain growth, twinning, diffusionless transformation (martensite reaction), solution and reprecipitation of phases, grain anisotropy by tinting by selective oxidation, graphitization of iron and steels, phase changes due to reaction with the matrix, and diffusion zones is possible with many metal and alloy systems using a heating stage metallograph. Much work has been done in Russia and Germany in this field.[8,9]

The metallography specimen is positioned in a small water-cooled vacuum furnace with a quartz viewing window. With the appropriate long-working-distance objective lenses, the specimen surface can be examined on a metallograph at temperatures up to 1800°C. This furnace operated at a vacuum of 5×10^{-5} torr or with an inert atmosphere.

Figure 38.4 is an overall view of the metallograph with the complete heating stage assembly. It is possible to make photomicrographs with either a 35-mm camera or standard 4- × 5-in. conventional film or Polaroid, or a 16-mm movie camera can be attached for conventional or time-lapse movies. Figure 38.5 shows the inside of the furnace with a specimen in place. The heating is done by a molybdenum strip heater. The heating stage was used in an examination of UAl_3-aluminum simulated fuel compacts to determine the cause of swelling. The results are summarized in Part III, Chap. 20 of this report.

METALLOGRAPHIC PREPARATION OF CERIUM CARBIDES[6]

T. M. Kegley, Jr.

Special procedures were required to prepare cerium carbides metallographically because of their strong reactivity with moisture. A chemical,

[8] M. G. Lozinskii, *High Temperature Metallography*, Pergamon Press, New York, 1961 (translated by Litterdan from Russian).

[9] R. Mitschi, R. Gabler, and W. Wurz, "High-Temperature Microscopy in Light and Heavy Metal Research," *Aluminum* 7(10), 652–62 (1961).

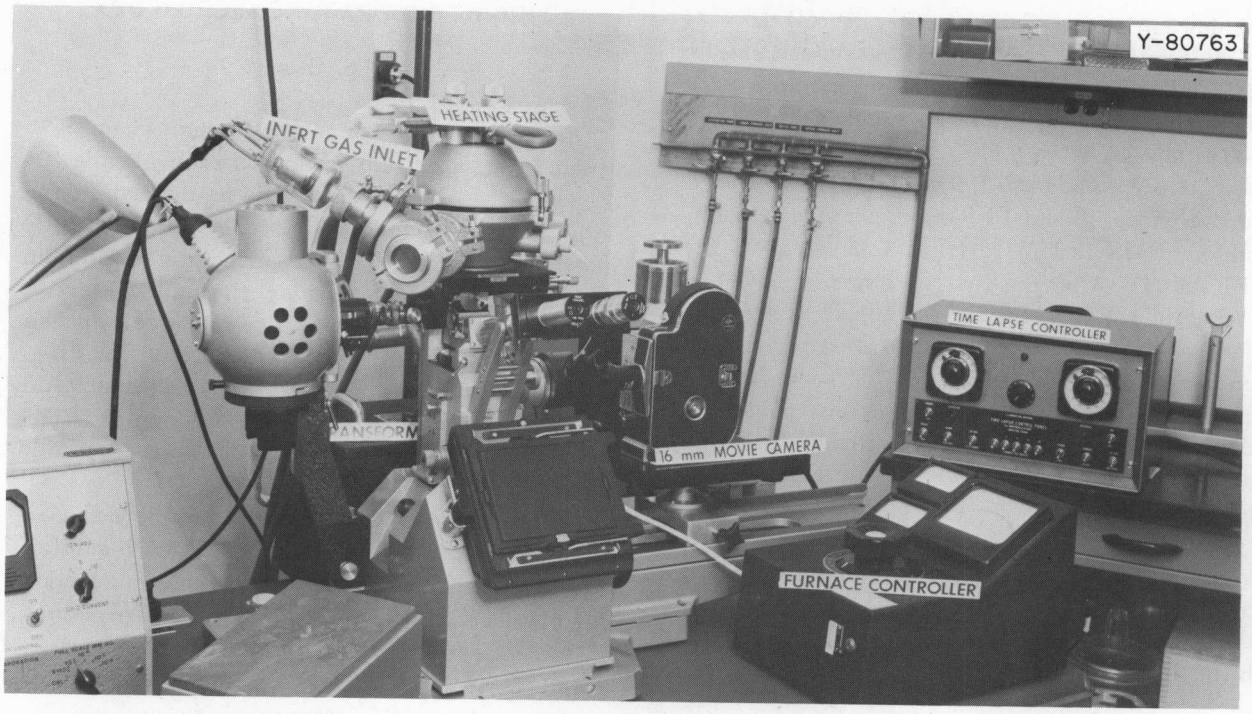

Fig. 38.4. Heating Stage Metallograph with Time-Lapse Movie Camera in Place.

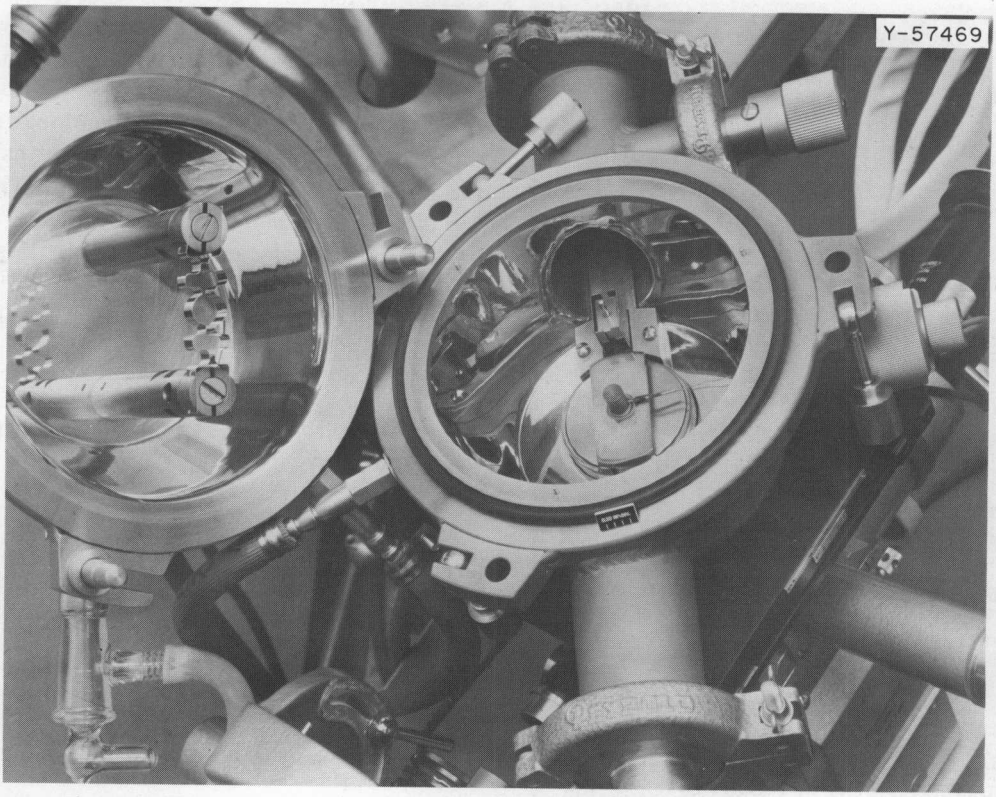

Fig. 38.5. Heating Stage Furnace Open, Showing Specimen in Place. Heating elements are shown at the left side of the picture. The scale of the flange measures 0.1 in./division.

an electrolytic, and a protective oil method were developed for preparing these carbides for examination. In both the chemical and electrolytic methods a stainless steel screw serves as a contact with the CeC_2.

By immersion in equal parts acetic, lactic, and nitric acids, cerium dicarbide is either chemically polished or passivated, depending upon whether the mount is partially or totally immersed. If the CeC_2 specimen is partially immersed so that the stainless steel screw does not contact the solution, only chemical polishing takes place. If the mounted specimen is totally immersed, a galvanic cell is created in which CeC_2 is the anode and stainless steel is the cathode. The emf developed by this cell provides the necessary potential for passivation of the CeC_2.

In the electrolytic method the CeC_2 is anodized at 5 v for 10 sec in equal parts acetic, lactic, and sulfuric acids.[10]

In the protective oil method CeC_2 is chemically polished in acetic-lactic-nitric acids and then washed with ethyl alcohol. Silicone oil is added to displace the ethyl alcohol, and a cover glass is placed on the CeC_2 specimen. For two-phase specimens containing CeC_2 and Ce_2C_3, the protective oil procedure is followed, but with the exception that chemical polishing is not employed.

---

[10]T. M. Kegley, Jr., *Metals and Ceramics Div. Ann. Progr. Rept. June 30, 1966*, ORNL-3970, p. 234.

39. Rover Rocket Nozzle Materials

E. A. Franco-Ferreira

We are continuing[1] to provide materials and fabrication support to the AEC-NASA Space Nuclear Propulsion Office on the Rover Nuclear Rocket Program. In general, we provide technical liaison between NASA and its contractors, and, where necessary, perform appropriate experimental studies. This assistance has been directed mainly toward the fabrication of nozzles to be used in static reactor test firings at the Nevada test site.

Two types of nuclear rocket engines are involved: Phoebus II (a 5000-Mw, 250,000-lb-thrust system primarily for reactor development) and NERVA II (a 5000-Mw, 250,000-lb-thrust engine development system ultimately aimed at a flight mission).

The work may be divided into two broad categories: studies in direct support of NASA contractor operations and studies aimed at developing a generalized rocket materials technology. Some aspects of the general experimental program will be discussed below.

THERMAL FATIGUE TESTING OF NOZZLE TUBE CONFIGURATIONS

D. G. Harman A. E. Carden[2]
E. A. Franco-Ferreira

The nozzles used with nuclear rockets are typical of most regeneratively cooled nozzles. That is, the interior surface of the nozzle which is in contact with the hot propellant gas is made up of a multiplicity of suitably shaped thin-walled tubes which are bonded to each other. The cryogenic coolant passes through the insides of these tubes to prevent them from melting. In many cases it is necessary, in order to provide greater strength to resist high chamber pressures, to bond a relatively heavy reinforcement jacket to those portions of the tubes that make up the outer surface of the nozzle. A schematic diagram of a typical cross section of such a configuration is shown in Fig. 39.1.

It is apparent that, in a nozzle of the type described above, there will be a very large temperature difference between the tube crowns on the hot gas side and those portions of the tubes bonded to each other and to the jacket. The temperature differences experienced in normal modes of operation are capable of producing calculated thermal strains of as much as 2%. Due to the restraint provided by the jacket, it is likely that a significant portion of the longitudinal thermal strain will be converted into mechanical deformation of the tube crowns. Thus, under conditions of cyclic nozzle operation, low-cycle thermal fatigue failures may be induced in the tubes.

A scale-model test was devised[3] to measure the effects of all the important parameters operative in an actual nozzle. In the case of thermal-cycling stresses, as discussed here, the important considerations include (1) the temperature distribution, (2) the physical and mechanical properties of the nozzle material, (3) the operating environment, (4) the geometry of the nozzle elements, and (5) the loading conditions.

A schematic diagram of the specimen is shown in Fig. 39.2. Each test specimen consisted of a planar array of six thin-walled Hastelloy X tubes brazed to

[1] E. A. Franco-Ferreira, *Metals and Ceramics Div. Ann. Progr. Rept. June 30, 1966*, ORNL-3970, pp. 236–44.

[2] Summer participant from the University of Alabama.

[3] A. E. Carden, D. G. Harman, and E. A. Franco-Ferreira, "Thermal Fatigue Analysis of a Cryogenically Cooled Rocket Nozzle," pp. 102-1–102-12 in *Proceedings of the Southeastern Symposium on Missiles and Aerospace Vehicles Sciences, Dec. 5–7, 1966, American Astronautical Society, Huntsville, Alabama*, American Astronautical Society, Southeast Section, Huntsville, Ala., 1966.

each other and to a thick Hastelloy X baseplate. The tubes were $\frac{1}{2}$ in. in diameter with a 0.012-in. wall, and the baseplate was $4 \times 10 \times \frac{7}{8}$ in. Both ends of each tube were plugged. Entry and exit ports for the coolant were drilled through the baseplate and into the tubes near opposite ends of each specimen. Suitable thermocouple instrumentation was added to the tubes and baseplate.

The heat source used in these experiments was a quartz-lamp radiant furnace. It was positioned parallel to and approximately $\frac{1}{2}$ in. above the tube crowns. The furnace had a lamp area of $8 \times 2\frac{1}{2}$ in. and an electrical power input to the lamps of 13.2 kw. This produced a measured heat flux at the specimen surface of approximately 700 w/in.^{2}. The specimen baseplate was kept at or near the liquid nitrogen coolant temperature by bolting it to a massive copper heat sink. Coolant flow was introduced into the tubes through a copper manifold.

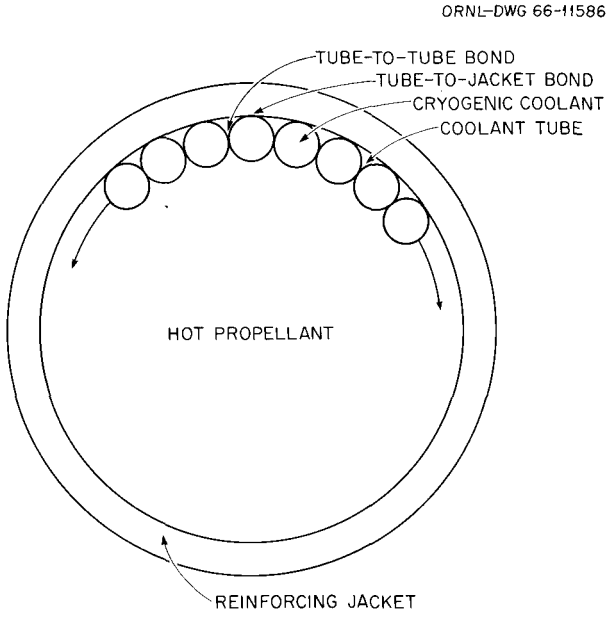

Fig. 39.1. Typical Cross Section of a Cryogenically Cooled Rocket Nozzle.

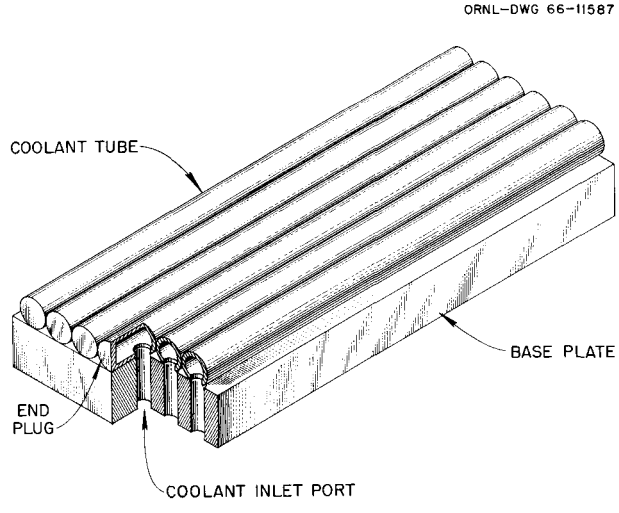

Fig. 39.2. Thermal Cycle Test Specimen. Baseplate is about 4 in. wide, 10 in. long, and $\frac{7}{8}$ in. thick. Coolant tubes are $\frac{1}{2}$-in. diam with 0.012-in. wall.

A test run for a given specimen was characterized by thermally cycling the tube crowns from liquid-nitrogen temperature to an elevated temperature and back. A number of identical cycles were reproduced until the tube failed. A typical test thermal cycle, as traced by a strip-chart recorder connected to the specimen thermocouples, is shown in Fig. 39.3. This particular cycle was for the 5-min hold time.

The results of all the tests are detailed in Table 39.1. For undented tubes, local creep buckling in the form of ripples occurred in the tube crowns in approximately 15 to 30 cycles, depending on hold time. The ripples stabilized in location but increased in amplitude as the cycling progressed. Failure was always associated with a ripple and normally occurred in a valley rather than on a peak. Failure was defined as a crack through the tube wall capable of passing liquid nitrogen.

A transverse section of a tube crown through a typical failure is shown in Fig. 39.4. This failure

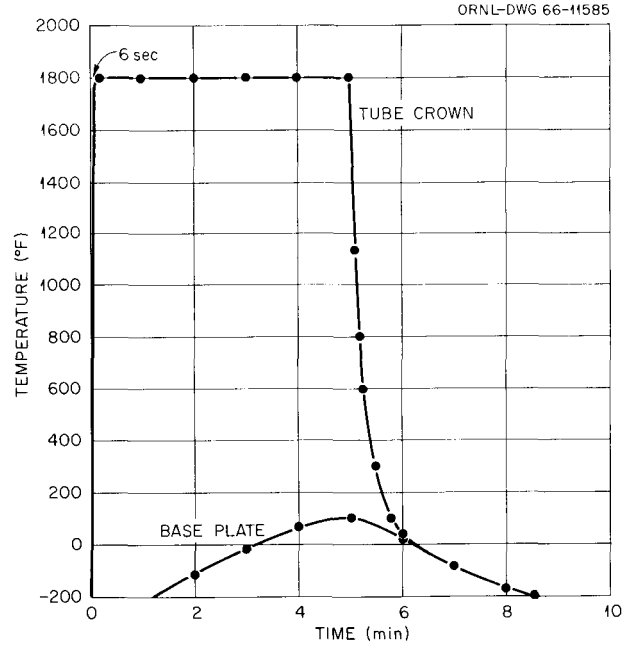

Fig. 39.3. Typical Test Cycle Showing Tube-Crown and Baseplate Temperatures.

Table 39.1. Thermal Cycle Data[a]

Specimen	Maximum Temperature (°F)	Hold Time at Temperature (min)	Tube Condition	Number of Thermal Cycles to Failure		
				First Visible Wrinkling	First Visible Crack	Crack Through Wall
X-1	1800	5	Smooth	14	41	50
X-2	1800	0.25	Smooth	30	70	80
X-3	1900	5	Smooth	11	32	42
			20-mil dent[b]		18	22
			20-mil dent[b]		21	26
X-4	1800	5	Smooth	14	49	57
			Small sharp dent[c]		25	33
			Medium deep dent[c]		39	49
			Large shallow dent[c]		56	*d*
			20-mil dent[b]		19	28
			20-mil dent[b]		22	30
			20-mil dent[b]		25	33
			10-mil dent[b]		25	35
			5-mil dent[b]		*d*	*d*
X-5	1600	5	Smooth	15	75	79
			20-mil dent[b]		23	35
			20-mil dent[b]		25	38

[a]Tube crown heating time from −200°F, the common minimum temperature, to maximum temperature was approximately 5 sec each cycle.

[b]Depth of controlled dent made in top of tube crown with a $\frac{1}{4}$-in.-diam indenter.

[c]Description of dent in as-received specimen.

[d]No failure.

Fig. 39.4. Cross Section of a 42-Cycle Failure Crack in a Smooth Tube from Specimen X-3. 100×. As polished.

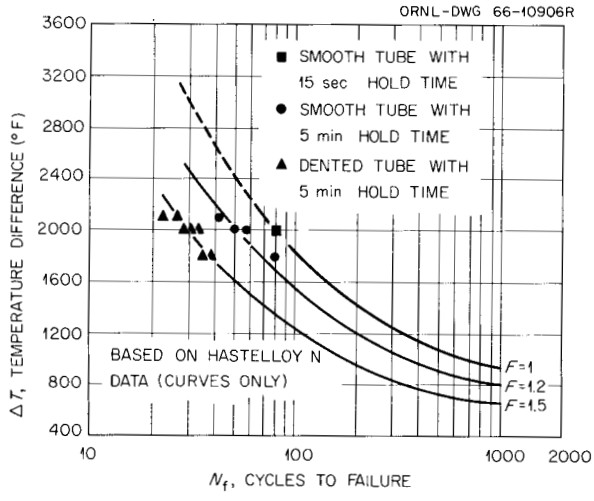

Fig. 39.5. Thermal Cycle Data for Hastelloy X Thin-Wall Tube Bundles Cycled Between −200°F and 1600, 1800, and 1900°F. Hastelloy N constraint curves are shown for comparison. Failure is defined as a crack through a tube wall capable of passing liquid nitrogen.

occurred in 42 cycles in a smooth tube in specimen X-3. Note that this is an intergranular tension failure, indicating that it occurred while the tube was cooling down from peak temperature and in the temperature range 1200 to 1500°F.

We tried to relate the data obtained in these tests to existing fatigue data. Appropriate information,[4] obtained by thermal cycle testing of tubular specimens, was available for a similar alloy, Hastelloy N. This was used for correlations with our test results.

The data generated by these tests were superimposed on a family of thermal fatigue curves for Hastelloy N, plotted for three different constraint factors: $F = 1$, 1.2, and 1.5. This is shown in Fig. 39.5. The data for the 15-sec hold time and the $F = 1$ curve correlate quite well. The data for the longer hold time of 5 min indicate that the effective constraint factor has been increased to near $F = 1.2$. We feel that this is due primarily to stress relaxation of the tube crowns, which can occur under the conditions of time and temperature studied. The results for the dented tubes show constraint factors in the vicinity of $F = 1.5$, due to the strain-concentrating effects of the dents.

[4]A. E. Carden, "Thermal Fatigue of a Nickel-Base Alloy," *J. Basic Eng.* **87**, 237–44 (1965).

RADIATION DAMAGE TO BRAZING ALLOYS

W. R. Martin E. E. Bloom

The coolant tubes in a nuclear rocket are brazed in place with precious-metal-base brazing alloys. The braze joints must be able to withstand structural loads in the presence of a high neutron flux. Thus, there is an interest in the effects of radiation damage on these brazing alloys. A modest program was conducted to study this problem.

Miller-Peaslee specimens were made of Hastelloy-X base metal and brazed with three different brazing alloys. The specimen was designed to load the braze joint in shear, and shear-stress–strain data were generated. The three brazing alloys studied were Nioro (Au–18% Ni), Palniro 7 (Au–8% Pd–22% Ni), and Nicoro 80 (Au–16.5% Cu–2% Ni).

One specimen of each brazing alloy was tested in the unirradiated condition at liquid-nitrogen, room, and 400°C testing temperatures. The irradiated specimens were all irradiated at a temperature of 50°C to a dose of 9×10^{19} neutrons/cm^2 thermal and 5×10^{18} neutrons/cm^2 fast (>2.9 Mev). The irradiated specimens of each brazing alloy were then tested at the same three temperatures.

The data were analyzed by comparing the stress-strain curves generated during the tests. The areas under those curves are proportional to the total energy absorbed to fracture the specimens.

The stress-strain curves for the specimens brazed with Nioro are shown in Fig. 39.6. Curves are shown for both irradiated and unirradiated specimens at all three testing temperatures. Radiation damage can be seen at all test temperatures, as evidenced by the greatly reduced areas under the three curves for the irradiated specimens.

Similar behavior is shown in Fig. 39.7 for Palniro 7. The strengths and ductilities of the unirradiated specimens are comparable to those for the Nioro, although there may be a slight bias toward less strength and greater ductility for the Palniro 7. There is no question that damage is evident in the 400°C and room-temperature tests. However, in the liquid-nitrogen test, only a slight strengthening and slight loss in ductility were shown.

The curves for Nicoro 80 are shown in Fig. 39.8. The 400°C tests show a relatively large amount of damage, while the room- and liquid-nitrogen-temperature tests show little if any damage. Although this may appear to be the most radiation resistant of the three brazing alloys tested, the mechanical properties of this alloy are inferior to those of the

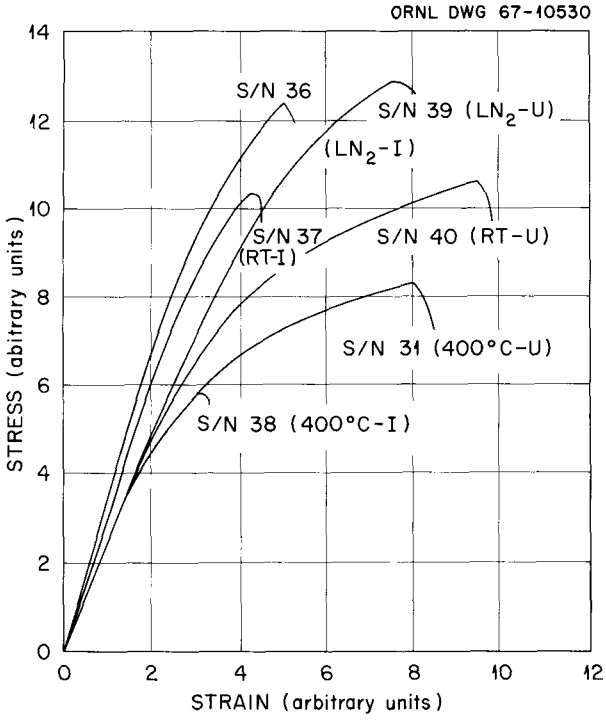

Fig. 39.6. Stress-Strain Curves for Joints Brazed with Nioro. Curves are identified by specimen serial number, testing temperature, and whether irradiated (I) or unirradiated (U).

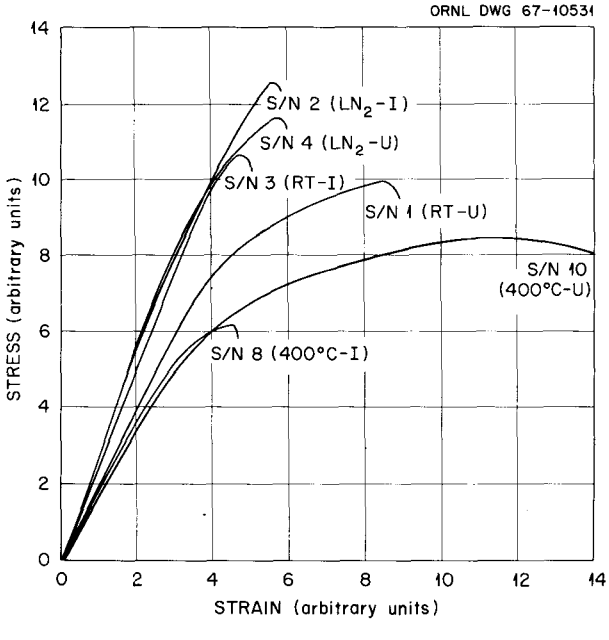

Fig. 39.7. Stress-Strain Curves for Joints Brazed with Palniro 7. Curves are identified by specimen serial number, testing temperature, and whether irradiated (I) or unirradiated (U).

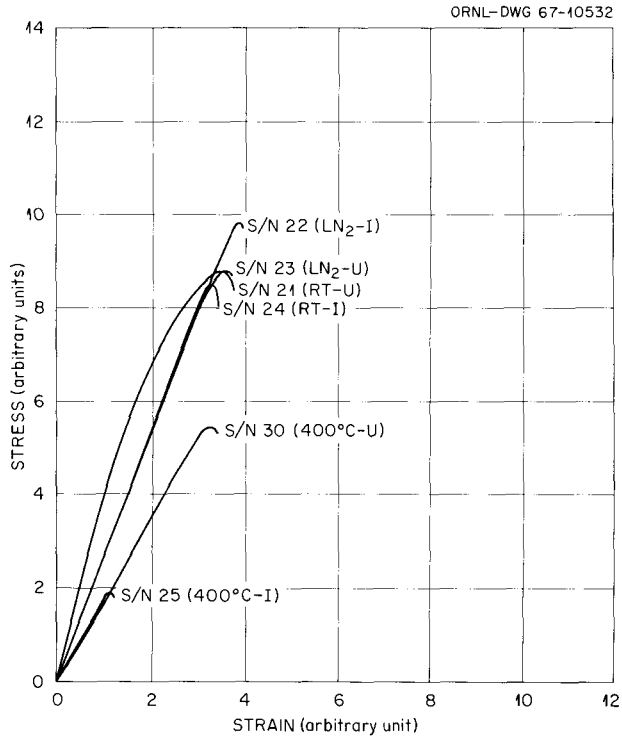

Fig. 39.8. Stress-Strain Curves for Joints Brazed with Nicoro 80. Curves are identified by specimen serial number, testing temperature, and whether irradiated (I) or unirradiated (U).

other two throughout the entire range of test variables.

No data are available regarding the boron contents of the three brazing alloys, as all specimens were supplied in the brazed form by Aerojet General Corporation. It is likely, though, that the damage is a result of the transmutation of ^{10}B to helium by a thermal-neutron (n, α) reaction rather than by the transmutation of the gold in the brazing alloys into mercury. This statement is based primarily on the great similarity of the behavior seen here to that reported by Martin and Slaughter.[5]

ELEVATED-TEMPERATURE TESTING OF TUBING MATERIAL

D. G. Harman

As the performance of the nuclear rocket is upgraded, the nozzle coolant tubes will have to oper-

[5]W. R. Martin and G. M. Slaughter, "Irradiation Embrittlement of Welds and Brazes at Elevated Temperatures," *Welding J. (N. Y.)* **45**(9), 385-s–391-s (September 1966).

Table 39.2. Short-Time Tensile Properties of 0.012-in.-Thick Allvac 625 Sheet (Heat 5940) and Hastelloy X Sheet (Heat 261-5-4002)

Property	Value of Property at					
	Room Temperature	1200°F	1400°F	1600°F	1800°F	2000°F
Allvac 625						
As received, at 0.05 min^{-1}						
0.2% yield strength, psi	53,530	34,280	35,790			
Upper yield strength, psi				33,080	20,750	8,330
Lower yield strength, psi				30,370	17,830	7,520
Ultimate tensile strength, psi	117,290	66,160	59,250	33,080	20,750	8,330
Uniform elongation, %	58.8	22.3	21.7	5.6	1.5	7.1
Total elongation, %	58.8	25.9	53.3	58.2	19.0	22.9
Braze cycle treated, at 0.05 min^{-1}						
0.2% yield strength, psi	53,530	35,190	33,980			
Upper yield strength, psi				29,770	22,650	8,720
Lower yield strength, psi				27,070	18,650	8,270
Ultimate tensile strength, psi	118,190	90,220	55,340	30,070	22,650	8,720
Uniform elongation, %	63.9	59.8	21.0	5.3	2.0	2.3
Total elongation, %	64.1	59.8	45.9	35.7	23.0	30.0
Braze cycle treated, at 0.005 min^{-1}						
0.2% yield strength, psi		33,980	31,880		11,730	
Upper yield strength, psi				20,450		5,050
Lower yield strength, psi				16,840		4,540
Ultimate tensile strength, psi		71,580	39,100	20,450	12,330	5,170
Uniform elongation, %		35.5	4.6	2.2	2.0	4.2
Total elongation, %		41.5	40.7	33.4	25.3	22.0
Hastelloy X						
As received, at 0.05 min^{-1}						
0.2% yield strength, psi	78,200	49,620	43,000	30,980	18,650	9,380
Ultimate tensile strength, psi	115,790	78,190	52,330	31,580	19,850	10,070
Uniform elongation, %	35.3	36.5	11.0	4.6	4.0	3.5
Total elongation, %	38.2	38.6	46.5	39.3	42.3	40.0
Braze cycle treated, at 0.05 min^{-1}						
0.2% yield strength, psi	51,430	39,400	38,500	27,370	17,380	9,770
Ultimate tensile strength, psi	112,780	80,300	52,930	29,320	18,590	10,380
Uniform elongation, %	38.1	35.7	11.0	3.2	3.0	4.2
Total elongation, %	35.3	43.0	55.8	65.0	41.0	47.9
Braze cycle treated, at 0.005 min^{-1}						
0.2% yield strength, psi		40,900	34,590	18,050	10,830	5,260
Ultimate tensile strength, psi		70,070	40,000	19,550	11,940	6,230
Uniform elongation, %		23.9	4.9	2.8	5.8	4.2
Total elongation, %		53.8	60.5	46.5	31.5	27.4

ate at ever-increasing tube-crown temperatures. Thus, there is an interest in the ability of candidate tubing materials to retain useful mechanical properties to a temperature as high as 2000°F. Elevated-temperature tensile tests were conducted on two promising candidate materials, Hastelloy X and Allvac 625, in the temperature range from 1200 to 2000°F.

Testing was done in an Instron testing machine using constant cross-head speeds corresponding to strain rates of 0.05 and 0.005 min^{-1} at room temperature, 1200, 1400, 1600, 1800, and 2000°F. The specimen axis was parallel to the rolling direction of the 0.012-in.-thick sheet. Each specimen was given the standard three-stage braze cycle. In addition, as-received sheet was tested at the same temperatures at a strain rate of 0.05 min^{-1}.

The tensile strength data are listed in Table 39.2. For Allvac 625, an upper and a lower yield stress are reported at the higher temperatures because of the unusual shape of the stress-strain curve for this alloy. The ultimate tensile strength is taken as the maximum in the curve and quite often coincides with the upper yield stress. The uniform elongation is taken as the plastic strain beyond which no increase in load occurs.

The data show that the two alloys are very similar in tensile properties over the temperature range investigated. Allvac 625 has some advantage in yield strength up to about 1800°F but has a lower yield strength at 2000°F than does Hastelloy X. The ultimate tensile strengths are about the same for these two alloys in the 1400 to 1800°F region. Below this range Allvac 625 has an advantage in ultimate tensile strength, and above it Hastelloy X is stronger. Hastelloy X has slightly better ductility, especially at the higher temperatures. Both alloys are satisfactory in this regard.

EFFECTS OF SPACE ENVIRONMENT ON NERVA MATERIALS

R. E. Clausing

A committee composed of representatives of Aerojet General Corporation, Westinghouse Astronuclear Laboratory, NASA Space Nuclear Propulsion Office at Cleveland, Oak Ridge National Laboratory, and Thompson-Ramo-Wooldrige has been reviewing the possible effects of the space environment on the material and components to be used in NERVA. The goal of the committee is to define the possible problem areas and to establish suitable means of assuring the satisfactory operation of materials and components in space.

The committee has recognized the tendency of atomically clean surfaces to adhere strongly to each other as one of the most important phenomena to be considered. Because adherence itself and its relationship to friction are only beginning to be understood, the committee decided to support a basic experimental program to better define the importance of various environmental parameters and lay the groundwork for future materials and component testing.

This program is being conducted through an ORNL subcontract with the Syracuse University Research Corporation. Dr. R. G. Aldrich is the principal investigator, and the contract is being monitored by R. E. Clausing of the ORNL Metals and Ceramics Division. The initial emphasis is on the influence of controlled surface contamination from gaseous environments upon the adhesion of various types of graphite to themselves and to other materials. The adherence of type 440C stainless steel to itself and to other materials is also being determined. Next year the program will be expanded to include additional combinations of materials.

The experiment is based on a technique developed by D. V. Keller of Syracuse University.[6] The experiment is based upon (1) starting with surfaces that are initially atomically clean, (2) measuring the adherence, (3) exposing the surfaces to known gaseous contamination, and (4) measuring changes in adherence as contamination proceeds. The gases presently being used are oxygen and hydrogen. Hydrogen will be a naturally occurring contaminant in the NERVA system and oxygen could be supplied in some circumstances.

The experimental program is well begun; however, the initial data on PO3 graphite vs PO3 graphite is not sufficiently complete to allow definite results to be reported.

---

[6]K. I. Johnson and D. V. Keller, "The Effect of Contamination on the Adhesion of Metallic Couples in Ultrahigh Vacuum," *J. Appl. Phys.* **38**, 1896–904 (March 1967).

40. Thermonuclear Project

R. E. Clausing W. J. Leonard

Both applied research and engineering assistance have been supplied for the Controlled Thermonuclear Program. The decision to use superconducting magnets has made the design of components for use at liquid-helium temperatures necessary. A brief summary of the results of a weldability study for the 5083 aluminum alloy is given as a typical example of the engineering assistance provided. The desorption of gases by electron bombardment is of interest because of the importance of adsorbed gases in determining the vacuum conditions in many experimental thermonuclear devices.

ENGINEERING AND DESIGN

W. J. Leonard

A number of small engineering and development projects were conducted this year: these included the casting of OFHC copper around a graphite sleeve for the so-called "burnout" experiments; the controlled surface hydriding of titanium and zirconium for use in proton sources; the possible use of electron-beam-heated titanium sublimators to replace resistance-heated sublimators in vacuum pumping applications; the preparation of braze welding specifications for copper, copper-nickel, and austenitic stainless steel and qualification of operators for this work; and the development of procedures for welding 5083 aluminum alloy. The latter project is briefly described as typical of the kind of engineering assistance provided.

The DCX-3 IMP (Injection Microwave Plasma) experiment will use superconducting coils for generating the magnetic fields necessary for containment of the energetic particles used in this experiment. The inner liner where reactions occur and are contained will be surrounded by a liquid-helium system which contains the magnet coils. The material for this liquid-helium containment and liner is a non-heat-treatable aluminum alloy, 5083. Data on this alloy indicate that it should support the mechanical stresses resulting from the magnetic fields, and that the other physical and mechanical properties of this alloy at 4.2°K are quite suitable for this application. Many weld joints occur in the design, but no local plant welding specifications had existed for this material.

A welding development program was initiated to screen candidate weld filler metals. The bases for selection are (1) good weldability and (2) production of welds whose mechanical and physical properties closely match those of the base metal at liquid-helium temperatures. Figure 40.1 shows a joint welded with ER-5183 filler metal. This material more closely satisfied the above criteria than the others tested. Further studies are needed, but we feel that a satisfactory welding procedure can be prepared for this equipment.

DESORPTION OF GASES FROM METALLIC SURFACES BY ELECTRON BOMBARDMENT

R. E. Clausing

The desorption of gas from the surfaces of vacuum systems is often the controlling factor in determining the pressure in the system. It has been shown that electrons per se (apart from thermal effects) can cause the desorption of large quantities of gases from such surfaces. This phenomenon can be very detrimental to the performance of systems when electron or plasma bombardment of surfaces occurs. On the other hand, this phenomenon may be used, in some

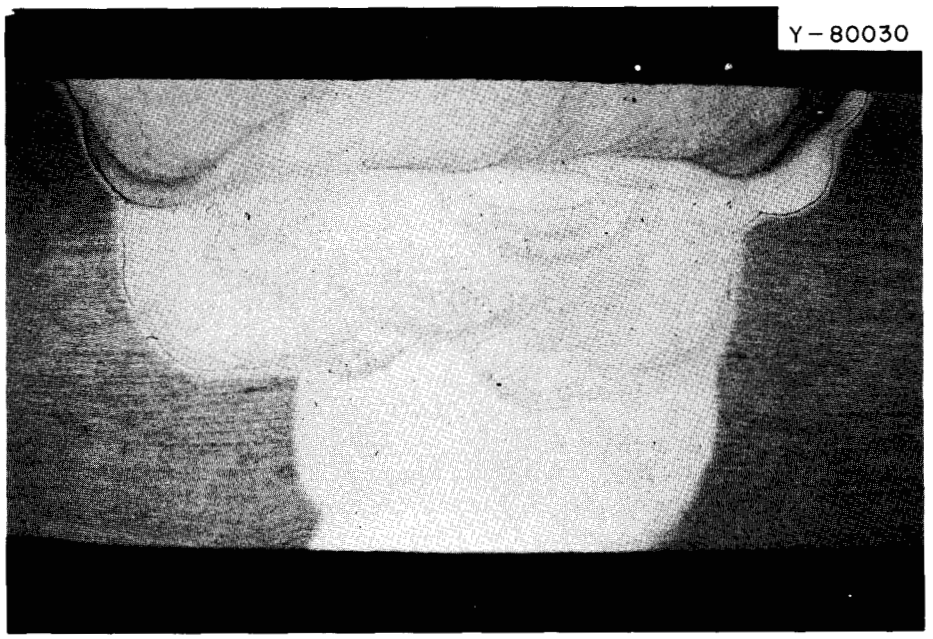

Fig. 40.1. Aluminum Alloy Plate TIG Weldment Using ER-5183 Filler Metal. 3×.

situations, to deplete the gases from vacuum vessels prior to normal operation. The desorption of gases by electron bombardment may also be used as an analytical method to follow changes in surface conditions, since the yield and kind of gas desorbed are quite sensitive to change in surface cleanliness.

Several preliminary experiments were conducted to explore the application of electron bombardment to vacuum technology,[1] and additional experiments are in progress. The release of gases from the surfaces of engineering materials, such as stainless steel, by electron impact appears to be very complex. It involves the decomposition of adsorbed hydrocarbons, the desorption of physically and chemically adsorbed gases and water, the decomposition of the surface oxide, the diffusion of gases and carbon to the surface, and probably even other phenomena.

Because of the complexity of engineering systems, the main emphasis during the past year has been to measure desorption in a simple well-defined system. The desorption of hydrogen, deuterium, and carbon monoxide from tungsten was chosen in the hope that the various processes of desorption could be isolated and studied independently.

Figure 40.2 is a schematic diagram of the present experimental apparatus. Both a narrow collimated electron beam and an uncollimated electron source are incorporated in the design. The target is located immediately adjacent to the ion source of a General Electric model 22PC110 mass spectrometer so as to give the maximum sensitivity to gases and ions desorbed from the target. Both electron sources have been used, but only data from the uncollimated source are given here, since its interpretation is more straightforward. The electron source is biased positive with respect to all its surroundings except the target. When the target is pulsed to a voltage more positive than the source, electrons are drawn to it from the source. Their energy is determined by the difference between the source and target potentials, and the current is determined by the filament temperature. All secondary and reflected electrons from the target return to it because of the electric fields; hence, the data include desorption by all three classes of electrons.

Control of secondary and reflected electrons is more difficult when the electron beam is used, and large spurious signals can arise when these electrons strike surfaces other than the target. Because the use of a collimated beam can give much

[1] R. E. Clausing, *Exploratory Experiments Concerning the Desorption of Gases by Bombardment with Electrons*, ORNL-TM-1166 (November 1965).

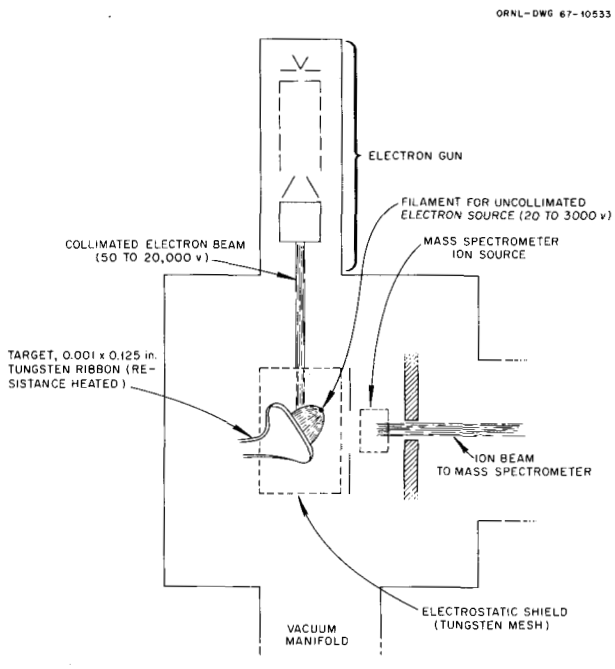

Fig. 40.2. Schematic Diagram of Apparatus for Studying Desorption of Gases from Tungsten by Electron Bombardment.

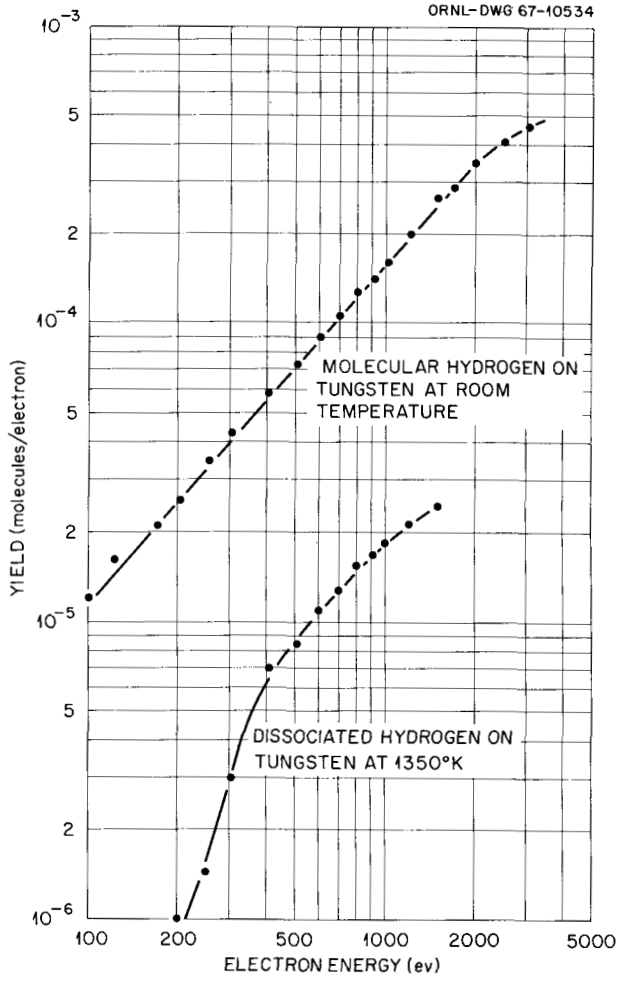

Fig. 40.3. Desorption of Hydrogen from Tungsten by Electron Impact.

better information concerning some effects, such as the importance of the angle of incidence, its use will be continued and its operation improved.

Figure 40.3 shows some typical results for the desorption of hydrogen from a tungsten surface. The ratio of the number of gas molecules produced by the bombardment to the number of electrons striking the target is plotted as a function of the energy of the primary electrons.

The results obtained for deuterium at room temperature are similar to those shown for hydrogen. Preliminary results indicate that the yields of carbon monoxide from a room-temperature target are much greater (i.e., approximately 10^{-2} molecule per incident 1000-ev electron).

The above results are given as typical; however, changes in experimental parameters or specimen preparation may shift these yield values by a factor of 2 in either direction. It is still too early to apply these results to a discussion of the mechanisms of desorption.

Future experiments will include additional data on the three gases mentioned above, with attention to elevated-temperature results (since one can see the effect on different adsorbed states easily in this manner), and will be extended to oxygen also. An attempt will be made to interpret these results in terms of the mechanisms involved. The secondary electron production will be characterized, and the effects of these secondary electrons on the total yield will be determined; or, alternatively, the effect of secondary electrons will be eliminated by an appropriate experimental design so that the yield of gas from the primary beam alone may be studied.

Papers and Publications

Papers and Oral Presentations

Compiled by Frances A. Scarboro

Atomic Energy Commission Review Meeting, Corrosion Center, Ohio State University, Columbus, Ohio, July 13–15, 1966

E. E. Bloom,* "Factors Affecting Radiation Damage in Stainless Steels"

International Symposium on Microscopy, Chicago, Ill., August 15–19, 1966

M. L. Picklesimer* and P. L. Rittenhouse, "Pole Figures by Quantitative Microscopy"

Thirteenth Sagamore Army Materials Research Conference, Raquette Lake, N. Y., August 23–26, 1966

J. V. Cathcart,* G. F. Petersen, and C. J. Sparks, "Oxidation Rate and Oxide Structural Defects"

XIVth Colloque Ampere, Ljubljana, Yugoslavia, September 5–11, 1966

M. M. Abraham,* C. B. Finch, L. J. Raubenheimer, Z. M. El Saffar, and R. A. Weeks, "Electron Spin Resonance Spectra of Dysprosium(III) Ion in Thorium Dioxide and Cerium(IV) Oxide"

1966 American Institute of Mining, Metallurgical, and Petroleum Engineers Nuclear Metallurgy Symposium on High-Temperature Nuclear Fuels, Delavan, Wis., October 3–5, 1966

M. N. Burkett,* W. P. Eatherly, and W. O. Harms, "Fueled-Graphite Elements for the German Pebble-Bed Reactor (AVR)"

1966 American Welding Society National Fall Meeting, St. Louis, Mo., October 3–6, 1966

D. A. Canonico,* R. W. Swindeman, and G. M. Slaughter, "Behavior of Stainless Steel Welds in Cyclic Loading"

W. R. Martin* and G. M. Slaughter, "Strength and Ductility of Irradiated Welds and Brazes"

J. W. Tackett, R. G. Donnelly, and G. M. Slaughter,* "Development of Solidified Metal Seals"

Symposium on Engineering Problems of Controlled Thermonuclear Research, Gatlinburg, Tenn., October 3–6, 1966

W. J. Leonard,* "Investigation of Material Failures in DCX-1 Liner"

Fall Meeting of the American Ceramic Society, University Park, Pa., October 9–11, 1966

C. S. Morgan* and D. H. Bower, "Inert Gas Bubbles in Neutron Irradiated Magnesium Oxide"

---

*Speaker

Philadelphia Meeting of the Electrochemical Society, Philadelphia, Pa., October 9–14, 1966

J. C. Banter,* "Spectrophotometric Determination of Properties of Anodic Oxide Films Formed on Zirconium in Various Electrolytes"

J. V. Cathcart* and G. F. Petersen, "Oxide Structural Defects and the Oxidation Rates of the (111) of Copper"

R. E. Pawel* and J. J. Campbell, "The Effect of Anodic Films on the Gaseous Oxidation of Tantalum"

12th Meeting of Refractory Composites Working Group, Denver, Colo., October 17–19, 1966

R. L. Heestand,* "Some Recent Developments in the Thermochemical Deposition Studies at the Oak Ridge National Laboratory"

6th Thermal Conductivity Conference, Dayton, Ohio, October 19–21, 1966

W. Fulkerson,* J. P. Moore, R. S. Graves, and D. L. McElroy, "Heat Transport in Silicon from 100 to 1300°K"

W. Fulkerson and R. K. Williams* "The Separation of the Electronic and Lattice Contributions to the Thermal Conductivity of Metals and Alloys"

D. L. McElroy* and W. Fulkerson, "A Brief Examination of the State of the Art of the Thermal Conductivity Conference Studies on Metals and Alloys – 1966"

J. P. Moore,* D. L. McElroy, and M. Barisoni, "Thermal Conductivity Measurements Between 78 and 340°K on Al, Fe, Pt, Mo, and W"

"Progress Report: Oak Ridge National Laboratory (Physical Properties Group)" (D. L. McElroy Speaker)

Nuclear Division, 19th Pacific Coast Regional Meeting of the American Ceramic Society, Portland, Ore., October 26–28, 1966

R. A. Potter,* T. G. Godfrey, and J. M. Leitnaker, "Precipitates in Uranium Nitride"

Annual Fall Meeting of the American Institute of Mining, Metallurgical, and Petroleum Engineers, Chicago, Ill., October 30–November 3, 1966

R. J. Arsenault,* "Hardening Mechanisms and Dislocation Distribution in Tantalum and Tantalum-Base Alloys"

R. O. Williams,* "Sheet Inverse Pole Figures"

American Nuclear Society Winter Meeting, Pittsburgh, Pa., October 31–November 4, 1966

D. D. Cannon, F. C. Davis,* and J. D. Sease, "A Machine to Remotely Fill and Compact Nuclear Fuel Tubes by Vibration"

J. H. Coobs,* R. L. Beatty, A. R. Olsen, H. L. Krautwedel, J. W. Prados, and J. L. Scott, "Testing of a Design Analysis for Coated-Particle Fuels"

F. C. Davis,* W. A. Pate, and J. D. Sease, "A Machine to Transfer Powdered Radioactive Fuel Remotely"

C. G. Lawson,* R. J. Kedl, and R. E. McDonald, "Enhanced Heat Transfer Tubes for Horizontal Condensers with Possible Applications in Nuclear Power Plant Design"

A. L. Lotts, M. K. Preston,* J. D. Sease, and J. E. Van Cleve, Jr., "Remotely Operated Equipment for Fabricating HFIR Target Elements"

J. W. Prados,* "Calculation of Creep in Spherical Pyrolytic-Carbon Shells Under Combined Radiation Damage and Internal Pressure"

J. D. Sease,* R. B. Pratt, F. C. Davis, and A. L. Lotts, "Design of a Remote System for Fabrication of (Th-^{233}U)O_2 Metal-Clad Fuel Elements"

*Speaker

26th National Convention of the Society for Nondestructive Testing, Chicago, Ill., October 31–November 4, 1966

K. V. Cook* and R. W. McClung, "Electro-Discharge-Machined Reference Discontinuities"

S. D. Snyder* and B. E. Foster, "An X-Ray Technique for Measuring Thickness of Tungsten on Copper"

Annual Technical Meeting of the Indian Institute of Metals, Bombay, India, November 1966

P. Rodriguez,* "High-Temperature Creep Behavior of Type 304 Stainless Steel in Argon-Oxygen Environment of Different Oxygen Partial Pressures"

Committee on Reactor Safety Testing (CREST), Paris, France, November 2–4, 1966

A. E. Goldman and S. I. Kaplan, "U. S. Research on the Oxidation and Irradiation Behavior of Carbon I. Graphite Oxidation"

A. E. Goldman and S. I. Kaplan, "U. S. Research on the Oxidation and Irradiation Behavior of Carbon II. Graphite Properties and Irradiation Behavior"

A. E. Goldman and S. I. Kaplan, "U. S. Research on the Oxidation and Irradiation Behavior of Carbon III. Fueled Graphite" (presented by H. Haymester)

1966 Thermionic Conversion Specialist Conference, Houston, Texas, November 2–4, 1966

J. R. DiStefano* and W. D. Box, "Compatibility Studies for High-Temperature Radioisotopic Power Source Applications"

J. I. Federer,* A. C. Schaffhauser, and C. F. Leitten, Jr., "Thermochemical Deposition and Evaluation of Rhenium and Tungsten-Rhenium Alloys"

A. C. Schaffhauser* and R. L. Heestand, "Effect of Fluorine Impurities on the Grain Stability of Thermochemically Deposited Tungsten"

Annual Meeting of the Tennessee Academy of Science, University of Tennessee, Knoxville, November 3, 1966

Otto C. Kopp,* "Recent Advances in the Methods of Hydrothermal Synthesis and Some Applications to Geological Problems"

1966 Pittsburgh Diffraction Conference, Mellon Institute, Pittsburgh, Pa., November 9–11, 1966

W. W. Beeman, H. Brumberger, R. W. Hendricks,* P. W. Schmidt, and A. M. Wims, "Current Status of Collimation Corrections in Small-Angle X-Ray Scattering"

Cullie J. Sparks, Jr.,* and Bernard Borie, "The Interpretation of Diffuse Scattering from Disordered Binary Alloys"

Annual Meeting of the Geological Society of America, San Francisco, Calif., November 14–16, 1966

T. F. Lomenick* and O. C. Kopp, "Thermal Effects and Stratigraphic Relations on the Deformation of Rock Salt"

7th General Meeting on the Irradiation Effects on Reactor Materials, Columbus, Ohio, November 16–21, 1966

E. E. Bloom* and J. R. Weir, Jr., "Behavior of Titanium-Bearing Stainless Steels at Elevated Temperatures"

J. R. Weir* and W. R. Martin, "Ductility of Stainless Steels Irradiated in LAMPRE and EBR-II"

---

*Speaker

International Atomic Energy Agency Symposium on Alkali Metal Coolants – Corrosion Studies and System Operating Experience, Vienna, Austria, November 28–December 2, 1966

J. H. DeVan,* "Corrosion of Iron- and Nickel-Base Alloys in High-Temperature Sodium and NaK"

J. H. DeVan,* A. P. Litman, J. R. DiStefano, and C. E. Sessions, "Lithium and Potassium Corrosion Studies with Refractory Metals"

23rd High Temperature Fuels Committee Meeting, Lawrence Radiation Laboratory, Livermore, Calif., November 29–December 1, 1966

J. L. Scott* (compiler), "Coated-Particle Fuel Development at the Oak Ridge National Laboratory"

22nd Annual Southwest Regional Meeting, American Chemical Society, Albuquerque, N. M., November 30–December 2, 1966

Niels J. Bjerrum, Harold L. Davis, Charles R. Boston, and G. Pedro Smith,* "Lower Oxidation States of Bismuth. Bi^+ and $[Bi_5]^{3+}$ in Solution and the Ligand-Field Theory of $p^{2,4}$ Configurations"

J. M. Leitnaker,* R. A. Potter, and H. Inouye, "Thermodynamic Properties of UN"

C. H. Liu* and G. P. Smith, "The Coordination Chemistry of Nickel(II) in Molten Dimethylsulfone"

Fall Meeting of the Southeastern Section of the American Ceramic Society, Chattanooga, Tenn., December 1–3, 1966

D. M. Hewette,* J. H. Coobs, R. L. Beatty, J. W. Prados, and J. L. Scott, "Recent Developments in Fuel Elements for Advanced Gas-Cooled Reactors"

Southeastern Symposium in Missiles and Aerospace Vehicles Sciences, American Astronautical Society, Huntsville, Ala., December 5–7, 1966

A. E. Carden, D. G. Harman, and E. A. Franco-Ferreira,* "Thermal Fatigue Analysis of a Cryogenically Cooled Rocket Nozzle"

International Symposium on Atomic, Molecular, and Solid State Theory, University of Florida, Sanibel Island, Fla., January 16–21, 1967

H. W. Joy,* J. S. Faulkner, and H. L. Davis, "Korringa-Kohn-Rostoker Band Theory Calculations"

Symposium on Nondestructive Testing of Welds, Illinois Institute of Technology, Chicago, Ill., January 30–February 1, 1967

R. W. McClung,* "Inspection of Small Specialty Welds and Brazed Joints for Nuclear Service"

American Physical Society Meeting, New York, N. Y., January 30–February 2, 1967

G. Czjzek,* J. L. C. Ford, Jr., J. C. Love, F. E. Obenshain, and H. H. F. Wegener, "Mössbauer Effect with Coulomb Excited, Recoil Implanted Germanium-73"

H. L. Davis,* H. W. Joy, and J. S. Faulkner, "Detailed Band Theory Calculations on Metallic Copper Using a Constant Energy Search"

3rd Annual Symposium on Low-Angle Scattering, New York, N. Y., February 1, 1967

R. W. Hendricks,* "X-Ray Monochromatization for Small-Angle Scattering Experiments"

Annual Meeting of the Metallurgical Society of the American Institute of Mining, Metallurgical, and Petroleum Engineers, Los Angeles, Calif., February 19–23, 1967

R. J. Arsenault,* "The Possibility of Irradiation Damage Affecting the Rate Controlling Mechanism for Slip in Body-Centered Cubic Metals and Solid Solutions"

---

*Speaker

J. Askill,* "Self Diffusion in Chromium-Nickel Alloys"

R. W. Hendricks,* "Kinetics of Precipitation in NaCl-AgCl Alloys"

C. C. Koch,* "Superconductivity in the Technetium-Vanadium Alloy System"

J. Larsen-Badse,* "The Time-Dependent Hardness of Soft Metals"

G. R. Love,* "Alloy Superconductors"

J. F. Murdock, "Self-Diffusion in Body-Centered Cubic Ti-V Alloys" (presented by C. J. McHargue)

J. C. Ogle* and R. A. Vandermeer, "The Development of Preferred Orientation in Cold-Rolled Columbium"

R. A. Vandermeer,* "Recrystallization and the Role of Precipitates in Gold-Doped, Zone-Refined Aluminum"

A. Wolfenden,* "The Energy Stored in Copper Crystals"

5th Temperature Measurements Society Conference, Los Angeles, Calif., March 14–15, 1967

D. L. McElroy, "Thermocouple Drift Tests to 800°C at 10^{-7} torr on Chromel-P vs Constantan" (presented by W. Fulkerson)

Twelfth Atomic Energy Commission Coated-Particle Working Group Meeting, Nevada Test Site, March 14–15, 1967

J. H. Coobs* and O. Sisman,* (compilers), "Coated-Particle Fuels Development at Oak Ridge National Laboratory for Period May 15, 1966, to January 15, 1967"

American Physical Society Meeting, Chicago, Ill., March 27–30, 1967

J. S. Faulkner,* Harold L. Davis, and H. W. Joy, "Energy Band Calculations Using the KKR Method"

Southeastern Section of Geological Society of America, Tallahassee, Fla., March 30–April 1, 1967

Otto C. Kopp* and Lawrence A. Harris, "Synthesis of Grunerite and Other Phases in the System SiO_2-NaOH-Fe-H_2O Near the Critical Temperature of Water"

American Chemical Society Meeting, Miami Beach, Fla., April 9–14, 1967

Niels J. Bjerrum and G. Pedro Smith,* "Lower Oxidation States of Bismuth. $[Bi_8]^{2+}$ Formed in $AlCl_3$-NaCl Melts"

Charles R. Boston,* Jorulf Brynestad, and G. Pedro Smith, "Effect of Melting on the Optical Spectra of $CsNiCl_3$ and Cs_3NiCl_5"

Jorulf Brynestad,* Charles R. Boston, and G. Pedro Smith, "The Coordination Geometry of Nickel(II) in Liquid KCl-LiCl Mixtures"

D. R. Cuneo,* E. L. Long, Jr., J. A. Conlin, C. A. Brandon, and G. B. Engle, "Compatibility of Graphite Under Irradiation with (1) Uranium(IV) Oxide-Thorium Dioxide at 1650°C and (2) Beryllium Oxide at 1500°C"

Atomic Energy Commission Nondestructive Testing Meeting, Oak Ridge National Laboratory, April 11–13, 1967

R. W. McClung, "Nondestructive Test Development at the Oak Ridge National Laboratory"

Pacific Northwest Metals and Minerals Conference, Portland, Ore., April 19–21, 1967

P. L. Rittenhouse,* "Biaxial Yield Locus Construction for Zircaloy-2 from a Uniaxial Test"

---

*Speaker

American Physical Society Meeting, Washington, D. C., April 24–27, 1967

Harold L. Davis,* H. W. Joy, and J. S. Faulkner, "Effect of Hydrostatic Pressure on the Fermi Surface of Metallic Copper"

American Welding Society, 48th Annual Meeting, Detroit, Mich., April 24–28, 1967

D. A. Canonico* and W. R. Martin, "The Effect of Heat Input on Austenitic Stainless Steel Weldments"

H. E. McCoy and D. A. Canonico,* "Studies on the Weldability of Hastelloy N"

American Ceramic Society, 69th Annual Meeting, New York, N. Y., April 29–May 4, 1967

H. Beutler* and R. L. Hamner, "Heat Treatment of Pyrolytic-Carbon-Coated Oxide Fuel Particles"

E. S. Bomar* and P. E. Potter, "The Compatibility of Plutonium Carbides with Silicon Carbide" (work performed at Harwell)

R. B. Fitts,* A. B. Meservey, J. D. Sease, and A. L. Lotts, "Extrusion of Thoria Bodies from Sol-Gel Clay"

J. M. Leitnaker* and C. M. Fitzpatrick, "Reaction of Nitrogen with Uranium Carbide at 1500°C"

C. S. Morgan* and L. L. Hall, "Effect of Isostatic Pressing on Sintering"

R. A. Potter* and V. D. Fréchette, "Sintering Behavior of Uranium Mononitride"

J. M. Robbins and J. G. Stradley,* "Fabrication of Sol-Gel Derived Thoria-Uranium by Cold-Pressing and Sintering"

Sixth Rare Earth Research Conference, Gatlinburg, Tenn., May 3–5, 1967

C. C. Koch* and C. J. McHargue, "A Metallographic Study of the Allotropic Phase Transformations in Cerium"

Materials Advisory Board Tubing Committee Meeting, Westinghouse Astronuclear Laboratory, Pittsburgh, Pa., May 9, 1967

W. O. Harms,* R. E. McDonald, G. A. Reimann, and W. R. Martin, "Status Report: Fabrication Development Studies on Refractory Metal Alloys at the Oak Ridge National Laboratory"

Ninth Annual Symposium on Electron, Ion, and Laser Beam Technology, Berkeley, Calif., May 9–11, 1967

C. W. Dean,* R. E. McDonald, and C. F. Leitten, Jr., "High-Purity Shape Casting with an Electron-Beam Furnace"

21st Atomic Energy Commission Metallography Group Meeting, Brookhaven National Laboratory, May 10–12 1967

James B. Buhr, T. M. Kegley, Jr.,* and R. J. Gray, "Potentiostatic Metallographic Etching Experiments"

R. E. Gehlbach* and J. T. Houston, "Application of Electron Metallography to Precipitation Studies of Hastelloy N"

T. M. Kegley, Jr.,* "Metallographic Preparation of Cerium Carbides"

24th High-Temperature Fuels Committee Meeting, United Nuclear Corporation Facility, Elmsford, N. Y., May 16–18, 1967

J. L. Scott* (compiler), "High-Temperature Fuel Work at the Oak Ridge National Laboratory"

American Institute of Chemical Engineers National Meeting, Salt Lake City, Utah, May 21–24, 1967

R. B. Fitts,* J. D. Sease, and A. L. Lotts, "Preparation of Ceramic Nuclear Fuels by Sol-Gel Extrusion"

P. A. Haas,* F. G. Kitts, and H. Beutler, "Preparation of Reactor Fuels by Sol-Gel Processes"

*Speaker

Fifth International Conference on Nondestructive Testing, Montreal, Canada, May 21–26, 1967

C. V. Dodd III* and W. E. Deeds, "Computer Design of Eddy-Current Tests"

H. L. Whaley,* K. V. Cook, R. W. McClung, and L. S. Snyders, "Optical Methods for Studying Ultrasonic Propagation in Transparent Media"

13th Annual Meeting, American Nuclear Society, San Diego, Calif., June 11–15, 1967

G. M. Adamson, Jr.,* J. Binns, and R. W. Knight, "Production of High-Flux Isotope Reactor Fuel Elements"

R. J. Beaver,* C. F. Leitten, Jr., and G. M. Adamson, "The Development of Aluminum-Base Eu_2O_3 Control Rods for the High Flux Isotope Reactor"

E. E. Bloom* and J. R. Weir, "In-Reactor and Postirradiation Creep-Rupture Properties of Type 304 Stainless Steel"

M. T. Morgan,* E. L. Long, Jr., and D. M. Hewette II, "Fuel Migration into Coatings of Pyrolytic Carbon Coated UO_2 and UC_2 Particles as a Result of Irradiation and Heat Treatment"

A. R. Olsen,* J. H. Coobs, D. M. Hewette II, H. L. Krautwedel, A. W. Longest, E. L. Long, Jr., J. W. Prados, and J. L. Scott, "Performance of Pyrolytic-Carbon-Coated Sol-Gel UO_2 Microspheres in High-Burnup Irradiation Tests"

J. L. Scott* and R. L. Beatty, "Pyrolytic-Carbon Coatings Formed at High Deposition Rates"

J. N. Siltanen,* F. R. McQuilkin, E. L. Long, Jr., and J. R. Lindgren, "Irradiation Testing of Candidate Fuel Rods for the GCFR"

J. W. Tackett,* J. R. Barker, and G. M. Slaughter, "Welding of Fuel Elements for the High Flux Isotope Reactor"

J. R. Weir* and E. E. Bloom, "The Nature of Radiation Damage in Materials"

J. R. Weir and R. T. King,* "The Effect of Cyclotron-Injected Helium on the Mechanical Properties of Stainless Steel"

International Conference on Vacuum Metallurgy, New York City, June 13–16, 1967

D. T. Bourgette,* "Vaporization Behavior of Haynes Alloy No. 25 in High Vacuum at Elevated Temperatures"

H. Inouye,* "High-Temperature Sorption of Nitrogen by Nb–1% Zr in Ultrahigh Vacuum"

International Symposium on Special Topics in Ceramics, Alfred, N. Y., June 18–23, 1967

C. S. Morgan,* "Densification Kinetics During Nonisothermal Sintering of Oxides"

American Physical Society, University of Toronto, Toronto, Canada, June 21–23, 1967

S. T. Sekula,* R. H. Kernohan, and C. C. Koch, "Superconductivity in the Technetium-Vanadium System"

American Society for Testing Materials Symposium on Nondestructive Testing of Graphite, Boston, Mass., June 25–30, 1967

C. V. Dodd,* "Eddy Current and Infrared Inspection of Graphite"

R. W. McClung,* "Low Voltage Radiographic and Microradiographic Techniques for Graphite"

Libby/Cockcroft Graphite Physics Meeting, Oak Ridge National Laboratory, June 26–27, 1967

W. H. Cook,* "Molten Salt Reactors and Graphite"

C. R. Kennedy,* "The Irradiation Creep of Graphite for Temperatures of 150°C to 1000°C"

C. R. Kennedy,* "Strength Variations in Large Blocks of Graphite"

J. W. Prados,* "Theoretical Analysis of Spherical Pyrolytic Coatings on Fuel Particles"

---

*Speaker

Publications

Compiled by Meredith R. Hill

Abraham, M. M., R. A. Weeks, G. W. Clark, and C. B. Finch, "Electron Spin Resonance of Rare Earth Ions in CeO_2: Yb^{3+} and Er^{3+}," *Phys. Rev.* **148**, 350–52 (August 1966).

Abraham, M. M., L. A. Boatner, C. B. Finch, E. J. Lee, and R. A. Weeks, "Paramagnetic Resonance of Gd^{3+} in CeO_2 Single Crystals," *J. Phys. Chem. Solids* **28**(1), 81–92 (January 1967).

Adamson, G. M., Jr., J. Binns, and R. W. Knight, "Production of High-Flux Isotope Reactor Fuel Elements," *Trans. Am. Nucl. Soc.* **10**(1), 124–25 (June 1967).

Arsenault, R. J., "An Investigation of the Mechanism of Thermally Activated Deformation in Tantalum and Tantalum-Base Alloys," *Acta Met.* **14**(7), 831–38 (July 1966).

Arsenault, R. J., "Dislocation Dynamics Applied to the Problem of Overshoot," *Acta Met* **14**(11), 1635–36 (November 1966).

Arsenault, R. J., "The Double-Kink Model for Low-Temperature Deformation for BCC Metals and Solid Solutions," *Acta Met.* **15**(3), 501–11 (March 1967).

Arsenault, R. J., and A. Lawley, "Work Hardening and Dislocation Structure in Ta and Ta-base Alloys," *Phil. Mag.* **15**(135), 549–65 (March 1967).

Askill, J., "Environmental Effects on the Diffusion of Ta^{182} in B.C.C. Titanium," *Phys. Stat. Sol.* **16**(1), K63–K65 (July 1966).

Askill, John, "Grain Boundary Self-Diffusion in Chromium Near the Melting Point," *Appl. Phys. Letters* **9**(2), 82 (July 1966).

Askill, J. A., "Tracer Diffusion in Metals," pp. F-44–F-50 in *Handbook of Chemistry and Physics*, 47th ed., ed. by R. C. Weast and S. M. Selby, The Chemical Rubber Company, Cleveland, Ohio, 1966–1967.

Askill, John, *A Bibliography on Tracer Diffusion in Metals: Part III. Self and Impurity Diffusion in Alloys*, ORNL-3795, Part III (February 1967).

Askill, John, *A Bibliography on Tracer Diffusion in Metals, Supplement II to Parts I, II, and III*, ORNL-3795, suppl. II (June 1967).

Banter, J. C., "Incorporation of Ions in Anodic Oxide Films on Zirconium and Their Effect on Film Behavior," *J. Electrochem. Soc.* **114**(5), 508–11 (May 1967).

Barrett, L. K., and C. S. Yust, "Discussion of 'Measurement of Topological Parameters for Description of Two-Phase Structures with Special Reference to Sintering,'" *Trans. Met. Soc. AIME* **236**(9), 1385–86 (September 1966).

Beatty, R. L., *Pyrolytic Carbon Deposited from Propane in a Fluidized Bed*, ORNL-TM-1649 (January 1967), MS thesis, the University of Tennessee.

Beaver, R. J., *Estimated Large-Scale Production Costs for Cladding Uranium Metal Fuel Tubes*, ORNL-TM-596 (November 1966).

Beaver, R. J., C. F. Leitten, Jr., and G. M. Adamson, "The Development of Aluminum-Base Eu_2O_3 Control Rods for the High-Flux Isotope Reactor," *Trans. Am. Nucl. Soc.* **10**(1), 137–38 (June 1967).

Beutler, H., R. L. Beatty, and J. H. Coobs, "Low-Density Pyrolytic-Carbon Coatings for Nuclear Fuel Particles," *Electrochem. Technol.* **5**(5–6), 189–94 (May, June 1967).

Binns, J., G. M. Adamson, Jr., and R. W. Knight, *Fabrication Procedures for Manufacturing High Flux Isotope Reactor Fuel Elements*, ORNL-TM-1628 (November 1966).

Bjerrum, N. J., C. R. Boston, and G. P. Smith, "Lower Oxidation States of Bismuth. Bi^+ and $[Bi_5]^{3+}$ in Molten Salt Solutions," *Inorg. Chem.* **6**(6), 1162–72 (June 1967).

Bjerrum, N. J., and G. P. Smith, "Bismuth in the Oxidation State One-Fourth. The Entity $[Bi_8]^{2+}$ Formed in Molten $AlCl_3$-NaCl Media," *Inorg. Nucl. Chem. Letters* **3**(5), 165–67 (May 1967).

Bloom, E. E., W. R. Martin, J. O. Stiegler, and J. R. Weir, "The Effect of Irradiation Temperature on Strength and Microstructure of Stainless Steel," *J. Nucl. Mater.* **22**(1), 68–76 (April 1967).

Bloom, E. E., *Effect of Titanium Additions on the Stress-Rupture Properties of Type 304 Stainless Steel*, ORNL-TM-1807 (June 1967).

Bloom, E. E., and J. R. Weir, "In-Reactor and Postirradiation Creep-Rupture Properties of Type-304 Stainless Steel," *Trans. Am. Nucl. Soc.* **10**(1), 131 (June 1967).

Bomar, E. S., and P. E. Potter, *The Compatibility of Plutonium Carbides with Silicon Carbide*, AERE-R 5214 (June 1966).

Borie, B., "The Theory of the Borrmann Effect in Terms of Difference Equations," *Acta Cryst.* **21**(Part 4), 470–72 (October 1966).

Borie, B., and C. J. Sparks, Jr., "Analysis of Thin Films," pp. 341–49 in *Local Atomic Arrangements Studied by X-Ray Diffraction* (proceedings of a symposium sponsored by the Physics and Chemistry of Metals Committee of the Institute of Metals Division, the Metallurgical Society, American Institute of Mining, Metallurgical, and Petroleum Engineers, Chicago, Illinois, February, 1965) ed. by J. B. Cohen and J. E. Hilliard, Gordon and Breach, Science Publishers, New York, 1966.

Bourgette, D. T., *Vaporization Phenomena of Haynes Alloy No. 25 to 1150°C*, ORNL-TM-1786 (May 1967).

Bourgette, D. T., "High-Temperature Chemical Stability of Refractory-Base Alloys in High Vacuum," *Trans. Vacuum Met. Conf. 8th, New York, 1965*, 57–73 (1966).

Briggs, N. H., E. L. Long, Jr., and F. R. McQuilkin, "Summary of Experience with High-Temperature Thermocouples Used in the ORNL-GCR Program Fuel Irradiation Experiments," paper 1 in *High Temperature Thermometry, Papers Presented at a Seminar at AEC Headquarters, Washington, D. C., on February 24–26, 1965*, WASH-1067 (March 1966).

Brynestad, J., H. L. Yakel, and G. P. Smith, "Temperature Dependence of the Absorption Spectrum of Nickel(II)-Doped $KMgCl_3$ and the Crystal Structure of $KMgCl_3$," *J. Chem. Phys.* **45**(12), 4652–64 (December 1966).

Cannon, D. D., F. C. Davis, and J. D. Sease, "A Machine to Remotely Fill and Compact Nuclear Fuel Tubes by Vibration," (summary) *Trans. Am. Nucl. Soc.* **9**(2), 614 (October–November 1966).

Cannon, D. D., F. C. Davis, and J. D. Sease, "A Machine That Will Remotely Fill and Compact Nuclear Fuel Tubes by Vibration," pp. 60–65 in *Proceedings of the 14th Conference on Remote Systems Technology, 1966*, American Nuclear Society, Hinsdale, Illinois, 1966.

Carden, A. E., D. G. Harman, and E. A. Franco-Ferreira, "Thermal Fatigue Analysis of a Cryogenically Cooled Rocket Nozzle," pp. 102-1–102-12 in *Southeastern Symposium on Missiles & Aerospace Vehicles Sciences*, Vol. II, American Astronautical Society, Southeast Section, Huntsville, Ala., 1966.

Coobs, J. H., and O. Sisman, *Coated-Particle Fuels Development at Oak Ridge National Laboratory for Period May 15, 1966, to January 15, 1967*, ORNL-TM-1772 (March 1967).

Coobs, J. H., R. L. Beatty, A. R. Olsen, H. L. Krautwedel, J. W. Prados, and J. L. Scott, "Testing of a Design Analysis for Coated-Particle Fuels," *Trans. Am. Nucl. Soc.* **9**(2), 421–22 (October–November 1966).

Cook, K. V., and R. W. McClung, "Nondestructive Testing of Small-Diameter Refractory Alloy Tubing," pp. 79–97 in *AEC-NASA Liquid Metals Information Meeting held in Gatlinburg, Tennessee, April 21–23, 1965,* CONF-650411 (September 1966).

Cook, K. V., and R. W. McClung, "Electro-Discharge Machined Reference Discontinuities," *Mater. Evaluation* **25**(2), 36–40 (February 1967).

Crouse, R. S., "Bausch and Lomb Research Metallograph Modifications," pp. 97–105 in *Advances in Metallography,* ed. by R. J. Jackson and A. E. Calabra, Technical Papers of the Twentieth Metallographic Conference, The Dow Chemical Company, RFP-658 (October 1966).

Crouse, R. S., and R. J. Gray, "An Effect of Curing Stresses in Epoxy Resins," pp. 118–23 in *Advances in Metallography,* ed. by R. J. Jackson and A. E. Calabra, Technical Papers of the Twentieth Metallographic Conference, The Dow Chemical Company, RFP-658 (October 1966).

Cunningham, J. E., and J. W. Ullmann, "Cladding and Dispersion Fuel Development at ORNL," pp. 16.1–16.16 in *Fast Flux Test Facility Driver Fuel Meeting, Richland, Washington, March 8, 9, and 10, 1966,* BNWL-268 (June 1966).

Czjzek, G., J. L. C. Ford, Jr., J. C. Love, F. E. Obenshain, and H. H. F. Wegener, "Coulomb Recoil Implanation Mössbauer Experiments with ^{73}Ge," *Phys. Rev. Letters* **18**(14), 529–31 (April 1967).

Davis, F. C., W. A. Pate, and J. D. Sease, "A Machine to Transfer Powdered Radioactive Fuel Remotely," (summary) *Trans. Am. Nucl. Soc.* **9**(2), 613–14 (October–November 1966).

Davis, F. C., W. A. Pate, and J. D. Sease, "A Machine to Transfer Powdered Radioactive Fuel Remotely," pp. 55–59 in *Proceedings of the 14th Conference on Remote Systems Technology, 1966,* American Nuclear Society, Hinsdale, Illinois, 1966.

Davis, H. L., N. J. Bjerrum, and G. P. Smith, "Ligand Field Theory of $p^{2,4}$ Configuration and Its Application to the Spectrum of Bi^+ in Molten Salt Media," *Inorg. Chem.* **6**(6), 1172–78 (June 1967).

DeVan, J. H., and C. E. Sessions, "Mass Transfer of Niobium-Base Alloys in Flowing Nonisothermal Lithium," *Nucl. Appl.* **3**(2), 102–9 (February 1967).

DeVan, J. H., A. P. Litman, J. R. DiStefano, and C. E. Sessions, *Lithium and Potassium Corrosion Studies with Refractory Metals,* ORNL-TM-1673 (December 1966).

DiStefano, J. R., and D. H. Jansen, "Refractory Metal–Boiling Potassium Compatibility Studies," pp. 316–22 in *AEC-NASA Liquid Metals Information Meeting held in Gatlinburg, Tennessee, April 21–23, 1965,* CONF-650411 (September 1966).

DiStefano, J. R., *Mass-Transfer Effects in Some Refractory-Metal–Alkali-Metal–Stainless Steel Systems,* ORNL-4028 (November 1966).

Dodd, C. V., *Solutions to Electromagnetic Induction Problems,* ORNL-TM-1842 (June 1967). PhD Thesis, the University of Tennessee.

Dodd, C. V., and W. E. Deeds, *Electromagnetic Forces in Conductors,* ORNL-TM-1835 (May 1967).

Donnelly, R. G., "Filler Metals," chap. 95 in *Welding Handbook,* 5th ed., sect. 5, ed. by A. L. Phillips, American Welding Society, New York, 1967.

Douglas, D. A., "Cladding and Dispersion Fuel Development at ORNL," pp. 17.1–17.10 in *Fast Flux Test Facility Driver Fuel Meeting, Richland, Washington, March 8, 9, and 10, 1966,* BNWL-268 (June 1966).

DuBose, C. K. H., and J. O. Stiegler, "Semi-Automatic Preparation of Specimens for Transmission Electron Microscopy," (summary) p. 159 in *Advances in Metallography,* ed. by R. J. Jackson and A. E. Calabra, Technical Papers of the Twentieth Metallographic Conference, The Dow Chemical Company, RFP-658 (October 1966).

DuBose, C. K. H., and J. O. Stiegler, *Semiautomatic Preparation of Specimens for Transmission Electron Microscopy,* ORNL-4066 (February 1967).

DuBose, C. K. H., and J. O. Stiegler, "Controlled Jet Polishing of Specimens for Transmission Electron Microscopy," *Rev. Sci. Instr.* **38**(5), 694–95 (May 1967).

Erwin, J. H., S. Peterson, and C. F. Leitten, Jr., *Development of a Forming Method for Curved ATR Fuel Plates,* ORNL-3983 (August 1966).

Federer, J. I., A. C. Schaffhauser, and C. F. Leitten, Jr., "Thermochemical Deposition and Evaluation of Rhenium and Tungsten-Rhenium Alloys," pp. 222–27 in *1966 IEEE Conference Record of the Thermionic Conversion Specialist Conference Nov. 3 and 4, 1966, Houston, Texas,* Institute of Electrical and Electronics Engineers, New York, 1966.

Finch, C. B., and G. W. Clark, "Single-Crystal Growth of Cerium Dioxide from Lithium Ditungstate Solvent," *J. Appl. Phys.* **37**(10), 3910 (September 1966).

Fleischer, B., A. Taboada, W. R. Huntley, H. W. Savage, and R. E. MacPherson, "Compatibility Studies of Materials in SNAP-8 Primary System," pp. 119–20 in *AEC-NASA Liquid Metals Information Meeting held in Gatlinburg, Tennessee, April 21–23, 1965,* CONF-650411 (September 1966).

Fleming, J. D., W. C. Robinson, and C. F. Leitten, Jr., *Thermochemical Analysis of Vapor Plating Processes,* ORNL-TM-1454 (July 1966).

Franco-Ferreira, E. A., *The Fabrication of a Potassium Vapor Radiator for the Medium-Power Reactor Experiment Large Potassium System,* ORNL-TM-1600 (November 1966).

Franco-Ferreira, E. A., and G. M. Slaughter, "The Welding of Refractory-Metal Components for Liquid Metal Service," *Welding J. (N.Y.)* **45**(10), 835–42 (October 1966).

Fulkerson, W., and J. P. Moore, "The Seebeck Coefficients of Iron from 0 to 1000°C and Tungsten from 0 to 1300°C," paper 16 in *High Temperature Thermometry, Papers Presented at a Seminar at AEC Headquarters, Washington, D.C., on February 24–26, 1965,* WASH-1067 (March 1966).

Fulkerson, W., J. P. Moore, R. S. Graves, and D. L. McElroy, "Heat Transport in Silicon from 100 to 1300°K," pp. 429–78 in *Proceedings of the Sixth Conference on Thermal Conductivity* (October 19–21, 1966, Dayton, Ohio), Materials Applications Division, Air Force Materials Laboratory, Wright-Patterson Air Force Base, Ohio.

Fulkerson, W., and R. K. Williams, "The Separation of the Electronic and Lattice Contributions to the Thermal Conductivity of Metals and Alloys," pp. 807–19 in *Proceedings of the Sixth Conference on Thermal Conductivity* (October 19–21, 1966, Dayton, Ohio), Materials Applications Division, Air Force Materials Laboratory, Wright-Patterson Air Force Base, Ohio.

Gilliland, R. G., and G. M. Slaughter, "The Welding of New Solution-Strengthened Nickel-Base Alloys," *Welding J. (N.Y.)* **45**(7), 314-s–320-s (July 1966).

Gilliland, R. G., *Joining of Tungsten,* ORNL-TM-1606 (October 1966).

Godfrey, T. G., and J. M. Leitnaker, *An Explanation of the Anomalous Heat Capacity of Uranium Dicarbide,* ORNL-TM-1595 (October 1966).

Godfrey, T. G., J. A. Woolley, and J. M. Leitnaker, *Thermodynamic Functions of Nuclear Materials: UC, UC_2, UO_2, ThO_2, and UN,* ORNL-TM-1596 (October 1966).

Godfrey, T. G., and J. M. Leitnaker, *A Computer Program to Calculate High-Temperature Thermodynamic Functions,* ORNL-TM-1599 (September 1966).

Goeddel, W. V., and J. L. Scott, "Design of Coated-Particle Fuel for High-Temperature Gas-Cooled Reactors," *Trans. Am. Nucl. Soc.* **10**(1), 168–69 (June 1967).

Gordon, P., and R. A. Vandermeer, "Grain-Boundary Migration," Chap. 6, pp. 205–66 in *Recrystallization, Grain Growth and Textures* (papers presented at a seminar of the American Society for Metals, October 16 and 17, 1965), American Society for Metals, Metals Park, Ohio, 1966.

Gregg, J. L., R. S. Crouse, and W. J. Werner, *Swelling of UAl_3-Al Compacts,* ORNL-4056 (January 1967).

Hamner, R. L., R. L. Pilloton, and T. M. Kegley, "A Method for Preparing Dense Spherical Particles of Thorium and Thorium-Uranium Dicarbides," *Nucl. Appl.* **3**(5), 287–93 (May 1967).

Harman, D. G., *Mechanical Properties of Al-Al_2O_3 Alloys: Testing Procedures and Evaluation of Data,* ORNL-TM-1802 (May 1967).

Harms, W. O., and D. B. Trauger, "Fabrication Variables, Performance and Cost Considerations for HTGR Coated-Particle Fuels," pp. 27–49 in *Proceedings of the Conference "Fuel cycles of high temperature gas-cooled reactors," Brussels, June 10–11, 1965,* ed. by D. Tygat, European Atomic Energy Community (Euratom), Brussels, May 1966. EUR 2780.e.

Harris, L. A., and H. L. Yakel, "The Crystal Structure of Y_2BeO_4," *Acta Cryst.* **22**(Pt. 3), 354–60 (March 1967).

Haynes, V. O., and A. E. Richt, *Preirradiation Data for the Fuel Specimens for the Army PM Fuel Experiment in the ORR Pressurized-Water Loop,* ORNL-TM-1783 (June 1967).

Heitkamp, D., W. Biermann, and T. S. Lundy, "Effect of Alpha Bombardment on the Diffusion of Lead in Silver," *Acta Met.* **14**(10), 1201–12 (October 1966).

Hendricks, J. W., and D. L. McElroy, "High-Temperature High-Vacuum Thermocouple Drift Tests," paper 9 in *High Temperature Thermometry, Papers Presented at a Seminar at AEC Headquarters, Washington, D.C., on February 24–26, 1965,* WASH-1067 (March 1966).

Hendricks, J. W., and D. L. McElroy, "High Temperature–High Vacuum Thermocouple Drift Tests," *Environ. Quart.* **13**(1), 34–37 (March 1967).

Hewette, D. M., II, R. L. Beatty, J. H. Coobs, T. M. Kegley, and B. C. Leslie, *Preirradiation Evaluation of the Pyrolytic-Carbon-Coated Fuel and the Assembly for the ORR-A9-4 Capsule,* ORNL-TM-1713 (February 1967).

Hobson, D. O., V. O. Haynes, and R. S. Crouse, *Characterization of Army PM-1 Type Reactor Fuel Elements,* ORNL-TM-1676 (December 1966).

Hobson, D. O., and C. F. Leitten, Jr., *Characterization of U_3O_8 Dispersions in Aluminum,* ORNL-TM-1692 (February 1967).

James, D. W., and G. P. Smith, "Apparatus for Absorption Spectroscopy of Liquids Under Gas Pressures up to 300 atm at Temperatures up to 600°C," *Appl. Spectry.* **20**(5), 317–19 (September–October 1966).

Joy, H. W., L. J. Schaad, and G. S. Handler, "Hartree-Fock-Roothaan Wavefunctions for Lithium," *J. Chem. Phys.* **46**(10), 4156–57 (May 1967).

Kasten, P. R., R. E. Adams, R. S. Carlsmith, R. H. Chapman, E. P. Epler, E. H. Gift, F. E. Harrington, M. L. Myers, R. C. Olson, J. T. Roberts, R. Salmon, J. P. Sanders, R. S. Stone, D. R. Vondy, C. S. Walker, T. N. Washburn, L. B. Yeatts, and F. C. Zapp, *An Evaluation of Heavy-Water-Moderated Organic-Cooled Reactors,* ORNL-3921 (January 1967).

Klueh, R. L., and D. H. Jansen, *Effects of Liquid and Vapor Cesium on Structural Materials,* ORNL-TM-1813 (June 1967).

Koch, C. C., and C. J. McHargue, "A Metallographic Study of the Allotropic Phase Transformations in Cerium," *Proc. Conf. Rare Earth Res., 6th, Gatlinburg, Tenn.,* 416–27 (1967).

Koch, C. C., and G. R. Love, "The Electrical Resistivity of Technetium from 8.0° to 1700°K," *J. Less-Common Metals* **12**(1), 29–35 (January 1967).

Koch, C. C., and M. L. Picklesimer, "A Metallographic Technique for Lanthanum and Cerium," *Trans. Met. Soc. AIME* **239**, 759–61 (May 1967).

Kollie, T. G., and R. S. Graves, "The Effect of Cold Working of $Pt_{90}Rh_{10}$/Pt Thermocouples," paper 13 in *High Temperature Thermometry, Papers Presented at a Seminar at AEC Headquarters, Washington, D.C., on February 24–26, 1965,* WASH-1067 (March 1966).

Kopp, O. C., and G. W. Clark, "Synthetic Pollucites in the System $Cs_2O{\cdot}Al_2O_3{\cdot}4SiO_2$-$Cs_2O{\cdot}Fe_2O_3{\cdot}4SiO_2$-$H_2O$ – Their Phase Relationship and Physical Properties: A Discussion," *Am. Mineralogist* **51**, 1243–45 (July 1966).

Koppenaal, T. J., and R. J. Arsenault, "Some Notes on the Strengthening Mechanism in Neutron Irradiated Copper Single Crystals," *Phys. Status Solidi* **17**(1), 27–33 (1966).

Krautwedel, H., S. Peterson, and R. W. McClung, translators and editors of *The Results of Ultrasonic Testing in the Practice of Machine and Boiler Construction Concerning the Material and Strength Properties of Components,* by Hans-Juergen Meyer [a German dissertation, approved by the Faculty for Mechanical Engineering at the Technische Hochschule Darmstadt, to obtain the degree of Doctor of Engineering Science (Dr.-Ing.), Darmstadt, 1965], ORNL-tr-1369 (May 1967).

Larsen-Badse, J., *Time-Dependent Hardness of Soft Metals,* ORNL-TM-1771 (April 1967).

Larson, L. T., and M. L. Picklesimer, "Determination of the Basal-Pole Orientation in Zirconium by Polarized-Light Microscopy," *Trans. Met. Soc. AIME* **236**, 1104–6 (August 1966).

Lawson, C. G., R. J. Kedl, and R. E. McDonald, "Enhanced Heat-Transfer Tubes for Horizontal Condensers with Possible Applications in Nuclear Power Plant Design," *Trans. Am. Nucl. Soc.* **9**(2), 565–66 (October–November 1966).

Leitnaker, J. M., and T. G. Godfrey, "Thermodynamic Properties of Uranium Carbides via the U-C-O System," *J. Chem. Eng. Data* **11**(2), 392–94 (April 1966).

Leitnaker, J. M., and T. G. Godfrey, "Thermodynamic Properties of Uranium Carbides," *J. Nucl. Mater.* **21**(2), 175–89 (February 1967).

Leitten, C. F., Jr., A. E. Richt, and R. J. Beaver, *Irradiation Behavior of Eu_2O_3-Stainless Steel Dispersions,* ORNL-4104 (June 1967).

Leonard, W. J., "Investigation of Material Failures in DCX-1 Liner," pp. 373–79 in *Proceedings of the 1966 Symposium on Engineering Problems of Controlled Thermonuclear Research,* CONF-661016 (1966).

Litman, A. P., "Interactions in the Niobium-Oxygen-Potassium System," pp. 61–62 in *AEC-NASA Liquid Metals Information Meeting held in Gatlinburg, Tennessee, April 21–23, 1965,* CONF-650411 (September 1966).

Long, E. L., Jr., "Three Metallographic Observations," paper 3 in *High Temperature Thermometry, Papers Presented at a Seminar at AEC Headquarters, Washington, D.C., on February 24–26, 1965,* WASH-1067 (March 1966).

Lotts, A. L., D. A. Douglas, Jr., and R. L. Pilloton, "Refabrication Technology and Costs for High-Temperature Gas-Cooled Reactor Fuels," pp. 167–97 in *Proceedings of the Conference "Fuel cycles of high temperature gas-cooled reactors," Brussels, June 10–11, 1965,* ed. by D. Tytgat, European Atomic Energy Community (Euratom), Brussels, May 1966. EUR 2780.e

Lotts, A. L., M. K. Preston, J. D. Sease, and J. E. Van Cleve, Jr., "Remotely Operated Equipment for Fabricating HFIR Target Elements," pp. 233–43 in *Proceedings of the 14th Conference on Remote Systems Technology, 1966,* American Nuclear Society, Hinsdale, Illinois, 1966.

Lotts, A. L., M. K. Preston, J. D. Sease, and J. E. Van Cleve, Jr., "Remotely Operated Equipment for Fabricating HFIR Target Elements," (summary) *Trans. Am. Nucl. Soc.* **9**(2), 627–28 (October–November 1966).

Love, G. R., "Near-Surface Effects in Superconducting Niobium-Zirconium Alloys," *J. Appl. Phys.* **37**(9), 3361–66 (August 1966).

Love, G. R., and M. L. Picklesimer, "Color Metallography in Black and White," *Trans. Met. Soc. AIME* **236**(10), 1505–7 (October 1966).

Lundy, T. S., and F. R. Winslow, "Atomic Transport Problems of Interest in Nuclear Systems," pp. 23–41 in *Thermodynamics, Vol. II,* International Atomic Energy Agency, Vienna, 1966.

Martin, W. R., and J. R. Weir, "Postirradiation Creep and Stress Rupture of Hastelloy N," *Nucl. Appl.* **3**(3), 167–77 (March 1967).

Martin, W. R., and G. M. Slaughter, *Irradiation Embrittlement of Welds and Brazes at Elevated Temperatures,* ORNL-TM-1526 (July 1966).

Martin, W. R., and G. M. Slaughter, "Irradiation Embrittlement of Welds and Brazes at Elevated Temperatures," *Welding J.(N.Y.)* **45**(9), 385-s–391-s (September 1966).

McClung, R. W., and K. V. Cook, "Development of Ultrasonic Inspection Techniques for Tapered Tubing," *Mater. Evaluation* **24**(10), 573–76 (October 1966).

McCoy, H. E., *Creep-Rupture Properties of the Tantalum-Base Alloy T-222,* ORNL-TM-1576 (September 1966).

McCoy, H. E., and J. R. Weir, *Evaluation of Hastelloy N Tubes for SNAP-8 Applications,* ORNL-TM-1763 (April 1967). CLASSIFIED

McCoy, H. E., Jr., and J. R. Weir, Jr., *Materials Development for Molten-Salt Breeder Reactors,* ORNL-TM-1854 (June 1967).

McCoy, H. E., Jr., "Influence of CO-CO_2 Environments on the Calibration of Chromel-P–Alumel Thermocouples," paper 11 in *High Temperature Thermometry, Papers Presented at a Seminar at AEC Headquarters, Washington, D.C., on February 24–26, 1965,* WASH-1067 (March 1966).

McCoy, H. E., *Creep-Rupture Properties of Tungsten and Tungsten-Base Alloys,* ORNL-3992 (August 1966).

McCoy, H. E., and D. O. Hobson, "The Influence of Neutron Irradiation on Twinning in a Niobium-Vanadium Alloy (40% V)," *Am. Soc. Metals Trans. Quart.* **59**(3), 568–70 (September 1966).

McCoy, H. E., "Carburization of Niobium- and Tantalum-Base Alloys," *J. Less-Common Metals* **12**(2), 139–45 (1967).

McCoy, H. E., "Creep-Rupture Properties Under Conditions of Constant and Varying Stresses," *Nucl. Appl.* **2**, 481–85 (December 1966).

McCoy, H. E., Jr., and J. R. Weir, Jr., "Influence of Irradiation on the Tensile Properties of the Aluminum Alloy 6061," *Nucl. Sci. Eng.* **25**, 319–27 (August 1966).

McElroy, D. L., "General Progress Report: Oak Ridge National Laboratory," pp. 1173–78 in *Proceedings of the Sixth Conference on Thermal Conductivity* (October 19–21, 1966, Dayton, Ohio), Materials Applications Division, Air Force Materials Laboratory, Wright-Patterson Air Force Base, Ohio.

McElroy, D. L., and W. Fulkerson, "Introductory Paper: A Brief Examination of the State of the Art of the Thermal Conductivity Conference Studies on Metals and Alloys – 1966," pp. 797–805 in *Proceedings of the Sixth Conference on Thermal Conductivity* (October 19–21, 1966, Dayton, Ohio), Materials Applications Division, Air Force Materials Laboratory, Wright-Patterson Air Force Base, Ohio.

McElroy, D. L., "Thermocouple Drift Test to 800°C at 10^{-7} torr on Chromel-P vs Constantan," paper V-E-1 in *Proceedings of the Fifth Temperature Measurements Society Conference at Hawthorne, California, March 14 and 15, 1967.*

Melton, C. E., and H. W. Joy, "Mass-Spectrometric and Theoretical Evidence for NH_4 and H_3O," *J. Chem. Phys.* **46**(11), 4275–83 (June 1967).

Moore, J. P., D. L. McElroy, and M. Barisoni, "Thermal Conductivity Measurements Between 78 and 340°K on Aluminum, Iron, Platinum, and Tungsten," pp. 737–78 in *Proceedings of the Sixth Conference on Thermal Conductivity* (October 19–21, 1966, Dayton, Ohio), Materials Applications Division, Air Force Materials Laboratory, Wright-Patterson Air Force Base, Ohio.

Moore, J. P., and D. L. McElroy, "Contamination of Platinum-Rhodium Transducers," paper 12 in *High Temperature Thermometry, Papers Presented at a Seminar at AEC Headquarters, Washington, D.C., on February 24–26, 1965,* WASH-1067 (March 1966).

Moore, J. P., T. G. Kollie, R. S. Graves, and D. L. McElroy, *Thermal Conductivity Measurements on Solids Between 20 and 150°C Using a Comparative-Longitudinal Apparatus: Results on MgO, BeO, ThO_2, $Th_xU_{1-x}O_{2+y}$ and Al-UO_2 Cermets,* ORNL-4121 (June 1967).

Morgan, C. S., and D. H. Bowen, *Inert Gas Bubbles in Neutron Irradiated Magnesium Oxide,* AERE-R 5223 (June 1966).

Morgan, M. T., E. L. Long, Jr., and D. M. Hewette II, "Fuel Migration into Coatings of Pyrolytic-Carbon-Coated UO_2 and UC_2 Particles as a Result of Irradiation and Heat Treatment," *Trans. Am. Nucl. Soc.* **10**(1), 97–98 (June 1967).

Morgan, C. S., Jr., and L. L. Hall, "Effect of Isostatic Pressing on Sintering," (abstract) *P/M Newsletter* **1**(2), 5 (June 1967).

Murdock, J. F., "A Constant Power Annealing Furnace," paper 14 in *High Temperature Thermometry, Papers Presented at a Seminar at AEC Headquarters, Washington, D.C., on February 24–26, 1965,* WASH-1067 (March 1966).

Murdock, J. F., *Compatibility of Uranium Nitride with Various Refractory Metals and Alloys,* ORNL-TM-1814 (June 1967). CLASSIFIED

Olsen, A. R., D. A. Douglas, Y. Hirose, J. L. Scott, and J. W. Ullmann, "Properties and Prospects of Thoria-based Nuclear Fuels," *Proc. Brit. Ceram. Soc.* **7**, 289–310 (February 1967).

Olsen, A. R., J. H. Coobs, D. M. Hewette II, H. L. Krautwedel, A. W. Longest, E. L. Long, Jr., J. W. Prados, and J. L. Scott, "Performance of Pyrolytic-Carbon-Coated Sol-Gel UO_2 Microspheres in High-Burnup Irradiation Tests," *Trans. Am. Nucl. Soc.* **10**(1), 96–97 (June 1967).

Olsen, A. R., J. H. Coobs, and J. W. Ullmann, *Current Status of Irradiation Testing of Thorium Fuels at Oak Ridge National Laboratory,* ORNL-TM-1631 (September 1966).

Olsen, A. R., and J. W. Prados, *Estimation of Resonance Effects in Fuel Burnup Analysis,* ORNL-TM-1760 (March 1967).

Patterson, F. H., W. C. Robinson, Jr., and C. F. Leitten, Jr., *Conversion of Uranium Chlorides to Urania by Gas-Phase Reduction Hydrolysis,* ORNL-TM-1701 (April 1967).

Pawel, R. E., and J. J. Campbell, "Stress Measurements During the Oxidation of Tantalum and Niobium," *Acta Met.* **14**(12), 1827–33 (December 1966).

Pawel, R. E., and J. J. Campbell, "The Effect of Anodic Films on the Gaseous Oxidation of Tantalum," *J. Electrochem. Soc.* **113**(11), 1204–9 (November 1966).

Peterson, S., "Ignition and Combustion of Reactor Fuels, Coolants, and Structural Materials," *Nucl. Safety* **8**(1), 25–30 (Fall 1966).

Picklesimer, M. L., "Deformation, Creep, and Fracture in Alpha-Zirconium Alloys," *Electrochem. Technol.* **4**(7-8), 289–300 (July–August 1966).

Picklesimer, M. L., and G. Hallerman, *The Influence of the Preparation of Metal Specimens on the Precision of Electron Probe Microanalysis,* ORNL-TM-1591 (October 1966).

Pilloton, R. L., *Calculated Densities of Coated Nuclear Fuel Particles,* ORNL-TM-1513 (July 1966).

Poteat, L. E., and C. S. Yust, "Creep of Polycrystalline Thorium Dioxide," *J. Am. Ceram. Soc.* **49**(8), 410–14 (August 1966).

Prados, J. W., and J. L. Scott, "Mathematical Model for Predicting Coated-Particle Behavior," *Nucl. Appl.* **2**(5), 402–14 (October 1966).

Prados, J. W., and J. L. Scott, *The Influence of Pyrolytic-Carbon Creep on Coated-Particle Fuel Performance,* ORNL-TM-1787 (April 1967).

Prados, J. W., "Calculation of Creep in Spherical Pyrolytic-Carbon Shells Under Combined Radiation Damage and Internal Pressure," (summary) *Trans. Am. Nucl. Soc.* **9**(2), 382–83 (October–November 1966).

Reagan, P. E., R. L. Beatty, and E. L. Long, Jr., "Performance of Pyrolytic Carbon-Coated Uranium Oxide Particles During Irradiation at High Temperature," *Nucl. Sci. Eng.* **28**(1), 34–41 (April 1967).

Rittenhouse, P. L., and M. L. Picklesimer, "Research on the Mechanical Anisotropy of Zircaloy-2," *Electrochem. Technol.* **4**(7-8), 322–29 (July–August 1966).

Rittenhouse, P. L., *Characterization of the Three-Dimensional Anisotropy of Yielding and Flow in Zircaloy-2 from a Single Uniaxial Test,* ORNL-TM-1553 (August 1966).

Robinson, W. C., Jr., and W. R. Martin, *A Feasibility Study – Formation of Uranium Nitride Compounds Using Chemical Vapor Deposition Techniques,* ORNL-TM-1812 (May 1967).

Robinson, R. A., R. J. Beaver, D. W. Burton, T. C. Chapman, C. W. Craven, Jr., S. T. Ewing, A. J. Miller, J. P. Nichols, and R. L. Stephenson, *Brayton Cycle Radioisotope Heat Source Design Study Phase I (Conceptual Design),* ORNL-TM-1691 (June 1967). CLASSIFIED

Schaffhauser, A. C., "Low-Temperature Ductility and Strength of Thermochemically Deposited Tungsten and Effects of Heat Treatment," pp. 261–76 in *Summary of the Eleventh Refractory Composites Working Group Meeting,* Tech. Rept. AFML-TR-66-179 (July 1966).

Schaffhauser, A. C., and R. L. Heestand, "Effect of Fluorine Impurities on the Grain Stability of Thermochemically Deposited Tungsten," pp. 204–11 in *1966 IEEE Conference Record of the Thermionic Conversion Specialist Conference, Nov. 3 and 4, 1966, Houston, Texas,* Electrical and Electronics Engineers, New York, 1966.

Schaffhauser, A. C., and K. Farrell, "Gas Bubbles in Thermochemically Deposited Tungsten," *J. Nucl. Mater.* **22**(1), 106–8 (April 1967).

Scott, J. L., and R. L. Beatty, "Pyrolytic-Carbon Coatings Formed at High Deposition Rates," *Trans. Am. Nucl. Soc.* **10**(1), 96 (June 1967).

Sease, J. D., *The Fabrication of Target Elements for the High-Flux Isotope Reactor,* ORNL-TM-1712 (March 1967).

Sease, J. D., R. B. Pratt, F. C. Davis, and A. L. Lotts, "Design of a Remote System for Fabrication of (Th-^{233}U)O_2 Metal-Clad Fuel Elements," (summary) *Trans. Am. Nucl. Soc.* **9**(2), 613 (October–November 1966).

Sease, J. D., R. B. Pratt, F. C. Davis, and A. L. Lotts, "Design of a Remote System for Fabrication of (Th-^{233}U)O_2 Metal-Clad Fuel Elements," pp. 47–54 in *Proceedings of the 14th Conference on Remote System Technology, 1966,* American Nuclear Society, Hinsdale, Illinois, 1966.

Sekula, S. T., R. H. Kernohan, and G. R. Love, "Superconducting Properties of Technetium," *Phys. Rev.* **155**(2), 364–69 (March 1967).

Sessions, C. E., "Metal Reactions with Al_2O_3," paper 10 in *High Temperature Thermometry, Papers Presented at a Seminar at AEC Headquarters, Washington, D.C., on February 24–26, 1965,* WASH-1067 (March 1966).

Sessions, C. E., "Corrosion of Advanced Refractory Alloys in Lithium," pp. 143–48 in *AEC-NASA Liquid Metals Information Meeting held in Gatlinburg, Tennessee, April 21–23, 1965,* CONF-65041 (September 1966).

Siltanen, J. N., F. R. McQuilkin, E. L. Long, Jr., and J. R. Lindgren, "Irradiation Testing of Candidate Fuel Rods for the GCFR," (summary) *Trans. Am. Nucl. Soc.* **10**(1), 104–5 (June 1967).

Slaughter, G. M., E. A. Franco-Ferreira, E. C. Kirstowsky, K. K. Klindt, E. L. Long, Jr., and G. M. Tolson, *Fabrication of Rebuilt Bonus Reactor Superheater Fuel Assembly,* ORNL-4072 (June 1967).

Smith, C. O., and J. M. Robbins, "Impact Resistance of Fuelled Graphite Spheres for Pebble-Bed Reactor Applications," pp. 594–607 in *Second Industrial Carbon and Graphite Conference, Proceedings, April 7–9, 1965,* Society of Chemical Industry, London, 1966.

Smith, G. P., C. R. Boston, and J. Brynestad, "Electronic Spectra and Coordination Geometry in Molten Mixtures of CsCl and $NiCl_2$ Containing up to 60 Mole % $NiCl_2$," *J. Chem. Phys.* **45**(3), 829–34 (August 1966).

Snyders, L. S., *The Photoelastic Observation of Ultrasonic Waves in a Transparent Plate,* ORNL-TM-1671 (January 1967). MS Thesis, the University of Tennessee.

Sparks, C. J., and B. Borie, "Methods of Analysis for Diffuse X-Ray Scattering Modulated by Local Order and Atomic Displacements," chap. 1, pp. 5–50 in *Local Atomic Arrangements Studied by X-Ray Diffraction* (proceedings of a symposium sponsored by the Physics and Chemistry of Metals Committee of the Institute of Metals Division, the Metallurgical Society, American Institute of Mining, Metallurgical, and Petroleum Engineers, Chicago, Illinois, February, 1965) ed. by J. B. Cohen and J. E. Hilliard, Gordon and Breach, Science Publishers, New York, 1966.

Stephenson, R. L., *Creep-Rupture Properties of FS-85 Alloy and Their Response to Heat Treatment,* ORNL-TM-1456 (July 1966).

Stephenson, R. L., *Creep-Rupture Properties of Cb-752 Alloys and Their Response to Heat Treatment,* ORNL-TM-1577 (August 1966).

Stephenson, R. L., *Effect of Heat Treatment on the Creep-Rupture Properties of D-43 Alloy,* ORNL-TM-1587 (September 1966).

Stephenson, R. L., *An Approximate Method for Determining Allowable Stress Rates for Capsules Containing Helium-Producing Isotopes,* ORNL-TM-1436, Rev. (November 1966).

Stephenson, R. L., and R. G. Donnelly, *Effect of Aging on the Creep-Rupture Properties of D-43 Welds,* ORNL-TM-1708 (January 1967).

Stiegler, J. O., and R. J. Gray, "Microstructural Discrimination by Deposition of Surface Films," pp. 11–17 in *Advances in Metallography,* ed. by R. J. Jackson and A. E. Calabra, Technical Papers of the Twentieth Metallographic Conference, The Dow Chemical Company, RFP-658 (October 1966).

Stiegler, J. O., and C. K. H. DuBose, "Stress Dependence of Dislocation Configuration in Deformed Niobium," *Acta Met.* **15**(5), 953–55 (May 1967).

Tackett, J. W., J. R. Barker, and G. M. Slaughter, "Assembly and Welding of Fuel Elements for the High-Flux Isotope Reactor," (summary) *Trans. Am. Nucl. Soc.* **10**(1), 125 (June 1967).

Unger, W. E., F. E. Harrington, J. R. May, S. F. Scott, and T. N. Washburn, *On-Site Fuel Processing and Recycle Plant – Design Study,* ORNL-3959 (April 1967).

Vandermeer, R. A., "A Transient Effect in Grain-Boundary Migration During Recrystallization in Aluminum," *Acta Met.* **15**(3), 447–58 (March 1967).

Venard, J. T., *Compatibility of Dispersion Strengthened Aluminum with Uranium Monocarbide – A Review of the Literature,* ORNL-TM-1705 (January 1967).

Weir, J. R., Jr., "Radiation Damage at High Temperatures," *Science* **156**(3783), 1689–95 (June 30, 1967).

Weir, J. R., and R. T. King, "The Effect of Cyclotron-Injected Helium on the Mechanical Properties of Stainless Steel," (summary) *Trans. Am. Nucl. Soc.* **10**(1), 130–31 (June 1967).

Weir, J. R., and E. E. Bloom, "The Nature of Radiation Damage in Materials," *Trans. Am. Nucl. Soc.* **10**(1), 161 (June 1967).

Werner, W. J., and J. R. Barkman, *Characterization and Production of U_3O_8 for the High Flux Isotope Reactor,* ORNL-4052 (April 1967).

Williams, R. O., *Methods of Reduction of Texture Data to Inverse Pole Figures,* ORNL-3979 (August 1966).

Williams, R. O., "Determination of the Stored Energy of Deformation of Metals and Alloys," pp. 251–78 in *Experimental Methods of Materials Research,* ed. by H. Herman, Interscience Publishers, New York, May 1967.

Wolfenden, A., "Nomenclature of Metallic Elements," *Nature* **211**(5049), 632 (Aug. 6, 1966).

Wolfenden, A., "The Energy Stored in Copper Single Crystals," *Acta Met.* **15**(6), 971–78 (June 1967).

Woods, J. W., "In-Reactor Mechanical Properties Experiments," paper 1.6 in *International Symposium on Developments in Irradiation Capsule Technology, Held at Pleasanton, California, May 3–5, 1966,* CONF-660511 (March 1967).

Wymer, R. G., and D. A. Douglas, Jr., *Status and Progress Report for Thorium Fuel Cycle Development for Period Ending December 31, 1965,* ORNL-4001 (October 1966).

Wymer, R. G., and J. H. Coobs, "Preparation, Coating, Evaluation, and Irradiation Testing of Sol-Gel Oxide Microspheres," *Proc. Brit. Ceram. Soc.* **7**, 61–79 (February 1967).

Yust, C. S., and L. L. Hall, "The $Pt_{60}Rh_{40}/Pt_{80}Rh_{20}$ Thermocouple," paper 15 in *High Temperature Thermometry, Papers Presented at a Seminar at AEC Headquarters, Washington, D.C., on February 24–26, 1965,* WASH-1067 (March 1966).

Yust, C. S., and C. S. Morgan, "Formation of Dislocation Clusters During Sintering of Calcium Fluoride," *Trans. Met. Soc. AIME* **236**(10), 1504–5 (October 1966).

The following quarterly progress reports have been issued during this reporting period:

Patriarca, P., *Fuels and Materials Development Program Quart. Progr. Rept. June 30, 1966,* ORNL-TM-1570; *Sept. 30, 1966,* ORNL-TM-1700; *Dec. 31, 1966,* ORNL-TM-1720; *March 31, 1967,* ORNL-TM-1825 (Official Use Only).

Harms, W. O., *High-Temperature Materials Program Quart. Progr. Rept. Jan. 31, 1966,* ORNL-TM-1455, Pt. 2 (Classified); *April 30, 1966,* ORNL-TM-1520, Pt. 1 (Official Use Only) and Pt. 2 (Classified).

METALS AND CERAMICS DIVISION

NOVEMBER 1, 1967

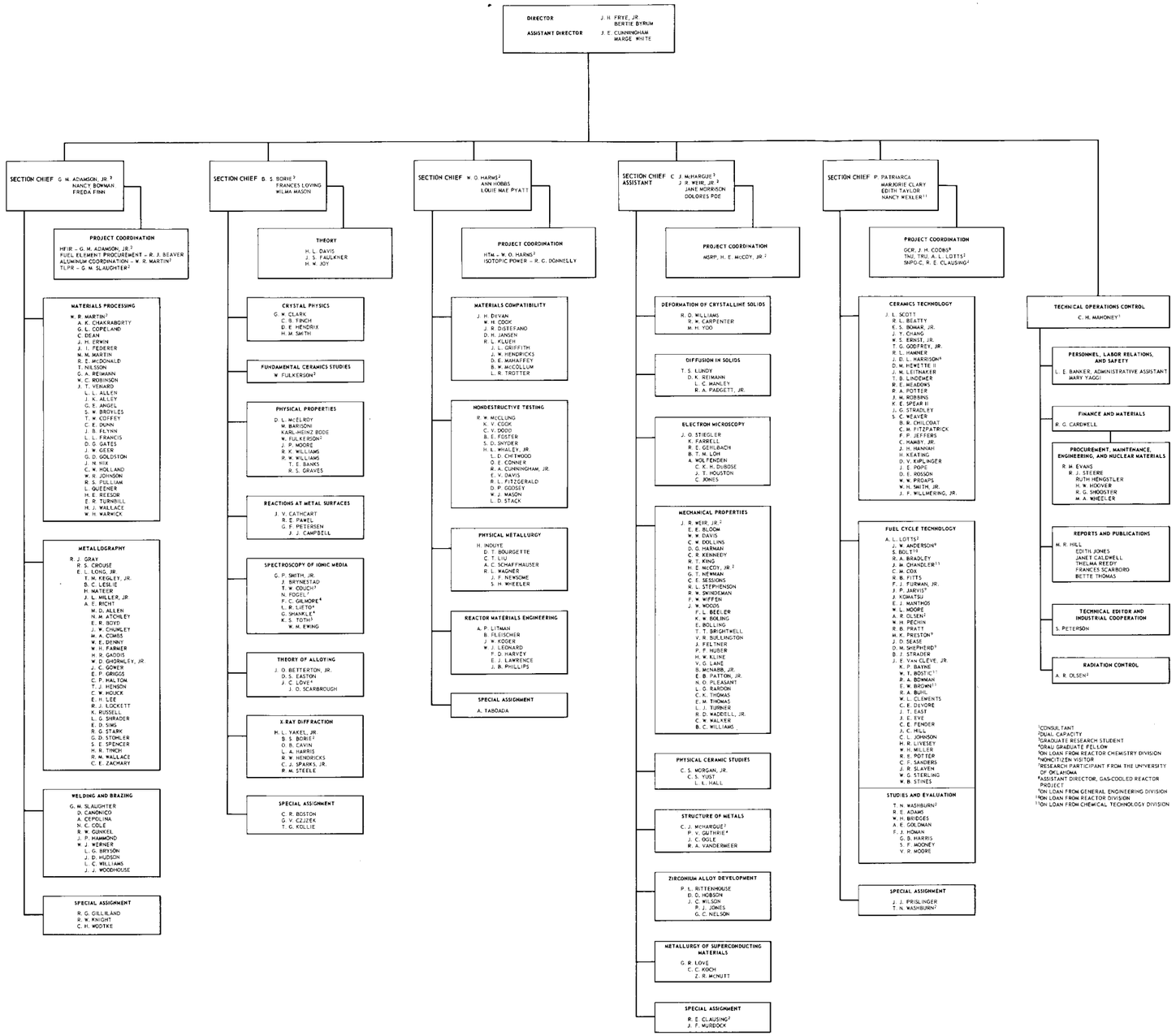

[1]CONSULTANT
[2]DUAL CAPACITY
[3]GRADUATE RESEARCH STUDENT
[4]ORAU GRADUATE FELLOW
[5]ON LOAN FROM REACTOR CHEMISTRY DIVISION
[6]NONCITIZEN VISITOR
[7]RESEARCH PARTICIPANT FROM THE UNIVERSITY OF OKLAHOMA
[8]ASSISTANT DIRECTOR, GAS-COOLED REACTOR PROJECT
[9]ON LOAN FROM GENERAL ENGINEERING DIVISION
[10]ON LOAN FROM REACTOR DIVISION
[11]ON LOAN FROM CHEMICAL TECHNOLOGY DIVISION

INTERNAL DISTRIBUTION

1–3. Central Research Library
4–5. ORNL – Y-12 Technical Library, Document Reference Section
6–30. Laboratory Records Department
31. Laboratory Records, ORNL R.C.
32. ORNL Patent Office
33. Laboratory Shift Supervisor
34. G. M. Adamson, Jr.
35. L. G. Alexander
36. R. J. Beaver
37. J. O. Betterton, Jr.
38. D. S. Billington
39. A. L. Boch
40. E. G. Bohlmann
41. E. S. Bomar
42. B. S. Borie
43. G. E. Boyd
44. E. J. Breeding
45. R. B. Briggs
46. J. V. Cathcart
47. J. M. Chandler
48. G. W. Clark
49. J. H. Coobs
50. J. A. Cox
51. F. L. Culler
52. J. E. Cunningham
53. G. V. Czjzek
54. J. H. DeVan
55. J. H. Erwin
56. J. S. Faulkner
57. D. E. Ferguson
58. G. W. Flack
59. A. P. Fraas
60. J. H Frye, Jr.
61. J. H. Gillette
62. A. E. Goldman
63. R. J. Gray
64. J. L. Gregg
65. W. R. Grimes
66. J. P. Hammond
67. W. O. Harms
68. C. S. Harrill
69–74. M. R. Hill
75. N. E. Hinkle
76. A. S. Householder
77. A. P. Huber (K-25)
78. H. Inouye
79. R. G. Jordan (K-25)
80. M. A. Kastenbaum
81. M. T. Kelley
82. E. M. King
83. R. B. Korsmeyer
84. J. A. Lane
85. C. E. Larson
86. A. P. Litman
87. R. S. Livingston
88. A. L. Lotts
89. T. S. Lundy
90. H. G. MacPherson
91. W. R. Martin
92. R. W. McClung
93. H. C. McCurdy
94. D. L. McElroy
95. C. J. McHargue
96. A. J. Miller
97. E. C. Miller
98. C. S. Morgan
99. K. Z. Morgan
100. M. L. Nelson
101. S. M. Ohr
102. A. R. Olsen
103–104. R. B. Parker
105. P. Patriarca
106. S. Peterson
107. J. W. Prados
108. P. L. Rittenhouse
109. A. W. Savolainen
110. O. Sisman
111. J. L. Scott
112. H. E. Seagren
113. J. D. Sease
114. G. M. Slaughter
115. G. P. Smith, Jr.
116. J. T. Stanley
117. P. E. Stein (K-25)
118. J. O. Stiegler
119. D. A. Sundberg
120. E. H. Taylor
121. D. B. Trauger
122. J. E. Van Cleve

123. T. N. Washburn
124. M. S. Wechsler
125. A. M. Weinberg
126. J. R. Weir, Jr.
127. G. D. Whitman
128. G. C. Williams
129. R. O. Williams
130. J. C. Wilson
131. H. L. Yakel
132. M. B. Bever (consultant)
133. A. R. Kaufmann (consultant)
134. J. A. Krumhansl (consultant)
135. L. S. Darken (consultant)

EXTERNAL DISTRIBUTION

136. C. M. Adams, Jr., MIT
137. I. Berman, USAMRA, Watertown
138. Leo Brewer, University of California
139. R. B. Burlin, AEC, Washington
140. E. D. Calvert, U.S. Bureau of Mines, P.O. Box 492, Albany, Oregon
141. G. Champier, E.N.S.M.I.M. Laboratoire de Physique, Parc de Saurupt, Nancy (M.-&-M.), France
142. D. F. Cope, RDT, SSR, AEC, Oak Ridge National Laboratory
143. J. F. Elliott, MIT
144. N. Engel, Georgia Institute of Technology
145. H. B. Finger, AEC, Washington
146. J. D. Fleming, Georgia Institute of Technology
147. V. D. Frechette, Alfred University
148. Angelo Giambusso, AEC, Washington
149. R. G. Gilliland, MIT
150. W. W. Grigorieff, Assistant to the Executive Director, Oak Ridge Associated Universities
151. R. F. Hehemann, Case Institute of Technology
152. E. E. Hoffman, GE, Cincinnati
153. O. C. Kopp, University of Tennessee
154. J. Korringa, Ohio State University
155. W. J. Larkin, AEC, Oak Ridge Operations
156. C. F. Leitten, Jr. Linde Division, Union Carbide Corporation
157. J. J. Lombardo, NASA, Lewis Research Center
158. W. D. Manly, Union Carbide Corporation, New York
159. P. W. McDaniel, AEC, Washington
160. A. J. Mortlock, Australian National University, P.O. Box 4, Canberra, A.C.T., Australia
161. Peter Murray, AERE, Harwell
162. R. R. Nash, NASA, Washington
163. E. F. Nippes, Rensselaer Polytechnic Institute
164. H. M. Otte, Martin Company, Mail Point No. 105, Orlando, Florida
165. R. E. Pahler, AEC, Washington
166. R. M. Parke, MAB, National Academy of Science, Washington
167. J. Pheline, Centre d'Etudes Nucleaires de Saclay
168. J. M. Prosser, AEC, Washington
169. H. B. Rahner, Savannah River Operations
170. R. E. Reed-Hill, University of Florida

171. F. N. Rhines, University of Florida
172. W. L. Rice, Technical Assistant, AGMR, AEC, Washington, D.C.
173. R. W. Schroeder, NASA, Lewis Research Center
174. F. C. Schwenk, AEC, Washington
175. A. A. Shoudy, Atomic Power Development Associate, Inc.
176. J. Simmons, AEC, Washington
177. E. E. Sinclair, AEC, Washington
178. L. M. Slifkin, University of North Carolina
179. E. E. Stansbury, University of Tennessee
180. D. K. Stevens, AEC, Washington
181. Dorothy Smith, AEC, Washington
182. J. A. Swartout, Union Carbide Corporation, New York
183. A. Van Echo, AEC, Washington
184. Watt Webb, Union Carbide Metals
185. J. Weertman, Northwestern University
186. G. W. Wench, AEC, Washington
187. M. J. Whitman, AEC, Washington
188. C.H.T. Wilkins, University of Alabama
189. Laboratory and University Division, AEC, Oak Ridge Operations
190–452. Given distribution as shown in TID-4500 under Metals, Ceramics, and Materials category (25 copies – CFSTI)